Springer Transactions in Civil
and Environmental Engineering

Srinivasan Gopalakrishnan
Yapa Rajapakse *Editors*

Blast Mitigation Strategies in Marine Composite and Sandwich Structures

Springer

Springer Transactions in Civil and Environmental Engineering

More information about this series at http://www.springer.com/series/13593

Srinivasan Gopalakrishnan
Yapa Rajapakse
Editors

Blast Mitigation Strategies in Marine Composite and Sandwich Structures

Springer

Editors
Srinivasan Gopalakrishnan
Department of Aerospace Engineering
Indian Institute of Science
Bangalore, Karnataka
India

Yapa Rajapakse
Programme Manager, Solid Mechanics Program
Office of Naval Research
Arlington, VA
USA

ISSN 2363-7633 ISSN 2363-7641 (electronic)
Springer Transactions in Civil and Environmental Engineering
ISBN 978-981-10-7169-0 ISBN 978-981-10-7170-6 (eBook)
https://doi.org/10.1007/978-981-10-7170-6

Library of Congress Control Number: 2017957190

Printed on acid-free paper

This Springer imprint is published by Springer Nature
The registered company is Springer Nature Singapore Pte Ltd.
The registered company address is: 152 Beach Road, #21-01/04 Gateway East, Singapore 189721, Singapore

Preface

Blast mitigation is essentially a strategic system designed to reduce the aftereffects of a blast event. During a blast event, a tremendous amount of energy is released into the atmosphere (or fluid medium) in the form of high-intensity pressure pulses or shock waves as well as high-velocity fragments/projectiles. These can result in severe damage and destruction to human life as well as to infrastructure, and can result in collapse of buildings and other structures. Although the effects of blast cannot be completely eliminated, its effects can be reduced to a certain degree using innovative methodologies. The main focus of this book is to address certain novel methodologies to reduce the adverse effects of blast.

There are certain classes of structures that are susceptible to such harsh loading conditions. For example, naval ship structures are designed to resist high-intensity dynamic loads. In order for these structures to be lightweight and efficient in energy absorption, and to ensure reduced life-cycle costs, they are expected to be made of composite materials and sandwich construction. Understanding the mechanics of a blast event and its effects on these composite and sandwich structures is still an open area for research. Understanding many phenomena, such as damage progression resulting from a blast event, modeling aspects of a blast phenomenon, blast response estimations, underwater explosions, and constitutive material modeling under high strain rates, is essential to devise efficient mitigation strategies. Many of these topics are addressed in this book.

Realizing the importance of the subject "composite marine structures," the Office of Naval Research (ONR), USA through its Solid Mechanics program, has supported research with the focus on blast effects and blast mitigation in composite structures, over the last two decades. Some of the world's leading researchers in the field are participating in this program. Many of the chapters presented in this book are based on their ONR-supported research.

This book has a total of 23 chapters covering various aspects of blast mitigation in marine composites and sandwich structures including modeling of blast phenomena, fluid–structure interactions, structural and material damage initiation and progression, underwater explosions, novel computational methods based on higher-order sandwich theories, and innovative blast mitigation strategies.

This book is targeted for practicing engineers, academic faculty, and higher-level graduate students. The nature of the timely topics covered in this area of blast mitigation is what makes this book unique. We would like to thank all the primary contributors and their coworkers who spent considerable time in preparing these chapters and helped to finalize this unique book. We would also like to thank the ONR for their help in bringing together some of the world's leading researchers in this area to contribute to this book.

Bangalore, India — Srinivasan Gopalakrishnan
Arlington, USA — Yapa Rajapakse
September 2017

Contents

Editors and Contributors

About the Editors

Prof. Srinivasan Gopalakrishnan received his master's degree in Engineering Mechanics from the Indian Institute of Technology Madras and Ph.D. from the Purdue University School of Aeronautics and Astronautics. Subsequently, he was a postdoctoral fellow at the Department of Mechanical Engineering at Georgia Institute of Technology. He is currently the Chairperson of the Department of Aerospace Engineering at Indian Institute of Science. His main areas of interest are wave propagation in complex media, computational mechanics, smart structures, structural health monitoring, MEMS, and nanocomposite structures. He has extensively published his works including 182 international journal papers, six graduate-level textbooks, and two undergraduate books. He is on the editorial board of nine international journals and is the Associate Editor of Smart Materials and Structures and Structural Health Monitoring. He has received numerous awards and honors including Structural Health Monitoring Person of the Year Award 2016, Distinguished Alumnus Award, Indian Institute of Technology, Technology Madras, Chennai, Satish Dhawan Young Scientist Award by Government of Karnataka, Alumni Award for excellence in research at IISc and had been a Fellow of Indian National Academy of Engineering, a Fellow of Indian Academy of Sciences, an Associate Fellow-AIAA, and a Fellow of the Royal Academy of Engineering, and received UK Distinguished Visiting Fellowship. He is one of the most highly cited aerospace researchers in the world. He was the head of the Aerospace Project Assessment and Review Committee of the National Programme of Micro and Smart Systems (NPMASS), DRDO, Government of India, and a member of the Structures panel of the Aeronautical Research & Development Board, Government of India. He is currently the President of Institute for Smart Structures and Systems. He has attracted research funding from top aerospace companies including Boeing Aircraft Company; Pratt & Whitney Corporation, USA; the U.S. Office of Naval Research (ONR), USA; Air Force Office for Advanced Research, Tokyo; and the Aeronautical Research and Development Board.

Dr. Yapa Rajapakse is the Program Manager of the Solid Mechanics program at the Office of Naval Research (ONR). The current focus of this research program is the thermomechanical behavior of composite materials and composite sandwich structures in severe marine environments (in the presence of high levels of humidity, seawater, hydrostatic pressure, dynamic loading, and temperature extremes). He completed his graduate studies at Stanford University, and received M. S. in Mathematics and Ph.D. in Applied Mechanics. His doctoral dissertation in the area of fracture mechanics was supervised by the late Prof. J.N. Goodier.

He has been elected as a fellow of four technical societies: the American Society of Mechanical Engineers (ASME), the American Academy of Mechanics (AAM), the Society of Engineering

Science (SES), and the American Society for Composites (ASC). He has served as president, vice-president, and member of the board of directors of the SES. He was also Chairman of the Composites Committee, Applied Mechanics Division of ASME, and the Polymer Matrix Composites Division of ASC. He has served on the editorial boards of several journals including Composite Science and Technology, the Journal of Sandwich Structures and Materials, the Journal of Composite Materials, the Journal of Reinforced Plastics & Composites, Composites Part B, Engineering Fracture Mechanics, and the International Journal of Plasticity.

He has delivered numerous presentations at national/international conferences. He is the editor/coeditor of 32 books including the recently published "Dynamic Failure of Materials and Structures", "Dynamic Failure of Composite and Sandwich Structures", "Blast Mitigation: Experimental and Numerical Studies", and "Durability of Composites in a Marine Environment".

Contributors

Serge Abrate Mechanical Engineering and Energy Processes, Southern Illinois University, Carbondale, IL, USA

Deepak Alapur Department of Aerospace Engineering, Indian Institute of Science, Bangalore, India

Moshabab Alkhtany The University of Akron, Akron, OH, USA

Luca Ansuini Composite Materials and Mechanics Laboratory, Mechanical and Aerospace Engineering Department, New York University, Tandon School of Engineering, Brooklyn, NY, USA

Hari Arora Department of Mechanical Engineering, Imperial College London, South Kensington Campus, London, UK

Siddharth Avachat The George W. Woodruff School of Mechanical Engineering, Atlanta, USA; School of Materials Science and Engineering, Georgia Institute of Technology, Atlanta, GA, USA

M. V. Barnhart Department of Mechanical and Aerospace Engineering, University of Missouri, Columbia, MO, USA

Romesh C. Batra Department of Biomedical Engineering and Mechanics, Virginia Polytechnic Institute and State University, Blacksburg, VA, USA

H. Chen Department of Mechanical and Aerospace Engineering, University of Missouri, Columbia, MO, USA

Y. Y. Chen Department of Mechanical and Aerospace Engineering, University of Missouri, Columbia, MO, USA

John P. Dear Department of Mechanical Engineering, Imperial College London, South Kensington Campus, London, UK

V. Eliasson Department of Structural Engineering, University of California, San Diego, La Jolla, CA, USA

Nikhil Gupta Composite Materials and Mechanics Laboratory, Mechanical and Aerospace Engineering Department, New York University, Tandon School of Engineering, Brooklyn, NY, USA

Sathya Hanagud School of Aerospace Engineering, Georgia Institute of Technology, Atlanta, GA, USA

Brian Hayman Technical University of Denmark, Kongens Lyngby, Denmark

S. R. Hiremath Department of Aerospace Engineering, Indian Institute of Science, Bangalore, India

W. D. Hodo US Army ERDC-GSL, Vicksburg, MS, USA

Michelle S. Hoo Fatt The University of Akron, Akron, OH, USA

Paul A. Hooper Department of Mechanical Engineering, Imperial College London, South Kensington Campus, London, UK

Zhen Hu Vanderbilt University, Nashville, TN, USA

G. L. Huang Department of Mechanical and Aerospace Engineering, University of Missouri, Columbia, MO, USA

G. Jagadeesh Department of Aerospace Engineering, Indian Institute of Science, Bangalore, India

H. Jeon Department of Aerospace and Mechanical Engineering, University of Southern California, Los Angeles, CA, USA

George A. Kardomateas School of Aerospace Engineering, Georgia Institute of Technology, Atlanta, GA, USA

Mark Kelly Department of Mechanical Engineering, Imperial College London, South Kensington Campus, London, UK

K. Kontis Aerospace Sciences Division, University of Glasgow, Glasgow, UK

James LeBlanc Naval Undersea Warfare Center (Division Newport), Newport, RI, USA

Dung D. Luong Composite Materials and Mechanics Laboratory, Mechanical and Aerospace Engineering Department, New York University, Tandon School of Engineering, Brooklyn, NY, USA

Sankaran Mahadevan Vanderbilt University, Nashville, TN, USA

Pavitra Manghaiapathy School of Aerospace Engineering, Georgia Institute of Technology, Atlanta, GA, USA

Roberta Massabò Department of Civil, Chemical and Environmental Engineering, University of Genova, Genoa, Italy

Helio Matos Dynamic Photomechanics Laboratory, Department of Mechanical, Industrial and Systems Engineering, University of Rhode Island, Kingston, RI, USA

Nilanjan Mitra Department of Civil Engineering & Center for Theoretical Studies, Indian Institute of Technology Kharagpur, Kharagpur, West Bengal, India

A. Mohamed Department of Nanoengineering, Joint School of Nanoscience and Nanoengineering, North Carolina A&T State University, Greensboro, NC, USA

R. Mohan Department of Nanoengineering, Joint School of Nanoscience and Nanoengineering, North Carolina A&T State University, Greensboro, NC, USA

M. D. Nelms University of Mississippi, Oxford, MS, USA

I. Obed Samuelraj Department of Aerospace Engineering, Indian Institute of Science, Bangalore, India

Michael Pinto Dynamic Photomechanics Laboratory, Department of Mechanical, Industrial and Systems Engineering, University of Rhode Island, Kingston, RI, USA

Pavana Prabhakar University of Wisconsin-Madison, Madison, WI, USA

Tao Qu The George W. Woodruff School of Mechanical Engineering, Atlanta, USA; School of Materials Science and Engineering, Georgia Institute of Technology, Atlanta, GA, USA

B. Raja Sekhar Department of Aerospace Engineering, Indian Institute of Science, Bangalore, India

A. M. Rajendran University of Mississippi, Oxford, MS, USA

J. Rivas Murillo Department of Nanoengineering, Joint School of Nanoscience and Nanoengineering, North Carolina A&T State University, Greensboro, NC, USA

Nunthadech Rodcheuy School of Aerospace Engineering, Georgia Institute of Technology, Atlanta, GA, USA

Emily Rolfe Department of Mechanical Engineering, Imperial College London, South Kensington Campus, London, UK

D. Roy Mahapatra Department of Aerospace Engineering, Indian Institute of Science, Bangalore, India

Arun Shukla Dynamic Photomechanics Laboratory, Department of Mechanical, Industrial and Systems Engineering, University of Rhode Island, Kingston, RI, USA

Dushyanth Sirivolu The University of Akron, Akron, OH, USA

Min Zhou The George W. Woodruff School of Mechanical Engineering, Atlanta, USA; School of Materials Science and Engineering, Georgia Institute of Technology, Atlanta, GA, USA

Mitigation of Energy Emanating from Imploding Metallic and Composite Underwater Structures

Helio Matos, Michael Pinto and Arun Shukla

1 Introduction

This chapter experimentally investigates the energy mitigation of hydrostatically initiated implosions of metallic and composite structures. Energy mitigation is achieved by placing polyurea (PU) coatings of different thicknesses at different locations onto imploding structures [1, 2]. This work is motivated from the concern of damage to naval and marine structures such as underwater pipelines, submarines, and unmanned underwater vehicles (UUVs). The implosion of a thin-walled body occurs when an applied external pressure reaches a critical value, resulting in a rapid structural collapse. During this collapse, the contacting fluid is accelerated, causing a drop in local pressure via Bernoulli's Principle. When opposing walls of the implodable structure make contact with one another their velocities rapidly drop to zero. This abrupt change in momentum is transferred to the surrounding fluid, causing the release of pressure waves with considerable strength [3, 4].

The pressure pulse released from an implosion has been studied for many decades, with some of the first work focusing on explosive-less underwater acoustic sources [5–7]. Recently, interest in implosion has been rekindled due to a 2001 accident in a Japanese neutrino observatory. Here, at the Super-Kamiokande facility, the implosion of a single photomultiplier tube released a shockwave powerful enough to trigger a chain reaction of collapses, resulting in the implosion of nearly 7000 adjacent tubes [8]. This accident renewed the efforts to characterize the pressure pulse released during the implosion of glass spheres and tube structures, as well as their potential to damage nearby structures [9, 10]. Turner and Ambrico identified key stages of the implosion event about the local pressure about

H. Matos · M. Pinto · A. Shukla (✉)
Dynamic Photomechanics Laboratory, Department of Mechanical, Industrial and Systems Engineering, University of Rhode Island, Kingston RI 02881, USA
e-mail: shuklaa@uri.edu

S. Gopalakrishnan and Y. Rajapakse (eds.), *Blast Mitigation Strategies in Marine Composite and Sandwich Structures*, Springer Transactions in Civil and Environmental Engineering, https://doi.org/10.1007/978-981-10-7170-6_1

the collapsing structure and developed robust fluid-structure computational models that agreed with experimental data [4]. Farhat et al. studied the implosion of aluminum cylinders with varying lengths to produce both mode 2 and mode 4 failures and used these experiments to verify computational models [11]. Most recently, Ikeda et al. studied the free-field implosion of aluminum and brass tubes with varying geometries, to examine the effect of collapse mode on the emitted pressure pulse [12].

Over the past decade, interest in using composite structures in marine applications has increased due to their advantages over traditional metals, such as light weight and corrosion resistance. Several authors performed both experimental and analytic studies to determine critical collapse pressures and mode shapes for composite tubes under external hydrostatic pressure [13–18]. More recently, the authors have performed experimental studies on the hydrostatic collapse of composite tubes, with particular attention paid to measurements of real-time deformations and local pressure history. The hydrostatic implosion of both carbon-fiber and glass-fiber composite tubes was characterized for different geometries and reinforcement architecture [19, 20]. The work on carbon-fiber implosion was then extended to study the shock-initiated implosion of composite tubes to reveal failure mechanisms unique to these materials [21].

In recent decades, several authors have examined the blast performance of materials with polymeric coatings (PU coatings in particular). Tekalur et al. [22] studied E-Glass composites coated with PU subjected to air blast loading and showed that the coating reduced deflection and damage levels as compared to the uncoated material. Sandwich composites have also been studied with PU interlayers by multiple authors. Bahei-El-Din et al. [23] showed PU interlayers reduce the kinetic energy and core damage as compared to control panels. Gardner et al. [24] studied the effect of location of the PU about a graded foam core in sandwich composites and showed PU layers located near the back face of the panel dramatically improved blast resistance.

This chapter shows how PU coatings can mitigate the strength of the pressure pulse released during the implosion of composite and metallic structures. Layers of controlled thicknesses were applied to carbon/epoxy and aluminum tubes onto their interior or exterior surfaces to determine the mitigation effects of coating thicknesses and locations. The energy emanating from the implosion structure is recorded through a series of pressure transducers. Also, the behavior of the implodable structures is quantified by a Digital Image Correlation (DIC) technique which captures real-time high-speed deformation during the collapse. The performance of the PU coated tubes discussed in this chapter can be used as guidelines for designing marine composite structures susceptible to implosion.

2 Experimental Details

2.1 Implodable Structures

The implodable volumes studied are filament wound carbon/epoxy composite and aluminum tubular structures. The carbon/epoxy tubes consist of seven layers of unidirectional carbon fabric reinforcement arranged in a [±15/0/±45/±15] layup with a 60.3 mm (2.36 in) inner diameter, 381 mm (15 in) unsupported length, and 1.63 mm (0.064 in) nominal wall thickness. The composite cylinders are manufactured by Rock West Composites (West Jordan, UT) and sanded for a smooth surface finish and tight tolerances. Moreover, the aluminum tubes consist of 6061-T6 Al with a 61.0 mm (2.4 in) inner diameter, 381 mm (15 in) length, and 1.24 mm (0.049 in) nominal wall thickness. These specimen dimensions are selected to provide specimens with a relatively low expected collapse pressure, a high radius-to-thickness ratio so that thin-wall assumptions may be used, and high comparability between the composite and metallic structures.

The expected collapse pressure can be calculated for the aluminum structures using Eq. (1), which is derived from the classic Von Mises eigenvalue solution [25]. In this case, critical collapse pressure, P_c, is a function of: elastic modulus, E; poisons ratio, υ; unsupported length, L; mean radius, r; and nominal thickness, h. Moreover, Eq. (1) assumes a mode 2 collapse (two buckling lobes in the circumferential direction) and the ends of the cylinder are held circular but are free to contract radially [25]. For composite structures, Eq. (1) was modified into Eq. (2) to account for the anisotropy of the laminates and the nonuniform distribution of stresses through the thickness of the laminate [26]. Here, E_1 and E_2 are the longitudinal and transverse moduli, respectively; υ_{12} and υ_{21} are Poisson's ratios of the two major axes; r and r_o are the mean and outer radii of the laminate, respectively; and G is the shear modulus. The material properties and collapse pressure for the aluminum and composite tubes used in this study are given in Table 1.

Table 1 Implodable structure details

Material	Inner diameter (mm)	Wall thickness (mm)	L/D	Modulus (GPa)	Theoretical P_c (MPa)	Actual P_c (MPa)
Aluminum	60.3	1.63	6.35	68.9	1.05	0.97 ± 0.03
Carbon/ Epoxy	61.0	1.24	6.25	73 (hoop) and 27 (axial)	1.76	1.68 ± 0.01

$$P_c = \frac{2.424E}{(1-\upsilon^2)^{0.75}}\left(\frac{h}{2r}\right)^{2.5}\left(\frac{1}{\frac{L}{2r}-0.45\left(\frac{h}{2r}\right)^{0.5}}\right) \quad (1)$$

$$P_c = \frac{0.85\sqrt{E_1E_2}h^{2.5}}{(1-\upsilon_{12}\upsilon_{21})^{0.75}Lr^{0.5}r_o}\left(\frac{1}{1+\frac{\sqrt{E_1E_2}h^2}{12rr_oG}}\right) \quad (2)$$

2.2 Polyurea Coating

Specimens with polyurea coatings have a uniform coating placed on the exterior or interior of the tube. Specimens were coated with a two-part polyurea supplied by Specialty Products, Inc. (Lakewood, WA). The specific blend used was the HM-VK hand mix series, which has a long enough gel time to be applied manually. This material has a low stiffness (10 MPa in quasistatic conditions), but an elongation of ~500%; which is why the HM-VK is suitable for energy absorption applications. The PU coating was manually applied to the cylindrical specimens as they rotated longitudinally. Before application, each tube was lightly sanded and cleaned with acetone to improve adhesion. Masking tape was used at each end of the tube (set to a predetermined thickness) as a scraper guide wipes off the excess polyurea. For interior coating, the entire setup is angled so the polyurea can be poured, and gravity fed, from the elevated end. The coating system schematic, as well as the coating locations, are shown in Fig. 1.

There are four PU coating configurations for each tube material; two different thicknesses for the interior and exterior coatings. The coating thicknesses are based a 1:1 and 2:1 PU to tube material volume ratio. The interior and exterior coatings have slightly different thicknesses due to their locations on the tube, but their volumes and masses are approximately the same. Moreover, due to geometrical differences, the composite tubes have slightly thicker coatings than its respective aluminum tubes. There are five aluminum (AL) and five carbon/epoxy (CE) cases analyzed in this study as shown in Table 2. Also, the composite material (density = 1600 kg/m^3) is more sensitive to the PU (density = 1050 kg/m^3) mass gain as compared to the aluminum (density = 2700 kg/m^3); hence their relatively higher mass gain in Table 2. Additionally, Table 2 shows that the PU coating had a strong

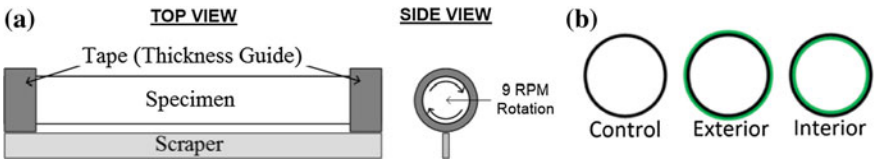

Fig. 1 Polyurea coating **a** setup **b** cross-sectional coating locations

Table 2 Experimental cases details

Case	Material	Polyurea coating location	Polyurea: specimen volume ratio	Mass increase (%)	P_c (MPa)
AL1	Aluminum 6061-T6	Uncoated	N.A.	N.A.	1.68 ± 0.01
AL2		Interior	1:1	34 ± 2	1.69 ± 0.01
AL3			2:1	59 ± 1	1.70 ± 0.02
AL4		Exterior	1:1	32 ± 1	1.67 ± 0.03
AL5			2:1	58 ± 1	1.72 ± 0.02
CE1	Filament wound carbon/epoxy	Uncoated	N.A.	N.A.	0.97 ± 0.03
CE2		Interior	1:1	50 ± 2	1.02 ± 0.10
CE3			2:1	90 ± 1	1.17 ± 0.10
CE4		Exterior	1:1	43 ± 6	1.18 ± 0.04
CE5			2:1	80 ± 6	1.20 ± 0.01

impact on the collapse pressure of the composite tube (further discussed in the results section). Each experimental case has been repeated three times to validate the accuracy of the results.

2.3 Experimental Facility

All implosion experiments are conducted in a 2.1 m diameter semi-spherical pressure vessel with a maximum pressure rating of 6.89 MPa designed to provide constant hydrostatic pressure throughout the collapse event. Several optically clear acrylic windows mounted about the midspan of the pressure vessel allow the specimens to be viewed by cameras and adequately lit by two high-powered lights as shown in Fig. 2. The specimens are sealed from both ends with aluminum end caps to prevent water penetration. Therefore, during the experiments, high-pressure water surrounds the specimen while low-pressure air resides inside. As shown in Fig. 2, the specimen is then suspended at the center. The tank is filled with water and slowly (0.083 MPa/min) pressurized with compressed nitrogen gas which is introduced from the top of the tank. This simulates increasing water depths in a marine environment. For the experiments performed in this study, the specimens were subjected to hydrostatic pressures ranging from 0.95 to 1.75 MPa (equivalent to 96–176 m below sea level, respectively).

To measure the changes in local pressure during the collapse event, several high-pressure blast transducers (PCB 138A05, PCB Piezotronics, Inc., Depew, NY) are mounted at different locations about the specimen both axially and circumferentially as shown in Fig. 3. The amplified outputs of this sensor are monitored by an Astro-med Dash® 8HF-HS portable data recorder (Astro-Med Inc., West Warwick, RI) at a sampling rate of 2 MHz.

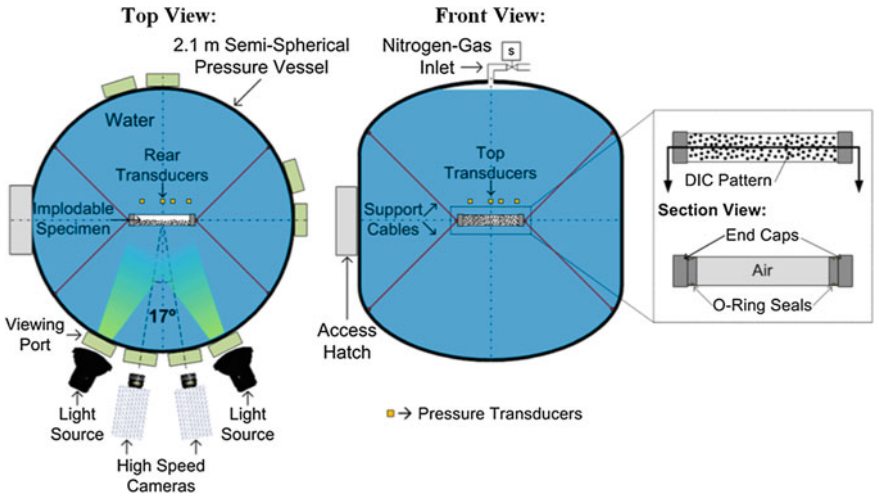

Fig. 2 Detailed schematic of the experimental implosion facility

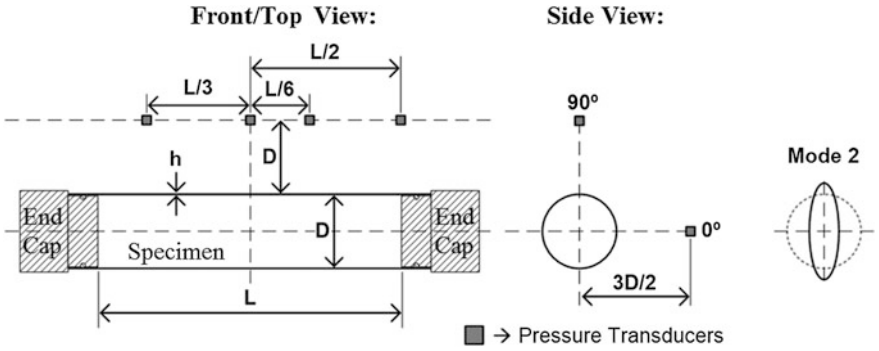

Fig. 3 Sensor locations and side view of the implodable setup inside the pressure tank

2.4 Digital Image Correlation Analysis

Before the experiments, a random, high-contrast speckle pattern is created by randomly placing flat black paint dots (sized 9–12 pixels per dot) on a flat white painted background until approximately 50% of the viewable surface area of the specimens is covered by the black dots. Two high-speed cameras (Photron SA1, Photron USA, Inc.) positioned at a stereo angle of 17° are used to capture images of the patterned region of the specimen at a frame rate of 50,000 frames/second. The stereo images are analyzed using commercially available DIC software, VIC3D 7 (Correlated Solutions, Inc., Columbia, SC) to measure full-field displacements across the viewable surface of the specimen. 3D Digital image correlation (DIC) is

a well-known, noncontact optical technique to determine real-time, full-field displacements across the viewable surface of a specimen [27]. Previous work [28] outlines the calibration procedures that validate the accuracy of the DIC results in the underwater environment (where changes in refractive index are present). It was found that the flat surface windows (located at the midspan of the pressure vessel) need to be perpendicular to the viewing axis to minimize DIC displacement errors [28]. In-plane displacement errors inherent to underwater DIC are 1.2% and the out-of-plane errors are 2.5%.

2.5 Energy Calculation

The energy emitted/released during implosion can be obtained from the measured pressure, p, as a function of time, t [1, 2]. The energy flux, E_F, from a collapsing volume is calculated from the integral of pressure squared times the inverse of the fluid density, ρ_0, and two times the sensor's standoff distance, R_s, as shown in Eq. (3). The flux in Eq. (3) represents the energy released during the under-pressure region of the pressure history ($t < 0$), which is also the energy stored in the implodable (in the form of compressed air) during collapse [29, 30]. All the stored energy is released during the over-pressure region of the pressure history ($t > 0$) similarly to a gas bubble collapse; in other words, the impulse from $t < 0$ is equal and opposite of the impulse from $t > 0$ [3, 4]. For this reason, the flow energy of the local pressure history is calculated for the under-pressure region of each specimen type. Moreover, knowing that the time integral of pressure is equal to impulse, I, then Eq. (3) can be simplified to Eq. (4).

$$E_F = \frac{1}{2\rho_0 R_s}\left[\int_0^t \Delta p dt\right]^2 \tag{3}$$

$$E_F = \frac{I^2}{2\rho_0 R_s} \tag{4}$$

The pressure pulse emanating from an implodable cylindrical structure is spherical [2–4]. Therefore, energy is also spherical, and the flux from Eq. (4) is multiplied by the area of a sphere with radius equal to the standoff distance of the pressure sensor to find the total energy, E_T, as shown in Eq. (5).

$$E_T = 4\pi R_s^2 E_F \tag{5}$$

To account for differences in the collapse pressure of different implosion cases, the total energy is normalized with respects to the available potential energy, E_p, of each case. The potential energy available is defined in Eq. (6).

$$E_H = P_c V_{tube}, \tag{6}$$

where P_c is the hydrostatic collapse pressure and V_{tube} is the volume of fluid displaced by the tube. In this way, the energy released in the pressure pulse may be presented as a percentage of the available hydrostatic energy at the collapse pressure.

3 Results and Discussion

3.1 Emanating Pressures

3.1.1 Pressures from Aluminum Structures

The tubular structure's cross section during implosion is illustrated alongside local dynamic pressure in Fig. 4a. The vertical axis in this figure is in terms of dynamic

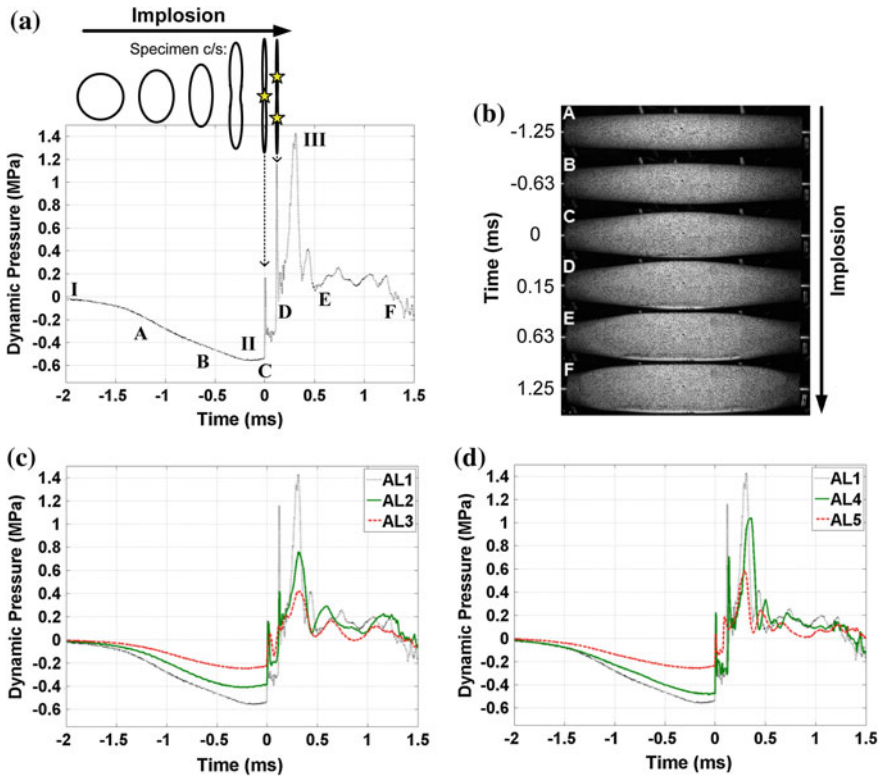

Fig. 4 Dynamic pressure histories taken from sensor 1; **a** of the AL1 case and tubular cross section during implosion; **b** still images that correlate with the pressure history; **c** of interior PU coating cases; and **d** exterior PU coating cases

pressure where the value of 0 represents hydrostatic pressure (1.68 ± 0.01 MPa). The pressure history can be broken down into three main stages: (I) Structure becomes unstable, (II) emission of low-pressure pulses due to the decrease in potential energy, and (III) emission of high-pressure pulses due to the abrupt change in water momentum. Immediately after the low-pressure region, there is a high acoustic spike (at $t = 0$ ms) caused by structural contact. A second acoustic spike is also seen when the opposing walls of the structure come into full contact shortly after the initial contact. Figure 4b shows the captured images that can be associated with the pressure history in Fig. 4a. Note that Fig. 4b is an in-plane image that illustrates out-of-plane deformation; hence, by focusing on the vertical dimension change, the out-of-plane change can be intuitively understood.

The interior and exterior PU coating effects on the AL cases are shown in Fig. 4c, d, respectively (see Table 2 for case details). Applying coatings to the exterior or the interior of the structure shows mitigating effects to the low and high-pressure regions of the pressure history. Interior coating has a stronger effect than the exterior coating. By doubling the coating volumes, this effect increases for both cases.

The loading profile can also be represented in terms of impulse by integrating the pressure signal [3, 4]. Doing so will take into account the duration of acoustic spikes as well as their magnitude. After integration, an impulse per unit area is given in terms of Pa•s. The areal impulse taken from Sensor 1 (pressure sensor at the midspan of the specimen at 0°) of the interior and exterior PU coating cases are illustrated in Fig. 5a, b. It is shown that the structures coated with polyurea have the same behavior as the non-coated structure. Also shown is the impulse with diminishing strength as PU is added (more so with interior coating).

In summary, the minimum and maximum pressures, as well as the maximum impulses for the AL cases, are given in Table 3. Based on the metrics shown in

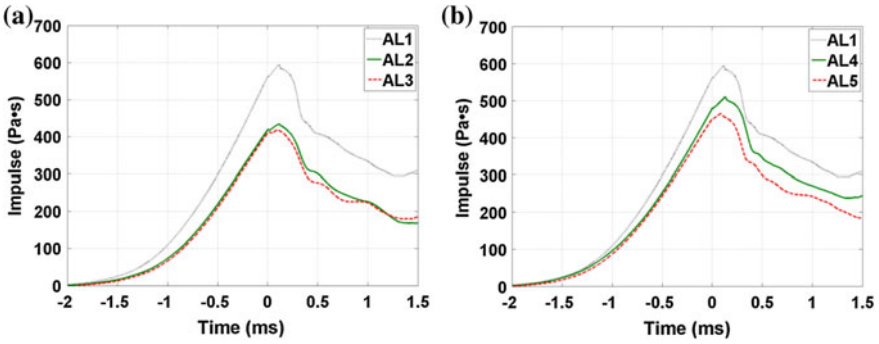

Fig. 5 Impulse histories of the **a** interior PU coating cases; and **b** exterior PU coating cases

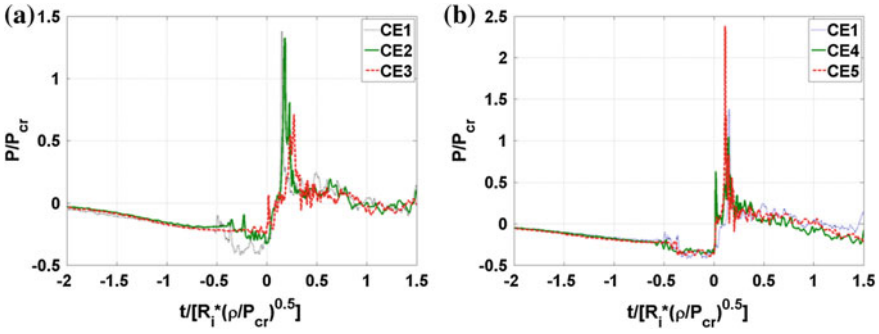

Fig. 6 Local normalized pressure histories (from Sensor 1) plotted against normalized time for the CE tubes with PU coating in the **a** interior and **b** exterior

Table 3, interior PU coatings on aluminum tubes yield a higher performance when compared to exterior coatings in terms of mitigating pressure pulses. Additionally, doubling the volume of the PU coating does not scale the mitigating effect; therefore there must be an optimal PU coating volume based on impulse (or energy) reduction to added mass for any given application.

3.1.2 Pressures from Carbon/Epoxy Structures

All coatings provided a moderate increase in collapse pressure for the composite structures as shown in Table 2. The coatings increase both the effective thickness of the tube walls as well as the mass of the structure, thereby altering the critical collapse pressure. In comparison, the collapse pressure of aluminum structures was not notably affected by the PU coating because they had relatively thinner coatings (due to differences in tube geometry) and they were less sensitive to the PU mass gain (due to their higher density). Additionally, the collapse pressure of the aluminum structures was far greater than the composites. Structures that fail in relatively lower pressures are sensitive to changes in their structural content. It is likely that a relatively thicker PU coating for the AL cases would also alter the aluminum's collapse pressure; especially exterior coatings based on Eq. (6).

Table 3 Pressure results details for the aluminum cases

Case	Polyurea coating location	Polyurea: specimen volume ratio	P_c (MPa)	P_{min} (MPa)	P_{Max} (MPa)	I_{Max} (Pa S)
AL1	Uncoated	N.A.	1.68 ± 0.01	0.56 ± 0.03	1.42 ± 0.08	595 ± 37
AL2	Interior	1:1	1.69 ± 0.01	0.42 ± 0.03	0.76 ± 0.05	433 ± 21
AL3		2:1	1.70 ± 0.02	0.25 ± 0.01	0.42 ± 0.04	418 ± 17
AL4	Exterior	1:1	1.67 ± 0.03	0.49 ± 0.04	1.04 ± 0.10	509 ± 24
AL5		2:1	1.72 ± 0.02	0.26 ± 0.02	0.58 ± 0.05	464 ± 15

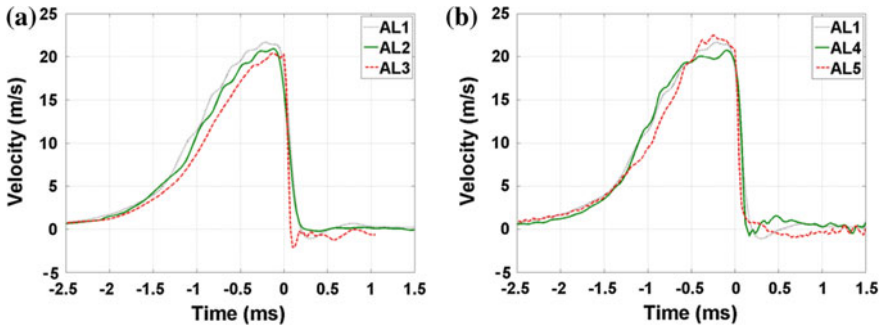

Fig. 7 Center point collapse velocity measured for the AL tubes with PU coating in the **a** interior and **b** exterior

The pressure history for the interior and exterior PU coated CE cases is plotted in Fig. 6a, b, respectively (see Table 2 for case details). The vertical axes in these figures are in terms of normalized pressure; which is simply a ratio of recorded pressure over collapse pressure (P/P_c). Due to the differences in collapse pressure, normalized pressure needs to be used instead of dynamic pressure, so the cases in Fig. 6 are comparable to each other [20]. Similarly, time was also normalized using classic bubble dynamics theory [31] to account for the changes in collapse mechanics in different collapse pressures. The normalized time, $\bar{t}$, is given in Eq. 7.

$$\bar{t} = \frac{t}{R_i \sqrt{\frac{\rho_0}{P_{cr}}}}, \tag{7}$$

where R_i is the internal tube radius. Here, the time is scaled by the collapse time of a spherical bubble with radius R_i, collapsing under an external pressure equal to the collapse pressure of the tube under study. In these plots in Fig. 6, $\bar{t} = 0$ ms represents the moment of wall contact; similar to previous pressure plots for the AL cases.

The interior coatings plotted in Fig. 6a show significant differences in the under-pressure region. Some elements of the two-phase characteristic remain but are significantly altered. Both interior coating thicknesses reduce the pressure drop seen in this region, with the thicker coating showing an even smaller pressure drop. This suggests that interior PU coatings lower the acceleration of the structure (consequently the acceleration of the surrounding fluid), and increasing the thickness of the coating enhances this effect. In addition, the thick interior coating appears to suppress the second phase of the under-pressure associated with damage development. In contrast, the exterior coatings plotted in Fig. 6b show little differences from the under-pressure of the uncoated specimens. In these cases, there is a two-phase under-pressure characteristic of the implosion of carbon composite tubes. The pressure first drops smoothly as the tube deforms without damage. At approximately 0.5 ms prior to wall contact, there is a very sudden drop in pressure

then a small plateau region until wall contact is made. This coincides with large-scale damage occurring in the structure. At this time, longitudinal cracks form on the lobes of the buckling shape in regions of high tensile stress. This causes a sudden loss in structural stability and allows for the rapid acceleration of the walls, and consequently, a rapid drop in local pressure. Both thin and thick exterior coatings show these same characteristics and similar minimum pressures, however, it is seen that the thick exterior coating seems to reduce the duration of the second phase. This suggests the exterior coating has some effect on the development of damage and will be further investigated in the following sections.

The changes to the over-pressure region brought on by different coating types are also illustrated in Fig. 6a, b. For exterior coatings, thin coatings have little effect on the peak pressure, while the thicker coatings produce a significantly higher magnitude pressure peak. The maximum pressure for the thicker exterior coating case is approximately 80% greater than the uncoated case which gives more evidence that thick exterior coatings actually intensify the collapse of the structure. This is due to a containment of the damage within the structure and is further discussed in a later section.

The interior coatings show even more interesting changes to the over-pressure. Not only is the magnitude of the pressure pulse altered, but so is the timing of the pulse. As the thickness of the coating increases, the magnitude of the pressure pulse decreases, and the arrival of the pulse is delayed. The mitigation of the peak pressure again gives evidence that these coatings slow the collapse of these tubes, thereby lessening the severity of the pressure pulse. The change in timing of the peak suggests these coatings extend the contact event itself; meaning that it takes longer to arrest the structure. Therefore, the tube has a lower deceleration. This observation is further explored using DIC measurements of velocities of the CE tubes.

In summary, the minimum and maximum pressures are given in Table 4. PU coatings appear to have a complex impact on composite tubes. It increases collapse pressures which is good in terms of increasing the operating depth of underwater structures. The released pressure is also increased in the case of exterior coatings. The interior coating shows a higher performance in terms of mitigating pressure pulses while increasing operating depth. Additionally, doubling the volume of the

Table 4 Pressure results details for the Carbon/Epoxy cases

Case	Polyurea coating location	Polyurea: specimen volume ratio	P_c (MPa)	P_{min} (MPa)	P_{Max} (MPa)
CE1	Uncoated	N.A.	0.97 ± 0.03	0.52 ± 0.05	2.5 ± 0.6
CE2	Interior	1:1	1.02 ± 0.10	0.71 ± 0.04	1.77 ± 0.4
CE3		2:1	1.17 ± 0.10	0.92 ± 0.09	1.76 ± 0.2
CE4	Exterior	1:1	1.18 ± 0.04	0.75 ± 0.02	2.56 ± 0.4
CE5		2:1	1.20 ± 0.01	0.73 ± 0.03	3.38 ± 0.6

PU coating can have a detrimental effect in the mitigation process; hence, there is an optimal coating thickness for a given application similar to the AL cases.

3.2 Collapse Velocities

3.2.1 Velocities of Aluminum Structures

The decrease of the under-pressure region for PU coated AL structures in Fig. 4 implies a decrease in potential energy; in turn, a decrease in kinetic energy in the form of lower collapse velocities is expected. For the AL2 and AL4 cases, a 25 and 15% reduction was observed in the under-pressure region compared to the AL1 case (see Table 3). The velocities do not have the same drastic reduction as pressures. The velocities measured with DIC from the center point (V_{cp}; the valley at the tube's midspan where structural contact happens when $t = 0$) for all the aluminum cases are similar but have small differences as illustrated in Fig. 7; where the center point velocities for the interior and exterior PU coated tubes are plotted versus time in parts (a) and (b), respectively. For interior PU coatings, a subtle decrease in initial acceleration and peak velocities; increasing coating thickness increases this effect. For exterior PU coatings, the thickness of the coating had different effects. The thinner coating in the AL4 case had the same initial acceleration and a subtle decrease in peak velocity. The thicker PU coating in the AL5 case had a subtle decrease in initial acceleration and an increase in peak velocity. Exterior coatings seems to have the following competing factors: (1) reduction in the rate of deformation due to the strain rate sensitivity of the polyurea coating; and (2) increase in volume which leads to higher potential energy for the same collapse pressure as shown by Eq. (6). It is worth noting that Fig. 7 shows a representative experiment from three experiments for each case; the observations mentioned are based on the

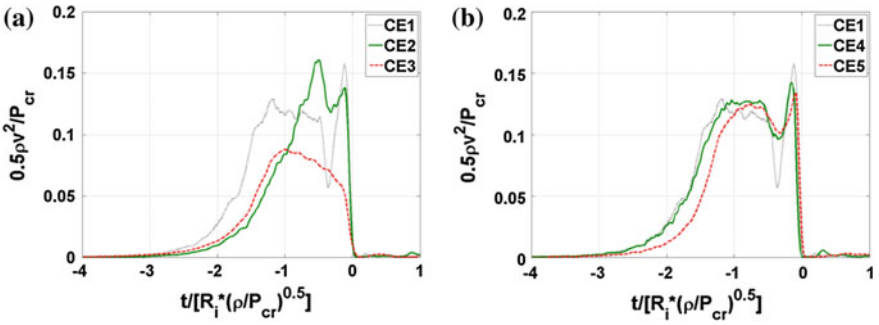

Fig. 8 Center point dimensionless velocity plotted against normalized time for the CE tubes with PU coating in the **a** interior and **b** exterior

Table 5 Velocity results details for the aluminum cases

Case	Polyurea coating location	Polyurea: specimen volume ratio	V_{cp} *(m/s)*	V_{lb} (MPa)
AL1	Uncoated	N.A.	21.6 ± 1.4	249 ± 5
AL2	Interior	1:1	20.8 ± 1.8	198 ± 3
AL3		2:1	20.3 ± 1.1	179 ± 6
AL4	Exterior	1:1	20.6 ± 1.6	217 ± 4
AL5		2:1	22.4 ± 1.9	207 ± 4

average trend, and the differences shown are smaller than the standard deviation for peak velocities (in the order of 1 m/s).

The PU coating is a strain rate sensitive material; which leads to a notable reduction in velocities during high strain rate events. The center point experiences relatively low strain rates due to its location on the collapse valley. However, the collapse lobes (90° from the valley; see Fig. 3) experience high strain rates. After wall contact, the buckle starts to propagate longitudinally. This longitudinal propagation is roughly 10 times faster than the wall collapse velocity as shown by the mean buckle velocity for each case in Table 5. The highest strain rates during collapse can be found at the longitudinal buckle front [28]. Thus, it is during this time that the strain rate sensitive properties of the polyurea can have a strong impact. The polyurea coating slows down the longitudinal buckle propagation by roughly 25 and 15% for the interior and exterior PU coating cases, respectively (note that a similar reduction in magnitude is seen in the pressure profile).

3.2.2 Velocities of Carbon/Epoxy Structures

To compare the velocities of the composite structures during the collapse, the data must first be scaled, both in terms of velocity magnitude and time, to account for differences caused by changing collapse pressure. Time is scaled using Eq. 7 as previously discussed. To scale velocities into a dimensionless parameter, Eq. 8 is used.

$$\overline{v} = \frac{\rho_0 v^2}{2P_{cr}}, \tag{8}$$

where v is the magnitude of the measured velocity. This dimensionless velocity term is similar to a normalized kinetic energy and removes the effect of pressure on the velocity.

The dimensionless center point velocity is plotted against normalized time for each interior and exterior PU coated CE cases in Fig. 8a, b, respectively. The differences observed in the composite tubes are much more prominent than the ones seen in the aluminum tubes due to its increased sensitivity to PU as mentioned previously. Interior PU coatings on the CE tubes have a dramatic effect on the center point velocity of the composite structure. The thinner interior coating shown

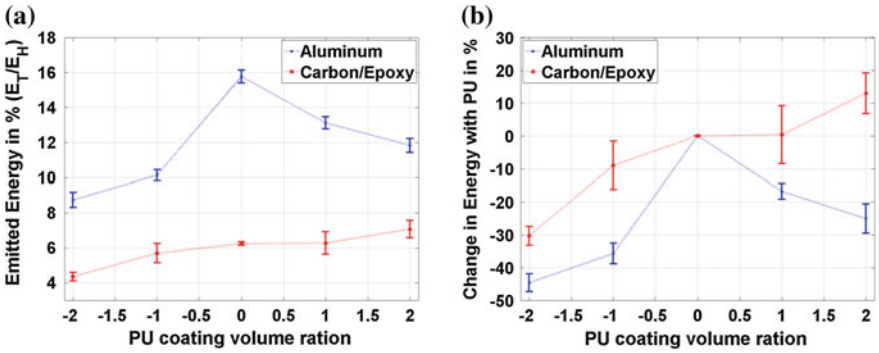

Fig. 9 Energy emanating from imploding metallic and composite structures **a** normalized with respect to potential energy and **b** as a ratio relative to the uncoated specimen

in the CE2 case has little effect on the peak velocity; however, the character of the velocity history is significantly different. The plateau region normally associated with damage in the tube is absent, and instead, the tube continues to accelerate to its maximum value. Interestingly, the acceleration of interior coated specimens is less than that of uncoated tubes, showing the resistive effect of the coating. For the exterior PU coatings, little differences are seen in the velocity profiles. Some of the acute responses of the uncoated velocity are smoothed out, but their magnitudes are roughly the same. For the thicker exterior PU coating shown in CE5, the duration of the plateau region prior to wall contact is shorter than the other cases. This plateau region is caused by large-scale damage occurring in the structure at this time; the thicker coating suppresses that feature of the failure process to some degree.

Specimens with thick interior coatings show even more difference in center point velocity. These specimens exhibit a significantly lower maximum velocity, and the velocity trace has a much more smooth character. Both of these qualities indicate that for this thickness of the interior coating, the mechanical behavior of the PU layer begins to dominate the collapse. PU is a highly strain rate sensitive material and becomes stiffer as strain rate increases. Therefore, as the collapse accelerates, the PU coating is better able to resist the deformation and reduce the structural velocity.

3.3 Implosion Energy

As mentioned previously, the impulse from an imploding structure can be obtained by the signal obtained from the dynamic pressure transducers [3, 4]. After integration, an impulse per unit area is given in terms of Pa•s. The maximum impulse which is obtained by the integration of the under-pressure region is equal in magnitude to the impulse obtained from the over-pressure region. This phenomenon has been observed in several studies on the implosion of glass spheres as well as the implosion of aluminum tubes [4, 11, 28]. The maximum impulse from

Fig. 10 Postmortem images of uncoated tubes showing **a** through-thickness axial cracks and **b** smaller circumferential cracks

Sensor 1 is used to calculate the flow energy with Eq. (4). The energy as a percentage of the total available hydrostatic potential energy is plotted for the different material cases in Fig. 9a. Also, energy is plotted as a percentage of the energy emitted by the uncoated specimen in Fig. 9b. For horizontal axis in Fig. 9a, b, the negative coating volume ratio represents interior PU coatings and positive ratio represents exterior coatings. Moreover, the total energy can be obtained by multiplying the flow energy to the spherical surface area of the pressure wave as shown in Eq. (5). The total energy can then be normalized with respect to the potential energy (Eq. (6)) to account for differences in collapse pressure and with respect to the non-coated specimens (AL1 and CE1) to visualize full-scale mitigation effects from the PU coatings as shown in Fig. 9.

For metallic tubes, the energy emanating during the implosion of polyurea coated aluminum structures can be mitigated regardless of coating locations; in terms of normalized and relative emitted energy as seen in Fig. 9a, b. Interior coatings have a higher performance in terms of mitigating released energy than exterior coatings. Doubling the coating volume on aluminum structures does not significantly improve the mitigation effects of the polyurea for both interior and exterior coatings. Therefore, as mentioned previously, there is an optimum coating thickness for any given application in terms of reduction of emitted energy over added mass.

For the composite tubes with the thinner PU coatings (CE2 and CE4), it is seen that PU coatings have little effect on the energy developed. Though there is some change in mean value, any change from the CE1 (control case) case lies within the error bars; which are consistent with other observations made in previous sections. Both minimum pressure and maximum collapse velocity for CE2 and CE4 (thinner coated cases) show little difference from the CE1, suggesting that coatings of this thickness had a small impact on the collapse mechanics of the composite tube.

However, for cases, CE3 and CE5 (thicker coated cases), a significant effect on the energy released is observed. Thick interior coatings show a significant (30%) reduction in energy developed in the collapse. This implies that this coating drastically reduces the severity of the collapse as previously discussed. The tubes with thick interior coatings (CE3) showed less of a pressure drop and reduced collapse velocity. All of these factors contribute to lessening the intensity of the failure event, and in turn reducing the energy released. Lastly, the CE5 (thick exterior coating case) show a significant (14%) increase in energy. This is unexpected as the maximum normalized collapse velocity is similar to the CE1 case. However, a much higher peak pressure is observed for CE5. To better explain and understand this observation, postmortem analysis is conducted to examine the states of damage on the composite tubes (see Sect. 3.4).

The overall increase in performance, in terms of energy reduction, is due to the PU coating and not the increased mass of the implodable structures. The percent increase in mass shown in Table 2 for the thin (AL2, AL4, CE2, and CE4) and thick (AL3, AL5, CE3, and CE5) coatings are approximately the same regardless of the location of the coating (interior or exterior). Though the added mass is the same, the effects on the pressure history, collapse velocity, and energy released are widely different. This shows that these effects are brought on by the specific coating itself rather than simply the added mass of the PU layer.

3.4 Composite Implodable Damage

The effects of PU coatings (interior or exterior) on the damage of aluminum tubes were not visually notable after the experiment. Thus, a postmortem analysis was only conducted for the composite structures. The exterior PU coatings (CE4 and CE5) effects on the composite tubes may be further understood by examining postmortem specimens. Figure 10 shows typical postmortem images for the case of an uncoated carbon/epoxy tube. The most prominent form of damage seen in these specimens is longitudinal, through-thickness cracks, marked as “A” in Fig. 10. These cracks show significant opening, as well as additional cracking and pullout in adjacent tows. In addition, some circumferential cracking is present, indicated by “B” in the image. These cracks appear less severe than the longitudinal cracks and initiated as the buckle propagated along the tubes’ length.

To observe how exterior coatings affect the damage in the structure, the coatings on postmortem specimens are carefully removed while preserving the state of damage on the tube surface. Postmortem images of tubes with a thin exterior coating are shown in Fig. 11.

On the outside of the coating, areas of delamination of the PU coating are seen where cracks exist in the tube underneath (see A in Fig. 11a). The extreme bending at these sites caused the delamination, and in some cases, the fractured tube then

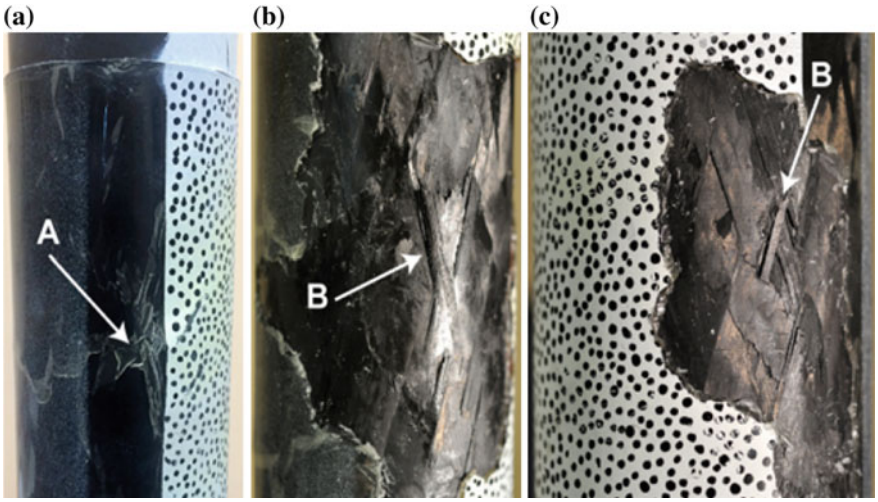

Fig. 11 Postmortem images of tubes with thin exterior coatings showing **a** coating delamination and puncture and **b** axial cracking (note: coating has been peeled to expose composite surface)

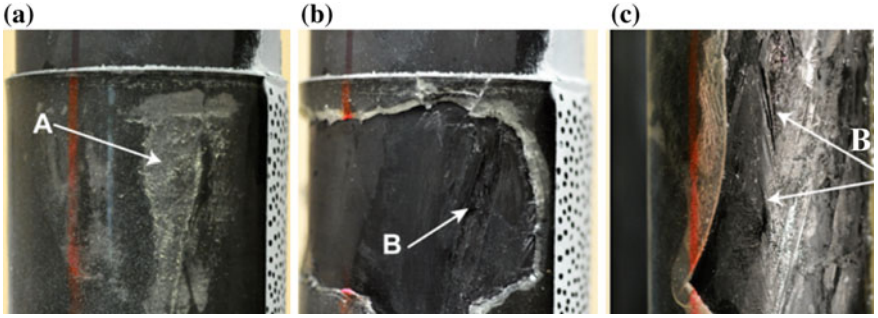

Fig. 12 Postmortem images of tubes with thick exterior coatings showing **a** coating delamination and **b** crimping in the outer ply with some cracking (coating has been peeled to expose composite surface)

punctured the PU coating. With the coating peeled back, the state of damage underneath is readily visible. Here, through-thickness cracks are seen with carbon tows fraying from the surface (labeled as B in Fig. 11b, c), which are responsible for rupturing the PU layer. Most importantly, the cracks for this case do not seem as severe as in the uncoated case. Uncoated tubes show much more fraying of carbon tows and opening in the crack faces. This indicates that the thin outer coating has a suppressive effect on the damage in the tube due to the confinement offered by the PU. To examine the effect of thickness on this phenomenon, postmortem images of tubes with a thick exterior coating are shown in Fig. 12.

The areas of delamination of the PU coating are seen where cracks exist, however for the thick outer coatings the PU layer was never punctured at these sites (see A in Fig. 12a). Peeling back the outer layer, the state of damage is seen in the center and right-most images. Here, the main longitudinal crack is indicated by "B" in Fig. 12 and is seen to be much less severe than either of the previous cases. There is significantly less fiber fraying along the crack, and no separation of tube walls is seen. In fact, in some cases, the crack does not appear to penetrate completely through the thickness. Instead, a slight bend is observed in the outer layer indicating the location of the crack. Thus, the thick outer coating provides an even greater suppressing effect on the damage mechanisms present in these structures. The suppressing effect causes less energy to be dissipated in the implosion event and contributes to the increased energy released in the pressure pulse as previously discussed.

4 Conclusions

The hydrostatic implosion of metallic and composite tubes with polymeric coatings on the interior and exterior surfaces was studied to examine differences caused by the specific type of coating. High-speed photography, DIC measurements, and dynamic pressure sensors were used to characterize the effects of the thickness and location of the coating on the mechanics of collapse as well as local pressure fields, with the goal of mitigating the pressure pulse. The completion of this work has resulted in the following findings:

- The collapse of layered composite tubes was well characterized using measurements of local pressure in conjunction with optical displacement measurements.
- The implosion energy can be obtained directly as a function of pressure and is a useful tool for comparing the total energy emitted during the implosion process.
- Polyurea coatings did not have a striking effect on the collapse pressure for aluminum structures. However, all coating types increase the collapse pressure for composites due to its higher sensitivity to the parameters of this study.
- The energy emanating during the implosion of polyurea-coated aluminum structures can be mitigated regardless of coating locations. Interior coatings have a higher performance in terms of mitigating released energy than exterior coatings.
- For the aluminum structures, doubling the coating volume does not significantly improve the mitigation effects of the polyurea for both interior and exterior coatings. There is an optimum coating thickness for any given application in terms of reduction of emitted energy over added mass.
- Highly increasing exterior coatings can lead to adverse effects by increasing: collapse pressure; structural velocity; and energy emitted. This is better shown

by the composite structure; however, metallic structures with much higher volume ratio than the ones in this study could have similar effects.

- On composites, interior polyurea coatings are successful in mitigating implosion pressure pulses, whereas, exterior coatings amplify their strength.
- Polyurea coating with a 1:1 volume ratio on composites have little effect on pressure pulses emitted following implosion, regardless of the location of the coating.
- Exterior polyurea coating with a 2:1 volume ratio on composites increase the energy released following implosion due to suppression of the damage mechanisms that dominate failure.
- Interior polyurea coating with a 2:1 volume ratio on composites decrease the energy released from implosion due to a reduction in collapse velocity and a softening of wall-to-wall contact.
- The overall increase in performance, in terms of energy reduction, is due to the PU coating (in the inner surface specifically) and not the increased mass of the implodable structures.

Acknowledgements The authors kindly acknowledge the financial support provided by Dr. Yapa D.S. Rajapakse and Dr. Thomas Fu under the Office of Naval Research (ONR) Grant Nos. N00014-10-1-0662 and N00014-15-1-2046.

References

1. Pinto, M., & Shukla, A. (2015). Mitigation of pressure pulses from implosion of hollow composite cylinders. *Journal of Composite Materials, 50*(26), 3709–3718. https://doi.org/10.1177/0021998315624254.
2. Matos, H., & Shukla, A. (2016). Mitigation of implosion energy from aluminum structures. *International Journal of Solids and Structures, 100–101,* 566–574. https://doi.org/10.1016/j.ijsolstr.2016.09.030.
3. Turner, S. E. (2007). Underwater implosion of glass spheres. *The Journal of the Acoustical Society of America, 121*(2), 844–852. https://doi.org/10.1121/1.2404921.
4. Turner, S. E., & Ambrico, J. M. (2012). Underwater implosion of cylindrical metal tubes. *Journal of Applied Mechanics, 80*(1), 011013. https://doi.org/10.1115/1.4006944.
5. Urick, R. J. (1963). Implosions as Sources of Underwater Sound. The Journal of the Acoustical Society of America, 35(11), 1903–1903. https://doi.org/10.1121/1.2142767.
6. Orr, M. (1976). Acoustic signatures from deep water implosions of spherical cavities. *The Journal of the Acoustical Society of America, 59*(5), 1155. https://doi.org/10.1121/1.380977.
7. Harben, P., Boro, C., Dorman, L., & Pulli, J. (2000). *Use of Imploding Spheres: An Alternative to Explosives as Acoustic Sources at Mid-Latitude SOFAR Channel Depths*. https://doi.org/10.2172/793868.
8. Physicsworld.com. (2001). Accident grounds neutrino lab. Retrieved March 23, 2017, from http://physicsworld.com/cws/article/news/2001/nov/15/accident-grounds-neutrino-lab.
9. Ling, J., Bishai, M., Diwan, M., Dolph, J., Kettell, S., Sexton, K., Sundaram, S. (2013). Implosion chain reaction mitigation in underwater assemblies of photomultiplier tubes. *Nuclear Instruments and Methods in Physics Research Section A: Accelerators, Spectrometers, Detectors and Associated Equipment*, *729*, 491–499. https://doi.org/10.1016/j.nima.2013.07.056.

10. Diwan, M., Dolph, J., Ling, J., Sharma, R., Sexton, K., Simos, N., Turner, S. (2012). Underwater Implosions of Large Format Photo-multiplier Tubes. *Physics Procedia*, *37*, 715–721. https://doi.org/10.1016/j.phpro.2012.03.721.
11. Farhat, C., Wang, K., Main, A., Kyriakides, S., Lee, L., Ravi-Chandar, K., et al. (2013). Dynamic implosion of underwater cylindrical shells: Experiments and Computations. *International Journal of Solids and Structures, 50*(19), 2943–2961. https://doi.org/10.1016/j.ijsolstr.2013.05.006.
12. Ikeda, C. M., Wilkerling, J., & Duncan, J. H. (2013). The implosion of cylindrical shell structures in a high-pressure water environment. *Proceedings of the Royal Society A: Mathematical, Physical and Engineering Sciences*, *469*(2160), 20130443–20130443. https://doi.org/10.1098/rspa.2013.0443.
13. Moon, C., Kim, I., Choi, B., Kweon, J., & Choi, J. (2010). Buckling of filament-wound composite cylinders subjected to hydrostatic pressure for underwater vehicle applications. *Composite Structures, 92*(9), 2241–2251. https://doi.org/10.1016/j.compstruct.2009.08.005.
14. Ross, C. T., Little, A. P., Haidar, Y., & Waheeb, A. A. (2009). Buckling of carbon/glass composite tubes under uniform external hydrostatic pressure. *Strain*, *47*. https://doi.org/10.1111/j.1475-1305.2008.00475.x.
15. Smith, P. T., Ross, C. T., & Little, A. P. (2009). Collapse of composite tubes under uniform external hydrostatic pressure. *Journal of Physics: Conference Series, 181,* 012043. https://doi.org/10.1088/1742-6596/181/1/012043.
16. Hernández-Moreno, H., Douchin, B., Collombet, F., Choqueuse, D., & Davies, P. (2008). Influence of winding pattern on the mechanical behavior of filament wound composite cylinders under external pressure. *Composites Science and Technology, 68*(3–4), 1015–1024. https://doi.org/10.1016/j.compscitech.2007.07.020.
17. Hur, S., Son, H., Kweon, J., & Choi, J. (2008). Postbuckling of composite cylinders under external hydrostatic pressure. *Composite Structures, 86*(1–3), 114–124. https://doi.org/10.1016/j.compstruct.2008.03.028.
18. Yang, C., Pang, S., & Zhao, Y. (1997). Buckling analysis of thick-walled composite pipe under external pressure. *Journal of Composite Materials, 31*(4), 409–426. https://doi.org/10.1177/002199839703100405.
19. Pinto, M., Gupta, S., & Shukla, A. (2015). Study of implosion of carbon/epoxy composite hollow cylinders using 3-D Digital Image Correlation. *Composite Structures, 119,* 272–286. https://doi.org/10.1016/j.compstruct.2014.08.040.
20. Pinto, M., Gupta, S., & Shukla, A. (2015). Hydrostatic implosion of GFRP composite tubes studied by digital image correlation. *Journal of Pressure Vessel Technology, 137*(5), 051302. https://doi.org/10.1115/1.4029657.
21. Pinto, M., & Shukla, A. (2015). Shock-initiated buckling of carbon/epoxy composite tubes at sub-critical pressures. *Experimental Mechanics, 56*(4), 583–594. https://doi.org/10.1007/s11340-015-0033-1.
22. Tekalur, S. A., Shukla, A., & Shivakumar, K. (2008). Blast resistance of polyurea based layered composite materials. *Composite Structures, 84*(3), 271–281. https://doi.org/10.1016/j.compstruct.2007.08.008.
23. Bahei-El-Din, Y. A., Dvorak, G. J., & Fredricksen, O. J. (2006). A blast-tolerant sandwich plate design with a polyurea interlayer. *International Journal of Solids and Structures, 43*(25–26), 7644–7658. https://doi.org/10.1016/j.ijsolstr.2006.03.021.
24. Gardner, N., Wang, E., Kumar, P., & Shukla, A. (2011). Blast mitigation in a sandwich composite using graded core and polyurea interlayer. *Experimental Mechanics, 52*(2), 119–133. https://doi.org/10.1007/s11340-011-9517-9.
25. Mises, R. V. (1933). *The critical external pressure of cylindrical tubes under uniform radial and axial load* (D.F. Windenburg, Trans.). https://doi.org/10.5962/bhl.title.47713.
26. Koudela, K., & Strait, L. (1993). Simplified methodology for prediction of critical buckling pressure for smooth-bore composite cylindrical shells. *Journal of Reinforced Plastics and Composites, 12*(5), 570–583. https://doi.org/10.1177/073168449301200507.

27. Schreier, H., Orteu, J., & Sutton, M. A. (2009). Image correlation for shape. *Motion and Deformation Measurements*. https://doi.org/10.1007/978-0-387-78747-3.
28. Gupta, S., Parameswaran, V., Sutton, M., & Shukla, A. (2014). Application of 3-D digital image correlation technique to study underwater implosion. In *Dynamic Behavior of Materials*. Conference Proceedings of the Society for Experimental Mechanics Series, (Vol. 1, pp. 351–356). https://doi.org/10.1007/978-3-319-06995-1_49.
29. Cole, R. (1948). *Underwater Explosions*. Princeton: Princeton Univ. Press.
30. Arons, A. B., & Yennie, D. R. (1948). Energy partition in underwater explosion phenomena. *Reviews of Modern Physics, 20*(3), 519–536. https://doi.org/10.1103/revmodphys.20.519.
31. Plesset, M. S. (1963). *Bubble dynamics*. Engineering Division: California Institute of Technology.

Underwater Explosion Response of Sandwich Structures with Compliant Cores

Brian Hayman

1 Introduction

Sandwich structures using polymer foams as the core material have been utilised in naval ships since the 1970s. Such foams give a stiffness in the thickness direction that is appreciably lower than many other potential core materials. Some foams have the potential to absorb large amounts of energy during crushing or other forms of deformation. Thus, foam-cored sandwich may offer possibilities for reducing the effect of shock and blast loadings, i.e. for shock mitigation. However, the task of establishing the real potential of these materials for shock mitigation, especially with regard to underwater explosions (UNDEX) presents several challenges, some of which will be presented here.

2 Brief History of Foam-Cored Sandwich in Naval Ships

According to Hellbratt and Gullberg [22] and Gullberg and Olsson [18], Swedish research and development work on foam-cored GRP sandwich structures for naval ships began in the mid to late 1960s in a collaboration between the Swedish Defence Materiel Administration and the Royal Institute of Technology (KTH). The core materials considered were structural rigid PVC foams. Shock testing showed that this kind of construction performed better than single-skin glass fibre reinforced plastics (GFRP) and traditional wooden construction. The semi-scale 24 m mine countermeasure vessel (MCMV) *Viksten*, which used this concept, was delivered in 1974. After further development and testing, including UNDEX shock

B. Hayman (✉)
Technical University of Denmark, Kongens Lyngby, Denmark
e-mail: bhayman@mek.dtu.dk

S. Gopalakrishnan and Y. Rajapakse (eds.), *Blast Mitigation Strategies in Marine Composite and Sandwich Structures*, Springer Transactions in Civil and Environmental Engineering, https://doi.org/10.1007/978-981-10-7170-6_2

testing of two full-scale test sections, seven *Landsort* Class MCMVs were built for the Swedish Navy, and four more for the Singapore Navy, at the naval shipyard in Karlskrona. The first vessel was delivered in 1984; extensive details are provided by Sjögren et al. [41]. The *Landsort* Class MCMVs were followed by the smaller *Styrsö* Class (four vessels) and by a series of 50 m *Standard Flex* multipurpose vessels for the Danish Navy.

Hellbratt and Gullberg [22] and Gullberg and Olsson [18] referred also to several other Swedish ships, including two 50 m coastguard vessels delivered in the late 1970s and two high-performance surface effect ships (SES) delivered in 1987–1988 for passenger ferry service. A 30 m, 40 km experimental SES with stealth properties, *Smyge*, was due for delivery in 1990–1991; further details were provided by Hellbratt and Gullberg [21] and Olsson and Lönnö [35]. This vessel was designed for dynamic loadings including slamming, but not UNDEX.

In spite of the favourable experience gained in Scandinavia, few other countries adopted the sandwich concept for MCMVs or other naval ships. The main exception was the Australian *Bay Class* inshore minehunter [19, 36, 37].

In the UK, the first major application of fibre composites in a naval ship was the Royal Navy's prototype MCMV *HMS Wilton*, which was commissioned in 1973. Before that, numerous small patrol boats and landing craft had been built in composites, but it was recognised in the late 1960s that the non-magnetic properties of composites could be exploited in MCMV applications, replacing wood as the main structural material. HMS *Wilton* was followed by the *Hunt* Class MCMVs. These were all of stiffened (framed) single-skin GFRP laminate construction. According to Henton [23], Dixon et al. [12] and Chalmers et al. [5], foam-cored sandwich construction had been evaluated but found to have inadequate fire and shock performance. However, the 'sandwich' concept tested appears to have been more like a cellular construction, with internal GFRP webs connecting the inner and outer face sheets [12]; with such internal stiffening the advantage of through-thickness compliance is lost. The discussion of the papers by Sjögren et al. and Chalmers et al. (RINA [38], Vol III) provides an insight into the different perceptions of fire and shock threats, and the different levels of achievement with sandwich hull structures, in the UK and Sweden at that time. However, in the UK, sandwich construction was later used in the superstructure of the *Sandown* Class minehunters [13]. In Italy, a thick GFRP monocoque design, the *Lerici* Class [43], was adopted for MCMVs and later developed into the *Osprey* Class MCMVs for the US Navy [44]. In 1984, the US Navy had previously ordered a lightweight SES concept with 'glass-reinforced plastic structure based on proven Swedish technology' [1, 2] but this programme was cancelled in 1986.

In Norway, a series of high-speed passenger ferries were built in the 1980s, based on the SES concept with PVC foam-cored GFRP composite construction. Meanwhile, the Royal Norwegian Navy (RNON) identified a need to replace its wooden *Sauda* Class MCMVs. Following the success of the *Landsort* MCMV design, together with the Swedish and Norwegian lightweight concepts for passenger ferries using SES technology, RNON began studying the feasibility of using foam-cored sandwich in a relatively lightweight, moderately high-speed concept

that would suit the long Norwegian coastline. The concept was finally adopted and seven vessels were built in the 1990s. These were followed by the development of the *Skjold* Class fast attack craft, but these did not have an UNDEX requirement.

A comprehensive overview of the application of reinforced polymer composites in naval vessels up to about year 2000 is provided by Mouritz et al. [32].

3 Norwegian MCMV Development Programme

In the late 1980s, Det Norske Veritas (DNV, now DNV GL) participated in the series of projects to establish the feasibility of building the Royal Norwegian Navy's new fleet of MCMVs as surface effect ships in foam-cored GFRP sandwich. In a preliminary study, the author attempted to simulate the response of foam-cored sandwich panels to underwater explosions and investigate whether their resistance to such events would be adequate for use in the MCMV hulls. In contrast to steel ship structures, little published work was found at that time on UNDEX response of composite ship structures, and no detailed information was found regarding the response of foam-cored sandwich panels.

The initial studies concluded that the response could be considered in two main phases: the initial, 'very early time' response as the incident shock wave strikes the panel and induces deformations with strain rates of the order $10^3\ s^{-1}$ in the thickness direction of the sandwich composite, and the later 'global' response of the panel as a whole involving bending and transverse shear deformations. In the first phase, the maximum pressure of the incident pulse appeared to be the dominant factor, while in the later phase the total impulse imparted to the panel was more important. The simulations for the initial phase indicated maximum compressive and tensile stresses in the thickness direction that were far in excess of the published static compressive and tensile strengths of available foam cores; thus it was decided that studies of the strain rate dependence of the foam core would be needed. The simulations of the global panel response involved a large degree of uncertainty; it was concluded, in particular, that the modelling of fluid–structure interaction (FSI) must take proper account of cavitation in the water. On the basis of these preliminary studies, it was clear that future simulations must be accompanied by realistic UNDEX tests on full-scale panels, both to validate the simulations and to demonstrate the performance of the final choice of layup.

3.1 UNDEX Tests

The Norwegian UNDEX tests were performed on air-backed panels representing the anticipated bottom panels of the MCMVs. The face sheets were GFRP laminates and the cores were of cross-linked, closed cell Divinycell PVC foam. Based on some early considerations, the panel size (the exposed area between supports)

was chosen as 1500 mm × 1600 mm. The tests were performed jointly by DNV and RNON at the Haakonsvern Naval Base.

More than 50 UNDEX tests were performed. It was necessary to investigate solutions that would satisfy a serviceability type criterion (the event should not cause significant permanent damage, and the ship should be able to withstand repeated shocks at this level) as well as a more extreme survivability criterion. Thus, many of the tests were performed at levels low enough to avoid noticeable damage, so the materials could be modelled as elastic, while others were at levels expected to cause significant, permanent damage. The tests were performed on full-scale panels with realistic charges and (far field) standoffs, and were to a large extent concerned with finding the most severe shocks that could be sustained while retaining full structural integrity, as well as providing detailed data for validating simulation methods. This contrasts with the emphasis that is often laid on maximising energy absorption and providing structural protection, with the sandwich possibly being treated as a sacrificial appendage that must be replaced when damaged.

The three test series involved in all six panels.

Series 1 Two nominally identical, instrumented panels were subjected to 14 UNDEX tests. The face sheets were of GFRP combimat, a combination of E-glass woven roving and chopped strand mat (CSM), with an iso-polyester matrix. The core was Divinycell H200 cross-linked PVC foam. The panels were placed vertically, with their centres 5 m below the water surface. The charges were placed at the same depth, directly in front of the panel centre. A range of charges and standoffs was used, the smallest standoff being 16 m. Only the primary shock wave was expected to affect the critical part of the panel response, so the measurements were mainly confined to this phase of the response. Several tests were performed at relatively low to medium shock levels in order to test repeatability and gather data for comparison with simulations before the shock level was increased to establish the shock capacity. Based on these tests, the simulation methods were modified and attempts were made to determine the layups that would be required to meet the design criteria for the MCMV bottom panels.

Series 2 Two panels, with thicker laminates and denser cores, and two different core thicknesses, were subjected to 16 UNDEX tests. The primary objective was to demonstrate the required shock resistance for application in the MCMVs. However, a few low-medium level shocks were also applied. The tests were mainly similar to those of Series 1, but a few were performed with the panel just below the water surface, to check the effects of surface cut-off (due to the negative reflected wave from the water surface). After the low-medium level shock tests, 100 kg TNT charges were used at decreasing standoffs until failure was observed.

Series 3 Two further panels, with modified face sheet materials compared to Series 1 and 2, were subjected to a total of 21 UNDEX tests. One panel was similar to those in Series 1, but with somewhat thicker face sheets containing a finer woven fabric and only a minimum of CSM. The other panel had thicker face sheets and a

heavier core material. This series included some tests similar to those of the earlier series, but also a large number of tests giving a range of angles of attack and panel and charge depths.

The panels were bolted to one face of an air-filled, welded steel box. This face of the box was open, but fitted with steel flanges 150 mm wide at each edge. The outermost 150 mm of each edge of the test panel were clamped between steel strips and these flanges, leaving the desired area 1500 mm × 1600 mm unsupported between the flanges. The box and TNT charges were held in position by wire ropes, a concrete block on the sea bed and a series of buoys. Figure 1 shows the arrangement for Series 1; minor modifications were made in the subsequent series.

All panels were fitted with strain gauges on the inside and outside face laminates and inside the core. The core gauges were placed so as to record strains in the thickness direction and at ±45°; the latter type of core gauges were intended to measure out-of-plane shear strains, which can be critical for panel performance (though this was not performed successfully in the first test series). A pressure transducer was suspended approximately 920 mm in front of the panel centre.

The strain gauges and pressure transducer were connected to twin-channel transient recorders, which were the only data capture devices available at that time that were fast enough to record the signals. In Series 1 and 2, a total of eight data channels were recorded. In Series 3, an extended arrangement allowed recording of up to 12 additional channels. Recording by the transient recorders was triggered by the incoming pressure signal. Sampling intervals in the range 1–10 μs were used, with the shortest intervals for the pressure and through-thickness strain signals; in

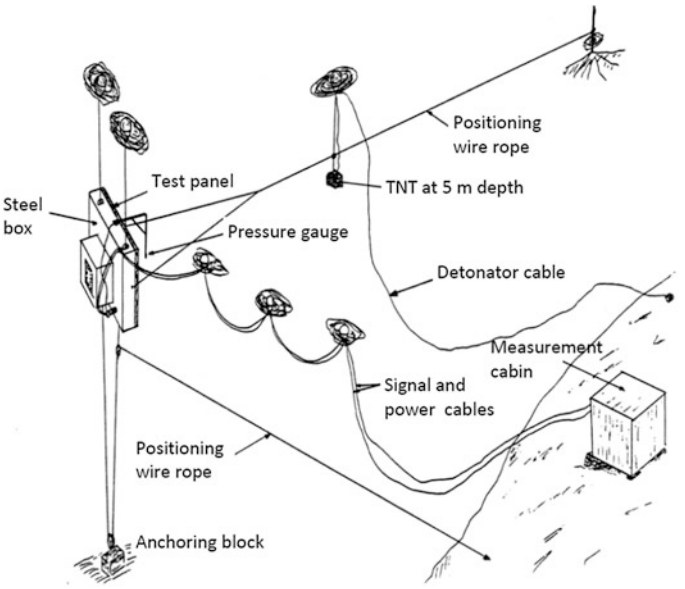

Fig. 1 Test arrangement for first Norwegian UNDEX test series

most cases, the duration recorded was 4096 samples. Paper plots were generated and the data were stored on 3½ inch diskettes in a now obsolete Hewlett Packard format. However, almost all of the test data have recently been retrieved and transferred to modern storage media.

3.2 UNDEX Simulations

At the time of the Norwegian studies, modelling of response and resistance to underwater explosions for composite vessels seems to have been considered unrealistic, although a considerable body of knowledge had been built up concerning the UNDEX response of steel ship hulls during and after the Second World War. Thus, investigation of the suitability of different composite concepts was mainly confined to experimental testing. Furthermore, as mentioned by Mouritz et al. [33], such investigations were often based on simple pass/fail tests and little was done during testing to measure the response or examine closely the failure mechanisms.

The first *published* reports on modelling of UNDEX response of foam-cored sandwich composite structures, to the author's knowledge, appeared in the early 1990s, after the Norwegian studies were completed. Moyer et al. [34] reported on a series of UNDEX tests performed in Sweden on instrumented 2 m × 2 m full-scale ship hull panels mounted on a rebuilt submarine hull section. They also described simulations of these tests using a modified version of DYNA3D based on a doubly asymptotic approximation (DAA) approach [16] and including the effects of surface cut-off (when the wave reflected from the water surface cancels or modifies the tail of the incoming wave) and associated cavitation. The simulations were confined to early times, before fluid flow effects become significant. Good agreement with the corresponding test results was demonstrated. This and later simulations are discussed in Sect. 4.

In parallel with the Norwegian UNDEX tests, analyses were carried out to simulate the panel responses and to perform parametric studies investigating the effects of changing the sandwich layup and the panel dimensions. The simulations were carried out using the finite element program FENRIS, which was coupled to the SESAM suite. FENRIS was an advanced FE program for nonlinear static and dynamic structural analysis; it was used partly for its geometrically nonlinear analysis capabilities and partly because it had good facilities for analysis of transient dynamic response. Composite materials were not implemented; the face sheets were modelled using a combination of bar and membrane elements that approximated the orthotropic elastic properties of the laminates. Attention was confined to the response to the primary shock wave as it was clear that the most severe part of the panel response would occur before the arrival of the subsequent bubble pulses.

The loading was defined with the aid of the empirical approximate formula for the pressure history due to a TNT charge W kg at standoff R m

$$p_i(t) = p_0 e^{-\alpha t}, \tag{1}$$

where

$$p_0 = 52.4\left(W^{1/3}/R\right)^{1.13} \tag{2}$$

and

$$\alpha = 1000/\left(0.0925 W^{0.26} R^{0.22}\right) \tag{3}$$

Here, p_i and p_0 are pressures in MPa, t is time in seconds and α (the reciprocal of the decay time constant) is in s^{-1}.

In the initial studies, various ways of modelling the fluid–structure interaction, as the shock wave struck the panel, were attempted. It was noted that, *for a thin plate*, the early time response could be adequately modelled using the acoustic equation for the resultant pressure on the plate surface [25, 42]:

$$p(t) = 2p_i(t) - \rho c v(t), \tag{4}$$

where ρ and c are the density and acoustic speed for the water and $v(t)$ is the velocity of the plate surface. In combination with the equation of motion for the plate, this predicts that, almost as soon as the plate is set in motion, the pressure just in front of the plate becomes negative, implying that cavitation will occur. Attempts were made to apply this directly in the FE analysis of a sandwich panel by using dashpot elements to represent the second term on the right-hand side of the above equation, and then assuming cavitation occurs as soon as the pressure at the panel surface drops to zero. The plate was then allowed to vibrate freely without any connection to the water. The effect of nonzero cavitation pressures was also investigated; the main effect of this is to move the cavitation site a short distance away from the plate surface. When compared with the first test results, this approach was found to give responses with timescales up to the maximum plate deflection that were much too short. If, instead, cavitation was suppressed and an added mass was assumed in accordance with accepted practice for vibrating, air-backed plates, the simulation gave far too slow a response. It appeared that a response with the correct timescale could only be obtained if it was assumed that a layer of water with thickness of the order 20 cm moved with the plate. The simulations were then performed in two stages: a first phase in which Eq. 1 is applied to the panel with dashpot elements representing the acoustic term, and a second stage in which the dashpots were removed and an extra mass corresponding to 20 cm of water was added to the panel surface.

A possible explanation for this was later given by Hayman [20]. An analysis was presented in which the one-dimensional, linear wave propagation equation was applied to the incoming pressure pulse, its transmission through the face sheet on the water side (assumed to be thin but with mass) and into the core, then its

reflection from the air side face sheet, and finally the wave transmitted back through the wet face sheet and into the water, combining with the tail of the initial incoming wave and the first reflection. This showed that the pressure in the water would drop to zero at *two* sites, one close to the panel surface and one about 10–20 cm away from it. Thus, a body of water of thickness 10–20 cm would be separated from both the panel and the remaining water. Study of the particle velocity of this body of water indicated that it would catch up with the panel as soon as the panel started to slow down as a result of its boundary constraints. This work demonstrated that the through-the-thickness compliance of the foam core has a fundamental influence on the fluid–structure interaction, the incidence of cavitation and the resulting panel response. This analysis is summarised in Sect. 3.3.

In the same analysis, equations were provided for calculating the thickness of the water layer and the 'kick-off' velocity given to this and the panel itself. Approximate, explicit expressions for these quantities were also provided. Under the assumption that the thickness of water moving with the panel remained constant, the subsequent panel motion and stress histories could be easily calculated.

The general approach, in which the occurrence of cavitation was calculated based on one-dimensional wave theory, was subsequently used by Mäkinen in a more detailed analysis in which movement of the cavitation boundaries was also taken into account (see Sect. 4.1). More recent investigations elsewhere have taken cavitation into account with varying degrees of accuracy.

3.3 Simulations: Summary of Analysis by Hayman [20]

The analysis presented by Hayman [20] contained some minor errors in the presented equations. A shortened, corrected version is provided here

3.3.1 Governing Equations

The free field pressure due to the incident pressure wave as it approaches the panel is assumed to be of the form

$$p_i(x,t) = p_0 e^{\alpha(x-ct)/c} \tag{5}$$

in which t is the time, measured from the instant at which the wave arrives at the panel surface, x is the distance from the panel surface (taken as positive into the panel), and c, p_0 and α are as defined previously. It is assumed that all distances x considered in the analysis are small compared with the standoff, so that the wave can be considered plane, and its amplitude can be considered constant as it travels. It is further assumed that the shock wave can be described by linear wave theory. This gives a uniform pressure at the panel surface given by Eq. 1.

On reaching the panel surface, the wave is partly transmitted into the panel and partly reflected. If the outer (water-exposed) skin laminate is thin compared to the sandwich core, it can be approximated by an infinitely thin sheet having a mass per unit area m_f. Then, it is only necessary to consider a transmitted wave in the core and a reflected wave in the water. The pressures at the skin laminate associated with the transmitted wave in the core and the reflected wave in the water are denoted by $p_{c1}(t)$ and $p_{r1}(t)$, respectively. These, and waves generated subsequently, are illustrated in Fig. 2.

The equation of motion for the skin laminate can be written as

$$p_i(t) + p_{r1}(t) - p_{c1}(t) = m_f \dot{v}_1(t) \tag{6}$$

in which $v_1(t)$ is the velocity of the laminate in the positive x direction. The particle velocities at the panel surface for the incident, reflected, and transmitted waves, u_i, u_{r1} and u_{c1}, respectively, are given by

$$u_i = \frac{p_i(t)}{\rho c}, u_{r1} = -\frac{p_{r1}(t)}{\rho c}, u_{c1} = \frac{p_{c1}(t)}{\rho' c'}, \tag{7}$$

where c' and ρ' are the acoustic speed and density for the foam core. The equations for this phase of the response are completed by the compatibility relationships between velocities:

$$u_i(t) + u_{r1}(t) = u_{c1}(t) = v_1(t) \tag{8}$$

When combined with the initial condition $v_1(t) = 0$, Eqs. 5–8 give

$$p_{c1}(t) = \rho' c' v_1(t) = A\left(e^{-\alpha t} - e^{-\beta t}\right) \tag{9}$$

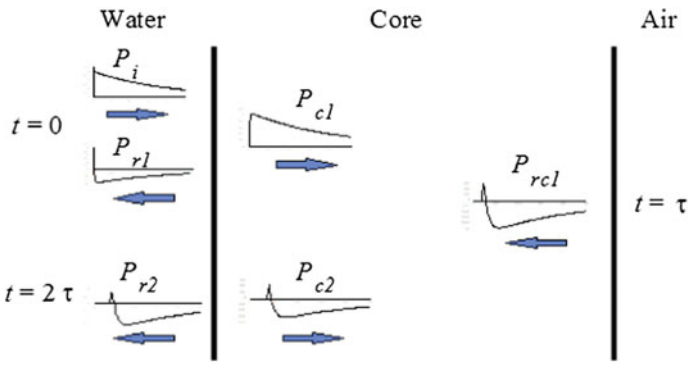

Fig. 2 Waves passing through water and sandwich core. From Hayman [20]

and

$$p_{r1}(t) = p_i(t) - \rho c v_1(t) = B_1 e^{-\alpha t} + B_2 e^{-\beta t}, \tag{10}$$

where

$$A = \frac{2\gamma p_0}{\beta - \alpha}; \quad B_2 = \frac{2(\beta - \gamma) p_0}{(\beta - \alpha)}; \quad B_1 = p_0 - B_2 \tag{11}$$

and

$$\beta = (\rho c + \rho' c')/m_f; \quad \gamma = \rho' c'/m_f \tag{12}$$

Full expressions for the transmitted and reflected waves $p_{c1}(t\text{-}x/c)$ and $p_{r1}(t+x/c)$ as functions of x and t are obtained if t is replaced by $(t\text{-}x/c)$ in Eq. 9 and by $(t+x/c)$ in Eq. 10, respectively.

The transmitted wave is assumed to pass through the core without attenuation, i.e. damping in the core is neglected. The wave reaches the rear (air side) laminate after a time interval τ, where

$$\tau = h_c/c' \tag{13}$$

in which h_c is the core thickness. What happens when the wave reaches the rear laminate (Fig. 2) can be described in a similar way to that used for the front laminate. However, there is a time-shift τ, and the wave that is transmitted into the air behind the panel can be neglected. For simplicity, the rear laminate will be assumed identical to the front laminate.

Then, it can be shown that the velocity of the rear laminate, w_1, is given by

$$w_1(t) = C_1 e^{-\alpha t'} + C_2 e^{-\beta t'} + C_3 e^{-\gamma t'} \tag{14}$$

and the wave that is reflected back through the core, p_{rc1}, is given by

$$p_{rc1}(t) = D_1 e^{-\alpha t'} + D_2 e^{-\beta t'} + D_3 e^{-\gamma t'} \tag{15}$$

in which

$$C_1 = \frac{4\gamma p_0}{(\beta - \alpha)(\gamma - \alpha) m_f}; \quad C_2 = \frac{4\gamma p_0}{(\beta - \alpha)(\beta - \gamma) m_f}; \quad C_3 = -(C_1 + C_2) \tag{16}$$

$$D_1 = \frac{-2\gamma(\alpha + \gamma) p_0}{(\beta - \alpha)(\gamma - \alpha)}; \quad D_2 = \frac{-2\gamma(\beta + \gamma) p_0}{(\beta - \alpha)(\beta - \gamma)}; \quad D_3 = -(D_1 + D_2) \tag{17}$$

and

$$t' = t - \tau \tag{18}$$

When the wave that has been reflected back through the core reaches the front skin laminate after a further time interval τ, a similar event occurs to that described previously. A wave $p_{r2}(x, t)$ is transmitted back into the water and a new reflected wave $p_{c2}(x, t)$ is generated in the positive x direction in the core (Fig. 2). It can be shown that pressures at the front laminate due to these two waves, and the additional velocity generated in the laminate, v_2, are given by

$$p_{r2}(t) = -\rho c v_2(t) = E_1 e^{-\alpha t''} + \left(E_2 + E_3 t''\right) e^{-\beta t''} + E_4 e^{-\gamma t''} \tag{19}$$

and

$$p_{c2}(t) = F_1 e^{-\alpha t''} + \left(F_2 + F_3 t''\right) e^{-\beta t''} + F_4 e^{-\gamma t''}, \tag{20}$$

where

$$E_1 = \frac{2(\beta - \gamma) D_1}{\beta - \alpha}; \quad E_4 = 2D_3; \quad E_2 = -(E_1 + E_4); \quad E_3 = 2(\beta - \gamma) D_2 \tag{21}$$

$$F_1 = D_1 \left(1 - \frac{2\gamma}{\beta - \alpha}\right); \quad F_4 = D_3 \left(1 - \frac{2\gamma}{\beta - \gamma}\right); \quad F_2 = -(F_1 + F_4); \quad F_3 = -2\gamma D_2 \tag{22}$$

and

$$t'' = t' - \tau = t - 2\tau \tag{23}$$

After a further interval τ, $p_{c2}(x, t)$ reaches the rear laminate and generates a new reflected wave $p_{cr2}(x, t)$ in the core and an additional velocity w_2 in the laminate. The process repeats itself indefinitely, the pressure waves and additional velocity components having progressively smaller amplitudes. The resultant pressure and velocity histories at a given location can be found by superimposing the separate waves or velocity components.

3.3.2 Resultant Pressure Distributions and Histories

The resulting pressure histories in the water at various distances from the panel have been calculated for a number of explosion cases and typical sandwich layups using a spreadsheet program. The program also allows study of the through-the-thickness stresses and strains in the core and the motions of the skin laminates. The case of a

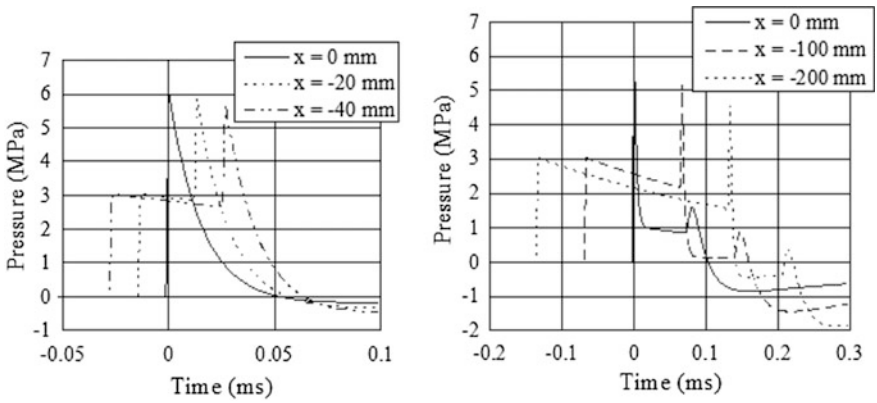

Fig. 3 Pressure histories in water at various distances from panel surface: thin plate (left) and sandwich plate (right). From Hayman [20]

thin plate or single-skin laminate can be analysed using the same program. Only the waves shown in Fig. 2 are included. Thus, the program does not give valid results for times when $p_{cr2}(x, t)$ or subsequently generated waves have reached the point in question. This means that, at the panel surface, $x = 0$, the results are only valid for $t \leq 4\tau$.

Figure 3 (left) shows the pressure histories at positions 0–40 mm from a thin plate having mass 24 kg/m^2 that is exposed to a shock wave with $p_0 = 3.0$ MPa and $\alpha = 2580$ s^{-1}. This shows that negative pressures are first generated at the plate surface, 0.05 ms after the shock wave arrives at the plate. Thus, if the cavitation tension is zero, cavitation can be expected at the plate surface. If a cavitation tension of 1 bar (0.1 MPa) is assumed, cavitation starts about 10 mm away from the panel.

Figure 3 (right) shows the corresponding case with a sandwich panel having approximately the same *total* mass per unit area. This panel has 4 mm thick GFRP skins and a 60 mm thick core of 200 kg/m^3 PVC foam. The analysis shows that, for zero cavitation tension, cavitation first occurs at the panel surface, about 0.10 ms after the shock wave arrives at the panel. The delay as compared to the thin plate is due to the time taken for the transmitted wave in the core to reach the rear skin and be reflected back to the panel/water interface ($2\tau \approx 0.07$ ms for this panel). However, at about the same time, cavitation also occurs independently at 125 mm from the panel as the negative part of the first reflected wave cancels the 'tail' of the incoming shock wave.

The influence of a nonzero cavitation tension can be studied from Fig. 3 (right) and the associated analysis. For a cavitation tension of 1 bar (0.1 MPa), there is little change. Cavitation is still initiated at the panel surface, at a time that is only a few microseconds later than for zero cavitation tension. The second cavitation site is moved about 15 mm further away from the panel, with initiation occurring at $t \approx 0.11$ ms, i.e. about 0.01 ms later than with zero cavitation tension.

Similar analyses with different shock waves show some interesting features. Increasing p_0 without changing α simply scales all the pressure histories up in proportion with p_0. This has no effect on the prediction of cavitation for the case of zero cavitation tension. However, it reduces the influence of a given nonzero cavitation tension. Reducing α (larger charges and/or standoffs) increases the distance between the second cavitation site and the panel, and delays cavitation initiation at this position. Increasing α (smaller charges and/or standoffs) leads to smaller cavitation distances, and can result in cavitation being initiated at the more remote position before it is initiated at the panel surface. For typical explosion cases considered in design of MCMV hulls, and typical sandwich layups for this application, the distance of the second cavitation site from the panel appears to be in the range 100–300 mm, in agreement with the observation mentioned in Sect. 3.2.

3.3.3 Subsequent Behaviour of Cavitated Region

Bleich and Sandler [4] considered the behaviour of a region of water between a submerged explosive charge and a thin plate suspended horizontally above it at the water surface. They showed that cavitation was first initiated just below the plate, and subsequently expanded and contracted with the upper and lower boundaries of the cavitated region migrating in a complex fashion, before the cavitated region finally closed. For the case of the vertical sandwich panel with cavitation occurring at two sites, the behaviour may be more complicated still. For this case, it was considered desirable to establish whether the mass of water between the two cavitation sites remains constant, and how long it remains detached from the panel and the main body of water.

By considering particle velocities associated with the respective pressure waves, it is possible to argue that the main body of water (outside the cavitated region) is moving towards the panel and slowing down. The water between the two cavitation sites has a zero resultant force acting on it as the pressures in the two cavitated regions can be assumed equal. This mass of water must therefore continue moving with a constant mean velocity once cavitation is established at the two locations, so the gap between this and the main body of water must continue to increase. Initially, the central region of the panel, which is uncoupled from the water, moves with constant velocity but then the boundary restraints cause the panel to slow down. The uncoupled water then catches up with the panel and the cavitated region adjacent to the panel closes. The panel and the water mass are now moving together, but are still separated from the main body of water.

The panel continues to slow down. Eventually, it reaches its maximum deflection and begins to swing back again towards its original position. Sooner or later, the main body of water and the panel will come to the same position. Observations in the DNV shock tests suggested that final cavitation closure occurred after the maximum deflection and stresses had been reached in the panel. (Later assessments are discussed in Sect. 4.3).

3.3.4 Formulae for Cavitation Initiation Time and Location

Cavitation at the panel surface will occur at time t_{cav1}, which is shortly after the reflected wave from the rear skin reaches the panel/water interface. This occurs at a time interval 2τ after arrival of the incoming shock wave, so

$$t_{\mathrm{cav1}} = 2\tau = 2h_c/c' \tag{24}$$

Cavitation at the second site occurs when the combined pressure from the incoming shock wave and the first reflected wave drop to a critical value p_{cav}, i.e. when

$$p_0 e^{-\alpha(t-x/c)} + B_1 e^{-\alpha(t+x/c)} + B_2 e^{-\beta(t+x/c)} = p_{\mathrm{cav}} \tag{25}$$

The location of the second cavitation site and the time at which cavitation is initiated there are found by calculating the smallest value of t that satisfies Eq. 25, and finding the corresponding value of x. This is achieved by differentiating Eq. 25 with respect to time, setting $dt/dx = 0$, and solving the resulting equation simultaneously with Eq. 25 itself. When $p_{\mathrm{cav}} \neq 0$, this requires numerical solution. However, when $p_{\mathrm{cav}} = 0$ explicit solutions exist for the position x_{cav2} (or distance ahead of the panel, $X_{\mathrm{cav2}} = -x_{\mathrm{cav2}}$) and the time t_{cav2} at which cavitation occurs

$$t_{\mathrm{cav2}} = \frac{1}{\beta-\alpha}\left[\frac{\alpha+\beta}{2\alpha}\ln\left(\frac{\alpha+\beta}{\alpha+\beta-2\gamma}\right) + \ln\left(\frac{\beta-\gamma}{\alpha}\right)\right] \tag{26}$$

and

$$X_{\mathrm{cav2}} = -x_{\mathrm{cav2}} = \frac{c}{2\alpha}\ln\left(\frac{\alpha+\beta}{\alpha+\beta-2\gamma}\right) \tag{27}$$

3.3.5 Formulae for Impulse and Kick-off Velocity

The kick-off velocity V_0 of the panel can be obtained by calculating first the impulse imparted to a unit area of the panel and water that moves with it, and then dividing by the combined mass per unit area M. The impulse J is calculated by integrating the pressure at the cavitation position with respect to time, from the instant the incoming shock wave arrives there to the time t_{cav2}. The main contribution J_i is from the incoming shock wave, but there is also a small, negative contribution J_{r1} from the first reflected wave

$$J = J_i + J_{r1}, \tag{28}$$

where

$$J_i = \frac{p_0}{\alpha}\left(1 - e^{-\alpha(t_{\text{cav2}} - x_{\text{cav2}}/c)}\right) \tag{29}$$

and

$$J_{r1} = p_0\left[\frac{2(\beta-\gamma)}{\beta(\beta-\alpha)}\left(1 - e^{-\beta(t_{\text{cav2}} + x_{\text{cav2}}/c)}\right) - \frac{\alpha + (\beta - 2\gamma)}{\alpha(\beta-\alpha)}\left(1 - e^{-\alpha(t_{\text{cav2}} + x_{\text{cav2}}/c)}\right)\right] \tag{30}$$

The kick-off velocity is then

$$V_0 = J/M, \tag{31}$$

where

$$M = 2m_f + \rho' h_c + \rho X_{\text{cav2}} \tag{32}$$

3.3.6 Simplified Expressions

Some approximations can be made that simplify some of the above expressions. In practice $\beta \gg \alpha$, so that Eqs. 26 and 27 give

$$t_{\text{cav2}} \approx \frac{1}{2\alpha}\ln\left(\frac{\beta}{\beta - 2\gamma}\right) + \frac{1}{\beta}\ln\left(\frac{\beta-\gamma}{\alpha}\right) \tag{33}$$

and

$$X_{\text{cav2}} = -x_{\text{cav2}} \approx \frac{c}{2\alpha}\ln\left(\frac{\beta}{\beta - 2\gamma}\right) \tag{34}$$

A more approximate estimate of t_{cav2} is obtained by neglecting the second term on the right-hand side of Eq. 33. This is equivalent to taking

$$t_{\text{cav2}} \approx -x_{\text{cav2}}/c \tag{35}$$

In calculating the impulse, a good approximation is to neglect J_{r1} while using the simple relationship for t_{cav2}, Eq. 35, in Eq. 28:

$$J \approx J_i \approx \frac{P_0}{\alpha}\left(1 - e^{2\alpha x_{\text{cav2}}/c}\right) \tag{36}$$

3.3.7 Subsequent Global Panel Response

If it is assumed that the mass of water moving with the panel remains constant following cavitation initiation at the remoter cavitation site, analytical or numerical methods can be used, together with the above equations to estimate the subsequent response of the panel. Rough estimates can be obtained using the following formulae, which consider bending deformations but neglect both out-of-plane shear deformations and local bending of the individual skin laminates.

The period of oscillation, T, the maximum deflection, $\Delta_{\max}$ and the maximum laminate strain at the centre of the panel, $\varepsilon_{\max}$ can thus be estimated from

$$T = K_T \sqrt{\frac{M a^4}{E_f h_f \left(h_c + h_f\right)^2}}; \tag{37}$$

$$\Delta_{\max} = K_\Delta V_0 \sqrt{\frac{M a^4}{E_f h_f \left(h_c + h_f\right)^2}}; \tag{38}$$

$$\varepsilon_{\max} = K_\varepsilon V_0 \sqrt{\frac{M}{E_f h_f}} \tag{39}$$

In the above, the coefficients K_T, K_Δ and K_ε are functions of the plate aspect ratio and boundary support conditions and of Poisson's ratio for the skin laminates, and a is one of the panel dimensions.

3.3.8 Comparisons with Test Results and Other Analysis Methods

Figure 4 shows histories of compressive strain in the core of a sandwich panel resulting from (a) use of the above theory, without the simplifying approximations, (b) use of a one-dimensional finite element model consisting of 13 bar elements connected end-to-end and (c) measurements using a strain gauge embedded in the sandwich core. In case (b), the front laminate is modelled with four elements, the core with eight elements and the rear laminate by a single element. The applied shock load is simulated using Eq. (4): the free field pressure is doubled and a damper element used to give the velocity term.

The principal difference between curves (a) and (b) is the initial part of the response associated with the transmission of the shock wave through the front laminate, model (b) taking account of the finite thickness of this laminate. Also, case (a) is not valid after a time of about 0.12 ms, when the second reflection from the air side laminate reaches the point in question. Nevertheless, case (a) models the important aspects quite well.

The measured strain history (c) is very similar to curve (b). The differences may be partly due to the fact that the properties of the core were not measured accurately

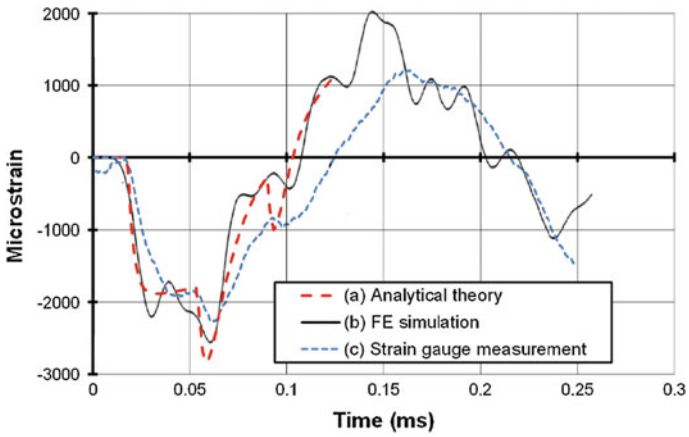

Fig. 4 Strain histories in the core by theory and experiment

at the relevant strain rates. There may also be some error in the measurement due to stiffening of the core by the strain gauges, though calibration tests suggested that this error is unlikely to be more than a few percent for the type of foam core and strain gauge used. Also, the position of the strain gauge does not correspond exactly to the Gauss point at which the FE analysis results are taken, and damping of the waves by the core is not taken into account in the models.

A further indication of the validity of the analytical model was obtained by studying how well Eqs. 37 and 39 agreed with experimental data from the UNDEX tests described in Sect. 3.1. The coefficients in the equations were obtained from thin plate solutions given in data books. Thus, the periods of oscillation estimated from strain gauge readings on four sandwich panels with the same overall dimensions but different layups, and with a wide range of shock loads, were plotted against values from Eq. 37, and maximum measured strains from the same tests were compared with those given by Eq. 39. The resulting plots are not included here as they contain a considerable degree of uncertainty, especially in relation to the assumed panel boundary conditions. Nonetheless, the trends predicted by the analyses were confirmed.

3.3.9 Effect of Sandwich Layup

The simple model described above allows rapid evaluation of the influence of such aspects as sandwich layup on underwater explosion response.

Influence of core density For typical PVC foam cores, increasing the density leads to a corresponding increase in elastic modulus, so that the acoustic speed is scarcely affected. However, the increased density itself results in reflected and transmitted waves of higher amplitude. This leads to higher through-thickness stresses in the

core, and slightly higher pressures in the water. There is a marked increase in the distance X_{cav2} of the more remote cavitation site from the panel. For the same incoming shock wave, this distance is roughly proportional to the core density. The impulse applied to the panel and water layer is also increased, so that the panel deflection and laminate stresses are increased somewhat.

Influence of core thickness Changing the core thickness has no effect on cavitation at the more remote site but has a major influence on the time at which cavitation occurs at the panel surface. For a very thick core, cavitation at the more remote site is likely to occur first. For very thin cores, the situation approaches that of a thin plate, and cavitation may occur so early at the plate surface that the reflected wave is prevented from generating cavitation at a more remote position. Provided the behaviour does not change fundamentally, the main visible effect of an increase in core thickness predicted by the present theory is a reduction in panel deflection, but the maximum stress in the laminates is scarcely affected.

Influence of laminate thickness Increasing or decreasing the mass per unit area of the skin laminates has a similar effect to increasing or decreasing the core thickness, except that the laminate stresses are reduced proportionately with the maximum deflection.

3.3.10 Comments and Conclusions from the Study

Simple wave theory was used to derive cavitation conditions, and hence to estimate the kick-off velocity of a sandwich panel when subjected to underwater shock loadings, together with the mass of water that moves with the panel. The theory appeared to explain several observations from explosion tests:

- It showed why a layer of water with thickness of order 20 cm moves with the panel.
- It demonstrated that the thickness of this layer, and hence the period of oscillation, varies with the applied shock load.
- It explained the observed variation of both period and maximum laminate strain with panel layup and shock load.

In the original paper, it was noted that, in principle, it would be quite straight forward to include waves generated by further encounters with the skin laminates. However, the analytical expressions become more complex. This is only needed if prediction of pressures, stresses, etc., are needed for later times. The analytical theory presented works best for sandwich panels with thin skin laminates. For thicker skins, it may be necessary to correct the results for the time delays as the stresses due to the respective waves build up in the skin laminates.

In many practical applications involving hulls of surface ships, the incoming primary shock wave is truncated by the arrival of a tensile reflected wave from the free water surface. This effect is easily included in the analytical model.

The major question that was left open concerned the possible movement of cavitation boundaries following initial cavitation at the two sites as described previously. To provide insight into this point, it was suggested that analyses of the type performed by Bleich and Sandler [4] or Driels [14] would need to be performed for some typical cases. In fact, Mäkinen and others have taken up this point, as discussed in Sect. 4.

4 Subsequent Simulation Studies

Several studies of the response of sandwich panels to UNDEX loading have been published since 1995. Some follow directly on from Hayman [20], by considering primarily elastic response of hull panels with polymer foam cores. Others are more concerned with providing strength and energy absorption as a protection against UNDEX shock, and consider a wider range of materials (in particular utilising the ductility of metals). The following summarises studies of both types, with focus on the modelling of FSI effects and associated cavitation.

4.1 Studies by Mäkinen and Colleagues

At the same conference as that at which the work summarised in Sect. 3.3 was presented, Mäkinen [27] also presented the results of some tests and simulations on a foam-cored GFRP sandwich panel. The simulation was carried out using the DAA method as implemented in the USA-STAGS software. The surface cut-off effect was included, as was cavitation at the panel surface, but the possibility of cavitation at other locations does not seem to have been considered. The author commented that because of surface cut-off effects the important parts of the response all occurred at early times, so that the use of simpler methods, such as that described by Moyer et al. [34], referred to in Sect. 3.2, could be expected to give good results.

Mäkinen followed up the above work in a doctoral thesis [29] that included two published journal articles, one conference paper and one paper that does not appear to have been published outside the thesis. First, he investigated [28] the formulation of relevant cavitation models and compared their predictions. Second [30], he applied an appropriate model to the incidence of a primary shock wave on a 1-D model for the through-thickness response of a foam-cored sandwich panel, taking account of movement of the cavitation boundaries. Thus, Hayman's analysis was modified and extended to include movement of the cavitation boundaries and also to include further internal reflections of the shock wave inside the sandwich core. This treatment was still entirely one-dimensional. It gave predictions very similar to

Hayman's in terms of stress and strain values inside the core. A further paper by Mäkinen and Kadyrov [31] applied this one-dimensional fluid–structure interaction model (with cavitation) to simulate an experimental test carried out in the Swedish MCMV programme. The test arrangement was that described by Moyer et al. [34]. Rather few details are provided from the tests, but the agreement between modelling and testing appears to have been very satisfactory. Unfortunately, it is not possible to compare the analysis directly with Hayman's simpler model. Note that this modelling is still essentially considering an early time approximation since it is an acoustic model and fluid flows across the plate are not considered. Mäkinen's thesis includes a further paper that does not appear to have been published; this applies the same approach in a parametric study of sandwich beams (as opposed to panels) with differing layups.

4.2 Studies Concerned with Protection and Energy Absorption

In the late 1990s, interest was aroused in the potential of sandwich structures to absorb energy in collisions and under blast loadings. The main objective was to establish the extent to which sandwich beams or panels would perform better than solid beams or plates of the same mass. Some of the studies performed were funded by the US Office of Naval Research (ONR). They were primarily concerned with metal sandwich structures, including some with (mainly metal) foam cores, and considered nonlinear, inelastic behaviour. They are briefly described here because they show how the FSI and cavitation modelling has been developed since Hayman's and Mäkinen's studies.

Deshpande and Fleck [8] presented constitutive laws for metal (aluminium alloy) foams that might in future be used in sandwich cores. The same authors subsequently [9] investigated the multiaxial yield behaviour of some PVC foams.

Xue and Hutchinson [45] appear to be among the first to consider specifically blast loading on metal sandwich structures. They considered a metal sandwich, with properties appropriate to truss cores, and focused on achieving high strength and energy absorption. They neglected strain rate dependence and FSI, while referring briefly to Mäkinen [29, 30], but mentioned that these simplifications could be expected to lead to pessimistic results in the case of UNDEX loadings. The same authors [46] later published a comparative study of blast-resistant metal sandwich plates.

Deshpande and Fleck [10] considered both metal and PVC foam-cored sandwich beams under air blast loading. They considered two phases—core compression (treated as inelastic) and global beam bending and stretching. They suggested that the results could be applied to UNDEX loadings but mentioned that FSI would have a beneficial effect. Fleck and Deshpande [15] compared a series of competing metallic core concepts. They divided the response into three stages: Stage I,

fluid–structure interaction (the initial primary shock transient, during which they assumed that the core and back face would remain stationary); Stage II, core crushing; and Stage III, overall bending and stretching. Stages I and II were treated one dimensionally, as in Hayman [20], Mäkinen and Kadyrov [31] and Mäkinen [30]. For UNDEX cases, they also introduced an 'FSI parameter', $\psi = \rho c/\alpha m_f$ (using the notation of Sect. 3.2), by which the theoretical impulse transmitted to a fixed, rigid structure would be reduced by the motion of the skin laminate. The sandwich cores they considered were relatively thick (0.1–1.0 m).

Hutchinson and Xue [24] studied the optimisation of metal sandwich plates for resistance to short pressure pulses. They followed the approach of Fleck and Deshpande [15], but improved on the FSI description of Stage I by accounting for the resistance the core offers to the motion of the front face sheet. They note that this results in cavitation being initiated some way from the plate surface, rather than at the plate surface itself. They then assume that the layer of water between the plate and the cavitation plane moves with the plate and remains with constant thickness —just as assumed by Hayman [20]. They note that the cavitated region will in fact close after some time, causing an additional transmitted impulse, but argue that this is small compared to the main impulse. Liang et al. [26] made further refinements to the model of Hutchinson and Xue [24], to give a better estimate of the momentum transmitted to the panel from the water taking account of the motion of the cavitation boundaries. Deshpande and Fleck [11] also used one-dimensional models to explore the FSI effects, including cavitation, for metal sandwich panels with crushable foam cores. They developed extensive maps showing differing regimes of behaviour. They treated the cores as inelastic, and observed that in practical cases of interest the core can be treated as an ideally plastic-locking solid (i.e. as rigid-plastic with a densification limit). It should be noted that the explosion cases they considered as typical have appreciably shorter pulse durations (around 0.1 ms) than in the Norwegian and Swedish studies.

Schiffer [39], in a recent doctoral thesis, investigated the response of both water- and air-backed composite laminates using both 1-D models (with FSI and modelling of moving cavitation boundaries) and corresponding tests using a shock tube. Based on a part of this work, Schiffer and Tagarielli [40] considered the specific case of a foam-cored sandwich layup with metal face sheets. FSI experiments and FE calculations were performed in order to examine the one-dimensional response of both water-backed and air-backed sandwich plates subject to blast loading in either deep or shallow water. The sandwich plates had rigid face sheets and low-density metal and polymer foam cores. The experiments were conducted in a transparent shock tube, allowing measurements of both structural responses and cavitation processes in the fluid. The simulations focused on estimation of the position of cavitation initiation, movement of the cavitation fronts, and the transmitted impulse and its dependence on parameters such as the core strength and stiffness and water pressure. It represented a further refinement of the approach of Liang et al. [26]. The study was more nuanced than previous ones, and showed that the sandwich solutions did not always perform better than corresponding solid plates.

4.3 Recent Work

Extensive studies, supported by the ONR, have been carried out in recent years at Imperial College London (ICL) into the underwater and air blast performance of polymer foam-cored sandwich panels. The work has largely involved physical testing [3, 7], and modelling has mainly been confined to air blast cases. The UNDEX testing has been confined to quite small panels (0.4 m × 0.3 m) exposed to blasts from small charges (1.0–1.4 kg of C4 explosive) at small standoffs generating peak pressures (30–43 MPa) that are far higher than in the Norwegian tests reported in Sect. 3.1. The resulting response involved severe compression of the SAN foam cores combined with face sheet damage.

In a recent collaboration between the present author and researchers from ICL and Nanyang Technological University, Singapore, attempts have been made to simulate some of the UNDEX tests reported in Sect. 3.1 using the explosion modeller and acoustic elements in ABAQUS. The initial trials are described below. Further trials have been conducted but are not reported here. The purpose of the studies has been to establish whether the proposed modelling approach can reproduce the main features of the response of foam-cored sandwich panels to a primary shock wave. The approach is confined to 'early times', in the sense that fluid flow effects are not included; however, use of a three-dimensional model removes some of the restrictions imposed by one-dimensional modelling of the acoustic phase in earlier analyses. Inclusion of the test box in the model reduced the uncertainties regarding panel boundary conditions.

4.3.1 Test Case Considered

Data from the two similar tests in Series 1 (Sect. 3.1) were used to validate the model results. Each face sheet laminate consisted of one layer of 300 g/m^2 chopped strand mat (CSM), two layers of 800 g/m^2 woven roving (WR) fibres each with an additional 300 g/m^2 CSM and a final 300 g/m^2 CSM layer. The matrix was iso-polyester Norpol 72–80, and the fibre weight fraction was approximately 50%. The total thickness of each face sheet was approximately 3.5 mm. A 60 mm thick Divinycell H200 closed cell PVC foam core was used, giving a total panel thickness of 67 mm. The blast pressures were generated with 14 kg of TNT at 30 m standoff distance. This relatively low blast level was chosen in order to validate the modelling method without the need for implementing accurate material failure and degradation laws.

4.3.2 FEA Models

The FEA models were built using ABAQUS 6.9 (Dassault Systèmes [6]). Initially, the test panel was modelled in isolation, assuming clamped boundary conditions.

While this was seen to give promising results, it was found that improved agreement between tests and simulation could be achieved by including the steel test box in the model. A quarter model of the panel and test box with appropriate symmetry boundary conditions was used (Fig. 5), though this does not allow accurate modelling of the variation of static pressure with depth. The core was modelled using 3D hexahedral stress elements with reduced integration and hourglass control. Quadrilateral shell elements with reduced integration and hourglass control were used for the skin laminates and for the steel box components. An element size of 10 mm was used throughout.

The water surrounding the test box and panel was modelled separately using tetrahedral acoustic elements. These elements have a pressure degree of freedom and are therefore able to model the blast wave propagation. Additionally, cavitation can be simulated by setting a minimum pressure the medium can sustain. The degree of FSI that is modelled corresponds to the 'early time' solution for a thin plate presented by Taylor [42]; it does not include fluid flow effects.

The parameters for the material models were obtained from tests performed on the same material types used in the panel manufacture. For simplicity, the H200 foam core was modelled with an isotropic, linear elastic material. The assumed Young's modulus was 250 MPa and the Poisson's ratio was 0.39. Each face laminate was modelled as a single layer shell. A laminar anisotropic elastic model was used, so that appropriate damage models could be used in later analyses. However, the same overall properties were applied in both directions. The Young's modulus and the shear modulus were assumed to be 14.6 GPa and 2.8 GPa, respectively, whilst the Poisson's ratio used was 0.17. The steel box was modelled with a linear elastic material with density 7800 kg/m^3, Young's modulus 210 GPa and Poisson's ratio 0.3. The density of the sea water was assumed to be 1025 kg/m^3 and the bulk modulus to be 2.1 GPa, whilst the cavitation limit was set at −75 kPa (tension, absolute pressure). Note that, because of the static ambient pressure of approximately 150 kPa due to atmospheric pressure and the 5 m water depth, this

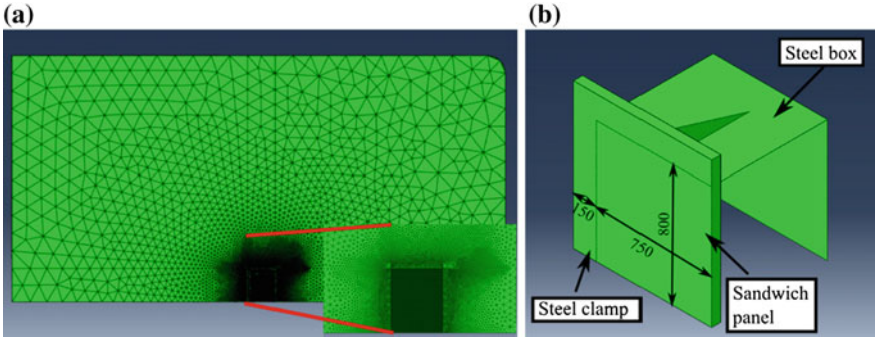

Fig. 5 Images of the FEA quarter model showing: **a** the acoustic mesh around the box structure, and **b** the test panel and the steel box providing the key dimensions of the panel

requires the shock wave to induce a pressure of −225 kPa in order to initiate cavitation.

The inbuilt underwater blast simulation tool in ABAQUS was employed to simulate the blast pressure waves. The tool uses equations derived by Geers and Hunter [17] to simulate both the initial shock wave and the dynamics of the gas bubble created at the charge location. In this case, the bubble pulses were neglected due to the large charge distance, and the analysis was confined to the effects of the initial shock wave. The software required the input of similitude parameters for the explosive used as well as the physical characteristics of the blast, including its position and the quantity of explosive material. The relevant parameters were obtained from Geers and Hunter [17], based on 1.52 g/cm^3 TNT.

4.3.3 Results

The results from the FE models were compared to the strain and pressure histories recorded during the blast tests. The FE pressure results were extracted at a location close to that of the pressure gauge. The maximum simulated pressure was 2.75 MPa, compared to recorded values of 3.0 MPa in both tests. Whilst the simulated peak is lower than the measured data by approximately 10%, the FE pressure rise time was longer, with a smoother rise and peak. The impulse recorded in the experimental tests was approximately 800 Pa s in the first millisecond, shortly after which the reflected wave from the target reached the sensor and the recorded signals became chaotic. The FE impulse in the same time period was 1050 Pa s. Note that this is the integral of the incoming pressure at the gauge with respect to time, and is not the same as the impulse actually imparted to the panel.

The strains at the centre of the panel on the water side and on the air side were compared, as shown in Figs. 6 and 7. The FE results for the water side strains matched closely the experimental data until about 15 ms. The air side data matched the experimental results up to the first peak at about 6 ms. Following this, the results diverge, with the strains decreasing less rapidly in the numerical analysis data.

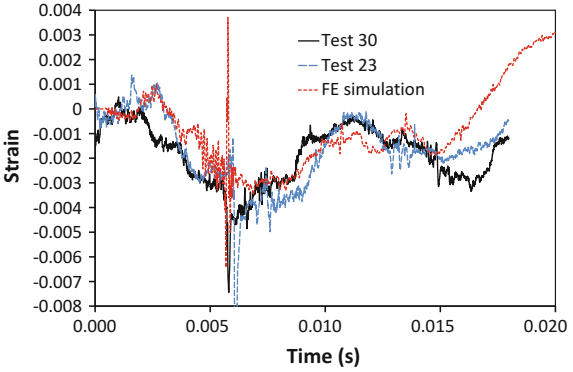

Fig. 6 Water side vertical strains. The FEA results are compared to two sets of experimental data

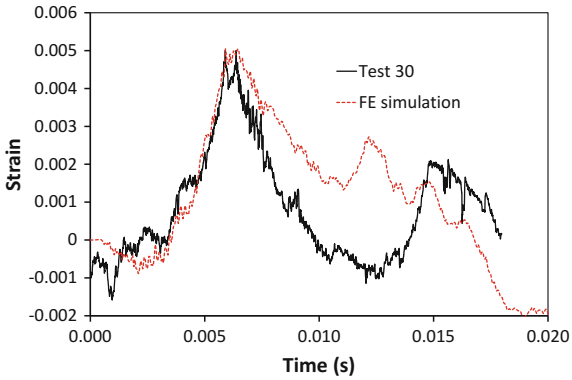

Fig. 7 Air side vertical strains. The FEA results are compared to the test results

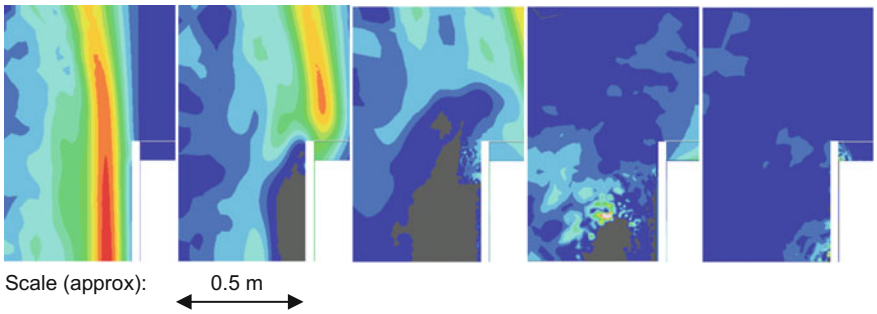

Fig. 8 Simulated pressure fields at time instants $t = 0$, 0.25, 0.5, 2.5 and 5.5 ms from arrival of incident shock wave at panel surface. Cavitated regions are shown in grey

The pressure fields at successive time instants have also been studied (Fig. 8). Immediately after arrival of the shock wave at the panel surface, the simulation indicates a region of cavitation adjacent to the front skin laminate. However, after less than 0.25 ms, a layer of uncavitated water appears at the panel surface, with a region of cavitation beyond this. The thickness of this uncavitated water layer grows rapidly to about 150 mm over the next millisecond or so. Then a cavitation layer reappears at the panel surface, while the thickness of the region of uncavitated water increases to a maximum between 200 and 250 mm while its boundary becomes more irregular. The picture becomes more chaotic, until eventually the last region of cavitation collapses, at about 5 ms after arrival of the shock wave. This probably explains the sharp spike in the strain histories (both measured and simulated) seen in Fig. 6. Thus, over a significant part of the response there appears to have been an uncavitated layer of water adjacent to the panel surface, as predicted by the simplified theory of Hayman [20]. However, whereas Hayman's early theory predicts an uncavitated layer with thickness approximately 150 mm for the present

case, and assumes this to remain constant, the FE simulation shows that it varies with time, reaching a maximum value somewhat greater than this magnitude before the picture becomes chaotic and the cavitation begins to close again.

4.3.4 Discussion and Conclusions

The FE analysis showed that many of the important features of the measured response could be replicated using the UNDEX simulation option in ABAQUS, combined with the use of acoustic elements for the water. The measured strain histories at the centre of the wet face laminate were well reproduced to times well beyond the peak deformation. That at the centre of the air side laminate was also accurately reproduced up to a time just after the peak response, but then the simulation gave a less rapid fall in strain values than the measurements. The UNDEX simulation option of ABAQUS approximately replicated the peak of the generated pressure pulse, though the numerical result was somewhat lower than the measured value, and the rise time was longer, which affected the impulse and the pulse shape. This may have changed the conditions regulating the cavitation of the medium. Whilst this introduces some inaccuracy in the model, the strain results obtained indicate that the system might be relatively insensitive to this in the simulation. The results suggest that the 'early time' acoustic model with cavitation is able to predict the maximum panel deformations and stresses, but effects due to the fluid flows around the target need to be taken into account, using a full computational fluid mechanics model, if the response at later times is to be investigated.

The simulation showed the formation and eventual closure of a region of cavitation ahead of the target panel, while for the major part of the response up to the peak deformation, an uncavitated layer of water moves with the panel. This is consistent with the predictions by Hayman [20] using simple one-dimensional plane wave propagation theory. However, while Hayman assumed that the thickness of the uncavitated layer would remain constant, the present simulation shows that the cavitation boundaries move and the thickness varies with time.

Some differences between the predicted and measured responses may be due to inaccuracies in the model of the box, which had to be simplified in the simulation. Additionally, the air medium inside the box was not included in this model.

5 Conclusions and Implications for Shock Mitigation Studies

An attempt has been made to trace the history of naval (and some relevant civilian) vessels using foam-cored sandwich, with particular focus on those with UNDEX requirements, and on the associated testing and modelling. The early modelling work performed by the author around 1990 has been summarised, as have the

developments of this by Mäkinen, and the work performed by Hutchinson and colleagues at Harvard and by Fleck, Deshpande and others at Cambridge, which focused especially on metallic sandwich with inelastic cores but included progressively improved FSI and cavitation descriptions. It culminates with quite recent work at the University of Oxford and Imperial College London, the latter in collaboration with the author.

Several points have arisen that have implications for shock mitigation studies:

- There are significant differences between modelling requirements for MCMV hull design and those for blast protection, and the results and conclusions cannot necessarily be transferred between these types of applications. Hull design for MCMVs focuses on avoidance of damage and maintenance of predominantly elastic behaviour, while blast protection focuses on use of inelastic behaviour to absorb energy.
- Sandwich panel responses for both types of application deviate from the classical theory by Taylor for thin plates, but in different ways.
- Changing the sandwich layup may be used to reduce the transferred impulse, but may at the same time reduce the resistance to global deformations.
- Trends observed for air blast cannot usually be transferred to water blast.
- Failure mechanisms for sandwich panels with UNDEX loading include.
  - Excessive crushing and damage to the core, possibly resulting in reduction or elimination of tensile through-thickness strength.
  - Failure under global panel deformation, due to either laminate tension/compression or core shear failure.

Changing the UNDEX shock case (e.g. between small charges at small standoffs and large charges at large standoffs), the panel size and support conditions, or the test or model configuration, may change the critical mechanism. Thus, it is important to ensure that shock mitigation studies reproduce conditions as close as possible to the envisaged application.

Acknowledgements Thanks are due to the Norwegian Defence Logistics Organisation/Naval Systems for permission to use the UNDEX measurement data. The work at Imperial College London (ICL) is led by Prof. John Dear, and at the time was supported by ONR Grant no. N00014-12-1-0403 as part of the Solid Mechanics Program (SMP) under Program Manager Dr. Yapa D.S. Rajapakse. Dr. Hayman's work is also supported by the SMP/Dr. Rajapakse. This support is gratefully acknowledged. The FE modelling presented in Sect. 4.3 was performed by the Dr. Paolo Del Linz (formerly of ICL) at Nanyang Technological University, Singapore. Advice on the FE modelling was provided by Dr. Hari Arora of the Department of Bioengineering, ICL. These contributions are also gratefully acknowledged.

References

1. Anon. (1985). Navy awards Bell Aerospace Textron $27.3-million contract for new minesweeper hunter. *Maritime Reporter & Engineering News 47*(2), 28–29.

2. Anon. (2011). MSH-1 *Cardinal* Minesweeper Hunter (MSH). http://www.globalsecurity.org/military/systems/ship/msh-1.htm.
3. Arora, H., Hooper, P. A., & Dear, J. P. (2012). The effects of air and underwater blast on composite sandwich panels and tubular laminate structures. *Experimental Mechanics, 52,* 59–81. https://doi.org/10.1007/s11340-011-9500-z.
4. Bleich, H. H., & Sandler, I. S. (1970). Interaction between structures and bilinear fluids. *International Journal of Solids and Structures, 6,* 617–639.
5. Chalmers, D. W., Osborn, R. J., & Bunny, A. (1984). Hull construction of MCMVs in the United Kingdom. In: Proceedings of International Symposium on Mine Warfare Vessels and Systems, 12–15 June 1984. London: Royal Institution of Naval Architects.
6. Dassault Systèmes Simulia Corp. (2009). Abaqus analysis manual v6.9. Providence, RI.
7. Dear, J. P., Rolfe, E., Kelly, M., Arora, H., & Hooper, P. A. (2017). Blast performance of composite sandwich structures. *Procedia Engineering, 173,* 471–478. https://doi.org/10.1016/j.proeng.2016.12.065.
8. Deshpande, V. S., & Fleck, N. A. (2000). Isotropic constitutive models for metallic foams. *Journal of the Mechanics and Physics of Solids, 48,* 1253–1283.
9. Deshpande, V. S., & Fleck, N. A. (2001). Multi-axial yield behaviour of polymer foams. *Acta Materialia, 49,* 1859–1866.
10. Deshpande, V. S., & Fleck, N. A. (2003). Blast resistance of sandwich beams. In *Proceedings of the 6th International Conference on Sandwich Construction*, *fort lauderdale* 31 March–2 April 2003.
11. Deshpande, V. S., & Fleck, N. A. (2005). One-dimensional response of sandwich plates to underwater shock loading. *Journal of the Mechanics and Physics of Solids 53*.
12. Dixon, R. H, Ramsey, B. W., & Usher, P. J. (1972). Design and build of the GRP hull of HMS *Wilton*. In *Symposium on GRP Ship Construction*, October 1972, London: Royal Institution of Naval Architects.
13. Dodkins, A. R. (1989). The structural design of the single role minehunter. In *Proceedings of Warship '89 International Symposium on Mine Warfare Vessels and Systems* 2, 8–10 May 1989. London: Royal Institution of Naval Architects.
14. Driels, M. R. (1980). The effect of a non-zero cavitation tension on the damage sustained by a target plate subject to an underwater explosion. *Journal of Sound and Vibration, 73*(4), 533–545.
15. Fleck, N. A., & Deshpande, V. S. (2004). The resistance of clamped sandwich beams to shock loading. *Journal of Applied Mechanics, 71,* 386–401.
16. Geers, T. L. (1978). Doubly asymptotic approximations for transient motions of submerged structures. *Journal of the Acoustic Society of America, 64*(5), 1500–1508.
17. Geers, T. L., & Hunter, K. S. (2002). An integrated wave-effects model for an underwater explosion bubble. *Journal of the Acoustical Society of America 111*, 1584–1601. https://doi.org/10.1121/1.1458590.
18. Gullberg, O., & Olsson, K.-A. (1990). Design and construction of GRP sandwich ship hulls. *Marine Structures, 3,* 93–109.
19. Hall, D. J., & Robson, B. L. (1984). A review of the design and materials evaluation programme for the GRP/foam sandwich composite hull of the RAN minehunter. *Composites, 15*(4), 266–276.
20. Hayman, B. (1995). Underwater explosion loading on foam-cored sandwich panels. In *Sandwich Construction 3*, *Proceedings of the 3rd International Conference on Sandwich Construction*, Southampton, 11–15 September 1995.
21. Hellbratt, S.-E, & Gullberg, O. (1988). The high speed passenger ferry *SES Jet Rider*. In *Proceedings of the 2nd International Conference on Marine Applications of Composite Materials*, Melbourne, Florida, USA, 21–23 March 1988.
22. Hellbratt, S.-E, & Gullberg, O. (1989). The development of the GRP-sandwich technique for large marine structures. In *Proceedings of the 1st International Conference on Sandwich Constructions*, Stockholm, 19–21 June 1989.

23. Henton, D. (1967). Glass reinforced plastics in the Royal Navy. *Transactions of the Royal Institution of Naval Architects, 109,* 487–501.
24. Hutchinson, J. W., & Xue, Z. (2005). Metal sandwich plates optimized for pressure impulses. *International Journal of Mechanical Sciences, 47,* 545–569.
25. Keil, A. H. (1961). *The response of ships to underwater explosions,* 16–17 November 1961. New York: Society of Naval Architects and Marine Engineers Annual Meeting.
26. Liang, Y., Spuskanyuk, A. V., Hayhurst, D. R., Hutchinson, J. W., McMeeking, R. M., & Evans, A. G. (2007). The response of metallic sandwich panels to water blast. *Journal of Applied Mechanics, 74,* 81–99.
27. Mäkinen, K.-E. (1995). Numerical and experimental results for shock loaded sandwich panels. In *Sandwich Construction 3*, *Proceedings of the 3rd International Conference on Sandwich Construction*, Southampton, 11–15 September 1995.
28. Mäkinen, K.-E. (1998). Cavitation models for structures excited by a plane shock wave. *Journal of Fluids and Structures, 12,* 85–101.
29. Mäkinen, K.-E. (1999). *Underwater shock loaded sandwich structures*. Doctoral Thesis, Report 99–01, Royal Institute of Technology Department of Aeronautics: Sweden.
30. Mäkinen, K.-E. (1999). The transverse response of sandwich panels to an underwater shock wave. *Journal of Fluids and Structures, 13*(5), 631–646. https://doi.org/10.1006/jfls.1999.0222.
31. Mäkinen, K.-E., & Kadyrov, S. (1998). A 1-D fluid sandwich interaction model for the early time underwater shock loading. In *Proceedings of the 4th International Conference on Sandwich Construction*, Stockholm, Sweden, 9–11 June 1998.
32. Mouritz, A. P., Gellert, E., Burchill, P., & Challis, K. (2001). Review of advanced composite structures for naval ships and submarines. *Composite Structures, 53,* 21–41.
33. Mouritz, A. P., Saunders, D. S., & Buckley, S. (1993). The damage and failure of GRP laminates by underwater explosion shock loading. In *5th Australian Aeronautical Conference,* Melbourne, 13–15 September 1993. The Institution of Engineers, Australia, National Conference Publication No. 93/6.
34. Moyer, E. T., Amir, G. G., Olsson, K. A., & Hellbratt, S. E. (1992). Response of GRP sandwich structures subject to shock loading. In *Proceedings of the 2nd International Conference on Sandwich Constructions*, Gainesville, USA, March 9–12 1992.
35. Olsson, K.-A., & Lönnö, A. (1992). Sandwich constructions—recent research and development: GRP-sandwich technology for high-speed marine vessels. In *Proceedings of the 2nd International Conference on Sandwich Constructions*, Gainesville, USA, 9–12 March 1992.
36. Robson, B. L. (1984). The RAN GRP minehunter—a status report. In *Proceedings of International Symposium on Mine Warfare Vessels and Systems*, 12–15 June 1984. London: Royal Institution of Naval Architects.
37. Robson, B. L. (1989). The Royal Australian Navy inshore minehunter—lessons learned. In *Proceedings of the 1st International Conference on Sandwich Construction*, Stockholm, 19–21 June 1989.
38. Royal Institution of Naval Architects. (1984). In *Proceedings*, *International Symposium on Mine Warfare Vessels and Systems* (3 Vols.). London: RINA.
39. Schiffer, A. (2013). *The response of submerged structures to underwater blast*. Thesis submitted for the degree of D.Phil in Engineering Science: University of Oxford, UK.
40. Schiffer, A., & Tagarielli, V. L. (2014). One-dimensional response of sandwich plates to underwater blast: Fluid-structure interaction experiments and simulations. *International Journal of Impact Engineering, 71,* 34–49.
41. Sjögren, J., Celsing, C.-G., Olsson, K.-A., Levander, C.-G., & Hellbrat, S.-E. (1984). Swedish development of MCMV-hull design and production. In *Proceedings of International Symposium on Mine Warfare Vessels and Systems*, 12–15 June 1984. London: Royal Institution of Naval Architects.
42. Taylor GI (1941). The pressure and impulse of submarine explosion waves on plates. In: Underwater explosion research: a compendium of British and American reports. US Office of

Naval Research, Washington, DC, USA, 1950. Also in Taylor, G. I. (1963) *The scientific papers of G. I. Taylor*, (Vol. III, pp. 287–303). Cambridge University Press: Cambridge, UK.
43. Trimming, M. (1984). Monocoque GRP minehunters. In *Proceedings of International Symposium on Mine Warfare Vessels and Systems*, 12–15 June 1984. London: Royal Institution of Naval Architects.
44. Trimming, M., Fantacci, G., & Buccianti, A. (1989). US Navy minehunter coastal (MHC) O*sprey* class. In *Proceedings of Warship '89 International Symposium on Mine Warfare Vessels and Systems*, 8–10 May 1989. London: Royal Institution of Naval Architects.
45. Xue, Z., & Hutchinson, J. W. (2003). Preliminary assessment of sandwich plates subject to blast loads. *International Journal of Mechanical Sciences, 45,* 687–705.
46. Xue, Z., & Hutchinson, J. W. (2004). A comparative study of impulse-resistant metal sandwich plates. *International Journal of Impact Engineering, 30,* 1283–1305.

The Effects of Polyurea Coatings on the Underwater Explosive Response of Composite Plates

James LeBlanc and Arun Shukla

1 Introduction

Composite materials are increasingly being employed in a wide range of industries and applications due to their numerous advantages over traditional construction materials, namely high strength-to-weight ratios, improved corrosion resistance, and overall reduced maintenance costs. Historically, the civilian marine industry has utilized composite materials in the construction of leisure and commercial watercraft. There has been a recent and increasing desire by multiple worldwide navies to implement these materials in military applications such as advanced ship hull designs, ship decks, unmanned underwater vehicles, and submarine components. However, structures which are employed in military environments are inherently at risk for being subjected to blast-type loading events. In the specific case of underwater explosions, these may occur either at large or very small standoff distances depending on the relative location of the explosive source and the structure of interest. The loading resulting from an UNDEX event is both complex and highly transient, signified by high peak pressures, rapid rise times, and spherical wavefronts. Due to the complex nature of both the mechanisms associated with these loadings, and a reduced knowledge base of the response of these advanced materials when subjected to high loading rates (10^{-1} to 10^{3}), including the evolution of damage, and the load carrying capacity in these materials, there is an inherent conservativeness in design. An extensive review of the use of composite materials in naval ships and submarines has been presented by Mouritz et al. [1].

J. LeBlanc (✉)
Naval Undersea Warfare Center (Division Newport), 1176 Howell Street, Newport, RI 02841, USA
e-mail: james.m.leblanc@navy.mil

A. Shukla
University of Rhode Island, 92 Upper College Road, Kingston, RI 02881, USA

S. Gopalakrishnan and Y. Rajapakse (eds.), *Blast Mitigation Strategies in Marine Composite and Sandwich Structures*, Springer Transactions in Civil and Environmental Engineering, https://doi.org/10.1007/978-981-10-7170-6_3

When composite materials are subjected to severe loading conditions, they may experience damage in the form of several distinct mechanisms occurring in the in-plane and through thickness directions. The in-plane mechanisms consist of fiber breakage and matrix cracking, while the through thickness damage is dominated by delamination of the plies. These damage mechanisms and their evolution in these materials have been studied through various experimental methods. The response of composites subject to UNDEX type loading is typically conducted in the laboratory-scale environments [2–10]. These studies have investigated different parameters associated with the structural response including charge standoff, impulse levels, material properties, and panel curvature. The effects of impact loading on damage mechanisms and energy absorption were studied in [11].

The finite-element modeling of damage in composites has been performed primarily on models simulating strain rates up to those representing drop test experiments with some work performed at the high strain rate regimes expected in shock loading. Analytical damage models, including implementation into computational codes for composites have been widely developed and are continually being refined and updated [12–17]. In general, these models assign an internal damage variable to each of the types of damage of interest (i.e., matrix cracking, fiber rupture) which, in simple form, are ratios of the stress state to a failure criterion. Early validation work focused on the low strain rate regime, rates below which blast/shock loading conditions would generate [18–21]. More recently, computational work has been performed on materials subject to higher loading rate events including UNDEX and high-speed impacts [22, 23] although the material inputs are derived from mechanical testing under quasi-static conditions. The through thickness strain rates for blast and ballistic impact events are significantly higher and the approach of using material inputs from quasi-static test data should be improved.

The use of elastomeric materials to increase the resistance of structures subjected to high rate loading such as blast and shock has become a recent topic of interest. One such material of interest is polyurea, a synthetic, high strength/high elongation coating that is typically spray cast onto existing structures. The armed forces have begun to investigate the suitability of these materials for use on military and naval vehicles such as Humvees, troop carriers, and ship hulls, Hodge [24]. Research efforts have recently studied the effectiveness of polyurea when applied to various substrates. Studies involving composite and sandwich construction applications [25–28] showed that the effect of the coating on the transient response and damage levels of these materials is dependent upon both coating thickness as well as location. Rate-sensitive constitutive models of these elastomeric materials have been developed to allow for numerical modeling of the coating effects under various high rate loading environments [29–33].

2 Composite Material

The composite material used in this study is Cyply® 1002, a cured epoxy composite with a nonwoven, parallel fiber construction with continuous E-Glass filaments. The specific laminate is a cross-ply construction with alternating plies of 0° and 90°, each ply having a thickness of 0.254 mm (0.01 in.). The cured material has a specific gravity of 1.85 and a resin content of 36 ± 3%. Mechanical properties of the material are provided in Table 1.

The composite laminate serves as the baseline substrate to which polyurea coatings are applied. The polyurea used is Dragonshield-BC which is a 2-part spray cast material that can be applied to a wide range of surfaces and materials. Mechanical characterization in both tension and compression for strain rates from 0.01 to 2000 s^{-1} has been conducted. Characterization up to 100 s^{-1} was performed using standard material testing machine whereas a split Hopkinson pressure bar was used to characterize the response of the material at 2000 s^{-1}. The response of the material at 2000 s^{-1} was only characterized in compression and is assumed to be similar in tension. At the lower strain rates, unique tests were conducted for both tension and compression. The full material characterization is shown in Fig. 1. From this figure, it is seen that the material exhibits strong strain rate dependence and becomes stiffer with increasing loading rate. Furthermore, the material displays a stiffening effect in compression above 300%, whereas in tension the response exhibits a stress plateau-like behavior. In this study, both the thickness and location of the coating is varied to determine relative effects.

3 Experimental Methods

The experiments that are the basis for the work described in the following sections are designed to subject composite panels to shock loading conditions representative of far and near field underwater explosions. A conical shock tube facility is utilized to impart blast loading conditions representative of far field UNDEX events and a water-filled blast tank is employed for the conduct of near field experiments. During all experiments, the DIC methodology is used to capture the transient response of the back face of the panels. These measurements form the basis for correlation between the experiments and corresponding finite-element simulations.

Table 1 Cyply 1002 cross-ply—mechanical properties

	N/m^2 (lb/in^2)
Tensile modulus (0°)	23.4e9 (3.4e6)
Tensile modulus (90°)	23.4e9 (3.4e6)
Tensile strength (0°)	482e6 (70e3)
Tensile strength (90°)	482e6 (70e3)
Compressive strength (0°)	689e6 (100e3)
Compressive strength (90°)	689e6 (100e3)

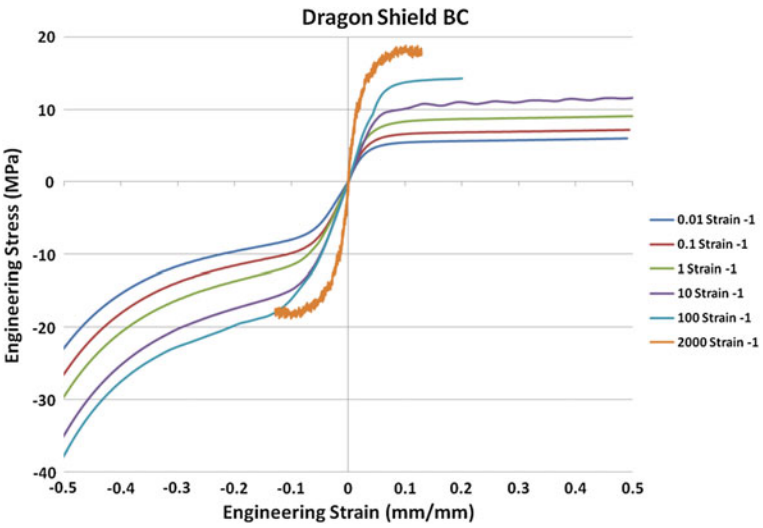

Fig. 1 Dragon shield BC polyurea stress–strain behavior

3.1 Conical Shock Tube—Far Field UNDEX Loading

The conical shock tube (CST) facility located at the Naval Undersea Warfare Center Division Newport (NUWCDIVNPT), has been utilized to generate shock loading conditions representative of explosions occurring at large standoff distances. The shock tube is a horizontally mounted, water-filled tube with a conical internal shape as seen in Fig. 2. The tube geometry represents a solid angle segment of the free field spherical pressure front resulting from the detonation of an underwater explosive charge. In an open water environment (free field), the pressure wave expands from the charge location as a spherically propagating wave. In the shock

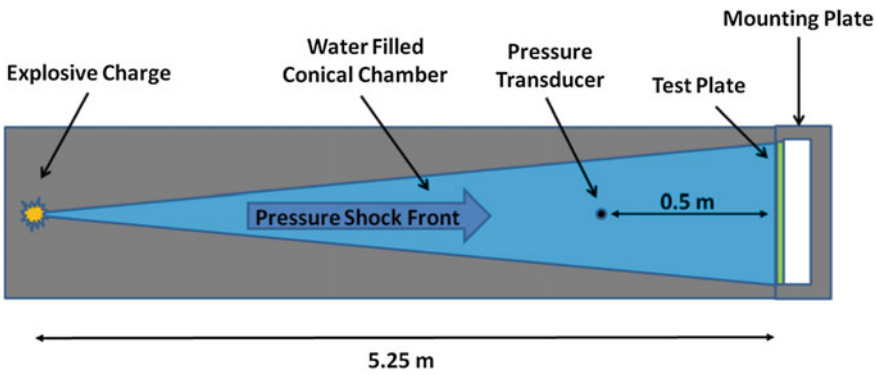

Fig. 2 Conical shock tube schematic (not to scale)

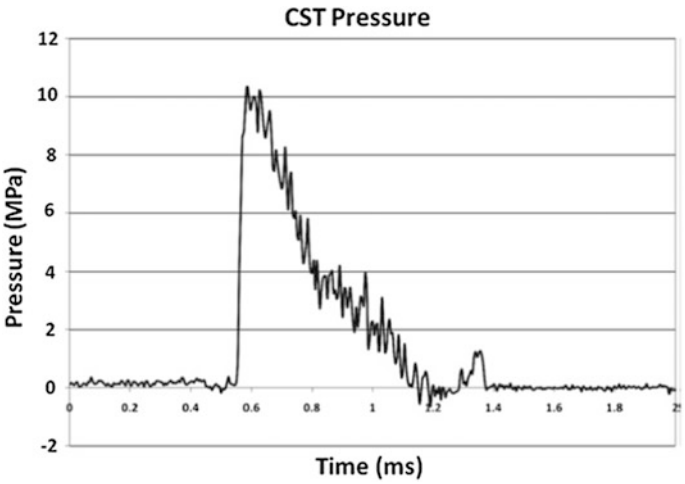

Fig. 3 Typical pressure profile generated in the conical shock tube

tube, the rigid wall acts to confine the expansion of the pressure wave in a manner that simulates a conical sector of the pressure field. The internal cone angle of the shock tube used in the current work is 2.6°. The pressure shock wave is initiated by the detonation of an explosive charge at the breech end of the tube (left side of Fig. 2) which then proceeds down the length of the tube. Peak shock pressures from 10.3 to 20.6 MPa (3000 lb/in^2) can be obtained depending on the amount of explosive charge used. A typical pressure profile, as obtained from the pressure transducers, is shown in Fig. 3. This figure illustrates the rapid pressure increase associated with the shock front followed by the exponential decay of the wave. A detailed description of the tube and underlying theoretical considerations are presented in [26, 34, 35]. A mounting fixture has been designed so the test specimens are air backed with fully clamped edges. The specimens have an overall diameter of 26.54 cm (10.5 in.) with a 22.86 cm (9.0 in.) unsupported middle section.

3.2 Water-Filled Blast Facility—Near Field UNDEX Loading

The near field UNDEX experiments in this study were conducted in a water-filled tank, Fig. 4. The tank has internal dimensions of 1.21 m × 1.21 m × 1.21 m with 6.35 mm thick steel walls and is supported on a reinforced wooden stand. The tank contains ~1500 L of water when filled. Four window ports allow for the lighting and high-speed photography of the UNDEX event and plate motion. Mounted to the inner surface of one wall is a 304.8 mm × 304.8 mm, rectangular tunnel with a

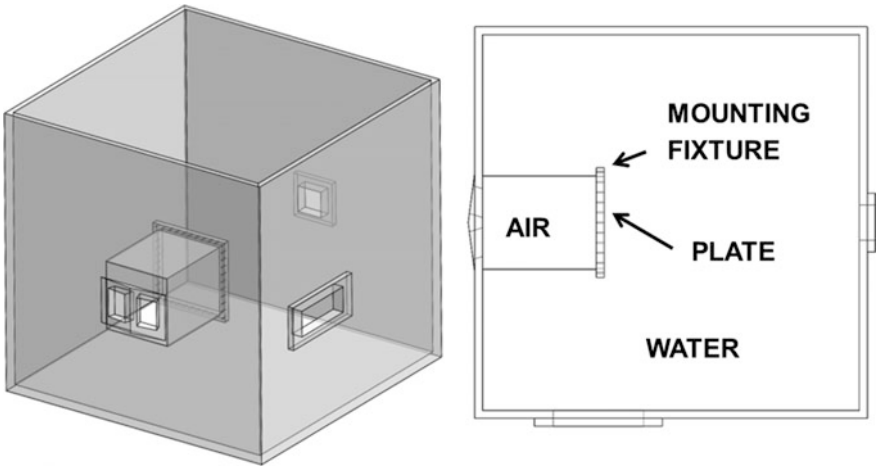

Fig. 4 UNDEX test tank

wall thickness of 12.7 mm, which serves as the base for the mounting of the composite plates. The tunnel extends 394 mm into the tank from the wall and a 38.1 mm wide flange is welded to the end of the tunnel. The flange has a series of through holes around the perimeter which allow for bolting of the test plates to the flange. The test plates are sandwiched between the flange and a second steel frame and are secured to the flange with a series of 1.59 mm diameter through bolts spaced at 38.1 mm. The use of the tunnel and mounting flange provide a watertight seal around the test plate and allows for the plates to be air backed.

The explosive used in the near field blast experiments is an RP-503 charge which is comprised of 454 mg RDX and 167 mg PETN contained within an outer plastic sleeve.

3.3 Transient Plate Response Measurements

In all experiments, the digital image correlation method is utilized for the capture of the transient response of the back face of all panels. Digital image correlation is a nonintrusive, optical technique for capturing the full field, transient response of the panels through the use of high-speed photography and specialized software. A detailed discussion of the DIC process and setup for each of the respective test facilities are presented in [26, 36]. The post-processing is performed with the VIC-3D software package (Correlated Solutions) which matches common pixel subsets of a random speckle pattern between the sequential deformed images. The matching of pixel subsets is used to calculate the three-dimensional location of distinct points on the face of the panel throughout time. Two high-speed digital cameras, Photron SA1, are utilized in each setup with frame rates of 20,000 fps.

4 Finite-Element Modeling

The numerical modeling of the two loading conditions requires different approaches to be employed. In the case of the far field loading experiments (CST) the tube geometry is explicitly captured and the incident shock wave is approximated as planar. In the modeling of the near field experiments, due to the close proximity of the charge to the plates, it is critical to capture the detonation of the charge as well as the bubble growth and spherical pressure wave expansion. The following is a brief overview of each approach. In all cases, the modeling of the experiments has been performed utilizing the LS-Dyna software code.

In all simulations, the material model utilized for the composite plate is Mat_Composite_Failure_*Option*_Model. This is an orthotropic material definition capable of modeling the progressive failure of the material due to any of several failure criteria including tension/compression in the longitudinal and transverse directions, compression in the through thickness direction, and through thickness shear. The material model for the polyurea coating is Mat_Simplified_Rubber which is a viscoelastic material definition that captures both the strain and strain rate effects through the use of a family of load curves. The model reproduces the uniaxial tension and compression behavior as obtained through material testing at discreet strain rates (see material section for properties). The model determines the appropriate strain rate curve from the family of curves through an internal calculation.

4.1 Far Field UNDEX Modeling

The complete finite-element model of the CST test setup is shown in Fig. 5. The model consists of the composite plate, polyurea coating, mounting fixture

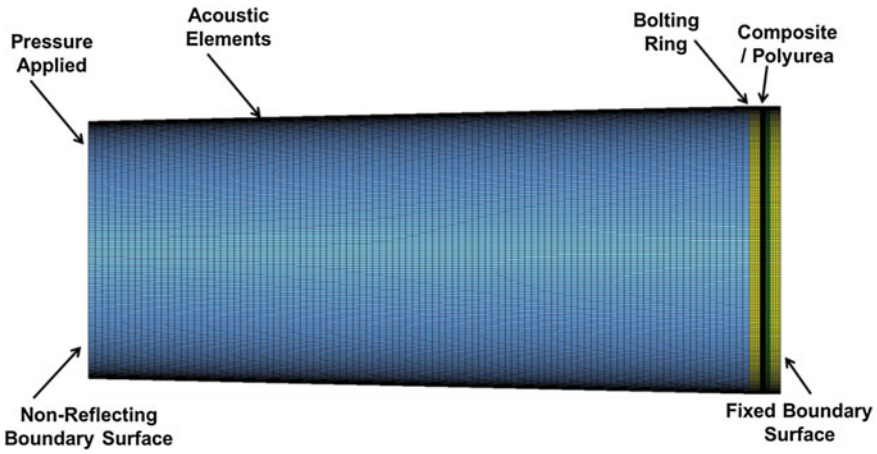

Fig. 5 Finite-element model of CST

(including the bolts) and the internal fluid of the shock tube up to the location of the pressure transducer used to record the UNDEX pressure profile. The fluid within the tube is considered in the simulation so as to capture the fluid structure interaction (FSI) at the interface of the fluid and test plate. The fluid is modeled with solid elements utilizing an acoustic element formulation which more accurately propagate the shock wave than the use of a structural element formulation combined with an equation of state (EOS) material definition. The pressure load is applied as a plane wave at the location of the test pressure transducer (left face of the fluid domain) and is taken to be the pressure profile that was measured during the test. The fluid–structure interaction is handled by utilizing a mesh that is equivalenced at the boundary between the fluid domain and composite plate. The mounting plate and fastening bolts are explicitly included in the model to obtain the correct interaction with the test plates. The polyurea coatings are assumed to be perfectly bonded to the composite plate and are thus meshed directly to the composite. The composite plate in the simulations is modeled using layers of solid brick elements with each layer representing a 0° and 90° combined ply. The polyurea is also represented in the model by solid elements.

4.2 Near Field UNDEX Modeling

The near field UNDEX models utilize the coupled Lagrange–Eulerian formulation of the code, which allows for the accurate representation of the detonation of the explosive charge as well as the fluid structure interaction between the fluid and the composite plate. The finite-element model of the UNDEX test setup is shown in Fig. 6. The model consists of the test plate, tank water, air, and the RP-503 charge. The model represents a sub-domain of the full experimental test tank for computational efficiency. The use of a sub-domain for the modeling of the corresponding

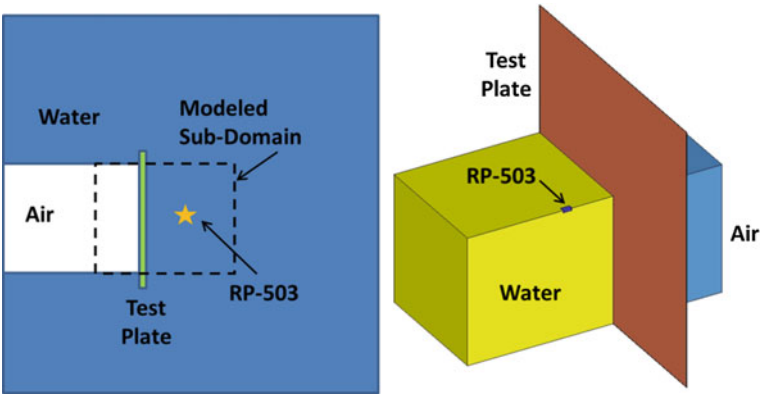

Fig. 6 Finite-element model of UNDEX experiment (3 Quadrants of Fluid Domain Hidden)

experiments is deemed appropriate as the loading of the plate and subsequent response occurs sufficiently fast that reflections from the tank walls do not affect the overall transient response of the plate. In the model, the outer surface of the fluid sub-domain is prescribed a non-reflecting boundary condition (*BOUNDARY_NON_REFLECTING). The composite plate in the simulations is modeled using a single layer of shell elements and the polyurea material is represented in the model by solid elements. Furthermore, the polyurea coatings are assumed to be perfectly bonded to the composite plate and are thus meshed directly to the composite.

The water, air, and explosive charge are modeled with solid elements utilizing the LS-Dyna ALE multi-material element formulation. The water and air utilize the *Mat_Null material definition with the density of the water and air given as 1 g/cm^3 and 0.0013 g/cm^3 respectively. The Gruneisen EOS is used for the definition of the water with the speed of sound taken to be 149,000 cm/s. A Linear Polynomial EOS defines the air domain in the model with the parameters defined in Table 2. By defining C_0, C_1, C_2, C_3, and C_6 equal to zero, and C_4, and C_5 equal to γ-1, a gamma law EOS is achieved. Finally, the explosive charge is modeled with the *Mat_High_Explosive_Burn material model combined with the JWL EOS. Although the RP-503 charge contains both RDX (454 mg) and PETN (167 mg), the model assumes a charge comprised of only RDX, with the overall charge weight being maintained. The Material and EOS parameters for the RDX are provided in Tables 3 and 4.

Table 2 Air EOS parameters

C0	0
C1	0
C2	0
C3	0
C4	0.4
C5	0.4
C6	0

Table 3 RDX material parameters

ρ (g/cm^3)	1.77
D (cm/s)	850e3
Chapman–Jouget pressure (dyn/cm^2)	3.41e13

Table 4 RDX EOS (JWL) parameters [37]

A	7.78e12 (dyn/cm^2)
B	7.07e10 (dyn/cm^2)
R1	4.485
R2	1.068
ω	0.3
E_o	5.93e10
V_o	1.0

5 Far Field UNDEX Response of Flat Composite Plates

The response of flat E-Glass/Epoxy plates subjected to far field explosive loading, including the effects of the polyurea coatings is presented in the following section. In the investigation, 5 unique panel configurations are considered as shown in Fig. 7. The goal is to determine the effects of both coating thickness and position with respect to the incoming shock wave. The response of the each of the composite plates, coated and uncoated, is characterized in terms of the transient displacements of the back face of the panel and the deformation mechanisms during the displacement. The correlation between the experiments and numerical models is discussed.

The center point displacement–time history as obtained from the DIC data for the five-panel configurations tested is shown in Fig. 8. In general, the response of both the coated and uncoated panels is approximately the same in terms of peak center point deflection. However, it can be seen that overall the panel with the thicker coating (4.8 mm) located on the back provides a slightly improved response as compared to the baseline. Conversely, the thin coating (2.4 mm) on the front face results in a minor degradation in the transient panel response as compared to the uncoated composite plate. These trends, although not as pronounced, are in agreement with previous observations of experimental data [25]. Similar to the current investigation these studies also showed that, up to a certain thickness, a coating on the front face (towards loading) of a panel under shock loading can degrade the performance of the plate as compared to a panel with no coating at all. Furthermore, a thicker coating on the back face can improve the response of the panel subjected to shock loading. Potential reasons for the lack of significant differentiation of the experimental peak displacements include: (1) the coating

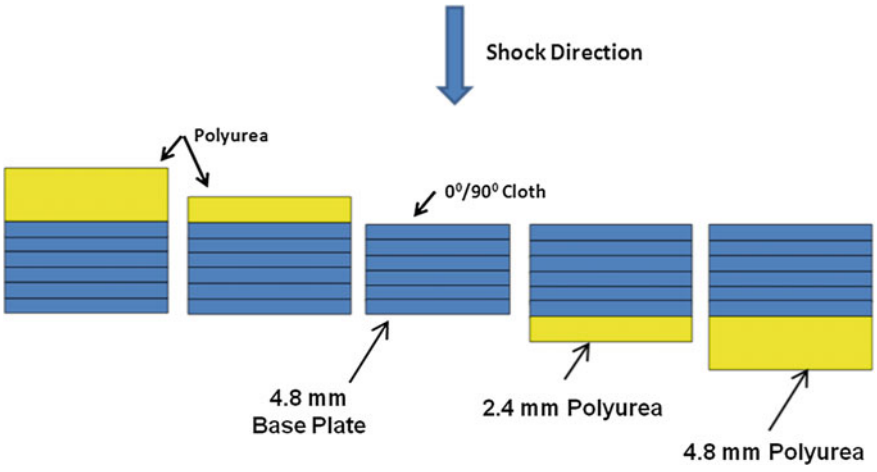

Fig. 7— Composite plate construction—schematic (not to scale)

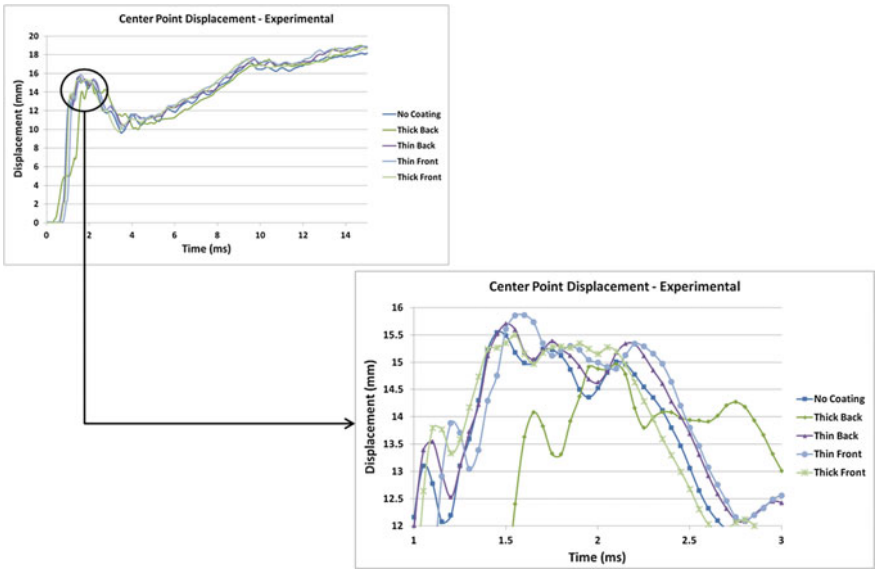

Fig. 8 Time history deformation comparison

thicknesses chosen for this study are not sufficient to meaningfully improve the shock response of the plates, or (2) the in-plane strains realized by the coatings during deformation are not sufficient for the coating to experience the significant strain stiffening as seen in the material characterization.

The deformation of the uncoated composite plate as measured along a horizontal cut through the center point (c) is shown in Fig. 9b. The deformed shape along the cross-section is shown for 5 distinct points in time as indicated by the black dots in the time history in the upper Fig. 9a. From this figure, it is shown that for a plate subjected to a shock front with a plane wave profile, the plate motion initiates at the outer edge and progresses inwards. During the early deformation phase, a knee-like hinge develops at the outer edge as seen for the 0.9 ms deformation contour. As this hinge continues to progress toward the center point the deformation tends toward a mode I plate flexure. The significant observation is that the expected mode I flexure deformation profile does take a finite time to develop and is not the initial deformation mechanism.

The finite-element simulation of the shock tube testing allows for a visual full field representation of the interaction between the pressure wave and the composite plate. The pressure field in the fluid as it interacts with and loads the plate, for the case of the plate with the 4.8 mm polyurea coating is shown on the left side of Fig. 10. The associated plate response is shown in right side of the figure. Figure 10 illustrates several key points. First, although the pressure wave is uniform (planar) prior to its impact with the test plate, the pressure becomes both complex and nonuniform when it interacts with and loads the plate itself. It is evident that there is

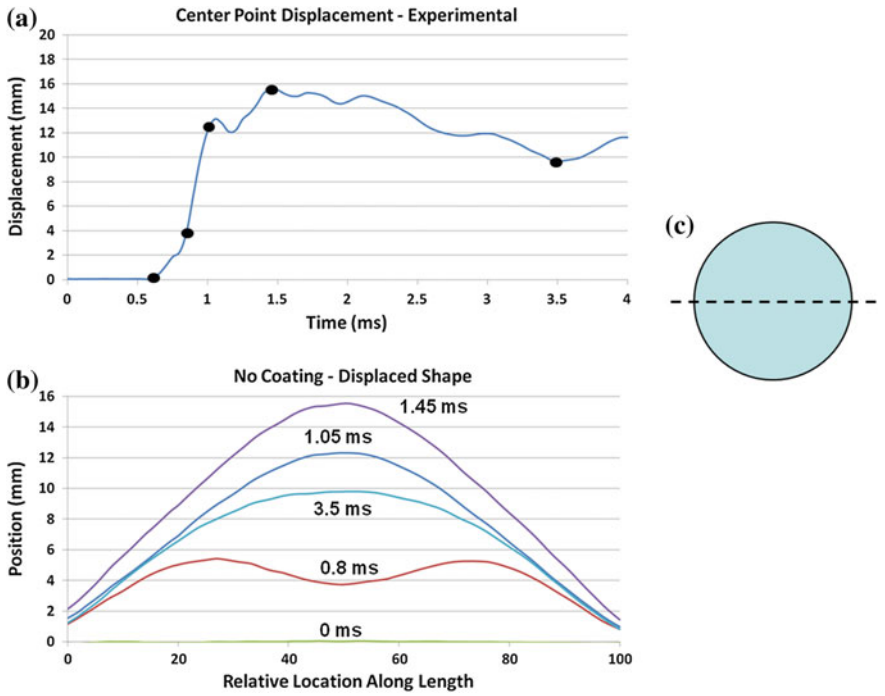

Fig. 9 Plate deformation profiles for centerline

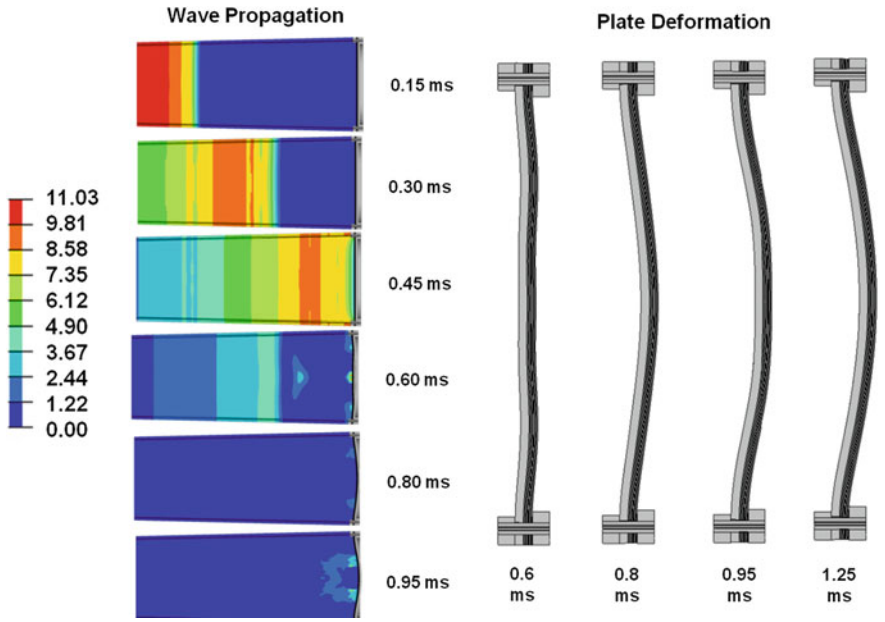

Fig. 10 Fluid structure interaction (contours of MPa) and associated plate response

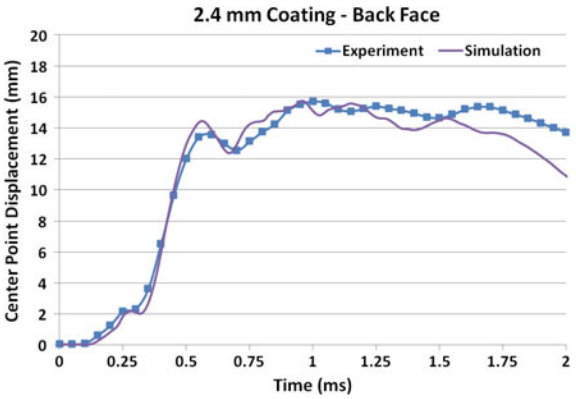

Fig. 11 Computational model correlation for 2.4 mm back face coating

a low-pressure area that develops in the center of the plate while the clamped edge is loaded with high pressure. The second point is that the loading of the plate and the associated response can be separated into two distinct time regimes. The plate does not start to deform until 0.6 ms which roughly corresponds to the point in time at which the pressure wave is nearly fully reflected. Furthermore, from the cross-section view of the plate deformation it is seen that plate in the simulation also develops a hinge which propagates inwards from the clamped edge. These are the same deformation mechanisms which were observed from the DIC data of the experiments.

The center point displacement data comparison between the experimental and numerical simulation for the CST test performed with a thin (2.4 mm) coating on the back face of the composite panel is shown in Fig. 11. From this graphical comparison, it is seen that there is a high level of correlation between the experimental results and the computational simulations. This level of agreement between the test and finite-element data demonstrates that the computational methodology utilized to simulate the testing is suitable for the accurate predictions of these types of loading conditions.

6 Near Field UNDEX Response of Flat Composite Plates

The effects of polyurea coatings on the near field UNDEX response of flat E-Glass/Epoxy plates subjected to near field explosive loading is presented in the following section. Based on the previously observed results of greater performance obtained when the coating is applied to back face of the structure, only a rear face coating is considered for this part of the study. In addition to the coated panel, a thicker structural configuration is also considered. The 3 unique panel configurations are shown in Fig. 12. The goal is to determine the relative effects of both a rear face coating and a thicker structural laminate.

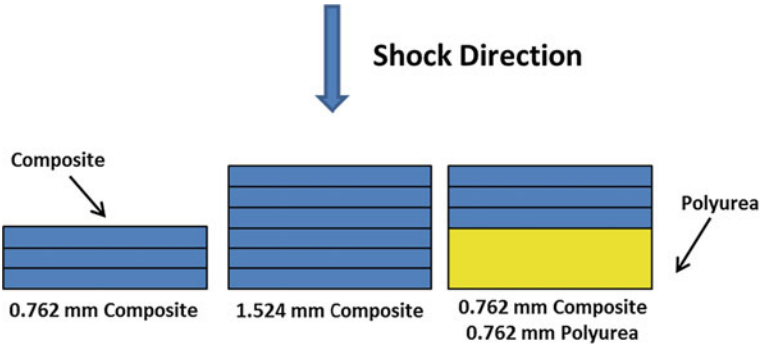

Fig. 12 Composite plate construction—schematic (not to scale)

The center-point displacement for each respective plate configuration is shown in Fig. 13. From this figure, it is observed that there are several distinct differences in the overall plate response as influenced by the plate construction. It is evident that, as compared to the baseline 0.762 mm plate, increasing the plate thickness or including a polyurea coating reduces the peak overall deflection for a given level of loading. It is noted that the center-point velocity during the initial deflection is nearly constant for each configuration. The main difference is the time that it takes for the plate to arrest its outward motion and begin to recover, with the 1.524 mm uncoated and the 0.762 mm polyurea coated plates arresting their outward motion ~0.25 ms sooner than the baseline 0.762 mm plate. The center-point deflection comparison between the 1.524 mm uncoated plate and the 0.762 mm plate with a 0.762 mm coating of polyurea indicate that for a plate thickness it is more advantageous to utilize additional structural plies rather than an elastomeric coating. However, when a structure has previously been designed and further thickening of the structural shape is not possible, the application of a polyurea coating can improve the transient response to shock loading. A second primary difference in the

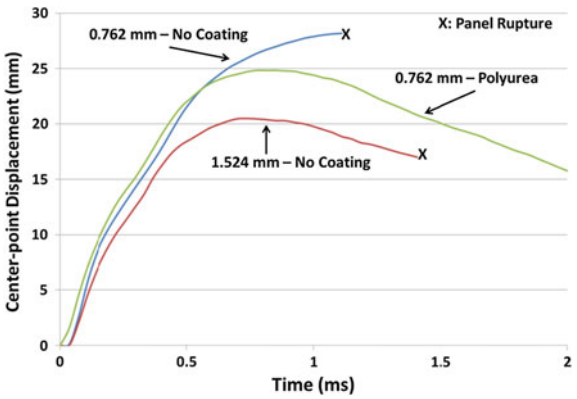

Fig. 13 Plate center-point deflections

response of the plate configurations is the onset of material damage. Both the uncoated 0.762 and 1.524 mm specimens experienced significant through thickness tearing at the plate boundaries. It is further observed that although the 0.762 mm plate with the polyurea coating did experience larger deflections than the 1.524 mm uncoated plate, there was no edge tearing of the plate itself. Thus in terms of reducing material damage itself, the polyurea coatings offer an advantage over a thicker uncoated plate.

The deformation history of the baseline 0.762 mm uncoated composite plate as measured along a horizontal cut through the center of the plate is shown in Fig. 14. From this figure, it is seen that for a plate subjected to a centralized near field UNDEX loading, the deformation is initially dominated by localized deflections at the center with minimal deflection near the boundaries. As the plate responds to the pressure loading, it gradually transitions to an overall plate flexure mode as shown by the cross-sectional shape at 0.63 and 1.11 ms. The significant observation is that the initial plate deformation is governed by the highly localized pressure loading and then subsequently shifts to a mode I flexure deformation profile later in time.

The center-point time history correlation between the experimental data and the corresponding computational simulation for each respective plate configuration is shown in Fig. 15. The correlations presented in the figure show that there is a high level of correlation between the experiment and simulations, both temporally and in terms of displacement magnitudes. The simulation and experiment results exhibit consistent results in the early time frame of the event (0–0.4 ms) in terms of displacement and velocity, with some deviation beyond this point, although the deviation is somewhat minor. Additionally, for both of the uncoated plates (0.762 and 1.524 mm) it is seen that the onset of edge tearing occurs slightly later (0.1 ms) in time as compared to the experimental results. The timing differences in the onset of damage are expected as the model assumes a uniform plate in terms of material properties and does not account for manufacturing variability or minor internal defects which can contribute to the onset of damage or slightly weaker/stronger areas of the plates as compared to the gross material strengths. That the model is

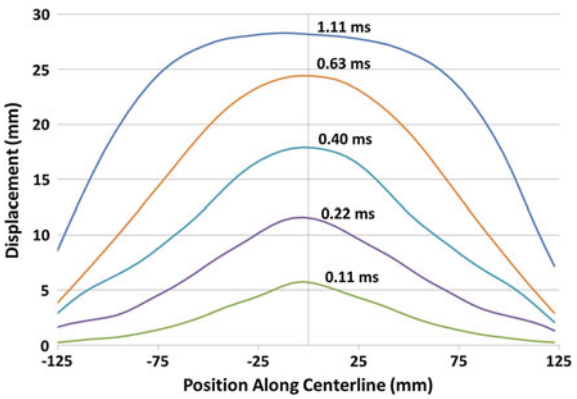

Fig. 14 Plate deformation—horizontal centerline

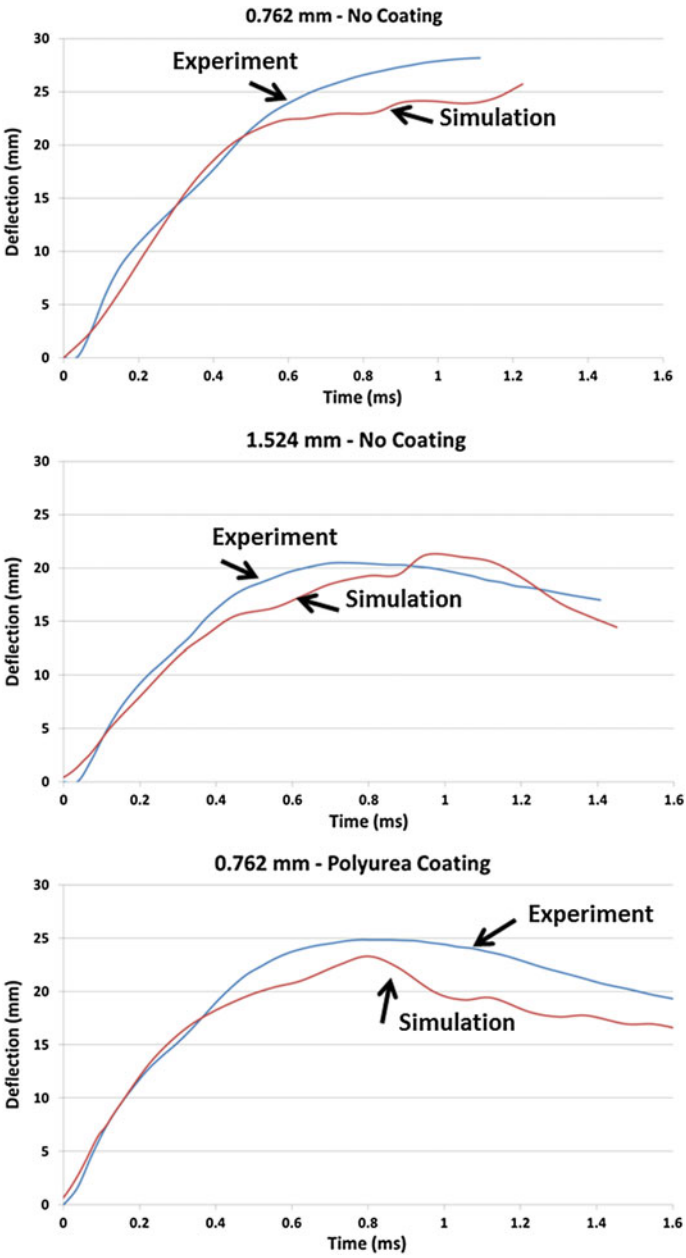

Fig. 15 Center-point displacement model correlation

able to predict the onset of damage in a consistent manner as observed during the testing, namely edge tearing, is encouraging.

7 Summary

This research has studied the response of E-Glass/Epoxy composite plates subjected to UNDEX loading, specifically far and near field conditions. The work consists of experimental testing with corresponding numerical simulations. The primary objectives of the study were to (1) determine the effects of polyurea coatings on the transient response and damage mechanisms of the plates during loading and (2) develop a computational modeling methodology that is able to accurately simulate the behavior of the plates. The relevant findings resulting from the present study are presented below.

(1) Experimental methods have been developed which subject flat composite plates to loading conditions representative of underwater explosions. Far field loading conditions are generated through the use of a conical shock tube facility which replicates the free field expansion of pressure waves resulting from the explosion. A water-filled blast chamber is utilized for the controlled detonation of small charges in close proximity to the plates to replicate near field loading conditions. In all experiments the real-time dynamic response of the back face of the specimens is captured through the use of high-speed photography coupled with the digital image correlation technique.
(2) A computational modeling methodology, utilizing the commercial finite-element code LS-Dyna, has been developed that is able to accurately simulate the response of the composite material and polyurea coatings subject to UNDEX conditions. Unique modeling methods have been employed for the simulation of the far and near field loading experiments. All simulations include explicit representations of the plate, coating, and a sufficient amount of the surrounding fluid to accurately capture the fluid structure interaction between the pressure wave and structure. The models are shown to be able to simulate the dynamic loading of the plate and the corresponding transient response.
(3) The effects of polyurea surface coatings have been studied to determine the effects of parameters including coating thickness and location with respect to the incident shock front. In general, it was shown that greater performance increases are obtained when the back face of the panels are coated as compared to the front face in terms of peak deflections and velocity decay times. Furthermore, as the coating thicknesses were increased the performance was further increased but at the cost of added weight and panel thickness.

The work discussed in this chapter has provided a basis for experimental and computation techniques which can be applied to the study of the dynamic response of composite materials subjected to underwater explosive loading conditions. However, there remains a significant body of work to be completed in this area before the dynamic response of these materials matures to an equivalent level of understanding as that for metallic materials. This work includes further experimental and computational studies as well as validation efforts which correlates the

two. These efforts will ultimately lead to validated modeling practices that can be applied during the design phase of composite structures.

Acknowledgements The financial support of the Naval Undersea Warfare Center (Division Newport) In-house Laboratory Independent Research program (ILIR) directed by Mr. Neil Dubois is greatly acknowledged. The support provided by Dr. Y.D.S. Rajapakse of the Office of Naval Research under Grant Nos. N00014-10-1-0662 (University of Rhode Island) and N00014-14-WX00730 (Naval Undersea Warfare Center, Division Newport) is acknowledged. The contributions of Dr. Erin Gauch, Christopher Shillings, and Frank Livolsi are acknowledged.

References

1. Mouritz, A. P., Gellert, E., Burchill, P., & Challis, K. (2001). Review of advanced composite structures for naval ships and submarines. *Composite Structures, 53,* 21–41.
2. Latourte, F., Gregoire, D., Zenkert, D., Wei, X., & Espinosa, H. (2011). Failure mechanisms in composite plates subjected to underwater impulsive loads. *Journal of the Mechanics and Physics of Solids, 59,* 1623–1646.
3. Espinosa, H., Lee, S., & Moldovan, N. (2006). A novel fluid structure interaction experiment to investigate deformation of structural elements subjected to impulsive loading. *Experimental Mechanics, 46*(6), 805–824.
4. Schiffer, A., & Tagarielli, V. (2015). The Response of circular composite plates to underwater blast: Experiments and Modeling. *Journal of Fluids and Structures, 52,* 130–144.
5. Avachat, S., & Zhou, M. (2014). Response of cylindrical composite structures to underwater impulsive loading. *Procedia Engineering, 88,* 69–76.
6. Avachat, S., & Zhou, M. (2015). High-speed digital imaging and computational modeling of dynamic failure in composite structures subjected to underwater impulsive loads. *International Journal of Impact Engineering, 77,* 147–165.
7. LeBlanc, J., & Shukla, A. (2010). Dynamic response and damage evolution in composite materials subjected to underwater explosive loading: An experimental and computational study. *Composite Structures, 92,* 2421–2430.
8. LeBlanc, J., & Shukla, A. (2011). dynamic response of curved composite plates to underwater explosive loading: Experimental and computational comparisons. *Composite Structures, 93,* 3072–3081.
9. Franz, T., Nurick, G., & Perry, M. (2002). Experimental investigation into the response of chopped-strand mat glassfibre laminates to blast loading. *International Journal of Impact Loading, 27,* 639–667.
10. Mouritz, A. P. (1995). The effect of underwater explosion shock loading on the fatigue behaviour of GRP laminates. *Composites, 26,* 3–9.
11. Dear, J., & Brow, S. (2003). Impact damage processes in reinforced polymeric materials. *Composites Part A Applied Science and Manufacturing, 34,* 411–420.
12. Matzenmiller, A., Lubliner, J., & Taylor, R. L. (1995). A constitutive model for anisotropic damage in fiber-composites. *Mechanics of Materials, 20,* 125–152.
13. Zako, M., Uetsuji, Y., & Kurashiki, T. (2003). Finite element analysis of damaged woven fabric composite materials. *Compos Sci Technol, 63,* 507–516.
14. Dyka, C. T., & Badaliance, R. (1998). Damage in marine composites caused by shock loading. *Compos Sci Technol, 58,* 1433–1442.
15. O'Daniel, J. L., Koudela, K. L., & Krauthammer, T. (2005). Numerical simulation and validation of distributed impact events. *International Journal of Impact Engineering, 31,* 1013–1038.

16. McGregor, C. J., Vaziri, R., Poursartip, A., & Xiao, X. (2007). Simulation of progressive damage development in braided composite tubes under axial compression. *Compos Part A, 38,* 2247–2259.
17. Williams, K. V., & Vaziri, R. (2001). Application of a damage mechanics model for predicting the impact response of composite materials. *Computers & Structures, 79*(2001), 997–1011.
18. Gama, B., Xiao, J., Haque, M., Yen, C., & Gillespie, J. (2004). *Experimental and numerical investigations on damage and delamination in thick plain weave S-2 glass composites under quasi-static punch shear loading*. Center for Composite Materials, University of Delaware.
19. Xiao, J., Gama, B., & Gillespie, J. (2007). Progressive damage and delamination in plain weave S-2 glass/SC-15 composites under quasi-static punch-shear loading. *Composite Structures, 78,* 182–196.
20. Donadon, M. V., Iannucci, L., Falzon, B. G., Hodgkinson, J. M., & de Almeida, S. F. M. (2008). A progressive failure model for composite laminates subjected to low velocity impact damage. *Computers & Structures, 86,* 1232–1252.
21. Hosseinzadeh, R., Shokrieh, M. M., & Lessard, L. (2006). Damage behavior of fiber reinforced composite plates subjected to drop weight impacts. *Composites Science and Technology, 66,* 61–68.
22. Batra, R. C., & Hassan, N. M. (2007). Response of fiber reinforced composites to underwater explosive loads. *Composites Part B: Engineering, 38,* 448–468.
23. Chan, S., Fawaz, Z., Behdinan, K., & Amid, R. (2007). Ballistic limit prediction using a numerical model with progressive damage capability. *Composite Structures, 77,* 466–474.
24. Hodge, N. (2004). Military experimenting with 'spray on' armor for humvees. *Defense Today*, *25*.
25. LeBlanc, J., Gardner, N., & Shukla, A. (2013) Effect of polyurea coatings on the response of curved e-glass/vinyl ester composite plates to underwater explosive loading. *Composites Part B: Engineering, 44,* 565–574.
26. LeBlanc, J., & Shukla, A. (2015). Response of Polyurea Coated flat composite plates to underwater explosive loading. *Journal of Composite Materials, 49,* 965–980.
27. Tekalur, A., Shukla, A., & Shivakumar, K. (2008). Blast resistance of polyurea based layered composite materials. *Composite Structures, 84,* 271–281.
28. Gardner, N., Wang, E., Kumar, P., & Shukla, A. (2012). Blast mitigation in a sandwich composite using graded core and polyurea interlayer. *Experimental Mechanics, 52,* 119–133.
29. Amirkhizi, A., Isaacs, J., McGee, J., & Nemat-Nasser, S. (2006). An experimentally-based viscoelastic constituitve model for polyurea, including pressure and temperature effects. *Philosophical Magazine, 86,* 5847–5866.
30. Amini, M. R., Isaacs, J. B., & Nemat-Nasser, S. (2010). Experimental investigation of response of monolithic and bilayer plates to impulsive loads. *International Journal of Impact Engineering, 37,* 82–89.
31. Xue, L., Mock, W., & Belytschko, T. (2010). Penetration of DH-36 steel plates with and without polyurea coating. *Mechanics of Materials, 42,* 981–1003.
32. Grujicic, M., Pandurangan, B., He, T., Cheeseman, B. A., Yen, C. F., & Randow, C. L. (2010). Computational investigation of impact energy absorption capability of polyurea coatings via deformation-induced glass transition. *Materials Science and Engineering: A, 527,* 7741–7751.
33. Bahei-El-Din, Y. A., Dvorak, G. J., & Fredricksen, O. J. (2006). A blast-tolerant sandwich plate design with a polyurea interlayer. *International Journal of Solids and Structures, 43,* 7644–7658.
34. Coombs, A., & Thornhill, C. K. (1967). An underwater explosive shock gun. *Journal of Fluid Mechanics, 29,* 373–383.
35. Poche, L., & Zalesak, J. (1992). *Development of a water-filled conical shock tube for shock testing of small sonar transducers by simulation of the test conditions for the heavyweight MIL-S-901D (Navy)*. NRL Memorandum Report 7109, 10 October 1992.

36. LeBlanc, J., Shillings, C., Gauch, E., Livolsi, F., & Shukla, A. (2016). Near field underwater explosion response of polyurea coated composite plates. *Experimental Mechanics, 56,* 569–581.
37. Dobratz, B. (1972). *Properties of chemical explosives and explosive simulants*. Lawrence Livermore National Laboratory.

Sandwich Structures Subjected to UNDEX Loading

B. Raja Sekhar and S. Gopalakrishnan

1 Introduction

The design of navy vessels primarily involves resistance to underwater blast loads. Sandwich structures if properly designed show high energy absorption capabilities compared to monolithic counterparts, making them suitable for use in Navy structures. However, the design and modeling of sandwich structures is more involved and depends on the type of layers used. Also, studying the effects of an UNDEX load on the sandwich structure is still more complex and involves the modeling of blast wave and its interaction with the surrounding environment and the structure. Its an extremely complex phenomenon with multiple possibilities dictating the final result.

In this chapter, we cover the modeling of sandwich structure, where a computational model based on a more comprehensive theory— extended high order sandwich panel theory (EHSAPT) is explained followed by the treatment of the blast phenomena. Blast loading is simplified with certain assumptions and the subsequent UNDEX loading effects on the sandwich structure are explained. The differences in the fluid–structure interaction (FSI) for the case of both sandwich and monolithic structures is highlighted and a design process is brought out for the sandwich structures.

B. Raja Sekhar · S. Gopalakrishnan (✉)
Department of Aerospace Engineering, Indian Institute of Science,
Bangalore 560012, India
e-mail: krishnan@aero.iisc.ernet.in

B. Raja Sekhar
e-mail: rajsekhargitm@gmail.com

S. Gopalakrishnan and Y. Rajapakse (eds.), *Blast Mitigation Strategies in Marine Composite and Sandwich Structures*, Springer Transactions in Civil and Environmental Engineering, https://doi.org/10.1007/978-981-10-7170-6_4

2 Sandwich Structures

Sandwich structures are widely used in aerospace, marine, and automobile industry. The use of thin face sheets and lightweight core provides good stiffness and yet reduce the weight of the structure way below its monolithic alternatives [1]. Other advantages like tailoring the composite laminated face sheets for thermal isolation, suitable embedments in the core for heat dissipation, etc., gives flexibility to the designer. Due to this design flexibility, the study of sandwich structures has grown enormously in the recent past.

Naval structures are designed to bear UNDEX loading. Earlier the designs to these loads were addressed with monolithic structures, where simple analytical models were developed such as the one-dimensional fluid–structure interaction model [2]. Presently, the advantages of the sandwich over monolithic structures direct the study of sandwich structures to underwater shock loads.

In the next section, modeling of sandwich structure is addressed with the main focus on the flexible core formulation presented by the authors in [3]. This formulation includes detailed coupled kinematic deformations and is suitable for both a flexible and a rigid core.

3 Modeling Sandwich Structures

Sandwich structures are typically modeled by assuming the displacement kinematics which are known as displacement-based theories. These displacement-based theories are classified as the equivalent single layer (ESL) theories and the layer-wise theories. The most common ESL theories are the classical laminate theory (CLT) and the first-order shear deformation theory (FSDT). The Euler–Bernoulli theory for beams and Kirchoff theory for plates are the CLT counterparts for monolithic structures. Similarly, Timoshenko theory for beams and Reisnner–Mindlin theory for plates are the FSDT counterparts for monolithic structures. Other higher order shear deformation theories classified as the ESL theories for sandwich members are reviewed in detail in [4]. In the ESL theories, the core is assumed to be incompressible and the cross-sectional stiffness is obtained by through thickness integration. Alternatively, in layer-wise theories, each layer is analyzed using independent kinematic assumptions and the continuity between the adjacent layers is imposed either through the displacement or stress/strain. The usage of these theories is suited for softer cores.

For a compliant core, a mixed model for sandwich beam is presented in [5], where the transverse normal and transverse shear stress is taken into account and is popularly known as the higher order sandwich panel theory (HSAPT). This theory uses the classical theory of the face sheets and 3D elasticity for the core. Frostig and Baruch [6] enhanced the same model to investigate the localized load effects in the sandwich panels. Due to the complexity in the kinematic assumptions the consideration

of the in-plane rigidity is ignored in both the above-cited references. Experimentally it is shown in [7] that the compliant core absorbs energy and undergoes significant transverse deformation and HSAPT can be used in the case of compliant core as compared to the ESL theories mentioned above. However, in dynamic problems, especially high transient loading cases, the axial acceleration, and the core density is not negligible. When the axial inertial terms are included, the constant shear stress distribution through the height of the core is not valid and an extended high order sandwich panel theory (EHSAPT) is proposed in [8], by taking into account the axial rigidity of the core. Thus, in their work, the results for static responses are presented and compared with that of the elasticity solutions; demonstrating the superior accuracy of this theory. Later, the same theory is used to study wrinkling behavior in sandwich panels and is presented in [9]. The results are compared with the elasticity solutions and experiments, where close match is observed. Phan et al. [10] used the same theory by considering both the static and dynamic parts of the equations. Here the blast loading case is presented, demonstrating the cavitation-like phenomena in sandwich beams and a good comparison of dynamic response with elasticity solutions is made. The HSAPT and the EHSAPT mentioned above have assumed a very thin face sheets and hence the assumption of the classical theory for face sheets holds good.

Tailoring of the composite laminate face sheets based on the design requirement leads to increase in layers with different orientation making the laminate thicker and hence the shear deformation effect cannot be neglected. By including the shear deformation in the face sheets, a more general higher order sandwich panel theory is proposed in [11]. Here, the face sheets of the sandwich panel can be modeled with a composite lamina of arbitrary orientation in the lay-up sequence and also different cores can be implemented through the thickness of the sandwich panel. The theory assumes the face sheets to be thick where the shear deformation is taken into account by modeling the face sheets on the assumptions made in FSDT. Similar to the HSAPT and EHSAPT, the displacement functions are made compatible with the core interfaces of the top face sheet and at the bottom face sheet. With regard to the composite laminated face sheets, there is one significant difference in this theory, that is the reference plane is at the mid-surface of the sandwich panel and therefore the computation of the laminate cross-sectional stiffnesses (A_{ij}, B_{ij}, D_{ij}) are relative to the reference plane, which leads to the fact that even though the face sheet laminate is symmetric B_{ij} does not vanish; except when the symmetry is present only if the entire sandwich panel is symmetric. Although the theory suggested here is general, only the static part has been formulated and the examples of static problems were demonstrated using finite-element method (FEM).Though FEM is very efficient, highly transient loading cases make it computationally expensive and methods like spectral element method (SEM) are more useful [12], reasons for which are given in the next section.

In the following sections, a complete general higher order sandwich panel theory is developed by extending the above-mentioned theory proposed in [11] with the inclusion of the inertial terms, which enables us to address dynamic and wave propagation problems. Based on this extended theory SEM model is formulated.

3.1 Computational Model for Sandwich Beam Using SEM

In this section, a brief explanation of the spectral element method and its advantages are given after which the spectral element formulation for a sandwich beam with flexible orthotropic core based on Oskooei et al. [11] formulation extended to include dynamics is explained.

3.1.1 Spectral Element Method (SEM)

In high-frequency analysis, the wavelength is very small. The finite- element (FE) codes with linear/quadratic Lagrangian interpolant shape functions, known as *h*-type elements provide increased accuracy as the number of elements are increased. While employing *p*-type FEs, the accuracy increases as the polynomial order is increased. Many *p*-type FEs employ hierarchical shape functions and do not constitute a nodal basis like the Lagrangian interpolants do and these are well suited for adaptive refinement [13]. However, the *p*-type FEs show large errors at the ends of the element as we increase the order of the polynomial-*p*. This can be seen in the Fig. 1a, where seventh degree FEM shape functions show undesired oscillations at the element ends. This is called Runge phenomena and due to this high errors are induced at the element ends.To overcome this, the nodal position should be altered unlike the conventional equidistant FE node distribution. The density of the nodes should be high at the ends in order to nullify this error. This kind of nodal distribution is arrived by using the nodes which are the roots of Legendre polynomials [14] and the Lobatto node distribution is given as,

$$(1 - \xi_i^2) P'_p(\xi_i) = 0 \tag{1}$$

where P'_p is the derivative of the Legendre polynomial of the order "p" with respect to its independent variable ξ. These node distributions are spaced $O(1/N^2)$ apart, near the end points versus the $1/N$ spacing that is conventionally maintained. Figure

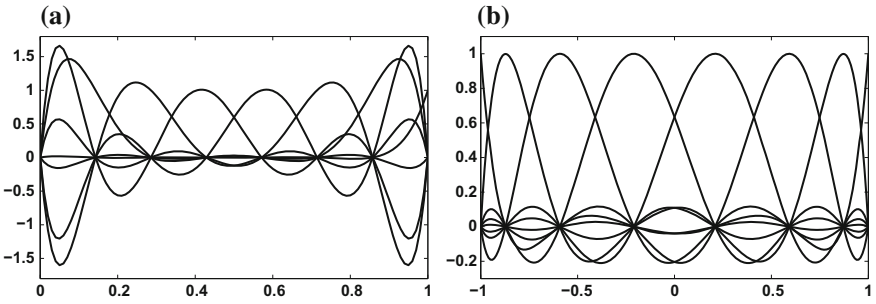

Fig. 1 **a** Conventional FEM shape functions derived by taking 8 equidistant nodes; **b** shape functions based on Lobatto node distribution

1b shows the Lobatto node distribution interpolants which, do not show any end oscillations unlike the FEM shape functions. The interpolants formed based on the Lobatto node distribution have a discrete orthogonal property given as

$$\int_{-1}^{1} \phi_i(\xi)\,\phi_j(\xi)\,dx = \sum_{k=1}^{p+1} w_k\,\phi_i\left(\xi_k\right)\phi_j\left(\xi_k\right) = w_k\delta_{ij} \tag{2}$$

where δ_{ij} denotes the Kronecker symbol and w_k denotes the weights of the Gauss–Lobatto–Legendr (GLL) quadrature:

$$w_k = \frac{2}{p(p+1)}\frac{1}{\left(P_p\left(\xi_k\right)\right)^2},\quad k = 1, 2, \ldots p+1$$

This discrete orthogonality property of the Lobatto polynomials cuts down the computational cost intensely by rendering the mass matrix diagonal, removing the need to resort to diagonalization schemes. The GLL quadrature is exact for a $2n-3$ degree polynomial [15], where n is the number of points.

Spectral elements are also p-type FEs, but their shape functions are Lagrangian interpolants with node locations like the above mentioned Lobatto nodes. These have the accuracy of global spectral methods with geometric flexibility of h-type FEs. The use of Legendre polynomial spectral element to isotropic rod is presented in [12], for wave propagation problems using beam elements which are formulated based on Timoshenko beam theory is presented in [12, 13] and more recently for Reisnner–Mindlin composite plates in [16].

3.1.2 Spectral Element Formulation

To solve computationally demanding wave propagation problems, spectral elements with seventh-degree interpolants, obtained by Lobatto node distribution as shown in Fig. 2 are considered. The geometry of the sandwich beam or wide panel is shown in Fig. 3, where the core is bonded between two laminated composite face sheets. The thickness of the top face sheet is denoted by f_t, the bottom face sheet thickness by f_b and core thickness as $2c$. The displacement function of the face sheet is expressed based on the assumptions made in FSDT and are given as,

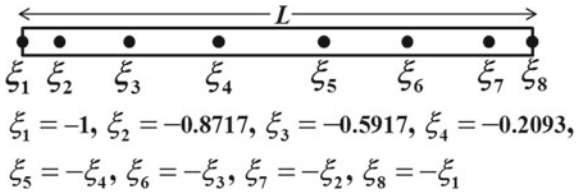

Fig. 2 Lobatto node distribution in the GLL quadrature domain [−1, 1], for a 8-node beam Spectral element scheme

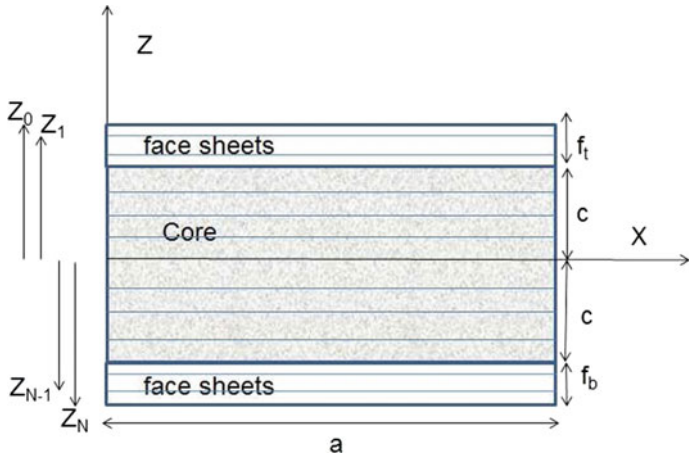

Fig. 3 Sandwich beam configuration

For top face sheet:
$c \leq z \leq c + f_t$,

$$u^t(x,z,t) = u_0^t(x,t) - \left(z - c - \frac{f_t}{2}\right)\psi_0^t(x,t), \tag{3a}$$

$$w^t(x,z,t) = w_0^t(x,t) \tag{3b}$$

For bottom face sheet:
$-(c + f_b) \leq z \leq -c$,

$$u^b(x,z,t) = u_0^b(x,t) - \left(z + c + \frac{f_b}{2}\right)\psi_0^b(x,t), \tag{4a}$$

$$w^b(x,z,t) = w_0^b(x,t) \tag{4b}$$

The use of FSDT introduces shear locking effect in the conventional FE formulations and is alleviated by reduced integration or by choosing unequal higher order polynomials for the in-plane and out-of-plane displacements [17]. Here, it is to be mentioned that the use of higher order polynomials in the SEM avoids this shear locking behavior in the face sheets [16]. The core is modeled with a cubic polynomial in "z" for in-plane and a quadratic polynomial in "z" for out-of-plane displacement functions and are taken as

For core:
$-c \leq z \leq c$,

$$u^c(x,z,t) = u_0^c(x,t) + z\,\phi_0^c(x,t) + z^2\,u_2^c(x,t) + z^3\,u_3^c(x,t), \tag{5a}$$

$$w^c(x,z,t) = w_0^c(x,t) + z\, w_1^c(x,t) + z^2\, w_2^c(x,t) \tag{5b}$$

In the above equations $u(x,z,t)$ indicates the axial displacement function, $w(x,z,t)$ the transverse displacement function, $\psi_0(x,t)$ the rotation of the transverse normal about the Y axis, u_0 and w_0 indicates displacement of the point at $z=0$, ϕ_0 is the mid-plane rotation and u_2, u_3, w_1, w_2 are the Taylor's series expansion of the respective axial and transverse displacement fields. The superscripts ^{t}, ^{b} and ^{c} indicate the top face sheet, bottom face sheet and the core respectively. These displacement results in quadratic transverse shear stress and cubic axial stress resulting to 2D elasticity profiles. Enforcing displacement compatibility conditions at the interfaces between the top face sheet and the core ($z=c$) and similarly on the bottom face sheet and the core ($z=-c$), the core in-plane and out-of-plane displacement fields are thus given as

$$\begin{aligned} u^c(x,z,t) = {} & z\left(1-\frac{z^2}{c^2}\right)\phi_0^c(x,t) + \frac{z^2}{2c^2}\left(1-\frac{z}{c}\right)u_0^b(x,t) + \left(1-\frac{z^2}{c^2}\right)u_0^c(x,t) \\ & + \frac{z^2}{2c^2}\left(1+\frac{z}{c}\right)u_0^t(x,t) + \frac{f_b z^2}{4c^2}\left(-1+\frac{z}{c}\right)\psi_0^b(x,t) \\ & + \frac{f_b z^2}{4c^2}\left(1+\frac{z}{c}\right)\psi_0^t(x,t) \end{aligned} \tag{6a}$$

$$\begin{aligned} w^c(x,z,t) = {} & \left(-\frac{z}{2c}+\frac{z^2}{2c^2}\right)w_0^b(x,t) + \left(1-\frac{z^2}{c^2}\right)w_0^c(x,t) \\ & + \left(\frac{z}{2c}+\frac{z^2}{2c^2}\right)w_0^t(x,t) \end{aligned} \tag{6b}$$

Considering linear terms, the strain displacement relations are given as

For face sheets:

$$\left\{\epsilon^{t,b}\right\} = \begin{Bmatrix} \epsilon_{xx}^{t,b} \\ \gamma_{xz}^{t,b} \end{Bmatrix} = \begin{Bmatrix} \frac{\partial u^{t,b}}{\partial x} \\ \frac{\partial u^{t,b}}{\partial z} + \frac{\partial w^{t,b}}{\partial x} \end{Bmatrix} = [Z^{t,b}]\,[\partial^{t,b}] \begin{Bmatrix} u_0^{t,b} \\ w_0^{t,b} \\ \psi_0^{t,b} \end{Bmatrix} \tag{7}$$

For core:

$$\{\epsilon^c\} = \begin{Bmatrix} \epsilon_{xx}^c \\ \epsilon_{zz}^c \\ \gamma_{xz}^c \end{Bmatrix} = \begin{Bmatrix} \frac{\partial u^c}{\partial x} \\ \frac{\partial w^c}{\partial x} \\ \frac{\partial u^c}{\partial z} + \frac{\partial w^c}{\partial x} \end{Bmatrix} = [Z^c]\,[\partial^c] \begin{Bmatrix} u_0^t \\ w_0^t \\ \psi^t \\ u_0^c \\ w_0^c \\ \phi_0^c \\ u_0^b \\ w_0^b \\ \psi_0^b \end{Bmatrix} \tag{8}$$

where the matrices $[Z^{t,b,c}]$ and $[\partial^{t,b,c}]$ are given in the appendix. The orthotropic constitutive relations are given as
For face sheets:

$$\begin{Bmatrix} \sigma_{xx}^{t,b} \\ \tau_{xz}^{t,b} \end{Bmatrix} = \begin{bmatrix} Q_{11}^{t,b} & 0 \\ 0 & Q_{55}^{t,b} \end{bmatrix} \begin{Bmatrix} \epsilon_{xx}^{t,b} \\ \gamma_{xz}^{t,b} \end{Bmatrix} \tag{9}$$

For core:

$$\begin{Bmatrix} \sigma_{xx}^{c} \\ \sigma_{zz}^{c} \\ \tau_{xz}^{c} \end{Bmatrix} = \begin{bmatrix} Q_{11}^{c} & Q_{13}^{c} & 0 \\ Q_{13}^{c} & Q_{33}^{c} & 0 \\ 0 & 0 & Q_{55}^{c} \end{bmatrix} \begin{Bmatrix} \epsilon_{xx}^{c} \\ \epsilon_{zz}^{c} \\ \gamma_{xz}^{c} \end{Bmatrix} \tag{10}$$

where the matrix $[Q_{ij}]$, is the stiffness matrix.

Using the principle of virtual work,

$$\delta\, W_I \;=\; \delta\, W_E$$

where W_I is the work done due to internal forces or strain energy stored and W_E is the work done due to inertial forces and external forces applied to the beam. The same procedure that formulates a typical finite element equations is followed resulting in 9 degrees of freedom (DOF) per node. This leads to the equilibrium equation of the form as

$$\begin{aligned} &\left[\int_0^a b\,\Big(\,[B^t]^T\,[C^t]\,[B^t] + [B^c]^T\,[C^c]\,[B^c]\; + [B^b]^T\,[C^b]\,[B^b]\,\Big)dx\right]\{\bar{u}\} + \\ &\left[\int_0^a b\,\Big(\,[N^t]^T[R^t][N^t] + [N^c]^T[R^c][N^c] + [N^b]^T[R^b][N^b]\,\Big)dx\right]\{\ddot{\bar{u}}\} \\ &= \{F\} \end{aligned} \tag{11}$$

where $[B^x]$ is the strain-displacement matrix, $[R^x]$ is the inertia matrix $[N^x]$ is the shape functions matrix, $[C^x]$ is the through thickness integrated, transformed stiffness matrix and are given in the appendix. The superscript $(^x)$ is "t" for top face sheet, "b" for bottom face sheet, "c" for the core and $\{F\}$ is the force vector. The above equation is written in standard form as

$$[M]\{\ddot{\bar{u}}\} + [K]\{\bar{u}\} = \{F\} \tag{12}$$

where superscript $(\cdots)$ represents double time derivative, $[M]$ the mass matrix, $[K]$ the stiffness matrix and $\bar{u}$ represents the nodal displacement vector given as

$$\begin{aligned}\{\bar{u}\} = \{&{}^{1}u_0^t,\ {}^{1}w_0^t,\ {}^{1}\psi_0^t,\ {}^{1}u_0^c,\ {}^{1}w_0^c,\ {}^{1}\phi_0^c,\ {}^{1}u_0^b,\ {}^{1}w_0^b,\ {}^{1}\psi_0^b,\\ &{}^{2}u_0^t,\ {}^{2}w_0^t,\ {}^{2}\psi_0^t,\ {}^{2}u_0^c,\ {}^{2}w_0^c,\ {}^{2}\phi_0^c,\ {}^{2}u_0^b,\ {}^{2}w_0^b,\ {}^{2}\psi_0^b \ldots\\ &\ldots {}^{8}u_0^t,\ {}^{8}w_0^t,\ {}^{8}\psi_0^t,\ {}^{8}u_0^c,\ {}^{8}w_0^c,\ {}^{8}\phi_0^c,\ {}^{8}u_0^b,\ {}^{8}w_0^b,\ {}^{8}\psi_0^b\}^T\end{aligned} \tag{13}$$

where superscript ($^1, \ldots, ^8$) denotes the node numbers for each element.

4 UNDEX Phenomena and FSI

UNDEX is a complex phenomenon with multiple consequences. Hence, studies on this are mostly made with lot of simplifications and assumptions. In this section, the UNDEX phenomena, pressure load quantification, and the interaction of the structure with the fluid pressure load is explained. This forms the basis for analysis of the behavior of sandwich structure subjected to an UNDEX.

4.1 UNDEX Phenomena

Underwater explosion results in a spherical compression shock wave and a spherical gas bubble both having the point of explosion as the center. However, the shock wave is very rapid and lasts for a few milliseconds whereas the gas bubble dynamics last upto a second [18]. Even the pressure magnitudes due to these two effects differ significantly.

First, the shock wave interacts with its surroundings producing reflections which interfere to produce pressure loading again. These reflections may be a compression shock wave or a tension shock wave. For example, reflection from the sea bottom produces a compression shock wave where as reflection from surface produces a tension shock wave due to changes in the impedance. The action of these reflected shock waves bears a time lag with the incident shock wave but can cause high pressures. Another phenomenon which occurs due to the reflected tension shock wave is cavitation. Water cannot take tensile pressure and a huge region through which this reflection passes would cavitate. However, this cavitated region does not stay so for long before it closes and produces a water hammer kind of effect generating pressure waves again. These pressure waves would interact with the surroundings and generate reflections which can repeat the whole thing again.

While the repercussions of the incident shock wave continue, the spherical gas bubble also adds to the dynamics. The spherical gas bubble shows a behavior similar to a spring–mass system where the mass is stretched and left to oscillate. The gas bubble too expands and contracts due to the interplay of inertia and pressure differences inside and outside the bubble. This causes pressure to vary in the surrounding along with the diameter of the gas bubble with maximum pressure at minimum diameter. Finally, these pulsations stop once the energy gets dissipated or the gas bubble

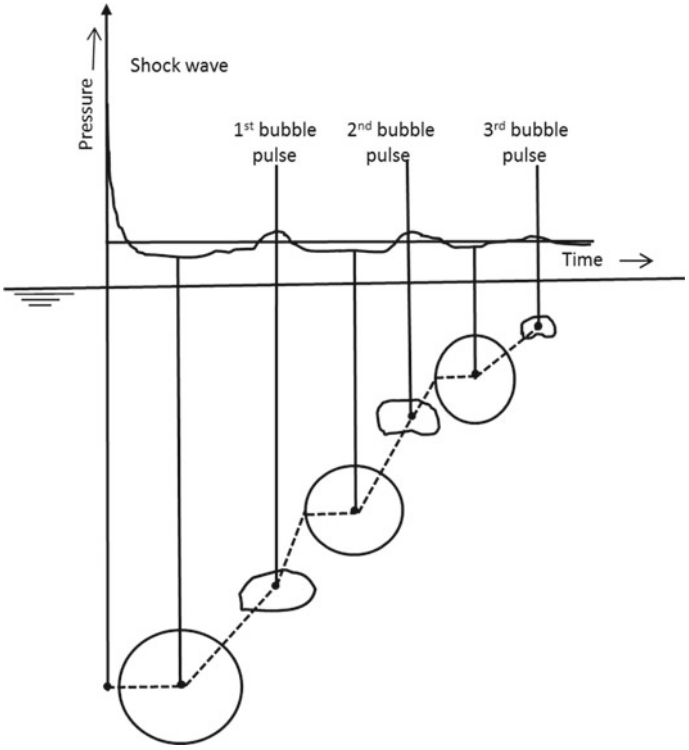

Fig. 4 Pressure–time plot due to shock wave and the pulsating bubble phenomena [19]

reaches the surface. However, during these pulsations considerable pressure force is created on the vicinity though not as high in magnitude as the incident shock wave. A qualitative idea of the pressure-time plot is illustrated in Fig. 4.

As can be seen from Fig. 4, the maximum damage would be caused due to the high peak pressure generated by incident shock wave. Hence, most of the damage prediction studies isolate this shock loading and study its effects. This shock wave pressure–time variation is conveniently modeled by an exponentially decaying curve and perfectly matches the shock wave till the time θ (decay constant) when peak pressure (P_m) decays to $1/e$ of its value. Figure 5 shows the exponential fit (Curve II) to the shock wave load. The shockwave parameters P_m and θ depend on the type of explosive, quantity of explosive and distance of the point where the pressure is measured [19].

$$P(x,t) = P_m\, e^{-\frac{t}{\theta}} \tag{14}$$

where

$$P_m = 52.4\left(\frac{m^{1/3}}{R}\right)^{1.13} \text{MPa},\ \theta = 0.084\, m^{1/3}\left(\frac{m^{1/3}}{R}\right)^{-0.23} \text{ms}$$

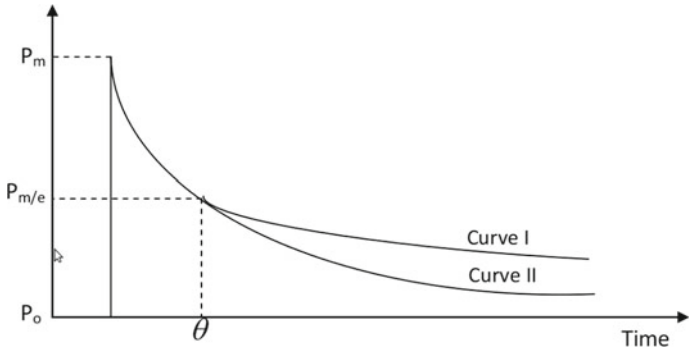

Fig. 5 Primary shock parameters: Peak pressure P_m, decay constant θ. Curve I is the actual plot and Curve II is the exponential fit to it which is good enough up to one decay constant [19]

and m, R are the mass of the TNT explosive in kg and the distance of the point of observance from it.

4.2 Fluid–Structure Interaction

The incident shock wave and the subsequent pressure waves due to reflections makes the whole blast scenario complex and difficult to study. However, the high impact is due to the primary shock wave and hence only this is considered to study the blast effects. Still, modeling the shock wave propagation and the fluid–structure interaction is a daunting task. In case of contact explosions, it is much more difficult owing to the nonlinear wave effects. In the present chapter, fluid–structure interaction for noncontact explosions is presented. This assumption allows to model the blast wave using linear acoustic theory. Also, the shock wave is assumed to be a plane wave in both the models presented.

In the next section, most widely used analytical models for the fluid–structure interaction are presented. For the monolithic structures the very old and popular model by Taylor [2] and for the sandwich structures the Hayman's model [20] are explained. Based on these FSI models, the structure behavior is studied in many works. Makinen [21] studied the fluid–structure interaction by using a simplified 1D finite element model of a sandwich section. Fleck and Deshpande [22] developed an approximate analytical methodology to analyze the dynamic response of metallic sandwich beams subject to both air and water blasts. Librescu et al. [23] studied the dynamic response of anisotropic sandwich flat panels subjected to underwater and in-air explosions.

4.2.1 Taylor's Model

Taylor developed a model for the response of a free-standing plate undergoing rigid body motion due to a blast loading. Total pressure that the plate is subjected to is the

summation of incident pressure, reflected pressure, and rarefaction pressure developed as a result of the acceleration of the plate. The reflection is assumed to be perfect and the resistance due to the end supports is neglected because of the highly transient nature of loading. Hence, the total pressure on the plate is

$$P(x,t) = P_{incident} + P_{reflected} + P_{rarefaction}$$

$$= P_m e^{-\frac{(t-x/c_w)}{\theta}} + P_m e^{-\frac{(t+x/c_w)}{\theta}} - \rho_w c_w \dot{w}\left(t + x/c_w\right) \tag{15}$$

where ρ_w is the density of water, c_w is the speed of blast wave in water, $x = 0$ at the side of the plate first in contact with the blast wave, positive x-direction is the incident wave direction, and w is the deflection of the plate. Using Newton's second law, the equation of motion for the rigid plate with mass per unit area (m_f) is given as

$$m_f \ddot{w}(x,t) = P_m e^{-\frac{(t-x/c_w)}{\theta}} + P_m e^{-\frac{(t+x/c_w)}{\theta}} - \rho_w c_w \dot{w}\left(t + x/c_w\right) \tag{16}$$

Taylor's model fairly predicts the behavior of a rigid plate and hence does not consider the energy dissipation due to deformation of the structure. However, in the case of sandwich structures, major blast mitigation is achieved with suitable core and hence this contribution of internal strain energy due to deformation of the structure has to be considered.

4.2.2 Hayman's Model

Hayman developed an analytical model for the FSI of sandwich structure and UNDEX created shock wave. The blast shock is assumed as a plane wave and linear wave theory concepts are applied. Facesheets are assumed to be infinitely thin and hence transmission through them is neglected. Using the equilibrium and compatibility relations at the fluid–facesheet and facesheet–core junctions the expression for pressure variation are arrived. The analysis can be divided into three stages before arriving at the final pressure in the fluid. This is represented pictorially in the Fig. 6.

The incident pressure wave impinging on the front face sheet $P_i(t)$ in positive x direction, is reflected at the front face sheet surface $P_{r1}(t)$, and a part is transmitted into the core $P_{c1}(t)$, which impinges on the rear face sheet as shown in the first column of Fig. 6. Transmission through the front face sheet is neglected as it is assumed that facesheets are infinitely thin sheets having mass per unit area m_f kg/m^2.

The equilibrium equation for the front face sheet moving at a speed $v_f(t)$ is

$$P_i(t) + P_{r1}(t) - P_{c1}(t) = m_f \dot{v}_f(t)$$

The particle velocities at the front face sheet due to the three pressure waves are u_i, u_{r1} and u_{c1}, respectively, and are related to the pressures by the impedance of the medium as

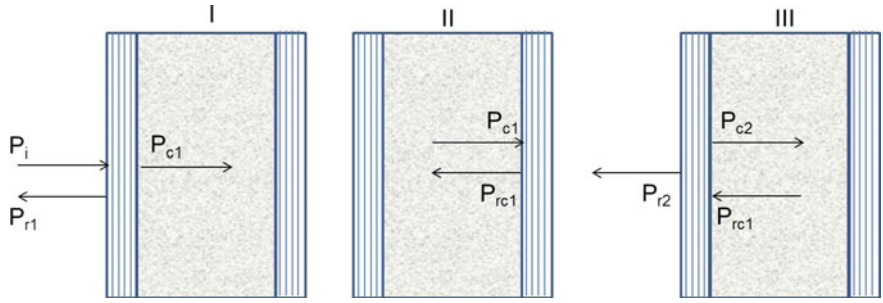

Fig. 6 Reflections and transmissions of the incident shock wave at the fluid–facesheet and facesheet–core junctions

$$u_i = \frac{P_i}{\rho_w c_w},\ u_{r1} = -\frac{P_{r1}}{\rho_w c_w},\ u_{c1} = \frac{P_{c1}}{\rho_c c_c}$$

where ρ_w, ρ_c are the densities of water and core, respectively, and c_w, c_c are the acoustic velocities in water and core respectively.

These particle velocities should obey the following relationship in order to ensure compatibility at the front face sheet:

$$u_i(t) + u_{r1}(t) = u_{c1}(t) = v_f(t)$$

Using the above two equilibrium and compatibility relations, the expressions for the reflected and transmitted pressure waves, $P_{r1}(t)$ and $P_{c1}(t)$ are found by solving a first-order differential equation with constant coefficients and using the initial condition $v_f(0) = 0$.

$$\begin{aligned} P_i(x,t) &= P_o e^{-\alpha\left(t-\frac{x}{c_w}\right)} \\ P_{r1}(x,t) &= B_1 e^{-\alpha\left(t+\frac{x}{c_w}\right)} + B_2 e^{-\beta\left(t+\frac{x}{c_w}\right)} \\ P_{c1}(x,t) &= A\left(e^{-\alpha\left(t-\frac{x}{c_w}\right)} - e^{-\beta\left(t-\frac{x}{c_w}\right)}\right) \end{aligned}$$

where the constants are given by

$$\alpha = \frac{1}{\theta};\quad \beta = \frac{(\rho_w c_w + \rho_c c_c)}{m_f};\quad \gamma = \frac{\rho_c c_c}{m_f}$$

$$A = \frac{2\gamma P_o}{(\beta - \alpha)};\quad B_2 = \frac{2(\beta - \gamma) P_o}{(\beta - \alpha)};\quad B_1 = P_o - B_2$$

The transmitted wave $P_{c1}(t)$ reaches the rear face sheet after a certain time and is assumed to be reflected back $P_{rc1}(t)$ without any transmission as shown in the second column of Fig. 6. As the rear facesheet is supported on the other side by air this is a

good assumption. Hence, the equilibrium and the compatibility relationships at the rear facesheet moving with a velocity $v_r(t)$ are given by

$$P_{c1}(t) + P_{rc1}(t) = m_r \dot{v}_r(t), \quad u_{c1}(t) + u_{rc1}(t) = v_r(t)$$

and the pressure wave velocities, u_{c1} and u_{rc1} are related to the pressures by the impedance of the medium, i.e.,

$$u_{c1} = \frac{P_{c1}}{\rho_c c_c}, \quad u_{rc1} = -\frac{P_{rc1}}{\rho_c c_c}$$

Using these two equilibrium and compatibility equations at the rear facesheet and the expression for the reflected wave $P_{c1}(t)$ found previously, the transmitted pressure wave, $P_{rc1}(t)$ is found by solving a first order differential equation with constant coefficients and using the initial condition $v_r(0) = 0$.

$$P_{rc1}(x,t) = D_1 e^{-\alpha(t+\frac{x}{c_w}-\frac{h_c}{c_c})} + D_2 e^{-\beta(t+\frac{x}{c_w}-\frac{h_c}{c_c})} + D_3 e^{-\gamma(t+\frac{x}{c_w}-\frac{h_c}{c_c})}$$

where the constants are given by

$$D_1 = \frac{-2\gamma(\alpha+\gamma)P_o}{(\beta-\alpha)(\gamma-\alpha)}; \; D_2 = \frac{-2\gamma(\beta+\gamma)P_o}{(\beta-\alpha)(\beta-\gamma)}; \; D_3 = -\left(D_1 + D_2\right)$$

The reflected wave $P_{rc1}(t)$ reaches the front face sheet after a time $2h_c/c_c$, where h_c is the thickness of the core and is partly reflected back $P_{c2}(t)$, and partly transmitted into the water $P_{r2}(t)$ as shown in the last column of Fig. 6. The equilibrium and compatibility equations of the front facesheet moving with a velocity v_{2f} and assuming this as an independent event are given as

$$P_{rc1}(t) + P_{c2}(t) - P_{r2}(t) = -m_f \dot{v}_{2f}(t), \quad u_{rc1}(t) + u_{c2}(t) = u_{r2}(t) = -v_{2f}(t)$$

and the corresponding pressure wave velocities u_{rc1}, u_{c2} and u_{r2} are related to the pressures by the impedance of the medium, i.e.,

$$u_{rc1} = \frac{P_{rc1}}{\rho_c c_c}, \quad u_{c2} = -\frac{P_{c2}}{\rho_c c_c}, \; u_{r2} = \frac{P_{r2}}{\rho_w c_w}$$

Using these two equilibrium and compatibility relations at the front facesheet, the expressions for the reflected and transmitted pressure waves $P_{c2}(t)$ and $P_{r2}(t)$ are found by solving a first-order differential equation with constant coefficients and using the initial condition $v_{2f}(0) = 0$.

$$P_{r2}(x,t) = E_1 e^{-\alpha(t+\frac{x}{c_w}-\frac{2h_c}{c_c})} + \left(E_2 + E_3\left(t - \frac{2h_c}{c_c}\right)\right) e^{-\beta(t+\frac{x}{c_w}-\frac{2h_c}{c_c})} + E_4 e^{-\alpha(t+\frac{x}{c_w}-\frac{2h_c}{c_c})}$$

This phenomenon takes place again and repeated reflections and transmissions take place at the facesheet–core junctions resulting in new pressure waves with reduced intensity. Hence, further pressure contributions are neglected and the total pressure in the water in front of the sandwich beam is taken as the summation of the three pressure waves P_i, P_{r1} and P_{r2}.

$$P(x,t) = P_i(t - x/c_w) + P_{r1}(t + x/c_w) + P_{r2}(t + x/c_w - 2h_c/c_c)$$

In case of neglecting the pressure wave transmission through the core as in the case of monolithic structures, the equilibrium and compatibility relationships for the front face sheet are arrived by treating it in the same manner as the rear face sheet in the sandwich structure which is supported on the other side by air and hence the expression for the reflected pressure can be obtained. The total pressure would then be the summation of the incident pressure and this reflected pressure only. Hence, equilibrium and the compatibility relationships at the front facesheet moving with a velocity $v_{1f}(t)$ are given by:

$$P_i(t) + P_{r1}(t) = m_f \dot{v}_{1f}(t), \quad u_i(t) + u_{r1}(t) = v_{1f}(t)$$

and the pressure wave velocities, u_i and u_{r1} are related to the pressures by the impedance of the medium, i.e.,

$$u_i = \frac{P_i}{\rho_w c_w}, \quad u_{r1} = -\frac{P_{r1}}{\rho_w c_w}$$

Using these two equilibrium and compatibility relations at the front facesheet, the expressions for the reflected pressure wave $P_{r1}(t)$ is found by solving a first order differential equation with constant coefficients and using the initial condition $v_{1f}(0) = 0$.

$$P_{r1}(t) = F_1 e^{(\gamma-\beta)t} + F_2 e^{-\alpha t}$$

where $F_1 = \frac{2P_o(\beta-\gamma)}{\beta-\gamma-\alpha}$, $F_2 = \frac{P_o(-\alpha+\gamma-\beta)}{\beta-\gamma-\alpha}$ and the total pressure in water in front of the sandwich beam is the summation of the incident and reflected pressures P_i and P_{r1}.

$$P(x,t) = P_i(t - x/c_w) + P_{r1}(t + x/c_w)$$

5 Fluid Pressure on Sandwich Structure

There are significant differences in the FSI of a sandwich structure and a monolithic structure. Due to transmission of pressure wave through core and subsequent reflections, the fluid pressure magnitude and duration vary considerably. The major

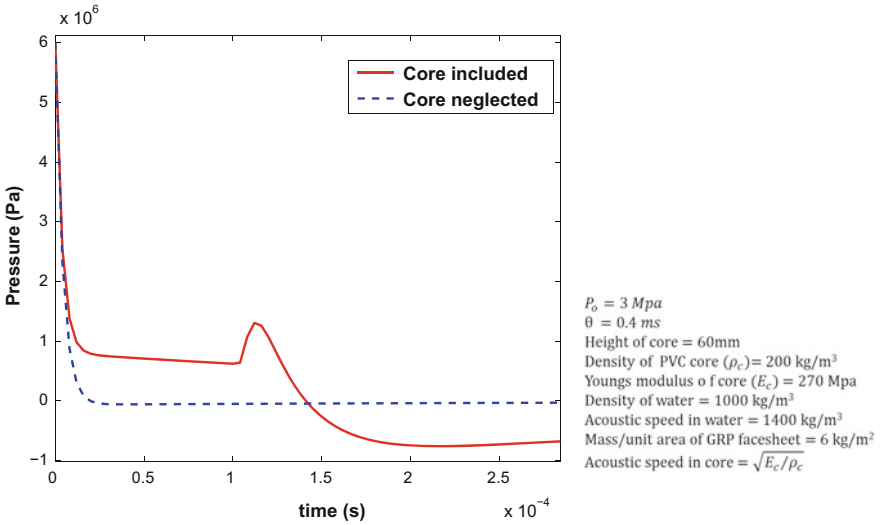

Fig. 7 Pressure–time plot for sandwich beam with GRP facesheet and PVC core. Effect on cavitation time when core effects are included and neglected

consequence is the difference in cavitation formation in the fluid. Tension created in the water due to the interaction of the incident and reflected waves leads to cavitation as water cannot sustain tensile pressure. This cavitation near the surface of the sandwich structure dictates the time until which fluid load is present on the structure. Cavitation time and hence loading differs in both these cases. In Fig. 7 the comparison is shown for the case of a sandwich beam with GRP facesheets and PVC core. The analysis is done considering wave propagation through the core and the one without the core, and we can see the significant variation in the times when pressure goes below zero and the pressure–time variation is also different. For the case where core effects are included cavitation may happen at 0.141 ms and for the other case it is 0.02 ms.

Another observation pointed by Hayman [20] is the formation of two cavitation zones in the case of a sandwich structure: one near the fluid–facesheet interface and other is at a small distance away in the fluid. This can be seen in the pressure variation in the fluid in front of the same sandwich structure in Fig. 8. The pressure variation snapshot at the three different times show the two cavitation zones developed at the fluid–facesheet junction and at a distance of 0.08 m ahead of the sandwich beam. In case there is considerable distance between these two cavitation zones, the water in between moves along with the sandwich beam adding to the structure's mass. Though cavitation formation is dependent on the kind of layers in the sandwich structure, its length and cavitation pressure of the fluid, there is a great difference in the phenomena when compared to monolithic structures.

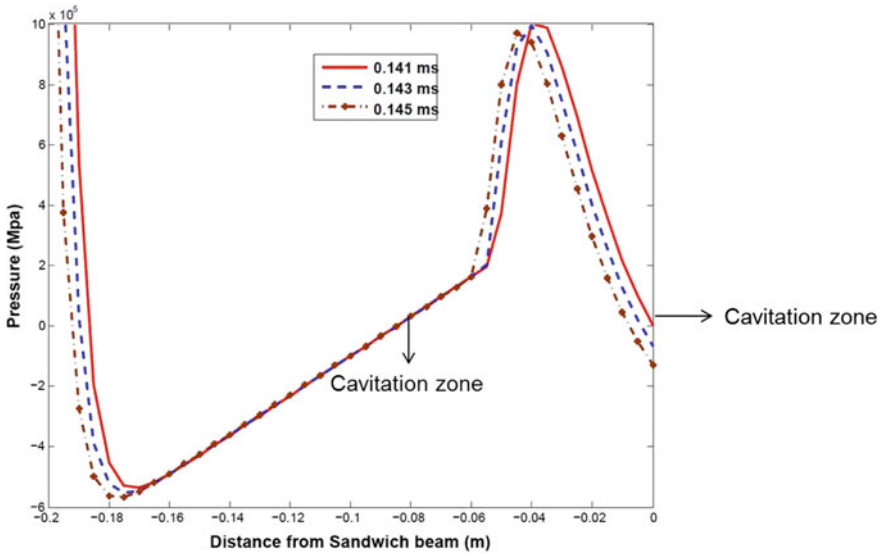

Fig. 8 Pressure variation in fluid before the sandwich beam at different time snapshots. Two cavitation zones can be seen: fluid–facesheet junction and in the fluid

5.1 Sandwich Structure Behavior and Design to UNDEX Loading

In this section, a numerical example is presented and analysis is done to show the behavior of sandwich structure subjected to UNDEX loading and a suggestive design process is presented. Material like fiber metal laminate (FML), which is a hybrid material consisting of alternate metal and fiber-reinforced composite is considered for the facesheet owing to its properties like high impact strength, resistance to crack propagation, increasing tensile strength with strain rate, etc., The response of sandwich beam with fiber metal laminate (FML) face sheets of GLARE 5 and aluminum low-density core subjected to the UNDEX loading with peak pressure $P_o = 1$ Mpa and $\theta = 0.1$ ms is obtained. Computational model for the sandwich beam and fluid pressure calculated as described in the previous section are used to obtain the responses.

GLARE5 FML constitutes of 3 layers of 2024-T3 aluminium alloy and 2 layers of S2-glass/epoxy laminates arranged alternately as shown in Fig. 9. Each S2-glass/epoxy layer has a layup of [0/90]s. The material properties of 2024-T3 Al alloy are $E = 72.2$ Gpa, $\rho = 2780$ kg/m^3, $\nu = 0.3$. The material properties of a unidirectional ply of S2-glass/epoxy prepreg are $\rho = 1980$ kg/m^3, $E_1 = 52$ Gpa, $G_{13} = G_{23} = G_{12} = 7$ Gpa, $E_2 = E_3 = 17$ Gpa.

The material properties of the GLARE5 are determined from the material properties of the 2024-T3 Al alloy and the S2-glass/expoxy prepreg using the rule of mix-

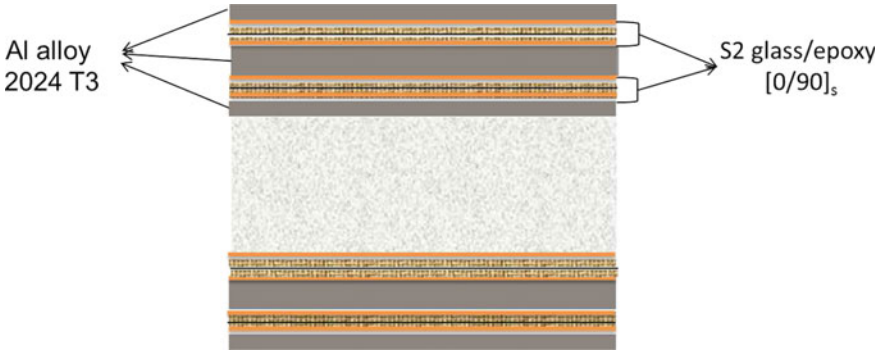

Fig. 9 Fiber metal laminate with Al and S2-glass epoxy laminates

tures method, which gives a good approximation of the FML properties [24, 25]. Hence, GLARE5 properties for the present case are $E_{1FML} = 57.12$ Gpa, $G_{FML} = 12.7$ Gpa and $\rho_{FML} = 2460\,\text{kg/m}^3$, found as:

$$\begin{aligned} E_{1\,FML} &= E_{Al} \times Metal\ Vol.fraction + E_{1\,S2} \times Vol.fraction\ of\ 0°\ plys \\ &\quad + E_{2\,S2} \times Vol.fraction\ of\ 90°\ plys \\ G_{FML} &= 1/(Metal\ Vol.fraction/G_{Al} + Vol.fraction\ of\ 0°\ plys/G_{13\,S2} \\ &\quad + Vol.fraction\ of\ 90°\ plys/G_{23\,S2}) \\ \rho_{FML} &= \rho_{Al} \times Metal\ Vol.fraction \\ &\quad + \rho_{S2} \times Vol.fraction\ of\ S2\ glass\ epoxy\ laminate \end{aligned}$$

Density of water is $\rho_w = 1000\,\text{kg/m}^3$, acoustic velocity in water is $c_w = 1400$ m/s, and in core is $c_c = \sqrt{E_c/\rho_c}$. The total height of the sandwich beam is taken as 50 mm with the ratio of the thickness of core to facesheet $(2c/f_t)$ as 10. The material properties of the Al low-density core are $E_1 = 4.0313 \times 10^{-2}$ Mpa, $E_3 = 520.54$ Mpa, $G_{31} = 100.45$ Mpa, $\nu_{31} = 0.3$, density $= 20.907\,\text{kg/m}^3$.

In Fig. 10 the comparison of the responses of sandwich structures to the same UNDEX loading with and without core transmission are shown. The maximum displacements are almost double when the propagation through core is considered, as the pressure on the front sandwich structure is more accurate and significantly different as pointed out in Fig. 7. Solid line is the front facesheet and dashed one is the rear facesheet response. The alternate core compression and expansion can also be seen because of the oscillating response of the two facesheets as in the Fig. 10.

A design methodology is proposed based on minimum weight and the maximum deflection of the rear facesheet. Here, a simply supported sandwich beam with FML face sheets and Al-high density core is taken and is subjected to the same blast loading on outer face sheet. The material properties of the Al high-density core are: $E_1 = 3.1734$ Mpa, $E_3 = 2230.9$ Mpa, $G_{31} = 430.51$ Mpa, $\nu_{31} = 0.3$, density$= 89.6\,\text{kg/m}^3$. The height of the sandwich beam is fixed to 0.11 m and the ratio of the core to face

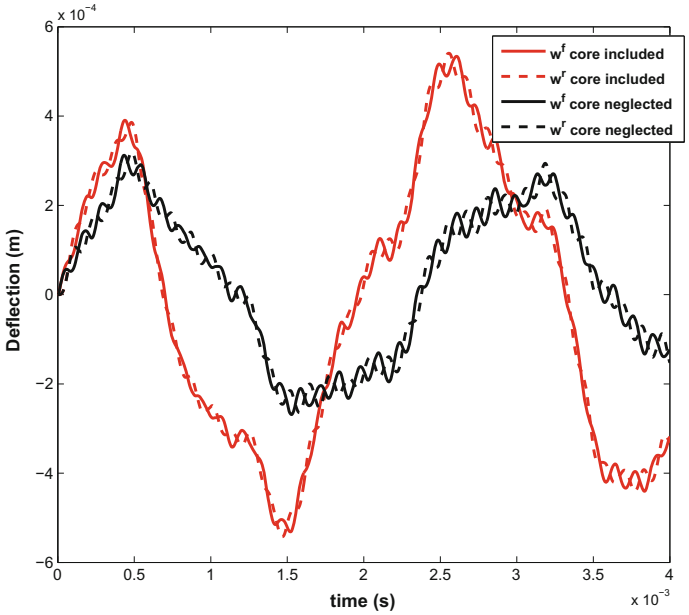

Fig. 10 Transverse displacements of front and rear facesheets when transmission of the pressure wave through core is considered and neglected

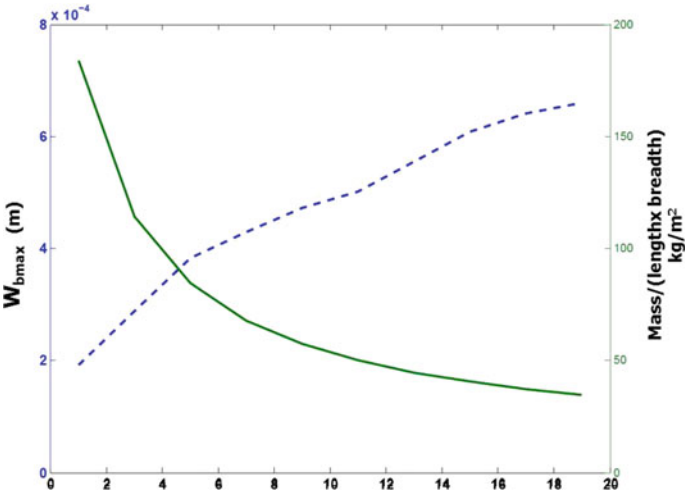

Fig. 11 Optimum point based on deflection criteria and weight

sheet thickness is varied. The maximum deflection undergone by the rear facesheet is plotted against this ratio. The response is shown in Fig. 11. In the same figure, the variation of the mass per unit base area $= 2c \times \rho_c + f_t \times \rho_t + f_b \times \rho_b$ with varying

geometry is superimposed. The point of coincidence of these two plots gives sandwich beam geometry with optimum deflection and weight. These kinds of design charts can be generated for different sandwich panel configurations of a given height and the optimum geometry can be arrived.

6 Conclusions

Spectral element formulation for a compliant core sandwich beam and an analytical model [20] for fluid–structure interaction are explained. The response of the compliant core sandwich beam to underwater transient shock loading is presented. The difference in the pressure on the front facesheet due to shock wave propagation through core and the resulting change in response of the sandwich structure are shown. The core compression and the damping effect are clearly demonstrated in the examples. Finally, a design methodology is proposed to arrive at an optimum configuration considering the face sheet to core ratio, mass and stiffness. Although the current work presented the pressure prediction, damping effect of the core, the blast impact mitigation is to be studied in detail by considering the geometry and material nonlinearity of fiber metal face sheets. The after cavitation effects have to be incorporated too. Additionally, a detailed computational model to study the coupled fluid–structure interaction has to be formulated so as to give a deeper insight in the response behavior of the sandwich structure.

Acknowledgements The authors gratefully acknowledge the Office of Naval Research and specially Dr. Y.D.S. Rajapakse for their continuous support under grant no. N6209-14-1-N139.

Appendix

The matrices of Eqs. (7) and (8) are given as,

$$[Z^{t,b}]_{2\times4} = \begin{bmatrix} 1 & 0 & z & 0 \\ 0 & 1 & 0 & z \end{bmatrix}$$

$$[Z^{c}]_{3\times12} = \begin{bmatrix} 1 & 0 & 0 & z & 0 & 0 & z^2 & 0 & 0 & z^3 & 0 & 0 \\ 0 & 1 & 0 & 0 & z & 0 & 0 & z^2 & 0 & 0 & z^3 & 0 \\ 0 & 0 & 1 & 0 & 0 & z & 0 & 0 & z^2 & 0 & 0 & z^3 \end{bmatrix}$$

$$[\partial^t]_{4\times3} = \begin{bmatrix} \frac{\partial}{\partial x} & 0 & \left(c + \frac{f_t}{2}\right)\frac{\partial}{\partial x} \\ 0 & \frac{\partial}{\partial x} & -1 \\ 0 & 0 & -\frac{\partial}{\partial x} \\ 0 & 0 & 0 \end{bmatrix}, \qquad [\partial^b]_{4\times3} = \begin{bmatrix} \frac{\partial}{\partial x} & 0 & -\left(c + \frac{f_b}{2}\right)\frac{\partial}{\partial x} \\ 0 & \frac{\partial}{\partial x} & -1 \\ 0 & 0 & -\frac{\partial}{\partial x} \\ 0 & 0 & 0 \end{bmatrix}$$

$$[\partial^c]_{12\times9} = \begin{bmatrix} 0 & 0 & 0 & \frac{\partial}{\partial x} & 0 & 0 & 0 & 0 & 0 \\ 0 & \frac{1}{2c} & 0 & 0 & 0 & 0 & 0 & -\frac{1}{2c} & 0 \\ 0 & 0 & 0 & 0 & \frac{\partial}{\partial x} & 1 & 0 & 0 & 0 \\ 0 & 0 & 0 & 0 & 0 & \frac{\partial}{\partial x} & 0 & 0 & 0 \\ 0 & \frac{1}{c^2} & 0 & 0 & \frac{-2}{c^2} & 0 & 0 & \frac{1}{c^2} & 0 \\ \frac{1}{c^2} & \frac{1}{2c}\frac{\partial}{\partial x} & \frac{ft}{2c^2} & -\frac{2}{c^2} & 0 & 0 & \frac{1}{c^2} & -\frac{1}{2c}\frac{\partial}{\partial x} & -\frac{f_b}{2c^2} \\ \frac{1}{2c^2}\frac{\partial}{\partial x} & 0 & \frac{f_t}{4c^2}\frac{\partial}{\partial x} & -\frac{1}{c^2}\frac{\partial}{\partial x} & 0 & 0 & \frac{1}{2c^2}\frac{\partial}{\partial x} & 0 & -\frac{f_b}{4c^2}\frac{\partial}{\partial x} \\ 0 & 0 & 0 & 0 & 0 & 0 & 0 & 0 & 0 \\ \frac{3}{2c^3} & \frac{1}{2c^2}\frac{\partial}{\partial x} & \frac{3f_t}{4c^3} & 0 & -\frac{1}{c^2}\frac{\partial}{\partial x} & -\frac{3}{c^2} & -\frac{3}{2c^3} & \frac{1}{2c^2}\frac{\partial}{\partial x} & \frac{3f_b}{4c^3} \\ \frac{1}{2c^3}\frac{\partial}{\partial x} & 0 & \frac{f_t}{4c^3}\frac{\partial}{\partial x} & 0 & 0 & \frac{-1}{c^2}\frac{\partial}{\partial x} & \frac{-1}{2c^3}\frac{\partial}{\partial x} & 0 & \frac{f_b}{4c^3}\frac{\partial}{\partial x} \\ 0 & 0 & 0 & 0 & 0 & 0 & 0 & 0 & 0 \\ 0 & 0 & 0 & 0 & 0 & 0 & 0 & 0 & 0 \end{bmatrix}$$

and the strain displacement matrix, $[B^x]$ in Eq. (11) is given as

$$[B^{t,c,b}] = [\partial^{t,c,b}]\,[N^{t,c,b}]$$

where

$$[N^t]_{3\times72} = \left[N_1[I]_{3\times3},\ [0]_{3\times6},\ N_2[I]_{3\times3},\ [0]_{3\times6},\ \ldots,\ N_8[I]_{3\times3},\ [0]_{3\times6}\right]$$

$$[N^c]_{9\times72} = \left[N_1[I]_{9\times9},\ N_2[I]_{9\times9},\ \ldots,\ N_8[I]_{9\times9}\right]$$

$$[N^b]_{3\times72} = \left[[0]_{3\times6},\ N_1[I]_{3\times3},\ [0]_{3\times6},\ N_2[I]_{3\times3},\ \ldots,\ [0]_{3\times6},\ N_8[I]_{3\times3}\right]$$

where, [0] is the matrix with zeros of size subscripted by the given dimension, $[I]$ is the identity matrix of size subscripted by the given dimension, $N_1, N_2, \ldots, N_8$ are the Lagrange interpolation functions of 7th degree in ζ and can be found in standard text on FEM/SEM [26].

The stiffness matrix C^x is given as

$$[C^{t,b}]_{4\times4} = \begin{bmatrix} [A^{t,b}] & [B^{t,b}] \\ [B^{t,b}] & [D^{t,b}] \end{bmatrix} \qquad [C^c]_{12\times12} = \begin{bmatrix} [A^c] & [B^c] & [D^c] & [E^c] \\ & [D^c] & [E^c] & [F^c] \\ & & [F^c] & [G^c] \\ \text{sym.} & & & [H^c] \end{bmatrix}$$

and

$$[A_{ij}^x] = \sum_{k=1}^{N_x} [\bar{Q}_{ij}^x]_k \, (h_{k-1} - h_k), \qquad [B_{ij}^x] = \frac{1}{2} \sum_{k=1}^{N_x} [\bar{Q}_{ij}^x]_k \, (h_{k-1}^2 - h_k^2),$$

$$[D_{ij}^x] = \frac{1}{3} \sum_{k=1}^{N_x} [\bar{Q}_{ij}^x]_k \, (h_{k-1}^3 - h_k^3), \qquad [E_{ij}^x] = \frac{1}{4} \sum_{k=1}^{N_x} [\bar{Q}_{ij}^x]_k \, (h_{k-1}^4 - h_k^4),$$

$$[F_{ij}^x] = \frac{1}{5} \sum_{k=1}^{N_x} [\bar{Q}_{ij}^x]_k \, (h_{k-1}^5 - h_k^5), \qquad [G_{ij}^x] = \frac{1}{6} \sum_{k=1}^{N_x} [\bar{Q}_{ij}^x]_k \, (h_{k-1}^6 - h_k^6),$$

$$[H_{ij}^x] = \frac{1}{7} \sum_{k=1}^{N_x} [\bar{Q}_{ij}^x]_k \, (h_{k-1}^7 - h_k^7)$$

where superscript "x" represents "t", "b", or "c" indicating top face sheet, bottom face sheet and core respectively. N_x indicates the number of layers in the considered face sheet or the core and $[\bar{Q}_{ij}]$, is the transformed stiffness matrix of the layer "k" and is given in [27].

The inertia matrix, $[R^x]$ in Eq. (11) is given as

$$[R^{t,b,c}] = [\partial Z^{t,c,b}]^T [CZ^{t,c,b}][\partial Z^{t,c,b}]$$

where

$$[\partial Z^t]_{4\times 3} = \begin{bmatrix} 1 & 0 & \left(c + \frac{f_t}{2}\right) \\ 0 & 1 & 0 \\ 0 & 0 & -1 \\ 0 & 0 & 0 \end{bmatrix}, \qquad [\partial Z^b]_{4\times 3} = \begin{bmatrix} 1 & 0 & -\left(c + \frac{f_b}{2}\right) \\ 0 & 1 & 0 \\ 0 & 0 & -1 \\ 0 & 0 & 0 \end{bmatrix},$$

$$[\partial Z^c]_{8\times 9} = \begin{bmatrix} 0 & 0 & 0 & 1 & 0 & 0 & 0 & 0 & 0 \\ 0 & 0 & 0 & 0 & 1 & 0 & 0 & 0 & 0 \\ 0 & 0 & 0 & 0 & 0 & 1 & 0 & 0 & 0 \\ 0 & \frac{1}{2c} & 0 & 0 & 0 & 0 & 0 & -\frac{1}{2c} & 0 \\ \frac{1}{2c^2} & 0 & \frac{f_t}{4c^2} & -\frac{1}{c^2} & 0 & 0 & \frac{1}{2c^2} & 0 & -\frac{f_b}{4c^2} \\ 0 & \frac{1}{2c^2} & 0 & 0 & -\frac{1}{c^2} & 0 & 0 & \frac{1}{2c^2} & 0 \\ \frac{1}{2c^3} & 0 & \frac{f_t}{4c^3} & 0 & 0 & -\frac{1}{c^2} & -\frac{1}{2c^3} & 0 & \frac{f_b}{4c^3} \\ 0 & 0 & 0 & 0 & 0 & 0 & 0 & 0 & 0 \end{bmatrix}$$

and

$$[CZ^{t,b}]_{4\times4} = \begin{bmatrix} [AZ^{t,b}]\ [BZ^{t,b}] \\ [BZ^{t,b}]\ [DZ^{t,b}] \end{bmatrix}, \qquad [CZ^{c}]_{8\times8} = \begin{bmatrix} [AZ^{c}] & [BZ^{c}] & [DZ^{c}] & [EZ^{c}] \\ & [DZ^{c}] & [EZ^{c}] & [FZ^{c}] \\ & & [FZ^{c}] & [GZ^{c}] \\ \text{sym.} & & & [HZ^{c}] \end{bmatrix}$$

where,

$$[AZ^{x}] = \sum_{k=1}^{N_x} \rho_k^x\,(h_{k-1} - h_k)[I_{2\times2}], \qquad [BZ^{x}] = \frac{1}{2}\sum_{k=1}^{N_x} \rho_k^x\,(h_{k-1}^2 - h_k^2)[I_{2\times2}],$$

$$[DZ^{x}] = \frac{1}{3}\sum_{k=1}^{N_x} \rho_k^x\,(h_{k-1}^3 - h_k^3)[I_{2\times2}] \qquad [EZ^{x}] = \frac{1}{4}\sum_{k=1}^{N_x} \rho_k^x\,(h_{k-1}^4 - h_k^4)[I_{2\times2}],$$

$$[FZ^{x}] = \frac{1}{5}\sum_{k=1}^{N_x} \rho_k^x\,(h_{k-1}^5 - h_k^5)[I_{2\times2}], \qquad [GZ^{x}] = \frac{1}{6}\sum_{k=1}^{N_x} \rho_k^x\,(h_{k-1}^6 - h_k^6)[I_{2\times2}],$$

$$[HZ^{x}] = \frac{1}{7}\sum_{k=1}^{N_x} \rho_k^x\,(h_{k-1}^7 - h_k^7)[I_{2\times2}]$$

The superscript "x" represents "t", "b", or "c" indicating top face sheet, bottom face sheet and N_x indicates the number of layers in the considered face sheet or core and ρ_k the density of the layer "k".

References

1. Zenkert, D. (1995). *An introduction to sandwich construction*. London: EMAS.
2. Taylor, G. I. (1963). The pressure and impulse of submarine explosion waves on plates. *The scientific* (Vol. 3, pp. 287–303).
3. Raja Sekhar, B., Gopalakrishnan, S., & Murthy, M. V. V. S. (2016). Wave transmission characteristics for higher-order sandwich panel with flexible core using time-domain spectral element method. *Journal of Sandwich Structures & Materials*, 1099636216664536 (2016).
4. Wanji, C., & Zhen, W. (2008). A selective review on recent development of displacement-based laminated plate theories. *Recent Patents on Mechanical Engineering*, *1*, 29–44.
5. Frostig, Y., Baruch, M., Vilnay, O., & Sheinman, I. (1992). High order theory for sandwich beam behaviour with transversely flexible core. *Journal of Engineering Mechanics*, *118*(5), 1026–1043.
6. Frostig, Y., & Baruch, M. (1996). Localized loads effects in high-order bending of sandwich panels with flexible core. *Journal of Engineering Mechanics*, *122*(11), 1069–1076.
7. Nemat-Naseer, S., Kang, W., McGee, J., Guo, W., & Issacs, J. (2007). Experimental investigation of energy absorption characteristics of components of sandwich structures. *International Journal of Impact Engineering*, *34*(6), 1119–1146.
8. Phan, C. N., Frostig, Y., & Kardomateas, G. A. (2012). Analysis of sandwich beams with a compliant core and with in-plane rigidity-extended high-order sandwich panel theory versus elasticity. *Journal of Engineering Mechanics*, *79*, 041001/1–041001/11.

9. Phan, C. N., Bailey, N. W., Kardomateas, G. A., & Battley, M. A. (2012). Wrinkling of sandwich wide panels/beams based on the extended high-order sandwich panel theory: Formulation, comparison with elasticity and experiments. *Archive of Applied Mechanics*, *82*, 1585–1599.
10. Phan, C. N., Kardomateas, G. A., & Frostig, Y. (2013). Blast response of a sandwich beam/wide plate based on the extended high-order sandwich panel theory and comparison with elasticity. *Journal of Applied Mechanics*, *80*, 061005/1–061005/11.
11. Oskooei, S., & Hansen, J. S. (2000). Higher-order finite element for sandwich plates. *AIAA Journal*, *38*(3), 525–533.
12. Kudela, P., Krawczuk, M., & Ostachowicz, W. (2007). Wave propagation modelling in 1-d structures using spectral finite elements. *Journal of Sound and Vibration*, *300*, 88–100.
13. Sprague, M. A., & Geers, T. L. (2008). Legendre spectral finite elements for structural dynamics analysis. *Communications in Numerical Methods in Engineering*, *24*, 1953–1965.
14. Boyd, J. P. (2001). *Chebyshev and Fourier spectral methods*. Mineola, Newyork: Dover Publications Inc.
15. Canuto, C., Hussaini, M. Y., Quarteroni, A., & Zang, T. A. (2007). *Spectral methods evolution to complex geometries and applications to fluid dynamics*. Springer.
16. Sprague, M. A., & Purkayastha, A. (2015). Legendre spectral finite elements for reissner-mindlin composite plates. *Finite Elements in Analysis and Design*, *105*, 33–43.
17. Chakraborty, A., Mahapatra, D. R., & Gopalakrishnan, S. (2002). Finite element analysis of free vibration and wave propagation in asymmetric composite beams with structural discontinuities. *Composite Structures*, *55*, 23–36.
18. Costanzo, F. A. (2011). Underwater explosion phenomena and shock physics. In *Structural dynamics* (Vol. 3, pp. 917–938). Springer.
19. Swisdak, M. M. (1978). *Explosion effects and properties-part ii: Explosion effects in water*. Technical report, Naval Surface Weapons Center, Dahlgren, VA.
20. Hayman, B. (1995). Underwater explosion loading on foam-cored sandwich panels. *Sandwich Construction*, *3*.
21. Makinen, K. (1999). The transverse response of sandwich panels to an underwater shock wave. *Journal of Fluids and Structures*, *13*, 631–646.
22. Fleck, N. A., & Deshpande, V. S. (2004). The resistance of clamped sandwich beams to shock loading. *Journal of Applied Mechanics*, *71*, 386–401.
23. Librescu, L., Sang-Yong, O., & Hohe, J. (2006). Dynamic response of anisotropic sandwich flat panels to underwater and in-air explosions. *International Journal of Solids and Structures*, *43*(13), 3794–3816.
24. Kamocka, M. (2015). Analytical and experimental determination of fml stiffness and strength properties. *Mechanics and Mechanical Engineering*, *19*(2), 141–159.
25. Wu, H. F., Wu, L. L., Slagter, W. J., & Verolme, J. L. (1994). Use of rule of mixtures and metal volume fraction for mechanical property predictions of fibre-reinforced aluminium laminates. *Journal of Materials Science*, *29*(17), 4583–4591.
26. Pozrikidis, C. (2005). *Introduction to finite and spectral element methods using MATLAB*. Boca Raton: Chapman and Hall.
27. Reddy, J. N. (1997). *Mechanics of laminated composite plates*. CRC Press.

Concentrated Load Impulse Response of a Sandwich Beam/Wide Plate: Dynamic Elasticity and Extended High Order Sandwich Panel Theory Solutions

Nunthadech Rodcheuy and George A. Kardomateas

1 Introduction

Sandwich composite structures are widely used in many industries, namely: aerospace, naval engineering, wind engineering, etc., due to their superior stiffness/strength-to-weight ratio in comparison with conventional metal alloys. And often these sandwich structures are exposed to sudden loads, such as bird strikes, ballistic, or blast impacts, etc., which can lead to catastrophic failures. In sandwich panel studies, the first-order shear deformation theory is generally applied due to its simplicity. While this may be acceptable when considering static response in sandwich structures with stiff cores, there is a big effect of core compressibility when it comes to sudden loading/impact problems as well as very large transverse shear effects when the core is of low stiffness, which makes simplified methods very inaccurate [1]. On the other hand, sandwich flexible foam cores play a crucial role in impact energy absorption Wang et al. [2]. Experiments on the impact response of sandwich foam core panels indicated various phenomena: localized deformations, local indentation failure, substantial compressible core, core crackings, interfacial delaminations, etc. [2, 3]. Therefore, more sophisticated theories that account for the core compressibility and core stiffness and include the core transverse normal stress in addition to the transverse shear are needed.

The theory of elasticity is regarded as the most accurate and is used as an accuracy assessment to other structural theories. Pagano [4] derived the static closed-form solutions for sandwich composite plates under restricted cases, then the remaining solution cases were treated in Kardomateas [5]. A semi-closed form dynamic elasticity solution of the sandwich subject to distributed transverse load (through thickness direction) is presented in Kardomateas et al. [6, 7] for beams and plates, respectively. Laplace transforms were applied to the elasticity equations in the time domain, then a closed-form solution was obtained in the Laplace domain before a numerical inversion back to time domain. These elasticity solutions, however, were restricted to only

N. Rodcheuy · G. A. Kardomateas (✉)
School of Aerospace Engineering, Georgia Institute of Technology, Atlanta, GA 30332-0150, USA
e-mail: george.kardomateas@aerospace.gatech.edu

S. Gopalakrishnan and Y. Rajapakse (eds.), *Blast Mitigation Strategies in Marine Composite and Sandwich Structures*, Springer Transactions in Civil and Environmental Engineering, https://doi.org/10.1007/978-981-10-7170-6_5

simply supported boundary conditions and a sinusoidal load distribution because there are great difficulties in solving elasticity equations for arbitrary cases of loading and end fixities. In addition, the inverse Laplace dynamic solution is valid during the transient only phase due to the specific numerical inversion technique employed in the problem. In such cases of complex loading and end fixity conditions, refined high order sandwich theories are at an advantage.

A recently developed compressible sandwich theory is the high order sandwich theory of Frostig et al. [8]. This theory neglects in-plane axial rigidity (zero in-plane stress), and, as a result, a closed-form core displacement field can be uniquely determined from local equilibrium. The assumption is valid for a very soft foam core; however, for a moderately stiff core, the assumption becomes inappropriate. Phan et al. [9] proposed the Extended High order Sandwich Panel Theory (EHSAPT), which includes the in-plane axial rigidity; this theory proved to be very accurate in comparison with elasticity. The EHSAPT was then applied to the study of a simply supported sandwich beam/wide plate subjected to a distributed half-sine blast load (Phan et al. [10]). Again, in all these studies a sinusoidally distributed load was applied, which made for a simple solution, since the differential equations degenerate into algebraic equations that can be solved directly.

In this article, we relax the sinusoidal distributed load assumption. Instead we provide the solution for a sandwich beam/wide plate subjected to a concentrated (point-wise) blast decay load. The solution is derived by use of the EHSAPT and also a dynamic elasticity solution is derived for accuracy assessment. The point load is expressed as a Fourier series, i.e., it becomes a series of distributed sinusoidal loads; then the same solution procedure as presented in Phan et al. [10] as well as the dynamic elasticity solution presented in Kardomateas et al. [6] is followed on the basis of superposition principle. Displacements and stresses are presented with materials and load profiles derived from the experimental studies in Gardner et al. [3].

2 Dynamic Extended High Order Sandwich Panel Theory (EHSAPT) Formulation and Solution

The Dynamic Extended High order Sandwich Panel Theory has been formulated in Phan et al. [10] where it was applied to the case of sinusoidally distributed loading; in the following we shall modify the formulation and solution for the case of a concentrated dynamic load applied at a specific location.

In the following, a sandwich beam configuration as in Fig. 1 is considered. Two-dimensional Cartesian coordinates (x, z) with origin at the beam left edge and mid-core, respectively, are defined. The sandwich beam consists of two thin stiff face sheets of thicknesses $f_{t,b}$ and a thick core of thickness $2c$. In the following, the superscript or subscript t, b, c denotes top face, bottom face, and core respectively. The sandwich beam has a length a and a width (out of plane) b and is subjected to a

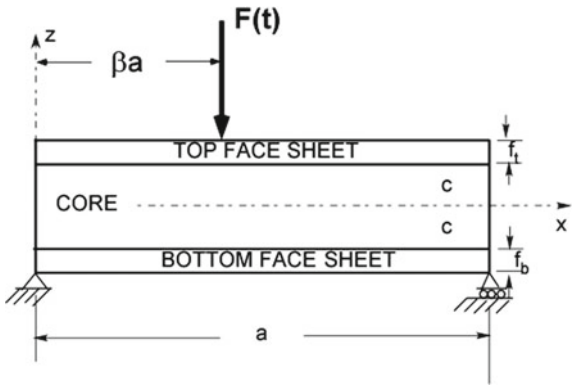

Fig. 1 Definition of the geometry for the sandwich beam/wide panel loaded by a concentrated dynamic load

dynamic concentrated load on the top face surface (in plane xz) at a distance βa from left end. There are two displacement components: transverse displacement in z direction, denoted by w, and axial displacement in x direction, denoted by u.

The two thin face sheets are assumed to follow the Euler–Bernoulli beam Theory; therefore, the top face displacements, $c \le z \le z + f_t$, are:

$$w^t(x,z,t) = w_0^t(x,t); \quad u^t(x,z,t) = u_0^t(x,t) - \left(z - c - \frac{f_t}{2}\right) w_{0,x}^t(x,t), \tag{1a}$$

and bottom face displacements, $-c - f_b \le z \le -c$, are:

$$w^b(x,z,t) = w_0^b(x,t); \quad u^b(x,z,t) = u_0^b(x,t) - \left(z + c + \frac{f_b}{2}\right) w_{0,x}^b(x,t). \tag{1b}$$

In correspondence with the Euler–Bernoulli beam assumptions, there is only an axial strain component in the face sheets:

$$\epsilon_{xx}^{t,b}(x,z,t) = u_{,x}^{t,b}(x,z,t), \tag{1c}$$

and the face sheets' constitutive relation is:

$$\sigma_{xx}^{t,b}(x,z,t) = E^{t,b}\epsilon_{xx}^{t,b}. \tag{1d}$$

where $E^{t,b}$ are the face sheets' Young's moduli.

While the face sheets are restricted to the classical beam theory which assumes through thickness incompressibility and neglects shear deformation, the core accounts for all transverse, shear, and axial rigidity via an assumed high order kinematic description, see Phan et al. [9]. A perfect bond is assumed between core and with face sheets (displacement continuity), and the core displacements are as follows:

$$w^c(x,z,t) = \left(-\frac{z}{2c} + \frac{z^2}{2c^2}\right) w_0^b(x,t) + \left(1 - \frac{z^2}{c^2}\right) w_0^c(x,t) + \left(\frac{z}{2c} + \frac{z^2}{2c^2}\right) w_0^t(x,t) \tag{2a}$$

$$u^c(x,z,t) = z\left(1 - \frac{z^2}{c^2}\right)\phi_0^c(x,t) + \frac{z^2}{2c^2}\left(1 - \frac{z}{c}\right) u_0^b(x,t) + \left(1 - \frac{z^2}{c^2}\right) u_0^c(x,t) + \\ + \frac{z^2}{2c^2}\left(1 + \frac{z}{c}\right) u_0^t(x,t) + \frac{f_b z^2}{4c^2}\left(-1 + \frac{z}{c}\right) w_{0,x}^b(x,t) + \frac{f_t z^2}{4c^2}\left(1 + \frac{z}{c}\right) w_{0,x}^t(x,t) \tag{2b}$$

The above displacement field results in three strain components for the core,

$$\epsilon_{xx}^c = u_{,x}^c(x,z,t); \quad \epsilon_{zz}^c = w_{,z}^c(x,z,t), \tag{3a}$$

$$\gamma_{xz}^c = u_{,z}^c(x,z,t) + w_{,x}^c(x,z,t), \tag{3b}$$

Core strain components (3) are written explicitly in [9].

Sandwich core materials are generally orthotropic. Let us denote $x \equiv 1$ and $z \equiv 3$. The constitutive relations for an orthotropic core are as follows:

$$\begin{bmatrix} \sigma_{xx}^c \\ \sigma_{zz}^c \\ \tau_{xz}^c \end{bmatrix} = \begin{bmatrix} c_{11}^c & c_{13}^c & 0 \\ c_{13}^c & c_{33}^c & 0 \\ 0 & 0 & c_{55}^c \end{bmatrix} \begin{bmatrix} \epsilon_{xx}^c \\ \epsilon_{zz}^c \\ \gamma_{xz}^c \end{bmatrix}, \tag{4a}$$

where the stiffness coefficients c_{ij}^c are derived from an inverse of the compliance matrix:

$$[C] = \begin{bmatrix} 1/E_1^c & -\nu_{31}^c/E_3^c & 0 \\ -\nu_{13}^c/E_1^c & 1/E_3^c & 0 \\ 0 & 0 & 1/G_{13}^c \end{bmatrix}^{-1}, \tag{4b}$$

This theory is in terms of seven generalized coordinates, the transverse and axial displacements at the reference line of the two faces and the core and $w_0^{t,b,c}$, $u_0^{t,b,c}$, and the rotation of the core reference line, ϕ_0^c.

The dynamic governing equation and associated boundary conditions are derive using Hamilton's Principle:

$$\int_{t_1}^{t_2} \delta(U + V - K)dt = 0, \tag{5a}$$

where U is the internal strain energy, V is external potential energy, and K is the kinetic energy.

The first variation of the internal strain energy δU is

$$\delta U = \int_0^a \left[\int_{-c+f_b}^{-c} \sigma_{xx}^b \delta\epsilon_{xx}^b dz + \int_{-c}^{c} (\sigma_{xx}^c \delta\epsilon_{xx}^c + \sigma_{zz}^c \delta\epsilon_{zz}^c + \tau_{zx}^c \delta\gamma_{zx}^c) dz + \int_{c}^{c+f_t} \sigma_{xx}^t \delta\epsilon_{xx}^t dz \right] b dx. \tag{5b}$$

The sandwich beam is subjected to a single concentrated load, as depicted in Fig. 1, thus the first variation of the external potential is

$$\delta V = \int_0^a F(x,t) \delta w_0^t dx. \tag{5c}$$

The external energy for general loading, i.e., distributed forces and moments and concentrated forces and moments are written in [10].

The first variation kinetic energy of the sandwich beam is

$$\delta K = \int_0^a \left[\int_{-c-f_b}^{-c} \rho_b (\dot{u}^b \delta\dot{u}^b + \dot{w}^b \delta\dot{w}^b) dz + \int_{-c}^{c} \rho_c (\dot{u}^c \delta\dot{u}^c + \dot{w}^c \delta\dot{w}^c) dz + \int_{c}^{c+f_t} \rho_t (\dot{u}^t \delta\dot{u}^t + \dot{w}^t \delta\dot{w}^t) dz \right] b dx \,. \tag{5d}$$

Substituting the constitutive relations and strain displacement relations into (5b), δU is written in terms of the generalized coordinates, $w_0^{t,b,c}$, $u_0^{t,b,c}$, and ϕ_0^c. Performing integration by parts at (11), results in 7 linear partial differential equations and associated 18 boundary conditions in x, t, see Phan et al. [10].

Given any boundary conditions, the governing equations can be solved. In order to compare with elasticity solutions, simply supported conditions at both ends are considered. In this case, solutions can be sought in the following form:

$$w_0^{t,b,c}(x,z,t) = \sum_{n=1}^{\infty} W_n^{t,b,c}(t) \sin \frac{n\pi x}{a}, \tag{6a}$$

$$u_0^{t,b,c}(x,z,t) = \sum_{n=1}^{\infty} U_n^{t,b,c}(t) \cos \frac{n\pi x}{a}, \tag{6b}$$

$$\phi_0^c(x,z,t) = \sum_{n=1}^{\infty} \Phi_n^c(t) \cos \frac{n\pi x}{a}. \tag{6c}$$

Note that these solution forms in (6) satisfy all 18 boundary conditions.

The concentrated load is applied at $x = \beta a$, and can be expressed as a Fourier series, for $0 \le x \le a$:

$$F(x,t) = P\delta(x-\beta a)T(t) = T(t)\sum_{n=1}^{\infty} q_{0n}\sin\frac{n\pi x}{a}, \tag{7a}$$

where P is the magnitude of the concentrated load and

$$q_{0n} = \frac{2}{a}\int_0^a P\delta(x-\beta a)\sin\frac{n\pi x}{a}dx = \frac{2P}{a}\sin n\pi\beta; \qquad n = 1,2,3,4,5,\ldots \tag{7b}$$

Next, substituting the simply supported solutions (6) and Fourier series load (7) and canceling out trigonometric functions on both sides of equations, results in n systems of 7 linear second-order ODEs:

$$[M_n]\{\ddot{\mathbf{U}}_n(t)\} + [K_n]\{\mathbf{U}_n(t)\} = \{\mathbf{F}_n(t)\}, \tag{8}$$

where $[M]$ and $[K]$ are 7×7 matrices; and $\mathbf{U}_n(t)$ is the vector of the 7 generalized coordinates: $\{U_n^b(t), U_n^c(t), \Phi_n^c(t), U_n^t(t), W_n^b(t), W_n^c(t), W_n^t(t)\}$.

Analytical solutions of the second-order linear ODEs (8) are very simple [10]; hence, procedure details are skipped.

Considering a specific blast decay dynamic load with $T(t)$ in Eq. (7a):

$$T(t) = e^{\alpha t}, \tag{9a}$$

with α negative as the force decays overtime, the corresponding solution to the ODEs is

$$\{\mathbf{U}_n(t)\} = \sum_{i=1}^{7}\{X_{in}\}\left(C_i\cos\omega_i t + S_i\sin\omega_i t\right) + e^{\alpha t}\{\mathbf{U}_n^F\}, \tag{9b}$$

where ω_i, $\{X_i\}$ are eigenvalues and eigenvectors of:

$$(-\omega^2[M_n] + [K_n])\{X\} = 0, \tag{9c}$$

and $\{\mathbf{U}_n^F\}$ is the particular solution:

$$\{\mathbf{U}_n^F\} = ([M_n]\alpha^2 + [K_n])^{-1}[Q_n], \tag{9d}$$

where

$$[Q_n] = [0,0,0,0,0,0,q_{0n}]^T, \tag{9e}$$

and C_i and S_i can be determined from zero initial conditions: $\{\dot{\mathbf{U}}_n(0)\} = \{\mathbf{U}_n(0)\} = 0$

After the solution $\{\mathbf{U}_n(t)\}$ is obtained for each n, the displacements functions (6) are then formed. In order to produce numerical results, a partial sum is considered and convergence is studied, which will be shown in the results section.

3 Dynamic Elasticity Formulation and Solution

The same sandwich configuration in Fig. 1 as previously described is considered. The dynamic elasticity formulation and solution follow the approach in [10], modified for the case of a concentrated load at the specific location βa from the left end. The two displacement components within each layer $i = t, b, c$ (top face, bottom face, and core, respectively) are the axial, $u(x, z, t)^i$, and the transverse displacement, $w(x, z, t)^i$; and the linear strain displacement relations are as follows:

$$\epsilon^i_{xx} = u^i_{,x}; \quad \epsilon^i_{zz} = w^i_{,z}; \quad \gamma^i_{xz} = u^i_{,z} + w^i_{,x}, \tag{10}$$

The orthotropic stress–strain relations apply now in each layer i:

$$\begin{bmatrix} \sigma^{(i)}_{xx} \\ \sigma^{(i)}_{zz} \\ \tau^{(i)}_{xz} \end{bmatrix} = \begin{bmatrix} c^i_{11} & c^i_{13} & 0 \\ c^i_{13} & c^i_{33} & 0 \\ 0 & 0 & c^c_{55} \end{bmatrix} \begin{bmatrix} \epsilon^{(i)}_{xx} \\ \epsilon^{(i)}_{zz} \\ \gamma^{(i)}_{xz}, \end{bmatrix} \tag{11a}$$

where the stiffness coefficients c^i_{nm} are derived from an inverse of compliance matrix:

$$[C] = \begin{bmatrix} 1/E^i_1 & -\nu^i_{31}/E^i_3 & 0 \\ -\nu^i_{13}E^i_1 & 1/E^i_3 & 0 \\ 0 & 0 & 1/G^i_{13}, \end{bmatrix} \tag{11b}$$

The two-dimensional dynamic equilibrium equations are as follows:

$$\sigma^i_{xx,x} + \tau^i_{xz,z} = \rho u^i_{,tt}, \tag{12a}$$

$$\tau^i_{xz,x} + \sigma^i_{zz,z} = \rho w^i_{,tt}, \tag{12b}$$

Substituting the strain displacement (10) and constitutive relations (11) into the equilibrium equations (12), displacement-based field equations for $i = t, b, c$ are obtained as follows:

$$c^i_{11}u^i_{,xx} + c^i_{55}u^i_{,zz} + (c^i_{13} + c^i_{55})w^i_{,xz} = \rho^i u^i_{,tt}, \tag{13a}$$

$$(c^i_{11} + c^i_{55})u^i_{,xz} + c^i_{55}w^i_{,xx} + c^i_{33}w^i_{,zz} = \rho^i w^i_{,tt}. \tag{13b}$$

In the following, the superscript i indicating each sandwich layer will be dropped for simplification. Therefore, it should be noted that the following derived relations hold within each layer.

We restrict end conditions to simply supported on both ends for all layers; then, the displacements are sought in the following form:

$$u = U(z, t)\cos px; \quad w = W(z, t)\sin px; \quad p = \frac{n\pi}{a}; \quad n = 1, 2, \ldots \tag{14}$$

Substituting the simply supported solution form (14) into (13), results in sin and cos terms cancelling out from both sides, thus eliminating the x dependence and resulting in two PDEs in (z, t). A Laplace transform is subsequently applied to the equations. We shall denote the Laplace transform of the function $g(t)$ by $\tilde{g}(s)$

$$\tilde{g}(s) = \int_0^\infty g(t)e^{-st}dt. \tag{15}$$

Taking the Laplace transform of the PDEs results in

$$(c_{11}p^2 + \rho s^2)\tilde{U} + c_{55}\tilde{U}_{,zz} + (c_{13} + c_{55})p\tilde{W}_{,z} = 0, \tag{16a}$$

$$-(c_{13} + c_{55})p\tilde{U}_{,z} - (c_{55}p^2 + \rho s^2)\tilde{W} + c_{33}\tilde{W}_{,zz} = 0. \tag{16b}$$

Assuming next that

$$[\tilde{U}(z), \tilde{W}(z)] = [\tilde{U}_0, \tilde{W}_0]e^{\lambda z}, \tag{17}$$

where $\tilde{U}_0$ and $\tilde{W}_0$ are constants, and substituting into (16) results in the following system of algebraic equations

$$(c_{11}p^2 + \rho s^2 - c_{55}\lambda^2)\tilde{U}_0 - (c_{13} + c_{55})p\lambda\tilde{W}_0 = 0, \tag{18a}$$

$$(c_{13} + c_{55})p\lambda\tilde{U}_0 + (c_{55}p^2 + \rho s^2 - c_{33}\lambda^2)\tilde{W}_0 = 0. \tag{18b}$$

Nontrivial solutions of this system exist only if the determinant of the coefficients vanishes, which leads to the following equation:

$$A_0\lambda^4 + A_1\lambda^2 + A_2 = 0, \tag{19}$$

where

$$A_0 = c_{33}c_{55}, \quad A_2 = (c_{11}p^2 + \rho s^2)(c_{55}p^2 + \rho s^2) \tag{20a}$$

$$A_1 = (c_{13} + c_{55})^2p^2 - (c_{11}p^2 + \rho s^2)c_{33} - (c_{55}p^2 + \rho s^2)c_{55}, \tag{20b}$$

With the substitution

$$\mu = \lambda^2, \tag{21a}$$

equation (19), which defines the parameter λ, can be written in the form of a quadratic equation as follows:

$$A_0\mu^2 + A_1\mu + A_2 = 0. \tag{21b}$$

Since the Laplace parameter, s, is in general complex, so are the coefficients of (21b), thus Eq. (21b) has two complex roots:

$$\mu_{1,2} = \frac{-A_1 \pm \sqrt{A_1^2 - 4A_0A_2}}{2A_0}. \tag{21c}$$

which results in four complex roots of (19):

$$\lambda_{1,2} = \pm\sqrt{\mu_1}; \quad \lambda_{3,4} = \pm\sqrt{\mu_2}. \tag{21d}$$

Corresponding to these four roots, the transformed displacement functions take the following form:

$$\tilde{U}(z) = \sum_{i=1,2,3,4} a_i e^{\lambda_i z}; \quad \tilde{W}(z) = \sum_{i=1,2,3,4} b_i e^{\lambda_i z}, \tag{22}$$

where a_i and b_i are complex constants.

Of the eight constants appearing in (22) only four are independent. The four relations that exist among these constants are found by substituting the transformed displacements (22) into the equilibrium equations (16). In this way, we obtain the following relations for the coefficients in the transformed displacement expression for $\tilde{W}(z)$, Eq. (22), in terms of the coefficients in the expression for $\tilde{U}(z)$:

$$b_i = f_i a_i, \tag{23a}$$

where,

$$f_i = \frac{(c_{11}p^2 + \rho s^2) - c_{55}\lambda_i^2}{(c_{13} + c_{55})p\lambda_i}, \tag{23b}$$

Because the Laplace parameter, s, is complex, the roots are two pairs of complex conjugates. Also, a_i are 4 unknowns to be determined for each individual layer; hence, 12 unknowns are posed for the three-layer sandwich configurations.

Thus, the two displacements components for phases $j = t, b, c$ in the Laplace domain are as follows:

$$\tilde{u}^j = \sum_{i=1}^{4} d_i^j e^{\lambda_i^j z} \cos px; \quad \tilde{w}^j = \sum_{i=1}^{4} f_i^j d_i^j e^{\lambda_i^j z} \sin px, \tag{24}$$

and the s-domain stresses and strains can be accordingly expressed in term of a_i^j. The 12 unknowns are determined by 12 boundary and face/core interface conditions are the following:

(a) two traction-free conditions at the bottom surface $z = -c - f_b$,

$$\tilde{\sigma}_{zz}^b = 0; \quad \tilde{\tau}_{xz}^b = 0, \tag{25a}$$

(b) two traction conditions and two displacement continuity at the lower face/core interface $z = -c$,

$$\tilde{\sigma}^b_{zz} = \tilde{\sigma}^c_{zz}; \quad \tilde{\tau}^b_{xz} = \tilde{\tau}^c_{xz}; \quad \tilde{U}^b = \tilde{U}^c; \quad \tilde{W}^b = \tilde{W}^c, \tag{25b}$$

(c) two traction conditions and two displacement continuity at the upper face/core interface $z = c$,

$$\tilde{\sigma}^t_{zz} = \tilde{\sigma}^c_{zz}; \quad \tilde{\tau}^t_{xz} = \tilde{\tau}^c_{xz}; \quad \tilde{U}^t = \tilde{U}^c; \quad \tilde{W}^t = \tilde{W}^c., \tag{25c}$$

(d) two traction conditions at the top-loaded boundary.

The Fourier series of the concentrated load in the Laplace domain is

$$\tilde{F}(x, s) = \tilde{T}(s) \sum_{n=1}^{\infty} q_{0n} \sin \frac{n\pi x}{a}, \tag{26a}$$

where q_{0n} is as previously derived in (7).

As previously stated in (9a), we study the point blast decay load and the Laplace transform of $T(t)$ is

$$\tilde{T}(s) = L(e^{\alpha t}) = \frac{1}{s - \alpha}. \tag{26b}$$

Thus, the last two traction conditions at the top bounding surface $z = c + f_t$, corresponding to the nth term in (26a), are

$$\tilde{\sigma}^t_{zz} = \frac{q_{0n}}{s - a} \sin \frac{n\pi x}{a}; \quad \tilde{\tau}^t_{xz} = 0, \tag{26c}$$

Note that from (24) the $\tilde{\sigma}^t_{zz}$ will have a $\sin px$ dependence, which will cancel the $x-$ dependence in (26c).

In this linear analysis, because of the infinite Fourier series (26a), there is an infinite set of 12 conditions and corresponding infinite set of 12 unknowns a^j_i. Then using the superposition principle, the displacements (24) become

$$\tilde{u}^j = \sum_{n=1}^{\infty} \sum_{i=1}^{4} a^j_i e^{\lambda^j_i z} \cos \frac{n\pi x}{a}; \quad \tilde{w}^j = \sum_{n=1}^{\infty} \sum_{i=1}^{4} f^j_i a^j_i e^{\lambda^j_i z} \sin \frac{n\pi x}{a}, \tag{27}$$

Details of the solution procedure and explicit forms of the stresses, strains, and boundary/interface conditions are presented in Kardomateas et al. [10].

The Laplace domain solutions are then numerically inverted to the time domain:

$$g(z, t) = L^{-1} \left[g(z, s) \right]. \tag{28}$$

There are various numerical inverse Laplace methods, and each is suitable for different physical problems. The Euler method, as described in Abate and Whitt [11] is chosen as it was proven to be exactly the theoretical results up to 10 ms [10]. The Euler method, so named because it employs Euler summation, is based on the Bromwich contour inversion integral, which can be expressed as the integral of a real-valued function of a real variable by choosing a specific contour [11]. The integral is calculated by use of the Fourier series method (the Poisson summation formula) and the Euler summation to accelerate convergence. The numerical accuracy of this method was confirmed in [10] by comparing to the closed form simple vibration equation, and also by comparing with the results from the Post-Widder method, again described in Abate and Whitt [11]. It should be noticed that both the Euler and the Post-Widder methods are variants of the Fourier series method, but are dramatically different so that they can be expected to serve as useful checks on each other.

4 Results

We consider a sandwich beam/wide panel simply supported on both ends, initially at rest (zero initial conditions) subjected to a point-wise blast decay load at the top face midspan, i.e., $x = a/2$ as depicted in Fig. 1. The sandwich panel consists of two thin orthotropic E-glass polyester faces of thickness $f_{t,b} = 5$ mm and of a Divinycell A300 foam core of thickness $2c = 38$ mm; it also has a length of $a = 152.4$ mm and a width (out of plane) of $b = 102$ mm. Details of the material properties are taken from [10] and presented in Table 1.

The concentrated load has a blast decay profile, so that less than 0.1% of its initial value remains after 5.5 ms; the profile is based on the impact blast experiments of Gardner et al. [3]. Specifically, the concentrated load is

$$F(x,t) = P\delta(x - \beta a)e^{\alpha t}, \tag{29}$$

where $\beta = 0.5$, $P = -46.48$ kN, $\alpha = -1.25$ ms^{-1}, and t is time in ms.

The point load can then be expressed as the Fourier series (7), where $T(t) = e^{\alpha t}$. Since in our case the force is applied at midspan, i.e., $\beta = 0.5$, (7b) gives

Table 1 Material properties, Moduli are in GPa and densities are in kg/m^3

	E_1	E_3	ν_{31}	G_{13}	ρ
E-Glass polyester face	40.0	10.0	0.26	4.5	2000
Divinycell A300 foam core	0.032	0.032	0.25	0.0128	58.5

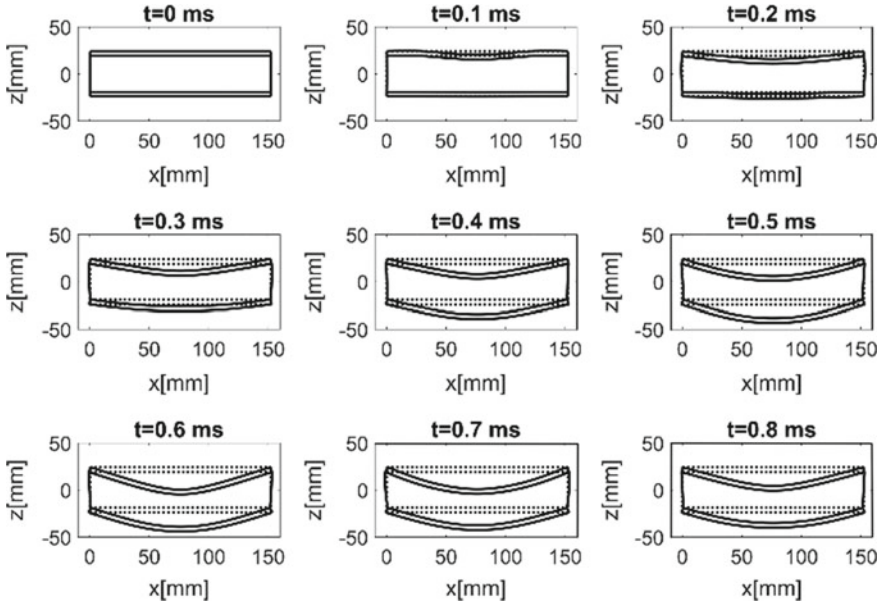

Fig. 2 Deformed configuration of a sandwich beam/wide panel subjected to a concentrated blast load at the top face surface midspan (from EHSAPT)

$$q_{0n-odd} = \frac{2P}{a}(-1)^{n+1}; \quad q_{0n-even} = 0. \tag{30}$$

Figure 2 shows the sandwich deformed configuration, initially at rest, up to 0.8 ms. Local deformation is observed at $t = 0.1$ ms and substantial core compression is observed at $t = 0.2$ ms.

Figure 3 presents the transverse displacement w during the first 2 ms after impact at midspan $x = a/2$ from both Dynamic EHSAPT and Dynamic Elasticity. Three curves are plotted, namely for the middle of the top face, $z = c + f_t/2$, the mid-core $z = 0$, and the middle of the bottom face, $z = -c - f_b/2$.

First, it can be observed that both Dynamic EHSAPT and Dynamic Elasticity agree very well. Second, although each displacement has similar overall tendency, each curve has its own path with the top face being displaced the most. During the first downward motion until 0.8 ms, there are substantial, up to 7 mm, differences between the top and the bottom face; this indicates that the core is significantly compressed. It should be noted that incompressible theories, for instance the first-order shear deformation theory (widely used to study sandwich panels), are incapable of the capturing the path variation and the associated compressibility effect, whereas the EHSAPT is capable and in very good agreement with elasticity.

Figure 4 presents the axial displacement, u, again for the middle of the each face and the core, at the left end $x = 0$; note that the problem has symmetry at midspan, therefore, the right end $x = a$ axial displacement is the symmetrical reflect of the left

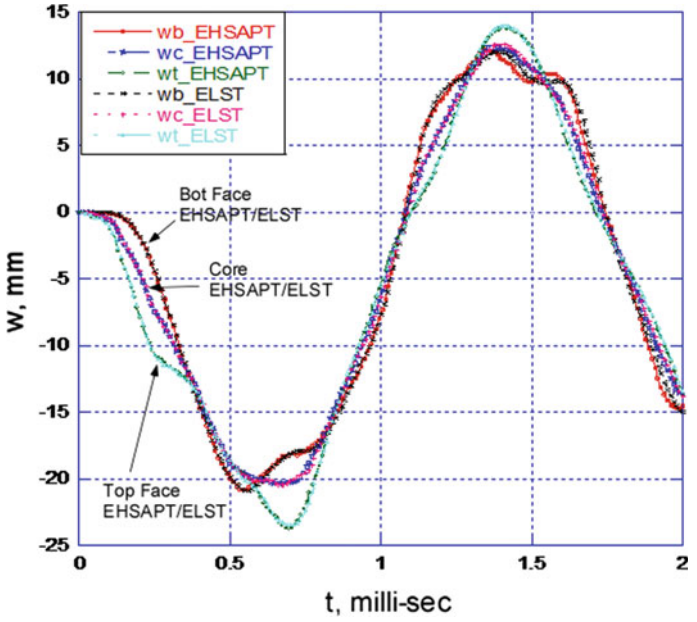

Fig. 3 The transverse displacement, w, at midspan: EHSAPT and elasticity

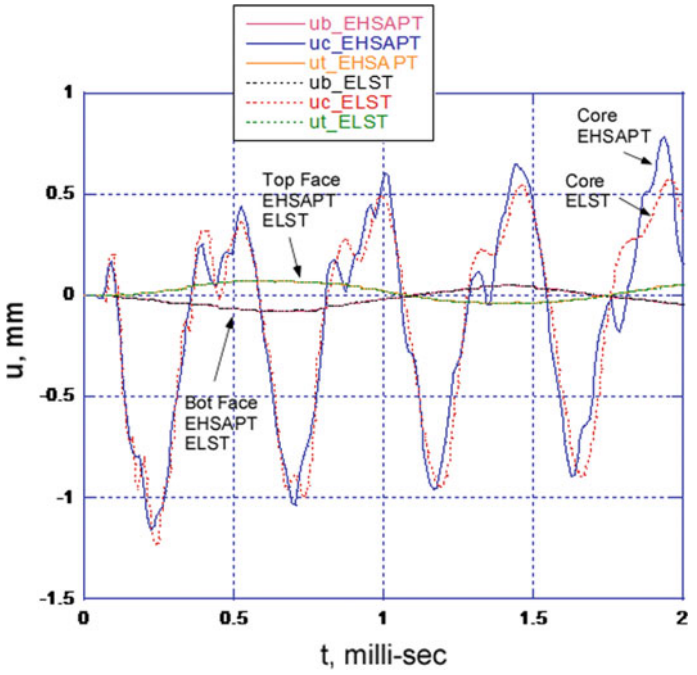

Fig. 4 Axial displacement, u, at left end, $x = 0$: EHSAPT and elasticity

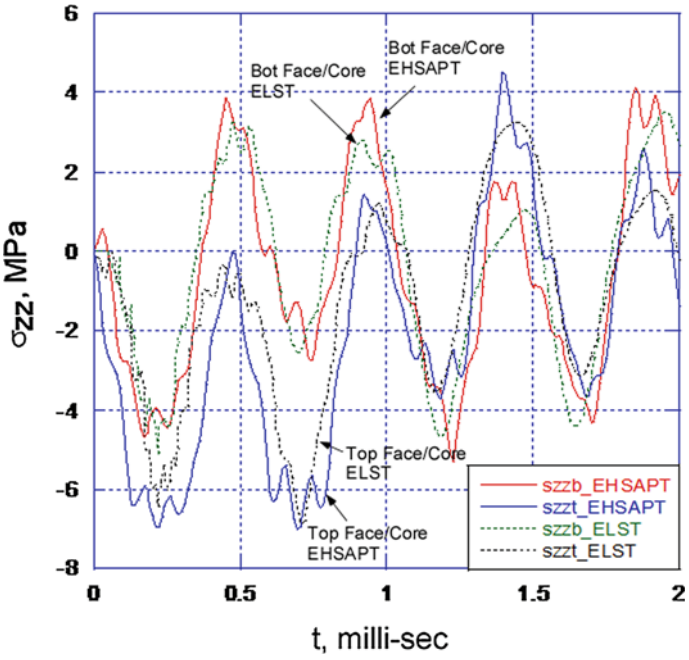

Fig. 5 Core transverse normal stress, σ_{zz}^{c} at midspan: EHSAPT and elasticity

end i.e., same magnitude but opposite sign. The EHSAPT shows good agreement with elasticity, although the agreement was better in the transverse displacement (Fig. 3). Notice that the core has highly cyclic behavior unlike the two face sheets. A comparison of Figs. 3 and 4 shows also that the overall amplitude of u is far lower than that of w.

One of the unique features of EHSAPT is the inclusion of core compressibility, thus the ability to provide the transverse normal stress for the core, σ_{zz}^{c}. Figure 5 shows the transverse stress at the core, σ_{zz}^{c}, at the top/bottom face/core interfaces at $x = a/2$. Highly cyclic behavior is observed, both interfaces experience compression and tension numerous times during the first 2 ms. While the sandwich first downward motion last until 0.8 ms, the top face/core interfacial transverse compression stress peaks twice at 0.2 and 0.7 ms. Also, the EHSAPT seems to have a slight phase lag-advance to elasticity during the first millisecond but this shift tends to diminish afterwards.

Despite these phase shifts, the EHSAPT predictions have an overall good agreement with elasticity. Figure 6 presents the EHSAPT transverse stress field, σ_{zz}^{c}, of the sandwich core at specific time instants. It is observed that at $t = 0.2$ and 0.7 ms a relatively large compression stress of 7 MPa locally develops on the top face/core interface at midspan (where the load is applied); this localized effect could lead to indentation failure. Another localized effect is a tension of 4 MPa, which is devel-

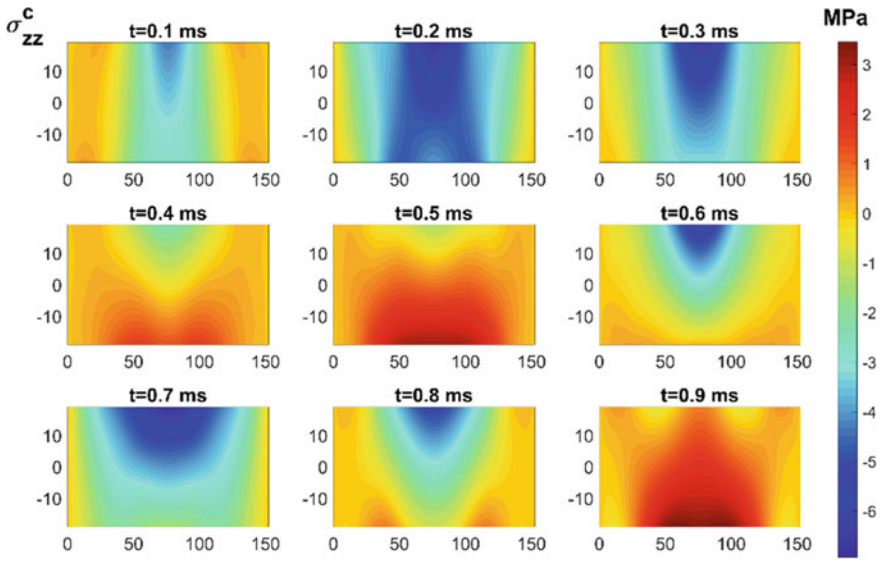

Fig. 6 Core transverse normal stress, σ^c_{zz} at various time instances (through thickness and along length profiles)

oped at the bottom face/core interface, midspan, and at times $t = 0.4$ and 0.9 ms; this tensile transverse normal stress could lead to local face/core delamination.

For sandwich composite panels, the shear rigidity is in general dependent on the core. Figures 7 and 8 shows the shear stress, τ^c_{xz}, at the top and bottom face/core interfaces, respectively, at $x = 0$. The ESHAPT shows a very good agreement with elasticity. The shear stress reaches a peak magnitude of 6.5 MPa at $t = 0.7$ ms. Slight fluctuations are also observed along the path of the major cycles. Figure 9 presents the EHSAPT shear stress field at the core, τ^c_{xz}, at specific time instants; it is shown that the shear stress is increasing toward both ends and has a slight through thickness variation.

This could lead to the entire core cracking toward both ends and to face/core debonding at the beam ends.

Lastly, while the sandwich core is responsible for the shear rigidity, the bending rigidity is provided by the two thin stiff face sheets. Figure 10 shows the axial stress, σ_{xx}, at the top and bottom face surfaces, i.e., at $z = c + f_t$ and $z = -c - f_b$ at midspan $x = a/2$. Highly cyclic behavior is observed in both face sheets, the stress peaking at the bottom face sheet with tension on bottom surface and compression at the face/core interface with a magnitude of approximately 1.6 GPa around $t = 0.7$ ms.

Figure 11 presents the same for the mid-core, the magnitudes of the axial stress being orders of magnitude less that that of the faces (of the order of 1.5 Mpa); high cyclic behavior is observed and the core experiences both tension and compression

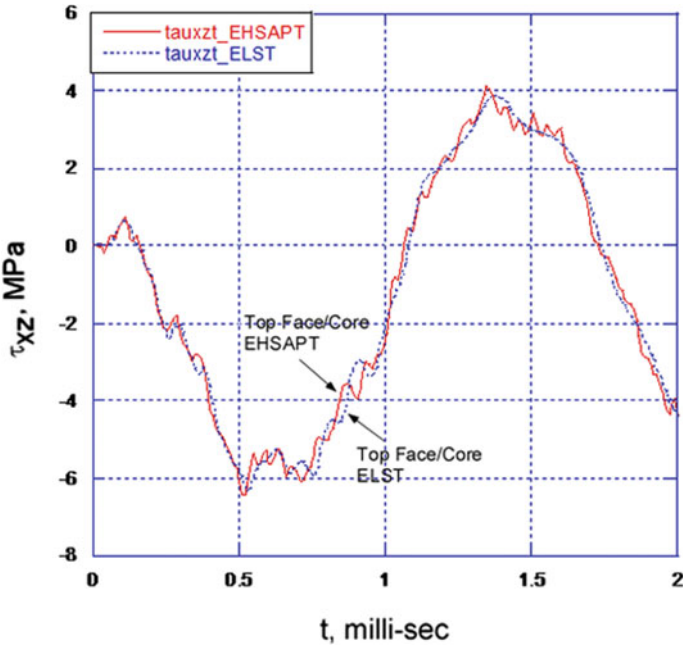

Fig. 7 Core transverse shear stress, τ^c_{xz} at the top face/core interface and at the left end, $x = 0$: EHSAPT and elasticity

slightly over 1 MPa whose magnitude is in the same order as the other stress components, σ^c_{zz} and τ^c_{xz}, in the core.

Considering that core is relatively much weaker than the face, this magnitude of the axial stress is nonnegligible and can contribute to failure under multiaxial loading. Also notice that in both Figs. 10 and 11, the elasticity and the EHSAPT follow the same trends but the agreement between them is not as good as in the transverse shear Figs. 7 and 8.

A discussion on the convergence and the number of terms in the series (10) or (27) follows next.

As it has been shown earlier the concentrated load is expressed as an infinite Fourier series (7a), and the solutions are also infinite series summation, e.g., (27). In order to produce numerical results, a finite number of terms is used. It is expected that the convergence of either the EHSAPT series solution, Eq. (6), or the dynamic elasticity series solution, Eq. (27), would yield a similar convergence rate because this is a linear analysis and solutions are composed on the basis of superposition principle.

Seven individual quantities are chosen, these are the partial summation (up to N) of the transverse displacement functions at midspan, $x = a/2$, and the axial displacement functions at left end, $x = 0$:

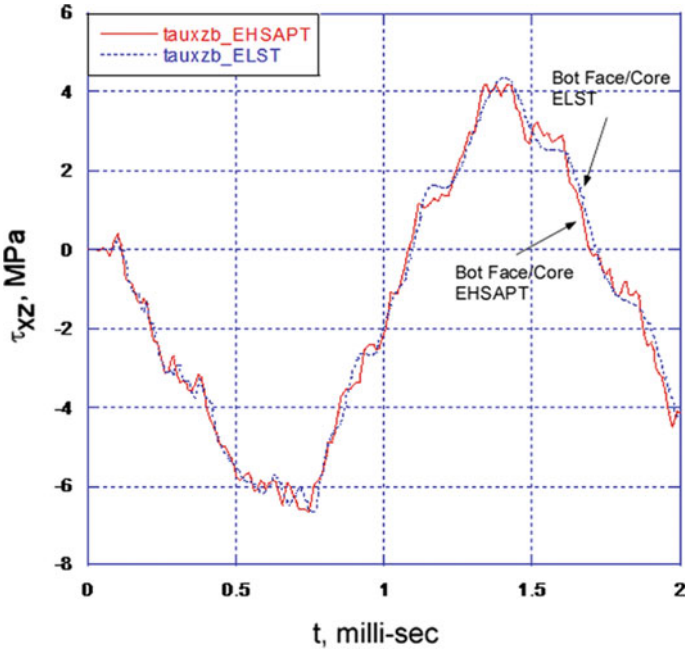

Fig. 8 Core transverse shear stress, τ^c_{xz} at the bottom face/core interface and at the left end, $x = 0$: EHSAPT and elasticity

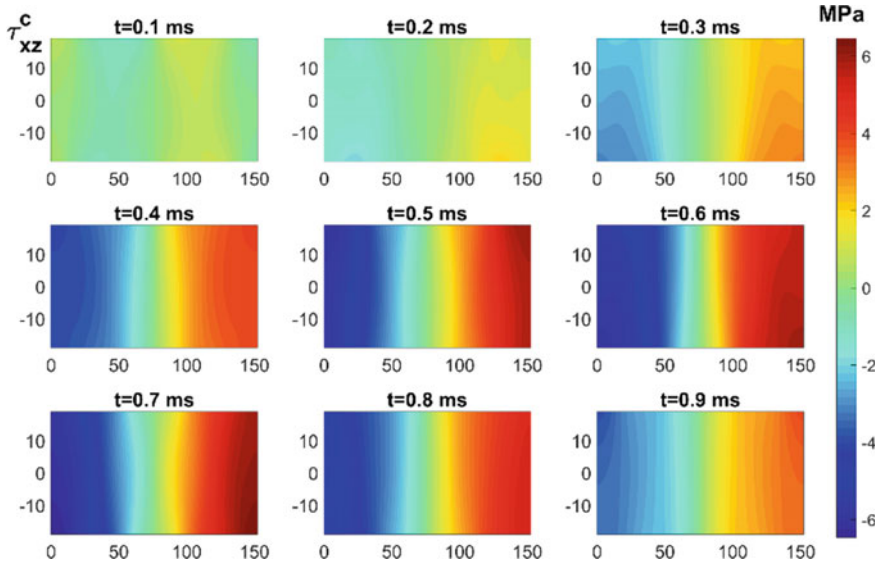

Fig. 9 Core transverse shear stress, τ^c_{xz} at various time instances (through thickness and along length profiles)

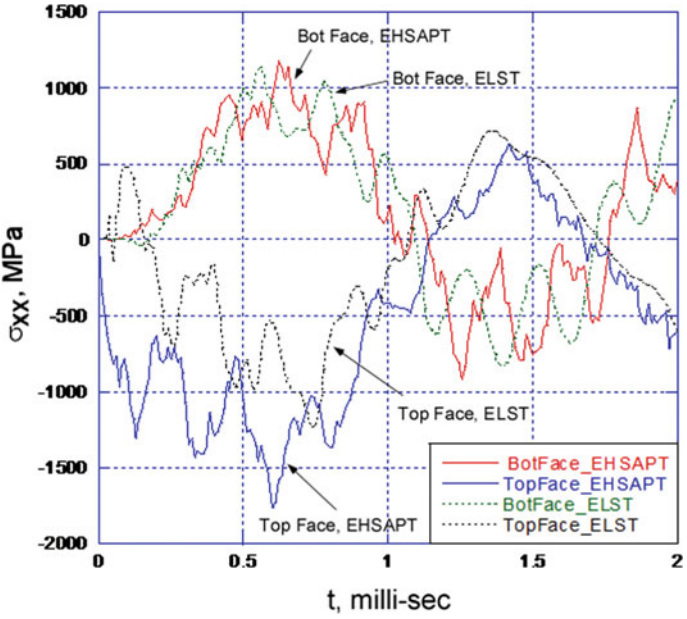

Fig. 10 The axial stress, $\sigma_{xx}^{t,b}$, at the top face surface and bottom face surface, and at midspan: EHSAPT and elasticity

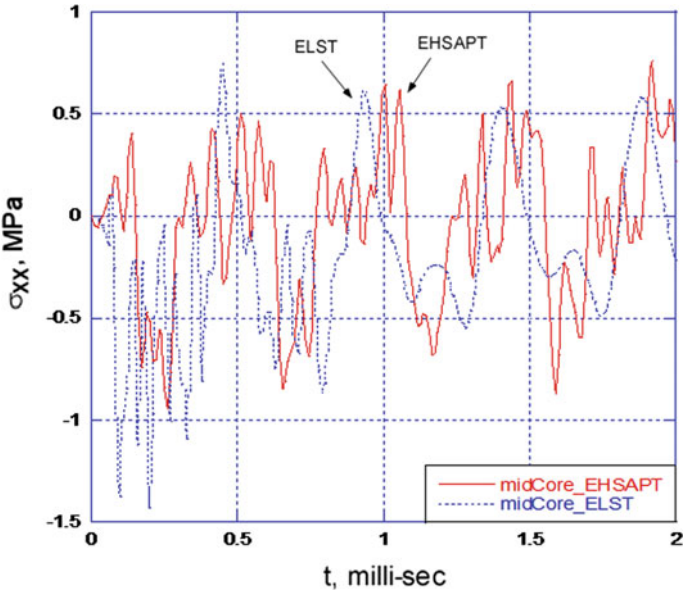

Fig. 11 The axial stress, σ_{xx}^{c}, at the core (middle) and at midspan: EHSAPT and elasticity

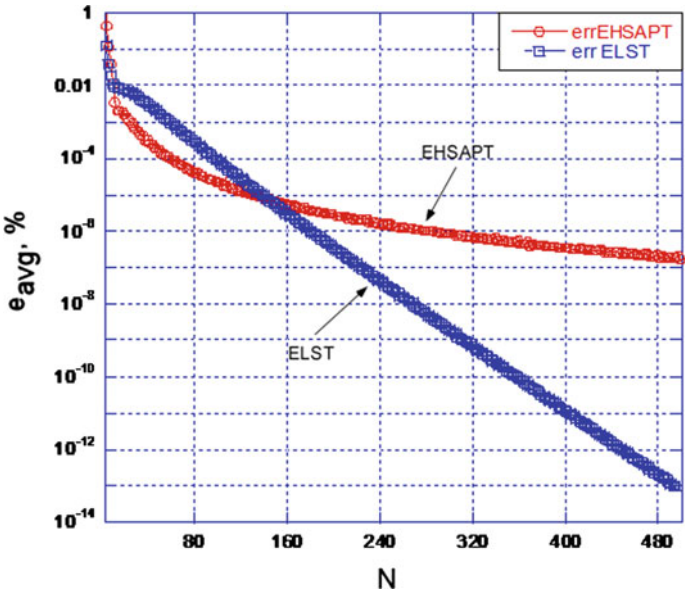

Fig. 12 Convergence of EHSAPT and elasticity: average cumulative error versus number of terms in the Fourier series

$$S_i^N(t) = [w_{0,N}^t(\frac{a}{2},t),\ w_{0,N}^c(\frac{a}{2},t),\ w_{0,N}^b(\frac{a}{2},t),\ u_{0,N}^t(0,t),\ u_{0,N}^c(0,t), u_{0,N}^b(0,t),\ \phi_{0,N}^c(0,t)], \tag{31a}$$

where,

$$w_{0,t}^t(\frac{a}{2},t) = \sum_{n=1}^{N} W_n^t(t)\sin\frac{n\pi}{2}, \tag{31b}$$

and other members in (31a) are defined in the same manner.

The individual subsequent cumulative error over the initial period of time up to 2 ms is defined as

$$e_i(N+1) = \int_{t=0}^{t=2ms} \left|\frac{S_i^{N+1}(t) - S_i^N(t)}{S_i^N(t)}\right| \times 100\, dt, \tag{31c}$$

and the average error for the seven quantities in (31a) is

$$e_{avg}(N) = \sum_{i=1}^{7} \frac{e_i(N)}{7}. \tag{31d}$$

It must be noted that, in this midspan point load case, even terms do not contribute to the solution as shown in (30). Therefore, the next term $N+1$ in (31c) shall be interpreted as the next odd term.

The convergence for both the EHSAPT and the Elasticity is shown in Fig. 12 on a semi-log plot. It can be seen that the Elasticity converges faster than the EHSAPT. Figure 12 shows that $N = 200$ gives an average percent error less than 3×10^{-6} for the EHSAPT and less than 4×10^{-7} for the Elasticity; therefore, in this paper, numerical results with $N = 200$ are produced.

5 Conclusions

The linear dynamic response of a simply supported sandwich composite beam/wide panel subjected to a concentrated blast decay load at the top face sheet is studied by use of (a) the Dynamic Extended High Order Sandwich Panel Theory (EHSAPT) and (b) the Dynamic Elasticity. The concentrated load is expressed as a Fourier Series (a series of distributed transverse sin functions over the beam length), then a closed form analytical solution of EHSAPT is derived. A semi-closed form of the dynamic elasticity transient response is also derived (closed form solution in the Laplace domain and numerical Laplace inversion). Specifically, the Laplace transform is applied to the elasticity formulation in the time domain, then a closed-form elasticity solution in the Laplace domain is obtained. Next, a numerical inverse Laplace transform is applied to obtain the solution in the time domain. Due to the inverse Laplace numerical technique being limited to specific time scales, i.e., not being valid for all time scales, only the transient response is obtained by the Euler method of inversion used in this study (as opposed to EHSAPT whose solution is valid for any $t > 0$). The EHSAPT shows very good accuracy in comparison with elasticity, and captures the unique sandwich response features i.e., the core compressibility and transverse shear; it accurately accounts for all stress components which are often neglected by other simplified sandwich theories, such as the first order shear deformation theory. Furthermore, the stress fields obtained from EHSAPT provide significant insights as to possible failure mechanisms of sandwich panels subjected to blast, i.e., local indentation, core cracking, interfacial debonding and are in agreement with such mechanisms reported in experimental studies.

Acknowledgements The financial support of the Office of Naval Research, Grant N00014-16-1-2831, and the interest and encouragement of the Grant Monitor, Dr. Y.D.S. Rajapakse, are both gratefully acknowledged.

References

1. Carlsson, L., & Kardomateas, G. A. (2011). *Structural and failure mechanics of sandwich composites*. Springer.
2. Wang, E., Gardner, N., & Shukla, A. (2009). The blast resistance of sandwich composites with stepwise graded cores. *International Journal of Solids and Structures*, *46*, 3492–3502.

3. Gardner, N., Wang, E., Kumar, P., & Shukla, A. (2012). Blast mitigation in a sandwich composite using graded core and polyurea interlayer. *Experimental Mechanics*, *52*, 119–133. https://doi.org/10.1007/s11340-011-9517-9.
4. Pagano, N. J. (1970). Exact solutions for rectangular bidirectional composites and sandwich plates. *Journal of Composite Materials*, *4*, 20–34. Jan.
5. Kardomateas, G. A. (2009) Three dimensional elasticity solution for sandwich plates with orthotropic phases: The positive discriminant case. *Journal of Applied Mechanics (ASME)*, *76*, 014505-1–014505-4.
6. Kardomateas, G. A., Frostig, Y., & Phan, C. N. (2013). Dynamic elasticity solution for the transient blast response of sandwich beams/wide plates. *AIAA Journal*, *51*(2), 485–491. https://doi.org/10.2514/1.J051885.
7. Kardomateas, G. A., Rodcheuy, N., & Frostig, Y. (2015) Transient Blast Response of Sandwich Plates by Dynamic Elasticity. *AIAA Journal*, *53*(6), 1424–1432. https://doi.org/10.2514/1.J052865. June.
8. Frostig, Y., Baruch, M., Vilnay, O., & Sheinman, I. (1992). High-order theory for sandwich beam behavior with transversely flexible core. *Journal of Engineering Mechanics*, *118*, 1026.
9. Phan, C. N., Frostig, Y., & Kardomateas, G. A. (2012). Analysis of sandwich panels with a compliant core and with in-plane rigidity-extended high-order sandwich panel theory versus elasticity. *Journal of Applied Mechanics (ASME)*, *79*(041001), 041001-1–041001-11.
10. Phan, C. N., Kardomateas, G. A., & Frostig, Y. (2012). Blast response of a sandwich beam/wide plate based on the extended high-order sandwich panel theory (EHSAPT) and comparison with elasticity. *Journal of Applied Mechanics (ASME)*, *80*(061005), 061005-1–061005-11. https://doi.org/10.1115/1.4023619.
11. Abate, J., & Whitt, W. (1995). Numerical inversion of Laplace transforms of probability distributions. *ORSA Journal on Computing*, *7*(1), 38–43.

Explosion-Induced Shock Waves Through a Medium and Associated Structural Response

Nilanjan Mitra

1 Introduction

Blast mitigation of a structure requires a detailed understanding of the process of explosion (which involves the type of explosive being used, detonation mechanism), the shock wave propagation through the medium resulting in fluid–structure interaction effects which eventually results in imparting loads to the structure, and eventually the structural response. It should be realized that any solution proposed is typically dependent on the above-mentioned conditions and thereby no solution in full-proof for different possible combinations that may arise. In this manuscript, I have concentrated on lightweight sandwich composite materials (which is being used currently for numerous defense applications based on the property of the polymeric foam to absorb the impact of shock waves). For consideration of the medium through which the shock wave propagates and reflects, I have considered the two most common mediums—air and water. Because of issues related to confidentiality, the topic of the type of high energy materials used as different types of explosives and their associated detonation mechanism has been kept outside the scope of this manuscript.

1.1 Medium Effects in an Explosion

The response of a structure subjected to the explosion is strongly dependent upon the medium. For an explosion in the air, we only obtain shock loading on the structure which typically translates to a sudden increase in pressure and temperature

N. Mitra (✉)
Department of Civil Engineering & Center for Theoretical Studies, Indian Institute of Technology Kharagpur, Kharagpur, West Bengal, India
e-mail: nilanjan@civil.iitkgp.ernet.in

S. Gopalakrishnan and Y. Rajapakse (eds.), *Blast Mitigation Strategies in Marine Composite and Sandwich Structures*, Springer Transactions in Civil and Environmental Engineering, https://doi.org/10.1007/978-981-10-7170-6_6

of structural components. The transmitted impulse to the structure depends both on the intensity of pressure pulse as well as on the decay time of the loading. The pressure pulse and decay time are typically dependent upon the weight of charge in TNT equivalents and the standoff distance. Empirical equations are available in the literature (such as the Friedlander's equation), which relate the charge weight and standoff distance to the pressure intensity and decay time witnessed by the structure using fluid–structure interaction concepts considering near incompressible medium. However, almost all these empirical equations are based on the theory by Taylor [1], which considers the medium as acoustic in nature. The effect of nonlinear compressibility (which may be more appropriate for high intensity and/or near field explosions) is not considered in the seminal work done by Taylor. Apart from that, Taylor's theory only considers constant back pressure to the plate on which the pressure pulse due to shock wave impinges. Constant back pressure situation typically arises if the movement of the plate subjected to shock loading is insignificant and there is no change in pressure on the back of the plate. With the development of new lightweight and high strength materials the assumption of constant back pressure requires to be revisited. Infact, the structures can move a certain distance with sufficient speed (being lightweight) and thereby the consideration of variable back pressure as a result of the movement of the structure should also be properly accounted for. The details of development along these lines for the case of air explosion has been discussed in this manuscript under section "air-shock loading."

It should be understood that there are significant differences between air and water medium. In a water medium, the molecules are much tightly packed compared to that of air and the dispersion of energy (transmitted by the explosion) by the associated molecules is also significantly different. Thereby direct applications of empirical equations (without a proper understanding) relating charge and standoff distance with peak pressure and decay time may be inappropriate. In this context, it should also be mentioned that underwater explosion events are much more complex events compared to that of an air explosion event. In an air explosion it is just the shock wave peak pressure and decay time, one is concerned about; however, in the case of an underwater explosion apart from direct shock wave effects there are other phenomenon, such as bulk cavitation, cavitation bubble dynamics, and so on [2]. The cavitation bubble that generates as a result of an underwater explosion also emits secondary shock wave like impulses which are significant and are known to cause the phenomenon of "hull whipping". If the frequency of the "hull whipping" matches with the natural frequency of the ship then it may result in resonance and eventual disaster of the ship structure. The cavitation bubbles are also known to "latch on" the ship/marine structure and jetting induced due to that may result in vertical cuts of the ship structure. In this manuscript, I will only concentrate on the phenomenon of shock waves that are induced as a result of underwater explosion under section "underwater shock loading". These shock waves may be considered either to be that of primary shock wave phenomenon from the explosion or resulting from cavitation bubble dynamics. It should be noted in this regard, that there is very less work done in the domain of

underwater shock wave propagation and its associated fluid–structure interaction phenomenon. One interested in the study of cavitation bubble dynamics is referred to the classic book by Brennen [3].

1.2 Air-Shock Loading

Taylor [1] demonstrated the beneficial effects of fluid–structure interaction in reducing the impulsive loads on a structure as a result of the explosion. However, the medium considered by Taylor was an acoustic medium in which the effects of compressibility of the medium were neglected. Group of researchers from Massachusetts Institute of Technology (MIT) argued the importance of consideration of nonlinear compressibility of air in an event of an explosion. Nonlinear compressibility effects in fluid–structure interaction and their implications in air-shock loading of structures were eventually demonstrated by the MIT group [4, 5]. It should be noted in this regard that the need for consideration of nonlinear compressibility of the medium had been identified much earlier in literature primarily from different experimental investigations [6–8] (Baker 1977). The study by the MIT group concentrated on the combined effects of fluid compressibility and fluid–structure interaction between a one-dimensional blast wave and a plate. A numerical method based on the Lagrangian formulation of Euler equations for a compressible flow and a shock capturing scheme based on the artificial viscosity (following classic approach by von Neumann and Richtmeyer [9] was utilized to solve the problem. The study eventually demonstrated that lightweight plates (typically sandwich type construction) are beneficial in reducing the impulse transmission to a plate with a given weight of TNT equivalent and standoff distance. The effects of nonlinear compressibility were observed to further enhance the mitigation of transmitted impulse provided by the fluid–structure interaction effects. The benefits were observed to be marginal for low-intensity blast waves compared to that of high-intensity blast waves.

Typically, if a lightweight plate is considered subjected to a shock wave, the plate will recede and there will be a resistance provided by the sudden pressure rise at the back of the plate. The theory by the MIT group did not account for the rise in pressure at the back of the plate and an assumption of constant atmospheric pressure at the back end of the plate was considered in their study. A group of researchers from the University of Nebraska Lincoln and US Army Research Lab [10] eventually established the theory considering the effects of nonlinear compressibility both front and back of the plate. They argued that in front of the plate, explosion-induced shock wave results in nonlinear compressibility of the medium (as earlier proposed by the MIT group) whereas at the back of the plate the pressure rises thereby resulting in the need for consideration of nonlinear compressibility due to the receding movement of the plate. They demonstrated that neglecting the resistance of the pressure build up in the back of plate significantly overpredicts the effectiveness of fluid–structure interaction.

The theories proposed by MIT group as well as by Peng et al. [10] consider the ideal gas equation of state. Thereby, the maximum value of reflection coefficient, C_R (ratio of reflected to that of the incident pressure) that could be achieved by these theories is limited to a value of 8. On the other hand, experiments carried out earlier demonstrates that the value of C_R can even be more around 20 [6, 11] and more. Early literatures [11–13] also suggest that for peak overpressures more than 6.9 atm the ideal gas EoS should not be utilized since dissociation and ionization of gasses may be responsible for an increase of the C_R values. It should also be noted that with rise of terrorist activities, the possibility of attaining higher peak pressures more than 6.9 atm is not a fiction. Infact as per FEMA specifications [14] and Kingery-Bulmash blast indicator the incident shock strength can easily reach more than 500 atm for vehicle/truck bombs placed near buildings. Thereby, there is a need to develop theories which can improve upon the theories by the MIT group and Peng et al. Infact, it should also be pointed out that there exist studies in the literature (peak overpressure of 200 atm by Vaziri and Hutchinson [15], 600 atm by Aleyaasin et al. [16]) which applies the theory of MIT group for their simulations. The ideal gas EoS (typically valid for small ranges of pressure and temperature rise) does not work at such high peak overpressures, and thereby, there is a need to remove these misconceptions in literature.

A theory has thereby been proposed by a group at IIT Kharagpur [17] in which a non-polytropic van der Walls EoS has been used to model shock wave propagation. A seven species air system (N_2, O_2, N, O, N^+, O^+, and e^-) has been modeled with a reference composition of 79% N_2 and 21% O_2 by volume. It should be noted that polytropic fluid assumption (specific heat at constant volume is constant) of an ideal gas EoS considers only translational and rotational motion of the molecules to be responsible for the internal energy of the system. On the other hand, the Real Gas EoS assumed in this work considers not only the effects of translation and rotation but also molecular vibration, dissociation, electronic excitation, and ionization of diatomic molecules considered for the work. It should be noted that the effects of reactions between gasses, the coupling of rotational and vibrational degrees of freedom, anharmonicity of vibrations have not been considered in this work. The study demonstrates (in line with suggestions by Brode [12] as well as Guzas and Earls [13]) that for peak overpressures greater than ~7 bar, the ideal gas EoS cannot be used since the contribution of vibrational degrees of freedom to internal energy cannot be neglected. The maximum value of reflection coefficient that be obtained considering vibrational degrees of freedom is ~10. For peak overpressure above 100 bar, the contributions of ionization and dissociation to the internal energy of the gas becomes important. Based on the simulation results, the study also shows that percentage change in transmitted impulse to a plate owing to real gas modeling of air instead of ideal gas assumption can result in an increase of 62% for the case of heavy plates and decrease up to 22% for lightweight plates considering a shock strength of 500 bar.

1.3 Water Shock Loading

The earliest studies of underwater shock wave propagation and reflection have been reported by Cole [2] and Swisdak [18]. Unlike air, Water is typically considered to be as a near incompressible medium. However, there exists there exists studies in which it has been reported both experimentally [19–26] and numerically that water under shock and/or static compression undergoes phase transition [27–29] which definitively indicates that under conditions of high pressure water may not demonstrate an isochoric behavior, thereby dispelling the assumption of incompressible medium for water. High pressure conditions not only occur under shock loading situations but also for water in ocean at large depths. Infact, it has been demonstrated that bulk liquid water undergoes phase transition to different polymorphs of water including ice VII under shock compression and hydrostatic compression loading [28, 30].

Apart from the work by Taylor [1] there appears to be no work looking into the fundamental aspects of shock loading in water. Extension to Taylors work was provided by Liu and Young [31] in which plate back side pressure was also included in the fluid–structure interaction parameter. However, both these theories are applicable for near incompressible water medium. It has been demonstrated that under high intensity loading situations or near field explosive situations or explosions at high depths water does behave as nonlinear compressible medium. Nonlinear compressibility of the water medium was explored by Ghoshal and Mitra [32] in which the pressure impulse to the submerged plate subjected to explosion-induced shock loading was determined considering both constant back pressure as well as variable pressure at the back side of the plate. The results obtained were compared to Taylor as well as Liu and Young theory and it was shown that nonlinear compressibility of the underwater medium further enhances the beneficial effects of FSI in reducing impulse transmitted to the structure. It was also demonstrated that FSI effect is more predominant for variable back pressure case in comparison to constant back pressure case thereby resulting in lower impulse transmission for light plates for different shock intensities. Maximum momentum transfer time was also observed to be lower for the case of variable back pressure case in comparison to the constant back pressure case. The importance of consideration of nonlinear compressibility of the medium was also demonstrated for deep underwater situations which may occur in oceans [33]. The amount of compression of the foam core material when sandwich composites are subjected to shock compression was also theoretically determined [34] considering the previous theory established by the authors group as well as the core compression model based on the rigid perfectly plastic locking idealization of the core material. It should be pointed out here that core compression reduces the back velocity of the plate and thereby non-consideration of this effect may lead to overestimation of the beneficial effects of fluid–structure interaction parameter for the case of sandwich composite panels. It is expected that the study will eventually help in better design of core region thicknesses of sandwich composite hull structure of marine ships.

Underwater shock loading of structures may not occur only at normal incidence but also at oblique incidence. The theoretical details behind oblique shock incidence underwater have been explored [35] in which transition lines are identified denoting regions of no shock reflection, irregular, and regular reflections and regions in which shock is not possible. The nature of irregular shock wave reflections under these situations of oblique incidence has also been done considering shock polar situations for the different intensity of shock and wedge angle incidence. This study of oblique underwater shock wave reflection may be beneficial in shock mitigation design of underwater structures, such as piers and/or floating/submerged platforms. This study on oblique underwater shock reflection also is one of the first extensive studies carried out for underwater situations; similar studies for shock reflections in air medium are present in [36].

1.4 Explosion-Induced Shock Wave Response of Structural Components

It should be noted that the theories developed above typically consider a one-dimensional formulation in which the structure is a point mass (except for study on oblique underwater shock reflection). Thereby, there is no consideration for structural deformations and/or delamination situations which may specifically arise as a result of shock loading on sandwich composite structures. Apart from that, there may be structural changes, phase change, and/or material dissociation when the material is subjected to shock waves. These issues have been considered as part of this manuscript. It should be noted that even though the situations of deformations and/or delaminations may be studied within the realm of conventional continuum mechanics but the issues of structural phase transformation, phase transformation (between different states of matter like solid $\rightarrow$ liquid) and/or material dissociation cannot be studied within the realm of conventional continuum mechanics and one needs a detailed study at a molecular or atomistic level. It should be realized that shock loading involves very high strain rates, thereby, the constitutive models that are utilized for material modeling should also account for that. For the case of metals, typically available high strain rate constitutive models include [37–41] models. All of these mentioned material models are not specific for different crystal structures that may be present within a metal, such as face-centered cubic, body centered cubic, hexagonal close packed as well as other different other crystal structures with the exception of Zerilli Armstrong [39]. It should be noted that all of these models have been developed based upon experimental tests carried out in Split Hopkinson test apparatus for strain rates at around $10^6\ s^{-1}$. Thereby, the suitability of these material models for strain rates above $10^6\ s^{-1}$ is yet to be investigated rigorously. One of the main issues that arise as a result of high strain rates above $10^6\ s^{-1}$ is the small timescale involved in the process. It should be noted that typically time-scales and length-scales are related to each other, thereby, if one reduces the time-scales then

length-scales should also be suitably reduced (e.g., being the Courant–Friedrichs–Lewy condition) and one thereby typically enters into the realm of molecular simulations rather than continuum simulations. Apart from that, it should also be noted that currently available constitutive models for continuum simulations cannot account for phase change in materials (such as situations in which liquid water undergoes a phase transformation to ice VII or even change of FCC Cu to BCT Cu under shock loading) and/or material dissociation. Thereby, as a word of caution it should be realized that continuum simulations for shock loading are only applicable for weak shocks in which the time-scales (decay time of shock) is not below millisecond, and there is no structural phase change (such as FCC → BCC), solid–liquid phase transformation and/or molecular dissociation of the material.

1.5 Delamination as a Result of Shock Loading of Sandwich Composites

Sandwich composites (made of GFRP face sheets, PVC foam core, and epoxy resin using vacuum resin infusion technology typically used for marine structures) when exposed to explosion-induced shock loads to undergo delamination in addition to deformations of the face exposed to the explosion. It should be noted that delamination cannot be easily captured in polymer sandwich composites since the conventional NDT techniques are ineffective. The foam core typically absorbs conventional ultrasonic waves and thereby detection of delamination in sandwich composites with polymer foam core cannot be done. One of the ways to investigate delamination is through microCT scans before and after the test. In situ observation of interfacial delamination can also be done through embedded optical sensors [42].

It should be mentioned that there are two different ways by which underwater explosive loads can be transmitted to a submerged structure each having it advantages and disadvantages: direct explosion loads by charging an explosive underwater (shown in Fig. 1 by experiments carried out by author) and through shock tube test setup. The direct explosion loads capture in reality the entire sequence of events that happens in the field which not only involves shock loading but also local and bulk cavitation, cavitation bubble response. However, this methodology of load application suffers from safety issues and primarily repeatability of experiments since the shape of the explosive, duration of preservation, and various other factors influence the pressure pulse loading to the structure. Thereby in a laboratory scale typically one goes in for shock tube test setups in which one can modulate precisely the intensity and decay time of the pressure impulse transmitted to the structure. However, this method typically suffers from not being able to model the other effects of underwater explosion such as local and bulk cavitation as well as cavitation bubble dynamics. It should be realized that unless the load is given properly to the structure (simulating real field experiments) the response obtained does not capture the intricate details of structure/material.

Fig. 1 Experiments carried out at National Underwater explosive testing facility at Naval Science and technology Limited, Defence Labs, Vishakhapatnam, India. The figures show the PETN explosive charge, arrangement of attachment to the sandwich composite panel, attachments of pressure transducers above the panel, immersion of the system underwater. The dimpled shape demonstrates the deformations sustained by the sandwich composite panel subjected to an real underwater explosion

From a modeling perspective, one needs to provide suitable constitutive models for the face sheet and the core. It should be remembered that even though there are high strain rate constitutive models available for metals but there are none for that of polymers so one is limited to using standard phenomenological plasticity models available for polymers [43, 44]. Otherwise, one can also develop new constitutive models for polymeric materials realizing the fact that plasticity in polymers is different from that of metals in which chain dynamics governs plasticity instead of dislocation and twinning mechanism in metals. The modeling of GFRP face sheet can be done through elastic materials (since it is not expected that the material will plastic levels) along with damage models (such as Hashin mode) to account for matrix cracking and fiber breakage. Delamination should be properly modeled in between the face sheet and the core by using some interface laws that has been calibrated for mixed mode loading situations (one may refer interfacial mixed mode loading experiments by the authors group—[45, 46]. As a word of caution, it should be mentioned that constitutive laws for interface considering mixed mode loads as well as damage models for the face sheet also depend on strain rates which is yet to be developed properly in the literature. Thereby numerical simulations of blast loading mimicking experimental tests still needs more work on the subject.

1.6 Shock-Induced Phase Transformations

In many situations, there may be phase transformation in materials subjected to shock loading. One of the cases of such transformation from bulk liquid water to

that of ice VII has been reported earlier [27]. Apart from such liquid to solid a phase transition, another type of phase transformation may happen in materials referred to as structural phase transformation. Typically for metallic structures, this means change from one crystal state to another, such as FCC → BCT. Prior to this type of structural phase transformation under shock loading, energy is dissipated through the formation of different types of dislocations and twinings in the crystal structure. A detailed exposition on the subject for Cu material can be obtained from a series of publications by the authors group [47–49] and references cited within those articles. It should be noted that the mechanism of deformation under shock loads differs from materials to materials thereby the behavior as observed in Cu may not the same for some other hexagonal close packed (HCP) materials such as Ti in which twinning is more predominant mode of plasticity compared to slippage [50]. The molecular simulation that has been carried out for different materials in the above literature review considers single crystal pristine materials; however, it should be realized that materials typically contains defects (which might be in the form of inclusions, voids, and initial dislocations or disinclinations) and the behavior of the material changes as a result of these defects. The effect of considering different types of voids (closed and open cells) in Cu material exposed to shock loads has been explored by the authors group [51]. It should also be realized that the materials considered so far are only single elements in single crystal form; in a macroscopic scale, we typically do not obtain single crystal materials but polycrystals. Polycrsytals are typically different single crystals (of different sizes) arranged in a random manner and the boundary between two single crystals is referred to as grain boundaries. These grain boundaries also influence the behavior of the material under different loading situations. Polycrsytals, which are typically found at a macroscopic level requires crystal plasticity codes for their simulations under different types of loading situations. These crystal plasticity-based codes applies homogenization techniques (such as the self-consistent approach) to model the constitutive behavior of polycrystals from single crystals also considering the effects of grain boundaries. Apart from that random defects should also be introduced to properly develop suitable constitutive model the material. It should be noted that many times, we require compounds and/or alloys instead of single elements; similar approaches can be used for these materials to investigate their behavior under shock or other type of loading situations. It should be realized that this methodology of structural phase transformations may also be effectively used to develop materials for shock mitigation [52–54].

1.7 Shock-Induced Molecular Dissociation

Another method by which energy from the shock is dissipated is through molecular dissociation of the material. A case such molecular dissociation was highlighted for air medium (if one considers air medium as a material) subjected to shock loads earlier [17]. Similarly, there are also studies in the literature in which water

(considering it as a material) also undergoes dissociation [30]. Apart from air and water, the structural material which is subjected to shock loads may also undergo dissociation. A case of such molecular dissociation has been demonstrated by the authors group for the case of Polyvinyl chloride—an important constituent of core material in sandwich composites [27]. The sequence of chain breakage which initiates after the glass transition temperature is reached when polyvinylchloride is shock loaded has been demonstrated by the authors.

2 Conclusion

The response of a structure under shock loading depends upon numerous factors which include the response of the medium, fluid–structure interaction and also the material response. Thereby, a proper understanding of all these are required prior to the development of efficient blast mitigation methodologies. The article demonstrates the utility of each of these factors that may play a decisive role in the development of blast mitigation technology.

References

1. Taylor, G. I. (1963). *Scientific papers*. In Batchelor, G. K. (Eds.), *The scientific papers of Sir Geofrey Ingham Taylor* (Vol. 3, pp. 287–303). *Aerodynamics and the mechanics of projectiles and explosions*. Cambridge University Press.
2. Cole, R. H. (1948). *Underwater explosions*. Princeton, New Jersey: Princeton University Press.
3. Brennen, C. E. (1995). *Cavitation and bubble dynamics*. Oxford University Press.
4. Kambouchev, N., Radovitzky, R., & Noels, L. (2006). Nonlinear compressibility effects in fluid-structure interaction and their implications on the air-blast loading of structures. *Journal of Applied Physics, 100,* 063519.
5. Kambouchev, N., Radovitzky, R., & Noels, L. (2007). Fluid-structure Interaction effects in the dynamic response of free standing plates to uniform shock loading. *ASME Journal of Applied Mechanics, 74,* 1042–1045.
6. Brode, H. L. (1959). Blast wave from a spherical charge. *Physics of Fluids, 2,* 217–229.
7. Vincenti, W. G., & Kruger, C. H. (1965). *Introduction to physical gas dynamics*. Malabar, Florida: Krieger Publishing Company.
8. Zeldovich, Y., & Razier, Y. (1966). *Physics of shock wave and high temperature hydrodynamic phenomena*. New York: Academic Press.
9. Von Neumann, J., & Richtmyer, R. (1950). A method for numerical computation of hydrodynamic shocks. *Journal of Applied Physics, 21,* 232–237.
10. Peng, W., Zhang, Z., Gogos, G., & Gazonas, G. (2011). Fluid-structure interactions for blast wave mitigation. *ASME Journal of Applied Mechanics, 78,* 031016.
11. Baker, W. E. (1973). *Explosions in air*. Austin, Texas: University of Texas Press.
12. Brode, H. L. (1977). Quick estimate of peak overpressure from two simultaneous blast waves. Technical Report DNA 4503T of Defense Nuclear Agency, Marina Del Ray, California.
13. Guzas, E. L., & Earls, C. J. (2010). Air blast load generation for simulating structural response. *Steel and Composite Structures, 10,* 429–455.

14. FEMA-426. (2003). *Reference manual to mitigate potential terrorist attacks against buildings*. Washington DC: Federal Emergency Management Agency.
15. Vaziri, A., & Hutchinson, J. W. (2007). Metal sandwich plates subject to intense air shocks. *International Journal of Solids and Structures, 44,* 2021–2035.
16. Aleyaasin, M., Harrigan, J., & Reid, S. (2015). Air blast response of cellular materials with a face plate: An analytical-numerical approach. *International Journal of Mechanical Sciences, 91,* 64–70.
17. Ghoshal, R., & Mitra, N. (2015). High-intensity air-explosion-induced shock loading of structures: Consideration of a real-gas in modelling a nonlinear compressible medium. *Proceedings of the Royal Society A, 471,* 20140825.
18. Swisdak, M. M. (1978). Explosion effects and properties—Part II: Explosion effects in water. Technical Report, Naval Surface Weapons Center, Dahlgren, Virginia.
19. Dolan, D., Johnson, J., & Gupta, Y. M. (2005). Nanosecond freezing of water under multiple shock wave compression: Continuum modeling and wave profile measurements. *The Journal of Chemical Physics, 123,* 064702.
20. Dolan, D., Knudson, M., Hall, C., & Deeney, C. (2007). A metastable limit for compressed liquid water. *Nature Physics, 3,* 339–342.
21. Men, Z., Fang, W., Li, D., Li, Z., & Sun, C. (2014). Raman spectra from symmetric hydrogen bonds in water by high intensity laser induced breakdown. *Science Report, 4,* 4606.
22. Hemley, R., Jephcoat, A., Mao, H., Zha, C., Finger, L., & Cox, D. (1987). Static compression of H_2O ice to 128 GPa. *Nature*, *737*.
23. Goncharov, A., Struzhkin, V., Somayazulu, M., Hemley, R., & Mao, H. (1996). Compression of ice to 210 gigapascals: Infrared evidence for a symmetric hydrogen bonded phase. *Science, 273*(5272), 218–220.
24. Salzmann, C. G., Radaelli, P. G., Hallbrucker, A., Mayer, E., & Finney, J. L. (2006). The preparation and structures of hydrogen ordered phases of ice. *Science, 311*(5768), 1758–1761.
25. Bogdanov, G., & Rybakov, A. (1992). Anomalies of shock compressibility of water. *Journal of Applied Mechanics and Technical Physics, 33,* 162–165.
26. Rybakov, A. (1996). Phase transformation of water under shock compression. *Journal of Applied Mechanics and Technical Physics, 37,* 629–633.
27. Neogi, A., & Mitra, N. (2016). Shock induced phase transition of water: Molecular dynamics investigations. *Physics of Fluids, 28,* 027104.
28. Aragones, J., Conde, M., Noya, E., & Vega, C. (2009). The phase diagram of water at high pressures as obtained by computer simulations of the TIP4P/2005 model: The appearance of plastic crystal phase. *Physical Chemistry Chemical Physics: PCCP, 11,* 543.
29. Goldman, N., Reed, E. J., Kuo, I.-F. W., Fried, L. E., Mundy, C. J., & Curioni, A. (2009). Ab-initio simulation of the equation of state and kinetics of shocked water. *The Journal of Chemical Physics, 130,* 124517.
30. Neogi, A., & Mitra, N. (2016). Shock compression of polyvinylchloride. *Journal of Applied Physics, 119,* 165903.
31. Liu, Z., & Young, Y. (2008). Transient response of a submerged plate subject to underwater shock loading: An analytical perspective. *ASME Journal of Applied Mechanics, 75,* 044504.
32. Ghoshal, R., & Mitra, N. (2012). Non-contact near-field underwater explosion induced shock-wave loading of submerged rigid structures: Nonlinear compressibility effects in fluid structure interaction. *Journal of Applied Physics, 112,* 024911.
33. Ghoshal, R., & Mitra, N. (2016). Underwater explosion induced shock loading of structures: Influence of water depth, salinity and temperature. *Ocean Engineering, 126,* 22–28.
34. Ghoshal, R., & Mitra, N. (2014). On core compressibility of sandwich composite panels subjected to intense underwater shock loads. *Journal of Applied Physics, 115,* 024905.
35. Ghoshal, R. (2015). *Non-contact explosion induced shock wave response of structures*. Ph.D. Thesis, Indian Institute of Technology Kharagpur, India.
36. Ben-Dor, G. (2007). *Shock wave reflection phenomena*. Berlin Heidelberg: Springer.

37. Johnson, G. R., & Cook, W. H. (1985). Fracture characteristics of three metals subjected to various strains, strain rates, temperatures and pressures. *Engineering Fracture Mechanics, 21,* 31–48.
38. Johnson, G. R., & Holmquist, T. J. (1994). An improved computational constitutive model for brittle materials. In Schwartz, S. C., Shaner, J. W., Samara, G. A., Ross, M. (Eds.), *High pressure science and technology*—1993, *American Institute of Physics conference proceedings,* no. 309, pp. 981–984. New York: AIP Press.
39. Zerilli, F. J., & Armstrong, R. W. (1987). Dislocation-mechanics based constitutive relations for material dynamics calculations. *Journal of Applied Physics, 61,* 1816–1825.
40. Steinberg, D. J., & Lund, C. M. (1989). A constitutive model for strain rates from 10^{-4} to 10^{6} s^{-1}. *Journal of Applied Physics, 65,* 1528–1533.
41. Preston, D. L., Tonks, D. L., & Wallace, D. C. (2003). Model of plastic deformation for extreme loading conditions. *Journal of Applied Physics, 93,* 211–220.
42. Patra, A. (2017). *Identification and mitigation of interfacial delamination in sandwich composites*. Ph.D. Thesis, Indian Institute of Technology Kharagpur, India.
43. Mitra, N. (2010). A methodology for improving shear performance of marine grade sandwich composites: Sandwich composite panel with shear keys. *Composite Structures, 92,* 1065–1072.
44. Mitra, N., & Raja, B. R. (2012). Improving delamination resistance capacity of sandwich composite panels with initial face/core debond. *Composites Part B, 43,* 1604–1612.
45. Patra, A., & Mitra, N. (2014). Interface fracture of sandwich composites: Influence of MWCNT sonicated epoxy resin. *Composites Science and Technology, 101,* 94–101.
46. Patra, A., & Mitra, N. (2016). Mixed mode fracture of sandwich composites: Performance improvement with multiwalled carbon nanotube sonicated resin. *Journal of Sandwich Structures*. http://doi.org/10.1177/1099636216656485.
47. Neogi, A., & Mitra, N. (2017). Evolution of dislocation mechanism in single crystal Cu under shock loading in different directions. *Modelling and Simulation in Materials Science and Engineering, 25,* 025013.
48. Neogi, A., & Mitra, N. (2017). Shock induced deformation response of single crystal copper: Effect of crystallographic orientations. *Computational Materials Science, 131,* 141–151.
49. Neogi, A., & Mitra, N. (2017). A metastable phase of shocked bulk single crystal copper: An atomistic simulation study. *Scientific Reports, 7,* 7337.
50. Rawat, S., & Mitra, N. (2017). Compression twinning and structural phase transformation of single crystal Titanium under uniaxial compressive strain conditions: Comparison of interatomic potentials. *Computational Materials Science, 126,* 228–237.
51. Neogi, A., & Mitra, N. (2014). On shock response of nano void closed/open cell Copper material: Nonequilibrium molecular dynamic simulations. *Journal of Applied Physics, 115,* 013504.
52. Grujicic, M., Bell, W. C., Pandurangan, B., et al. (2010). Blast wave impact mitigation capability of polyurea when used as helmet suspension pad material. *Materials and Design, 31,* 4050–4065.
53. Grujicic, M., Yavari, R., Snipes, J. S., et al. (2012). Molecular level computational investigation of shockwave mitigation capability of polyurea. *Journal Materials Science, 47,* 8197–8215.
54. Grujicic, M., Snipes, J., & Ramaswami, S. (2015). Mesoscale computational investigation of polyurea microstructure and its role in shockwave attenuation/dispersion. *AIMS Materials Science, 2*(3), 163–188.

Uncertainty in Structural Response Prediction of Composite Structures Subjected to Blast Loading: Modeling, Quantification, and Reduction

Zhen Hu and Sankaran Mahadevan

1 Introduction

A considerable amount of energy is released in a relatively short time period during a blast event [1]. Materials with the high strength-to-weight ratio, such as composite laminates and sandwich structures with thin face sheets and lightweight core, have shown promising performance in the energy absorption of marine structures subjected to blast loads [2]. Prediction of the structural response under blast events requires simulations of the blast event and wave propagation. It is quite often that the simulated structural responses are different from the actual experiment responses due to the complexity of the physics and the inherent variability and uncertainty sources in the nature and simulations.

Significant progress has been made in the structural analysis of composite/sandwich structures subjected to blast loads in the past decades. For instances, Frostig and Baruch [3] developed a higher order sandwich panel theory by considering the transverse normal and transverse shear stress during the structural analysis. Phan et al. [4] performed one-dimensional analysis for the blast response of a sandwich beam/wide plate with a compressible core using extended high-order sandwich panel theory. Sekhar et al. [2] studied the wave transmission characteristics of higher order sandwich panels with flexible core using time-domain spectral element method. Although these research efforts have improved the accuracy of the structural response prediction, it is almost impossible to eliminate the discrepancy between computer simulations and the actual experiments. To design reliable blast-resistant structures, various uncertainty sources need to be considered in the analysis and design of composite/sandwich structures subjected to blast loads.

Z. Hu · S. Mahadevan (✉)
Vanderbilt University, Box 1831, Station B, Nashville, TN 37235, USA
e-mail: sankaran.mahadevan@vanderbilt.edu

S. Gopalakrishnan and Y. Rajapakse (eds.), *Blast Mitigation Strategies in Marine Composite and Sandwich Structures*, Springer Transactions in Civil and Environmental Engineering, https://doi.org/10.1007/978-981-10-7170-6_7

Considering uncertainty in the analysis of composite/sandwich structures has been a popular research topic during the past decade due to its importance. For example, Murugan et al. [5] investigated the effect of uncertainty in composite material properties on the nonlinear aeroelastic response of a four-bladed composite helicopter rotor. Piovan et al. [6] studied the structural response uncertainty of composite thin-walled beams due to the uncertainty sources introduced by manufacturing, material properties, and boundary conditions. Eamon and Rais-Rohani [7] applied reliability-based optimization method to the design of a composite submarine structure in the presence of composite material property uncertainty. Motley and Young [8] found that marine self-adaptive composite structures tend to be susceptible to geometric, material, and loading uncertainty of the composite structures. Patel et al. [9] considered the uncertainty in the elastic properties and strength of the composite material in the damage analysis of composite beams under ballistic impact. Shaw et al. [10] evaluated the reliability of fiber-reinforced composites by accounting for the uncertainty in both micro and macro-mechanical analyses of the composite structure. Hu et al. [11] performed reliability analysis for a composite turbine blade by considering the uncertainty in the composite material properties. Chandrashekhar and Ganguli [12] presented a method for the damage assessment of composite structures under material and measurement uncertainty. Kim and Noh [13] performed a method for the design optimization of blast-resistant CFRP-steel composite structure based on reliability analysis. Similar to the above studies, Zhang et al. [14] studied the effect of ply thickness uncertainty on the reliability of laminated composite panels, and Altunc et al. [1] performed design optimization of a blast-resistant composite laminate incorporating carbon nanotubes using a reliability-based design optimization method. By including uncertainty sources in the composite structural analysis and design, the variability of the composite structural response can be quantified and specific reliability requirement can be satisfied.

The aforementioned studies in the uncertainty modeling of composite structures, however, mainly focus on the natural variability in the composite material properties such as modulus and ply orientation. Only a few of them concentrate on the uncertainty modeling of the structural response of marine structures subjected to blast loads. Two issues are important in the latter context. First, due to the complicated nature of blast event and structural response, there are many other types of uncertainty sources that need to be considered in addition to the composite material properties variability. Second, the uncertainty sources in the structural analysis under blast events occur at multiple levels of analysis, which requires more advanced uncertainty modeling and quantification methods than those used in the above studies. Therefore, a clear and comprehensive framework is needed for the analysis and design of composite structures subjected to blast loads in the presence of heterogeneous uncertainty sources, in order to guarantee the reliability of marine structures.

This chapter aims to provide a systematic uncertainty quantification (UQ) and uncertainty management (UM) framework for the design of composite marine structures subjected to blast loads. The remainder of this chapter is organized as follows. The background of composite structure design subjected to blast loads is

reviewed in Sect. 2. Based on the reviewed models, Sect. 3 first gives an overview of the UQ/UM framework and then explains each element of the framework in detail. Following that, Sect. 4 provides concluding remarks.

2 Composite Structure Subjected to Blast Loads

In this section, we briefly overview the structural response analysis of marine structures subjected to blast loads. Further details on such analysis can be found in the other chapters of this book.

2.1 Blast Load Modeling

During an underwater explosion, a bubble is formed that expands and contracts, producing shockwaves [15, 16]. Two main factors that characterize a pressure pulse are the peak pressure and pressure time history. To effectively model the blast load, the blast wave pressure time history and the structural response to the blast load need to be considered. In Ref. [17], the pressure above the ambient pressure is modeled over time as

$$P(x,\ t) = P_m e^{-\frac{t}{\theta}} \tag{1}$$

where P_m is the peak pressure, θ is a time constant, $P_m = 52.4(m^{1/3}/R)^{1.13}$ MPa, $\theta = 0.084m^{1/3}(m^{1/3}/R)^{-0.23}$ ms, and m, R are the mass of the TNT explosive in kg. and the distance of the point of observation from it.

Another widely used blast load model is by Taylor [18], where the total pressure on a plate during a blast event is given by

$$\begin{aligned} P(x,\ t) &= P_{incident} + P_{reflected} + P_{rarefaction} \\ &= P_m e^{-\frac{(t-x/c_W)}{\theta}} + P_m e^{-\frac{(t+x/c_W)}{\theta}} - \rho_w c_W \dot{w}(t + x/c_W) \end{aligned} \tag{2}$$

in which ρ_w is the density of water, c_W is the speed of the blast wave in water, and w is the deflection of the plate.

In this chapter, for the sake of illustration, we represent the blast load as $P(x,\ t,\ \boldsymbol{\alpha})$, where $\boldsymbol{\alpha}$ is a vector of parameters in the blast pressure model, such as θ and m in the model given in Eqs. (1) and (2). Based on the blast load modeling, the dynamic response of the composite/sandwich structures is analyzed.

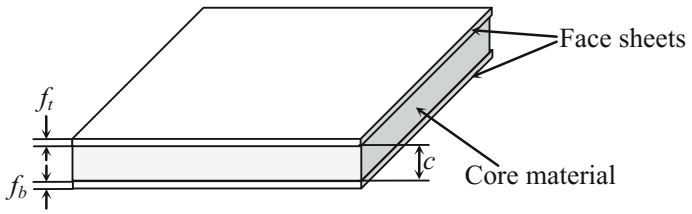

Fig. 1 Illustration of a sandwich plate

2.2 Composite/Sandwich Structural Response Analysis

Figure 1 shows a schematic sandwich structure, where the core material is bounded between two laminated composite face sheets [19]. The thicknesses of the top and bottom face sheets are f_t and f_b. The thickness of the core material is c.

Different types of materials can be used as the core material. To predict the displacement of the sandwich plate, various methods have been developed in the past decades, such as the higher order sandwich panel theory, the extended higher order sandwich panel theory, and the time-domain spectral element method [2–4]. In this chapter, we denote the displacement of the plate as $u(\mathbf{d}, P(x, t, \boldsymbol{\alpha}), t, \boldsymbol{\beta})$, where $\mathbf{d}$ is a vector of spatial coordinates and $\boldsymbol{\beta}$ is a vector of parameters related to the structural analysis including the geometry parameters, material parameters, initial boundary conditions, and other parameter during the analysis. In the next section, we discuss how to perform uncertainty quantification and uncertainty management based on the blast load modeling and structural response analysis.

3 Uncertainty Quantification (UQ) and Uncertainty Management (UM)

3.1 Overview of the UQ/UM Framework

We first identify the uncertainty sources in the modeling of composite structure behavior under blast loading and then provide an overview of the UQ/UM framework.

3.1.1 Uncertainty Sources Analysis

The uncertainty sources in the modeling of composite structure behavior under blast loading can be classified into two categories: *aleatory uncertainty* and *epistemic uncertainty* [20].

Aleatory uncertainty refers to natural variability, such as variability in composite material properties, ply angles, shockwave pressure, etc., which is irreducible. Epistemic uncertainty refers to the uncertainty caused due to lack of knowledge, manifested either due to inadequate data on the model inputs and parameters, or due to modeling approximations. Epistemic uncertainty can be reduced by collecting more information or by improved modeling. The modeling uncertainty sources include blast load model, composite material model, and stress/deformation analysis model, as reviewed in Sect. 2. The two categories of uncertainty sources are briefly summarized below.

Aleatory uncertainty: Natural variability is inherent in the blast events. There are numerous sources of such variability, such as peak pressure of the shock wave, the mass of the TNT explosive, modulus of the composite material, ply orientations, ply and laminate thickness, the material property of the core material, and measurement errors of the loading and structural properties.

Epistemic uncertainty: As shown in Fig. 2, epistemic uncertainty can be further divided into two groups, namely *data uncertainty* and *model uncertainty* [21]. Data uncertainty may come from limited measurement data or imprecise measurements. In the case of epistemic uncertainty with respect to model inputs and parameters, typically, the value of a quantity is not precisely known. This could refer to a deterministic quantity whose precise value is not known, or a stochastic quantity whose distribution type and parameters are not precisely known. For example, when the composite material properties are modeled as random variables to represent the natural variability (aleatory uncertainty), there will be epistemic uncertainty regarding the distribution type and distribution parameters of the random variables if the amount of data is sparse. Another example is epistemic uncertainty in the modeling of a deterministic blast event, such as the imprecise parameters of the blast load model.

The other important source of epistemic uncertainty is model uncertainty, which represents the difference between the computer simulation model and the experiment. Its quantification plays a role in correcting the simulation model to improve

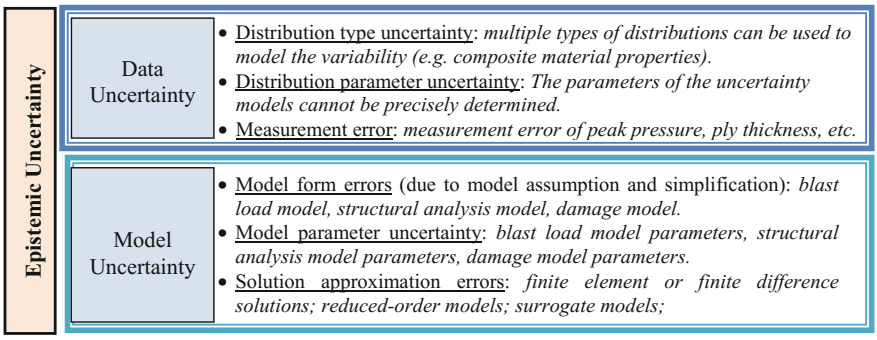

Fig. 2 Summary and examples of epistemic uncertainty sources in composites modeling

the accuracy of the simulation. The model uncertainty sources can be further classified into three groups, namely *model form*, *model parameters*, and *solution approximations.*

- *Model form*: Model form uncertainty comes from the assumptions and simplifications made in formulating the mathematical model. For example, Eqs. (1) and (2) are a simplified representation of the complex blast load model. This causes the discrepancy between the predicted wave pressure and the actual wave pressure.
- *Model parameters*: In some simulation models, we are not able to exactly determine the values of some parameters. For example, we may not precisely know the material property of the material used in the sandwich structure. In this situation, we have uncertainty in the simulation model output due to uncertainty in the model parameter values. In some cases, the model parameters may be physical quantities, but in some other cases, model parameters may simply be coefficients without a physical meaning, dictated by the choice of the model form. The latter is often the case with regression models of empirical data.
- *Solution approximations*: These come from numerical discretization, reduced order modeling, and other approximate solution procedures in the simulation models. For example, finite element or finite different simulation models solve the partial differential equations using numerical discretization (e.g., fluid–structure interaction analysis of marine structures, or structural analysis under blast loading). Further, when the simulation models are computationally expensive, often surrogate models are trained and used as substitutes. This introduces additional approximation and uncertainty in the model prediction.

3.1.2 Overview of the UQ/UM Framework

The above summarized uncertainty sources will affect the structural response of the marine composites. To mitigate the effect of the uncertainty sources on the output quantity of interest (e.g., the maximum displacement of the composite plate), we present a systematic UQ/UM framework in Fig. 3. There are mainly three elements, namely uncertainty modeling, uncertainty propagation, and uncertainty management.

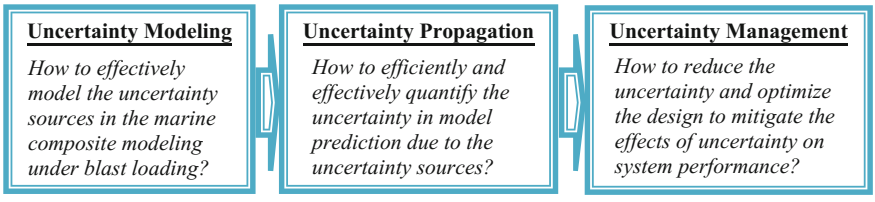

Fig. 3 Overview of UQ/UM framework for marine composite modeling under blast loading

- Uncertainty modeling: This element focuses on the modeling of the uncertainty sources summarized in Sect. 3.1.1 using advanced statistical approaches. For different types of uncertainty sources, the modeling methods are different. Section 3.2 provides details about different uncertainty modeling approaches.
- Uncertainty propagation: This element covers various research topics related to how to quantify the variability of the quantity of interest (QoI) due to the uncertainty sources modeled in the last element. A major challenge that needs to be solved in this element is how to reduce the required computational effort during the uncertainty propagation. Topics such as surrogate modeling, multi-level uncertainty propagation, and global sensitivity analysis, which has been widely used to improve the computational efficiency in uncertainty propagation, will be discussed in Sect. 3.3. Model validation and the inclusion of validation result in the prediction uncertainty quantification will also be covered in this element.
- Uncertainty management: After the variability of the QoIs is effectively quantified, the new questions that need to be answered include how to reduce the uncertainty based on the observations and how to optimize the design based on the uncertainty quantification (i.e., uncertainty modeling and uncertainty propagation) to satisfy specific reliability or robustness requirements. Solutions related to these two questions will be explained in details in Sect. 3.4.

Some techniques discussed below can be used in multiple elements to achieve different purposes. For instance, the Bayesian calibration method presented in Sect. 3.2 can be employed for the modeling of epistemic uncertainty in the uncertainty modeling element and can also be used to reduce the uncertainty in the uncertainty management element.

3.2 Uncertainty Modeling

3.2.1 Modeling of Aleatory Uncertainty

A natural way of modeling the aleatory uncertainty is to use random variables for time-independent quantities, stochastic fields for space-varying quantities, and stochastic processes for time-varying quantities, based on the classical frequentist probability theory [20]. The commonly used distributions for modeling of continuous random variables include normal distribution, lognormal distribution, Weibull distribution, and Beta distribution [20]. For discrete random variables, the widely used distributions include Binomial distribution, Geometric distribution, and Poisson distribution [20]. To determine an appropriate distribution, there are several approaches can be employed, such as probability paper and statistical tests (e.g., Chi-Square test, Kolmogorov–Smirnov test). Details of these methods can be found in Ref. [20].

To model the variability over time, such as the blast pressure at a specific location of the composite structure, the commonly utilized methods include the Karhunen–Loeve (KL) expansion method, Polynomial Chaos Expansion (PCE), Linear Expansion (LE) method, Orthogonal Series Expansion (OSE) method, Expansion Optimal Linear Estimation (EOLE) method, and time series models [22]. These methods can also be applied to the modeling of variability over space, such as the heterogeneous material properties with spatial variability [23]. If the time series models are used to represent the variability over time, depending on the characteristics of the stochastic process, there are several options including autoregressive (AR) model, moving average (MA) model, autoregressive moving average (ARMA) model, and autoregressive integrated moving average (ARIMA) model [24]. For instance, an ARMA(p, q) time series model can be used to model a stationary stochastic process as follows

$$Y(t_i) = \varphi^{(0)} + \varphi^{(1)} Y(t_{i-1}) + \varphi^{(2)} Y(t_{i-2}) + \cdots + \varphi^{(p)} Y(t_{i-p}) + \varepsilon(t_i) - \omega^{(1)} \varepsilon(t_{i-1}) - \cdots - \omega^{(q)} \varepsilon(t_{i-q}) \tag{3}$$

in which t_i is the ith time instant, $\varepsilon(t_i)$, $\varepsilon(t_{i-1})$, ... , $\varepsilon(t_{i-q})$, is a sequence of independent and identically distributed random variables with zero mean and finite standard deviation σ_ε, $\varphi^{(0)}$, $\varphi^{(1)}$, ..., $\varphi^{(p)}$, $\omega^{(1)}$, ..., $\omega^{(q)}$ are the coefficients of the time series model $Y(t)$, p is the order of the AR model, and q is the order of the MA model. The random variables, $\varepsilon(t_i)$, $\varepsilon(t_{i-1})$, ..., $\varepsilon(t_{i-q})$, can follow Weibull, Normal, or other distributions.

When there is variability in both space and time (e.g., the total pressure that a composite plate subjected to during a blast event), as discussed in Refs. [25, 26], the aforementioned stochastic process modeling methods can be combined with singular value decomposition or copula method to model the aleatory uncertainty sources. Next, we will introduce methods for the modeling of epistemic uncertainty sources.

3.2.2 Modeling of Data Uncertainty

(a) Distribution parameter uncertainty

When the data for the modeling of aleatory uncertainty is too limited, the epistemic uncertainty in the parameters of the random variables, stochastic processes, random fields, or time-dependent random fields, is modeled using the Bayes' theorem as [27]

$$f(\theta|\mathbf{D}) = P(\mathbf{D}|\theta) f(\theta) / \left[\int_\theta P(\mathbf{D}|\theta) f(\theta) d\theta \right] \propto P(\mathbf{D}|\theta) f(\theta) \tag{4}$$

where $\mathbf{D}$ is the observation data, θ is the vector of parameters of random variables, $P(\mathbf{D}|\theta)$ is the likelihood of observing the data $\mathbf{D}$, $f(\theta)$ is the prior distribution, $f(\theta|\mathbf{D})$ is the posterior distribution, and "$\propto$" stands for "proportional to."

For example, both coefficients and noise terms can be assumed to be random instead of deterministic in the ARMA model given in Eq. (3) to account for the epistemic uncertainty due to limited data. When no information is available about the prior distributions of the ARMA coefficients, they can be assumed to follow uniform distributions.

Assume that, we have n_{ts} trajectories of a stochastic loading $Y(t)$, and denote these trajectories as $\mathbf{D}^i$, $i=1,\ 2,\ \ldots,\ n_{ts}$, where $\mathbf{D}^i=[Y^i(t_1),\ Y^i(t_2),\ \ldots, Y^i(t_{nt})]$ and $Y^i(t_j)$, $j=1,\ 2,\ \ldots,\ n_t$ are the ith trajectory of the stochastic loading $Y(t)$ at time instant t_j. For given values of $\boldsymbol{\varphi},\ \boldsymbol{\omega}$, the standard deviation σ_ε is computed by comparing the model prediction and the observed data $\mathbf{D}_k$ as follows [28]

$$\sigma_\varepsilon^2=\frac{1}{n_{ts}(n-p-1)}\sum_{j=1}^{n_{ts}}\sum_{i=p+1}^{n_t}[Y^j(t_i)-\hat{Y}(t_i)]^2 \tag{5}$$

where n_t is the number of observations and $\hat{Y}(t_i)$ is the estimation of the time series model under given coefficients of $\boldsymbol{\varphi}$ and $\boldsymbol{\omega}$.

The likelihood $L(\mathbf{D}|\boldsymbol{\varphi},\boldsymbol{\omega})$ of observing data $\mathbf{D}=[\mathbf{D}^1,\ \ldots,\ \mathbf{D}^{n_{ts}}]$ given specific values of the coefficients of the time series model $\boldsymbol{\varphi}$ and $\boldsymbol{\omega}$ is given by [29]

$$L(\mathbf{D}|\boldsymbol{\varphi},\boldsymbol{\omega})=\prod_{i=1}^{n_{ts}}L(\mathbf{D}^i\big|\boldsymbol{\varphi},\boldsymbol{\omega}) \tag{6}$$

where

$$L(\mathbf{D}^i\big|\boldsymbol{\varphi},\boldsymbol{\omega})=L(Y^i(t_1),\ Y^i(t_2),\ \ldots, Y^i(t_{nt})\big|\boldsymbol{\varphi},\boldsymbol{\omega}) \tag{7}$$

Equation (7) can be further written as

$$L(Y^i(t_1),\ Y^i(t_2),\ \ldots, Y^i(t_{nt})\big|\boldsymbol{\varphi},\boldsymbol{\omega})=L(Y^i(t_{nt})\big|\boldsymbol{\varphi},\ \boldsymbol{\omega},\mathbf{Y}_{-t_{nt}})L(\mathbf{Y}_{-t_{nt}}|\boldsymbol{\varphi},\boldsymbol{\omega}) \tag{8}$$

where $\mathbf{Y}_{-t_{nt}}=[Y^i(t_1),\ Y^i(t_2),\ \ldots,\ Y^i(t_{t_{nt}-1})]$ is the stochastic loading at time instants before t_{nt}, $L(\mathbf{Y}_{-t_{nt}}|\boldsymbol{\varphi},\boldsymbol{\omega})=L(Y^i(t_1),\ Y^i(t_2),\ \ldots, Y^i(t_{nt-1})\big|\boldsymbol{\varphi},\boldsymbol{\omega})$ is computed similarly to Eq. (7), and $L(Y^i(t_{nt})\big|\boldsymbol{\varphi},\ \boldsymbol{\omega},\mathbf{Y}_{-t_{nt}})$ is computed based on $\boldsymbol{\varphi}$ and $\boldsymbol{\omega}$. Note that the probability given in Eq. (6) is usually very small. To make the computation of Eq. (6) possible, a logarithm operator can be used. More details related to the likelihood given in Eq. (7) can be found in [30].

Then, the joint distribution of the coefficients $\boldsymbol{\varphi}$ and $\boldsymbol{\omega}$ under given observation $\mathbf{D}$ is updated using Bayes' theorem as

$$p(\boldsymbol{\varphi},\ \boldsymbol{\omega}|\mathbf{D}) = \frac{L(\mathbf{D}|\boldsymbol{\varphi},\ \boldsymbol{\omega})\pi(\boldsymbol{\varphi})\pi(\boldsymbol{\omega})}{\int \cdots \iint L(\mathbf{D}|\boldsymbol{\varphi},\ \boldsymbol{\omega})\pi(\boldsymbol{\varphi})\pi(\boldsymbol{\omega}) d\boldsymbol{\varphi}\mathbf{d}\boldsymbol{\omega}} \tag{9}$$

where $\pi(\cdot)$ is the prior distribution.

Directly solving Eq. (9) is difficult due to the high-dimensional integration. Several methods have been developed to approximate the posterior distributions given by Eq. (9), such as Markov Chain Monte Carlo (MCMC) [31] and Particle Filter (PF) [32]. In these methods, the posterior samples are generated for $\boldsymbol{\varphi}$ and $\boldsymbol{\omega}$ based on the following proportional relationship

$$p(\boldsymbol{\varphi}, \boldsymbol{\omega}|\mathbf{D}) \propto L(\mathbf{D}|\boldsymbol{\varphi}, \boldsymbol{\omega})\pi(\boldsymbol{\varphi})\pi(\boldsymbol{\omega}) \tag{10}$$

We now use a simple example to illustrate the Bayesian updating technique for the above discussed ARMA model. Figure 4a shows 500 data points collected from an underlying time series model $Y(t_i) = 0.8231Y(t_{i-1}) - 0.1256Y(t_{i-2}) + 0.0812Y(t_{i-3}) + N(0,\ 2^2)$. Figure 4b–d present the prior and posterior distributions of the estimated coefficients given observations shown in Fig. 4a. Figure 4e gives the samples of φ_1 and φ_2 generated from MCMC, indicating that φ_1 and φ_2 are correlated.

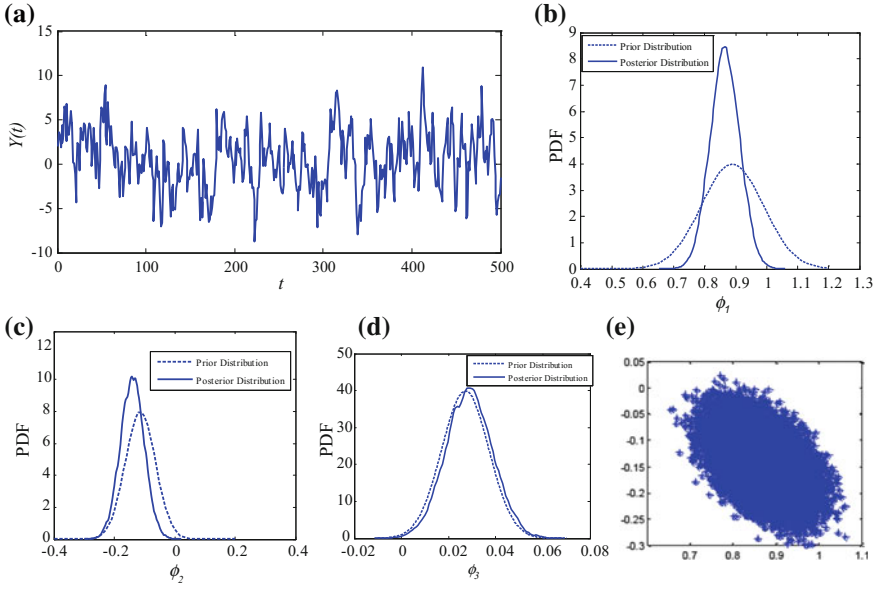

Fig. 4 Illustration of Bayesian updating of a time series model

(b) Distribution type and parameter uncertainty

When there is uncertainty in both distribution type and distribution parameters, the posterior distributions of the *i*th distribution and its associated parameters can also be obtained using the Bayes' theorem as [33]

$$f(\theta_i,\ M_i|\mathbf{D}) = \frac{P(\mathbf{D}|\theta_i,\ M_i)f(\theta_i|M_i)P(M_i)}{\sum_{j=1}^{m} P(M_j)\int_{\theta} P(\mathbf{D}|\theta_j,\ M_j)f(\theta_j|M_j)d\theta_j} \propto P(\mathbf{D}|\theta_i,\ M_i)f(\theta_i|M_i)P(M_i) \tag{11}$$

where M_i is the *i*th distribution type, θ_i is the vector of parameters of the *i*th distribution type, $f(\theta_i|M_i)$ is the probability that the parameters of the *i*th distribution type is θ_i, and m is the total number of distribution types.

If there are N competing distributions, the probability density function (PDF) $f_D(d)$ can be expressed as a weighted sum of the densities of the competing distributions using Bayesian model averaging [34] as

$$f_D(d) = \sum_{i=1}^{N} w_i f(d|\theta_i,\ M_i) \tag{12}$$

where w_i is the weight of the *i*th competing distribution, which can be obtained through Eq. (11) or through the likelihood ratio of competing distributions (known as Bayes factor) [34].

Epistemic uncertainty regarding models inputs and parameters can also be modeled using evidence theory [35], likelihood-based nonparametric method [36], and interval variables [37] depending on the degree of uncertainty in the collected data. For example, we may only know that the peak pressure of the shockwave is within a certain range. In that case, we can describe the uncertainty in the peak pressure as an interval variable.

The aforementioned methods focus on how to deal with aleatory uncertainty, and epistemic uncertainty due to data uncertainty. The handling of model uncertainty is more complicated than that of data uncertainty. In the subsequent section, we introduce the modeling of various sources of model uncertainty.

3.2.3 Modeling of Model Uncertainty

(a) Model form error and model parameter uncertainty

Model discrepancy or model form error comes from the assumptions and simplifications made in various simulation models. Some examples are: the assumption made in Taylor's blast load model and the simplification of fluid–structure interaction during the structural analysis. If there is only model discrepancy or model form uncertainty, the model discrepancy can be quantified by comparing the difference between the simulation model and experiment at different input settings.

However, often model parameter uncertainty and model discrepancy are present simultaneously in the simulation model. The two sources are coupled, making it difficult to quantify them together. A two-step approach for dealing with this challenge was proposed by Kennedy and O'Hagan (KOH) [38]. In this approach, the model discrepancy term is modeled in terms of only the input variables, through a Gaussian process model. The hyperparameters of the Gaussian process model are first estimated based on the maximum likelihood estimation (MLE) approach using the prior information of the unknown model parameters. In the next step, the unknown physics model parameters are estimated using Bayesian calibration, using the hyperparameters of the discrepancy term estimated in the first step. More details of the KOH framework are available in Ref. [38].

(b) Model verification

Model verification is the process of checking how close the code output is the true solution of the mathematical modeling of the physics [39]. In the verification process, the solution approximation errors such as discretization error and model approximation error need to be quantified. One of the commonly used methods for quantifying the discretization error is Richardson extrapolation [40, 41]. For a given input setting $\mathbf{x}$, the discretization error in the output $y_s(\mathbf{x})$ of an FEA simulation with mesh size h_1 can be quantified based on two more FEA simulations with finer mesh sizes h_2 and h_3 as [40, 41]

$$\varepsilon_{FEA}(\mathbf{x}) = \left[y_s^{(1)}(\mathbf{x}) - y_s^{(2)}(\mathbf{x})\right] / \left(r_{mesh}^{p_c} - 1\right), \tag{13}$$

where $y_s^{(k)}(\mathbf{x})$ is the result of FEA simulation with inputs $\mathbf{x}$ and mesh size h_k, $r_{mesh} = h_2/h_1 = h_3/h_2$ is the mesh refinement ratio, and the convergence p_c is estimated as $p_c = \ln[(y_s^{(3)}(\mathbf{x}) - y_s^{(2)}(\mathbf{x}))/(y_s^{(2)}(\mathbf{x}) - y_s^{(1)}(\mathbf{x}))]/\ln r_{mesh}$.

There are also other sources of uncertainty due to solution approximation, such as the errors due to reduced order and surrogate models in the analysis. Since the composite structural dynamics analysis model may be computationally expensive, surrogate models are often needed to substitute these simulation models since multiple runs are needed for UQ analyses. Due to the limited number of training points, in addition to bias error, we will also have uncertainty in the surrogate model prediction at untrained input settings. Quantification of the surrogate model uncertainty will be discussed in detail in the following section.

3.3 Uncertainty Propagation to the Structural Response

The purpose of uncertainty propagation is to quantify the uncertainty in the output quantities of interest such as the maximum displacement of the composite structure under blast loads, by aggregating the effects of all the uncertainty sources described in the last section. One of the biggest challenges during this process is how to

reduce the required computational effort since the structural analysis of the composite structure is usually computationally expensive. The commonly used techniques, such as surrogate modeling, dimension reduction, and multilevel uncertainty propagation, are briefly introduced in this section.

3.3.1 Surrogate Modeling for Uncertainty Propagation

There are two types of uncertainty propagation activities in the UQ of a single model: *local UQ* and *global UQ*. In local UQ, we are interested in a small range of the input/output, whereas, in global UQ, we are interested in the entire domain of the input/output. Reliability analysis, which quantifies the probability that an output quantity of interest is larger than a certain threshold, belongs to local UQ. Analyzing the statistical properties such as mean, standard deviation, and other moments falls into global UQ. Both local UQ and global UQ can be performed using Monte Carlo simulation (MCS). However, basic MCS is computationally expensive for most computer simulation models (e.g., marine structure fluid–structure interaction analysis). Therefore, often an inexpensive surrogate model is built and used as a substitute for the original simulation model. The widely used surrogate models in UQ studies include Gaussian process model (Kriging model) [42], polynomial chaos expansion (PCE) [43], support vector machine (SVM) [44], and neural networks. Here, we briefly introduce the Kriging model and PCE.

(a) Kriging surrogate modeling

A Kriging model approximates the response of a simulation model by assuming the approximated response as a Gaussian stochastic process [45, 46]. The Kriging surrogate of a simulation model $g(\mathbf{x})$ is given by [45]

$$\hat{g}(\mathbf{x}) = \mathbf{h}(\mathbf{x})^T \mathbf{v} + \varepsilon(\mathbf{x}) \tag{14}$$

where $\mathbf{d}$ is the vector of input variables, $\mathbf{v} = [v_1,\ v_2,\ \ldots,\ v_p]^T$ is a vector of unknown coefficients, $\mathbf{h}(\mathbf{x}) = [h_1(\mathbf{x}),\ h_2(\mathbf{x}),\ \ldots,\ h_p(\mathbf{x})]^T$ is a vector of regression functions, $\mathbf{h}(\mathbf{x})^T\mathbf{v}$ is the trend of prediction, and $\varepsilon(\mathbf{x})$ is usually assumed to be a Gaussian process with zero mean and covariance $Cov(\varepsilon(\mathbf{x}_i),\ \varepsilon(\mathbf{x}_j))$ given by

$$Cov(\varepsilon(\mathbf{x}_i),\ \varepsilon(\mathbf{x}_j)) = \sigma_\varepsilon^2 R(\mathbf{x}_i,\ \mathbf{x}_j) \tag{15}$$

in which σ_ε^2 is the process variance and $R(\mathbf{x}_i,\ \mathbf{x}_j)$ is the correlation function.

For a new point $\mathbf{x}$, the prediction of the Kriging model follows a Gaussian distribution with the mean and variance of the prediction given by

$$\hat{g}(\mathbf{x}) = \mathbf{h}(\mathbf{x})^T \mathbf{v} + \mathbf{r}(\mathbf{x})^T \mathbf{R}^{-1}(\mathbf{g} - \mathbf{H}\mathbf{v}) \tag{16}$$

$$MSE(\mathbf{x}) = \sigma_\varepsilon^2\{1 - \mathbf{r}(\mathbf{x})^T\mathbf{R}^{-1}\mathbf{r}(\mathbf{x}) + [\mathbf{H}^T\mathbf{R}^{-1}\mathbf{r}(\mathbf{x}) - \mathbf{h}(\mathbf{x})]^T(\mathbf{H}^T\mathbf{R}^{-1}\mathbf{H})^{-1}[\mathbf{H}^T\mathbf{R}^{-1}\mathbf{r}(\mathbf{x}) - \mathbf{h}(\mathbf{x})]\} \tag{17}$$

where $\mathbf{r}(\mathbf{x}) = [R(\mathbf{x},\ \mathbf{x}_1),\ R(\mathbf{x},\ \mathbf{x}_2),\ \ldots,\ R(\mathbf{x},\ \mathbf{x}_{n_s})]$, $\mathbf{d}_i$ is the ith training point, n_s is the number of training points, $\mathbf{R}$ is the correlation function evaluated at the training points, $\mathbf{H}$ is the regression function $\mathbf{h}(\mathbf{x})$ evaluated at the training points.

The hyperparameters of the Kriging model, which include unknown coefficients υ, σ_ε^2, and parameters of $R(\mathbf{x}_i,\ \mathbf{x}_j)$ can be estimated using maximum likelihood, least squares, or Bayesian estimation. More details about Kriging can be found in [45, 46], and a Kriging toolbox is available in both Python and MATLAB [47]. Advanced Kriging surrogate modeling methods have also been proposed to effectively perform local UQ [48, 49].

(b) Polynomial chaos expansion (PCE)

The PCE surrogate modeling method uses a polynomial orthogonal basis to approximate a simulation model. The PCE surrogate model is given by [43]

$$\hat{g}(\xi) = \sum_{j=0}^{n_b} \omega_j \Psi_j(\xi) \tag{18}$$

where $\Psi_j(\xi)$ is the ith orthogonal basis function, ω_j is the coefficient of the ith orthogonal basis function, and ω_j is the number of basis functions used. For different input distributions, different basis functions should be used. (For example, Hermite polynomials are used for the basis when the inputs are Gaussian). The orthogonal basis functions have the following property

$$\int \Psi_j(\xi)\Psi_k(\xi)\rho(\xi)d\xi = \delta_{j,k} \tag{19}$$

where $\delta_{j,k}$ is Kronecker delta and $\rho(\xi)$ is PDF of random variables.

The coefficients of the PCE model are solved using the following equation [43]

$$\omega_k = \frac{\langle g,\ \Psi_k\rangle}{\langle \Psi_k,\ \Psi_k\rangle} = \frac{1}{\int \Psi_k^2(\xi)\rho(\xi)d\xi}\int g(\xi)\Psi_k(\xi)\rho(\xi)d\xi \tag{20}$$

The above equation shows that the estimating the coefficients ω_k, $k = 1,\ 2,\ \ldots,\ n_b$ is basically solving the integration given in Eq. (20). Since the simulation model $g(\xi)$ is involved in the integration, tensor grid, and sparse grid approaches have been investigated to solve the integration [50]. Equation (20) has also been formulated into an optimization problem to minimize the overall regression error by estimating the coefficients using compressive sensing or least

squares [51]. Due to the orthogonal properties of the basis functions, the mean and standard deviation of the response variable can be estimated analytically.

Kriging and PCE have also been integrated to develop a PCE-Kriging surrogate modeling method in recent years [52]. For most of the current surrogate modeling methods, there exists a curse of dimensionality. When the dimension of the input variables is high, it is computationally very challenging to build surrogate models due to the need for a large number of training runs with the original simulation model. In that case, a method needs to be employed to reduce the dimension of the model.

3.3.2 Dimension Reduction

Dimension reduction aims to reduce the number of uncertainty sources considered in the UQ process since not all of the sources are important. An effective method for dimension reduction is variance-based global sensitivity analysis, which ranks the contribution of each input random variable (X) on the variance Var(Y) of an output quantity of interest (Y). Sobol' indices are commonly used in this context, which quantify the uncertainty contribution using two kinds of indices: first-order indices and total effects indices. The first-order index measures the contribution of an individual variable without considering its interactions with other variables and is given by [53]

$$S_i^I = \frac{Var_{X_i}(E_{X\sim i}(Y|X_i))}{Var(Y)} \tag{21}$$

where X_i is the ith input variable, $X_{\sim i}$ is the vector of variables excluding variable X_i, $Var(Y)$ is the variance of the quantity of interest (Y), and $E_{X\sim i}(Y|X_i)$ is the expectation by freezing X_i.

The total index measures the contribution of an individual variable including its interactions with all other variables. The total effect index is given by

$$S_i^T = 1 - \frac{E_{X_{\sim i}}(Var_{X_i}(Y|X_{\sim i}))}{Var(Y)} \tag{22}$$

Based on the results of GSA, the less important random variables can be fixed at certain specific values (usually nominal or mean values) without considering their variability. In addition, as discussed in Sect. 3.1, both aleatory and epistemic uncertainty sources are present in the structural analysis of the marine composite structure. The aleatory and epistemic uncertainty sources are usually coupled together. To perform GSA for models with both aleatory and epistemic uncertainty sources and to separately quantify the contributions of aleatory and epistemic uncertainty sources, the auxiliary variable approach presented in Ref. [54] can be employed. The auxiliary variable approach has also been extended to GSA of time-dependent problems [55]. The Kullback–Leibler divergence has also been

formulated similarly to Eqs. (21) and (22) to rank the contributions of different uncertainty sources [56].

3.3.3 UQ of the Structural Response

As mentioned in Sect. 2, the modeling of the composite structural response is a multilevel problem. The outputs of lower level models (explosive model, blast load model, and composite material model) are inputs to the upper level models (i.e., structural dynamic response analysis model). In order to propagate uncertainty from blast load model and composite material model to the quantities of interest at the top level, such as the maximum displacement or damage metric quantification of the composite structure, multilevel UQ methods are required.

As a flexible tool for the modeling of the multivariate joint probability density, Bayesian networks (BNs) can play a vital role in the multilevel UQ. BNs express the joint probability density of n random variables $X_1, X_2, \ldots, X_n$ in terms of conditional probabilities as below [27]

$$P(\mathbf{X}) = P(X_1, X_2, \ldots, X_n) = \prod_{i=1}^{n} P(X_i|\pi_i) \tag{23}$$

where π_i is the set of parent nodes of the node X_i and $P(X_i|\pi_i)$ is the conditional probability density function of the node X_i for a given realization of its parents. The nodes without parent nodes are called root nodes, such as blast load model parameters including peak pressure, time constant, and others. The probability density functions of the root nodes are obtained from the uncertainty sources modeling discussed in Sect. 3.2.

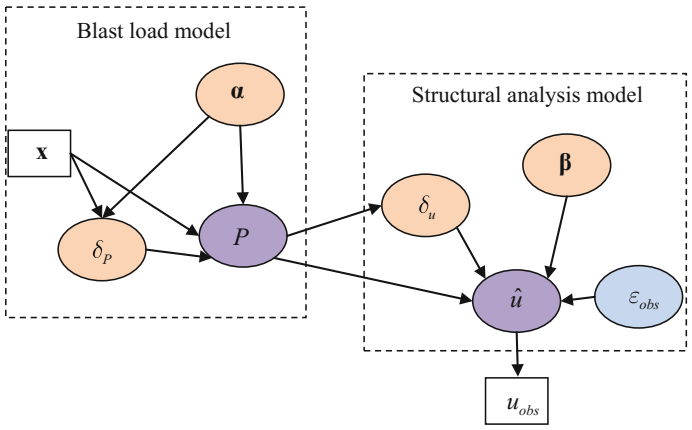

Fig. 5 Schematic Bayesian network of composite structural analysis at a time instant

Based on the definitions given in Sect. 2, we provide a schematic Bayesian network in Fig. 5 for the composite structural analysis at a time instant. When multiple time instants are considered, the Dynamic Bayesian network (DBN) method discussed in Ref. [57] needs to be employed.

There are several benefits of using BN for the UQ: (1) BN can effectively connect various simulation models and mathematical models to facilitate the UQ of the final structural response; (2) BN can also connect simulation models with models established from experiments and expert opinion to perform the UQ; (3) Heterogeneous sources of information can be aggregated through BNs to quantify the uncertainty in the quantity of interest; and (4) BN can facilitate the inverse problem of model calibration and uncertainty management to reduce the uncertainty in the structural response prediction. Next, we will discuss how to validate the model prediction after uncertainty propagation, before the model is applied for design optimization.

3.3.4 Model Validation of the Structural Response

Model validation is the process of determining the degree to which a model is an accurate representation of the real world from the perspective of the intended use of the model [58, 59]. Before applying the uncertainty quantification model of the composite structural response to the design optimization of the composite structure, the models need to validated to ensure that the models represent the actual physics. Model validation can be performed qualitatively or quantitatively. Graphical validation methods (i.e., plots comparing prediction and observation) describe the agreement visually, while quantitative methods (using a validation metric) numerically characterize the degree of agreement [60]. Commonly studied quantitative validation metrics include mean-based methods [61, 62], hypothesis testing-based methods [60], area metric [63], and distance or reliability metric [59, 64]. A detailed review of different validation metrics can be found in Ref. [59].

Since the response of the composite structure subjected to blast loads is a dynamic response, there are also several methods available to validation the dynamic response. For example, McFarland and Mahadevan [65] used the maximum absolute acceleration over the time series as the feature for model validation. Some researchers recognized the pattern of time series for model validation using statistical classification [66], autoregressive models [67, 68], neural networks [69, 70], etc. Numerous types of transformation have been explored for feature extraction in the frequency domain to facilitate the validation. Principal components analysis (PCA) [71], Karhunen–Loève (KL) expansion [20], and wavelet packet decomposition [72] have been applied to compute the features for validation assessment. Other transformation methods (e.g., Fourier transform, Fisher criterion minimization, divergence analysis, and wavelet–based methods) [73, 74] which are commonly used for damage detection in structural health monitoring can also be extended to model validation. To capture the features of a time series signal in both time and frequency domain, Jiang and Mahadevan [75] developed a wavelet

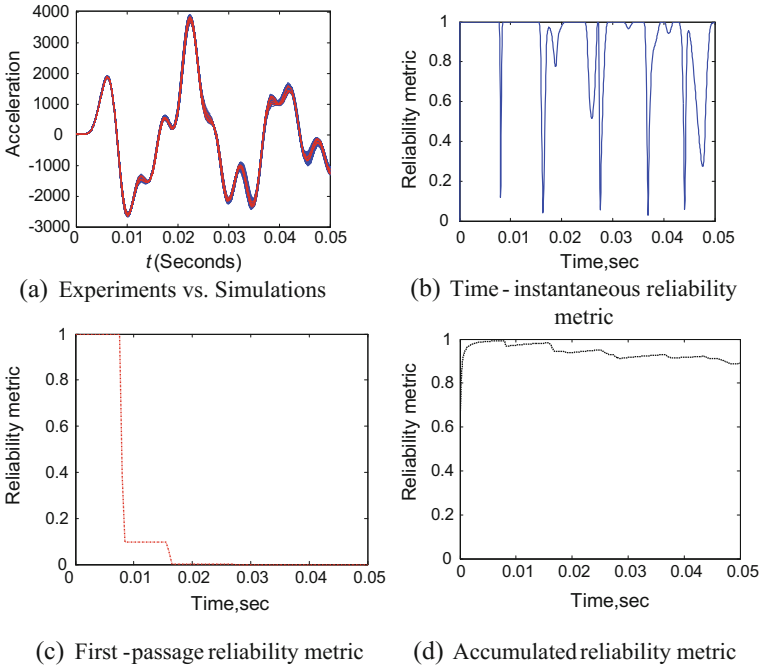

(a) Experiments vs. Simulations (b) Time - instantaneous reliability metric

(c) First -passage reliability metric (d) Accumulated reliability metric

Fig. 6 Illustration of a dynamic response and the associated validation results [76]

spectrum analysis approach. In addition, three new model validation metrics, namely time-instantaneous reliability metric, first-passage reliability metric, and accumulated reliability metric, have been recently developed for time-domain comparison based on the concept of reliability metric [76]. These three reliability metrics are able to quantify the validity of the dynamic model from three different perspectives. For a dynamic response shown in Fig. 6a, where "red" curves are the experimental observations and "blue" curves are the uncertainty realizations of the response obtained from uncertainty quantification, the validation results from the three validation metrics are given in Fig. 6b–d. The decision maker can choose the validation metric based on their interest and requirement of the model.

3.3.5 Uncertainty Aggregation

The UQ process consists of model calibration, verification, validation, and forward uncertainty propagation. The results of these different activities need to be aggregated to quantify the overall uncertainty in the prediction quantity of interest (QoI). An uncertainty aggregation method [39] has been recently developed for this purpose. Figure 7 gives an overview of the uncertainty aggregation procedure. As indicated in the figure, there are mainly four modules, namely surrogate modeling

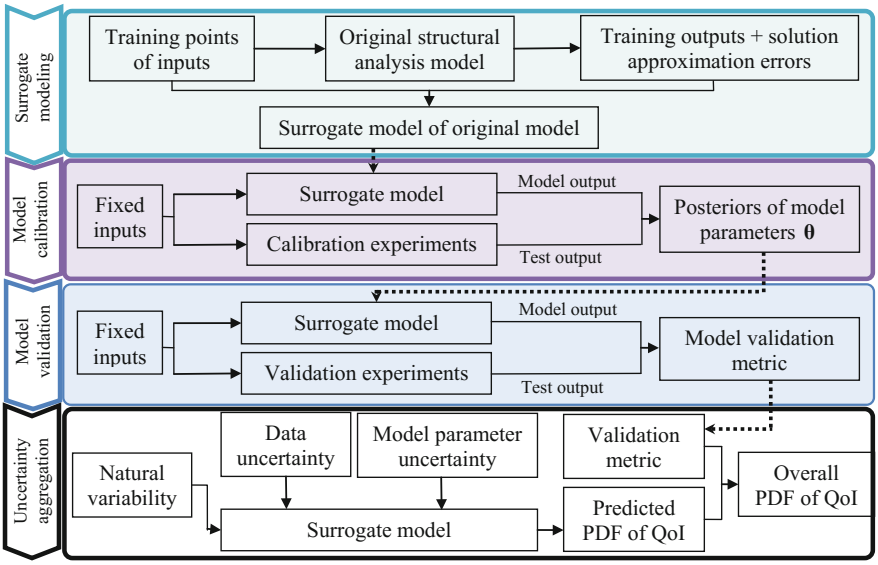

Fig. 7 Overview of the procedure of uncertainty aggregation

(Sects. 3.3.1–3.3.3), model calibration (Sect. 3.2.3), model validation (Sect. 3.3.4), and uncertainty aggregation. In the uncertainty aggregation module, various sources of uncertainty are aggregated into the distribution of QoI (e.g., deformation u defined in Sect. 2.2) first. After that, the model validation metric is combined with the distribution of QoI based on the uncertainty aggregation method, to quantify the overall uncertainty in the prediction QoI. More details about the uncertainty aggregation method can be found in Ref. [39].

3.4 Uncertainty Management in Blast Response Modeling

This section will focus on the third element of the UQ/UM framework. The topics related to uncertainty reduction and design optimization under uncertainty will be covered.

3.4.1 Resource Allocation for Uncertainty Reduction

As discussed in Sect. 3.1, among the two types of uncertainty, aleatory uncertainty is irreducible while epistemic uncertainty is reducible. For different types of epistemic uncertainty, the methods of uncertainty reduction are different. For instance, the epistemic uncertainty in the model parameters can be reduced by collecting more experimental data; and the epistemic uncertainty in the model can be reduced

by model refinement, (such as adding more training points to reduce the surrogate model uncertainty, using finer mesh to reduce the numerical error, and using advanced higher order modeling to reduce model form error).

In reality, we are usually limited by the available resources (computational and experimental). Given the limited resources, how to effectively reduce the epistemic uncertainty is an important ongoing research issue. It is also an important topic for uncertainty reduction in the composite structural response analysis subjected to blast loads. To achieve this purpose, the following research directions need be pursued.

- *Experimental design for model calibration*: Bayesian calibration represents the epistemic uncertainty in parameters and variables based on prior information and observation data collected from experiments. To maximize the information gain (reduction in the epistemic uncertainty), the experiment input settings need to be optimized [77–79].
- *Adaptive surrogate modeling*: Physics simulation models are usually computationally expensive. To reduce the epistemic uncertainty (bias and variance) introduced by the surrogate model, we need to adaptively determine the optimal input settings for computer simulations and thus maximize the information we obtain from the simulation model for training the surrogate model [48, 49].
- *Resource allocation for experiments and surrogate modeling*: Since both experiments and simulation models are expensive, given the limited computational and experimental resources, how to maximize the reduction of epistemic uncertainty and thus increase the quality of composite structural response prediction is a research topic that needs to be investigated [80, 81].
- *Experimental design for model validation*: As discussed in Sect. 3.3.4, model validation is needed to assess the credibility of the models, and the model validation data is collected through validation experiments. How to effectively collect data for validation and thus accelerate the product certification process is an important issue that needs to be addressed. In this regard, the validation experiment design methods developed in Ref. [82] can be explored for an extension to blast events model validation.
- *Resource allocation based on the integration of model calibration, verification, validation, and uncertainty quantification*: Resource allocation based on the uncertainty roll-up presented in Sect. 3.3.5 can effectively allocate resources for different activities (e.g., testing versus model refinement, or selection among multiple candidate tests) and thus reduce the uncertainty in the overall prediction of composite structural response in a systematic way.

After the uncertainty in the structural response is quantified and the epistemic uncertainty is reduced, the next issue is how to optimize the design to mitigate the effect of uncertainty on the response quantities of interest and thus satisfy the reliability and robustness requirements of the composite structure.

3.4.2 Design Optimization Under Uncertainty

Since aleatory uncertainty is irreducible, the composite structure needs to be optimized to reduce the effects of aleatory uncertainty on the variability of the quantity of interest (e.g., maximum displacement of the composite plate under blast loading). As shown in Fig. 8, the optimization under uncertainty can be pursued in two directions: reliability-based design optimization (RBDO) [83] and robust design optimization (RDO) [84]. In reliability-based design optimization, the design variables are optimized such that certain reliability constraints are satisfied. In robust design optimization, the design variables are optimized to minimize a certain quality loss function, which is a function of mean and variance of the quantity of interest.

The RBDO model is given by

$$\begin{aligned} &\min_{(\mathbf{d},\boldsymbol{\mu}_X)} f(\mathbf{d}) \\ &s.t.\ \Pr\{g_{P_i}(\mathbf{d},\mathbf{X}) \le 0\} \le [p_{fi}], i = 1,2,\ \ldots, n_p \\ &\quad g_{D_j}(\mathbf{d},\mathbf{X}) \le 0, j = 1,2,\cdots, n_d \end{aligned} \tag{24}$$

where $\mathbf{d}$ is a vector of deterministic design variables, $\boldsymbol{\mu}_X$ is a vector of mean values of the random variables $\mathbf{X}$, n_p is the number of probabilistic constraints, and n_d is the number of deterministic constraints.

The RDO model is given by

$$\begin{aligned} &\min_{(\mathbf{d},\boldsymbol{\mu}_X)} C(\mu_Z(\mathbf{d},\boldsymbol{\mu}_X), \sigma_Z(\mathbf{d},\boldsymbol{\mu}_X)) \\ &s.t. g_i(\mathbf{d},\mathbf{X}) \le 0, i = 1,2,\ \ldots, n_i \\ &\quad g_j(\mathbf{d},\mathbf{X}) = 0, j = 1,2,\ \ldots, n_e \end{aligned} \tag{25}$$

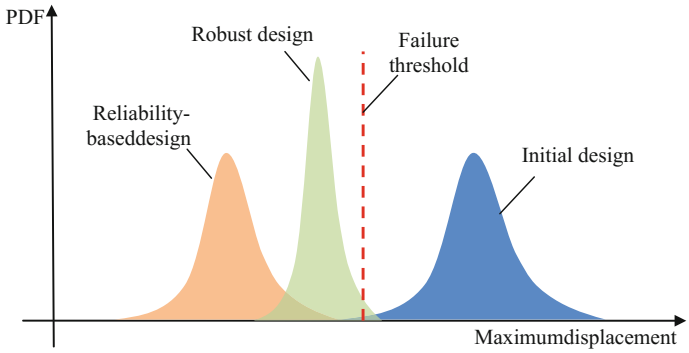

Fig. 8 Illustration of design optimization under uncertainty

in which $C(\mu_Z(\mathbf{d},\ \boldsymbol{\mu}_X),\ \sigma_Z(\mathbf{d},\ \boldsymbol{\mu}_X))$ is a quality loss function (QLF), $\mu_Z(\mathbf{d},\ \boldsymbol{\mu}_X)$ and $\sigma_Z(\mathbf{d},\ \boldsymbol{\mu}_X)$ are the mean and standard deviation of the quantify of interest, n_i is the number of inequality constraints, and n_e is the number of equality constraints. A commonly used QLF is given by

$$C(\mu_Z(\mathbf{d},\ \boldsymbol{\mu}_X),\ \sigma_Z(\mathbf{d},\ \boldsymbol{\mu}_X)) = w_1\mu_Z(\mathbf{d},\ \boldsymbol{\mu}_X) + w_2\sigma_Z(\mathbf{d},\ \boldsymbol{\mu}_X) \tag{26}$$

where $w_1 \geq 0$ and $w_2 \geq 0$ are the weights. $w_1 + w_2 = 1$.

In the RBDO and RDO models, the probabilistic constraints, the mean, and the standard deviation of the quantity of interest are obtained from the uncertainty quantification of the composite structure response as discussed in Sect. 3.3.

Until now, we have discussed details of all the three elements of the UQ/UM framework for the design of marine composite structures subjected to blast loading. Following the implementation procedure of the proposed framework, the uncertainty in the structural response prediction can be modeled, quantified, and reduced. The optimal design of the structure can then be accomplished to guarantee the reliability and robustness of the structure.

4 Conclusion

Composite/sandwich structures are being studied in marine structures to absorb the energy generated in a blast event. The structural response predicted from the structural analysis, however, varies significantly from one marine structure to another one due to the uncertainty involved in the composite material properties and blast event. Designing a highly reliable structure to withstand the blast event is an important issue that needs to be solved. To address this, a better understanding of the causes of the variation in the structural response is required. This chapter discussed the needs and opportunities in uncertainty quantification and uncertainty management of marine composite structures subjected to blast loads in order to improve their reliability. A UQ and UM framework is proposed for the composite structure in order to reduce the effects of uncertainty sources on the structural response. The UQ/UM framework encompasses three elements (uncertainty modeling, uncertainty propagation, uncertainty reduction, and design optimization) to comprehensively address the uncertainty in marine structures design.

Research needs include investigating the modeling of various sources of uncertainty in the marine structures subjected to blast loads, verification and validation of the various models used to assess composite structure performance under blast events, uncertainty quantification of the analysis models, and optimizing the marine structure to satisfy specific reliability and robustness requirements.

References

1. Altunc, A. B., Kim, J. J., Al-Haik, M., & Taha, M. M. R. (2011). Reliability-based design of blast-resistant composite laminates incorporating carbon nanotubes. *Composite Structures, 93* (8), 2042–2048.
2. Raja Sekhar, B., Gopalakrishnan, & S., Murthy, M. (2016). Wave transmission characteristics for higher-order sandwich panel with flexible core using time-domain spectral element method. *Journal of Sandwich Structures & Materials*, 1099636216664536.
3. Frostig, Y., & Baruch, M. (1996). Localized load effects in high-order bending of sandwich panels with flexible core. *Journal of Engineering Mechanics, 122*(11), 1069–1076.
4. Phan, C. N., Kardomateas, G. A., & Frostig, Y. (2013). Blast response of a sandwich beam/wide plate based on the extended high-order sandwich panel theory and comparison with elasticity. *Journal of Applied Mechanics, 80*(6), 061005.
5. Murugan, S., Harursampath, D., & Ganguli, R. (2008). Material uncertainty propagation in helicopter nonlinear aeroelastic response and vibratory analysis. *AIAA journal, 46*(9), 2332–2344.
6. Piovan, M., Ramirez, J., & Sampaio, R. (2013). Dynamics of thin-walled composite beams: Analysis of parametric uncertainties. *Composite Structures, 105,* 14–28.
7. Eamon, C. D., & Rais-Rohani, M. (2009). Integrated reliability and sizing optimization of a large composite structure. *Marine structures, 22*(2), 315–334.
8. Motley, M. R., & Young, Y. L. (2011). Influence of uncertainties on the response and reliability of self-adaptive composite rotors. *Composite Structures, 94*(1), 114–120.
9. Patel, S., Ahmad, S., & Mahajan, P. (2015). Probabilistic failure analysis of composite beams for optimum ply arrangements under ballistic impact. *Journal of Aerospace Science and Technology, 1,* 36–47.
10. Shaw, A., Sriramula, S., Gosling, P. D., & Chryssanthopoulos, M. K. (2010). A critical reliability evaluation of fibre reinforced composite materials based on probabilistic micro and macro-mechanical analysis. *Composites Part B Engineering, 41*(6), 446–453.
11. Hu, Z., Li, H., Du, X., & Chandrashekhara, K. (2013). Simulation-based time-dependent reliability analysis for composite hydrokinetic turbine blades. *Structural and Multidisciplinary Optimization, 47*(5), 765–781.
12. Chandrashekhar, M., & Ganguli, R. (2016). Damage assessment of composite plate structures with material and measurement uncertainty. *Mechanical Systems and Signal Processing, 75,* 75–93.
13. Kim, J. J., & Noh, H.-C. (2012). Design optimization of blast resistant CFRP-steel composite structure based on reliability analysis. *Journal of the Korean Society for Advanced Composite Structures, 3*(4), 10–16.
14. Zhang, S., Zhang, L., Wang, Y., Tao, J., & Chen, X. (2016). Effect of ply level thickness uncertainty on reliability of laminated composite panels. *Journal of Reinforced Plastics and Composites, 35*(19), 1387–1400.
15. Ngo, T., Mendis, P., Gupta, A., & Ramsay, J. (2007). Blast loading and blast effects on structures—An overview. *Electronic Journal of Structural Engineering, 7,* 76–91.
16. Avachat, S. (2015). Design of composite structures of blast mitigation. Doctoral dissertation, Georgia Institute of Technology.
17. Swisdak Jr, M. M. (1978). Explosion effects and properties. Part II. Explosion effects in water. DTIC Document, No. NSWC/WOL/TR-76-116, Naval Surface Weapons Center White Oak Lab Silver Spring, MD.
18. Taylor, G. (1963). The pressure and impulse of submarine explosion waves on plates. *The scientific papers of GI Taylor, 3,* 287–303.
19. Sekhar, B. R., Gopalakrishnan, S., & Murthy, M. (2017). Time domain spectral element method to study response of a sandwich beam with compliant core subjected to under water explosion. *Procedia Engineering, 173,* 1515–1522.

20. Haldar, A., & Mahadevan, S. (2000). *Probability, reliability, and statistical methods in engineering design*. New York: Wiley.
21. Sankararaman, S., Ling, Y., & Mahadevan, S. (2011). Uncertainty quantification and model validation of fatigue crack growth prediction. *Engineering Fracture Mechanics, 78*(7), 1487–1504.
22. Nelson, C. R., & Plosser, C. R. (1982). Trends and random walks in macroeconmic time series: Some evidence and implications. *Journal of monetary economics, 10*(2), 139–162.
23. Huang, S., Mahadevan, S., & Rebba, R. (2007). Collocation-based stochastic finite element analysis for random field problems. *Probabilistic Engineering Mechanics, 22*(2), 194–205.
24. Shumway, R. H., & Stoffer, D. S. (2009). *Time series analysis and its applications*. New York: Springer.
25. Hu, Z., & Mahadevan, S. (2017). Time-dependent reliability analysis using a vine-ARMA load model. *ASCE-ASME Journal of Risk and Uncertainty in Engineering Systems, Part B: Mechanical Engineering, 3*(1), 011007.
26. Devathi, H., Hu, Z., & Mahadevan, S. (2016). Snap-through buckling reliability analysis under spatiotemporal variability and epistemic uncertainty. *AIAA Journal*, 3981–3993.
27. Mahadevan, S., Zhang, R., & Smith, N. (2001). Bayesian networks for system reliability reassessment. *Structural Safety, 23*(3), 231–251.
28. Ling, Y., & Mahadevan, S. (2012). Integration of structural health monitoring and fatigue damage prognosis. *Mechanical Systems and Signal Processing, 28,* 89–104.
29. Hu, Z., Mahadevan, S., & Du, X. (2016). Uncertainty quantification of time-dependent reliability analysis in the presence of parametric uncertainty. *ASCE-ASME Journal of Risk and Uncertainty in Engineering Systems, Part B: Mechanical Engineering, 2*(3), 031005.
30. Box, G. E., Jenkins, G. M., & Reinsel, G. C. (2013). *Time series analysis: forecasting and control*. Wiley.
31. Gilks, W. R., Richardson, S., & Spiegelhalter, D. (1995). *Markov chain Monte Carlo in practice*. Washington, D.C.: CRC Press.
32. Carpenter, J., Clifford, P., & Fearnhead, P. (1999). Improved particle filter for nonlinear problems. *IEE Proceedings—Radar, Sonar and Navigation, 146*(1), 2–7.
33. Zhang, R., & Mahadevan, S. (2000). Model uncertainty and Bayesian updating in reliability-based inspection. *Structural Safety, 22*(2), 145–160.
34. Sankararaman, S., & Mahadevan, S. (2013). Distribution type uncertainty due to sparse and imprecise data. *Mechanical Systems and Signal Processing, 37*(1), 182–198.
35. Du, X. (2008). Unified uncertainty analysis by the first order reliability method. *Journal of Mechanical Design, 130*(9), 091401.
36. Sankararaman, S., & Mahadevan, S. (2011). Likelihood-based representation of epistemic uncertainty due to sparse point data and/or interval data. *Reliability Engineering & System Safety, 96*(7), 814–824.
37. Hu, Z., & Du, X. (2015). A random field approach to reliability analysis with random and interval variables. *ASCE-ASME Journal of Risk and Uncertainty in Engineering Systems, Part B: Mechanical Engineering, 1*(4), 041005.
38. Kennedy, M. C., & O'Hagan, A. (2001). Bayesian calibration of computer models. *Journal of the Royal Statistical Society: Series B (Statistical Methodology), 63*(3), 425–464.
39. Sankararaman, S., & Mahadevan, S. (2015). Integration of model verification, validation, and calibration for uncertainty quantification in engineering systems. *Reliability Engineering & System Safety, 138,* 194–209.
40. Richardson, L. F. (1911). The approximate arithmetical solution by finite differences of physical problems involving differential equations, with an application to the stresses in a masonry dam. *Philosophical Transactions of the Royal Society of London. Series A, Containing Papers of a Mathematical or Physical Character, 210,* 307–357.
41. Celik, I., & Karatekin, O. (1997). Numerical experiments on application of Richardson extrapolation with nonuniform grids. *Journal of Fluids Engineering, 119*(3), 584–590.
42. Jones, D. R., Schonlau, M., & Welch, W. J. (1998). Efficient global optimization of expensive black-box functions. *Journal of Global Optimization, 13*(4), 455–492.

43. Xiu, D., & Karniadakis, G. E. (2002). The Wiener-Askey polynomial chaos for stochastic differential equations. *SIAM Journal on Scientific Computing, 24*(2), 619–644.
44. Suykens, J. A., & Vandewalle, J. (1999). Least squares support vector machine classifiers. *Neural Processing Letters, 9*(3), 293–300.
45. Rasmussen, C. E. (2006). *Gaussian processes for machine learning*. The MIT Press, ISBN 0-262-18253-X.
46. Santner, T. J., Williams, B. J., & Notz, W. (2003). *The design and analysis of computer experiments*. Springer.
47. Lophaven, S. N., Nielsen, H. B., & Søndergaard, J. (2002). *DACE-A Matlab Kriging toolbox, version 2.0*. Lyngby, Denmark: Technical University of Denmark.
48. Bichon, B. J., Eldred, M. S., Swiler, L. P., Mahadevan, S., & McFarland, J. M. (2008). Efficient global reliability analysis for nonlinear implicit performance functions. *AIAA Journal, 46*(10), 2459–2468.
49. Hu, Z., & Mahadevan, S. (2016). Global sensitivity analysis-enhanced surrogate (GSAS) modeling for reliability analysis. *Structural and Multidisciplinary Optimization, 53*(3), 501–521.
50. Ganapathysubramanian, B., & Zabaras, N. (2007). Sparse grid collocation schemes for stochastic natural convection problems. *Journal of Computational Physics, 225*(1), 652–685.
51. Hampton, J., & Doostan, A. (2015). Compressive sampling of polynomial chaos expansions: convergence analysis and sampling strategies. *Journal of Computational Physics, 280,* 363–386.
52. Schöbi, R., Sudret, B., & Marelli, S. (2016). Rare event estimation using polynomial-chaos Kriging. *ASCE-ASME Journal of Risk and Uncertainty in Engineering Systems, Part A: Civil Engineering*, D4016002.
53. Li, C., & Mahadevan, S. (2016). An efficient modularized sample-based method to estimate the first-order Sobol′ index. *Reliability Engineering & System Safety, 153,* 110–121.
54. Sankararaman, S., & Mahadevan, S. (2013). Separating the contributions of variability and parameter uncertainty in probability distributions. *Reliability Engineering & System Safety, 112,* 187–199.
55. Li, C., & Mahadevan, S. (2016). Relative contributions of aleatory and epistemic uncertainty sources in time series prediction. *International Journal of Fatigue, 82,* 474–486.
56. Liu, H., Chen, W., & Sudjianto, A. (2006). Relative entropy based method for probabilistic sensitivity analysis in engineering design. *Journal of Mechanical Design, 128*(2), 326–336.
57. Li, C., Mahadevan, S., Ling, Y., Choze, S., & Wang, L. (2017). Dynamic Bayesian network for aircraft wing health monitoring digital twin. *AIAA Journal, 55*(3), 930–941.
58. Committee, A. S. (1998). AIAA guide for the verification and validation of computational fluid dynamics simuations (G-077-1998). AIAA.
59. Ling, Y., & Mahadevan, S. (2013). Quantitative model validation techniques: New insights. *Reliability Engineering & System Safety, 111,* 217–231.
60. Rebba, R., Mahadevan, S., & Huang, S. (2006). Validation and error estimation of computational models. *Reliability Engineering & System Safety, 91*(10), 1390–1397.
61. Kleijnen, J. P. (1995). Verification and validation of simulation models. *European Journal of Operational Research, 82*(1), 145–162.
62. Drignei, D., Mourelatos, Z. P., Kokkolaras, M., & Pandey, V. (2014). Reallocation of testing resources in validating optimal designs using local domains. *Structural and Multidisciplinary Optimization, 50*(5), 825–838.
63. Ferson, S., Oberkampf, W. L., & Ginzburg, L. (2008). Model validation and predictive capability for the thermal challenge problem. *Computer Methods in Applied Mechanics and Engineering, 197*(29), 2408–2430.
64. Rebba, R., & Mahadevan, S. (2008). Computational methods for model reliability assessment. *Reliability Engineering & System Safety, 93*(8), 1197–1207.
65. McFarland, J., & Mahadevan, S. (2008). Error and variability characterization in structural dynamics modeling. *Computer Methods in Applied Mechanics and Engineering, 197*(29), 2621–2631.

66. DeSimio, M., Miller, I., Derriso, M., Brown, K., & Baker, M. (2003). Structural health monitoring experiments with a canonical element of an aerospace vehicle. In *Proceedings of Aerospace Conference, 2003* (pp. 3105–3111). Proceedings. IEEE.
67. Sohn, H., Farrar, C. R., Hunter, N. F., & Worden, K. (2001). Structural health monitoring using statistical pattern recognition techniques. *Journal of Dynamic Systems, Measurement, and Control, 123*(4), 706–711.
68. Nichols, J., Nichols, C., Todd, M., Seaver, M., Trickey, S., & Virgin, L. (2004). Use of data-driven phase space models in assessing the strength of a bolted connection in a composite beam. *Smart Materials and Structures, 13*(2), 241.
69. Qian, Y., & Mita, A. (2008). Acceleration-based damage indicators for building structures using neural network emulators. *Structural Control and Health Monitoring, 15*(6), 901–920.
70. Sankararaman, S., & Mahadevan, S. (2013). Bayesian methodology for diagnosis uncertainty quantification and health monitoring. *Structural Control and Health Monitoring, 20*(1), 88–106.
71. Wold, S., Esbensen, K., & Geladi, P. (1987). Principal component analysis. *Chemometrics and Intelligent Laboratory Systems, 2*(1–3), 37–52.
72. Jiang, X., & Mahadevan, S. (2008). Bayesian wavelet method for multivariate model assessment of dynamic systems. *Journal of Sound and Vibration, 312*(4), 694–712.
73. Jiang, X., Mahadevan, S., & Guratzsch, R. (2009). Bayesian wavelet methodology for damage detection of thermal protection system panels. *AIAA journal, 47*(4), 942–952.
74. Guratzsch, R. F. (2007). *Sensor placement optimization under uncertainty for structural health monitoring systems of hot aerospace structures*. Citeseer.
75. Jiang, X., & Mahadevan, S. (2011). Wavelet spectrum analysis approach to model validation of dynamic systems. *Mechanical Systems and Signal Processing, 25*(2), 575–590.
76. Ao, D., Hu, Z., & Mahadevan, S. (2017). Dynamics model validation using time-domain metrics. *Journal of Verification, Validation and Uncertainty Quantification, 2*(1), 011004.
77. Hu, Z., Ao, D., & Mahadevan, S. (2017). Calibration experimental design considering field response and model uncertainty. *Computer Methods in Applied Mechanics and Engineering, 318,* 92–119.
78. Ao, D., Hu, Z., & Mahadevan, S. (2017). Design of validation experiments for life prediction models. *Reliability Engineering & System Safety, 165,* 22–33.
79. Nath, P., Hu, Z., & Mahadevan, S. (2017). Bayesian calibration of spatially varying model parameters with high-dimensional response. In *Proceedings of 19th AIAA Non-Deterministic Approaches Conference* (p. 1775).
80. Sankararaman, S., McLemore, K., Mahadevan, S., Bradford, S. C., & Peterson, L. D. (2013). Test resource allocation in hierarchical systems using Bayesian networks. *AIAA journal, 51* (3), 537–550.
81. Mullins, J., & Mahadevan, S. (2014). Variable-fidelity model selection for stochastic simulation. *Reliability Engineering & System Safety, 131,* 40–52.
82. Jiang, X., & Mahadevan, S. (2006). Bayesian cross-entropy methodology for optimal design of validation experiments. *Measurement Science and Technology, 17*(7), 1895.
83. Du, X., & Chen, W. (2004). Sequential optimization and reliability assessment method for efficient probabilistic design. *Journal of Mechanical Design, 126*(2), 225–233.
84. Zaman, K., McDonald, M., Mahadevan, S., & Green, L. (2011). Robustness-based design optimization under data uncertainty. *Structural and Multidisciplinary Optimization, 44*(2), 183–197.

Shock Interactions with Structures and Their Associated Induced Flows

K. Kontis

1 Introduction

Study of the reflection and attenuation characteristics of shock waves interacting with obstacles has always been an active area of research [4, 8]. Similarly, the presence of obstacles or multiple steps in the propagation path of a detonation wave front also leads to very interesting gas dynamics phenomena [1]. The propagation of explosive-driven blast wave on a grooved surface can result in very interesting fluid dynamics instabilities that might result in the acceleration of the flame front. From the viewpoint of safety engineering, it is essential to understand the complex propagation dynamics of explosive-driven blast waves in the presence of grooves.

Pressure waves occur frequently as unforeseen and undesired incidents leading to high loading on piping systems in industrial and nuclear power plants. These pressure waves when reflected on orifices, vessels, accumulators, closed tubes, cross-section reductions or valves may lead to considerable pressure increase [7]. Strong pressure waves after a lapse of time tend to form shock waves. These shock waves cause higher loads for short tubes compared to pressure waves of equal strength but longer extension due to their sharp front.

Attenuation of the pressure and shock waves is naturally present at the walls of the pipe system. The roughness of the wall in which a shock wave propagates is an effective way to produce pressure drop within the flow. Therefore, the natural assumption for suppressing pressure peaks is to increase the roughness or modify the walls with other types of elements. Another reason for the above methodologies to be favoured is because no obstructions are made to the cross-sectional area of the tube.

The main aim of this study is to investigate the effect of signature grooves on the propagation dynamics of shock waves and an explosive-driven micro-blast wave.

K. Kontis (✉)
Aerospace Sciences Division, University of Glasgow, Glasgow G12 8QQ, UK
e-mail: kostas.kontis@glasgow.ac.uk

S. Gopalakrishnan and Y. Rajapakse (eds.), *Blast Mitigation Strategies in Marine Composite and Sandwich Structures*, Springer Transactions in Civil and Environmental Engineering, https://doi.org/10.1007/978-981-10-7170-6_8

2 Experimental Set-up

Non-electric (NONEL) tube consists of a polymer tube with a thin explosive coating on the inner wall of the tube. The NONEL tubes have been used extensively in blasting and mining, quarrying, crew escape systems in military aircraft, ordnance systems in launch vehicles and missiles which require the highest repeatability [3, 10]. In the present study, a novel way of creating detonation inside a non-electric tube has been employed, allowing the products of detonation and the accompanying shock system to propagate over a grooved surface. Using this method, we have developed the ability to produce safe and repeatable detonation blast waves in the laboratory.

The flexible NONEL tube, with an outer diameter of 3 mm and an internal diameter of 1 mm, was inserted into an aluminium hypodermic tube with an internal diameter of 3.28 mm. This would ensure that the tube would not be loose during firing and also allow sufficient room for easy changing of the NONEL tube after each run. 0.9 m of NONEL tubing was used for each run. To initiate the detonation, a DynoStart 2 with a capacitance of 0.2 μF and the output voltage of 2500 V was used. Both DynoLine and DynoStart were manufacture by Dyno Nobel Sweden AB (now, Orica Mining Services). The DynoLine contains 16 mg/m of Octogen (HMX) and 2 mg/m of Aluminium powder.

Two different bottom walls surfaces were compared. The width of the plate was 24.8 mm. The grooves on the wall have the following dimensions 2.5 × 7.5 mm and 5 mm separations between each one. The dimensions of the grooves were scaled according to Igra et al. [2] who studied the effect of roughness on a double bend duct. The NONEL tube was placed at three different stand-off heights (h), from the bottom wall: 4, 8 and 12 mm, as shown in Fig. 1a.

A square-section shock tube consisting of a 24.8 × 24.8 mm internal cross section was used to generate shock waves for the purpose of the study. The driver (high-pressure chamber) and driven (low-pressure chamber) section lengths were 700 and 1750 mm, respectively. The high-and low-pressure chambers were separated by a diaphragm which was perforated manually with a plunger incorporated on the driver section. Three different diaphragm pressure ratios were used; P4/P1 = 4, 8 and 12, where P4 is the initial driver pressure and pressure and P1 the initial driven pressure. PMX980 polyester thin film (HiFi Industrial Film) was used as the diaphragm to separate these two components. The diaphragm thicknesses were: 23, 55 and 75 μm for P4/P1 = 4, 8 and 12, respectively. The diaphragm thickness used was the minimum that would sustain the desired pressure ratio. The driver and driven gas was air. Figure 2 shows the schematic of the shock tube. The theoretical shock wave Mach number, Ms, corresponding to each diaphragm ratio, P4/P1 was 1.34, 1.54 and 1.66, respectively. Three Kulite XT-190 transducers were mounted at 200, 645 and 1140 mm from the open end of the shock tube. The experimental incident shock Mach numbers were calculated by taking the ratio of distance and time for the shock to travel from one transducer location to the other.

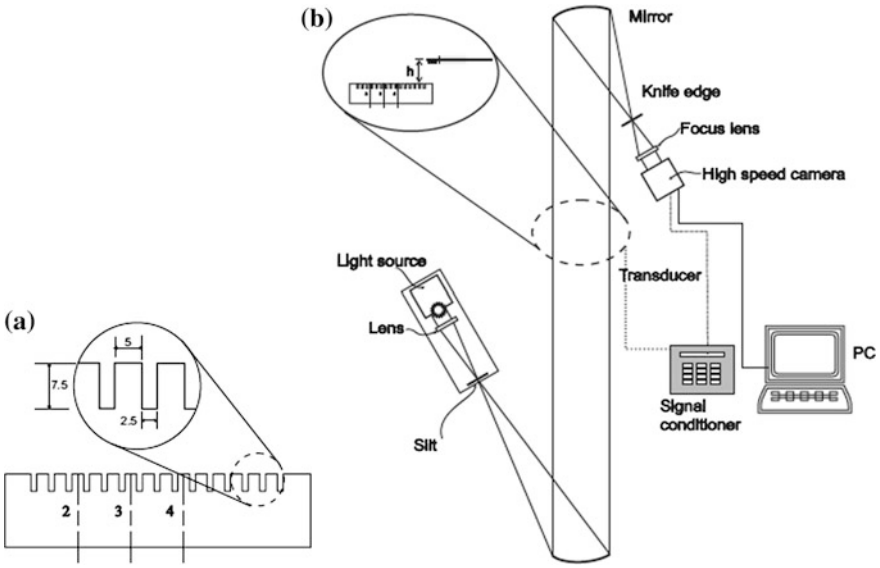

Fig. 1 **a** Dimensions of grooves; **b** Experimental set-up

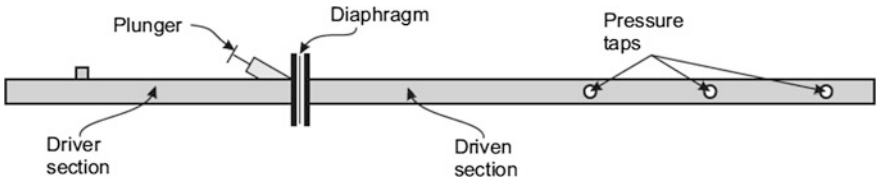

Fig. 2 Schematic of the shock tube

A test section to study the effects of shock interaction in junctions of an engine manifold, was placed at the end of the driven section. It consists of twelve interchangeable aluminium blocks which form different junctions: 0, 30, 45, 60 and 90°as shown in Fig. 3. The test section can be rotated which yields twelve configurations. Furthermore, the straight wall of the junctions can be a smooth or grooved surface. The combination of smooth walls and grooves with the bifurcations at different angles give a total of 24 configurations for testing. In the present paper, the results of the straight duct case only are discussed.

Optical quartz widows, 16 mm thick, were used on both sides of the junction to allow visualization of the flow. Kulite XT-190 pressure transducers were used to record the pressure history. The grooves on the side walls were 2.5 mm wide and 7.5 mm deep, with 5 mm separations between each one. The dimensions of the grooves were scaled based on the work of Igra et al. [2] which studied the effect of roughness on a double bend duct. Furthermore, in the straight case with no

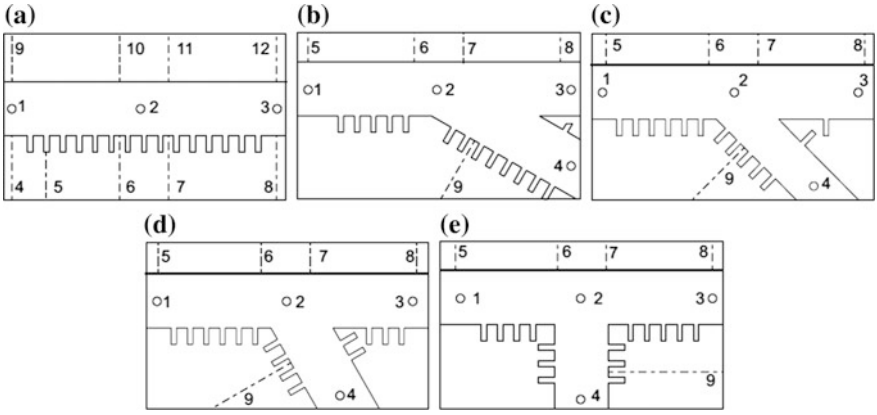

Fig. 3 Typical test section configurations **a** 0, **b** 30, **c** 45, **d** 60 and **e** 90° junctions

bifurcations, a pressure transducer was placed on the second groove. This allowed the effect of the oscillation of the transmitted shock wave inside the groove to be seen.

High-speed schlieren with an optical arrangement similar to that used by Kontis et al. [5] was employed to visualize the flow. The Shimadzu Hyper-Vision camera is capable of recording images at a frame rate of up to 1 Mfps with an exposure time of 0.50 μs. A motion picture, consisting of one hundred images with spatial resolution of 312 × 260 pixels, was produced of the flow field. Illumination for the Shimadzu camera was provided via a 300 W continuous Xenon lamp. The schematic diagram of the high-speed schlieren setup is shown in Fig. 1b.

3 Results

A. NONEL tube experiments

The combustion products decouple from the primary shock wave 20 μs after the initial detonation. The primary shock travels ahead of the products of combustion. Compression waves propagate between them, which with time coalesce to form a secondary shock front. The micro-blast wave produced by the NONEL is shown in Fig. 4.

Three stand-distances, 4, 8 and 12 mm, are used to visualize the effect of the blast wave and products of combustion with a planar and grooved surface. Figure 5 shows the schlieren results of the interaction of the blast wave with the planar surface. The time for each frame corresponds to the initial detonation of the NONEL tube in microseconds. The stand-off height, 4, 8 and 12 mm, corresponds to the first, second and third column, respectively. In the first 40 μs of the detonation, the primary shock wave has impinged on the planar surface. The detonation

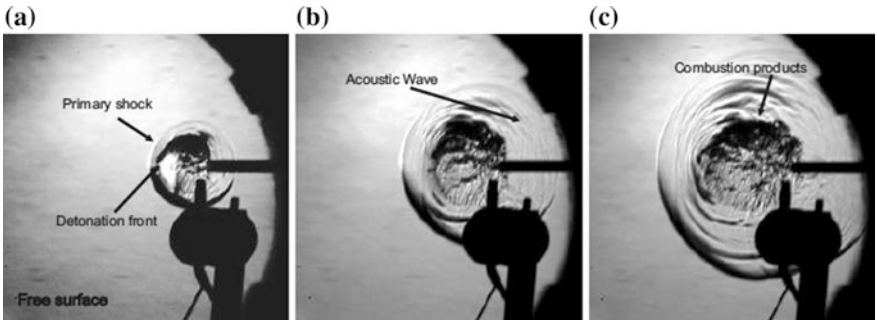

Fig. 4 Micro-blast wave free surface

front, which is close behind the primary shock wave, is deformed by its proximity. The reflection of the primary shock with the planar surface interacts with the combustion products which also influences the primary shock shape as it can seen in Fig. 5a–c.

The initial reflected shock wave at 80 μs forms Mach reflections for stand-off heights of 8 and 12 mm. The reflected shock and the contact with the planar wall lead the combustion products to 'stretch' in the case where the point source is 4 mm from the planar wall as it is shown in Fig. 5d and m. The combustion products are 'pushed' upwards for the two remaining heights. Interactions between compression waves with the products of combustion and planar surface are more prominent for h = 8 and 12 mm. In the lowest height, this reflection seems to be absorbed by the products of combustion which in turn accelerates it.

Compression waves, generated by the products of combustion, travel faster for the 4 mm and coalesce producing a weak shock wave, Fig. 5g. The radial compression waves are produced from the expansion of the combustion products which can be seen in Figs. 4 and 5i The emanating acoustic waves and reflection of the acoustic waves interact at the front of the combustion products producing an interweave pattern between the surface and the combustion products. These interactions can be seen clearly in the case of h = 12 mm. The velocity of the cloud of products of combustion are higher for the 4 mm, and slows down as the distance increases.

Secondary shock wave appears with more intensity in the case of the 4 mm stand-off height. At the bottom left of the cloud of combustion products, interaction with the reflected waves from the wall continues, increasing the temperature; visible as intense white patterns. The stand-off height affects the expansion of the combustion products. Further from the wall, the combustion products expand upwards.

The cloud of combustion products for a stand-off height of 4 mm expands near the planar wall. The secondary shock produced by the merging of acoustic waves accelerates as time elapses, for the three stand-off cases. However, this acceleration is more pronounced in the case of the highest stand-off height (h = 12 mm). As it was discussed previously, the reflection of the acoustic waves with the planar wall coalesces with the propagating acoustic waves at an earlier time for 4 and 8 mm.

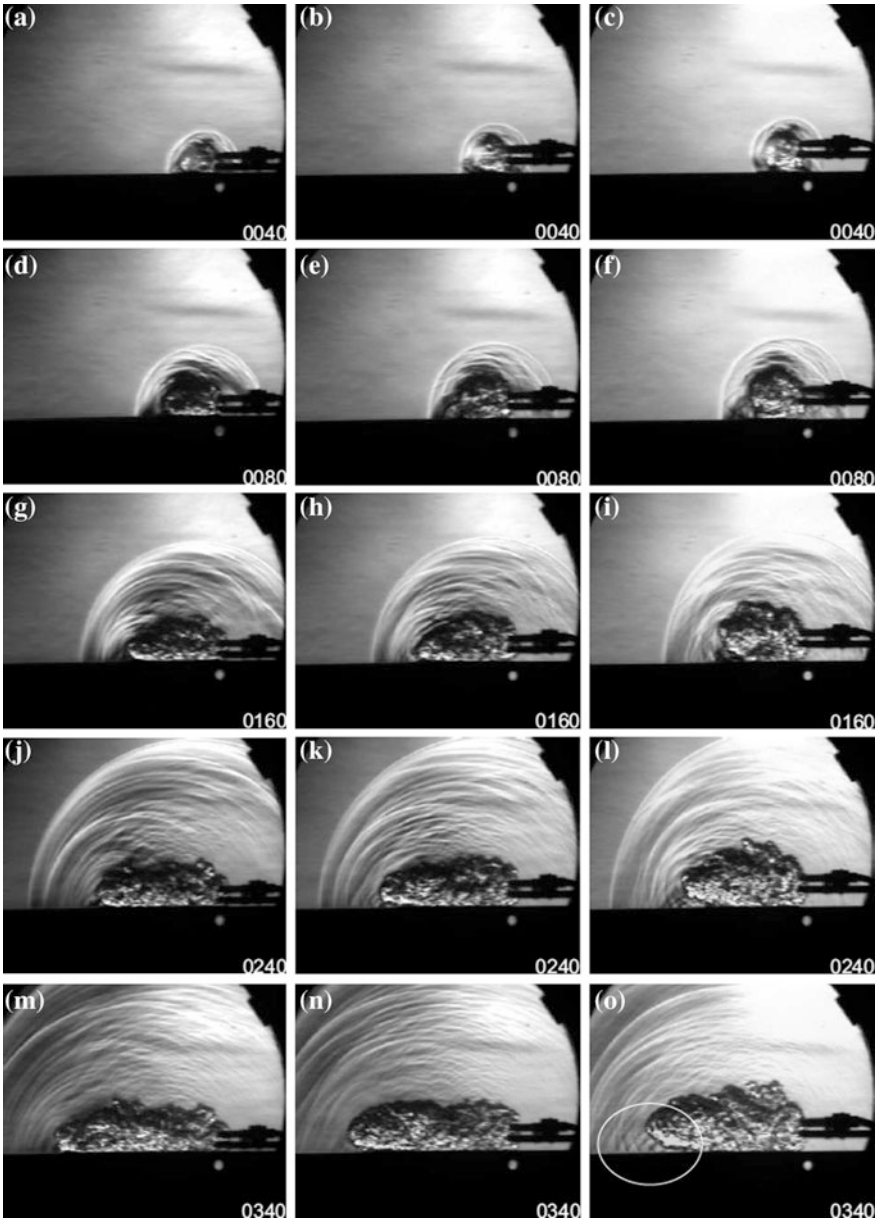

Fig. 5 Micro-blast wave propagation on planar surface for three stand-off heights 4, 8 and 12 mm

The energy release of the combustion products in the form of heat increases the speed of sound. Therefore, the velocity of the acoustic waves increases which explains the acceleration of the secondary shock. The exchange of the energy is

promoted by the distance between the combustion products and the wall. This is demonstrated in Fig. 6b where the velocities of the secondary shock wave with time are plotted for different stand-off heights. An initial deceleration of the secondary shock wave can be seen in the case of 12 mm. This is due to the expansion of the combustion products in the vertical direction, whereas for the two remaining heights, tend to propagate near to the wall. The reflection waves play an important role, as it was mentioned previously, they tend to 'push' the combustion products upwards. The bright zones near the wall, shown in Fig. 5d–f are due to the interaction of the reflected shock wave with the wall.

After 40 μs of detonation, the primary shock has decoupled from the combustion products. The primary shock has reached the bottom wall of the grooves. The primary shock wave front diffracts by the encounter with the grooves at 80 μs. Mach reflection can be seen to be generated by this interaction. The reflected waves interact with the combustion products, as with the previous case with the solid wall, these reflection 'pushes' the combustion products upwards and exchange of energy, as it can be seen in Fig. 7f (bright spots).

The continuous diffraction and reflection of the propagating primary shock wave form complicated patterns downstream. At time 160 μs, a Mach reflection can be seen formed by the acoustic waves diffracting from the primary shock wave, Fig. 7i. The secondary shock wave formed by the coalescence of the acoustic waves is stronger for the stand-off height of 4 and 12 mm as seen in Fig. 7g. The cloud of combustion products travels faster for a stand-off height of 8 mm. This is shown visually in Fig. 7 and Fig. 6c where the velocity is 314 m/s and 295.2 and 299.6 m/s for 4 and 12 mm, respectively. Compared to the planar surface, the expansion of the combustion products radially is slow as it is propagating downstream. For the 4 mm case, this expansion increased the velocity (307.9 m/s) considerably with respect to the other heights 275 and 258.1 m/s, 8 mm and 12 mm, respectively.

Figure 7j–l shows the snapshots at 240 μs after the initial detonation. Weak compression waves patterns behind the primary shock due to diffraction and reflection can be observed. The products of combustion propagation, on the other hand, have changed their shape. For 8 and 12 mm stand-off heights, the front of the combustion products has been elongated and presents a uniform height (at the exit of the NONEL tube there is still random expansion vertically caused by the exit of the combustion products). However, this uniform expansion cannot be seen for the 4 mm case. The tip of the combustion products is drawn into the grooves.

The primary shock wave produced by the detonation decreases with respect to time, is shown in Fig. 6a. In the case where the stand-off height is 12 mm with grooves, the velocity is reduced significantly compared with the other two stand-off heights, 4 and 8 mm. The combustion products decelerate from the initial detonation time. However, after some time has elapsed, the combustion products accelerate to a second peak value and then decelerate again. At the stand-off height

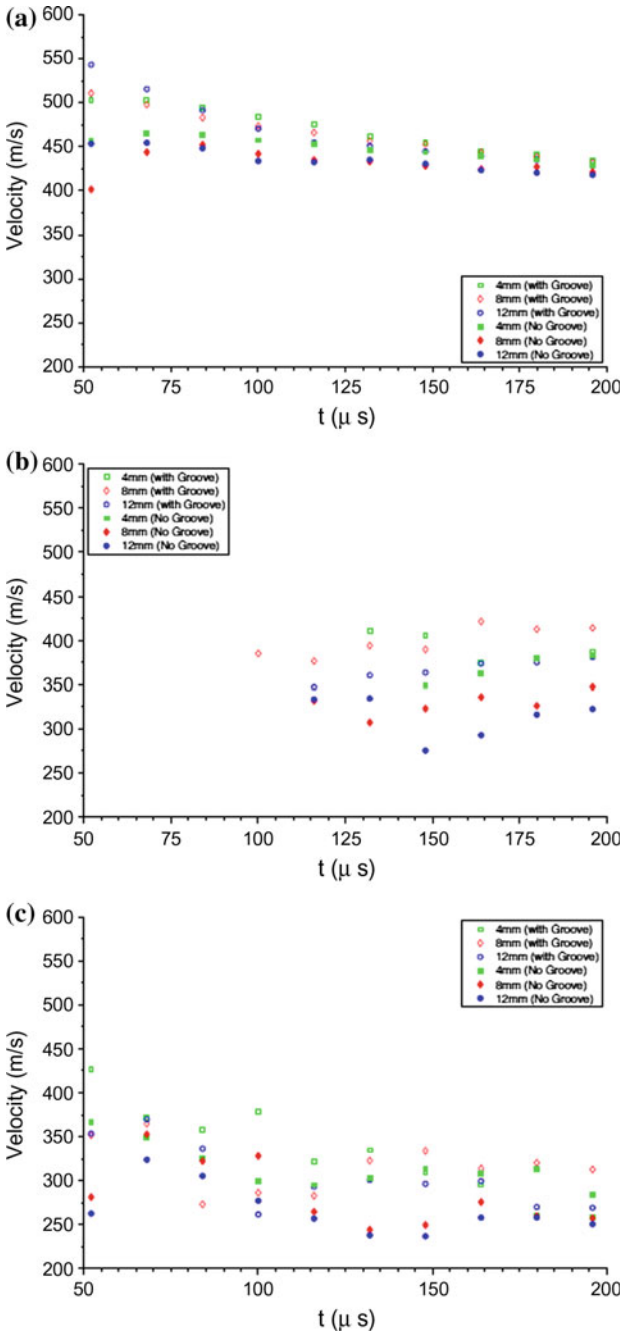

Fig. 6 Propagation velocity of the **a** primary shock wave, **b** secondary shock wave, **c** combustion products

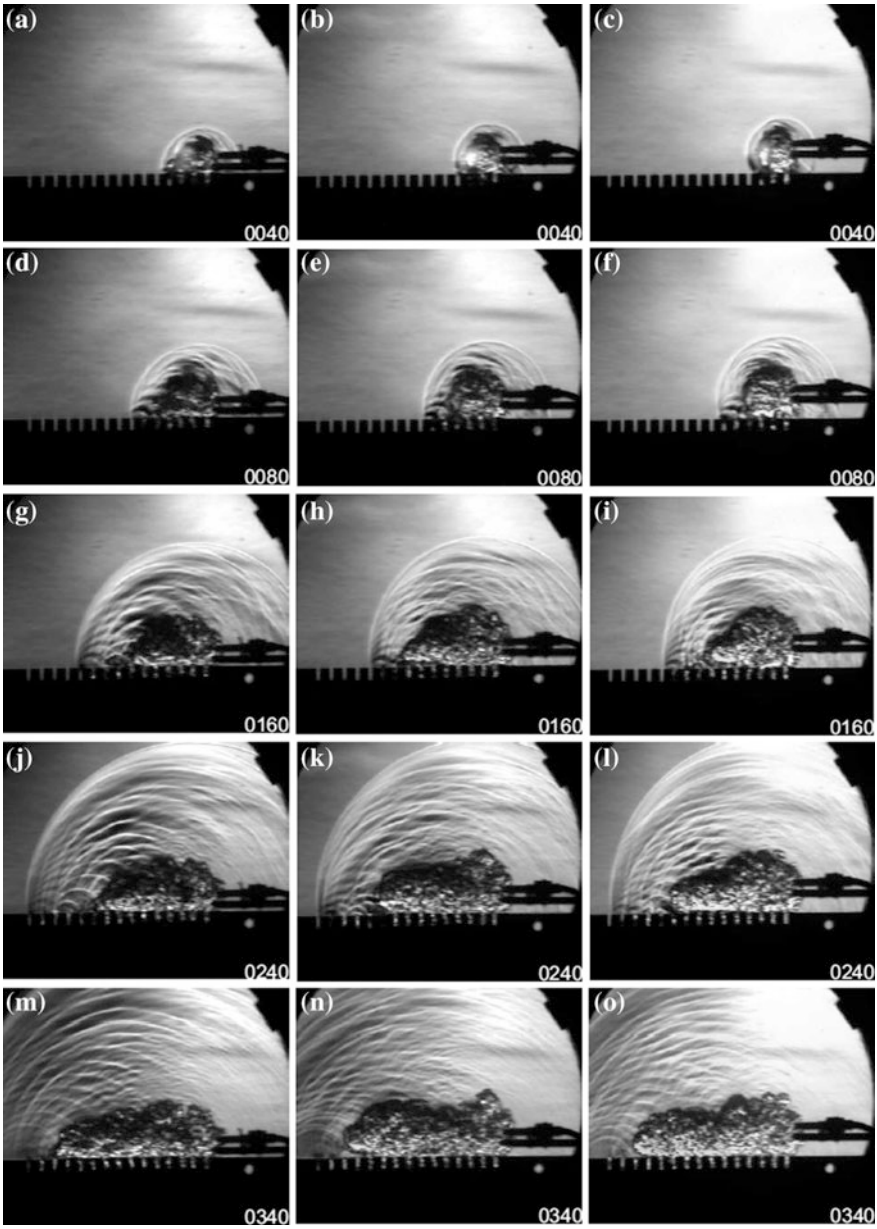

Fig. 7 Micro-blast wave propagation on grooved surface for three stand-off heights 4, 8 and 12 mm

of 8 and 12 mm with grooves, the deceleration of the combustion products tends to follow the same oscillation pattern, Fig. 6c.

B. Shock Tube Experiments

The effect of roughness in a straight duct on shock propagation was studied by incorporating grooves on either the upper and lower surface of a 2D pipe or on both surfaces. Figure 8 presents schlieren images at 60 and 220 μs with the incorporation of the grooves on both and one wall for P4/P1 = 4. The time of the schlieren images is taken with reference to the first appearance of the incident shock front on the test section. The shape of the incident shock wave when encountering the grooves is the first indication of shock attenuation in Fig. 8a: the bottom part of the shock front slows down caused by the diffraction of the shock wave with the grooves. Multiple diffracted and reflected sound waves travel upstream, by-product of the encounter of the shock front with the grooves as it propagates downstream.

At 220 μs, in Fig. 8b, the decrease of the velocity on the grooved surface of the shock front is apparent, compared to the shape of the incident shock wave with the groove–groove wall configuration in Fig. 8d. The reflected sound waves or Mach waves m, which have a cylindrical shape grow radially with time and reflect from the upper wall of the pipe. However, this does not affect the propagation of the incident shock front. The influence of Mach waves, m', which are the result of the reflected shock waves travelling inside the individual grooves is shown in Fig. 9.

The diffracted D and reflected R waves are indicated with the corresponding groove number which produces them after the incident shock wave encounter. In groove 3, the diffracted shock wave is propagating downward and R4 is reflecting of the right corner producing R'3. In the second groove, the transmitted shock

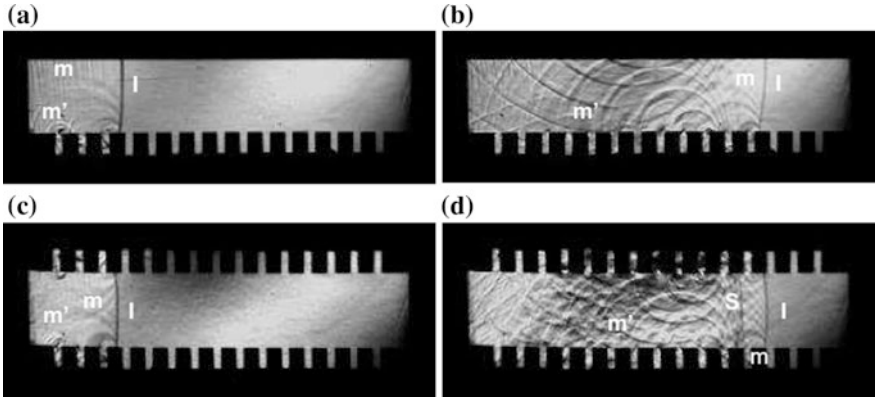

Fig. 8 Schlieren images for P4/P1 = 4 with solid and grooved wall: **a** and **b** solid-groove walla **c** and **d** groove-groove walls

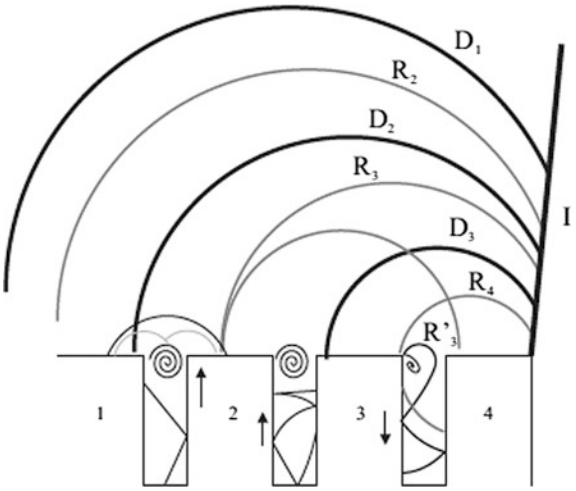

Fig. 9 Schematic of transmitted waves behaviour

waves are traveling upwards and becoming normal to the side walls of the groove. By the third groove, the transmitted shock wave has exited the groove forming a cylindrical compression wave growing radially.

According to Onodera and Takayama [9] the distance between the incident shock wave from the reflected shock waves from the grooves emerge is not time-dependent, this distance is determined by the incident shock wave Mach number Ms, the depth, and width of the groove. The remaining transmitted shock waves in the groove will exit with time, forming compression waves m', which is stronger than the reflected waves m propagating behind the incident shock wave. The intensity of the compression waves is higher than that for the reflected waves m indication of the strength. The same pattern occurs after the third groove which the incident shock wave has passed. The coalescence of the compression waves results in the formation of a normal secondary shock wave seen in Fig. 8d for groove-groove wall configuration. An oblique shock wave is formed in the case of a solid-groove wall. For diaphragm pressure ratios of 8 and 12, a similar behaviour occurs. However, the formation of the secondary shock occurs earlier in time, because they travel faster.

Figure 10 shows the propagation velocity of the incident shock wave for both cases and secondary shock wave. The velocity decreases linearly for P4/P1 = 4 and 8. The appearance of the secondary shock wave result of the coalescence of compression waves m' varies for the three shock Mach numbers. The Mach waves surpass the speed of sound and keep accelerating until it catches up with the incident shock wave, strengthening the initial shock front.

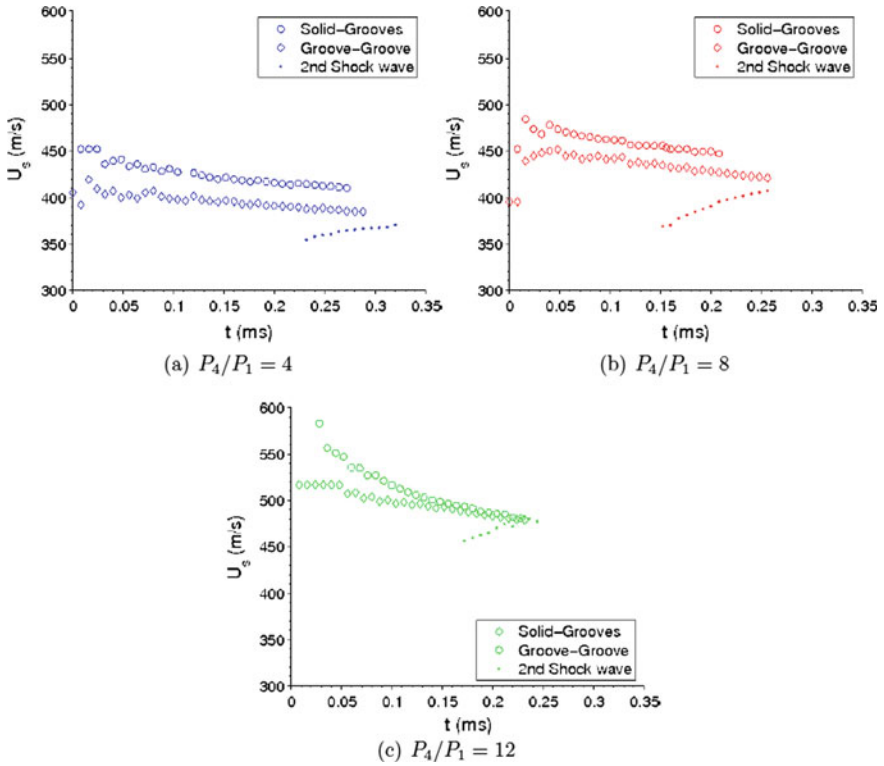

Fig. 10 Velocity plots of the propagation of the incident shock wave and second shock wave P4/P1: **a** 4, **b** 8 and **c** 12

Figure 11 shows the pressure histories for transducer location T5 at the bottom wall of the 'second' groove and T9 at the top wall. Transducer T5 indicates the accumulation of pressure on the grooves and the slow release of the stored energy for all pressure ratios. When the incident shock wave first encounters the groove, it creates a pressure peak in both the groove–groove and solid-grooved test cases. For P4/P1 = 4 case, this leads to a peak value of 2.1 bar and for cases P4/P1 = 8 and 12, peak values of 2.6 and 3.0 bar. However, in the groove-groove case, the pressure fluctuations are stronger with increasing of the pressure upstream. As the shock tube evacuates the remaining flow, the pressure fluctuations inside the grooves are still dissipating energy. The accumulation of pressure in the grooves is evident for higher pressures. From the solid-groove pressure history, the pressure fluctuation dissipates faster than that for the groove-groove case.

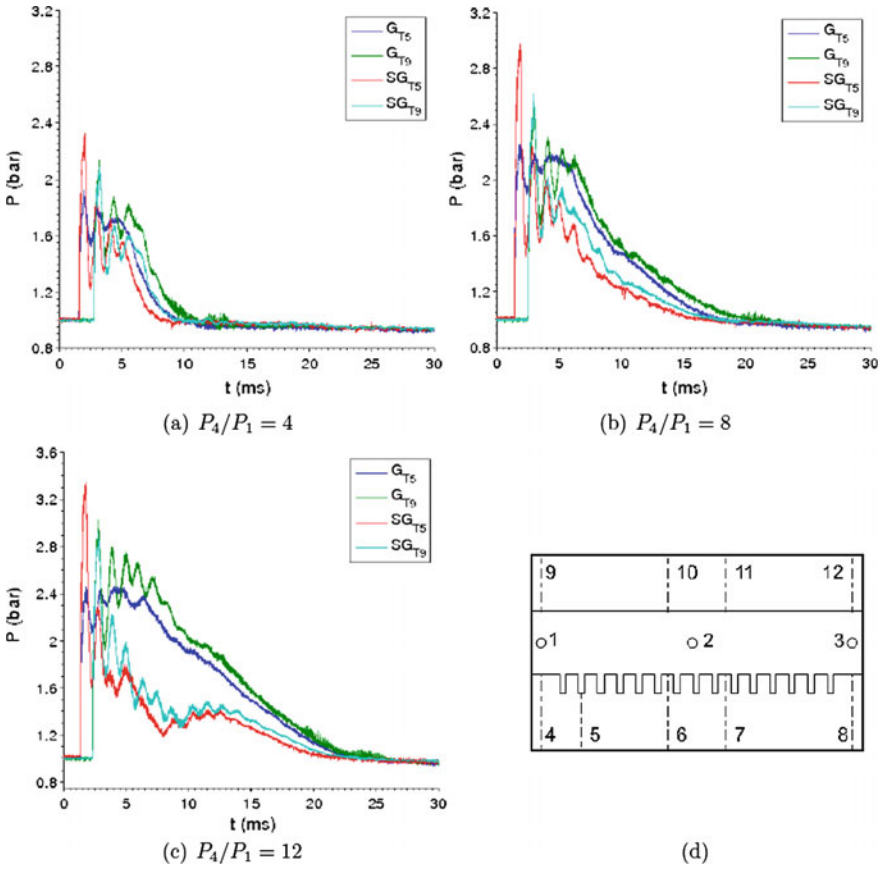

Fig. 11 Pressure history at the entrance of the test section (T9) and at the bottom wall of the groove (T5): **a** P4/P1 = 4 **b** P4/P1 = 8, and **c** P4/P1 = 12

4 Conclusions

The velocity of the primary shock wave, secondary shock wave and products of combustion are greatly influenced by the height of the detonation source to the surface and the surface geometry. The shape of the products of combustion and velocity are influenced by the grooved surface. The propagation of the combustion products for stand-off height of 8 mm with grooved walls is faster, increasing the velocity of the compression waves which coalesce with the secondary shock wave incrementing its velocity. In the case of a planar surface, the closer the source of detonation is to the wall, the influence in the flow field travelling ahead is greater due to the speeding of the combustion products which are responsible for the flow motion in the system. The influence of the wall for greater height minimizes this influence due to the expansion products in both x and y direction.

The attenuation of pressure jumps of the shock front is successfully reduced by incorporating grooves to the upper and lower wall of the duct. Multiple compression and expansion waves are produced due to the interaction of the shock front with the grooves leading to: a highly unsteady flow field, an increase in pressure at the entrance of the test section, and the coalescence of the waves to form a secondary shock wave propagating behind the shock front.

The number of grooves is varied by using two configurations: solid-groove and groove–groove walls which correspond to upper and lower wall, respectively. The multiple pressure jumps of the flow field are reduced by the capacity of the grooves to store energy momentarily. The implication of this is the slow release of the energy from the grooves, which affects the time for the pressure to settle at ambient conditions.

Acknowledgements The author is indebted to his former PhD students Dr. N. Gongora-Orozco and Dr. H. Zare-Behtash for their research contributions.

References

1. Cicarrelli, G., & Dorofeev, S. (2008). Flame acceleration and transition to detonation ducts. *Progress in Energy and Combustion Science, 34,* 499–550.
2. Igra, O., Wu, X., Falcovitz, J., Takayama, K., & Heilig, W. (1986). Experimental and theoretical study of shock wave propagation through double-bend ducts. *Journal of Fluid Mechanics, 437,* 225–282.
3. Jagadeesh, G., Onodera, O., Ogawa, T., & Takayama, K. (2001). Visualizing micro-air blasts using double exposure holographic interferometry. In: *24th International Congress on High-Speed Photography and Photonics*, *4183*.
4. Kobayashi, S., & Adachi, T. (2004). Visualization of shock wave formation processes during shock reflection at obstacles with multiple steps. *Experimental in Fluids, 36,* 297–298.
5. Kontis, K., An, R., Zare-Behtash, H., & Kounadis, D. (2008). Head-on collision of shock wave induced vortices with solid and perforated walls. *Physics of Fluids, 20*.
6. Lee, J. H. S. (2008). *The detonation phenomenon*.
7. Movahed, M. A., & Groenig, H. (1986). Pressure wave damping in branched pipes with arbitrary angles. *International Journal of Pressure Vessels and Piping, 23*(3), 215–255.
8. Ohtomo, K., Ohtani, K., & Takayama, K. (2005). Attenuation of shock waves propagating over arrayed baffle plates. *Shock Waves, 14,* 379–390.
9. Onodera, H., & Takayama, K. (1990). Interaction of a plane shock wave with slitted wedges. *Experiments in Fluids, 10*(2–3), 109–115.
10. Yang, L. C., & Do, I. H. P. (2000). Nonelectrical tube explosive transfer system. *AIAA, 38,* 2260–2267.

Dynamic Response of Syntactic Foams and Sandwich Composites: Blast and High Strain Rate Loading

Dung D. Luong, Luca Ansuini and Nikhil Gupta

1 Introduction

Foams are extensively used in weight sensitive applications. A variety of open and closed cell foams are used in marine systems. For example, closed-cell foam core sandwich structures are used in constructing ships and boats. One of the limitations of closed cell foams containing gas porosity is that the moisture can diffuse in the polymer and accumulate inside the gas pores, which can increase the effective density of the foam and result in degradation of the foam material over a long exposure period.

Some of these limitations are overcome by developing a special variety of closed cell foams, where thin-walled hollow particles are incorporated in a matrix material to create a foam-like microstructure. Existing applications of syntactic foams have been discussed in some of the available publications [1, 2]. Advantages of syntactic foams over conventional gas porosity foams include close control over the cell shape, size, and distribution. In addition, particle shell thickness and volume fraction can be controlled as two independent parameters in syntactic foams, which results in greater control over their properties. A combination of theoretical and experimental approaches has enabled methods of tailoring the properties of syntactic foams over a wide range, which is useful for the current and potential future applications of syntactic foams.

This chapter is focused on discussing the dynamic behavior of syntactic foam core materials under high strain rate compression and blast loading conditions. These loading conditions are relevant to their applications in lightweight armors and marine structures.

D. D. Luong · L. Ansuini · N. Gupta (✉)
Composite Materials and Mechanics Laboratory, Mechanical and Aerospace Engineering Department, New York University, Tandon School of Engineering, 6 MetroTech Center, Brooklyn, NY 11201, USA
e-mail: ngupta@nyu.edu

S. Gopalakrishnan and Y. Rajapakse (eds.), *Blast Mitigation Strategies in Marine Composite and Sandwich Structures*, Springer Transactions in Civil and Environmental Engineering, https://doi.org/10.1007/978-981-10-7170-6_9

2 Syntactic Foams

A solid model representation of syntactic foam microstructure is shown in Fig. 1a, where hollow particles of various wall thicknesses can be observed dispersed in a matrix material. Figure 1b and c show examples of microstructures of polymer and metal matrix syntactic foams, respectively.

In both cases, hollow particles of different size scale are randomly dispersed in a matrix material. Polymer matrix syntactic foams have been extensively studied in the available literature to understand their mechanical, thermal, and electrical properties with respect to the parameters, such as matrix modulus, and particle modulus wall thickness and volume fraction. The lessons learned from polymer matrix syntactic foams are being extended to designing metal matrix syntactic foam microstructures.

In many applications, especially in structural applications that may be subjected to bending loads, syntactic foams are used in the form of sandwich structures. An example of a metal matrix syntactic foam core sandwich is shown in Fig. 2. In the present case, a carbon fabric is used as reinforcement in the skins. This sandwich is synthesized by one-step infiltration of the particle and fabric preform, so there is no interfacial layer between core and skins. Such sandwich structures are expected to have superior performance compared to the sandwich structures that contain skins adhesively bonded with the core.

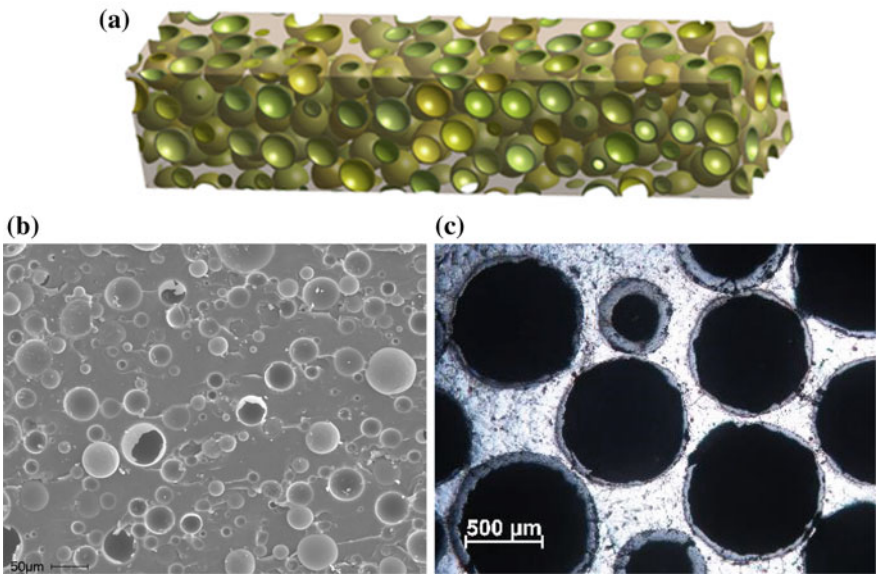

Fig. 1 **a** 3D model of syntactic foams filled hollow particles, **b** vinyl ester-glass microballoon syntactic foam, and **c** A356-SiC syntactic foam

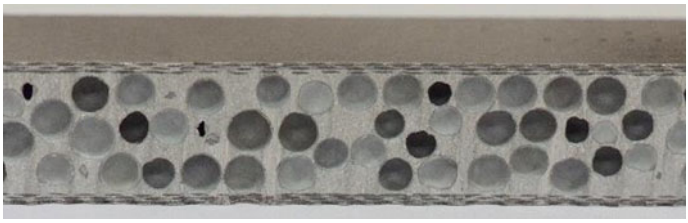

Fig. 2 A metal matrix syntactic foam core sandwich containing carbon fabric skins

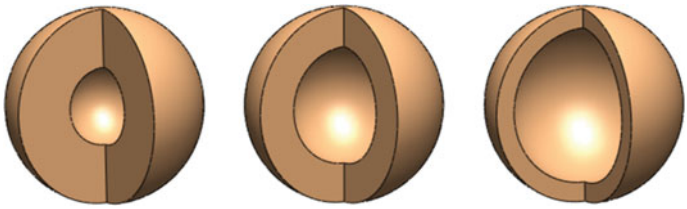

Fig. 3 Illustration of variation in wall thickness of particles of the same outer diameter. The true density of particles depends on the wall thickness

Although hollow particles of shapes such as cuboids, cylinders, and cones are available, only spherical particles have been used in synthesizing syntactic foams because spherical particles flow well in the mixture and provide isotropic properties to syntactic foams [3]. Figure 3 illustrates that particles of the same outer radius may have different wall thicknesses, which implies that the particle diameter, wall thickness, and volume fraction can be controlled independently in the syntactic foam.

Most of the available studies on polymer matrix syntactic foams have used glass particles of 1–300 μm diameter. The ratio of inner (r_i) to outer (r_o) radius of hollow particles is defined as radius ratio η. The available studies have mostly used particles of η greater than 0.85 to benefit from the low density of particles in that range. Increase in particle wall thickness increases the syntactic foam density, while a decrease in particle volume fraction increases the syntactic foam density. Studies are available that have focused on understanding the effects of these parameters on syntactic foam properties. An overview of properties of polymer and metal syntactic foams is presented in Fig. 4 and Fig. 5, respectively, where syntactic foams are grouped based on the matrix material. In most polymer syntactic foams glass microballoons (GMB) have been used as reinforcements. However, most studies on metal matrix syntactic foams have used SiC, Al_2O_3, or fly ash cenospheres as filler.

Figure 4 shows that polymer matrix syntactic foams are fabricated in the density range of 0.4–1.15 g/cm^3. It should be noted that particle wall thickness and volume fraction both can change the density of syntactic foams. In addition, fracture of particles during syntactic foam fabrication results in increased density, while entrapment of matrix porosity during mixing procedures results in a decreased

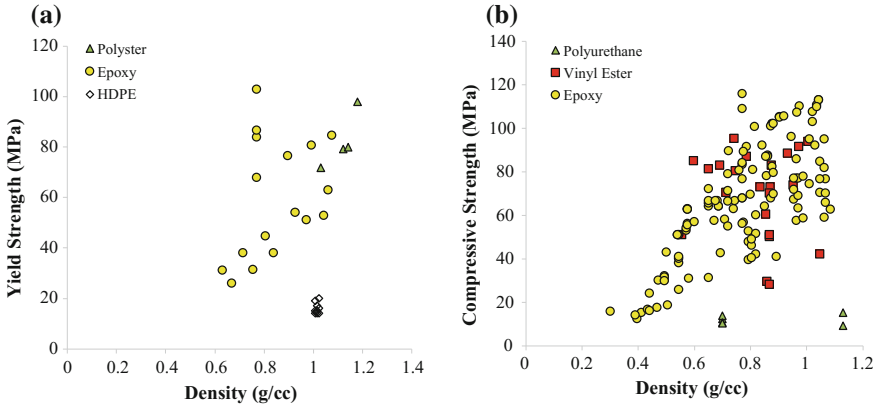

Fig. 4 **a** Yield strength (epoxy [4, 5], HDPE [6], polyester [7]), and **b** compressive strength (epoxy [4, 8–25], polyurethane [26, 27], vinyl ester [28–31]) of polymer matrix syntactic foams plotted against density

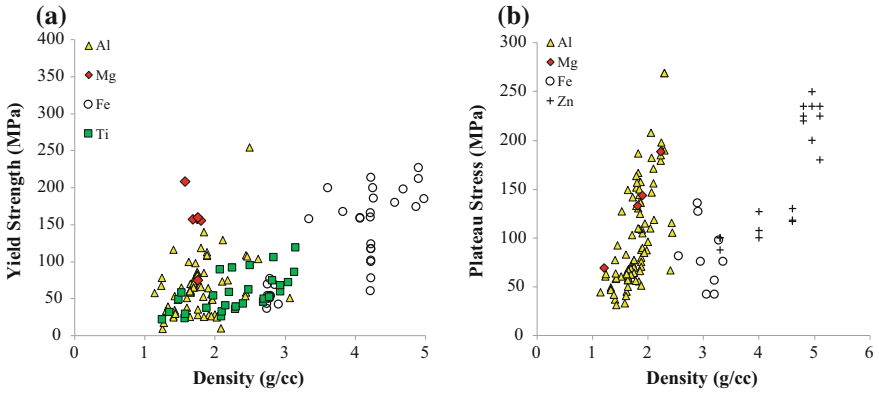

Fig. 5 **a** Yield strength (Al [32–42], Mg [43–45], iron [41, 46–55], Ti [56, 57]), **b** plateau stress (Al [34, 36, 38, 40, 42, 58–71], Mg [70, 72], iron [46, 71], Zn [73]) of metal syntactic foams plotted against density

density of the syntactic foam. The density in Fig. 4 includes the net effect of all these parameters on the density of the fabricated syntactic foams. In comparison, metal matrix syntactic foams have been fabricated in the density range of 1–5 g/cm^3 as observed in Fig. 5. The properties of many compositions of syntactic foams are found to be superior compared to that of the matrix material, which is usually of higher density than the syntactic foams. Such observations show the possibility of weight saving in the structural application by using syntactic foams. A recent study showed a metal matrix syntactic foam with a density of 0.9 g/cm^3 [74]. At such density levels, metal matrix syntactic foams start to compete with polymer matrix

syntactic foams in applications, where higher load bearing capacity or higher temperature withstanding capabilities are required.

The present chapter does not include discussion on particle-matrix interfacial bonding and particle to particle interactions. However, these effects have been studied by experimental and simulation methods [75–77].

3 High Strain Rate Properties of Syntactic Foams

The split-Hopkinson pressure bar (SHPB) setup has been widely used for high strain rate characterization of syntactic foams. This technique assumes one-dimensional wave propagation and neglects temperature rise and inertia effects in the specimens. Extensive literature is available on this technique that mostly reports on the strength parameters, not the modulus. Testing of syntactic foams using SHPB is especially challenging due to the high volume fraction of porosity in their structure, resulting in a weak transmitted signal. In addition, pulse shaping is very important in testing foams because it can provide enough time to obtain the stress equilibrium in the specimen during deformation.

Figure 6 shows the compressive strength of polymer matrix syntactic foams with respect to strain rate. The low strain rate results are obtained using universal test systems and the high strain rate results are obtained using the SHPB technique. The strength is found to increase with strain rate. In many cases, the high strain rate strength is found be to twice the quasi-static strength. These experimental measurements emphasize the need for using the correct properties of materials in designing armors and protective structures that are intended for use under high strain rate loading conditions.

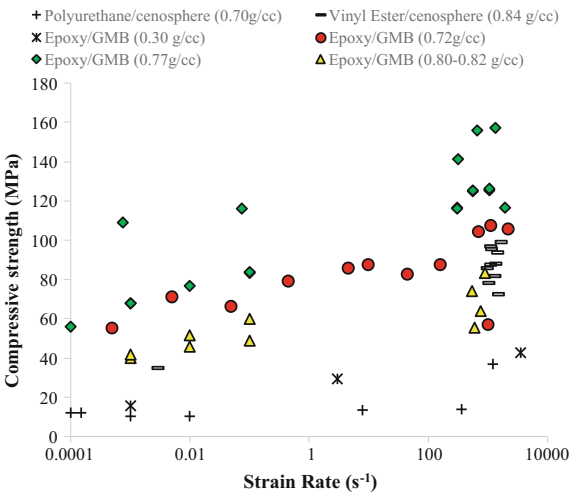

Fig. 6 Compressive strength of polymer matrix SFs [4, 11, 19, 22, 26, 30, 81] plotted against strain rate

Among the main effects of high strain rate loading of polymer matrix syntactic foams are suppression of elastic deformation and increase in brittleness. The effect of an increase in strain rate on material behavior is similar to decrease in temperature and previous studies have converted the temperature dependent mechanical property data to strain rate dependent material response [78, 79]. Understanding such effects is crucial for fully characterizing the materials across the entire spectrum of temperatures and strain rates.

Observations of polymer matrix syntactic foam failure behavior are shown in Fig. 7. It is observed that the failure mechanism of syntactic foams changes from shear to brittle failure as the strain rate is increased. Brittle failure results in less hollow particle crushing and increased specimen fragmentation. However, these trends are dependent on the total porosity present in the syntactic foam microstructure [80]. Highly porous foams have shown softening with increasing strain rate while foams with less porosity have shown stiffening effect with increasing strain rate.

The high strain rate behavior of some metal matrix syntactic foams is summarized in Fig. 8. Iron and aluminum matrix syntactic foams are covered in this figure. The body-centered cubic structure of iron is found to be strain rate sensitive while the face-centered cubic structure of aluminum is found to be relatively insensitive to strain rate in the range tested by split-Hopkinson pressure bar. The strength of iron syntactic foams is almost doubled from quasi-static compression to about 5000 s^{-1} strain rate. This figure also shows that the strength of iron and aluminum syntactic foams is over 100 MPa for many compositions, which can help in developing their load bearing applications. The properties measured at various strain rates can be used as input for the finite element analysis studies to conduct parametric studies and understand the behavior of the material over a wide range of composition and loading parameters.

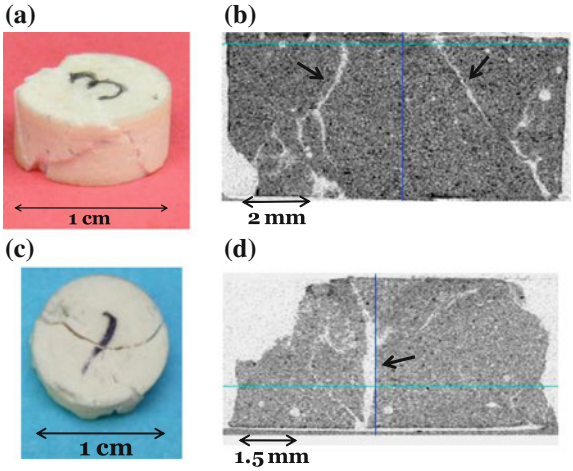

Fig. 7 Vinyl ester matrix syntactic foam containing 60 vol.% of 460 kg/m^3 GMB **a** tested at 920 s^{-1} strain rate, **b** CT scan showing shear cracks. The same material **c** tested at 1260 s^{-1} strain rate and **d** CT scan showing primarily brittle fracture

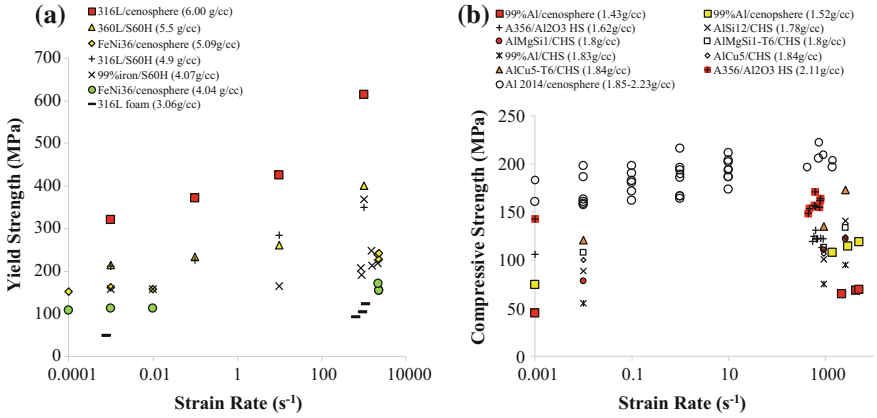

Fig. 8 **a** Yield strength of iron-based matrix SFs [41, 50, 52, 54, 55] and **b** compressive strength of aluminum SFs [39, 40, 60, 66, 82] plotted against strain rate

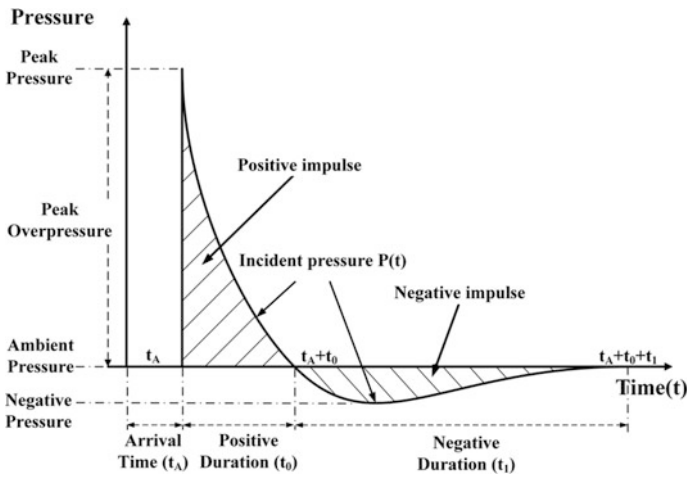

Fig. 9 A typical blast wave profile. Adapted from [83]

4 Blast Properties of Syntactic Foams

4.1 Shock Wave

A typical blast wave profile with respect to time is plotted in Fig. 9 [83]. The blast wave forms by a sudden release of energy, such as an explosion, and consists of a shock front in which pressure rises instantaneously from the ambient pressure (P_a) to a high value of P_s. The pressure decays exponentially with time. This is followed

by a negative pressure phase in which the air expands to return the pressure to the ambient value. The development and propagation of blast wave are expressed by the Friedlander equation [84, 85]

$$P(t) = (P_s - P_a)\left[1 - \frac{t - t_A}{t_0}\right] e^{-(t-t_A)/\theta} + P_a \tag{1}$$

where t_A is the arrival time of the blast wave, t_0 is the duration of the positive phase in which the pressure rises to the peak and then returns to the ambient value, and θ is a decay-time constant. The damage potential of a blast wave depends on its positive phase and the impulse loading, I, specified by

$$I = \int_0^{t_0} P(t)dt \tag{2}$$

The implications of expansion wave are significant on syntactic foams because of their low mechanical properties under tensile loading conditions. Particle-matrix debonding and matrix cracking may occur, especially for brittle resin systems during the tensile loading phase. Nonetheless, the standoff distance is one of the most important parameters in blast wave–structure interactions.

4.2 Shock Wave Propagation in Syntactic Foams

Finite element analysis (FEA) simulations are conducted to understand the shock wave-syntactic foam interactions and the material deformation and failure mechanisms. The simulations are conducted using Ansys AUTODYN commercial software (v.18.0). The results obtained from high strain rate testing of the matrix resin and syntactic foams are used as input parameters for these simulations to have a more realistic material behavior at the applied strain rates. The objective is to observe and predict the one-dimensional shock wave propagation in syntactic foams of pure iron matrix filled with 45 vol.% of 3M^{TM} S60HS soda lime GMBs as reported in [50, 54, 86]. Figure 10 depicts a 300 × 150 μm^2 2D domain

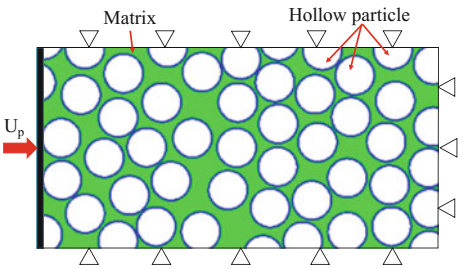

Fig. 10 The model of 1D blast propagation in syntactic foam

representing the microstructure of pure iron syntactic foams containing GMBs of 30 μm diameter and 1.3 μm wall thickness [50, 87]. The domain contains 49 particles, some of which are partially inside the domain. The GMBs are randomly dispersed in the matrix by using an in-house MATLAB code. In order to simulate the behavior of syntactic foams under shock wave, the Euler mesh is used to discretize the domain and the mesh size is set to 0.65 μm to make sure that the GMB walls contain at least two elements. Smaller mesh sizes took significantly longer time to converge.

The idealized 1D shock compression is generated by applying a particle velocity U_p to the left side of the model and roller support to other sides, as shown in Fig. 10 [88]. In Eulerian finite element model, the stress–strain constitutive model of the materials is separated and distinguished in the hydrostatic and deviatoric components. The hydrostatic component is represented by the equation of state (EOS). Both pure iron and soda lime glass materials use the Hugoniot linear EOS reposted in [89, 90], respectively. Besides the deviatoric component is calculated by the strength model. Hence, the Johnson-Cook strength model of pure iron [91] is applied.

Figure 11 shows the deformation microstructure of iron syntactic foams at four different time steps when the material is deformed with 1 km/s rate. The collapsed GMBs consolidate in the cavity and the material densifies as the shock wave

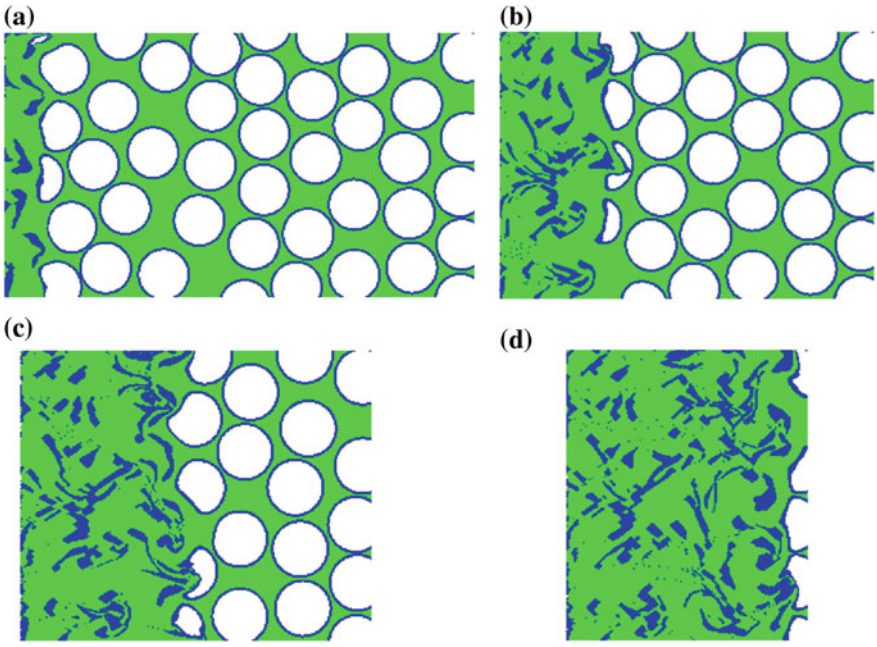

Fig. 11 The deformation microstructures of iron syntactic foams at time of **a** $t = 0.028$ μs **b** 0.085 μs **c** 0.113 μs **d** 0.170 μs for $U_p = 1$ km/s

propagates. The elastic nature of iron results in large deformation of the matrix being required for densification in the GMB cavity.

Results for incident shock velocities of 0.1 and 0.8 km/s are compared in Fig. 12, where the deformed microstructure and pressure distribution inside the microstructure are represented. At faster shock velocities, the microstructure completely densifies as the shock front propagates. In comparison, the densification front lags behind the shock front at slower shock velocities. The microstructure also shows that the material compression results in fracture of particles in the entire specimen at slow shock speed, whereas the particles are intact away from the shock interaction zone in the specimen subjected to faster shock velocity.

Figure 12c and d show that the pressure is distributed more uniformly in the microstructure at slower shock velocities, whereas the pressure concentration is observed close to the incident wave side of the microstructure at higher shock velocity. Uniform distribution of pressure in the entire microstructure results in particle fracture throughout the specimen.

In this study, the shock wave velocity (U_S) is determined by averaging the horizontal velocity at 12 measurement points that are located at the same horizontal location and along the vertical direction at the beginning and move following the deformation of the material in the domain. The U_S is found to be slightly higher than U_P, which is likely because the shock wave propagation in the syntactic foam is similar to the densification process of the cellular material.

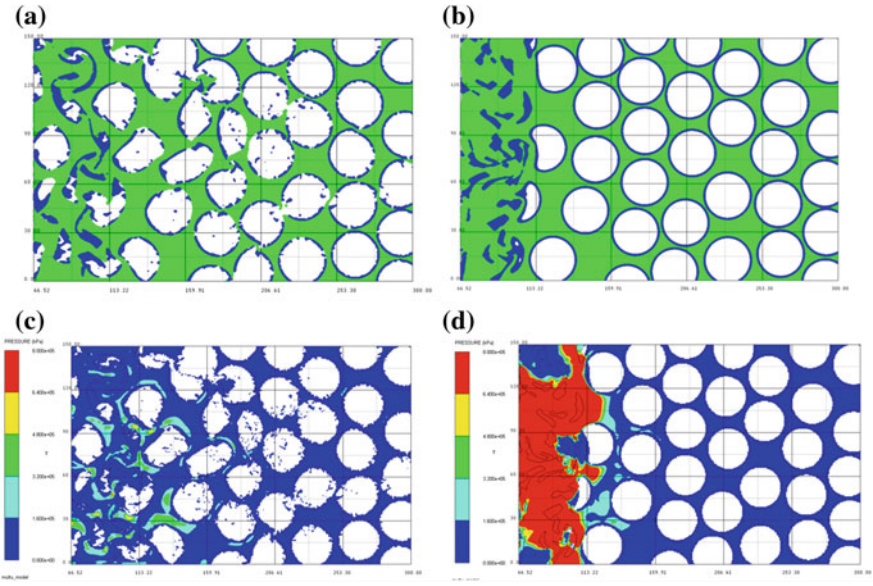

Fig. 12 The **a**, **b** deformed microstructures and **c**, **d** pressure distribution of iron syntactic foams having the same deformation of 66.52 μm for **a**, **c** U_p = 0.1 km/s and **b**, **d** 0.8 km/s

The results presented in Figs. 11 and 12 show the response of only a limited set of syntactic foams and loading conditions. However, syntactic foams can be tailored for a wide range of behaviors under shock loading by changing the particle wall thickness and volume fraction. One of the limitations of this approach can be that a given composition of syntactic foams may be most effective for energy absorption under a narrow range of shock properties. Functionally graded syntactic foams with a gradient in the wall thickness or volume fraction along the material thickness may be effective in mitigating the effects of a wide range of shock types [92, 93].

4.3 Blast Mitigation of Sandwich Composite

The dynamic response of a syntactic foam core sandwich composite panel under blast wave is simulated in ABAQUS. Syntactic foam core sandwich panels have been fabricated with a wide range of materials, including polymers and metals [94–96], and have been studied for various properties. In addition to the tailoring of the syntactic foams core by means of material selection and selection of particle properties, additional tailoring parameters are available in sandwich structures in the form of skin fabric, lay up sequence, and thickness of the skins. Optimization of all these parameters is a challenging task and can only be conducted based on a given threat level. Some of the fundamental aspects of modeling the sandwich behavior are presented below.

The quarter symmetry model is built as a rectangular panel of dimensions 100×75 mm^2 with a thickness of 20 mm for the syntactic foam core and 0.4 mm for the fiber reinforced laminate skins. The skins contain two layers of fabric in 0/90 orientation as shown in Fig. 13a. Figure 13b shows the symmetry boundary conditions applied to two edges and clamped supports applied to two other edges.

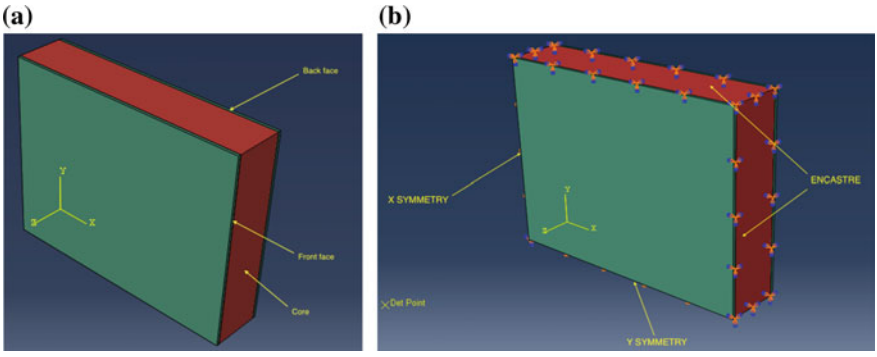

Fig. 13 **a** A representative syntactic foam core sandwich panel model used in simulations and **b** the applied boundary conditions

The blast load is created by a 50 g TNT explosion with the standoff distance of 90 mm by the CONWEP feature [97].

The syntactic foam core comprises vinyl ester (VE) matrix filled with glass microballoons. The properties of four types of core materials simulated in this study are presented in Table 1. These properties are obtained from an experimental study [28]. The constitutive model of core material includes a linear elastic model followed by a crushable foam model in the plasticity range [97] that was developed from the isotropic foam constitutive model published by Deshpande and Fleck [98]. The crushable foam parameters are estimated from the literature [28, 31] and are listed in Table 2.

The fiber reinforced laminated skin is modeled as a brittle material with orthotropic elastic behavior. Its Young's moduli (E), Poisson's ratios (ν), and shear moduli (G) are listed in Table 3. The failure criteria of the laminate is set up with Hashin damage model that contains four different modes of failure: fiber rupture in tension, fiber buckling and wrinkling in compression, matrix cracking under transverse tension and shearing, and matrix crushing under transverse compression and shearing. The parameters of the Hashin damage model include longitudinal tensile ($X^T = 270$ MPa), longitudinal compressive ($X^C = 200$ MPa), transverse tensile ($Y^T = 270$ MPa), transverse compressive ($Y^C = 200$ MPa), longitudinal shear ($S^L = 40$ MPa), and transverse shear ($S^T = 31.6$ MPa) strengths.

The von-Mises stress distribution on the face sheets is shown in Fig. 14a for VE-220-30 syntactic foam core sandwich. Part of the syntactic foam core reaches plastic condition as shown in Fig. 14b. As expected it happens in the proximity of the front face sheet, while the back face stress is lower. The plastic strain is maximum at the center of the front face and gradually reduces in magnitude toward the clamped edges. The sandwich panel reaches the maximum deflection in about 0.1 ms when the interaction with the blast wave takes place. After that, the core absorbed part of the kinetic energy coming from the blast by plastic deformation. When plastic deformation ended, the elastic response of the sandwich panel causes continuous oscillations that decay over time.

The front and back skin deflections of different VE syntactic foam core panels are plotted over time in Fig. 15. The equilibrium deflection values for syntactic foams are listed in Table 4. These values represent plastic strain in the material.

Tailoring the particle type and volume fraction affects the stiffness of the syntactic foam and helps in managing the deflection. In addition, as observed in the

Table 1 The mechanical VE syntactic foams

Material	Volume fraction (%)	Density (kg/m^3)	Peak stress (MPa)	E (GPa)	Plateau stress (MPa)
VE220-30	30	870	66.11	1.66	64.46
VE220-60	60	558	33.08	0.80	31.50
VE460-30	30	930	100.64	1.27	89.65
VE460-60	60	734	84.11	1.15	74.42

Table 2 The crushable foam parameters of polymer syntactic foam core materials.[a]

Material	k	k_t	R	$\dot{\overline{\varepsilon^{pl}}}$	Material	k	k_t	R	$\dot{\overline{\varepsilon^{pl}}}$
VE220-30	1.08	0.1	1	0.0001	VE460-30	1.5	0.1	1	0.0001
			1.158	0.001				1.103	0.001
			1.223	0.01				1.097	0.01
			1.172	0.1				1.178	0.1
			1.8	1024				1.565	793
			1.936	1155				1.609	1008
			1.785	1215				1.563	1127
			1.906	1457				1.559	1172
			1.694	1547				1.465	1401
								1.610	1535
								1.552	1796
VE220-60	1.2	0.1	1	0.0001	VE460-60	1.08	0.1	1	0.0001
			1.095	0.001				1.119	0.001
			1.146	0.01				1.151	0.01
			1.157	0.1				1.142	0.1
			1.663	1276				1.275	818
			1.451	1342				1.328	997
			1.632	1474				1.357	1236
			1.693	1579				1.386	1269
			1.602	1814				1.398	1286
			1.693	2121				1.378	1667
			1.511	2687				1.335	1851

[a]Notations: $k = \sigma_c^o / p_c^o$ is defined as the compressive yield strength ratio; $k_t = p_t^o / p_c^o$ is hydrostatic yield stress ratio; $R = \overline{\sigma}_c / \sigma_c$ is yield stress ratio; and $\dot{\overline{\varepsilon^{pl}}}$ is equivalent plastic strain rate. σ_c^o is the initial compressive yield stress; p_c^o and p_t^o are respectively the initial compressive yield stress under hydrostatic load and the initial tensile yield stress under hydrostatic load. R is given as the set of data corresponding to equivalent plastic strain rate $\dot{\overline{\varepsilon^{pl}}}$

Table 3 Orthotropic elastic properties of the fiber reinforced sheet

E_1 GPa	E_2 GPa	E_3 GPa	ν_{12}	ν_{13}	ν_{23}	G_{12} GPa	G_{13} GPa	G_{23} GPa
17	17	7.48	0.13	0.28	0.13	4	1.730	1.730

case of microstructure-based simulations of iron syntactic foams, the particle crushing behavior can be controlled by selecting particles of appropriate wall thickness. Such possibilities can provide the energy absorption capabilities as per the material design and develop syntactic foam core and sandwich structure as per the anticipated loading conditions.

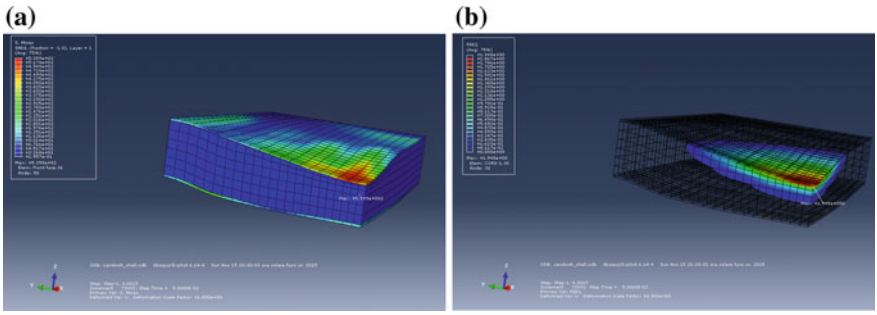

Fig. 14 **a** The distribution of von-Misses stress of VE220-30 and **b** equivalent plastic strain inside VE220-30 core plotted as isosurface contour

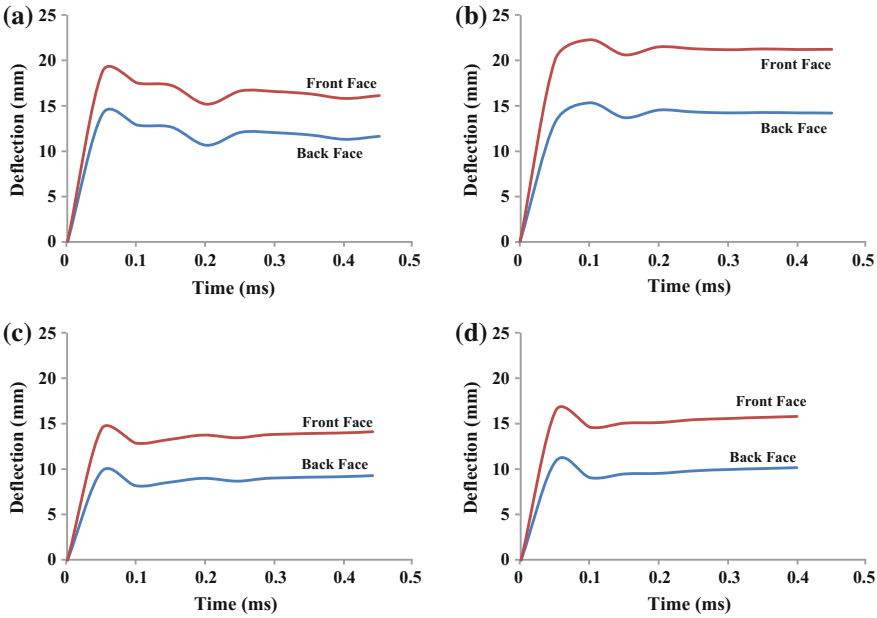

Fig. 15 Front and back sheet deflections of **a** VE220-30, **b** VE220-60, **c** VE460-30, and **d** VE460-60 core panel plotted against time

Table 4 Defection of front and back laminate sheets at equilibrium

Core material	Deflection of back face (mm)	Deflection of front face (mm)	Relative deflection (mm)
VE220-30	14.20	18.80	4.60
VE220-60	13.21	20.05	6.84
VE460-30	9.89	14.54	4.65
VE460-60	10.91	16.52	5.61

The effects of temperature on the blast loading response of structures can be significant, but have not been studied in detail so far. For example, the same panel loaded under arctic temperature conditions versus desert temperature conditions can produce very different results due to brittleness effects. Such parameters should be combined with the loading and microstructure-based parameters to fully characterize the material for a given scenario.

5 Conclusions

Thin-walled particles and porosity present in syntactic foam microstructure result in a difference in failure mechanisms as the loading condition is changed from quasi-static to high strain rate. Studies have shown that the failure mechanism of syntactic foams can change from shear to brittle fracture as the loading condition is changed from quasi-static to high strain rate. The strain rate sensitivity is also observed in the measured mechanical properties of syntactic foams. Studies are available on blast loading of syntactic foams and their sandwich structures. These materials need to be tailored as per a given threat level because of the number of parameters available to tailor their properties. For example, a number of combinations of particle wall thickness and volume fractions can provide the same density or mechanical properties which facilitate the selection of the most optimal material for the given loading condition.

Acknowledgements Authors acknowledge the Office of Naval Research grant N00014-10-1-0988. The views expressed in this article are those of authors, not of funding agencies. The authors thank the MAE Department at NYU for providing facilities and support. Steven E. Zeltmann is thanked for help with manuscript preparation and technical discussions.

References

1. Gupta, N., Zeltmann, S. E., Shunmugasamy, V. C., & Pinisetty, D. (2014). Applications of polymer matrix syntactic foams. *JOM, 66*(2), 245–254.
2. Gupta, N., Pinisetty, D., & Shunmugasamy, V. C. (2013). *Reinforced polymer matrix syntactic foams: Effect of nano and micro-scale reinforcement*. SpringerBriefs in Materials. Springer.
3. Gupta, N., & Rohatgi, P. K. (Eds.). (2014). *Metal matrix syntactic foams: Processing, microstructure, properties and applications*. DEStech Publications: Lancaster, PA.
4. Song, B., Chen, W., Yanagita, T., & Frew, D. J. (2005). Confinement effects on the dynamic compressive properties of an epoxy syntactic foam. *Composite Structures, 67*(3), 279–287.
5. Huang, C., Huang, Z., Qin, Y., Ding, J., & Lv, X. (2016). Mechanical and dynamic mechanical properties of epoxy syntactic foams reinforced by short carbon fiber. *Polymer Composites, 37*(7), 1960–1970.
6. Bharath Kumar, B. R., Singh, A. K., Doddamani, M., Luong, D. D., & Gupta, N. (2016). Quasi-static and high strain rate compressive response of injection-molded cenosphere/HDPE syntactic foam. *JOM, 68*(7), 1861–1871.

7. Rohatgi, P. K., Matsunaga, T., & Gupta, N. (2009). Compressive and ultrasonic properties of polyester/fly ash composites. *Journal of Materials Science, 44*(6), 1485.
8. Gupta, N., Woldesenbet, E., & Mensah, P. (2004). Compression properties of syntactic foams: effect of cenosphere radius ratio and specimen aspect ratio. *Composites Part A: Applied Science and Manufacturing, 35*(1), 103–111.
9. Woldesenbet, E., & Peter, S. (2009). Volume fraction effect on high strain rate properties of syntactic foam composites. *Journal of Materials Science, 44*(6), 1528–1539.
10. Woldesenbet, E., & Peter, S. (2008). Radius ratio effect on high-strain rate properties of syntactic foam composites. *Journal of Materials Science, 44*(6), 1551.
11. Li, P., Petrinic, N., Siviour, C. R., Froud, R., & Reed, J. M. (2009). Strain rate dependent compressive properties of glass microballoon epoxy syntactic foams. *Materials Science and Engineering: A, 515*(1–2), 19–25.
12. Xie, W., Yan, H., Mei, Q., Du, M., & Huang, Z. (2007). Compressive and fracture properties of syntactic foam filled with hollow plastic bead (HPC). *Journal of Wuhan University of Technology-Materials Science Edition, 22*(3), 499–501.
13. Ambika Devi, K., John, B., Reghunadhan Nair, C. P., & Ninan, K. N. (2007). Syntactic foam composites of epoxy-allyl phenol-bismaleimide ternary blend—Processing and properties. *Journal of Applied Polymer Science, 105*(6), 3715–3722.
14. Kishore, Shankar, R., & Sankaran, S. (2006). Effects of microballoons' size and content in epoxy on compressive strength and modulus. *Journal of Materials Science, 41*(22), 7459–7465
15. Wouterson, E. M., Boey, F. Y. C., Hu, X., & Wong, S.-C. (2005). Specific properties and fracture toughness of syntactic foam: Effect of foam microstructures. *Composites Science and Technology, 65*(11–12), 1840–1850.
16. Karthikeyan, C.S., Sankaran, S., Jagdish Kumar, M.N., & Kishore. (2001). Processing and compressive strengths of syntactic foams with and without fibrous reinforcements. *Journal of Applied Polymer Science, 81*(2), 405–411.
17. Dimchev, M., Caeti, R., & Gupta, N. (2010). Effect of carbon nanofibers on tensile and compressive characteristics of hollow particle filled composites. *Materials and Design, 31*(3), 1332–1337.
18. Gupta, N., & Maharsia, R. (2005). Enhancement of energy absorption in syntactic foams by nanoclay incorporation for sandwich core applications. *Applied Composite Materials, 12*(3), 247–261.
19. Song, B., Chen, W., & Frew, D. J. (2004). Dynamic compressive response and failure behavior of an epoxy syntactic foam. *Journal of Composite Materials, 38*(11), 915–936.
20. Viot, P., Shankar, K., & Bernard, D. (2008). Effect of strain rate and density on dynamic behaviour of syntactic foam. *Composite Structures, 86*(4), 314–327.
21. Peter, S., & Woldesenbet, E. (2008). Nanoclay syntactic foam composites—High strain rate properties. *Materials Science and Engineering: A, 494*(1–2), 179–187.
22. Song, B., Chen, W. W., & Lu, W. Y. (2007). Mechanical characterization at intermediate strain rates for rate effects on an epoxy syntactic foam. *International Journal of Mechanical Sciences, 49*(12), 1336–1343.
23. Drdlová, M., & Prachař, V. (2016). High strain rate characteristics of nanoparticle modified blast energy absorbing materials. *Procedia Engineering, 151,* 214–221.
24. Ahmadi, H., Liaghat, G. H., Shokrieh, M. M., Hadavinia, H., Ordys, A., & Aboutorabi, A. (2014). Quasi-static and dynamic compressive properties of ceramic microballoon filled syntactic foam. *Journal of Composite Materials, 49*(10), 1255–1266.
25. Ahmadi, H., Liaghat, G. H., Shokrieh, M. M., Aboutorabi, A., Hadavinia, H., & Ordys, A. (2014). Compressive properties of nanoclay-reinforced syntactic foams at quasi-static and high strain rate loading. *Polymer-Plastics Technology and Engineering, 53*(10), 990–999.
26. Pellegrino, A., Tagarielli, V. L., Gerlach, R., & Petrinic, N. (2015). The mechanical response of a syntactic polyurethane foam at low and high rates of strain. *International Journal of Impact Engineering, 75,* 214–221.

27. Luong, D. D., Shunmugasamy, V. C., Strbik III, O. M., & Gupta, N. (2014). High strain rate compressive behavior of polyurethane resin and polyurethane/Al_2O_3 hollow sphere syntactic foams. *Journal of Composites,* Article ID 795984.
28. Gupta, N., Ye, R., & Porfiri, M. (2010). Comparison of tensile and compressive characteristics of vinyl ester/glass microballoon syntactic foams. *Composites Part B: Engineering, 41*(3), 236–245.
29. Labella, M., Shunmugasamy, V. C., Strbik, O. M., & Gupta, N. (2014). Compressive and thermal characterization of syntactic foams containing hollow silicon carbide particles with porous shell. *Journal of Applied Polymer Science, 131*(17), 8593–8597.
30. Labella, M., Zeltmann, S. E., Shunmugasamy, V. C., Gupta, N., & Rohatgi, P. K. (2014). Mechanical and thermal properties of fly ash/vinyl ester syntactic foams. *Fuel, 121,* 240–249.
31. Shunmugasamy, V. C., Gupta, N., Nguyen, N. Q., & Coelho, P. G. (2010). Strain rate dependence of damage evolution in syntactic foams. *Materials Science and Engineering: A, 527*(23), 6166–6177.
32. Rohatgi, P. K., Kim, J. K., Gupta, N., Alaraj, S., & Daoud, A. (2006). Compressive characteristics of A356/fly ash cenosphere composites synthesized by pressure infiltration technique. *Composites Part A: Applied Science and Manufacturing, 37*(3), 430–437.
33. Sudarshan, & Surappa, M. K. (2008). Synthesis of fly ash particle reinforced A356 Al composites and their characterization. *Materials Science and Engineering: A, 480*(1–2), 117–124.
34. Tao, X. F., Zhang, L. P., & Zhao, Y. Y. (2009). Al matrix syntactic foam fabricated with bimodal ceramic microspheres. *Materials and Design, 30*(7), 2732–2736.
35. Luong, D. D., Gupta, N., Daoud, A., & Rohatgi, P. K. (2011). High strain rate compressive characterization of aluminum alloy/fly ash cenosphere composites. *JOM, 63*(2), 53–56.
36. Májlinger, K., & Orbulov, I. N. (2014). Characteristic compressive properties of hybrid metal matrix syntactic foams. *Materials Science and Engineering: A, 606,* 248–256.
37. Vogiatzis, C. A., Tsouknidas, A., Kountouras, D. T., & Skolianos, S. (2015). Aluminum–ceramic cenospheres syntactic foams produced by powder metallurgy route. *Materials and Design, 85,* 444–454.
38. Szlancsik, A., Katona, B., Májlinger, K., & Orbulov, I. (2015). Compressive behavior and microstructural characteristics of iron hollow sphere filled aluminum matrix syntactic foams. *Materials, 8*(11), 5432.
39. Myers, K., Katona, B., Cortes, P., & Orbulov, I. N. (2015). Quasi-static and high strain rate response of aluminum matrix syntactic foams under compression. *Composites Part A: Applied Science and Manufacturing, 79,* 82–91.
40. Licitra, L., Luong, D. D., Strbik III, O. M., & Gupta, N. (2015). Dynamic properties of alumina hollow particle filled aluminum alloy A356 matrix syntactic foams. *Materials and Design, 66, Part B*, 504–515.
41. Alvandi-Tabrizi, Y., Whisler, D. A., Kim, H., & Rabiei, A. (2015). High strain rate behavior of composite metal foams. *Materials Science and Engineering: A, 631,* 248–257.
42. Zhang, B., Lin, Y., Li, S., Zhai, D., & Wu, G. (2016). Quasi-static and high strain rates compressive behavior of aluminum matrix syntactic foams. *Composites Part B: Engineering, 98,* 288–296.
43. Daoud, A., Abou El-khair, M. T., Abdel-Aziz, M., & Rohatgi, P. (2007). Fabrication, microstructure and compressive behavior of ZC63 Mg-microballoon foam composites. *Composites Science and Technology, 67*(9), 1842–1853.
44. Rohatgi, P. K., Daoud, A., Schultz, B. F., & Puri, T. (2009). Microstructure and mechanical behavior of die casting AZ91D-Fly ash cenosphere composites. *Composites Part A: Applied Science and Manufacturing, 40*(6–7), 883–896.
45. Luong, D. D., Gupta, N., & Rohatgi, P. K. (2011). The high strain rate compressive response of Mg-Al alloy/fly Ash cenosphere composites. *JOM, 63*(2), 48–52.
46. Brown, J., Vendra, L., & Rabiei, A. (2010). Bending properties of Al-steel and steel-steel composite metal foams. *Metallurgical and Materials Transactions A, 41*(11), 2784–2793.

47. Weise, J., Baumeister, J., Yezerska, O., Salk, N., & Silva, G. B. D. (2010). Syntactic iron foams with integrated microglass bubbles produced by means of metal powder injection moulding. *Advanced Engineering Materials, 12*(7), 604–608.
48. Castro, G., & Nutt, S. R. (2012). Synthesis of syntactic steel foam using mechanical pressure infiltration. *Materials Science and Engineering: A, 535,* 274–280.
49. Castro, G., & Nutt, S. R. (2012). Synthesis of syntactic steel foam using gravity-fed infiltration. *Materials Science and Engineering: A, 553,* 89–95.
50. Peroni, L., Scapin, M., Avalle, M., Weise, J., & Lehmhus, D. (2012). Dynamic mechanical behavior of syntactic iron foams with glass microspheres. *Materials Science and Engineering: A, 552,* 364–375.
51. Rabiei, A., & Garcia-Avila, M. (2013). Effect of various parameters on properties of composite steel foams under variety of loading rates. *Materials Science and Engineering: A, 564,* 539–547.
52. Peroni, L., Scapin, M., Fichera, C., Lehmhus, D., Weise, J., Baumeister, J., et al. (2014). Investigation of the mechanical behaviour of AISI 316L stainless steel syntactic foams at different strain-rates. *Composites Part B: Engineering, 66,* 430–442.
53. Weise, J., Lehmhus, D., Baumeister, J., Kun, R., Bayoumi, M., & Busse, M. (2014). Production and properties of 316L stainless steel cellular materials and syntactic foams. *Steel Research International, 85*(3), 486–497.
54. Luong, D. D., Shunmugasamy, V. C., Gupta, N., Lehmhus, D., Weise, J., & Baumeister, J. (2015). Quasi-static and high strain rates compressive response of iron and Invar matrix syntactic foams. *Materials and Design, 66, Part B*, 516–531.
55. Luong, D., Lehmhus, D., Gupta, N., Weise, J., & Bayoumi, M. (2016). Structure and compressive properties of invar-cenosphere syntactic foams. *Materials, 9*(2), 115.
56. Xue, X. B., Zhao, Y. Y., Kearns, V., & Williams, R. L. (2010). Mechanical and biological properties of titanium syntactic foams. In *TMS 2010 Annual Meeting and Exhibition*. Warrendale.
57. Xue, X., & Zhao, Y. (2011). Ti matrix syntactic foam fabricated by powder metallurgy: Particle breakage and elastic modulus. *JOM, 63*(2), 43–47.
58. Santa Maria, J. A., Schultz, B. F., Ferguson, J. B., & Rohatgi, P. K. (2013). Al–Al2O3 syntactic foams—Part I: Effect of matrix strength and hollow sphere size on the quasi-static properties of Al-A206/Al2O3 syntactic foams. *Materials Science and Engineering: A, 582,* 415–422.
59. Santa Maria, J. A., Schultz, B. F., Ferguson, J. B., Gupta, N., & Rohatgi, P. K. (2014). Effect of hollow sphere size and size distribution on the quasi-static and high strain rate compressive properties of Al-A380–Al2O3 syntactic foams. *Journal of Materials Science, 49*(3), 1267–1278.
60. Goel, M. D., Mondal, D. P., Yadav, M. S., & Gupta, S. K. (2014). Effect of strain rate and relative density on compressive deformation behavior of aluminum cenosphere syntactic foam. *Materials Science and Engineering: A, 590,* 406–415.
61. Cox, J., Luong, D., Shunmugasamy, V., Gupta, N., Strbik, O., & Cho, K. (2014). Dynamic and Thermal properties of aluminum alloy A356/silicon carbide hollow particle syntactic foams. *Metals, 4*(4), 530.
62. Rocha Rivero, G. A., Schultz, B. F., Ferguson, J. B., Gupta, N., & Rohatgi, P. K. (2013). Compressive properties of Al-A206/SiC and Mg-AZ91/SiC syntactic foams. *Journal of Materials Research, 28*(17), 2426–2435.
63. Tao, X. F., & Zhao, Y. Y. (2009). Compressive behavior of Al matrix syntactic foams toughened with Al particles. *Scripta Materialia, 61*(5), 461–464.
64. Zou, L. C., Zhang, Q., Pang, B. J., Wu, G. H., Jiang, L. T., & Su, H. (2013). Dynamic compressive behavior of aluminum matrix syntactic foam and its multilayer structure. *Materials and Design, 45,* 555–560.
65. Luong, D. D., Strbik, O. M., III, Hammond, V. H., Gupta, N., & Cho, K. (2013). Development of high performance lightweight aluminum alloy/SiC hollow sphere syntactic

foams and compressive characterization at quasi-static and high strain rates. *Journal of Alloys and Compounds, 550,* 412–422.
66. Dou, Z. Y., Jiang, L. T., Wu, G. H., Zhang, Q., Xiu, Z. Y., & Chen, G. Q. (2007). High strain rate compression of cenosphere-pure aluminum syntactic foams. *Scripta Materialia, 57*(10), 945–948.
67. Zhang, L. P., & Zhao, Y. Y. (2007). Mechanical response of Al matrix syntactic foams produced by pressure infiltration casting. *Journal of Composite Materials, 41*(17), 2105–2117.
68. Mondal, D. P., Goel, M. D., & Das, S. (2009). Compressive deformation and energy absorption characteristics of closed cell aluminum-fly ash particle composite foam. *Materials Science and Engineering: A, 507*(1–2), 102–109.
69. Rabiei, A., & O'Neill, A. T. (2005). A study on processing of a composite metal foam via casting. *Materials Science and Engineering: A, 404*(1–2), 159–164.
70. Vendra, L., Neville, B., & Rabiei, A. (2009). Fatigue in aluminum–steel and steel–steel composite foams. *Materials Science and Engineering: A, 517*(1–2), 146–153.
71. Neville, B. P., & Rabiei, A. (2008). Composite metal foams processed through powder metallurgy. *Materials and Design, 29*(2), 388–396.
72. Newsome, D., Schultz, B., Ferguson, J., & Rohatgi, P. (2015). Synthesis and quasi-static compressive properties of Mg-AZ91D-Al2O3 syntactic foams. *Materials, 8*(9), 5292.
73. Daoud, A. (2008). Synthesis and characterization of novel ZnAl22 syntactic foam composites via casting. *Materials Science and Engineering: A, 488*(1–2), 281–295.
74. Anantharaman, H., Shunmugasamy, V. C., Strbik, O. M., III, Gupta, N., & Cho, K. (2015). Dynamic properties of silicon carbide hollow particle filled magnesium alloy (AZ91D) matrix syntactic foams. *International Journal of Impact Engineering, 82,* 14–24.
75. Tagliavia, G., Porfiri, M., & Gupta, N. (2011). Analysis of particle-to-particle elastic interactions in syntactic foams. *Mechanics of Materials, 43*(12), 952–968.
76. Bharath Kumar, B. R., Zeltmann, S. E., Doddamani, M., Gupta, N., Uzma, Gurupadu, S., & Sailaja, R. R. N. (2016). Effect of cenosphere surface treatment and blending method on the tensile properties of thermoplastic matrix syntactic foams. *Journal of Applied Polymer Science, 133*(35), n/a–n/a.
77. Tagliavia, G., Porfiri, M., & Gupta, N. (2010). Analysis of hollow inclusion–matrix debonding in particulate composites. *International Journal of Solids and Structures, 47*(16), 2164–2177.
78. Zeltmann, S. E., Prakash, K. A., Doddamani, M., & Gupta, N. (2017). Prediction of modulus at various strain rates from dynamic mechanical analysis data for polymer matrix composites. *Composites Part B: Engineering, 120,* 27–34.
79. Zeltmann, S. E., Bharath Kumar, B. R., Doddamani, M., & Gupta, N. (2016). Prediction of strain rate sensitivity of high density polyethylene using integral transform of dynamic mechanical analysis data. *Polymer, 101,* 1–6.
80. Gupta, N., & Shunmugasamy, V. C. (2011). High strain rate compressive response of syntactic foams: Trends in mechanical properties and failure mechanisms. *Materials Science and Engineering: A, 528*(25–26), 7596–7605.
81. Ahmadi, H., Liaghat, G., Shokrieh, M., Hadavinia, H., Ordys, A., & Aboutorabi, A. (2015). Quasi-static and dynamic compressive properties of ceramic microballoon filled syntactic foam. *Journal of Composite Materials, 49*(10), 1255–1266.
82. Goel, M. D., Peroni, M., Solomos, G., Mondal, D. P., Matsagar, V. A., Gupta, A. K., et al. (2012). Dynamic compression behavior of cenosphere aluminum alloy syntactic foam. *Materials and Design, 42,* 418–423.
83. Karlos, V., & Solomos, G. (2013). *Calculation of blast loads for application to structural components*. Publications Office of the European Union, Luxembourg, p. JRC Technical Reports: EUR 26456 EN.
84. Porfiri, M., & Gupta, N. (2010). A review of research on impulsive loading of marine composites. In I. M. Daniel, E. E. Gdoutos, & Y. D. S. Rajapakse (Eds.), *Major*

accomplishments in composite materials and sandwich structures (pp. 169–194). Springer Netherlands: Dordrecht.
85. Hause, T. (2012). Elastic structural response of anisotropic sandwich plates with a first-order compressible core impacted by a Friedlander-type shock loading. *Composite Structures, 94* (5), 1634–1645.
86. Peroni, L., Scapin, M., Avalle, M., Weise, J., Lehmhus, D., Baumeister, J., et al. (2012). Syntactic iron foams—on deformation mechanisms and strain-rate dependence of compressive properties. *Advanced Engineering Materials, 14*(10), 909–918.
87. 3M. (2017). *3M™ Glass Bubbles S60HS*. Retrieved April 28, 2017, from http://multimedia.3m.com/mws/media/184506O/3mtm-glass-bubbles-s60hs.pdf.
88. Ryan, A. A., David, L. M., & David, J. B. (2006). Numerical simulation of shock wave propagation in spatially-resolved particle systems. *Modelling and Simulation in Materials Science and Engineering, 14*(4), 537.
89. Marsh, S. P. (1980). *LASL shock Hugoniot data* (vol. 5). University of California Press.
90. Christou, G. A., Young, L. R., Goel, R., Vechart, A. P., & Jérusalem, A. (2012). Shock attenuation of PMMA sandwich panels filled with soda-lime glass beads: A fluid-structure interaction continuum model simulation. *International Journal of Impact Engineering, 47,* 48–59.
91. Johnson, G. R., & Cook, W. H. (1985). Fracture characteristics of three metals subjected to various strains, strain rates, temperatures and pressures. *Engineering Fracture Mechanics, 21*(1), 31–48.
92. Caeti, R., Gupta, N., & Porfiri, M. (2009). Processing and compressive response of functionally graded composites. *Materials Letters, 63*(22), 1964–1967.
93. Gupta, N. (2007). A functionally graded syntactic foam material for high energy absorption under compression. *Materials Letters, 61*(4–5), 979–982.
94. Omar, M. Y., Xiang, C., Gupta, N., Strbik, O. M., III, & Cho, K. (2015). Syntactic foam core metal matrix sandwich composite under bending conditions. *Materials and Design, 86,* 536–544.
95. Lamanna, E., Gupta, N., Cappa, P., Strbik, O. M., III, & Cho, K. (2017). Evaluation of the dynamic properties of an aluminum syntactic foam core sandwich. *Journal of Alloys and Compounds, 695,* 2987–2994.
96. Gupta, N., Kishore, & Sankaran, S. (1999). On the characterisation of syntactic foam core sandwich composites for compressive properties. *Journal of Reinforced Plastics and Composites, 18*(14), 1347–1357
97. Abaqus. (2012). *Abaqus Analysis User's Manual (6.12).*
98. Deshpande, V. S., & Fleck, N. A. (2000). Isotropic constitutive models for metallic foams. *Journal of the Mechanics and Physics of Solids, 48*(6–7), 1253–1283.

Wave Propagation and Dynamic Correction Factors for Composite Structures

Roberta Massabò

1 Introduction

Structural theories are extensively being used in the analysis and design of homogeneous and layered structures under different loading conditions, including impact and blast. The structural theories offer various advantages over three-dimensional theories when dealing with one- or two-dimensional bodies and within their regime of validity: the number of problems for which insightful closed-form solutions can be obtained is larger; and the computational modeling, especially when dealing with layered structures, is more efficient. The equivalent single layer theories have been developed as an extension to layered structures of well-known and used theories for homogeneous structures. Among the Equivalent Single Layer theories, the first-order theories assume first-order displacement fields in the thickness coordinate and offer the best compromise between accuracy and effectiveness. This is confirmed by their extensive use in the engineering community.

Due to the very simple kinematic description, the first-order theories require shear and/or normal correction factors, which are introduced to improve the treatment of the transverse strains and the accuracy. The definition of the best correction factors to use for different static and dynamic problems has been the topic of many research papers, which will be reviewed in the next section. The problem is complicated because the best correction factors are problem dependent, they differ between static, dynamic and wave propagation problems, and depend on the layup and elastic constants of the layers. For static problems, different methods and analytical and computational strategies have been proposed and implemented. On the other hand, the community has not paid similar attention to the definition of the best dynamic correction factors for layered systems and often dynamic correction factors

R. Massabò (✉)
Department of Civil, Chemical and Environmental Engineering, University of Genova, Genoa, Italy
e-mail: roberta.massabo@unige.it

S. Gopalakrishnan and Y. Rajapakse (eds.), *Blast Mitigation Strategies in Marine Composite and Sandwich Structures*, Springer Transactions in Civil and Environmental Engineering, https://doi.org/10.1007/978-981-10-7170-6_10

derived for homogeneous materials or static correction factors derived for layered systems are used for dynamic problems. The reason for this lack of attention is probably to be found in the complexity of the derivation of exact elasticity solutions for dynamic and wave propagation problems, which typically require complex computational strategies.

In this chapter, we propose an analytical strategy for the derivation of explicit expressions for the dynamic correction factors of cross-ply laminated plates in cylindrical bending. The strategy uses the method originally proposed by Mindlin et al. [1, 2], which is based on matching the first cut-off frequencies of the thickness-modes of wave propagation derived using the approximate equivalent single layer theory and the exact elasticity solutions for homogeneous plates. Since elasticity closed-form solutions of the cut-off frequencies are not available for layered plates, we propose the use of explicit solutions obtained through a homogenized structural model [3]. The model enriches the displacement field of an equivalent single layer theory through the inclusion of local zig-zag contributions which are defined to properly account for the effects of the layered material structure [4, 5]. Using a homogenization technique, macro-scale displacement fields and dynamic equilibrium equations are then derived which depends on the global variables only. This allows the closed-form solution of many problems, including wave propagation problems, and the derivation of explicit expressions for the cut-off frequencies of the first thickness-shear modes of wave propagation. The frequencies prove to be very accurate, also in plates with a large mismatch of the elastic properties of the layers.

The chapter is organized as follows. In Sect. 2 static and dynamic methods for the derivation of shear and normal correction factors of equivalent single layer theories are reviewed and their advantages and limitations discussed. The formulation of the multiscale homogenized structural model for plates with imperfect interfaces and delaminations presented in [4] is briefly recalled in Sect. 3. For plates with fully bonded, transversally incompressible layers the model coincides with the original zig-zag theory previously formulated by Di Sciuva [5]. In Sect. 4 the frequency equations of the first thickness-shear and thickness-stretch modes of wave propagation are derived and solved in closed form. They define the cut-off frequencies of the lowest cut-off frequency modes of propagation of plane-strain Rayleigh–Lamb waves. Explicit expressions for the dynamic correction factors are obtained by matching the frequencies of the first-order equivalent single layer theories and those of the homogenized model. The correction factors are compared with numerical predictions based on the exact elasticity solutions for bilayer plates in Sect. 5. A discussion on the applicability of the approach to other problems and on the possible use of the homogenized structural theory for the derivation of dynamic correction factors using different matching parameters is presented in Sect. 6.

2 Correction Factors of Equivalent Single Layer Theories

Equivalent Single Layer (ESL) theories are extensively being used by the engineering community to analyze the mechanical response of anisotropic layered structures, such as laminated and sandwich beams, plates, and shells under static and dynamic loadings. They are extensions to layered materials of the structural theories which were developed for homogeneous structures, with which they share the kinematic assumptions. The simplest theory is the Classical Plate Theory (CPT), which neglects transverse shear and normal strains. The theory leads to underestimations of the static deflections and overestimations of the vibration frequencies in structures which are not slender. The kinematic description of the CPT is improved in the first-order theories, which assume constant transverse strains across the thickness, and in the higher order theories. The equivalent single layer theories have been presented and discussed in many review papers over the years [6, 7].

The first-order shear deformation theory (FSDT) assumes constant transverse displacements and in-plane displacements which are linear functions of the thickness coordinate. This implies constant transverse shear strains and zero transverse normal strains [8]. The first-order shear, first-order normal deformation theory (FSNDT) additionally accounts for the transverse compressibility of the layers and assumes linear transverse displacements across the thickness, which implies thickness-wise constant transverse normal strains [9]. In dynamic problems, different assumptions are made to account for the inertia effects, by including or neglecting the rotational inertia in the dynamic equilibrium equations.

All first-order theories introduce *shear* and/or *normal correction factors* to partly overcome the limitations of the kinematic assumptions and improve predictions for certain loadings and frequency ranges. While in statically determinate problems the transverse stresses may be derived quite accurately a posteriori through the imposition of the local equilibrium equations, correction factors are needed for the accurate definition of the displacement field, the solution of statically indeterminate problems and vibration and wave propagation analyses. With the inclusion of the correction factors, the first-order theories offer the best compromise between accuracy, efficacy, and computational costs for a wide class of problems, even for moderately thick laminates. This explains their success within the engineering community.

The *correction factors* are introduced to modify the transverse shear and normal stiffnesses, which relate the transverse shear and normal stress resultants to the transverse shear and normal strains; the strains are derived from the displacement components through compatibility and are constant through the thickness. In a cross-ply laminated plate with $x_1 - x_2 - x_3$ the principal material directions and x_3 the thickness direction, the shear correction factors, k_{44} and k_{55}, of FSDT are introduced into the constitutive equations,

$$Q_1 = k_{55}^{ESL} \int_h C_{55} dx_3 (\varphi_1 + w_{0,1})$$

$$Q_2 = k_{44}^{ESL} \int_h C_{44} dx_3 (\varphi_2 + w_{0,2}), \tag{1}$$

which relate the transverse shear forces, $Q_i(x_1, x_2) = \int_h \sigma_{i3} dx_3$, with $i = 1, 2$, to the transverse strains, $\gamma_{i3}(x_1, x_2) = (\varphi_i + w_{0,i})$, where $w_0(x_1, x_2)$ is the transverse displacement, $\varphi_i(x_1, x_2)$ the rotation of the normal to the reference surface, and C_{jj}, with $j = 4, 5$, the components of the stiffness matrix. In the same cross-ply laminate, an additional normal correction factor, k_{33}^{ESL}, is introduced if the transverse compressibility of the layers is accounted for in accordance with a first-order theory (FSNDT) and the transverse displacement is assumed as $w(x_1, x_2, x_3) = w_0(x_1, x_2) + \varphi_3(x_1, x_2) x_3$. The factor in inserted into the constitutive equation which relates transverse normal force and transverse normal strain, φ_3, in a purely extensional motion of a plate of infinite extent:

$$N_3 = k_{33}^{ESL} \int_h C_{33} dx_3 (\varphi_3) \tag{2}$$

where $N_3(x_1, x_2) = \int_h \sigma_{33} dx_3$ and C_{33} the stiffness component [2]. Under general loading conditions the constitutive Eq. (2) modifies to account for the effects of the in-plane normal strains, e.g., [9]. Additional correction factors are required/introduced for plates under general loading conditions or with arbitrary stacking sequences, namely k_{45} in the FSDT, which relates the transverse shear force, Q_2, to the shear strain γ_{13}, or k_{13}, k_{23} in a FSNDT, which relate the transverse normal force, N_3, to the normal in-plane strains, $\varepsilon_{11}, \varepsilon_{22}$.

Many different approaches have been proposed over the years to define the correction factors of first-order theories for homogeneous and layered beams, plates and shells, and focus has been on the derivation of shear correction factors. The methods use static or dynamic approaches and for layered structures, they date back to the original works by Yang et al. [8], based on dynamic considerations, and by Chow [10] and Whitney [11], based on the statical considerations. The methods extend to layered structures the methods previously proposed for homogeneous structures by Reissner [12] and Mindlin [1].

The *static methods* are mostly based on the energy approaches and follow and extend the method in [10, 11], which defines the shear correction factors in layered plates subjected to cylindrical bending conditions by matching the shear strain-energy density obtained from the constitutive equations, Eq. (1), and that obtained from the transverse shear stresses which satisfy three-dimensional equilibrium; these stresses are related to the bending stresses/moment, and, through global equilibrium, to the transverse shear forces. The shear correction factors depend on the inhomogeneous material structure and layup and may differ, even

substantially, from the value $5/6 = 0.833$, which is obtained for homogeneous isotropic or orthotropic structures.

For general plate problems, the closed-form derivation in [10, 11] is not applicable, since the transverse shear forces are not known a priori, and depend on the shear factor themselves. The definition of the correction factors then become problem dependent. An iterative procedure (predictor–corrector) has been developed in [13] to define accurate correction factors starting from an initial guess and the procedure has been extended and implemented into a finite element framework for the solution of problems with complex geometries [14].

The literature on *dynamic methods* for the derivation of dynamic correction factors of first-order laminate structural theories is less extended, mainly because of the complexities involved in the derivation of exact solutions. For the derivation of the shear correction factors, some authors directly extend to dynamic problems the energy approach formulated for static problems, either by neglecting the rotary inertia in the derivation of the correction factors [10] or by accounting for the inertia terms within an iterative solution procedure [13]. The correction factors derived through these approaches are satisfactory for low modes of vibration in slender structures where the influence of shear deformations is small.

Other dynamic methods are based on the wave propagation analyses and extend to layered structures the method originally proposed by Mindlin for homogeneous crystal plates [1]. The shear correction factor is derived by imposing that the frequency of the first thickness-shear mode of propagation, predicted by the approximate structural theory, matches that of 3D elasticity, which is derived in closed form for homogeneous plates. The first thickness-shear mode is a mode of wave propagation in plates of the infinite extent which is characterized by anti-symmetric in-plane vibrations in the absence of transverse displacements and its frequency coincides with the cut-off frequency of the first cut-off frequency mode of propagation of Rayleigh–Lamb waves. At the cut-off frequency, there are important changes in the lowest flexural spectrum due to a strong coupling between flexural and shear-dominated modes. The shear correction factor obtained by matching the cut-off frequency predicted by the FSDT and the exact elasticity solution in a homogeneous plate is $\pi^2/12 = 0.822$. Using this factor extends the range of frequencies for which the first-order theory accurately predicts the lowest modes [15]. The normal correction factor may be defined using a similar procedure by matching the cut-off frequency of the first thickness-stretch mode of propagation [2, 9]. The first thickness-stretch mode is a symmetric wave propagation mode characterized by the absence of in-plane displacements and its first cut-off frequency coincide with the cut-off frequency of the second lowest cut-off frequency mode of Rayleigh–Lamb waves propagating in the plate. The normal correction factor obtained by matching the cut-off frequency predicted by FSNDT and the exact elasticity solution in a homogeneous plate is $\pi^2/12 = 0.822$.

The main difficulty in extending the method proposed by Mindlin to layered structures is that explicit expressions for the frequencies of the first thickness-modes are not available. A numerical solution of the frequency equation is required for

layered media, even with only two or three layers [8, 16], and in media, with a larger number of layers the frequencies are typically obtained using a matrix formalism and systematic computational procedures, e.g., transverse matrix method. The numerical solution of the elasticity frequency equation of the thickness-mode of vibration for bilayer media has been used in [8, 16] to define shear and normal correction factors. A transverse matrix method and a trial and error procedure have been applied in [17, 18] to define the thickness-shear frequencies and related shear correction factors for laminated plates with many layers and different layups. These results first highlighted the important effects that stacking sequence, number of layers, and material inhomogeneities have on the dynamic shear correction factors.

Another approach for the derivation of dynamic correction factors has been originally proposed by Stephen for homogeneous beams [19] and plates [20]. The method defines the best shear correction factor as the coefficient which provides agreement between the phase velocity associated to the lowest flexural mode of vibration and the exact Rayleigh–Lamb solution in the limit of the long wavelengths in plates of infinite extent. The method uses a consistent truncation procedure applied to the frequency equations and for a homogeneous isotropic plate yields a correction factor equal to $5/(6-\nu)$, with ν the Poisson coefficient, which gives 0.877, 0.862, 0.833 for ν equal to 0.3, 0.2, 0, respectively. The extension of this approach to layered systems has been suggested in [21] as the natural way to determine the dynamic shear correction factors of first-order theories for layered structures. Unfortunately, the complexities in the derivation of the elasticity solution for the lowest flexural branch make the approach scarcely applicable.

3 Multiscale Homogenized Structural Model

The first thickness-modes of wave propagation in cross-ply laminated plates are analyzed using the homogenized structural model which has been formulated in [4] for wide plates with imperfect interfaces and delaminations. The model is based on the original zig-zag theory formulated by Di Sciuva in [5] for fully bonded plates, and on the models in [22–24], where first attempts to apply the zig-zag theories to plates with imperfect interfaces were presented (the models were energetically inconsistent and have been corrected in [25]).

The homogenized model [4] has been applied to study the propagation of plane-strain Rayleigh–Lamb waves in multilayered plates of infinite in-plane extent and thickness h (Fig. 1) in [3], and the effects of interfacial imperfections on wave propagation modes and dispersion curves have been investigated; the solutions were limited to transversally incompressible plates with sliding interfaces. In this paper, the analysis is extended to account for the transverse compressibility of the layers, following [4], and used to define correction factors of ESL theories for fully bonded plates through the matching of the cut-off frequencies of the lowest cut-off frequency modes of Rayleigh–lamb waves.

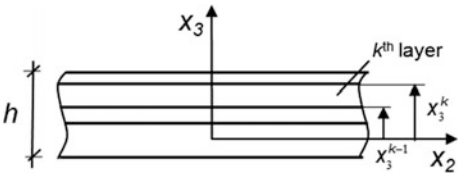

Fig. 1 Layered composite plate with n unequal orthotropic layers with principal material directions parallel to the geometrical axes

The plate in Fig. 1 consists of n layers joined by $n-1$ zero-thickness interfaces. The thickness of the layer k, with $k=1, \ldots, n-1$ numbered from bottom to top, is ${}^{(k)}h$ and the coordinates x_3^{k-1} and x_3^k defines its lower and upper interfaces. The interfaces are assumed as mathematical surfaces where the interfacial tractions and displacements are continuous while the materials properties may change discontinuously. The following assumptions are applied: plane-strain parallel to the plane $x_2 - x_3$; linearly elastic and orthotropic layers with principal material directions parallel to the geometrical axes and ${}^{(k)}C_{ij}$ the stiffness coefficients with respect to the axes of material symmetry, $i,j=2,3,4$; in-plane displacements which are piece-wise linear functions of the through-thickness coordinate (first-order theory); fully bonded layers.

The following small-scale displacement field is assumed in the generic layer k at the coordinate $\mathbf{x}=\{x_1,x_2,x_3\}^T$:

$$
\begin{aligned}
{}^{(k)}v_2(x_2,x_3,t) &= v_{02}(x_2,t)+x_3\varphi_2(x_2,t)+\sum_{i=1}^{k-1}\Omega_2^i(x_2)(x_3-x_3^i)\\
{}^{(k)}v_3(x_2,x_3,t) &= w_0(x_2,t)+x_3\varphi_3(x_2,t)+\sum_{i=1}^{k-1}\Omega_3^i(x_2)(x_3-x_3^i)
\end{aligned}
\tag{3}
$$

where $v_{02}(x_2,t)$, $w_0(x_2,t)$, $\varphi_2(x_2,t)$ and $\varphi_3(x_2,t)$ define the global displacement field, which is continuous with continuous derivatives in the thickness direction and coincides with the displacement field of first-order shear, first-order normal deformation theory, FSNDT. This global field is enriched by local contributions, given by the terms in the summations on the right-hand side. The functions $\Omega_j^i(x_2)(x_3-x_3^i)$ for $i=1, \ldots, k-1$ and $j=2,3$ define a piece-wise linear displacement field in x_3, which is introduced to reproduce the zig-zag patterns due to the multilayered material structure. In plates which are transversally incompressible, $\varphi_3=\Omega_3^i=0$ and the global displacements coincide with those of the FSDT.

The small-scale kinematic description of the problem is defined by a total of $4+2\times(n-1)$ unknown functions in the n layers. The $2\times(n-1)$ small-scale unknowns are defined as functions of the global unknowns, v_{02}, w_0, φ_2 and φ_3, by imposing, a priori, continuity of shear and normal tractions at the $n-1$ layer interfaces. The resulting macro-scale displacement field [4] is presented below:

- transversally incompressible plates:

$$\begin{aligned} {}^{(k)}v_2(x_2,x_3,t) &= v_{02}(x_2,t) + x_3\varphi_2(x_2,t) + [w_{0,2}(x_2,t) + \varphi_2(x_2,t)]R^k_{S22}(x_3) \\ {}^{(k)}v_3(x_2,x_3,t) &= w_0(x_2,t) \end{aligned} \tag{4}$$

- transversally compressible plates:

$$\begin{aligned} {}^{(k)}v_2(x_2,x_3,t) &= v_{02}(x_2,t) + x_3\varphi_2(x_2,t) \\ &\quad + [w_{0,2}(x_2,t) + \varphi_2(x_2,t)]R^k_{S22}(x_3) + \varphi_{3,2}(x_2,t)R^k_{N22}(x_3) \\ {}^{(k)}w(x_2,x_3,t) &= w_0(x_2,t) + \varphi_3(x_2,t)\left[x_3 + \sum_{i=1}^{k-1}\Lambda^{(i)}_{33}(x_3 - x^i_3)\right] \end{aligned} \tag{5}$$

where the coefficients, R^k_{S22}, R^k_{N22}, $\Lambda^{(i)}_{33}$, which control the zig-zag contributions, depend on geometry and layup and can be calculated a priori for any given laminate, are defined in Eq. (15) of the Appendix 1. The displacements depend on the global variables only. If the zig-zag contributions are neglected, which yields $R^k_{S22} = R^k_{N22} = \Lambda^{(i)}_{33} = 0$, Eq. (4) defines the displacement field of FSDT and Eq. (5) the displacement field of FSNDT.

The macro-scale displacements are used, along with the compatibility and constitutive equations of the layers, to derive the weak form of the dynamic equilibrium equations through Hamilton principle [4]. In plates with transverse incompressibility, $\varphi_3 = 0$, the system of equations can be decoupled to show that the transverse behavior is controlled by a sixth-order equation in w_0, which reduces to the classical fourth-order equation of first-order shear deformation theory when the zig-zag effect is neglected [26]. A similar behavior is observed in [27] where highly contrasted laminated plates are studied through a multiscale asymptotic approach.

To analyze the propagation of continuous, straight-crested waves in the x_2 direction, solutions of the form $y(x_2,t) = Y\exp i(kx_2 - \omega t)$ are assumed, with $y(x_2,t)$ the displacement variable and Y an unknown constant; k, the wave number, and ω, the radian frequency, are related to the wavelength, Λ, frequency, f, and the wave speed, c, by $\Lambda = 2\pi/k$, $f = \omega/2\pi$ and $c = \omega/k$. Substitution into the dynamic equilibrium equations [3] yields a system of homogeneous equations in the unknown constants whose nontrivial solution gives the frequency equation of the problem. The closed-form solution and relevant results have been presented in [3] for plates with transverse incompressibility of the layers and sliding interfaces.

In accordance with the assumed displacement field, Eq. (5), four wave types are operative in a multilayered plate. These types correspond to the two lowest branches of all frequency curves and to the branches of the first two cut-off frequencies. The theory also describes the first thickness-modes of propagation.

4 Thickness-Shear and Thickness-Stretch Propagation Modes

The *thickness-shear mode* is a wave propagation mode characterized by the absence of transverse displacements, $v_3 = 0$, and by in-plane displacements which are independent of the in-plane coordinates, $v_2 = v_2(x_3, t)$ [1]. The macro-scale displacement field, Eqs. (4) and (5), simplify in this mode and $w_0 = 0$, $\varphi_3 = 0$, $v_{02} = v_{02}(t)$ and $\varphi_2 = \varphi_2(t)$. The dynamic equilibrium equations of the homogenized theory (Eq. (22) in [4]) reduce to:

$$\begin{aligned} R_0 \ddot{v}_{02} + R_1 \ddot{\varphi}_2 &= 0 \\ A_{44}\varphi_2 + R_1 \ddot{v}_{02} + R_2 \ddot{\varphi}_2 &= 0 \end{aligned} \tag{6}$$

where the coefficients R_0, R_1, R_2, A_{44}, which depend on the elastic constants, inertia, and stacking sequence, are defined in Eq. 16 of the Appendix 1. The equations reduce to those of the FSDT [8] if the coefficients are modified as in Eq. 17 to neglect the zig-zag contributions.

The *thickness-stretch mode* is a propagation mode characterized by nonzero transverse displacements and the absence of in-plane displacements, $v_2 = 0$ and $v_3 = v_3(x_3, t)$. The macro-scale displacement field, Eq. (5), simplifies in this mode and $v_{02} = 0$, $\varphi_2 = 0$, $w_0 = w_0(t)$ and $\varphi_3 = \varphi_3(t)$. The dynamic equilibrium equations of the homogenized theory (Eq. 20 in [4]) reduce in this limit to:

$$\begin{aligned} R_0 \ddot{w}_0 + R_1^N \ddot{\varphi}_3 &= 0 \\ A_{33}\varphi_3 + R_1^N \ddot{w}_0 + R_2^N \ddot{\varphi}_3 &= 0 \end{aligned} \tag{7}$$

where the coefficients R_1^N, R_2^N, A_{33}, are defined in Eq. 16 of the Appendix 1. The equations reduce to those of the FSNDT [2, 9] if the coefficients are modified as in Eq. 17 to neglect the zig-zag contributions.

These thickness-shear and -stretch modes are the asymptotic limits, for infinitely long wavelengths, $k \to 0$, of the first two cut-off frequency modes of propagation of plane-strain Rayleigh–Lamb waves [3]. The radian frequency associated to the thickness-shear mode, Eq. (6), can be calculated by assuming solutions of the form:

$$v_{02}(t) = V_{02} \exp(i\omega^{SH} t),\ \varphi_2(t) = \Phi_2 \exp(i\omega^{SH} t),\ w_0 = \varphi_3 = 0 \tag{8}$$

and that of the thickness-stretch mode, Eq. (7), by assuming:

$$w_0(t) = W_0 \exp(i\omega^{ST} t),\ \varphi_3(t) = \Phi_3 \exp(i\omega^{ST} t),\ \mathrm{v}_{02} = \varphi_2 = 0 \tag{9}$$

with $V_{02}, \Phi_2, W_0, \Phi_3$ unknown constants. Substituting, Eqs. (8) and (9) into the equations of motion, (6) and (7), yields the frequency equations and associated radian cut-off frequencies:

$$\begin{cases} (\omega^{SH})^4 \left(R_2 - \dfrac{R_1^2}{R_0} \right) - (\omega^{SH})^2 A_{44} = 0 \\ \omega_{c.o.}^{SH} = \left(\dfrac{A_{44}}{R_2 - R_1^2/R_0} \right)^{1/2} \end{cases} \quad (\text{thickness} - \text{shear mode}) \qquad (10)$$

$$\begin{cases} (\omega^{ST})^4 \left(R_2^N - \dfrac{\left(R_1^N\right)^2}{R_0} \right) - (\omega^{ST})^2 A_{33} = 0 \\ \omega_{c.o.}^{ST} = \left(\dfrac{A_{33}}{R_2^N - \left(R_1^N\right)^2/R_0} \right)^{1/2} \end{cases} \quad (\text{thickness} - \text{stretch mode}) \qquad (11)$$

The frequency of the thickness-shear mode depends on the elastic constants and density of the layers, the layup, and the shear correction factor k_{44}, which appears in A_{44}, Eq. 16. In a homogeneous orthotropic plate, Eq. 10 yield $\omega_{c.o.}^{SH} = \sqrt{k_{44} C_{44}/(\rho r^2)}$ with $r = h/\sqrt{12}$. The shear correction factor k_{44} can be calculated so as to enforce the equivalence with the exact elasticity solution, $\omega_{co}^{SH} = \pi/h\sqrt{C_{44}/\rho}$ [1], which yields $k_{44} = \pi^2/12$. Similarly, the frequency of the thickness-stretch mode depends on the correction factor, k_{33}. Assuming $k_{33} = \pi^2/12$ in a homogeneous plate enforces the equivalence with the exact solution, $\omega_{c.o.}^{ST} = \pi/h\sqrt{C_{33}/\rho}$ with C_{33} the P-waves modulus [2]. Explicit expressions for the frequencies similar to those presented above have been derived in [28] by means of a higher order layer-wise zig-zag theory.

The cut-off frequencies associated with the first-order shear deformation theory and first-order shear and normal deformation theory, $\omega_{c.o.}^{SH,ESL}$ and $\omega_{c.o.}^{ST,ESL}$, can be easily recovered from Eqs. (10-11) by using the modified coefficients given in Eq. (17).

Figure 2 depicts the cut-off frequencies of Eq. 10, obtained by assuming $k_{44} = \pi^2/12$, for a plate with two fully bonded layers of thicknesses, f and c with $h = f + c$, and shear moduli in the plane $x_2 - x_3$, G_f and G_c. The dimensionless frequency is shown on varying the normalized thickness of one of the layers, f/h. The results are compared with the lowest root of the thickness-shear frequency equation of two-dimensional elasticity [8, 16], which is given in implicit form in Eq. 18 of Appendix 2. It is worth noting that the elasticity equation requires a numerical solution but for the limit case of a homogeneous plate and that it has an infinite number of roots.

Figure 2a refers to $G_c = G_f/2$ and $\rho_c = \rho_f$, which is the case examined in [8]. These ratios could represent a classical [0/90] cross-ply laminate with two unidirectionally reinforced carbon-epoxy layers. Under this assumption, the homogenized model accurately reproduces the exact solutions for all relative thicknesses. Results are also presented for the frequency obtained using first-order shear deformation plate theory and assuming $k_{44}^{ESL} = \pi^2/12$; they are also quite accurate for most relative thicknesses of the layers and the maximum relative error is around

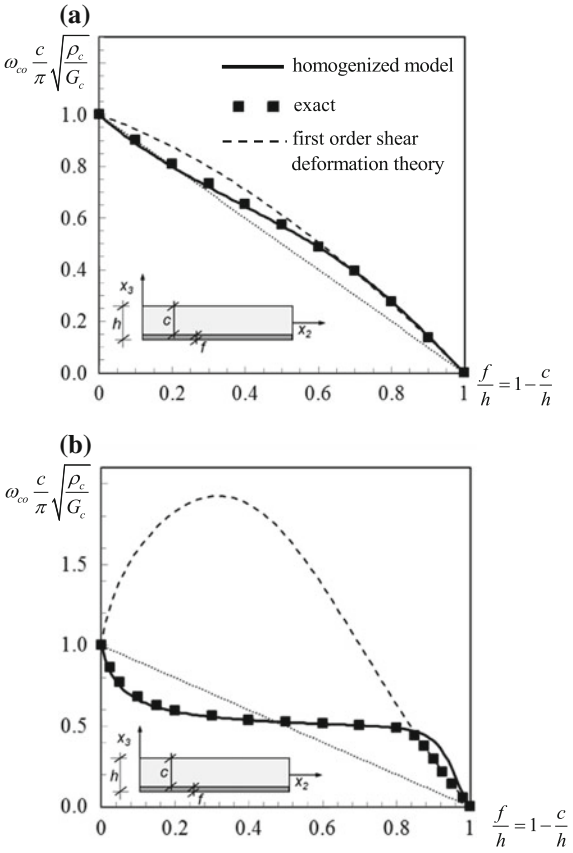

Fig. 2 Dimensionless cut-off frequency of thickness-shear mode in a bilayer with f and c the thicknesses of the layers, $h = f + c$, and G_f and G_c the corresponding shear moduli. Results obtained assuming $k_{44} = k_{44}^{ESL} = \pi^2/12$. **a** $G_c = G_f/2$ and $\rho_c = \rho_f$ (e.g., cross-ply laminate); **b** $G_c = 0.02G_f$ and $\rho_c = 0.15\rho_f$(e.g., for small f/h: composite sandwich with foam core). (after [3])

11%. The dotted line in the figure corresponds to a homogeneous plate of thickness c and material properties, G_c and ρ_c, for which $\omega_{c.o.}^{SH} = \pi/c(G_c/\rho_c)^{1/2}$ and highlights the effect of the presence of the lower layer on wave propagation.

Figure 2b refers to an extreme case, which could represent materials used in composite sandwich plates with foam cores (e.g., carbon-epoxy faces with Divinycell H250 foam core), with $G_c = 0.02G_f$ and $\rho_c = 0.15\rho_f$. The discrepancies between the exact solution and first-order shear deformation theory, in this case, are large over most relative thicknesses and the relative percent error goes up to 250%. This result confirms the need for a substantial modification of the shear correction factor derived for homogeneous materials when dealing with multilayered systems, where the shear rigidities of the layer largely differ, as already been noted in the literature [29]. The solution of the multiscale homogenized model obtained using $k_{44} = \pi^2/12$, are instead very accurate over most of the domain, for $c = (0.15 \div 1)h$. In the limiting case of a bilayer with a thin soft layer, $c = (0 \div 0.15)h$, the relative error between the homogenized model and the exact solution increases and goes up

to 40%. In this region, the influence of the thin soft layer becomes negligible and predictions using the first-order shear deformation theory with $k_{44}^{ESL}=\pi^2/12$ are instead very accurate.

Substituting the frequency of the first thickness-shear mode, Eq. (10), into the equations of motion, Eq. 6, shows that in a layered plate with a centroidal reference system and fully bonded layers, the motion is characterized by $W_0=0$ and $V_{02}, \Phi_2 \neq 0$, with $V_{02}=-(R_1/R_0)\Phi_2$, so that:

$$\begin{aligned} {}^{(k)}v_2(x_3,t) &= (-R_1/R_0 + x_3 + R_{S22}^k)\varphi_2(t) \\ {}^{(k)}v_3 &= 0 \end{aligned} \tag{12}$$

for $k=1, \ldots, n$. The global displacement field, which is controlled by the global rotation φ_2 as in a homogeneous plate, is enriched by local zig-zag contributions through R_{S22}^k, which varies in each layer. If the first-order shear deformation theory is used to define the cut-off frequency, Eq. (10) with coefficient given in Eq. (17), then Eq. 6 shows that the motion is characterized by linearly varying in plane displacements ${}^{(k)}v_2(x_3,t)=(-R_1/R_0+x_3)\varphi_2(t)$ and ${}^{(k)}v_3=0$ for $k=1, \ldots, n$ and coincides with the motion of an equivalent homogeneous plate with effective moduli when $R_1=0$. The first-order shear deformation theory is unable to describe the zig-zag fields which characterize the response of layered media.

Figure 3 shows the longitudinal displacement fields as predicted by the homogenized model and the first-order shear deformation theory for the case $f=h/3$ and $c=2/3h$ in Fig. 2b. The displacements are normalized to the maximum values at $x_3=h/2$. The homogenized model captures the zig-zag field due to the highly inhomogeneous material structure.

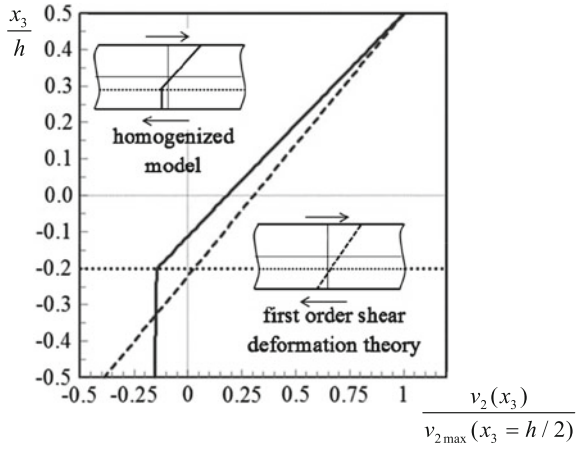

Fig. 3 Bilayer plate examined in Fig. 2 with $f=h/3$. Through-thickness in plane displacements derived with the approximate structural theories; the homogenized model captures the zig-zag pattern due the inhomogeneous material structure. (modified after [3])

Similar results and conclusions can be drawn by comparing the frequency of the thickness-stretch mode of propagation calculated using elasticity theory, Eq. 18 in Appendix 2, the homogenized multiscale model and first-order normal deformation theory [3].

5 Dynamic Correction Factors from Thickness-Modes

Given the excellent results obtained using the homogenized multiscale theory to define the frequencies of the thickness-shear and -stretch modes in cross-ply laminated plates, Eqs. 10 and 11, we propose to use these frequencies as matching frequencies for the evaluation of the shear and normal correction factors of ESL theories for plane-strain problems in cross-ply laminates, $k_{44}^{ESL}, k_{33}^{ESL}$. The correction factors can be used in the constitutive relations, Eqs. (1) and (2). The advantage compared with the use of elasticity solutions relies in the explicit expressions, Eqs. (10) and (11), which lead to explicit expressions for the correction factors of plates with an arbitrary number of layers and arbitrary layup. Imposing $\omega_{c.o.}^{SH,ESL} = \omega_{c.o.}^{SH}$ and $\omega_{c.o.}^{ST,ESL} = \omega_{c.o.}^{ST}$, yields:

$$\frac{k_{44}^{ESL}}{\pi^2/12} = \frac{C_{44}^P}{\int_h C_{44} dx_3} \frac{R_2^{ESL} R_0 - (R_1^{ESL})^2}{R_2 R_0 - (R_1)^2} \text{ (shear correction factor)} \tag{13}$$

$$\frac{k_{33}^{ESL}}{\pi^2/12} = \frac{C_{33}^P}{\int_h C_{33} dx_3} \frac{R_2^{N,ESL} R_0 - (R_1^{N,ESL})^2}{R_2^N R_0 - (R_1^N)^2} \text{ (normal correction factor)} \tag{14}$$

With coefficients given in the Appendix 1. The correction factors for ESL theories have been normalized to the correction factors of homogeneous plates, $k_{44} = k_{33} = \pi^2/12$ to highlight the influence of the inhomogeneous material structure on the behavior. The accuracy of the correction factor in Eq. (13) is verified through comparison with the correction factors obtained by matching the exact frequencies of 2D elasticity for the bilayer media examined above. Figure 4 shows the shear correction factors which should be used in a first-order shear deformation theory to match the thickness-shear frequency of a plate with two fully bonded layers. The results compare predictions obtained numerically using the exact frequency Eq. (18), and the frequency in Eq. 10 (homogenized model). The correction factors obtained using the homogenized structural model are very accurate over most of the domain but for $c/h = (0 \div 0.15)$ when the material of Fig. 2a is considered. This domain describes a plate with a very thin layer much more shear deformable of the thicker layer. In this limiting configuration, the effects of the inhomogeneity are negligible and the required correction factor, as predicted by 2D elasticity, coincides with that of a homogeneous plate. The inaccurate behavior predicted by the homogenized model, which is probably a consequence of the assumed first-order kinematic description, needs to be further investigated.

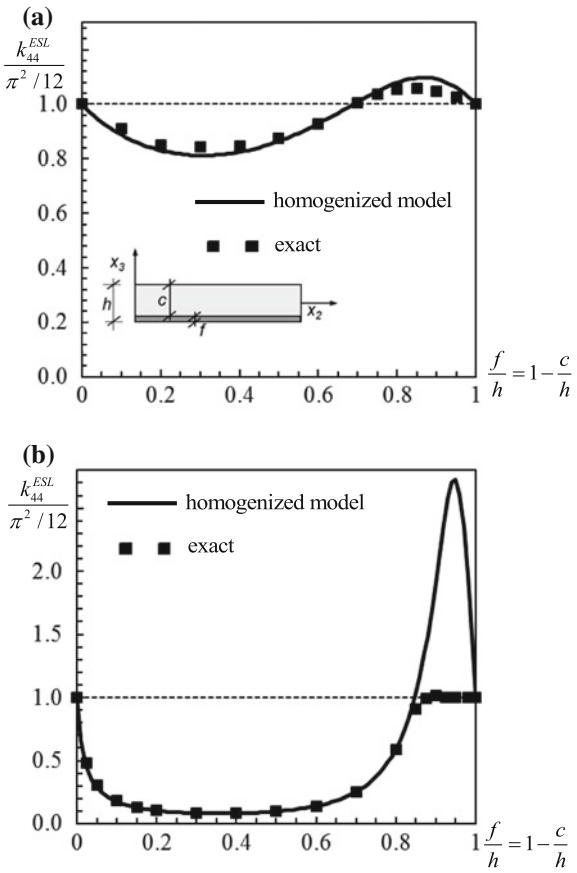

Fig. 4 Correction factors of first-order shear deformation theory necessary to match the first thickness-shear cut-off frequencies calculated using: homogenized model (solid line), Eq. 13; 2D elasticity (boxes) (Eq. 18 and [8, 16]). Correction factor of homogeneous plate: dotted line. **a** $G_c = G_f/2$ and $\rho_c = \rho_f$ (e.g., cross-ply laminate); **b** $G_c = 0.02G_f$ and $\rho_c = 0.15\rho_f$ (e.g., for small *f*/*h*: composite sandwich with foam core). (modified after [30])

6 Conclusions

An analytical strategy has been proposed for the derivation of dynamic shear and normal correction factors of first-order equivalent single layer theories for layered composite plates with cross-ply layups. The strategy applies the method originally proposed by Mindlin for homogeneous plates, which defines the best correction factors as those which lead to predictions of the cut-off frequencies of the first thickness-shear and thickness-stretch modes which match those obtained through 2D elasticity. Since closed-form elasticity solutions are not available for layered plates and the derivation would require complex computational approaches, we propose the use of the explicit expressions of the cut-off frequencies obtained through a multiscale homogenized structural theory. The accuracy of the results has been verified against elasticity solutions for highly inhomogeneous bilayers.

The proposed strategy is directly applicable to define the dynamic shear correction factors of first-order shear deformation theory for cross-ply beams or wide

plates deforming in cylindrical bending. The procedure can be extended to define the shear correction factors of plates with arbitrary layup deforming in cylindrical bending, for which the additional definition of the mixed correction factor is required. For plates under general dynamic loading conditions, the dynamic correction factors defined using the analytic strategy can be used for an approximate description of the behavior or as tentative values within iterative predictor–corrector procedures, as typically done for static correction factors. The closed-form results which can be obtained with the multiscale homogenized model also offer the possibility of using different strategies for the definition of the dynamic correction factors; they could be used, for instance, for matching the phase velocities of the first flexural mode in the limit of the infinitely long wavelengths, as suggested in [19] for homogeneous plates.

Acknowledgements The support of the U.S. Office of Naval Research, ONR, grants no: N00014-14-1-0254 and N00014-17-1-2914 monitored by Dr. Y. D. S. Rajapakse and of the (MURST) Italian Department for University and Scientific and Technological Research, MIUR Prin15 project 2015LYYXA8, are gratefully acknowledged.

Appendix 1

The coefficients in the expressions of the macro-scale displacement field of the homogenized model assuming perfect bonding of the layers are [4]:

$$R^k_{S22}(x_3) = \sum_{i=1}^{k-1} \left[\Lambda_{22}^{(1;i)} \left(x_3 - x_3^i \right) \right]$$

$$R^k_{N22}(x_3) = \sum_{i=1}^{k-1} \left[\Lambda_{22}^{(1;i)} x_3^1 + \sum_{l=2}^{i} \Lambda_{22}^{(l;i)} \left(x_3^l - x_3^{l-1} \right) \left(1 + \sum_{j=1}^{l-1} \Lambda_{33}^{(j)} \right) \right] \left(x_3 - x_3^i \right)$$

$$\Lambda_{22}^{(1;i)} = {}^{(1)}C_{44} \left(\frac{1}{{}^{(i+1)}C_{44}} - \frac{1}{{}^{(i)}C_{44}} \right) \tag{15}$$

$$\Lambda_{33}^{(i)} = - {}^{(1)}C_{33} \left(\frac{{}^{(i+1)}C_{33} - {}^{(i)}C_{33}}{{}^{(i+1)}C_{33}\,{}^{(i)}C_{33}} \right)$$

The coefficients in the equations of the homogenized model which describe the thickness-shear and -stretch modes assuming perfect bonding of the layers are given below [3, 30]:

$$(R_0, R_1, R_2, R_1^N, R_2^N) = \int_h \rho(1, x_3, x_3^2, x_3, x_3^2) dx_3 + (0, R^{0S}, 2R^{1S} + R^{S2}, R^{0N}, 2R^{1N} + R^{N2})$$

$$A_{44} = k_{44} C_{44}^P,$$

$$A_{33} = k_3 C_{33}^P,$$

$$C_{44}^P = \sum_{k=1}^{n} {}^{(k)}C_{44} \int_{x_3^{k-1}}^{x_3^k} \left(1 + \sum_{i=1}^{k-1} \Lambda_{22}^{(1;i)}\right)^2 dx_3$$

$$C_{33}^P = \sum_{k=1}^{n} {}^{(k)}C_{33} \int_{x_3^{k-1}}^{x_3^k} \left(1 + \sum_{i=1}^{k-1} \Lambda_{33}^{(j)}\right)^2 dx_3$$

$$R^{rS} = \sum_{k=1}^{n} {}^{(k)}\rho \int_{x_3^{k-1}}^{x_3^k} (x_3)^r \sum_{i=1}^{k-1} \left[\Lambda_{22}^{(1;i)}\left(x_3 - x_3^i\right)\right] dx_3$$

$$R^{S2} = \sum_{k=1}^{n} {}^{(k)}\rho \int_{x_3^{k-1}}^{x_3^k} \left(\sum_{i=1}^{k-1} \left[\Lambda_{22}^{(1;i)}\left(x_3 - x_3^i\right)\right]\right)^2 dx_3 \tag{16}$$

$$R^{rN} = \sum_{k=1}^{n} {}^{(k)}\rho \int_{x_3^{k-1}}^{x_3^k} (x_3)^r \sum_{i=1}^{k-1} \Lambda_{33}^{(i)}\left(x_3 - x_3^i\right) dx_3$$

$$R^{N2} = \sum_{k=1}^{n} {}^{(k)}\rho \int_{x_3^{k-1}}^{x_3^k} \left\{\sum_{i=1}^{k-1} \Lambda_{33}^{(i)}\left(x_3 - x_3^i\right)\right\}^2 dx_3$$

Under the assumptions of the first-order equivalent single layer theories the coefficients above simplify as:

$$(R_0, R_1^{ESL}, R_2^{ESL}, R_1^{N,ESL}, R_2^{N,ESL}) = \int_h \rho(1, x_3, x_3^2, x_3, x_3^2) dx_3,$$

$$A_{44}^{ESL} = k_{44}^{ESL} \int_h C_{44} dx_3,$$

$$A_{33}^{ESL} = k_{33}^{ESL} \int_h C_{33} dx_3. \tag{17}$$

Appendix 2

The elasticity frequency equation of the thickness-shear mode of propagation in an isotropic bilayer with f and c the thicknesses of the layers and G_f and G_c the corresponding shear moduli in the plane $x_2 - x_3$, has been derived in [8, 16] as the limit for wavelengths approaching infinity of the Rayleigh–Lamb equation:

$$\beta_f \sin(\beta_f f) \cos \beta_c c + \left(G_c/G_f\right) \beta_c \sin(\beta_c c) \cos(\beta_f f) = 0 \tag{18}$$

with $\beta_i^2 = \omega^2 \rho_i / G_i$. The exact cut-off frequency of the first thickness-stretch mode for a bilayer with M_f and M_c the P-waves moduli are defined by the first root of the frequency equation:

$$\left(\alpha_c/\alpha_f\right) \beta_f^2 \sin(\alpha_f f) \cos(\alpha_c c) + \left(G_c/G_f\right) \beta_c^2 \sin(\alpha_c c) \cos(\alpha_f f) = 0 \tag{19}$$

with $\alpha_i^2 = \omega^2 \rho_i / M_i$. The P-waves modulus in an isotropic material is given by $M_i = C_{33i} = \frac{E_i(1-\nu_i)}{(1+\nu_i)(1-2\nu_i)}$.

References

1. Mindlin, R. D. (1951). Thickness-shear and flexural vibrations of crystal plates. *Journal of Applied Physics, 22,* 316.
2. Kane, T. R., & Mindlin, R. D. (1956). High-frequency extensional vibrations of plates. *Journal of Applied Mechanics, 23,* 277–283.
3. Massabò, R. (2017). Propagation of Rayleigh-Lamb waves in multilayered plates through a multiscale structural model. *Int Journal of Solids and Structures, 124,* 108–124.
4. Massabò, R., & Campi, F. (2014). An efficient approach for multilayered beams and wide plates with imperfect interfaces and delaminations. *Composite Structures, 116,* 311–324.
5. Di Sciuva, M. (1986). Bending, vibration and buckling of simply supported thick multilayered orthotropic plates: An evaluation of a new displacement model. *Journal of Sound and Vibrations, 105*(3), 425–442.
6. Noor, A. K., & Burton, W. S. (1989). *Assessment* of shear deformation theories for multilayered composite plates. *Applied Mechanics Reviews, 42*(1), 1–13.
7. Ghugal, Y. M., & Shimpi, R. P. (2002). A review of refined shear deformation theories of isotropic and anisotropic laminated plates. *Journal of Reinforced Plastics and Composites*, *21*(9).

8. Yang, P. C., Norris, C. H., & Stavsky, Y. (1966). Elastic wave propagation in heterogeneous plates. *International Journal of Solids and Structures, 2,* 665–684.
9. Whitney, J. M., & Sun, C. T. (1973). A higher order theory for extensional motion of laminated composites. *Journal of Sound and Vibration, 30,* 85.
10. Chow, T. S. (1971). On the propogation of flexural waves in an orthotropic laminated plate and its response to an impulsive load. *Journal of Composite Materials, 5,* 306–319.
11. Whitney, J. M. (1973). Shear correction factors for orthotropic laminates under static load. *ASME Journal of Applied Mechanics, 40*(1), 303–304.
12. Reissner, E. (1945). The effect of transverse shear deformation on the bending of elastic plates. *ASME Journal of Applied Mechanics, 12,* 69–77.
13. Noor, A. K., & Burton, W. S. (1989). Stress and free vibration analyses of multilayered composite plates. *Computers & Structures, 11,* 183–204.
14. Auricchio, F., & Sacco, E. (1999). A mixed-enhanced finite-element for the analysis of laminated composite plates. *International Journal for Numerical Methods in Engineering, 44,* 1481–1504.
15. Mindlin, R. D., & Deresiewicz, H. (1953). Timoshenko's shear coefficient for flexural vibrations of beams. Technical Report, no. 10, ONR project NR 064-388, Columbia University.
16. Jones, J. P. (1964). Wave propagation in two-layered medium. *Journal of Applied Mechanics, 31,* 213.
17. Chatterjee, S. N., & Kulkarni, S. V. (1979). Shear correction factors for laminated plates. *AIAA Journal, 17,* 498–499.
18. Chatterjee, S. N., & Kulkarni, S. V. (1978). Effects of environment damping and coupling properties of composite laminates on panel flutter, ADA055753, AFORS-TR-78-1066.
19. Stephen, N. G. (1981). Considerations on second order beam theories. *International Journal of Solids and Structures, 17,* 325–333.
20. Stephen, N. G. (1997). Mindlin plate theory: best shear coefficient and higher spectra validity. *Journal of Sound and Vibration, 202,* 539–553.
21. Liu, L., & Bhattacharya, K. (2009). Wave propagation in a sandwich structure. *International Journal of Solids and Structures, 46,* 3290–3300.
22. Cheng, Z. Q., Jemah, A. K., & Williams, F. W. (1996). Theory for multilayered anisotropic plates with weakened interfaces. *Journal of Applied Mechanics, 63,* 1019–1026.
23. Di Sciuva, M. (1997). An improved shear-deformation theory for moderately thick multilayered anisotropic shells and plates. *AIAA Journal, 35*(11), 1753–1759.
24. Librescu, L., & Schmidt, R. (2001). A general theory of laminated composite shells featuring interlaminar bonding imperfections. *International Journal of Solids and Structures*, 3355–3375.
25. Massabò, R., & Campi, F. (2015). Assessment and correction of theories for multilayered plates with imperfect interfaces. *Meccanica, 50,* 1045–1061.
26. Viverge, K., Boutin, C., & Sallet, F. (2016). Model of highly contrasted plates versus experiments on laminated glass. *International Journal of Solids and Structures, 102–103,* 238–258.
27. Nanda, N., Kapuria, S., & Gopalakrishnan, S. (2014). Spectral finite element based on an efficient layerwise theory for wave propagation analysis of composite and sandwich beams. *Journal of Sound and Vibration,* 3120–3137.
28. Pelassa, M., & Massabò, R. (2015). Explicit solutions for multi-layered wide plates beams with perfect and imperfect bonding and delaminations under thermo-mechanical loading. *Meccanica, 50,* 2497–2524.
29. Sun, C.-T., & Whitney, J. M. (1972). On theories for the dynamic response of laminated plates. In *AIAA/ASNE/SAE 13th Structures, Structural Dynamics and Materials Conference*, San Antonio, Texas, AIAA paper no. 72-398.
30. Massabò, R. (2017). Cut-off frequencies and correction factors of equivalent single layer theories. *Procedia Engineering, 199,* 1466–1471.

Blast Performance and Damage Assessment of Composite Sandwich Structures

Emily Rolfe, Mark Kelly, Hari Arora, Paul A. Hooper and John P. Dear

1 Introduction

This chapter reviews and investigates the effect of altering face-sheets of composite sandwich panels on their blast performance [1–16].

Full-scale air blast experiments on composite sandwich panels have been carried out by Arora [2, 3]. The explosive resilience of glass-fiber reinforced polymer (GFRP) face-sheets with styrene acrylonitrile (SAN) foam cores was compared to that of carbon-fiber reinforced polymer (CFRP) face-sheets with the same cores. The CFRP face-sheet panel was found to deflect less than the GFRP face-sheet panel. Both panels suffered from core damage and face-sheet core delamination whilst the GFRP face-sheet panel suffered from a large face-sheet crack. Arora [4] investigated the edgewise compressive residual strength of the panels and found that the percentage drop in strength was greater for a CFRP face-sheet panel than for a GFRP face-sheet panel, which may be an influential result if residual strength is a key design factor in material choice.

Tekalur [15] and Gardner [7] used shock tube loading to simulate blast loading and demonstrated that the incorporation of a poly-urea layer into the layup of the face-sheets of composite sandwich panels improves the blast performance of the panels. Placing poly-urea either behind the front face-sheet or behind the core reduces back face-sheet deflection and in-plane strain hence maintaining structural integrity. A water filled conical shock tube (CST) has been used by LeBlanc et al. [8] to investigate the effects of poly-urea coatings in the underwater blast. The authors

E. Rolfe · M. Kelly · H. Arora · P. A. Hooper · J. P. Dear (✉)
Department of Mechanical Engineering, Imperial College London, South Kensington Campus, London SW7 2AZ, UK
e-mail: j.dear@imperial.ac.uk

E. Rolfe
e-mail: emily.rolfe11@imperial.ac.uk

S. Gopalakrishnan and Y. Rajapakse (eds.), *Blast Mitigation Strategies in Marine Composite and Sandwich Structures*, Springer Transactions in Civil and Environmental Engineering, https://doi.org/10.1007/978-981-10-7170-6_11

subjected the panels to shock loading with peak pressures of 10 MPa and found that a thick coating on the back face improved panel response whereas a thin layer on the front face degraded the response.

Tagarielli et al. [14] created a finite element (FE) model of composite sandwich beams under shock loading and compared the results to those of a previously reported experiment. The model and experiment showed good agreement and the authors concluded that the ultimate failure of the sandwich beams, face-sheet tearing, could be predicted using a maximum principal failure strain criterion. Hence, the shock resilience of composite sandwich structures would be maximized by implementing face-sheet materials with high failure strain. The hybridization of carbon and glass fibers, or other fibrous materials, may result in a composite material that has the optimal properties of the two constituent materials. In recent years, the development of tougher fiber reinforced polymer composites through hybridization has been revived as detailed by Swolfs [13].

Characterization of carbon/glass hybrids has been carried out by some authors. Murugan et al. [9] fabricated interlaminar carbon/glass hybrids and carried out characterization using tensile strength, flexural strength, impact strength and dynamic mechanical analysis. This revealed that the stacking sequence has an effect on the flexural properties of the hybrid composite. This result could be useful for improving the blast resilience of composites by stacking the composite layers in an order that utilizes the high strength and stiffness of CFRP and the failure strain of GFRP. Song [12] also investigated the performance of interlaminar carbon/glass and carbon/aramid composites using tensile and flexural tests. Song concluded that the tensile strength was dominated by the carbon fibers and whether the second fibrous material was glass or aramid made little difference. However, Song also identified that the stacking sequence has an effect on the mechanical properties of the composite.

The performance of ultra-high molecular weight polyethylene (UHMWPE), often known by its trade name Dyneema, and carbon intralayer hybrid composites was investigated by Bouwmeester et al. [5]. The authors concluded that the impact resistance of CFRP can be greatly increased by the replacement of carbon fibers with polyethylene fibers, however, this is at the expense of flexural strength. Nevertheless, the low density of UHMWPE enables the thickness of the composite to be increased for the same weight, thus the flexural strength and stiffness are only slightly reduced for a constant weight.

Aramid and UHMWPE fibers, and their hybrids, have been the subject of ballistics research due to their superior tensile properties, such as in research by Zhang [16] and Randjbaran [11] and thus an investigation into their blast performance has been the next line of research. Fallah et al. [6] subjected a 300 mm × 300 mm Dyneema panel to a close field air blast, delivered by a disc of plastic explosive 4 (PE4). The authors found that the use of Dyneema over mild steel would reduce plate permanent deflection by 30%.

This chapter reports on three blast studies that have been carried out. The first blast study investigated the effect of GFRP face-sheets, with plies of Innegra polypropylene (PP) incorporated into the front face-sheet. These PP plies were expected to reduce the damage to the front face-sheets during blast loading.

A GFRP/PP panel was directly compared to a second panel with GFRP skins containing no PP to assess the effect of these interlayers. Both panels had a 40 mm thick polyvinyl chloride (PVC) foam core.

The second blast study used panels with GFRP face-sheets and CFRP face-sheets against an underwater blast load. The panels had 30 mm thick styrene acrylonitrile (SAN) foam cores and had a similar areal density. These face-sheet materials were compared to see the effect of the increased strength but reduced strain to failure of the CFRP skins compared to GFRP skins.

The final blast study focused on the performance of a sandwich panel with glass- and aramid-fiber hybrid skins versus a panel with GFRP skins when subjected to an underwater blast load. The panels had a 30 mm thick SAN foam core but were smaller in size compared to the panels investigated in the second study.

2 Materials and Methods

The GFRP panels for the first two blast studies were manufactured using Gurit QE1200 quadriaxial glass fiber plies using vacuum consolidation. The glass fibers were mixed with SR 8500 epoxy resin and standard hardener before a vacuum and heat were applied for curing. The GFRP skin with PP Innegra interlayers was manufactured by simply incorporating the PP plies into the layup prior to curing. This sandwich panel had an asymmetrical layup. The thickness of a cured QE1200 ply was 1 mm and that of a cured Innegra PP ply was 0.35 mm. A diagram showing a detailed layup of the different panels used in the first study is shown in Fig. 1. The CFRP panel for the second study was manufactured using Gurit XC411 biaxial plies and SR 8500 epoxy resin and standard hardener by the same vacuum consolidation method. The GFRP and CFRP panels all had cured thicknesses of approximately 2 mm.

The material properties of the face-sheets were calculated using the rule of mixtures with the constituent properties taken from material data sheets. The fiber volume fraction of the QE1200 plies and Innegra PP plies were calculated as 47% and 62%, respectively. The density and compressive strength of the PP fibers were

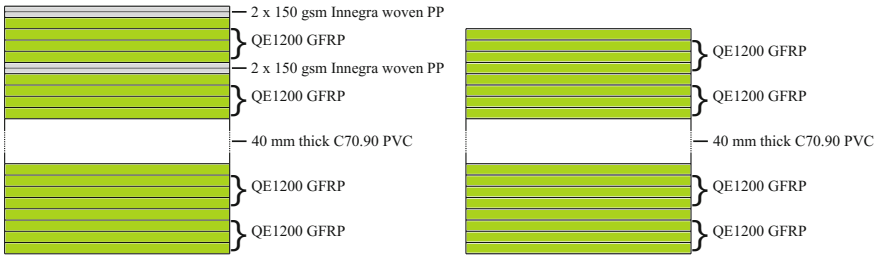

Fig. 1 Schematic diagram showing the layup of the PP/GFRP panel and GFRP panel

Table 1 Material properties for face-sheet constituent materials and manufactured plies

Material	Density (kg/m^3)	Elastic modulus (GPa)	Tensile fracture stress (MPa)	Interlaminar shear strength (MPa)	Compressive strength (MPa)
Glass Fibers	2550	80	2000	–	1450
SR 8500 Resin	984	3.35	83	59	114
QE1200/SR 8500 GFRP Ply	1720	15.88	396	59	316
Innegra IS-940 Fibers	900	14.8	667	–	39
Innegra/SR 8500 PP Ply	932	5.86	238	59	55
Carbon Fibers	1790	225	3350	–	2500
XC411/SR 8500 CFRP Ply	1355	40.62	623	59	493
Aramid RA320	1440	124	3600	–	410

unavailable from manufacturer data sheets so properties for bulk PP have been given. The properties of the face-sheets are detailed in Table 1.

The glass-fiber panel for the third study was manufactured using two plies of quadriaxial Gurit QE1200 for each skin, infused with Ampreg 22 epoxy resin. The glass-/aramid-fiber panel was constructed from one ply of QE1200 fabric and four plies of aramid RA320. Both panels were manufactured using a wet layup and consolidated under vacuum prior to curing. The skin constructions in this study were manufactured to ensure they had a similar weight. The glass and hybrid panels weighed 2.6 kg and 2.9 kg, respectively.

2.1 Air Blast Test Method

During air blast testing, the panels were subjected to a 100 kg nitromethane charge (100 kg TNT equivalent) at a 15 m standoff distance. The standoff was calculated to cause front face-sheet and core damage but leave the back face-sheet intact using a method outlined by Andrews and Moussa [1]. This was important as high-speed cameras were placed behind the panels to record their out-of-plane displacement using 3D digital image correlation (DIC) and it was necessary to protect these cameras from debris. In total, four cameras were positioned behind the two test panels, these were two Photron SA1.1's and two Photron SA5's. The two panels were placed side-by-side in a reinforced steel test cubicle. A schematic diagram of the test cubicle is shown in Fig. 2 showing the dimensions of the cubicle and panel

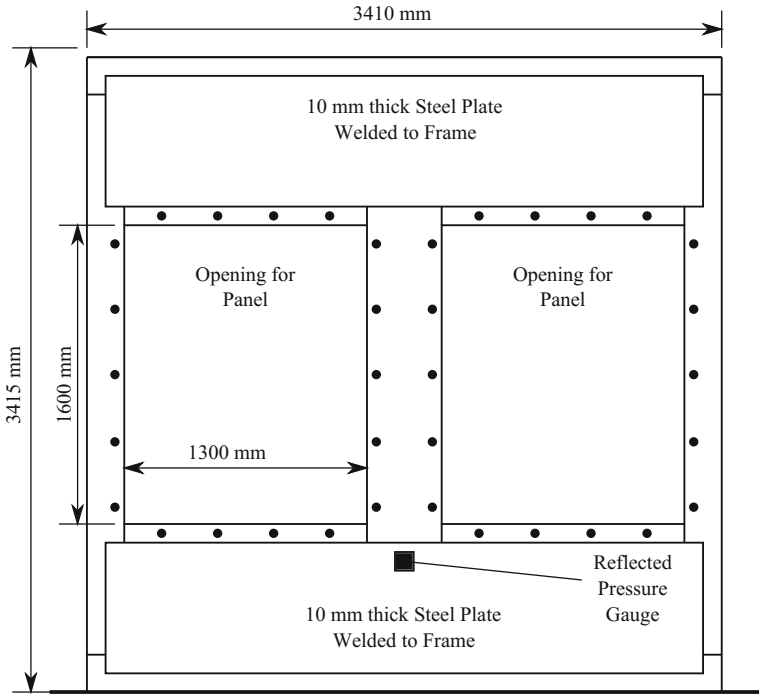

Fig. 2 Schematic of the air blast test cubicle

openings. The location of the reflected pressure gauge, which was bolted to the front of the test cubicle, is shown. A side-on pressure gauge was placed to the side of the cubicle at the same standoff distance and height from the charge as the center of the test panels. The panels were attached to the cubicle using M10 bolts and crushing of the panel core during tightening was prevented by placing steel tubes inside the bolt clearance holes. A steel plate was placed on the floor underneath the charge to create an elastic foundation for the blast wave. The charge was raised to a height of 1.2 m by placing it on polystyrene foam which absorbed a negligible amount of the blast energy. Following blast testing, the damage sustained by the panels was analyzed by visual inspection. The panels were cut into 112 pieces and maps of debonding and core damage were compared.

2.2 Underwater Blast Test Method (1)

The underwater blast panels were subjected to a smaller charge but at a much nearer standoff distance. Digital image correlation was not possible underwater, therefore, the panels were each instrumented with 30 foil strain gauges. The panels were

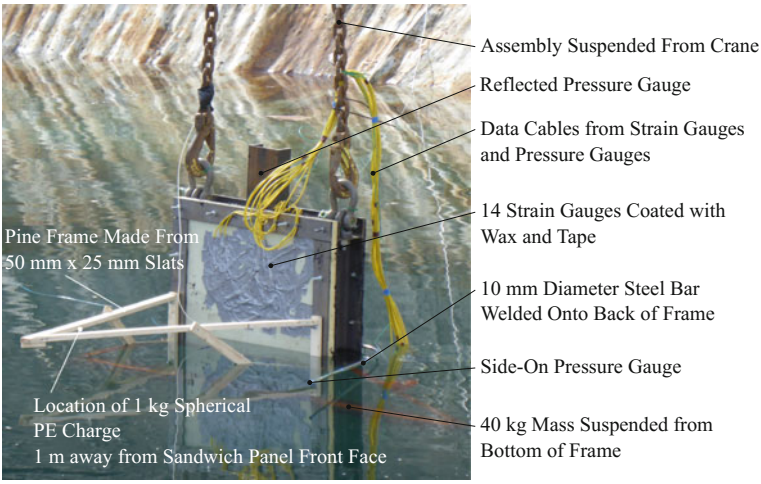

Fig. 3 Photograph showing the set up for the underwater blast experiments

0.8 m × 0.8 m in size with an unsupported area of 0.65 m × 0.65 m exposed to the blast. Since the panels were square in shape, only a quarter of each was instrumented as a symmetric response was expected. Fourteen strain gauges were adhered to the front and 16 to the rear face. The panels were mounted into a steel test frame which left an enclosed volume of air behind the panel and this assembly was fully submerged in the test pond. A 1 kg plastic explosive 4 (PE4) charge was mounted on a pine frame, 1 m away from the center of the panel, which was designed to break apart upon detonation and not load the panel. The charge and center of the panel were lowered to a depth of 3 m. Figure 3 shows a photograph of the GFRP test panel as it is being lowered into the test pond, prior to the charge being attached. A reflected pressure gauge was attached to the front of the test rig and a side-on gauge was attached to the end of a steel rod such that it was 1 m away from the charge. The post-blast damage to the panels was analyzed using X-ray computed tomography (CT) scanning at the micro-VIS center at the University of Southampton. The panels were divided into three sections and stacked in a polymer tube within custom Nikon hutch to capture the required level of detail and maximize scanning efficiency.

2.3 Underwater Blast Test Method (2)

These panels were smaller than the panels in the previous underwater blast study. An unsupported area of 0.4 × 0.3 m was left exposed to the blast and the edges were bolted into a steel frame. Once again an enclosed volume of air was sealed behind the panel. One-quarter of the panel was instrumented with 12 strain gauges,

fewer than the previous test due to a limitation of the data acquisition unit. A 1 kg C4 charge was held 1 m away from the center point of the panel from a gantry. The charge and center of the panel were lowered to a depth of 6 m. Side-on pressure measurements were taken on either side of the target, at the same height as the center point, using Neptune Sonar shock gauges. Two side-on transducers were used to monitor whether the underwater blast loading was uniform across the width of the panels. The gauges were attached to steel scaffolds and the whole assembly was lowered into the test pond from a gantry. A schematic diagram showing the test set up of this underwater blast test is shown in Fig. 4. The panel face-sheets were visually inspected for damage following the blast test and the panel was sectioned to record the extent of core crushing at the center point of the panel.

A summary of all the panels tested across the three different studies is presented in Table 2. Although the panels have different foam core materials, the foam core is constant within each test.

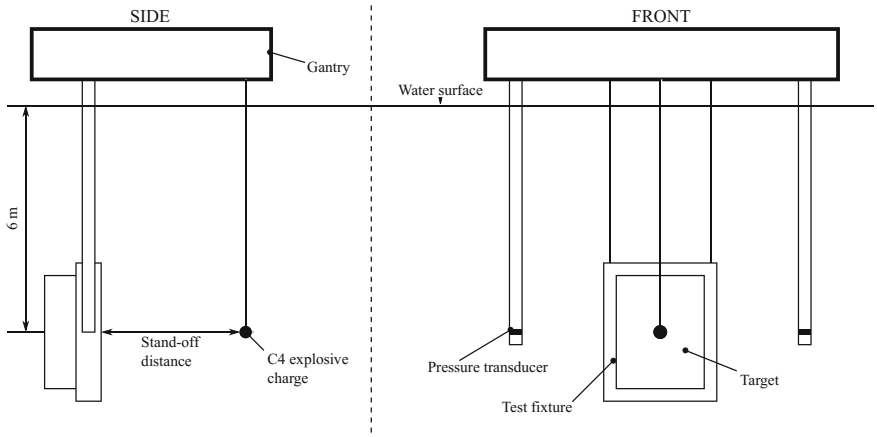

Fig. 4 Schematic of the test setup for the second underwater blast experiment

Table 2 Summary of composite sandwich panels tested in this study

Test method	Face-sheet material	Foam core material	Foam core thickness (mm)
Air Blast	GFRP	PVC C70.90	40
	GFRP/PP	PVC C70.90	40
Underwater Blast (1)	GFRP	SAN M130	30
	CFRP	SAN M130	30
Underwater Blast (2)	GFRP	SAN P800	30
	GFRP/Aramid	SAN P800	30

3 Results

This section details the results from each of the three blast studies and their subsequent damage analyses separately.

3.1 Air Blast Results

From the digital image correlation, it was possible to create plots of the horizontal center section displacement at discrete time intervals. The maximum amount of bending takes place across this horizontal center section. The positive displacement of the GFRP and GFRP/PP panels are shown in Fig. 5a and c, respectively. The rebound stroke for the GFRP and GFRP/PP panels are shown in Fig. 5b and d, respectively. The plots show that there is little difference between the initial displacement shapes. The panel with PP interlayers has a lower maximum

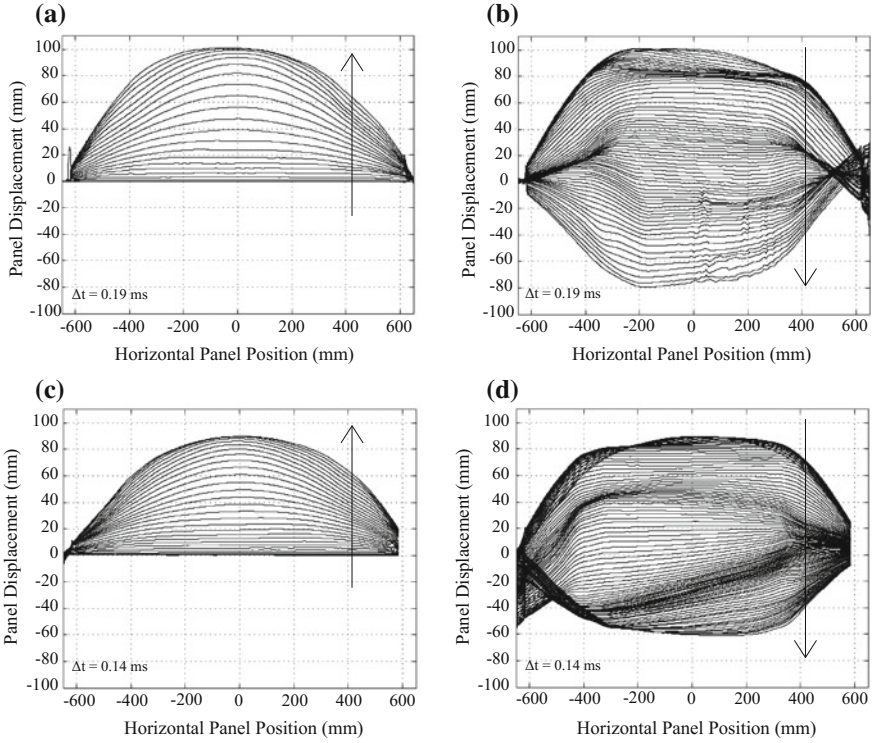

Fig. 5 Out-of-plane displacement of the horizontal center section of the panels during air blast showing **a** positive displacement and **b** rebound displacement for the panel with GFRP face-sheets, **c** positive displacement and **d** rebound displacement for the panel with GFRP/PP face-sheets

displacement in both cases. On the rebound stroke, the sharp gradient changes indicate the location of damage as cracks in the face-sheets and cores slow the rebound of the panel. The gradient discontinuities for both panels is similar implying that they suffer from a similar amount of damage. The cracking occurs at around one-quarter and three-quarters across the width of both panels.

The central point displacement for the two panels is shown in Fig. 6. Again, it can be seen that the panel with PP plies deflected less, this is expected to be due to the increased thickness of the front face-sheets. These traces indicate that the GFRP is more damaged that the GFRP/PP panel as the pull-out displacement is greater, along with the rebound time to reach the maximum pull-out.

The post-blast damage assessment maps for these two panels are shown in Fig. 7 and detailed in Table 3. Both panels suffer from a similar amount of core damage and debonding between the rear face-sheets and core. The panel with PP plies, however, suffered from less front face-sheet/core debonding and no front face-sheet cracking unlike the solely GFRP face-sheet panel. This result indicates that the incorporation of PP plies improves the front face-sheet integrity and would prevent water ingress into the sandwich panel.

3.2 *Underwater Blast Results (1)*

The strain against time for the strain gauge locations was recorded, a low-pass filter was applied, and the strain was interpolated between the discrete gauge locations to create contour plots. The contour plot for the front face-sheet strain of the GFRP and CFRP panels are shown in Fig. 8. The direction of the distance from the center of the panel is shown on the left-hand side of the figure. Upon arrival of the blast wave both the GFRP panel and CFRP panel front face-sheets are briefly put into tension as the foam core is crushed. Following this, the strain returns to

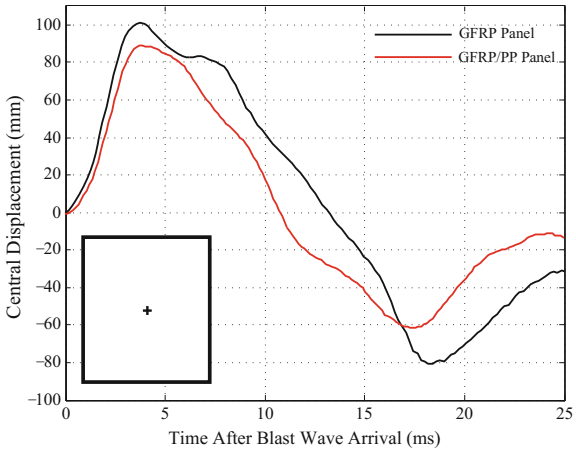

Fig. 6 Out-of-plane displacement of the central point of the two air blast panels

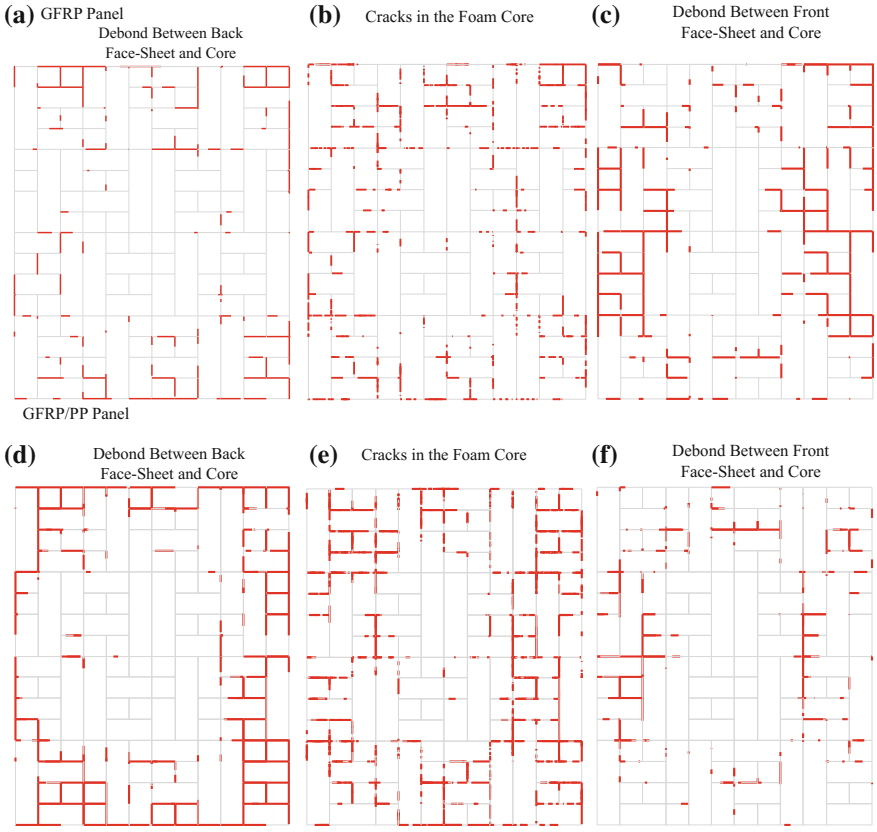

Fig. 7 Location of damage within the GFRP panel and GFRP/PP panel following air blast loading

Table 3 Summary of the damage experienced by the panels following air blast

Panel description	Total number of through thickness cracks	Total crack area (m^2)	Fraction of panel containing cracks (%)
GFRP skins with PVC core	121	2.45	41
GFRP/PP skins with PVC core	135	2.72	50

approximately zero, due to a mixture of membrane and bending loading. The outer edges experience compression due to the deflection of the panel. Figure 9 shows the contour plots for the back face-sheets of the GFRP and CFRP panels. The direction of the distance from the center of the panel is shown on the left-hand side of the figure.

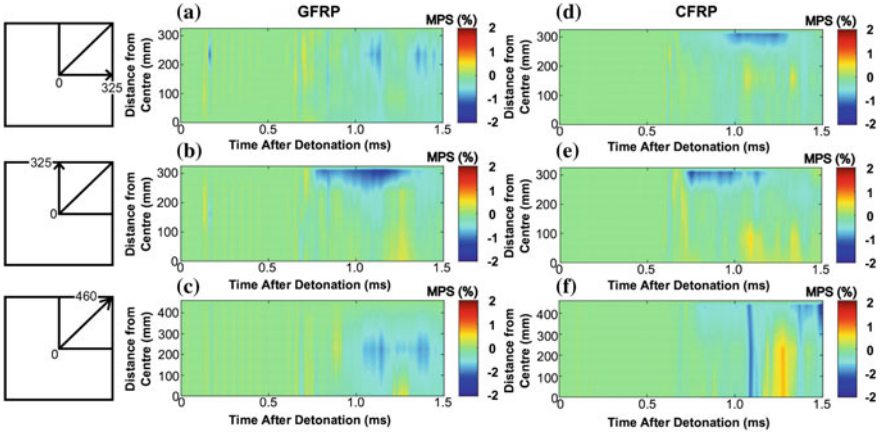

Fig. 8 Contour plots showing the magnitude of strain on the front face-sheet for **a** the horizontal direction, **b** the vertical direction and **c** the diagonal direction of the GFRP panel; **d** the horizontal direction, **e** the vertical direction and **f** the diagonal direction of the CFRP panel

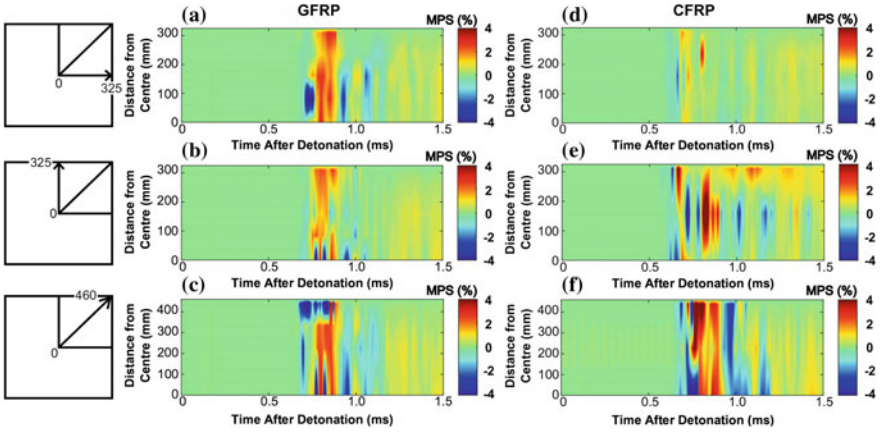

Fig. 9 Contour plots showing the magnitude of strain on the rear face-sheet for **a** the horizontal direction, **b** the vertical direction and **c** the diagonal direction of the GFRP panel; **d** the horizontal direction, **e** the vertical direction and **f** the diagonal direction of the CFRP panel

The blast waves arrive at the panels at approximately 0.7 ms after detonation and cause the panels to experience compression whilst the foam core is crushed. The back face-sheets are then put into tension and remain in tension until the panels fail. The GFRP panel fails due to shearing of the bolt holes and the CFRP panel fails due to fracture around the perimeter of the back face-sheet.

Front views of the 3D reconstructions of the panels from the X-ray CT scans are shown in Fig. 10. Substantial debonding between the skins and core, highlighted in

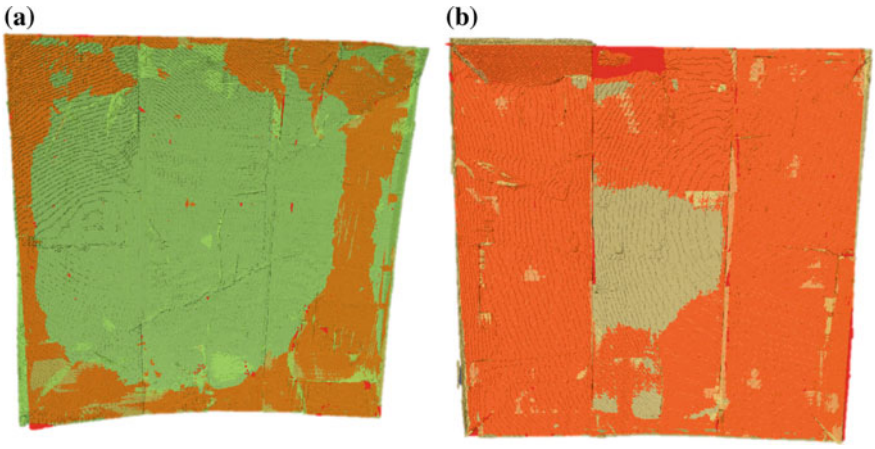

Fig. 10 Front view of the 3D reconstructions from X-ray CT scanning of the **a** GFRP panel and **b** CFRP panel following underwater blast, with debonding between front face-sheet and core highlighted in red

Table 4 Summary of the damage sustained by the panels following underwater blast loading

	GFRP panel	CFRP panel
Fraction of panel containing damage (%)	7.2	20.6
Fraction of panel with front skin and core debond (%)	26.9	76.0
Fraction of panel with rear skin and core debond (%)	18.2	15.2
Central point foam thickness (mm)	4.0	9.6

red, can be seen toward the edge of the panels along with front face-sheet fracture. The front face-sheet of the CFRP panel is almost completely debonded from the core. The core at the central point of the GFRP and CFRP panels crush to 4.0 mm and 9.6 mm, respectively. The damage to the panels was quantified and is detailed in Table 4. It is evident that the CFRP panel suffers from greater damage due to its lower strain to failure.

3.3 Underwater Blast Results (2)

Following the blast, the top edge of the GFRP panel was put into compression and the central section into tension. The compressive surface strain along the edges peaked at 3%. This is shown in Fig. 11, where gauge 6 is positioned at the top edge. The panel sustained a significant amount of damage and was permanently deformed into a curve. This is substantiated by gauge 6 remaining in compression indicating that the panel remained in the characteristic bath-tub shape. The core was uniformly

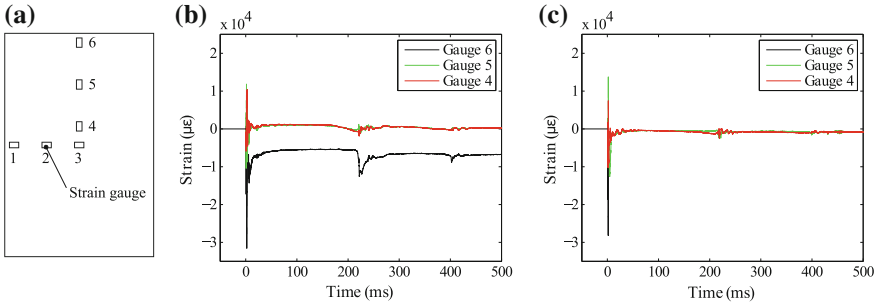

Fig. 11 **a** Strain gauge locations on the front face-sheet and strain gauge readings for **b** the GFRP panel and **c** the GFRP/aramid panel

crushed by 16 mm across the central section, this was the dominant failure mechanism overall. At the edges, the panel was only crushed by 8 mm as skin failure mechanisms, such as wrinkling and some cracking, absorbed a large portion of the blast energy.

The GFRP/aramid panel showed similar initial characteristic behavior. Following this, however, the entire GFRP/aramid panel formed a more parabolic deformed shape over a longer period of time. The core was crushed to a similar degree, by 19 mm. The face-sheet cracking, however, was far more severe in the GFRP/aramid panel. Both panels were subjected to a similar blast pressure, the magnitude was recorded as 43.5 MPa for the GFRP panel and 40.7 MPa for the GFRP/aramid panel. Figure 11 shows the location of the strain gauges and the strain against time for both panels. Figure 12 shows photographs of the panels after blast testing. The severe cracking to the edges of the GFRP/aramid panel is shown clearly in these photographs.

4 Discussion

The three studies performed have all aimed to identify whether alterations to the skins of composite sandwich panels can yield improved blast resilience. The first study investigated the effects of PP Innegra interlayers in the front face-sheet. The panel with PP interlayers had a reduced out-of-plane displacement. The initial out-of-plane displacement was reduced by 10% and the pull-out was reduced by 25%. This is due to the PP interlayers increasing the thickness of the front face-sheet, these interlayers increase the areal density of the panel by 14%. The damage to the core of both panels and debonding between the rear face-sheets and cores were similar for both panels. The PP interlayers, however, did reduce the damage experienced by the front face-sheet. Although the PP plies offer a negligible structural contribution, the increased strain to failure of the PP plies provides a seal against water. This result is useful for applications where the integrity of the front face-sheet is critical.

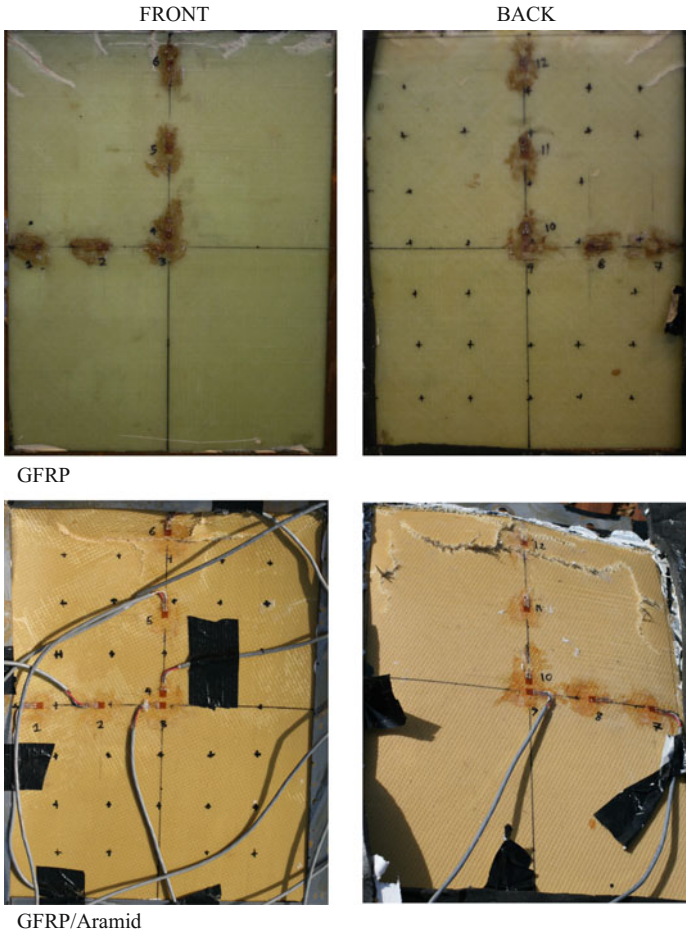

Fig. 12 Photographs of damage to the GFRP and GFRP/aramid panels following underwater blast loading

The first underwater blast experiments investigated glass-fiber versus carbon-fiber skins. The strain gauge data reveals that the two panels experienced similar strain on both the front and rear face-sheets as a result of the blast pressure. The CFRP panel, however, suffers from the severe fracturing of the rear face-sheet at the boundary and almost complete debonding between the front face-sheet and core. This damage results from the increased stiffness of the CFRP, which offers the blast wave more resistance, and the lower strain to failure of CFRP, which results in skin fracture. The experiment and damage assessment have revealed that there is a trade-off between carbon and glass fiber when selecting the face-sheet materials. Carbon-fiber face-sheets have a higher stiffness but this will result in greater damage, and hence, significantly reduce panel residual strength. Panels with

glass-fiber face-sheets will deform more as a result of blast loading but will not fracture as severely. This enables the sandwich panel to retain more of its original strength. In applications, where residual strength is important, it may be necessary to select glass-fiber skins which have a lower initial strength but retain a greater proportion of the strength following blast loading.

In the second set of underwater blast experiments both the GFRP and GFRP/aramid panels sustained visible damage as shown in the post-blast photographs. Both panels had their cores crushed to a similar extent by the shocks with pressures up to 43.5 MPa. The panels experienced high surface strain around the panel edges, up to 3%, caused by permanent deformation of the panel. The GFRP panel suffered mostly from skin wrinkling around the edges while the GFRP/aramid panel had more severe skin damage, fiber breakage, and skin tearing. The aramid skins did not absorb or redistribute sufficient blast energy through the front face which led to the formation of a highly deformed plate. As a result of this, the damage to the back face-sheet on this hybrid panel was more severe. The GFRP/aramid panel also transferred a more significant portion of the blast impulse through the core hence leading to more core crushing. These results indicate that this hybridization was not effective. The number of plies of aramid lessened the properties of the glass fibers instead of enhancing them and one ply of QE1200 GFRP was insufficient to withstand the blast.

Different energy absorption and failure mechanisms were observed when moving from air to underwater blast. In air the panels experienced core cracking and face-sheet/core debonding. Underwater the panels suffered from core crushing and severe skin fiber breakage in some cases. This is because the underwater blast pressure was 200 times greater than air blast. Additionally, the underwater impulse time period was less than one-tenth compared to the air blast. This drastically reduces the time available for the skins to activate their flexural response hence core compression dominates.

The results have demonstrated that GFRP skins have sufficient structural integrity to withstand blast loads. The response of GFRP skins can be improved through the addition of PP plies, however, the removal and replacement of GFRP plies with aramid fibers is disadvantageous. A combination of CFRP and GFRP may result in an ideal face-sheet. Both CFRP and GFRP have good blast resilience when implemented alone and their separate drawbacks may be reduced if they are combined in optimal proportions. Fabric plies that offer a negligible contribution to the structure of a composite sandwich panel should be used in addition to structurally sound materials rather than as a substitution.

5 Conclusions

These experiments have demonstrated the ability of composite sandwich panels to resist blast loading both in air and underwater. More advanced strain monitoring techniques, DIC, were adopted where possible while more conventional methods, strain gauges, were used in the underwater blast experiments.

The materials tested are readily available in the marine sector and were tested against real explosive charges. Additionally, the size of the panels tested was representative of the size of panels used in engineering structures (0.3–1.6 m). These experiments differ from other investigations into blast/shock since the panel size and explosive charges used approach real in-service conditions.

The failure mechanisms differed between the air and underwater blast experiments. This is due to the increased blast pressure underwater delivered in less than a tenth of the time compared to air blast.

Repeat experiments were not carried out which limits the sample data. This is due to the scale and nature of the experiments limiting the consumables available. Nevertheless, the multiple gauges used in the underwater blast experiments give confidence to the data recorded. Furthermore, DIC during air blast has been previously validated using two techniques to record point measurements. The results build upon years of composite research within the group, and worldwide, and experimental findings are being confirmed through analytical and numerical models.

The following bullet points summarize the main findings from these experiments:

- The addition of PP Innegra interlayers into a GFRP front face-sheet resulted in reduced out-of-plane displacement and reduced front face-sheet damage during air blast.
- The replacement of glass fibers with aramid fibers, however, led to an increase in panel damage during underwater blast.
- The CFRP panel suffered greater damage when subjected to underwater blast than an equivalent GFRP panel.
- This results in a trade-off between CFRP and GFRP as the latter has higher stiffness but this will result in greater damage and hence reduced residual strength.
- There may be an optimal combination of carbon- and glass fibers that result in a panel with good stiffness and good damage tolerance.

Acknowledgements The authors would like to acknowledge the support received from Dr. Yapa Rajapakse of the Office of Naval Research for supporting Dr. Hari Arora, Dr. Mark Kelly and Emily Rolfe during their Ph.Ds [N00014-08-1-1151, N00014-12-1-0403, and N62909-15-1-2004]; and EPSRC for supporting Emily Rolfe during her Ph.D. Much appreciated is the help and support from GOM UK, LaVision, Slomo Camera Hire, CPNI, and DNV for assistance with the full-scale blast experiments. The authors would also like to acknowledge the micro-VIS center at the University of Southampton for the provision of tomographic imaging facilities, supported by EPSRC grant EP-H01506X.

References

1. Andrews, E., & Moussa, N. (2009). Failure mode maps for composite sandwich panels subjected to air blast loading. *International Journal of Impact Engineering, 36*(3), 418–425.
2. Arora, H. (2012). Blast loading of fibre reinforced polymer composite structures. Ph.D. thesis, Imperial College London.
3. Arora, H., Hooper, P., Del Linz, P., et al. (2012). Modelling the behavior of composite sandwich structures when subject to air-blast loading. *International Journal of Multiphysics, 6,* 199–218.
4. Arora, H., Kelly, M., Worley, A., et al. (2015). Compressive strength after blast of sandwich composite materials. *Philosophical Transactions of the Royal Society A*, *372*, 20130212 https://doi.org/10.1098/rsta.2013.0212.
5. Bouwmeester, J., et al. (2008). Carbon/Dyneema intralaminar hybrids: New strategy to increase impact resistance or decrease mass of carbon fiber composites. In I. Grant (Ed.), *26th International Congress of the Aeronautical Sciences*. Alaska: Anchorage.
6. Fallah, A., Micallef, K., Langdon, G., et al. (2014). Dynamic response of Dyneema HB26 plates to localized blast loading. *International Journal of Impact Engineering, 73,* 91–100.
7. Gardner, N., Wang, E., Kumar, P., et al. (2012). Blast mitigation in a sandwich composite using graded core and polyurea interlayer. *Experimental Mechanics, 52*(2), 119–133.
8. LeBlanc, J., Gardner, N., & Shukla, A. (2013). Effect of polyurea coatings on the response of curved E-glass/vinyl ester composite panels to underwater explosive loading. *Composites Part B: Engineering, 44*(1), 565–574.
9. Murugan, R., Ramesh, R., & Padmanabhan, K. (2014). Investigation on static and dynamic mechanical properties of epoxy based woven fabric glass/carbon hybrid composite laminates. *Procedia Engineer, 97,* 459–468.
10. Radford, D., Deshpande, V., & Fleck, N. (2005). The use of metal foam projectiles to simulate shock loading on a structure. *International Journal of Impact Engineering, 31*(9), 1152–1171.
11. Randjbaran, E., Zahari, R., Abdul Jalil, N., et al. (2014). Hybrid composite laminates reinforced with Kevlar/carbon/glass woven fabrics for ballistic impact testing. *Scientific World Journal*. https://doi.org/10.1155/2014/413753.
12. Song, J. (2015). Pairing effect and tensile properties of laminated high-performance hybrid composites prepared using carbon/glass and carbon/aramid fibres. *Composites Part B—Engineering, 79,* 61–66.
13. Swolfs, Y., Gorbatikh, L., & Verpoest, I. (2014). Fibre hybridisation in polymer composites: A review. *Composites Part A—Applied Science, 67,* 181–200.
14. Tagarielli, V., Deshpande, V., & Fleck, N. (2010). Prediction of the dynamic response of composite sandwich beams under shock loading. *International Journal of Impact Engineering, 37*(7), 854–864.
15. Tekalur, S., Shukla, A., & Shivakumar, K. (2008). Blast resistance of polyurea based layered composite materials. *Composite Structures, 84*(3), 271–281.
16. Zhang, T., Satapathy, S., Vargas-Gonzalez, L., et al. (2015). Ballistic impact response of ultra-high-molecular-weight polyethylene (UHMWPE). *Composite Structures, 133,* 191–201.

Damage and Failure of Blast Loaded Fiber-Reinforced Composite Laminates Considering Material and Geometric Nonlinearities

Romesh C. Batra

1 Introduction

As summarized in the World-Wide Failure Exercise papers [1, 2] there are very few failure theories that accurately simulate damage initiation and propagation in unidirectional fiber-reinforced composites deformed under quasi-static loads. Transient problems involving shock loads are even more challenging because the propagation of deformation through a heterogeneous medium necessarily involves interactions among incident waves and those reflected from interfaces between distinct materials. There is a huge difference among acoustic impedances of fibers, the matrix, and the medium surrounding the structure. Furthermore, fibers are usually transversely isotropic with much higher modulus along the fiber axis than that in the transverse direction implying that wave speeds in fibers along and across their axes are quite different. Even though one can simulate these effects by studying 3-dimensional (3-D) deformations at the constituent level, the computational effort for a real size structure is prohibitively large because of the tiny time-step size needed to find a stable numerical solution. The consideration of damage initiation and propagation further stretches the extent of computational resources required for analyzing the problem. Studying experimentally transient deformations of blast loaded sandwich structures is equally challenging since taking in-situ strain and temperature measurements require using noncontacting, mostly optical, instruments. Focusing these instruments at critical locations requires a priori knowledge of points/regions of failure initiation. Thus, experimentalists, theoreticians, and numerical analysts need to collaborate closely for a comprehensive analysis of the problem.

R. C. Batra (✉)
Department of Biomedical Engineering and Mechanics,
Virginia Polytechnic Institute and State University, M/C 0219, Blacksburg,
VA 24061, USA
e-mail: rbatra@vt.edu

S. Gopalakrishnan and Y. Rajapakse (eds.), *Blast Mitigation Strategies in Marine Composite and Sandwich Structures*, Springer Transactions in Civil and Environmental Engineering, https://doi.org/10.1007/978-981-10-7170-6_12

An often-used strategy to simplify the problem is to homogenize material properties of the composite by using a micro-mechanics approach, and study transient deformations of the homogenized structure. This mitigates problems of wave reflections from fiber/matrix interfaces and of wide differences in wave speeds in the two materials. However, it replaces inhomogeneous face sheets and either a foam or a honeycomb core by homogenized media and removes stress singularities at contact surfaces between the different materials. Thus, one cannot accurately capture points of failure initiation especially with a stress- or a strain-based failure criterion. For using failure criteria at the constituent level, one can use a dehomogenization technique to find stresses and strains at the constituent level from those at the macro-level. Results depend upon the micro-mechanics approach, the failure initiation criteria, the ultimate failure or the structure collapse criteria, and the technique adopted for tracking failure propagation.

In numerical work, one usually simulates failure propagation by adopting one of the following techniques: deleting failed elements, releasing nodes where the material has failed, using singular surfaces, and employing a cohesive zone model (CZM). It is quite challenging to compute mesh-independent results unless the problem formulation involves a material characteristic length whose value cannot be easily ascertained.

Blast and water slamming loads on a structure induce large deformations necessitating the consideration of all material and geometric nonlinearities. Governing equations in the Lagrangian (or the material) description of motion involve nonlinear strain-displacement relations and those in the Eulerian (or the spatial) formulation have the particle acceleration as a nonlinear function of the particle velocity. Furthermore, the stress–strain relation is generally nonlinear in either formulation, and one must use materially objective (or frame-indifferent) constitutive relations. The time-step size for computing a stable solution of the governing equations must satisfy the Courant–Friedrichs–Levy (CFL) condition.

A possibility is to analyze deformations of the structure by modeling it as a plate/shell. Reissner [3] and Koiter [4] have emphasized the need to consider both transverse shear and transverse normal deformations. Reissner stated in 1947 that for a sandwich plate with $(t_f\, E_f)/(h_c\, E_c) \gg 1$ both transverse shear and transverse normal deformations should be considered. Here, t_f and E_f (h_c and E_c) equal, respectively, the thickness and the longitudinal modulus of the face sheet (core). Based on the energy considerations Koiter [4] recommended that any refinement of the Love first approximation theory must simultaneously consider both transverse shear and transverse normal stresses. Vel and Batra [5] have provided the exact solution for thermally loaded linearly elastic plates with material moduli only varying in the thickness direction. For plates with length/thickness = 5, they found that the transverse deflection computed with the classical plate theory, the first-order shear deformable theory and the third-order shear deformable theory deviates, respectively, from the exact solution by 26%, 26% and 28%. These large errors could be due to neglecting the transverse normal strain in the three theories. For the problem studied by Vel and Batra [5], Qian et al. [6] found that a fifth-order shear and normal deformable plate theory gives results very close to the analytical

solution of the problem. For 100 K temperature difference between the top and the bottom surfaces of the plate, the deflection of the centroid of the top surface equaled twice of that of the centroid of the bottom surface signifying an average transverse normal strain of $\sim 10^{-3}$. These examples signify the need for considering transverse normal deformations for moderately thick plates/shells.

We have considered material and geometric nonlinearities and simulated damage initiation and propagation and the consequent material degradation at the constituent level while analyzing transient 3-D deformations of composite laminates. The delamination between adjacent plies is modeled with a nodal-release technique. However, for sandwich shells subjected to water slamming loads we have used a layerwise third-order shear and normal deformable plate theory (TSNDT) and simulated mixed-mode delamination with a CZM. In each case, the failed material is not allowed to heal. The interpenetration of the material across an adjoining surface is prevented by joining "contacting" nodes with a spring that is very stiff in compression but weak in tension. We describe below some of the results from our two previously published papers.

2 Failure of Fiber-Reinforced Composite Laminate Due to Blast Loads

2.1 Material Models

2.1.1 Constitutive Relation

It is common to model, e.g., see [7, 8], the material nonlinearity by using a linear relation between the second Piola-Kirchhoff stress tensor, **S**, and the Green-St. Venant strain tensor, **E**. That is,

$$S_{ij} = C_{ijkl} E_{kl}, \quad i,j,k,l = 1,2,3 \tag{1}$$

where **C** is the matrix of elasticities. The material described by Eq. (1) is called St. Venant-Kirchhoff. Here and below, a repeated index implies summation over the range of the index. We note that **S** has no physical meaning but is convenient to use, **E** includes all nonlinear terms in displacement gradients, and **S** and **E** are work-conjugate tensors. The stress–strain relation (1) is materially objective, and one can easily implement it in a software. From **S** and displacement gradients, one finds the true or the Cauchy stresses needed to ascertain damage initiation at a point.

A unidirectional fiber-reinforced lamina, modeled as a transversely isotropic material with the fiber along the axis of transverse isotropy, has five material constants. With **S** and **E** written as 6-D vectors, values of elasticities in the 6×6 matrix of material parameters are such that the matrix is positive-definite. For simple extensional deformations of a cylindrical isotropic body made of the St. Venant-Kirchhoff material, the structure becomes unstable in compression when

the final length/initial length (or the axial stretch) equals 0.577 irrespective of values of material elasticities [9]. For simple shear deformations, this material exhibits strain hardening because the slope of the shear stress versus the shear strain curve increases with an increase in the shear strain [9]. For a transversely isotropic material loaded along the axis of transverse isotropy, the prismatic cylinder will become unstable at a compressive axial strain whose value depends upon the material elasticities.

2.1.2 Damage Modes and Initiation Criteria

Hassan and Batra [10] presumed that elasticities of the St. Venant-Kirchhoff material degrade with an increase in the damage, and deduced the degradation relations by using the mechanics of materials approach. They considered three internal variables—one each for fiber breakage, matrix cracking, and fiber/matrix debonding. The failure in a mode ensues when the corresponding internal variable reaches a material-dependent critical value. They found expressions for the work conjugate of an internal variable, called the thermodynamic force, by using the Clausius–Duhem inequality, and for the energy dissipated in each failure mode. They determined values of material parameters from the test data of Kyriakides et al. [11].

Hassan and Batra [10] postulated a delamination surface described by a homogeneous quadratic function of the tensile transverse normal and the transverse shear stresses acting at a point on an interface between two adjacent plies. Each stress component is normalized by its value at delamination initiation. Mixed-mode delamination can occur at the interface when the transverse normal stress is tensile but only sliding prevails when it is compressive. The energy dissipated during delamination is calculated from the energy balance, i.e., subtracting from the work done by external forces the total strain energy of elastic deformations and energies dissipated due to fiber breakage, matrix cracking, and fiber/matrix debonding.

2.2 Mathematical Model

The problem is formulated in the Lagrangian description of motion using a fixed set of rectangular Cartesian coordinate axes. With **x** and **X** denoting, respectively, the position vectors of a material point in the current and the reference configurations, and t the present time, equations governing deformations of a material point are

$$\rho_R \ddot{u}_i = \left[(\delta_{i\alpha} + u_{i,\alpha})(C_{\alpha\beta\gamma\delta} E_{\gamma\delta}) \right], _{\beta}, \;\; i, \alpha = 1, 2, 3 \tag{2}$$

In Eq. (2), $\mathbf{u} = \mathbf{x} - \mathbf{X}$, is the displacement of the material point **X**, ρ_R the mass density in the reference configuration, and $\delta_{i\alpha}$ the Kronecker delta. A superimposed

dot indicates material time derivative, and a comma followed by α implies partial differentiation with respect to X_α.

Boundary conditions pertinent to a test set-up, initial conditions (usually zero displacements and null velocities), Eq. (2), and the nonlinear strain-displacement relations provide three nonlinear partial differential equations (PDEs) for finding **u** as a function of **X** and t.

2.3 Computational Model

We use the Galerkin method to derive a weak form of Eq. (2) that reduces nonlinear PDEs to nonlinear ordinary differential equations (ODEs) in time. We employ 8-node brick elements, evaluate integrals on an element with the $2 \times 2 \times 2$ Gauss quadrature rule, integrate the resulting ODEs with respect to time t by using the freely available subroutine LSODE (Livermore Solver for ODEs) and set in LSODE the relative and the absolute error tolerance $= 1 \times 10^{-9}$.

2.3.1 Simulation of Material Failure

From the computed nodal displacements, we ascertain values of damage parameters at each integration point within an element. When a damage initiation criterion for fiber breakage, matrix cracking, and/or fiber/matrix debonding is satisfied at an integration point, we gradually degrade values of the relevant elastic constants there till they essentially become zero (i.e., very small as compared to that of the intact material) at damage parameter $= 1$. We do not delete the element from the analysis even when the material at all its eight integration points has failed. Thus, it has kinetic energy but negligible strength and essentially zero stresses. We refer the reader to Ref. [10] for the degradation of elasticities, and evolution equations for the damage parameters.

We simulate delamination by using the nodal-release criterion, and prevent non-interpretation of materials across an interface by connecting their corresponding two nodes with a spring element that is weak in tension but stiff in compression. The postulated constitutive relation for the spring is:

$$
\begin{aligned}
&F = k\, z_n \\
&\text{where,} \\
&k = \begin{cases} 0, & z_n/z_0 \geq 0, \\ E_3 l \left[1 + (\eta E_3 - 1)\left(\frac{z_n}{z_0}\right)^2\right], & -1 \leq z_n/z_0 < 0, \\ \eta E_3 l, & z_n/z_0 < -1. \end{cases}
\end{aligned} \tag{3}
$$

Here, F (z_n) is the normal force (relative displacement) between the two nodes, E_3 Young's modulus of the composite in the X_3-direction, l a characteristic length, and η a constant. Note that the value of l does not affect the mesh-dependence of results.

2.3.2 Verification of the Code

We verified the code by using the method of fictitious body forces or equivalently the method of manufactured solutions [13]. We also compared computed results for a few simple problems, such as wave propagation in a bar, with their analytical solutions. It ensures that the code correctly solves the governing equations but does not ensure that it incorporates all of the relevant physics of the problem.

2.3.3 Validation of the Mathematical Model

We compared with the test data computed results for configurations and loading conditions different from those used to deduce values of material parameters. The two sets of results agreed well with each other implying that the mathematical model incorporates in it most of the relevant physics of the problem.

2.4 Results

We present here a few results for the problem schematically shown in Fig. 1 and borrowed from Ref. [12] wherein values of material and other parameters are listed. The 22 cm × 22 cm × 1 cm unidirectional fiber-reinforced 4-ply panel with each ply 0.25 cm thick, clamped on all edges, is divided into 8-node brick elements with finer elements in the central portion. In practical applications, a thick laminate will

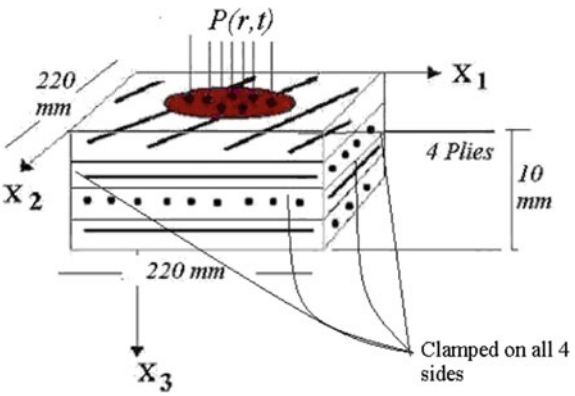

Fig. 1 Schematic sketch of the problem analyzed; reproduced from [12]

have 10^3 or more layers. The four-layer laminate studied in [12] was used to illustrate the theory within the available computational resources and the project duration.

We simulate the blast load due to underwater explosion by applying a time-dependent pressure field on the top surface of the specimen. The pressure variation with time t and the distance, r, from the centroid of the top surface of the panel has the expression

$$P(r,t) = P_{\max} e^{-t/\lambda}(-0.0005\mathrm{r}^4 + 0.01\mathrm{r}^3 - 0.0586\mathrm{r}^2 - 0.001\mathrm{r} + 1), \quad t > 0. \tag{4}$$

In Eq. (4), $\mathrm{P}_{\max}$ is the peak pressure in the shock front, t the time elapsed since the arrival of the shock wave, and λ the decay time constant. Cole [14] has given expressions for the peak pressure, P_{max}, and the decay constant, λ, in terms of the weight, material of the explosive, and the standoff distance. The spatial variation of $P(r,t)$ is a fit to the test data of Türkmen and Mecitolu [15]. The applied pressure is representative of an explosive event and does not necessarily correspond to the values measured in a test.

2.4.1 Effect of the Finite Element Mesh

For one loading, the laminate maximum centroidal deflection computed with the four FE meshes, 20 × 20 × 4 (2,205 nodes), 20 × 20 × 8 (3,969 nodes), 40 × 40 × 4 (8,405 nodes), and 40 × 40 × 8 (15,129 nodes), till $t = 230$ μs, differed at most by 4.8%. The maximum tensile (compressive) principal stress in the laminate equaled 1.393, 1.323, 1.234, and 1.246 GPa (−0.885, −0.894, −0.917, and −1.027 GPa) for the four FE meshes, and the total work done to deform the body equaled 378, 408, 398, and 405 J. By examining time histories (not exhibited here) of the deflection at centroids of planes $\mathrm{X}_3 = 0$ (bottom surface), $\mathrm{X}_3 = 0.5$ cm (midsurface), and $\mathrm{X}_3 = 1$ cm (top surface) we found that the deflections at these three points are very close to each other. It is due to the high speed of elastic waves in the transverse direction and very small laminate thickness.

The results given below are with the 20 × 20 × 4 elements mesh.

2.4.2 Effect of Fiber Orientation

For each ply making the same fiber angle θ with respect to the global X_1-axis aligned along a panel edge, we have computed results for θ = 0°, 10°, 30°, 45°, 60°, 75°, and 90°. Although the body is initially homogeneous, it becomes inhomogeneous because of the different damage evolved at various points, and the dependence of material properties upon the damage. As reported in [12], the fiber orientation angle has the most (least) effect on the time of initiation of the fiber/matrix debonding (the fiber breakage). However, the time of initiation and the

complete failure due to fiber breakage at specimen's centroid is virtually independent of the fiber orientation angle.

2.4.3 Fiber/Matrix Debonding

Fringe plots of the fiber/matrix debonding damage variable at t = 54, 108, 148, and 188 μs, displayed in Fig. 2, reveal that the debonding starts from edges perpendicular to the fibers and propagates along the fibers and toward the center. Plots of the time histories of the evolution of the debonding damage variable at centroids of the top, the middle, and the bottom surfaces of the laminate given in [12] suggest that the debonding instantaneously propagates in the thickness direction.

2.4.4 Matrix Cracking

By studying fringe plots of the matrix cracking damage variable at four times Hassan and Batra [12] concluded that the matrix cracking begins at approximately 108 μs at the bottom surface centroid and propagates faster along the fibers than in the transverse direction. These results agree with the experimental observations of Luo et al. [16].

We have exhibited in Fig. 3 fringe plots of the matrix cracking damage variable. These suggest that the matrix cracking ensues from points on clamped edges of the top surface that are parallel to the X_1-axis, and propagates inwards. The cracked matrix region on the top surface is centered about the X_2-axis and that on the bottom surface around its centroid as experimentally observed by Mouritz's [17]

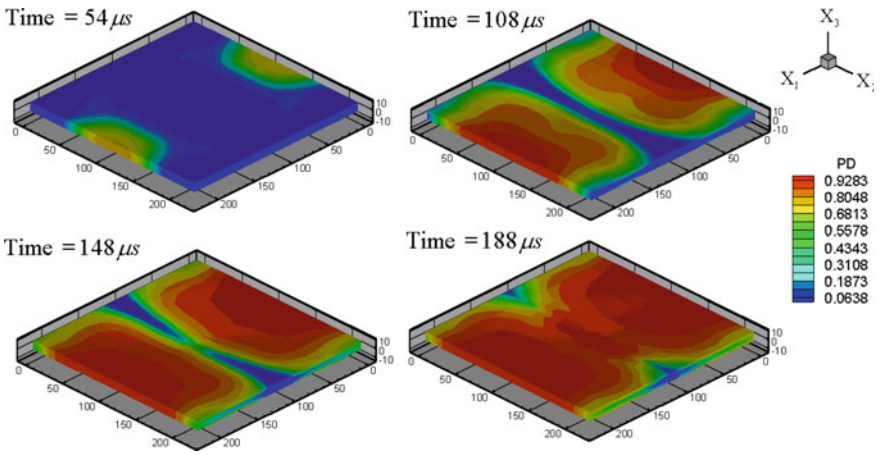

Fig. 2 Fringe plots of the fiber/matrix debonding damage variable, PD, at four different times; reproduced from [12]

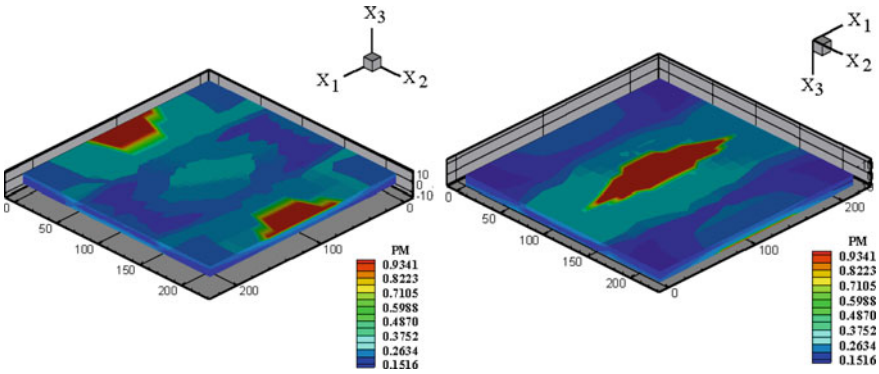

Fig. 3 Fringe plots of the matrix cracking damage variable, PM, at t = 160 μs; left: top surface; right: bottom surface; reproduced from [12]

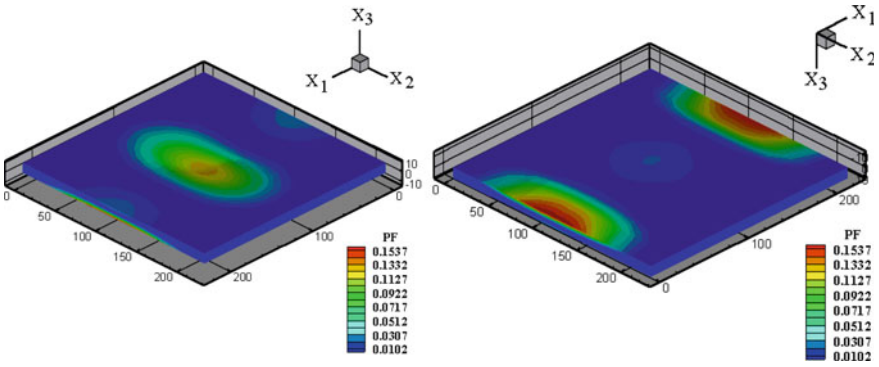

Fig. 4 Fringe plots of the fiber breakage damage variable, PF, at time = 160 μs; left: top surface; right: bottom surface; reproduced from [12]

who attributed it to high tensile bending stresses developed on the back surface. A compressive wave reflected from the traction-free back surface as a tensile wave induces more damage there causing the matrix cracking to initiate first on the bottom surface. The spalling failure mode, not considered here, can ensue at points on the bottom surface.

2.4.5 Fiber Breakage

We have depicted fringe plots of the fiber breakage damage variable at t = 160 μs in Fig. 4. These suggest that the fiber breakage is concentrated at points along the X_2-axis that are near the specimen's center. Similar to the damage variable for the matrix cracking, the damage variable for the fiber breakage also increases suddenly

from essentially 0.0 to 1.0. The time histories of the fiber breakage damage variable are given in [12].

2.4.6 Delamination Between Adjoining Layers

We have plotted in Fig. 5 fringe plots of the fiber/matrix debonding damage variable on planes $X_1 = 110$ mm, and $X_2 = 110$ mm for the 0^0 plies and $t = 220$ μs. The delamination between adjoining layers, indicated by solid lines, initiates from more than one point, not necessarily simultaneously, on an interface between two adjoining layers since these solid lines are not continuous through the entire laminate. The delamination started earliest at 128 μs for fiber orientations of 0° and 90°, and latest at 140 μs for the 45° fiber orientation.

2.4.7 Energy Dissipation Versus the Fiber Orientation Angle

Figure 6 displays the energy dissipated in the four failure modes and the total work done by external forces for different fiber orientation angles. In every case, the kinetic energy generally equals 20% of the total work done by external forces and the energy dissipated due to matrix cracking is negligible relative to that in other three damage modes. This is because the elastic moduli of the matrix are very small as compared to those of the fiber. The energy dissipated due to delamination increases but that due to fiber/matrix debonding and matrix cracking decreases as the fiber orientation angle is increased from 0° to 45°.

From results exhibited in Fig. 6, we find composite's *Figure of Merit* defined as the percentage of the work done by external forces that is dissipated in different failure modes. This metric suggests that clamped unidirectional AS4/PEEK

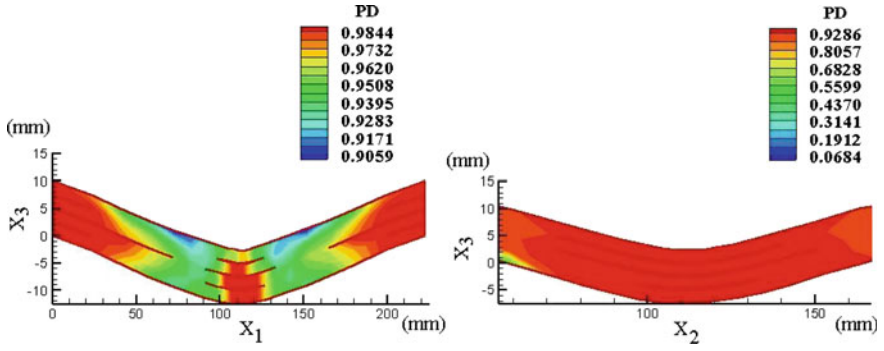

Fig. 5 At t = 220 μs, delamination/sliding between adjoining plies indicated by solid lines, and fringe plots of the fiber/matrix debonding damage variable, PD, on cross-sections $X_2 = 110$ mm (left), and $X_1 = 110$ mm (right); reproduced from [12]

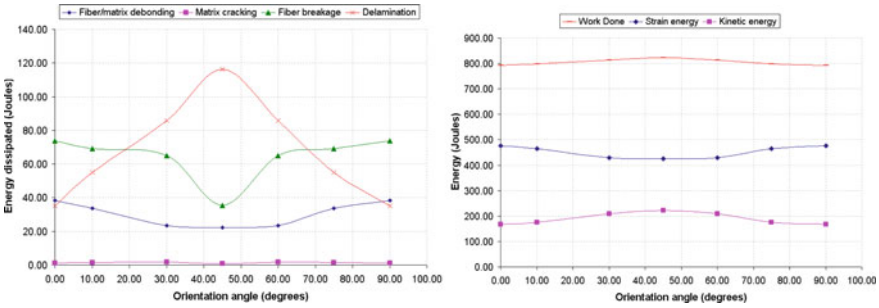

Fig. 6 Variation with the fiber orientation angle of (left) the energy dissipated in different failure modes and (right) total work done, strain energy, and kinetic energy; reproduced from [12]

composites with fiber orientations between 30° and 60° are equally effective in resisting explosive loads.

2.5 Limitations of the Model

The proposed model does not account for fiber pull out, fiber kinking, fiber buckling, and matrix crushing. The loading used to analyze the problem is a good approximation when the explosive charge is located far from the laminate. The mathematical model is not valid for composites reinforced with randomly distributed either short fibers or particulates, metal-matrix composites, and sandwich structures.

3 Delamination in Sandwich Hulls Due to Local Water Slamming Loads

We study local water slamming characterized by a large hydrodynamic load of short duration but sufficiently high intensity to cause significant structural damage, e.g., see Faltinsen [18]. In practical problems, the hull is generally curved and deformable. Hull's deformations affect the fluid motion and the hydroelastic pressure acting on the fluid/hull interface. Charca and Shafiq [19], amongst others, have experimentally studied the failure of sandwich composite panels including core shear, delamination, and damage of the face sheets due to water slamming.

We have exhibited in Fig. 7 a schematic sketch of the problem studied. The sandwich hull composed of stiff face sheets and a flexible core experiences localized slamming pressure. For hull speeds of 10 m/s, viscous effects in water are often neglected and the water compressibility plays a noticeable role only for a very short duration after the hull contacts the water. We assume the water to be

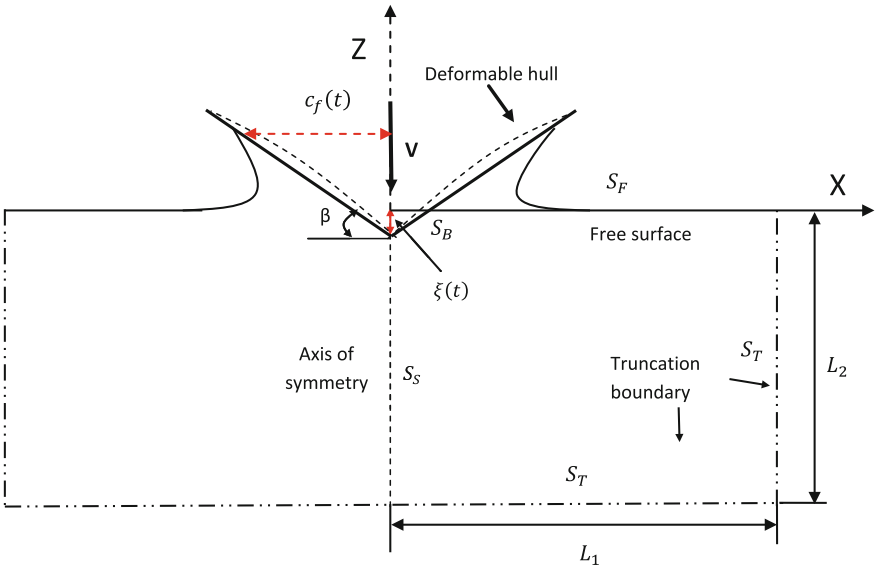

Fig. 7 Schematic sketch of the water slamming problem studied; reproduced from [20]

incompressible, inviscid, and undergoing irrotational motions. While analyzing deformations of a sandwich structure, as recommended by Reissner [3] and Koiter [4], we consider transverse normal and transverse shear deformations and use the CZM as well as coupled boundary element (BE) and FE methods to delineate delamination between adjacent plies induced by the hydroelastic pressure. We employ the BEM to analyze the fluid motion and the FEM in conjunction with the TSNDT to study transient deformations of the curved sandwich hull made of a St. Venant-Kirchhoff material. The continuity of the pressure and of the normal component of velocity at the water/hull interface couples hull's deformations with the water motion. The Rayleigh damping for the structure incorporated into the problem formulation reduces oscillations in the hydrodynamic pressure on the solid/fluid interface.

The assumptions of irrotational motion and incompressibility of the fluid imply that there exists a velocity potential φ such that the fluid velocity $\boldsymbol{v} = -\nabla\varphi$, where ∇ is the spatial gradient operator in the XZ-plane, and that φ satisfy the Laplace equation. The Laplace equation under pertinent boundary conditions is solved by the BEM with the fluid/structure interface updated after every time increment. The Bernoulli equation relating the pressure at a point to the kinetic energy density there is used to find the pressure.

We use the TSNDT and the FEM to analyze transient deformations of the St. Venant-Kirchhoff hull, and use the CZM for simulating delamination between adjacent layers of distinct materials.

The Table 1 and results described below are borrowed from Ref. [20]. In Table 1, we have compared features of our coupled BE-FE software with those of

Table 1 Comparison of LSDYNA and coupled BE-FE approaches for the water slamming problem

	LSDYNA	BE-FE methods
Fluid penetration into solid	Yes	No
Hull pressure oscillations	Yes	No
Dependence of results on contact algorithm	Yes	No
Water jet delineation	Difficult	Easy
Fluid flow assumptions	Compressible	Incompressible and irrotational
Finding strain rates in the fluid domain	Easy	Difficult

Table 2 Values of material parameters of the sandwich hull

	C_{1111} (GPa)	C_{1133} (GPa)	C_{3333} (GPa)	C_{1313} (GPa)	Mass density (kg/m^3)
Face sheet	140.3	3.77	9.62	7.10	31,400
Core	3.77	1.62	3.77	1.08	150

the commercial code, LSDYNA. It is clear that the in-house developed code avoids fluid penetration into the hull.

3.1 Water Slamming of Linearly Elastic Straight Sandwich Hull

We now analyze plane strain deformations of a clamped–clamped linearly elastic straight sandwich hull of deadrise angle, $\beta = 5°$, hull length = 1 m, thickness of each face sheet = 1.2 cm, core thickness = 3.0 cm, downward impact velocity = 10 m/s, and values of material parameters listed in Table 2. The face sheet mass density includes the dead weight of the ship. We discretize the sandwich beam into 60 uniform 2-node elements and the boundary of the 5 m × 15 m fluid domain into 2-node elements. We successively refined the mesh on the fluid boundary to get a converged solution.

For the Rayleigh damping coefficient $\alpha = 5 \times 10^{-6}$ and 5×10^{-7}, the time histories of the pressure at $y_1 = 0.35$ m plotted in Fig. 8 reveal a significant reduction in oscillations in the pressure and miniscule difference in results for the two values of α. The pressure computed without (with) using the added mass method exhibits (no) oscillations at $t = 4$ ms. The three pressure variations on the hull at $t = 2.72$, 4.79, and 5.75 ms are from the present BE-FE method, Qin and Batra's [21] semi-analytical approach, and the Das and Batra's [22] numerical solution computed using LSDYNA. The modified Wagner's theory employed in

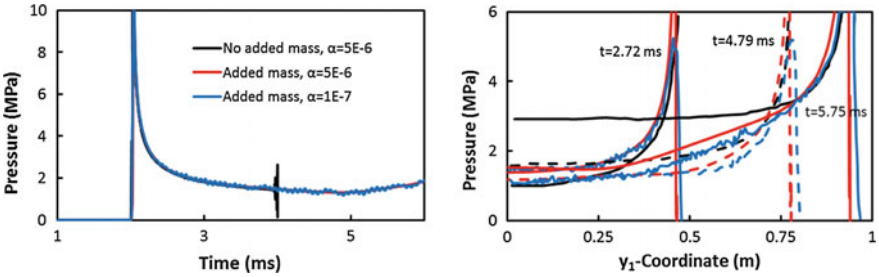

Fig. 8 For initial impact speed = 10 m/s, (left) time histories of the pressure on the hull at $y_1 = 0.35$ m for two values of the damping ratio, and with and without adding mass due to the acceleration of particles on the hull surface. The three curves overlap each other. Right: Pressure distribution on the hull at $t = 2.72$, 4.79 and 5.75 ms. Black, blue and red curves, respectively, represent results computed by Qin and Batra [20], Das and Batra [21], and the coupled FE-BE method. The y_1-axis is along the hull; reproduced from [20]

[21] gives singular pressure field and its peak value is approximated in the plot. Except for the peak pressure, the three methods give results close to each other. Hull's deformations are assumed to be infinitesimal in [21] but all geometric nonlinearities are considered in [22].

3.2 Water Slamming of Straight Sandwich Hull Made of St. Venant-Kirchhoff Material

We have simulated two water slamming problems to delineate the influence of geometric nonlinearities and hull stiffness on the hydrodynamic pressure acting on a sandwich hull. For problem 1 values of elastic constants are the same as those for the hull studied in Sect. 3.1, and for problem 2, values of all elastic parameters have been reduced by a factor of 10 and the mass density reduced to 2,000 kg/m^3. For problem 2 we set each face sheet thickness = 6 mm, core thickness = 7.5 mm, and hull length = 1 m. The first fundamental frequencies for the hulls of problems 1 and 2 without considering added mass are 110 and 101 Hz, respectively. The deadrise angle and the downward velocity of the hull for both problems, respectively, equal 10° and 10 m/s. Effects of geometric nonlinearities are considered only for problem 2. The time step = 0.75 μs was used to compute results for both problems.

Time histories of the mid-span deflection depicted in Fig. 9 (left), and the pressure distribution on the hull at two different times in Fig. 9 (right) vividly illustrate that the consideration of geometric nonlinearities significantly influences hull's deformations and its interaction with the surrounding fluid. Geometric nonlinearities reduce hull's mid-span deflection by 33% as compared to that found from the linear theory.

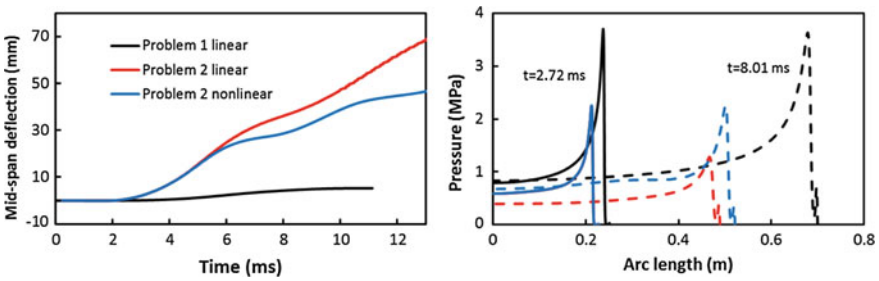

Fig. 9 Left: time histories of the mid-span deflection for the three problems studied; right: hydroelastic pressure on the hull at two different times. Black, red, and blue curves represent, respectively, results for linear problem 1, linear problem 2 and nonlinear problem 2; reproduced from [20]

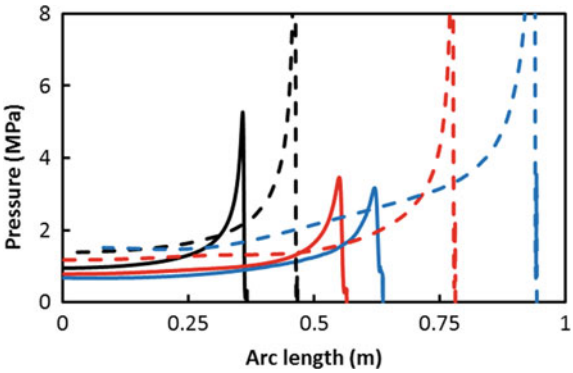

Fig. 10 Pressure distribution on circular hull with $R = 5$ m (solid curves) and flat (dashed curves) hulls. Black, red and blue curves, respectively, represent results at $t = 2.72$, 4.79 and 5.75 ms; reproduced from [20]

3.3 *Water Slamming of Linear Elastic Circular Sandwich Hull*

From the variation of the hydroelastic pressure on curved and straight hulls at three times depicted in Fig. 10, we see that the hull curvature noticeably influences the peak pressure and the pressure distribution on the hull. For each value of time, the peak pressure on the circular hull is considerably less than that on the flat hull and, as expected, occurs at different locations. The pressure distribution on the hull resembles a traveling wave with the peak pressure acting at the just wetted point, the pressure rapidly decreasing in its wake, and staying uniform over a significant part of the wetted length.

3.4 *Delamination in Linearly Elastic Straight Sandwich Hull Due to Water Slamming Loads*

We divide the clamped–clamped linearly elastic straight sandwich hull of length = 1 m, deadrise angle = 5° into 81 uniform 2-node elements. The geometric and material parameters, and the entry velocity for problem 1 are the same as those for the hull studied in Sect. 3.1. We set $\sigma_t^0 = \sigma_n^0 = 1$ MPa, $G_{Ic} = 625\,Jm^{-2}$, $G_{IIc} = 418\,Jm^{-2}$, where G_{Ic} and G_{IIc} are, respectively, the critical energy release rates for mode I and mode II failures, and σ_t^0 and σ_n^0 are the strength parameters. Values of various parameters used here are not necessarily for a real material. For problem 2, we take the thickness of each face sheet = 2 cm, core thickness = 6 cm, downward impact velocity = 10 m/s, deadrise angle = 10°, $\sigma_t^0 = 3.5$ MPa, $\sigma_n^0 = 7.1$ MPa, $G_{Ic} = 625\,Jm^{-2}$ and $G_{IIc} = 418\,Jm^{-2}$. Values of elasticities for the core and the interface strength are listed in Table 3.

For problem 1, we have compared in Fig. 11 time histories of the deflection of the hull centroid with and without considering delamination computed using the BE-FEM with those of [21] obtained by using LSDYNA. It is clear that the two sets of results are close to each other. The hull centroid deflection considering delamination is larger than that without accounting for delamination. The reduction in sandwich hull's stiffness due to delamination increases its deflections and decreases the hydroelastic pressure on the hull surface as shown in Fig. 12.

Table 3 Values of material parameters of the sandwich hull

	C_{1111} (GPa)	C_{1133} (GPa)	C_{3333} (GPa)	C_{1313} (GPa)	Mass density (kg/m^3)
Face sheet	13.4	2.40	5.92	1.92	1,850
Core	0.307	1.62	0.0923	0.107	200

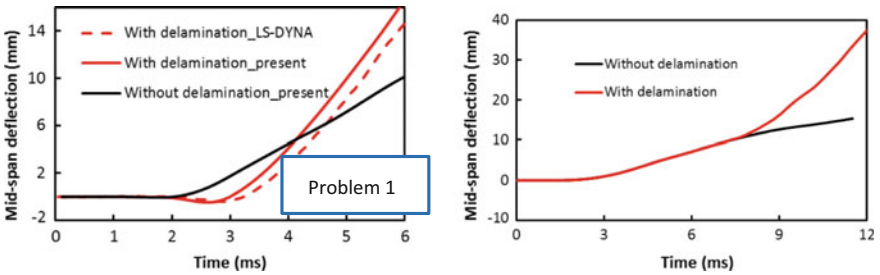

Fig. 11 Time histories of the straight hull centroid deflection with and without considering delamination; reproduced from [20]

In order to quantify delamination, we introduce a scalar, ω, that equals 1 (0) at a point for complete (no) delamination. For the two problems studied, we have plotted in Fig. 13 fringe plots of ω in ty_1-plane on the two interfaces. These plots

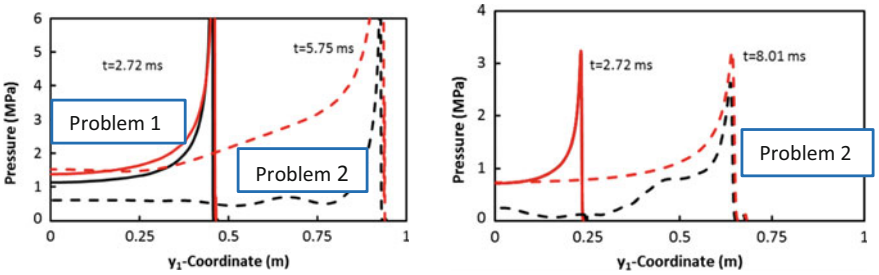

Fig. 12 Distribution of the hydroelastic pressure on the hull at two values of t. Black (red) curve represents results with (without) considering delamination. The red and black curves at t = 2.72 ms for problem 2 overlap as the beam has not been delaminated at this time; reproduced from [20]

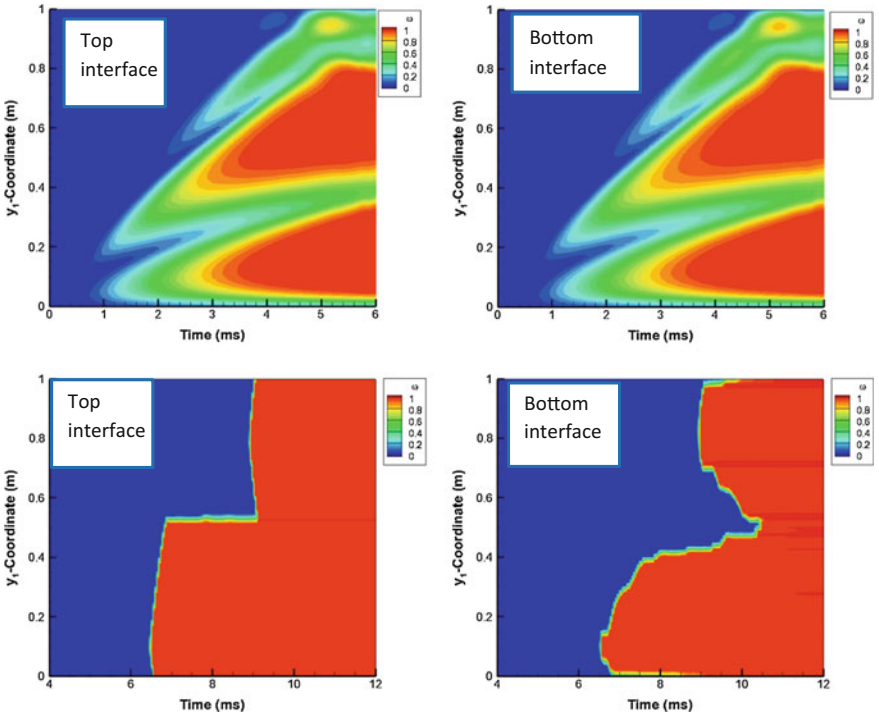

Fig. 13 Variation of the separation index ω with the y_1-coordinate and the time, on the top and the bottom interfaces for problems 1 (top 2) and 2 (bottom 2); reproduced from [20]

suggest that for problems 1 and 2 the complete delamination first occurs on both interfaces at points close to the left edge or near $y_1 = 0$ at $t = 3.6$ and 6.5 ms, respectively, and propagates to the right edge. At $t = 6$ ms, whereas most of the interfaces have been delaminated for problem 1, the delamination has not begun for problem 2. For problem 2, the two interfaces are delaminated at different rates with the top and the bottom interfaces completely delaminated at approximately $t = 9.5$ and 11 ms, respectively. The delamination process is unstable for problem 2 as evidenced by sharp increases followed by arrests in the delamination lengths.

4 Conclusions

Results presented here for the initiation and propagation of the fiber breakage, matrix cracking, fiber/matrix debonding, and delamination between adjacent plies in a clamped square composite laminate under a blast load suggest the following sequence for the failures:

(i) fiber/matrix debonding at edges of the bottom and the top surfaces that are perpendicular to the fibers,
(ii) matrix cracking at the bottom surface centroid, and at the top surface edges normal to the fibers,
(iii) fiber breakage at the top surface edges parallel to fibers followed by that at the bottom surface centroid,
(iv) debonding at the bottom and the top surfaces centroids,
(v) fiber breakage at the top surface centroid,
(vi) fiber breakage at the bottom surface sides, and
(vii) matrix cracking at the top surface centroid.

With all four plies having the same fiber orientation, the total energy dissipated in all failure modes is higher for fiber orientation angles between 30° and 60° with the panel edge than that for other fiber angles.

The slamming load on a straight sandwich hull induces delamination between stiff face sheets and the soft core with the mode II failure being unstable. The propagation of the hydroelastic pressure on the hull resembles a traveling wave with the peak pressure at the front. The pressure decay in the wake is different for intact and delaminated hulls.

Acknowledgements This work was partially supported by the ONR grant N00014-16-1-2309 to Virginia Polytechnic Institute and State University (VPI&SU) with Dr. Y. D. S. Rajapakse as the program manager. Views expressed herein are those of the author, and neither of ONR nor of VPI&SU.

References

1. Kaddour, A. S., & Hinton, M. J. (2007) The second world-wide failure exercise: Benchmarking of failure criteria under triaxial stresses for fiber-reinforced polymer composites. In *16th International Conference on Composite Materials* (pp. 2295–2312).
2. Kaddour, A. S., & Hinton, M. J. (2013). Maturity of 3D failure criteria for fiber-reinforced composites: Comparison between theories and experiments: Part B of WWFE-II. *Journal of Composite Materials, 47*(6–7), 925–966.
3. Reissner, E. (1947). Small bending and stretching of sandwich type shells. *National Advisory Committee for Aeronautics, Technical Note No*. 1832.
4. Koiter, W. T. (1960). A consistent first approximation in the general theory of thin elastic shells. In *Proceedings of IUTAM Symposium on the Theory of Thin Elastic Shells* (pp. 12–33). Amsterdam: North Holland Publishing Co.
5. Vel, S. S., & Batra, R. C. (2002). Exact solutions for thermoelastic deformations of functionally graded thick rectangular plates. *AIAA Journal, 40,* 1421–1433.
6. Qian, L. F., Batra, R. C., & Chen, L. M. (2003). Free and forced vibrations of thick rectangular plates by using higher-order shear and normal deformable plate theory and meshless local Petrov-Galerkin (MLPG) method. *Computer Modeling in Engineering and Science, 4,* 519–534.
7. Batra, R. C., & Xiao, J. (2013). Finite deformations of curved laminated St. Venant-Kirchhoff beam using layer-wise third order shear and normal deformable theory (TSNDT). *Composite Structures, 97,* 147–164.
8. Allix, O., & Corigliano, A. (1999). Geometrical and interfacial non-linearities in the analysis of delamination in composites. *International Journal of Solids and Structures, 36*(15), 2189–2216.
9. Batra, R. C. (2001). Comparison of results from four linear constitutive relations in isotropic finite elasticity. *International Journal of Nonlinear Mechanics, 36,* 421–432.
10. Hassan, N. M., & Batra, R. C. (2008). Modeling damage in polymeric composites. *Composites B, 39,* 66–82.
11. Kyriakides, S., Arseculeratne, R., Perry, E., & Liechti, K. (1995). On the compressive failure of fiber reinforced composites. *International Journal of Solids and Structures, 32*(6–7), 689–738.
12. Batra, R. C., & Hassan, N. M. (2007). Response of fiber reinforced composites to underwater explosive loads. *Composites: Part B, 38,* 448–468.
13. Batra, R. C., & Liang, X. Q. (1997). Finite dynamic deformations of smart structures. *Computational Mechanics, 20,* 427–438.
14. Cole, R. H. (1948). *Underwater explosions*. Princeton: Princeton University Press.
15. Türkmen, H. S., & Mecitolu, Z. (1999). Dynamic response of a stiffened laminated composite plate subjected to blast load. *Journal of Sound and Vibration, 221*(3), 371–389.
16. Luo, R., Green, E., & Morrison, C. (2001). An approach to evaluate the impact damage initiation and propagation in composite plates. *Composites Part B*, *32*, 513–520.
17. Mouritz, A. (1996). The effect of underwater explosion shock loading on the flexural properties of GRP laminates. *International Journal of Impact Engineering, 18*(2), 129–139.
18. Faltinsen, O. M. (1993). *Sea loads on ships and offshore structures*. Cambridge, UK: Cambridge University Press.
19. Charca, S., & Shafiq, B. (2010). Damage assessment due to single slamming of foam core sandwich composites. *Journal of Sandwich Structures and Materials, 12,* 97–112.
20. Xiao, J., & Batra, R. C. (2014). Delamination in sandwich panels due to local water slamming loads. *Journal of Fluids and Structures, 48,* 122–155.
21. Qin, Z., & Batra, R. C. (2009). Local slamming impact of sandwich composite hulls. *International Journal of Solids and Structures, 46,* 2011–2035.
22. Das, K., & Batra, R. C. (2011). Local water slamming impact on sandwich composite hulls. *Journal of Fluids and Structures, 27,* 523–551.

Stress Triaxiality in Damage Models

S. R. Hiremath, Deepak Alapur and D. Roy Mahapatra

1 Introduction

Impact dynamic response of structures has become an increasingly important consideration in structural design. Earlier, problems involving impact were primarily of military interest. In recent times, accidental impact problems have also become important in numerous civil, marine, and aerospace structural designs. The collision of two or more bodies can be anything from dropped objects, collision or grounding of vessels, collision of vehicles or aircrafts to accidental impacts like bird strikes in aviation and space debris and meteoroids in space. Due to the increasing focus on the impact problem, it is important to understand the material behavior when subjected to impulsive loading. The high strain rates and the elevated temperature associated with impact loading influence both the plastic flow stress and the failure mechanism of the material.

Simulation of large deformation and strain rate dependent fracture in alloys employs Johnson–Cook material model [16]. This type of prediction of large deformation behavior and fracture is based on the phenomenological viscoplasticity model. The plastic damages in this type of models are simulated based on fitting of uniaxial test data into constitutive model parameters and spall model parameters. The failure states are defined using spall model parameters, which use fitting of effective plastic strain data obtained from the test. Reported studies have shown that these parameters are primarily governed by the uniaxial tensile stress component under quasi-static loading conditions [9]. Stress triaxiality based failure modeling is widely used in modeling the failure in finite-element models, where unidirectional tensile test coupons with varying notches are used to determine the stress triaxiality during fracture. Effect of stress triaxiality on the fracture and its effects has been

S. R. Hiremath · D. Alapur · D. Roy Mahapatra (✉)
Department of Aerospace Engineering, Indian Institute of Science,
Bangalore 560012, India
e-mail: droymahapatra@aero.iisc.ernet.in

S. Gopalakrishnan and Y. Rajapakse (eds.), *Blast Mitigation Strategies in Marine Composite and Sandwich Structures*, Springer Transactions in Civil and Environmental Engineering, https://doi.org/10.1007/978-981-10-7170-6_13

shown in various studies. 3D-stress distribution near the tip of semi-infinite crack embedded in an infinite plate of arbitrary thickness was solved by Sin et al. [25], further numerical and analytical calculations were combined to solve more complex problems [5, 6, 15]. Variation of stress intensity and strain energy density factor along the crack front in a finite thickness plate having a central crack subjected to unidirectional loading studies showed the methodology for using finite-element method in conjugate with continuum mechanics [24]. Recently a phase-field model has been formulated where constitutive law prior to crack initiation is given by a cubic degradation function, kinematics of the body and the phase field are derived from general energy potential. Measure of stress triaxiality is chosen to be the driving force for crack initiating and propagation [7]. The accuracy of the prediction by the model considering the three-dimensional state of stress when the model is scaled to a different geometry is poorly understood. In the present work, we have used Johnson–Cook material model to numerically model various fracture and damage modes in coupon level. Here, J_2 plasticity approach is followed, which is wildly used for modelling multi-axial plasticity. In which effective deviatoric stress are used to check yield conditions. Further stresses are updated from radial return mapping algorithm. Material and damage parameters required in JC model are experimentally characterized from unidirectional tensile test. Further numerical modeling of the unidirectional tensile model and 3-point flexural model are carried out. Numerical and experimental models and further compared and analyzed.

1.1 Constitutive Model

1.1.1 Gurson Model

The Gurson model [12, 13] considers microvoid nucleation and growth, and Thomason [27] developed a physical model with microvoid coalescence criterion on the basis of plastic limit. Comparative studies based on finite-element simulation shows that the Gurson model is more accurate for both hardening and non-hardening materials [34]. The ductile failure in the Gurson model is entirely related to the microvoid nucleation parameter, and this parameter in many cases can be determined without any metallurgical/micromechanical experiments. According to the Gurson model, the yield function has the following form:

$$\Phi(q, \bar{\alpha}, f, \sigma_m) = \frac{q^2}{\bar{\sigma}^2} + 2q_1 f \cosh\left(\frac{3q_2\sigma_m}{2\bar{\sigma}}\right) - 1 - (q_1 f)^2 = 0 \tag{1}$$

where f is the void volume fraction, which is the average measure of a void-matrix aggregate, σ_m is the mean of normal stresses, q is the von Mises equivalent stress, $\overline{\alpha}$ is the flow stress of the matrix material, q_1, q_2 are the constants introduced by Tvergaard [23, 28]. For existing voids, the Gurson model can describe the softening

effect caused by the voids on material behavior, and at the same time can predict the void growth rate during plastic deformation. Because the matrix material is incompressible, the growth rate of the existing voids is given by

$$\mathrm{d}f_{growth} = (1-f)\mathrm{d}\varepsilon^{\mathrm{p}}:\mathrm{I} \tag{2}$$

where ε^{p} is the plastic strain tensor and I is the second-order unit tensor and f is the effective void volume fraction. Incremental of void growth is defined by multiplication of plastic strain tensor with effective void volume fraction (scaler value), which is further multiplied with a second-order unit tensor using double dot product. Void growth is preceded by nucleation of the voids, void nucleation model suggested by Needleman [11] is shown below.

$$f^{*} = \begin{cases} f & f \le \mathrm{f_c} \\ f_c + \frac{\mathrm{f_E} - \mathrm{f_c}}{\mathrm{f_F} - \mathrm{f_c}} & (f - f_c) f > \mathrm{f_c} \end{cases} \tag{3}$$

where f_c is the threshold value which indicates the onset of coalescence, f_F is the void volume fraction at the final state of fracture, where $f_E = 1/q_1$. Needleman [18] has shown that above form of void nucleation is accurate for low-stress triaxiality, but has poor accuracy for high-stress triaxialities.

1.1.2 Zerilli–Armstrong Model

The Zerilli–Armstrong-type models are physically based, and there are several generations of models. Initially, the model addressed metals with either fcc or bcc crystal structures [29, 33]. Formulation of constitutive relation is based on dislocation dynamics. The effects of grain size, strain hardening, strain rate hardening, and thermal softening have been incorporated into the formulation. The relation has a relatively simple expression and is applicable to a wide range of materials with the face-centered cubic crystal structure. A relation for iron has also been developed and is also applicable to other materials having body-centered cubic crystal structure. To address the problem of modeling ballistic impact on titanium alloys, Zerilli and Armstrong proposed a constitutive model with a hexagonal closely packed crystal structure. Shear instability and the resultant strain localization was also addressed in this model [21]. It has also been pointed out that each material structure type (fcc, bcc, hcp) will have its own constitutive behavior based on the dislocation dynamics of that particular crystal structure. The yield strength in Zerilli–Armstrong model is expressed as

$$\sigma_s = A + \left[C_1 + C_2\sqrt{3}\right] e^{\{-C_3 + C_4 \ln \dot{\varepsilon}\}T} + C_5 \varepsilon^{n} \tag{5}$$

where ε is the strain, $\dot{\varepsilon}$ is the strain rate and T is the temperature. A, C_1, C_2, C_3, C_4, C_5 are the choice of constants based on the crystal structure. This model has been used in the earlier works [22] for modeling the ballistic impact of titanium alloys. Zerilli and Armstrong extended the applicability of the fcc/bcc model by developing of a newer representation for hcp metals [30, 32]. Then they extended their hcp model to address shear instability, an important consideration for Ti-6Al-4 V alloy.

The localizing strength model proposed by Zerilli and Armstrong [31] for the strength of predominantly hcp Ti-6Al-4 V is somewhat different from Eq. (5)

$$\sigma_s = C_0 + C_1 e^{-\beta T} + C_2 \sqrt{\varepsilon_r (1 - e^{-.7ex\varepsilon/.7ex\varepsilon_r}) e^{-\alpha T}} \tag{6}$$

$$\alpha = \alpha_0 - \alpha_1 \ln \dot{\varepsilon} \tag{6a}$$

$$\beta = \beta_0 - \beta_1 \ln \dot{\varepsilon} \tag{6b}$$

where C_0, C_1, and C_2 are material constants, α and β are functions of strain rate, α_0, α_1, β_0, β_1 are material constants and T is the absolute temperature. The expression under the radical will be referred to as the "strain function". The material constant ε_r affects the strain at which saturation of the stress is achieved.

The square root in Eq. (6) comes from theoretical considerations of dislocation motion during the plastic deformation of crystals [26]. In that work, Taylor concluded that the yield stress depends on the square root of strain (and other factors). The problem with a simple square root function is that the stress will not saturate at high strains in a function of the form $\sigma_s = K\sqrt{\varepsilon}$. This type of strain hardening behavior is detrimental if modeling of plastic strain localization is desired, since localization depends on the thermal softening effects overtaking the strain hardening effects. In fact, hcp alloys like Ti-6Al-4 V do saturate at high strains, so Zerilli and Armstrong replaced the simple strain term in the Taylor strain hardening of earlier models with the strain function in Eq. 6, which shows saturation at high strains.

1.1.3 Johnson and Cook Material Model

The Johnson–Cook (JC) model [16] was developed during the 1980s to study the impact, ballistic penetration, and explosive detonation problems. The model has proven to be quite useful and it has been extensively used by many researchers and various industries to study high strain rate and large strain problems. The reasons for the popularity of this model are that it has a simple form of the constitutive equations and the parameters used in the equations for a number of materials are developed from macroscopic mechanical tests. The material constitutive model has an associated cumulative damage law which can be used to assess failure [19]. Both the constitutive model and the damage model are empirically based, where the flow stress and the failure strain are determined by conducting unidirectional tensile test

experiments by varying the stress triaxiality factor and the parameters involved in these two quantities are determined. According to the material model, the flow stress is represented as

$$\sigma_f = \left[A + B\left(\varepsilon_{eff}^{p}\right)^{N}\right](1 + C\ln\dot{\varepsilon})\left[1 - T_H^M\right] \tag{7}$$

where ε_{eff}^{p} is the equivalent plastic strain. The constant A is the yield stress, B and the exponent "N" represent the strain hardening effects. The exponent "M" in the last term in the brackets represents temperature softening of the material through homologous temperature defined as

$$\mathrm{T_H} = \frac{\mathrm{T} - \mathrm{T_{room}}}{\mathrm{T_{melt}} - \mathrm{T_{room}}} \tag{8}$$

The equivalent plastic strain at fracture (ε_f) is derived from the following cumulative damage law

$$\varepsilon_f = \left[D_1 + D_2 e^{D_3\sigma^*}\right]\left[1 + D_4\ln\varepsilon^*\right]\left[1 + D_5 T^*\right] \tag{9}$$

where σ^* is the stress triaxiality factor defined as pressure divided by effective stress, and D_1, D_2, D_3, D_4, and D_5 are the constants. These constants are determined by performing quasi-static tensile tests at various strain rates and also by varying the stress triaxiality.

Importance of triaxiality is evident for example in stress concentrations due to geometry and already initiated crack tips. To capture the effect of triaxiality, in an experimental procedure for estimation of the model parameters, the notched test specimen is subjected to tensile loading. In unidirectional tension test, the stress state prior to necking is due to the 3D stress state on the sample surface. The onset of necking is accomplished by the development of a triaxial state of stress in the neck. Theoretical and experimental studies have shown that stress triaxiality is the key parameter controlling the magnitude of the fracture strain. The effect of stress triaxiality on the fracture strain can be quantified by conducting a unidirectional tensile test on a smooth and notched round bar or flat specimens [17, 20]. Smooth and notched round bar specimens are mostly used to quantify the effect of stress triaxiality on fracture strain. Bridgman [10] analyzed for the first time the stress distribution in a round bar specimens with different notches and derived the formula of stress triaxiality for this type of specimen. At the neck cross section, which is the fracture initiation site, the Bridgman formula for stress triaxiality η is given by

$$\eta = \frac{1}{3} + \ln\left(1 + \frac{a}{2R}\right) \tag{10}$$

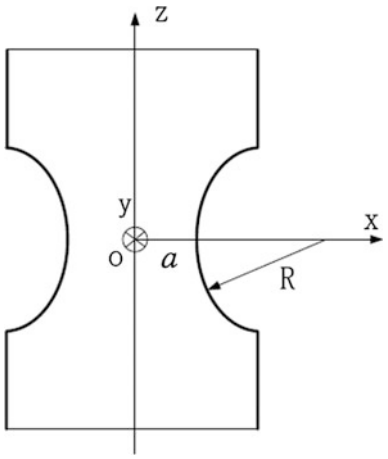

Fig. 1 Flat-grooved plane strain specimen [3]

where R is the local radius of the neck in the round bar specimen, and "a" is the radius of the necking cross section. A flat-grooved plane strain specimen with the sketch of its cross section is shown in Fig. 1 The thickness of the specimen at the groove is t = 2a, and the radius of the groove is "R". The thickness direction is in the x direction.

Bridgman also gave an approximate solution for stress triaxiality factor and the effective plastic strain for failure in flat specimen as shown below

$$\eta = \frac{\sigma_m}{\sigma} = \frac{1}{3} + \sqrt{2}\ln\left(1 + \frac{a}{2R}\right) \tag{11}$$

$$\varepsilon_f = \frac{2}{\sqrt{3}}\ln\frac{t_0}{t_f} \tag{12}$$

where a is the width and R is the radius of the groove. Where t_0 is the initial thickness of the specimen and t_f is the final thickness of the specimen at failure.

A choice of three spall models [14] were developed to represent material splitting, cracking, and failure under tensile loads. The pressure limiting model which limits the minimum hydrostatic pressure to the specified value $P \geq P_{min}$. If pressures are higher than this tensile limiting pressure than the pressure is reset to P_{min}. This option is not strictly a spall model since the deviatoric stresses are unaffected by the pressure reaching the tensile cutoff and the pressure cutoff value P_{min} remains unchanged throughout the analysis. The second one the maximum principal stress spall model which detects spall if the maximum principal stress σ_{max} exceeds the limiting value σ_P. Once spall in a solid is detected with this model, the deviatoric stresses are reset to zero and no hydrostatic tension is permitted. If tensile pressures are calculated, they are reset to 0 in the spalled material. Thus, the spalled material behaves as rubble. The third one is the hydrostatic tension spall model

which detects spall if the pressure becomes more tensile than the specified limit P_{min}. Once spall in a solid is detected with this model, the deviatoric stresses are set to zero and the pressure is required to be compressive. Hydrostatic stress is reset to 0 for that element.

The spall model used in Johnson–Cook model represent material damaging under tensile loads. The advantage of having spall model is it can accurately predict stress triaxiality-based failure in tensile mode. However, the failure strain is not strictly a material constant, but it also depends on the state of stress. Spall model controls the pressure in the element as explained earlier. One of the major disadvantages is mixed mode effects are poorly captured in these models. In the present studies, we are using maximum principle stress-based spall model.

2 Experimental Characterization of Triaxiality Effects and Model Parameter Extraction

The parameters for Johnson–Cook models are estimated through experimental measurements and data processing. Tensile test specimens are fabricated from aluminum 7075 alloy according to ASTM-E8 [1]. Smooth and notched tensile specimens with 40 mm gauge length, with varying notch radius of 0.8–2 mm were tested. Figure 2a shows the dimensions of the tensile test sample, Fig. 2b shows tensile test samples. Notches of the required radius are introduced in the test sample using electrical discharge machining (EDM).

Uniaxial tensile tests are conducted at room temperature using the universal testing machine. The experiment is carried out on un-notched samples with various strain rates varying from 0.05 to 0.0005 s^{-1} the test results are as shown in the Fig. 3. The experiment is carried out to obtain stress–strain curves for the material to extract Johnson–Cook model parameters. The experimental results are validated with the literature results and details are discussed in section.

Three-point flexural test samples are fabricated according to ASTM E290 [2] standards as shown in Fig. 4. The load P is applied at the mid-span of the test sample, stress distribution across the sample width is given by $\sigma_f = \frac{3PL}{2bd^2}$ where L is

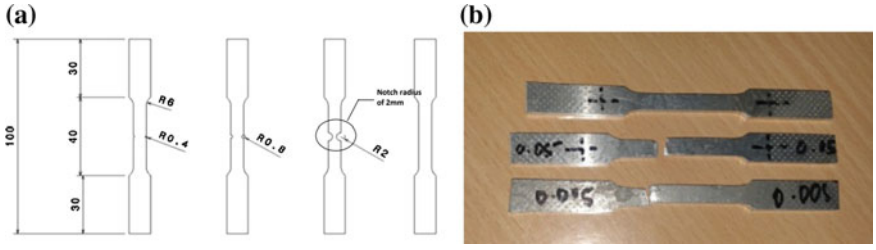

Fig. 2 **a** ASTM E-8 tensile test sample dimensions for notched and un-notched cases, **b** Al-7075 tensile samples

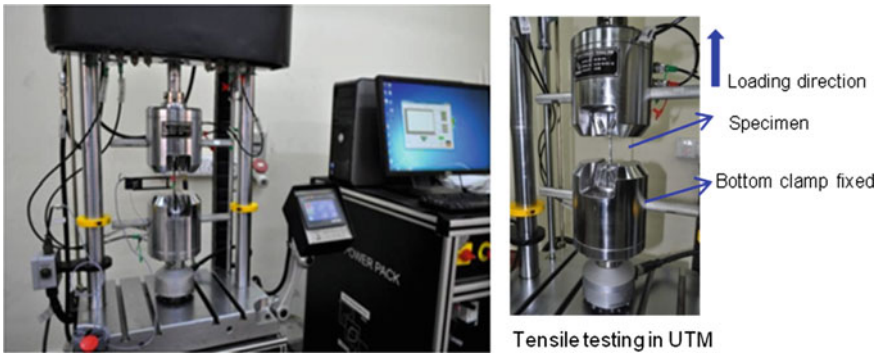

Fig. 3 Experimental setup for characterizing uniaxial tensile characteristics

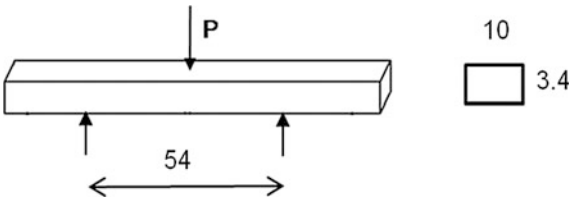

Fig. 4 Three-point bend flexural test sample dimension according to ASTM E290

the support span length, b is the width of the beam, and d is the thickness of the sample. The stress is essentially zero at the neutral axis. The flexural strain can be calculated as $\varepsilon_f = \frac{6Dd}{L^2}$ where D is the maximum deflection at the center of the sample. The flexural modulus is calculated as $E_f = \frac{L^3 m}{4bd^3}$ where m is the gradient load–deflection curve. Ductile materials, however, provide load–deflection curves which deviate from a linear relationship before a failure takes place.

The width and thickness of the samples are polished to maintain thickness to span ratios according to ASTM standards. The three-point bend flexural test is carried out using a universal testing machine as shown in the Fig. 5 until failure takes place. The load–deflection curve is obtained from the tests are further post-processed to obtain flexural properties. The bending stress, flexural strain, and flexural modulus are calculated according to the above equations. The load–deflection curves obtained from the experiments are discussed in the next section.

2.1 Determination of Flow Stress Parameters

Stress–strain plot for uniaxial tensile test of aluminium 7075 is shown in Fig. 6. Test data obtained from un-notched specimen are used in extracting Johnson–Cook flow stress parameters. The flow stress equation given by Eq. 7 is used. The flow stress parameters A, B, N, and C are extracted without considering the effect of

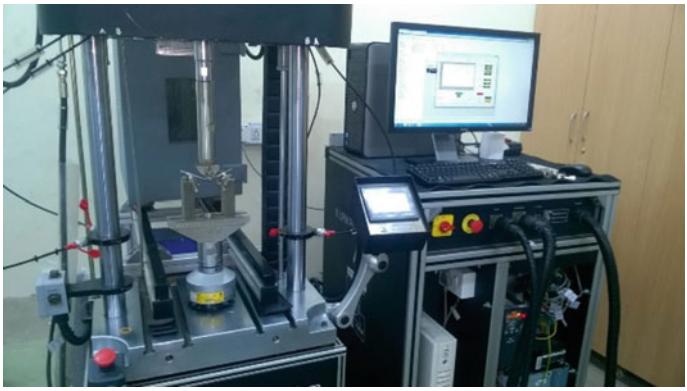

Fig. 5 Three-point bend flexural test setup

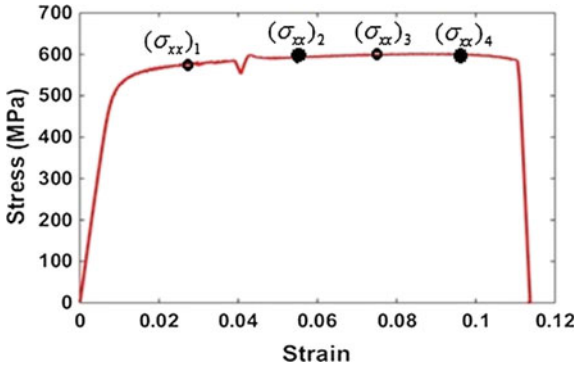

Fig. 6 Stress versus strain curve obtained from uniaxial tensile test of un-notched Al-7075 alloy

temperature. From the stress–strain results, the value of A (yield stress) is obtained, and the values for B, N, and C the flow stress equation is solved by rearranging it as

$$\ln\left(\sigma_f - A\right) = \ln B + n \ln \varepsilon_p \tag{13}$$

To obtain the values of B and n the variation of flow stress with respect to plastic strain is plotted, and Eq. 13 is solved by plugging-in various values of flow stress and their respect strain value.

The value of constant C in the Eq. 7 is obtained by rearranging the equation as

$$\left[\frac{\sigma_f}{\sigma_p} - 1\right] = c \ln \varepsilon \tag{14}$$

$$\sigma_p = A + B\left(\varepsilon_{eff}^p\right)^n \tag{15}$$

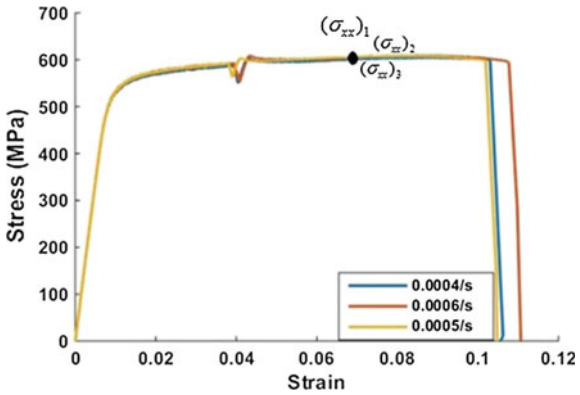

Fig. 7 Stress–strain response of the Al 7075 tensile samples for various strain rates

Table 1 Johnson–Ccook flow stress parameters

A	B	N	C
583 MPa	483 MPa	0.620	−0.004

Figure 7 shows the stress–strain response of the Al 7075 tensile samples for various strain rates. To obtain the value of constant C, Eq. 14 is solved for the particular value of plastic strain, with respective flow stress for various strain rates.

The flow stress parameters obtained are shown in Table 1.

2.2 *Determination of Damage Parameters*

Damage parameters are extracted from post-processing the uniaxial tensile test of notched samples at various strain rates. Three batches test samples with notch radius of 0.4, 0.8, and 2 mm are prepared as shown in Fig. 2. The notches in the specimen will introduce stress triaxiality. The stress triaxiality factor for the flat tensile specimen is calculated using Eq. 11. The Johnson–Cook damage model parameters D_1, D_2, D_3 are extracted by rearranging the Eq. 9. as

$$\varepsilon_f = \left[D_1 + D_2 e^{D_3 \sigma^*}\right] \tag{16}$$

In the above equation D_1, D_2, D_3 are the constants, ε_f and σ^* are the variables. To obtain the values of D_1, D_2, and D_3, plot of variation failure strain with respect to stress triaxiality factor is plotted. Curve fitting is done through the data points obtained as shown in the Fig. 8. The curve obtained from the curve fitting is used to obtain the new failure strain values for particular stress triaxiality factor and the Eq. 16 is solved obtain the values of D_1, D_2, and D_3.

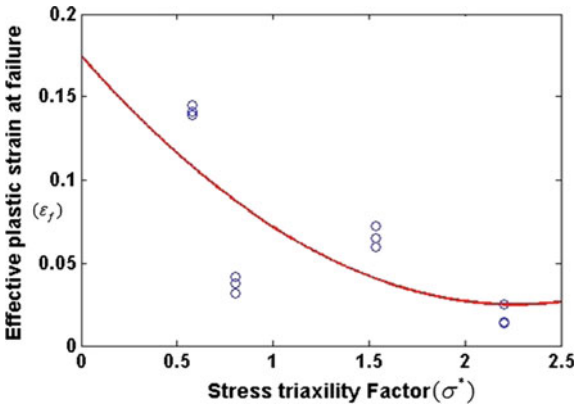

Fig. 8 Plot of stress triaxiality factor versus effective plastic strain at failure

Table 2 Johnson–Cook flow stress parameters

D_1	D_2	D_3	D_4
0.0117	0.2057	−1.2546	−0.0017

To obtain the value of D_4 plot of failure strain with respect to the strain rate is post-processed. Equation 9 is rearranged as the value of D_4 is obtained by solving Eq. 17.

$$\varepsilon_f = \left[1 + D_4 \ln \varepsilon^*\right] \tag{17}$$

The flow stress parameters and the damage parameters which are experimentally determined as discussed above are shown in Table 2, which will be further incorporated in LS-DYNA simulation to validate the simulation results with the experimental results. The objective of this comparative study is to evaluate the role on triaxiality on the predictive ability of the model regarding failure phenomena as observed in the experiment with various different boundary conditions and loading conditions.

3 Results and Discussion

The experimental tensile tests are conducted at a displacement rate of 0.5–2 mm/min. The strain was measured using an extensometer with a gauge length of 25 mm. Figure 9a shows the comparisons of stress versus strain graph obtained from experiments and reported literature results. The tensile test results obtained from the experiment are in consistent with the results obtained from the literature. Figure 9b shows the experimental stress–strain curves obtained from the uniaxial

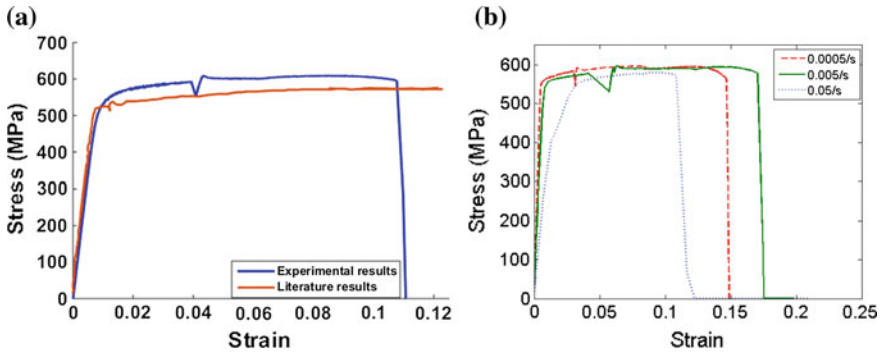

Fig. 9 **a** Stress–strain experimental data obtained from literature done on un-notched tensile test specimen [8] **b** Stress–strain experimental data obtained at different strain rates for un-notched tensile test specimen

Table 3 Tensile test results obtained by conducting test at various strain rates

Strain rate (s^{-1})	Yield stress (MPa)	Ultimate stress (MPa)	Failure strain
0.0005	541	580	0.18
0.005	538	580	0.15
0.05	530	550	0.12

tension test. In all cases, the specimens failed after very little necking and fractured along a surface slanted with respect to their longitudinal axes. The tensile test conducted at various strain rate shows, decrease in failure strain as the increase in the strain rate (Table 3).

The ultimate stress in case of the notched specimen is similar for various notch radius but the failure strain decreases with increase in the notch radius. The tensile tests with smooth and notched specimens showed that the tensile ductility decreases with increasing stress triaxiality, indicating a ductile fracture mode. Fracture mode changes as the stress triaxiality reduces. Similar fracture behavior has been reported for Al 2024-T351 [4]. The fracture locus has three distinct branches and possible slope discontinuities in the transition regime. It was concluded that for large triaxialities void growth is the dominant failure mode, while shear failure is dominant for negative stress triaxialities.

3.1 Validation of Unidirectional Tensile Response Simulation

Johnson–Cook material model parameters obtained from the experiments are used to model uniaxial tensile and three-point bend flexural simulation in LS-DYNA

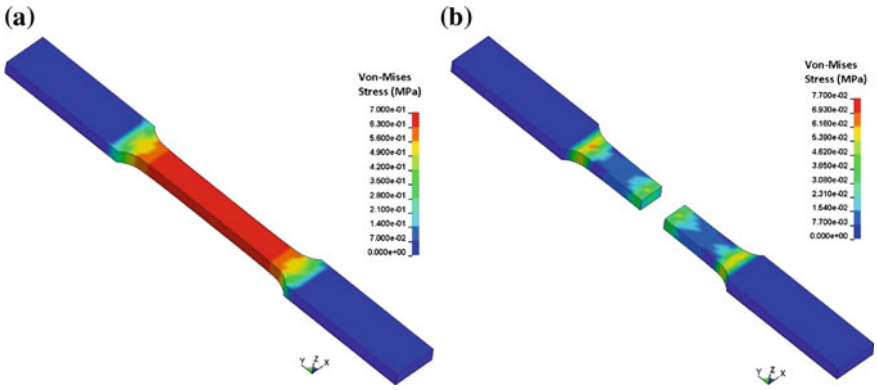

Fig. 10 von Mises stress distribution in uniaxial tensile test simulation model, **a** stress distribution before fracture, **b** stress distributions after fracture

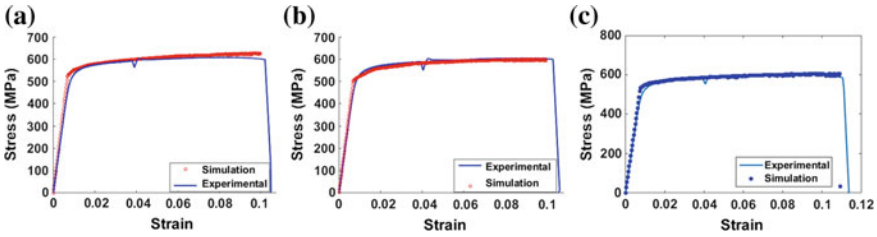

Fig. 11 Validation of tensile test simulation results with experimental results carried out at various strain rates, **a** stress versus strain graph for strain rate of 0.0004/s, **b** stress versus strain graph for strain rate of 0.0005/s, **c** stress versus strain graph for strain rate of 0.0006/s

software. Three-dimensional models of the test samples were created in CATIA software. Hexahedral elements with 8 nodes are used to generate the 3D mesh of the geometry using MSC PATRAN. The preprocessed 3D finite-element models are imported to LS-DYNA for applying material properties and boundary conditions. An implicit solver scheme is used to solve the quasi-static problem for mimicking the loading conditions applied in the experiments. Uniaxial tensile simulation model contains 88200 elements. The numerical model is constrained at one end and a prescribed displacement is applied at the other end. Johnson–Cook material model (MAT 15) is used in the simulation. The Young's modulus of Al-7075 alloy (70 GPa) obtained from experiments is used.

Figure 10 shows von-Mises stress distribution before and after fracture in the finite element model. The predicted stress–strain curves are shown in dotted line and compared with the experimental measurements in Fig. 11. The simulation results obtained are consistent with the experimental results. For the small variation in the Johnson–Cook model parameters, these results vary in larger scale. As these parameters can capture the damage much accurately, these parameters are future used in the validations of three-point bend flexural simulation.

3.2 *Validation of Mode-1 Fracture in 3-Point Bending Test Coupons*

Mode-1 fracture due to 3-point bend flexural loading is simulated to study the damage prediction capability of the Johnson–Cook model in various different boundary conditions. The model parameters obtained from the uniaxial tensile tests shown in Tables 1 and 2 are used in the flexural simulations. The indenter and the supports are assigned with rigid body condition. Figure 12 shows the finite element model with von-Mises distribution in flexural mode. The flexural test is carried out on UTM on samples fabricated according to ASTM E290 standards. The experiment is carried out to obtain load–displacement curves, and the results are validated with experimental results as shown in the Fig. 13.

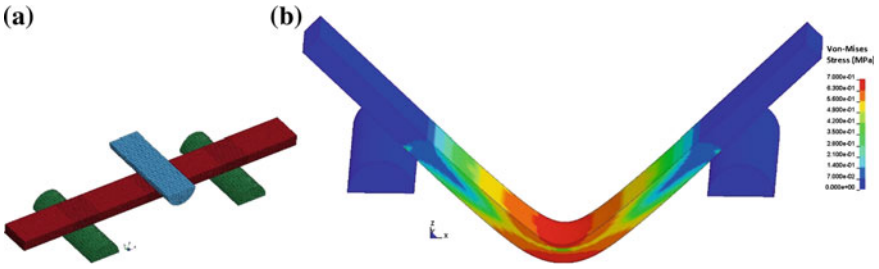

Fig. 12 **a** Finite-element model for three-point bend simulation, **b** von Misses stress distribution developed in the FE model due to applied loads

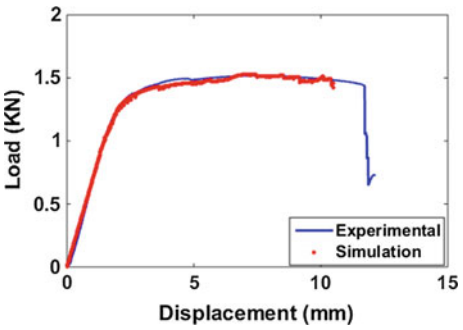

Fig. 13 Comparison of load versus displacement behavior from simulation and experimental results

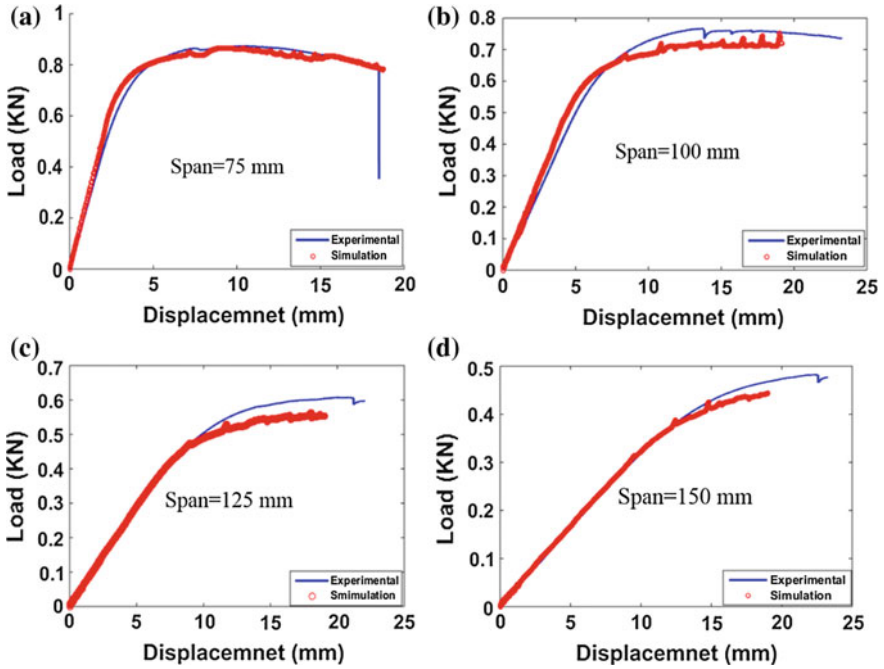

Fig. 14 Comparison of load versus displacement behavior obtained from experiments and simulations. **a** Load versus displacement curves for span length of 75 mm, **b** load versus displacement curves for span length of 100 mm, **c** load versus displacement curves for span length of 125 mm, **d** load versus displacement curves for span length of 150 mm

The simulation results are consistent with the experimental results. The yield, ultimate load are accurately predated in the simulation but the simulation lags in predicting the failure onset. The Johnson–Cook model parameters that were extracted using unidirectional tensile tests are incorporated in the simulation, which holds good in predicting failure in case of unidirectional tensile case but in case of three-point bending the simulation predicts early failure compared to the actual case (Fig. 14).

Three-point bend flexural test is carried out for the various aspect ratio of the samples. Four different aspect ratios were considered. The same configuration of samples is modeled in the simulations to compare the failure stress and strains. It is observed that the LS-DYNA simulation results have more error in predicting the flow stress and failure strain. The Johnson–Cook model parameters extracted using unidirectional tensile test does not predict the failure accurately as compared to that of unidirectional tensile test simulation (Fig. 15).

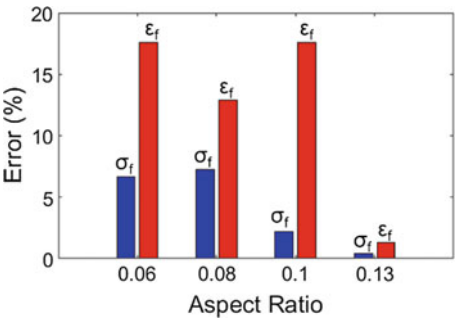

Fig. 15 Maximum error in predicting failure strain and flow stress in 3-point bending case

4 Conclusion

Structural components subjected to high strain loads such blast, the impact is modeled using various materials models available. Three material models which can handle complex material behavior are discussed. Johnson–Cook material model which is widely used across various industries to model high strain rate dependent behavior is used in the detailed investigation of failure prediction capability considering stress triaxiality effect. An extensive methodology for extracting the flow stress parameters and the damage parameters from uniaxial tensile test has been explained. We further validate the experimentally obtained data with reported literature data. Uniaxial tensile test simulations are carried out using simplified Johnson–Cook material model in LS-DYNA. Simulation results are validated against the experimental test results. We further investigated the modeling capability under different boundary conditions. Flow stress and damage parameters obtained from uniaxial tensile tests were used to model three-point bend flexural simulations. Even though the model was able to simulate uniaxial test cases accurately, it failed to capture flexural failure behavior for varying aspect ratios correctly. This study shows that the failure predictions using the Johnson–Cook model is highly dependent on the stress triaxiality. Hence, the flow stress and damage parameters for more complex boundary conditions and loading have to be experimentally or analytically estimated. One possible direction to develop more accurate and yet computationally efficient modeling scheme would be to incorporate fracture mechanics based updates of stress triaxiality in the fracture process zone.

Acknowledgements The authors thankfully acknowledge financial support Pratt and Whitney USA to carry out this research.

References

1. ASTM, E. (1991). 8 M: Standard test method for tension testing of metallic materials (Metric). *Annual book of ASTM standards, Philadelphia*.
2. ASTM, E. (1982). E290-92-standard test method for semi-guided bend test for ductility of metallic materials. *American society for testing and materials*.
3. Bai, Y., Teng, X., & Wierzbicki, T. (2009). On the application of stress triaxiality formula for plane strain fracture testing. *Journal of Engineering Materials and Technology, 131*(2), 21002.
4. Bao, Y., & Wierzbicki, T. (2004). On fracture locus in the equivalent strain and stress triaxiality space. *International Journal of Mechanical Sciences, 46*(1), 81–98.
5. Bažant, Z. P. (1974). Three-dimensional harmonic functions near termination or intersection of gradient singularity lines: A general numerical method. *International Journal of Engineering Science, 12*(3), 221–243.
6. Benthem, J. P. (1977). State of stress at the vertex of a quarter-infinite crack in a half-space. *International Journal of Solids and Structures, 13*(5), 479–492.
7. Borden, M. J. et al. (2016). A phase-field formulation for fracture in ductile materials : Finite deformation balance law derivation, plastic degradation, and stress triaxiality effects. *Computer Methods Applied Mechanical Engineering*, *312*, 130–166. Retrieved from http://dx.doi.org/10.1016/j.cma.2016.09.005.
8. Børvik, T., Hopperstad, O. S., & Pedersen, K. O. (2010). Quasi-brittle fracture during structural impact of AA7075-T651 aluminium plates. *International Journal of Impact Engineering, 37*(5), 537–551.
9. Brar, N. S., et al. (2009). Constitutive model constants for Al7075-T651 and Al7075-T6. *AIP Conference Proceedings, 1195*(1), 945–948.
10. Bridgman, P. W. (1952). *Studies in large plastic flow and fracture*. New York: McGraw-Hill.
11. Chu, C. C., & Needleman, A. (1980). Void nucleation effects in biaxially stretched sheets. *Journal of Engineering Materials and Technology (Transactions of the ASME)*, *102*(3), 249–256.
12. Gurson, A. L. (1977). Continuum theory of ductile rupture by void nucleation and growth: Part I—yield criteria and flow rules for porous ductile media. *Journal of Engineering Materials and Technology, 99*(1), 2–15.
13. Gurson, A. L. (1975). Plastic flow and fracture behavior of ductile materials incorporating void nucleation, growth and coalescence. *PhD Dissertation,* Brown University.
14. Hallquist, J. O. (2007). LS-DYNA keyword user's manual. *Livermore Software Technology Corporation*, *970*.
15. Hartranft, R. J., & Sih, G. C. (1973). Alternating method applied to edge and surface crack problems. *Methods of analysis and solutions of crack problems* (pp. 179–238). Springer.
16. Johnson, G. R., & Cook, W. H. (1983). A constitutive model and data for metals subjected to large strains, high strain rates and high temperatures. *Proceedings of the 7th international symposium on ballistics* (pp. 541–547). The Hague: The Netherlands.
17. Johnson, G. R., & Cook, W. H. (1985). Fracture characteristics of three metals subjected to various strains, strain rates, temperatures and pressures. *Engineering Fracture Mechanics, 21* (1), 31–48.
18. Koplik, J., & Needleman, A. (1988). Void growth and coalescence in porous plastic solids. *International Journal of Solids and Structures, 24*(8), 835–853.
19. Lesuer, D. R., Kay, G., & LeBlanc, M. (1999). Modeling large strain, high rate deformation in metals. *Engineering research, development and technology*.
20. Mackenzie, A. C., Hancock, J. W., & Brown, D. K. (1977). On the influence of state of stress on ductile failure initiation in high strength steels. *Engineering Fracture Mechanics*, *9*(1), 167IN13169–168IN14188.
21. Meyer, H. W. (2006). A modified Zerilli-Armstrong constitutive model describing the strength and localizing behavior of Ti-6Al-4 V.

22. Meyer, H. W., & Kleponis, D. S. (2001). Modeling the high strain rate behavior of titanium undergoing ballistic impact and penetration. *International Journal of Impact Engineering, 26*(1), 509–521.
23. Needleman, A. (1984). An analysis of ductile rupture in notched bars, (June 2017).
24. Sih, G. C., & Lee, Y. D. (1989). Review of triaxial crack border stress and energy behavior, *12*, 1–17.
25. Sih, G. H., Williams, M. L., & Swedlow, J. L. (1966). *Three-dimensional stress distribution near a sharp crack in a plate of finite thickness*, California Inst of Tech Pasadena Graduate Aeronautical Labs.
26. Taylor, G. I. (1934). The mechanism of plastic deformation of crystals. part i. theoretical. *Proceedings of the Royal Society of London. Series A*, *145*(855), 362 LP–387.
27. Thomason, P. F. (1985). A three-dimensional model for ductile fracture by the growth and coalescence of microvoids. *Acta Metallurgica, 33*(6), 1087–1095.
28. Tvergaard, V., & Needleman, A. (1984). Analysis of the cup-cone fracture in a round tensile bar. *Acta Metallurgica, 32*(1), 157–169.
29. Zerilli, F. J. et al. (1994). Constitutive relations for the plastic deformation of metals. *AIP conference proceedings* (pp. 989–992). AIP.
30. Zerilli, F. J. et al. (1996). Constitutive relations for titanium and Ti-6Al-4 V. *AIP conference proceedings* (pp. 315–318). AIP.
31. Zerilli, F. J., et al. (1998). Dislocation mechanics based constitutive equation incorporating dynamic recovery and applied to thermomechanical shear instability. *AIP Conference Proceedings, 429*(1), 215–218.
32. Zerilli, F. J., & Armstrong, R. W. (1995). Constitutive equation for HCP metals and high strength alloy steels. *High strain rate effects on polymer, metal and ceramic matrix composites and other advanced materials* (pp. 121–126).
33. Zerilli, F. J., & Armstrong, R. W. (1987). Dislocation-mechanics-based constitutive relations for material dynamics calculations. *Journal of Applied Physics, 61*(5), 1816–1825.
34. Zhang, Z. L., & Thaulow, C. (2000). A complete Gurson model approach for ductile fracture q (October 1998), *67*, 155–168.

Blast Mitigation Effects of Foam-Core, Composite Sandwich Structures

Michelle S. Hoo Fatt, Moshabab Alkhtany and Dushyanth Sirivolu

1 Introduction

Composite and composite sandwich panels used in ship hulls and deckhouses have higher stiffness and strength per unit weight than their metal counterparts, and this offers advantages of increased payload, longer range, as well as better speed and stability. In addition to this, glass and carbon fiber-reinforced plastics have reduced magnetic and acoustic signatures and are integral to the stealth technology of a ship. Lifecycle costs are dramatically reduced with composite structures because they do not corrode like metal ships. However, the advancement of composite materials into navy ships has been slow due to higher acquisition costs compared to conventional metals as well as other issues such as the fire, smoke, and toxicity that are associated with them.

An area that has been of interest to the navy is the behavior of composite structures and composite sandwich structures when they are subjected to blast loading in air and in water. Explosions underwater and near the water surface can cause serious damage to ship structures, and there has been much research concerning this topic with metal ship structures dating back to the early 1940s [1]. Few studies were also done to address this problem in the case of GRP and GRP sandwich mine hunters in the 1980s [2, 3], but there have been renewed interests of blast effects in navy composite structures over the past 15 years. Porfiri and Gupta

M. S. Hoo Fatt (✉) · M. Alkhtany · D. Sirivolu
The University of Akron, Akron, OH 44325-3903, USA
e-mail: hoofatt@uakron.edu

M. Alkhtany
e-mail: mma55@zips.uakron.edu

D. Sirivolu
e-mail: ds64@zips.uakron.edu

S. Gopalakrishnan and Y. Rajapakse (eds.), *Blast Mitigation Strategies in Marine Composite and Sandwich Structures*, Springer Transactions in Civil and Environmental Engineering, https://doi.org/10.1007/978-981-10-7170-6_14

[4] provide a fairly comprehensive review of experimental, numerical, and analytical concerning the blast response of marine composite materials and structures.

This research concerns the in air and underwater blast response of polymer foam-core composite sandwich panels. Structural polymer foams have been used as core material in lightweight sandwich panels for quite some time. Traditional sandwich theory suggests that the primary function of the polymer core is to transmit shear to the thin facesheets thereby rendering high bending stiffness and strength from a panel with a minimum weight penalty. Research has shown that on a per unit weight basis, the *in-vacuo* blast resistance of a foam-core composite sandwich structure is highest when it undergoes plastic core crushing [5, 6]. Recent analysis of the underwater blast response of PVC foam composite sandwich panel shows the blast mitigation effect of plastic core crushing is even more pronounced in an underwater blast because of fluid–structure interaction [7, 8]. Fluid–structure interaction (FSI) based on the work of Taylor [9] was used to examine the coupling between acoustic pressure waves in air or water and surfaces of the panel. Taylor showed that FSI reduces the amount of impulse transmitted to free-standing plates because a rarefaction or pressure relief wave is radiated by the structure due to its motion. The FSI method proposed by Taylor is restricted to a linear compressible, planar pressure wave in which fluid density does not change significantly. According to Kambouchev et al. [10], this assumption is applicable to cases of underwater explosions because the pressure level required for water to undergo significant density changes is on the order of 10 GPa. This magnitude is much higher than pressure levels of a planar shock wave from a faraway underwater explosion.

The following section highlights key findings on the behavior of foam-core composite sandwich panel underwater and air blasts. These results have led to ongoing investigations on the hysteresis effects of closed-cell PVC foams when they are subjected to combined transverse shear and compression. Experiments to obtain mixed-mode, cyclic stress–strain behavior are described in Sect. 3, and a transversely isotropic, viscoelastic–plastic damage constitutive model is proposed in Sect. 4. Concluding remarks are made in the final section.

2 Water and Air Blast Response

Consider the fully clamped composite sandwich plate with E-Glass/Vinyl Ester Woven Roving facesheets and Divinycell PVC H250 core shown in Fig. 1. The sandwich plate has $h = 5.08$ mm, $H = 25$ mm, and $a = b = 248.25$ mm. It is surrounded by an unbounded acoustic media, water or air, on either side of the facesheets. A planar shock wave is an incident to the front facesheet. When the shock wave is transmitted through water and air it is termed water blast and air blast, respectively. Three scenarios are of interest in this study: water blast/air back panel, water blast/water back panel, and air blast/air back panel.

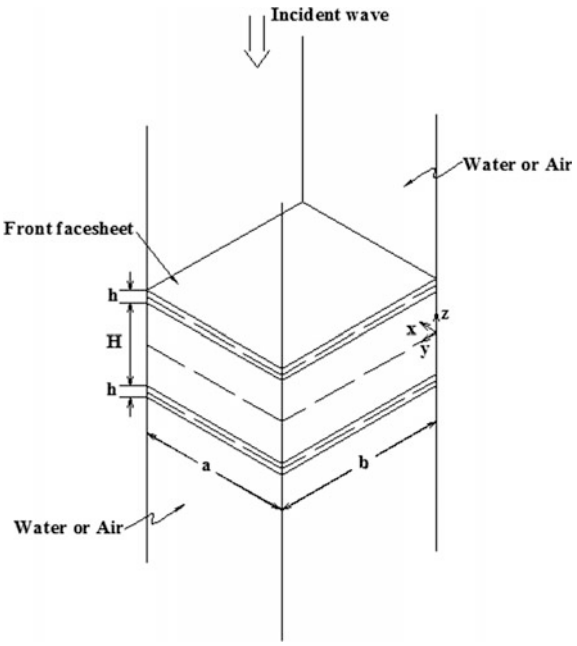

Fig. 1 Composite sandwich panel subjected to air and water blasts

Detailed analytical and finite-element analysis (FEA) solutions for the response of the composite sandwich panel under these three scenarios can be found in Hoo Fatt and Sirivolu [8] and Sirivolu [11]. In general, fluid–structure interaction (FSI) at the water–facesheet interfaces is dominated by radiation damping and for a fixed pressure pulse, panel deflections are substantially lower and peak out at later times during a water blast. Furthermore, through thickness stresses within the foam-core develop as a result of FSI and these affect the overall panel blast resistance, as will be elucidated in the next section.

2.1 Blast Resistance and Energy Absorption

Damage initiation in the panel can occur in the facesheets or the core. The pressure loads that would initiate damage for the air and water blast cases are given in Fig. 2a, and the associated plastic work dissipated by the PVC H250 foam is given in Fig. 2b. In all cases, failure was found to present in the facesheet. It is not surprising to see that the pressure load to initiate failure is higher due to radiation damping. However, it must be noted that energy absorption in the core due to plasticity is also higher in the water blast cases.

In the air blast/air back case, core yielding is primarily transverse shear. The stress distribution along the mid-span of the core is shown in Fig. 3a and b to show this. In-plane and out-of-plane stresses are separated for clarity. The stress

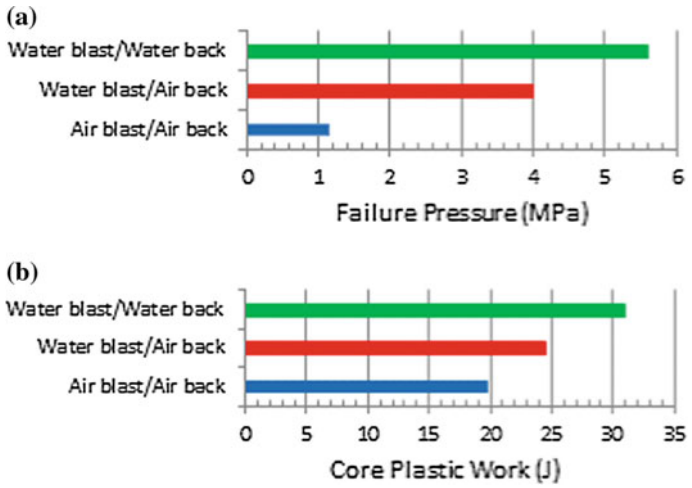

Fig. 2 Comparison of **a** pressure load to initiate failure and **b** energy absorption

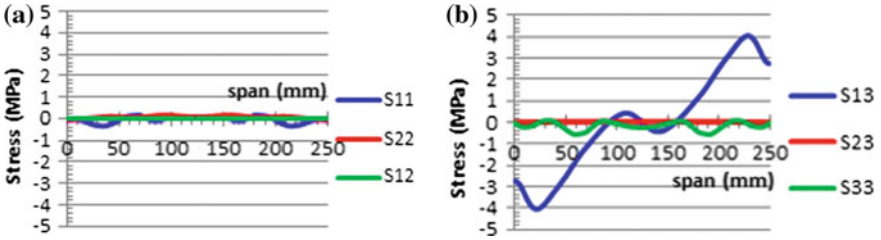

Fig. 3 Core mid-surface stresses at the onset of yielding in air blast/air back panel: **a** in-plane stresses and **b** out-of-plane stresses

distributions along the core mid-span in the water blast/air back and water blast/water back cases indicate that core yielding is due to combined transverse shear, transverse compression and/or hydrostatic pressure. Figures 4, 5, 6 and 7 show FEA quarter-models of the sandwich panel with fluid pressures and the stress distributions along the core mid-span. In the water blast/air back panel, core yielding is due to combining transverse shear and compression (Fig. 5). The pressure field on the front facesheet is altered by FSI (Fig. 4) and it causes local through thickness crushing. In the water blast/water back panel, pressure fields develop on both front and back facesheets (Fig. 6) and core yielding occurs under combined transverse shear and hydrostatic compression (Fig. 7).

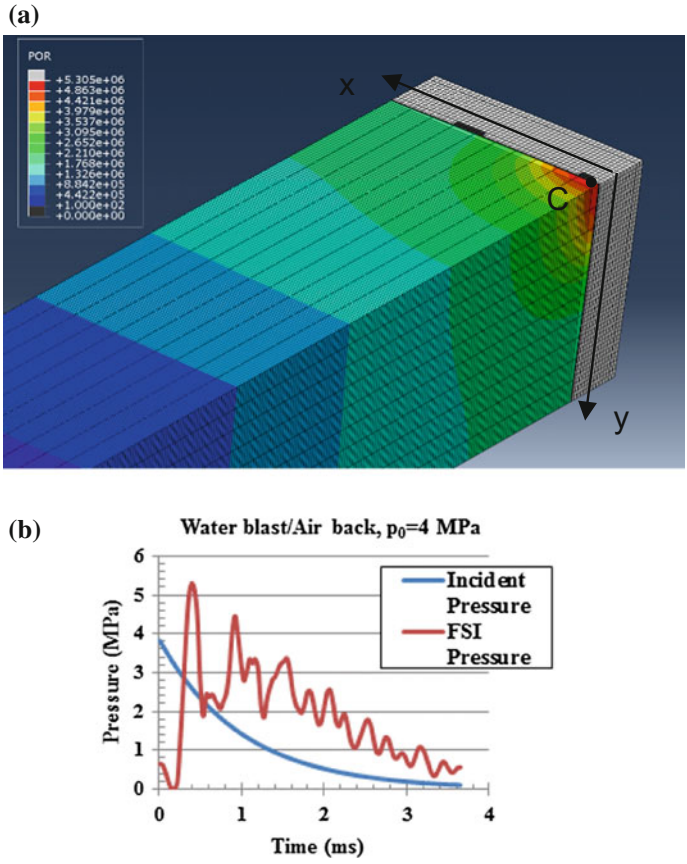

Fig. 4 Finite element analysis of water blast/air back panel: **a** pressure front and **b** transient pressure at front panel center, C

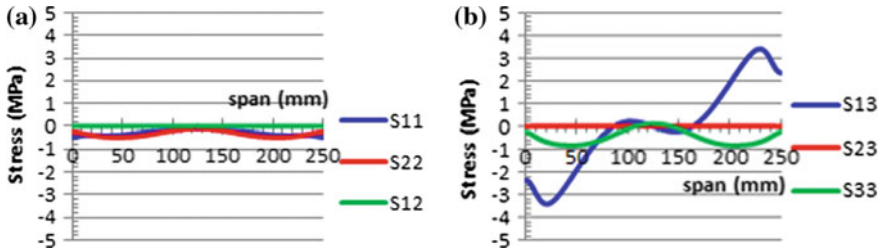

Fig. 5 Core mid-surface stresses at the onset of yielding in water blast/air back panel: **a** in-plane stresses and **b** out-of-plane stresses

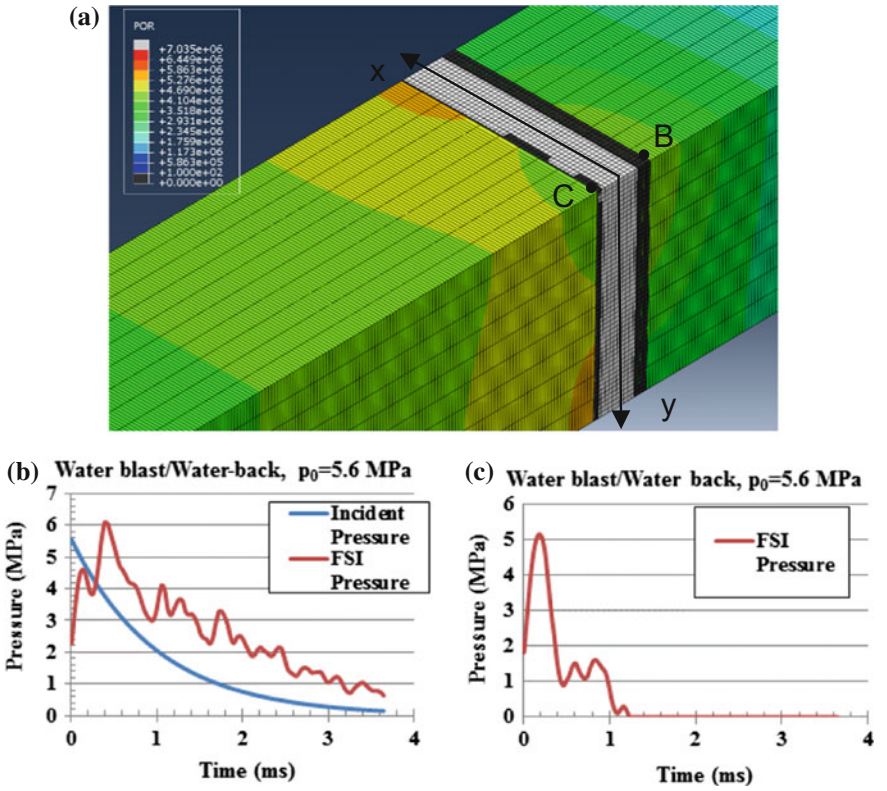

Fig. 6 Finite element analysis of water blast/water back panel: **a** pressure front and transient pressure at **a** front panel center, C, and **c** back panel center, B

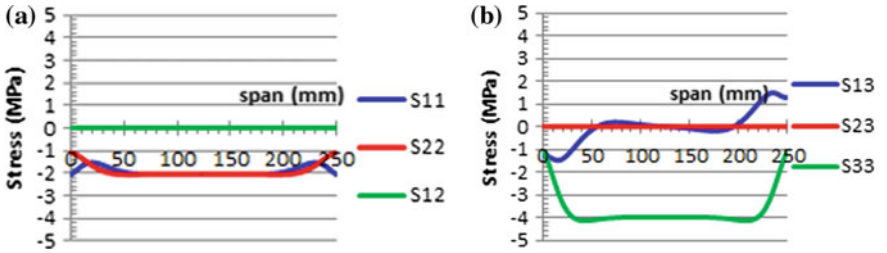

Fig. 7 Core mid-surface stresses at the onset of yielding in water blast/water back panel: **a** in-plane stresses and **b** out-of-plane stresses

3 Effect of Foam Type

A parametric study was done to examine blast resistance and energy absorption characteristic of sandwich panels with different cores. It was found that on a per unit areal weight density basis, panels with softer PVC H200 and H250 foams provided the better blast resistance in water blasts primarily because of the higher energy absorption due to core crushing (see Fig. 8a and b). Clearly, this effect is more pronounced in the water blast cases than in the air blast case.

An experimental program was developed to understand the energy absorption or hysteresis of PVC foam under combined transverse compression and shear because it was recognized as being an important mechanism affecting the underwater blast resistance of the sandwich panel. This is discussed in the following sections.

4 Foam Hysteresis Under Combined Compression and Shear

Experiments were done to examine the elastic–plastic response and hysteresis of Divinycell PVC H100 foam under combined transverse compression/shear (1–3 plane). Using a variety of angled specimens as shown in Fig. 9, cyclic stress–strain curves were obtained for the foam under prescribed strain amplitudes, strain rates and combinations of compression and shear on an MTS servo-hydraulic machine. The 1in-cubic specimen was glued to the test fixture in order to accommodate tensile stresses due to permanent core deformations. As a result of this, material properties of the foam were obtained under the constraints $\varepsilon_{11} = \varepsilon_{22} = 0$ and $\gamma_{12} = \gamma_{23} = 0$. These constraints are more realistic to the behavior of PVC foam sandwiched and bonded between facesheets. Displacement control of the actuator allowed prescribed time variation of ε_{33} and γ_{13}.

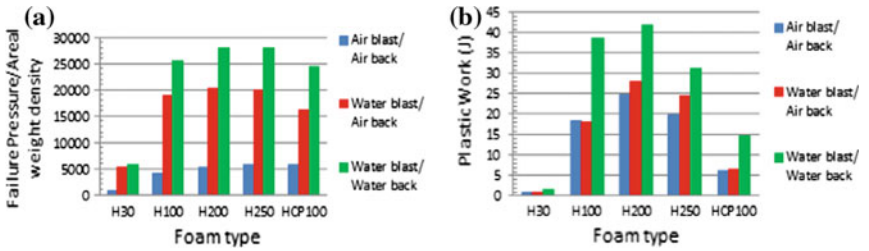

Fig. 8 Comparison of **a** blast resistance and **b** energy absorption up to failure for several panels with different cores

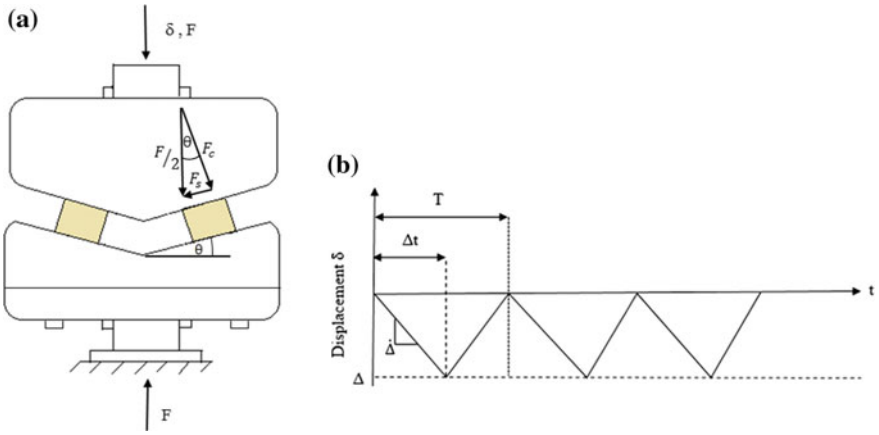

Fig. 9 Schematic of compression–shear test fixture for PVC H100 foam: **a** setup and **b** displacement control

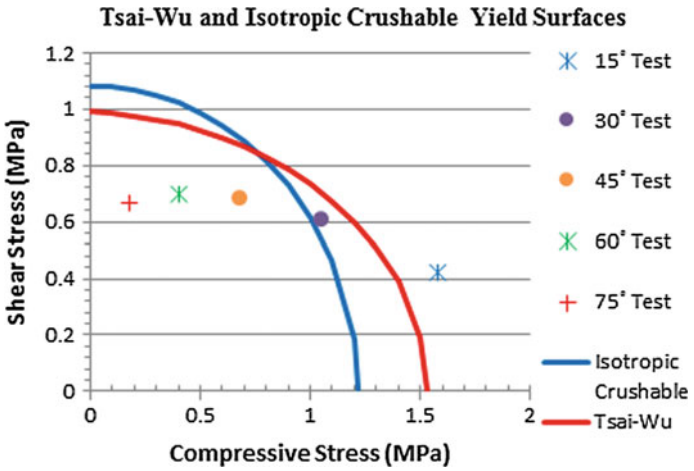

Fig. 10 Yield surface of foam specimen constrained by $\varepsilon_{11} = \varepsilon_{22} = 0$ and $\gamma_{12} = \gamma_{23} = 0$

4.1 Initial Yielding

Figure 10 shows the yield surface of the foam as predicted by isotropic crushable foam [12] and the Tsai–Wu failure [13]. Here yielding is defined by the onset of plastic or unrecoverable deformations. The data suggested that a Tsai–Wu failure criterion more accurately describes initial yield of the foam when it is bonded between facesheets. The Tsai–Wu failure criterion is currently being used to determine equivalent stress, strain, and strain rate in a three-dimensional constitutive equation for the foam.

4.2 Cyclic Response

Combined compression and shear stress–strain curves under constant displacement amplitude and varying Tsai–Wu strain rate are shown in Fig. 11a and b for the 60° angle specimen. The PVC H100 foam displayed viscoelasticity and then viscoplasticity with rate-dependent flow stress before unloading to a tensile stress. At zero stress or no load condition, the foam had permanent compressive and shear strains. Curiously these permanent strains had very little rate effect. The stress–strain curves of combined compression–shear loading for the specimen with constant Tsai–Wu strain and varying rate displacement amplitude are shown in Fig. 12a and b. The dissipation energy or hysteresis during cyclic loading–unloading increased with increasing displacement amplitude. The modulus also decreases with increasing displacement amplitude and this signifies permanent damage during yielding.

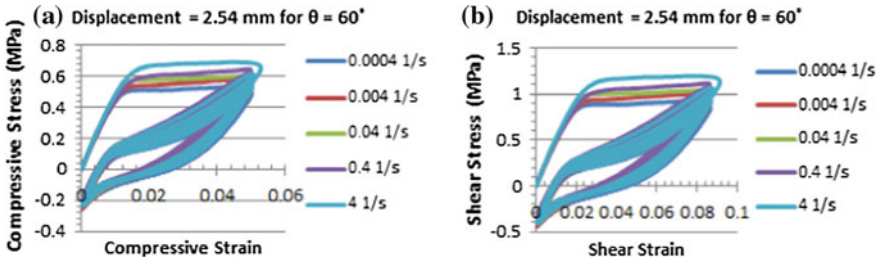

Fig. 11 PVC H100 elastic–plastic response and hysteresis with varying strain rate: **a** compression and **b** shear

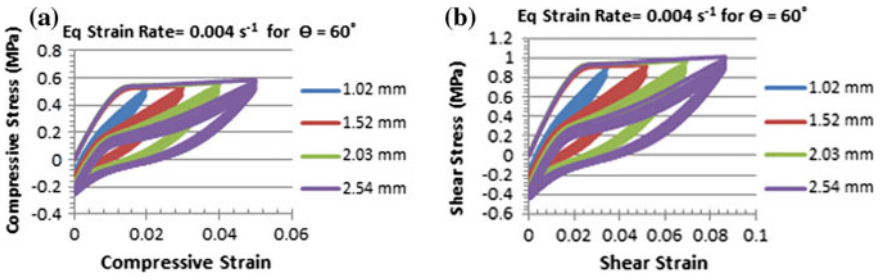

Fig. 12 PVC H100 elastic–plastic and hysteresis with varying displacement amplitude: **a** compression and **b** shear

4.3 Viscoelastic Hysteresis

In order to develop a constitutive material model that can be used to predict foam elastic–plastic and hysteresis response, additional tests were performed so that reversed yielding of the foam could be avoided. Results from these tests are shown for a $\theta = 30°$ specimen in Fig. 13a and b.

5 Constitutive Material Model

A phenomenological material model to describe the above foam behavior is shown in Fig. 14a and b. It is assumed that the onset of plasticity and damage occurs simultaneously. Stress–strain equations are derived below.

5.1 Behavior Before Yield/Damage: Viscoelastic Response

The total stress is given by

$$\boldsymbol{\sigma} = \boldsymbol{\sigma}_{\mathbf{eq}} + \boldsymbol{\sigma}_{\mathbf{ov}} \tag{1}$$

where boldface is used to denote a tensor quantity in Voigt notation. The equilibrium stress $\boldsymbol{\sigma}_{\mathbf{eq}}$ is

$$\boldsymbol{\sigma}_{\mathbf{eq}} = \mathbf{C}_{\mathbf{0}}\boldsymbol{\varepsilon} \tag{2}$$

where $\mathbf{C_0}$ is the stiffness matrix of the equilibrium spring given by

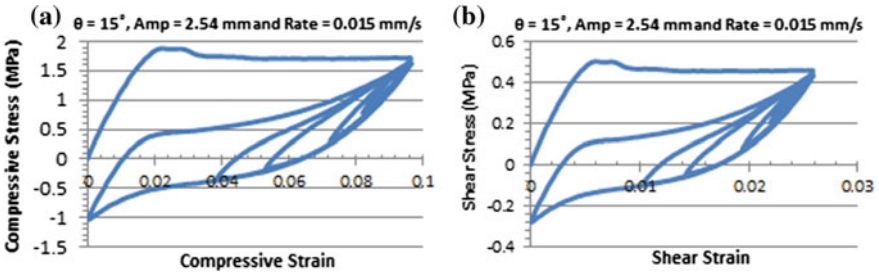

Fig. 13 Hysteresis curves with various displacement and rate = 0.015 mm/s for $\theta = 15°$: **a** compression and **b** shear

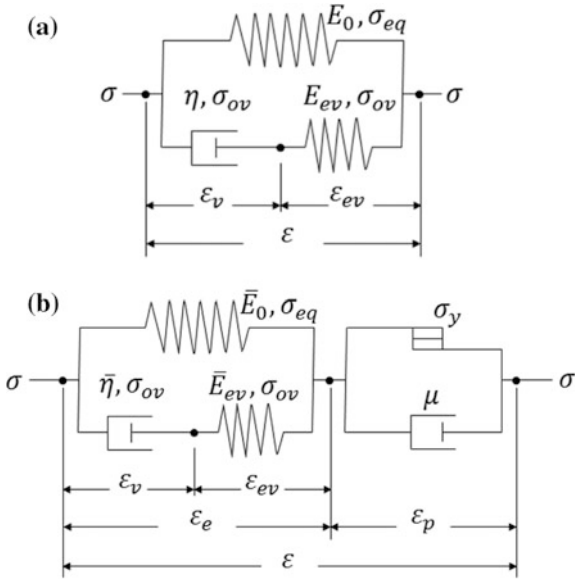

Fig. 14 Mechanical analogs: **a** before yielding/damage and **b** after yielding/damage

$$\mathbf{C_0} = \begin{bmatrix} C_{11} & C_{12} & C_{13} & 0 & 0 & 0 \\ C_{12} & C_{22} & C_{23} & 0 & 0 & 0 \\ C_{13} & C_{23} & C_{33} & 0 & 0 & 0 \\ 0 & 0 & 0 & C_{44} & 0 & 0 \\ 0 & 0 & 0 & 0 & C_{55} & 0 \\ 0 & 0 & 0 & 0 & 0 & C_{66} \end{bmatrix}$$

and

$$C_{11} = \frac{(E_{22} - \nu_{23}^2 E_{33})E_{11}^2}{\Omega} \qquad C_{12} = \frac{(\nu_{12}E_{22} + \nu_{13}\nu_{23}E_{33})E_{11}E_{22}}{\Omega}$$
$$C_{13} = \frac{(\nu_{12}\nu_{23} + \nu_{13})E_{11}E_{22}E_{33}}{\Omega} \qquad C_{22} = \frac{(E_{11} - \nu_{13}^2 E_{33})E_{22}^2}{\Omega}$$
$$C_{23} = \frac{(\nu_{23}E_{11} + \nu_{12}\nu_{13}E_{22})E_{22}E_{33}}{\Omega} \qquad C_{33} = \frac{(E_{11} - \nu_{12}^2 E_{22})E_{22}E_{33}}{\Omega}$$

$$C_{44} = G_{23} \quad C_{55} = G_{13} \quad C_{66} = G_{12}$$

and $\Omega = E_{11}E_{22} - \nu_{12}^2 E_{22}^2 - \nu_{13}^2 E_{22}E_{33} - \nu_{23}^2 E_{11}E_{33} - 2\nu_{12}\nu_{13}\nu_{23}E_{22}E_{33}$. Similarly, the overstress $\boldsymbol{\sigma_{ov}}$ is given by

$$\boldsymbol{\sigma_{ov}} = \mathbf{C_{ev}}\boldsymbol{\varepsilon_{ev}} \tag{3}$$

where $\mathbf{C_{ev}}$ is the stiffness matrix of the intermediate spring given by

$$\mathbf{C_{ev}} = \begin{bmatrix} C_{ev11} & C_{ev12} & C_{ev13} & 0 & 0 & 0 \\ C_{ev12} & C_{ev22} & C_{ev23} & 0 & 0 & 0 \\ C_{ev13} & C_{ev23} & C_{ev33} & 0 & 0 & 0 \\ 0 & 0 & 0 & C_{ev44} & 0 & 0 \\ 0 & 0 & 0 & 0 & C_{ev55} & 0 \\ 0 & 0 & 0 & 0 & 0 & C_{ev66} \end{bmatrix}$$

and

$$C_{ev11} = \frac{(E_{ev22} - \nu_{23}^2 E_{ev33})E_{ev11}^2}{\Phi} \qquad C_{ev12} = \frac{(\nu_{12}E_{ev22} + \nu_{13}\nu_{23}E_{ev33})E_{ev11}E_{ev22}}{\Phi}$$
$$C_{ev13} = \frac{(\nu_{12}\nu_{23} + \nu_{13})E_{ev11}E_{ev22}E_{ev33}}{\Phi} \qquad C_{ev22} = \frac{(E_{ev11} - \nu_{13}^2 E_{ev33})E_{ev22}^2}{\Phi}$$
$$C_{ev23} = \frac{(\nu_{23}E_{ev11} + \nu_{12}\nu_{13}E_{ev22})E_{ev22}E_{ev33}}{\Phi} \qquad C_{ev33} = \frac{(E_{ev11} - \nu_{12}^2 E_{ev22})E_{ev22}E_{ev33}}{\Phi}$$

$$C_{ev44} = G_{ev23} \quad C_{ev55} = G_{ev13} \quad C_{ev66} = G_{ev12}$$

and

$$\Phi = E_{ev11}E_{ev22} - \nu_{12}^2 E_{ev22}^2 - \nu_{13}^2 E_{ev22}E_{ev33} - \nu_{23}^2 E_{ev11}E_{ev33} - 2\nu_{12}\nu_{13}\nu_{23}E_{ev22}E_{ev33}.$$

5.2 *Initial Yield/Damage Criterion*

As shown in Fig. 10, the experimental results for different angles compared better with the theoretical Tsai–Wu criterion yield surfaces than the isotropic crushable foam yield surfaces. The tests do not appear to follow the trend-line of the isotropic crushable foam criterion. With the Tsai–Wu criterion, one sees relatively good agreements for $\theta = 15°$, $\theta = 30°$, $\theta = 45°$ tests, but the tests at $\theta = 60°$ and $\theta = 75°$ are lower than the theory predicted. However, it was noted in the experiments that cracks and debonding occurred near the edges of the foam and this may mean that the data for such high angles are unreliable. Subsequent FEA of the specimen indicates that stresses and strains are also not uniformly distributed in the midsection of 1in-cube specimen for $\theta = 60°$ and $\theta = 75°$, and this would also cause results to be unreliable for them.

5.3 *Behavior After Yield/Damage: Plastic Flow and Viscoelastic Damage Response*

The Tsai–Wu yield criterion comes from a special class of quadratic yield criteria for anisotropic material [14]. The Tsai–Wu plastic potential function is given by

$$\Phi = \frac{1}{2}\sigma \mathbf{P}\sigma^{\mathbf{T}} + \mathbf{q}^{\mathbf{T}}\boldsymbol{\sigma} - \bar{\sigma}^2 = 0 \tag{4}$$

where

$$\mathbf{P} = 2\begin{bmatrix} X_{11} & X_{12} & X_{13} & 0 & 0 & 0 \\ X_{12} & X_{22} & X_{23} & 0 & 0 & 0 \\ X_{13} & X_{23} & X_{33} & 0 & 0 & 0 \\ 0 & 0 & 0 & X_{44} & 0 & 0 \\ 0 & 0 & 0 & 0 & X_{55} & 0 \\ 0 & 0 & 0 & 0 & 0 & X_{66} \end{bmatrix}$$

$\mathbf{q} = [X_1 \quad X_2 \quad X_3 \quad 0 \quad 0 \quad 0]^T$, $\bar{\sigma} = \bar{\sigma}(\varepsilon_{\mathbf{p}})$ and $\varepsilon_{\mathbf{p}}$ is the equivalent plastic strain. The plastic strain rate $\dot{\varepsilon}_{\mathbf{p}}$ is given by an associate flow rule

$$\dot{\varepsilon}_{\mathbf{p}} = \lambda \frac{\partial \Phi}{\partial \boldsymbol{\sigma}} \tag{5}$$

where λ is the plastic multiplier. In terms of the $\mathbf{P}$ and $\mathbf{q}$, Eq. (4) reduces to

$$\dot{\varepsilon}_{\mathrm{p}} = \lambda \sqrt{\frac{2}{3}(\mathbf{P}\sigma + \mathbf{q})^{\mathbf{T}}\mathbf{Z}(\mathbf{P}\sigma + \mathbf{q})} \tag{6}$$

where

$$\mathbf{Z} = \begin{bmatrix} 1 & 0 & 0 & 0 & 0 & 0 \\ 0 & 1 & 0 & 0 & 0 & 0 \\ 0 & 0 & 1 & 0 & 0 & 0 \\ 0 & 0 & 0 & 1/2 & 0 & 0 \\ 0 & 0 & 0 & 0 & 1/2 & 0 \\ 0 & 0 & 0 & 0 & 0 & 1/2 \end{bmatrix}$$

An equivalent stress σ_* is defined from the Tsai–Wu potential as

$$\begin{aligned} \sigma_*^2 = {} & X_1\sigma_{11} + X_2\sigma_{22} + X_3\sigma_{33} + X_{11}\sigma_{11}^2 + X_{22}\sigma_{22}^2 + X_{33}\sigma_{33}^2 + X_{44}\tau_{23}^2 + X_{55}\tau_{13}^2 \\ & + X_{66}\tau_{12}^2 + 2X_{12}\sigma_{11}\sigma_{22} + 2X_{13}\sigma_{11}\sigma_{33} + 2X_{23}\sigma_{22}\sigma_{33} \end{aligned} \tag{7}$$

Initial yielding occurs when $\bar{\sigma} = 1$, but continued plastic flow occurs with strain hardening. The variation of plastic flow stress with an equivalent strain in separate compression and shear modes are shown in Fig. 15a. Data for these curves were obtained from [15]. The compression curve is projected (red dashed line) because

the data was very limited in range after converting to equivalent plastic strains. It is clearly seen that hardening is more prevalent in shear. Differences in hardening are due to the different micro-mechanisms causing plastic flow. In the case of compression, cells have buckled and are collapsing with compressive strain. Eventually, strain hardening in compression will be due to foam densification or compaction. This occurs at about 0.4 equivalent plastic strain and is not shown in Fig. 15a. In shear, cells bend and elongate. Strain hardening is due to this. The evolution of the yield surface due to the different plastic flow curves is shown in Fig. 15b.

During unloading the total stress is give again as the sum of equilibrium stress and overstress:

$$\boldsymbol{\sigma} = \boldsymbol{\sigma}_{\mathbf{eq}} + \boldsymbol{\sigma}_{\mathbf{ov}} \tag{8}$$

However, the equilibrium stress $\boldsymbol{\sigma}_{\mathbf{eq}}$ becomes

$$\boldsymbol{\sigma}_{\mathbf{eq}} = \bar{\mathbf{C}}_{\mathbf{0}}\left(\varepsilon - \varepsilon_{\mathbf{p}}\right) \tag{9}$$

where $\bar{\mathbf{C}}_{\mathbf{0}}$ is the damage stiffness matrix of the equilibrium spring, which is similar to $\mathbf{C_0}$ but with damage elastic moduli, $\bar{E}_{ij}$. Similarly, the overstress $\boldsymbol{\sigma}_{\mathbf{ov}}$ is

$$\boldsymbol{\sigma}_{\mathbf{ov}} = \bar{\mathbf{C}}_{\mathbf{ev}}\boldsymbol{\varepsilon}_{\mathbf{ev}} \tag{10}$$

where $\bar{\mathbf{C}}_{\mathbf{ev}}$ is the damage stiffness matrix of the intermediate spring, which again is similar in form to $\mathbf{C_{ev}}$ but with $\bar{E}_{evij}$. Compatibility of strain requires that

$$\boldsymbol{\varepsilon} = \boldsymbol{\varepsilon}_{\mathbf{p}} + \boldsymbol{\varepsilon}_{\mathbf{ev}} + \boldsymbol{\varepsilon}_{\mathbf{v}} \tag{11}$$

Substituting Eq. (11) into Eq. (10) gives

$$\boldsymbol{\sigma}_{\mathbf{ov}} = \bar{\mathbf{C}}_{\mathbf{ev}}\left(\boldsymbol{\varepsilon} - \boldsymbol{\varepsilon}_{\mathbf{p}} - \varepsilon_{\mathbf{v}}\right) \tag{12}$$

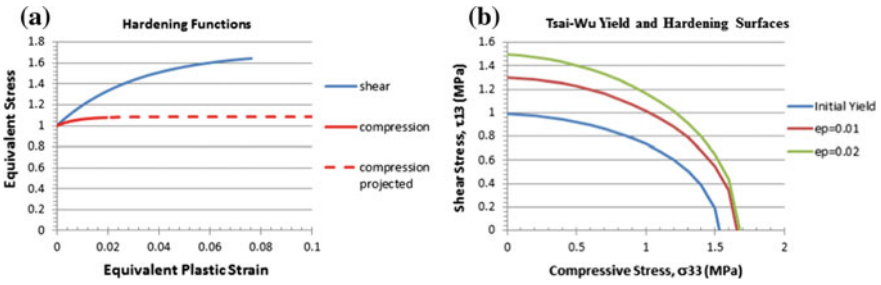

Fig. 15 Tsai–Wu plasticity for PVC H100 foam: **a** plastic flow stress in compression and shear modes and **b** expanding yield surfaces after plastic deformations

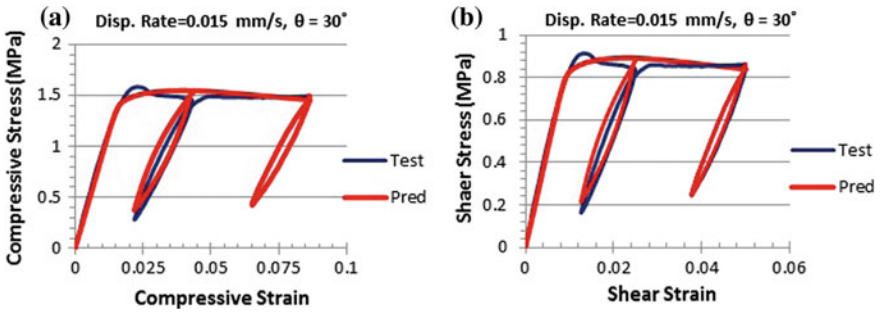

Fig. 16 Comparison of elastic–plastic, hysteresis stress–strain curves between analytical and experimental results for θ = 30°: **a** compression and **b** shear

The overstress is also governed by a linear viscosity law:

$$\sigma_{\mathbf{ov}} = \mathbf{V}\bar{\dot{\varepsilon}}_{\mathbf{v}} \tag{13}$$

where $\bar{\mathbf{V}}$ is the damage viscosity matrix, similar in form to $\mathbf{V}$ but with $\bar{\eta}_{ij}$. Combining Eqs. (12) and (13) give an evolution equation for $\boldsymbol{\varepsilon}_{\mathbf{v}}$:

$$\mathbf{V}\bar{\dot{\varepsilon}}_{\mathbf{v}} = \bar{\mathbf{C}}_{\mathbf{ev}}\left(\boldsymbol{\varepsilon} - \boldsymbol{\varepsilon}_{\mathbf{p}} - \boldsymbol{\varepsilon}_{\mathbf{v}}\right) \tag{14}$$

The total stress is represented as

$$\boldsymbol{\sigma} = \bar{\mathbf{C}}_{\mathbf{0}}\boldsymbol{\varepsilon} + \bar{\mathbf{C}}_{\mathbf{ev}}\left(\boldsymbol{\varepsilon} - \boldsymbol{\varepsilon}_{\mathbf{p}} - \boldsymbol{\varepsilon}_{\mathbf{v}}\right) \tag{15}$$

The predicted response based on the above constitutive model is shown for the test at θ = 30 in Fig. 16a and b. The Tsai–Wu plasticity is able to capture mixed-mode yielding.

6 Concluding Remarks

Analysis of the underwater blast response of PVC foam composite sandwich panel indicates that PVC foams have blast mitigation effects through energy absorption via plastic core crushing. Three-dimensional core plasticity is encountered in underwater blasts, and plastic work dissipation of the core plays a greater role in blast mitigation than in air blasts. In air blast/air back cases, core yielding is primarily transverse shear, but in water blast/air back and water blast/water back cases, core yielding is due to combined transverse shear, transverse compression, and/or hydrostatic pressure. As a result of these findings, experiments have been conducted to obtain the hysteresis effects of PVC H100 subjected to combined

transverse shear and compression. Under cyclic loading, PVC H100 foam displays plasticity, viscoelasticity, and permanent damage after yielding. A transversely isotropic, viscoelastic–plastic damage material model has been proposed to describe the behavior of foam operating in this environment.

Acknowledgements The authors would like to acknowledge financial support from Dr. Yapa Rajapakse at the Office of Naval Research under Grant N00014-11-1-0485.

References

1. Underwater explosion research: A compendium of British and American reports (Vols. 1–3). Office of Naval Research: Washington DC, (1950).
2. Lyson, J. D. (1979). The underwater explosion response of a GRP mine countermeasures vessel. *Journal of Naval Science, 5*(3), 182–190.
3. Hall, D. J. (1989). Examination of the effects of underwater blasts on sandwich composite structures. *Composite Structures, 11,* 101–120.
4. Porfiri, M., Gupta, N. (2010). A review of research on impulsive loading of marine composites. In: Gdoutos, E. E., Daniel, I. M., Rajapakse, Y. D. S. (Eds.), *Major accomplishments in composite materials and sandwich structures—an anthology of ONR sponsored research* (pp. 169–194). Springer.
5. Hoo Fatt, M. S., & Sirivolu, D. (2015). Blast response of double curvature, composite sandwich shallow shells. *Engineering Structures, 100,* 696–706.
6. Hoo Fatt, M. S., Gao, Y., & Sirivolu, D. (2013). Foam-core, curved composite sandwich panels under blast. *Journal of Sandwich Structures and Materials, 15,* 261–291.
7. Hoo Fatt, M. S., Sirivolu, D. (2015). Blast mitigation effects of foam-core, composite sandwich structures. *Indo-USA workshop on recent advances in blast mitigation strategies in civil and marine structures*. Bangalore, India, August 16–19, 2015.
8. Hoo Fatt, M. S., Sirivolu, D. (2017). Marine composite sandwich plates under air and water blasts. *Marine Structures* (to appear).
9. Taylor, G. I. (1941). The pressure and impulse of submarine explosion waves on plates. *Scientific papers of G. I. Taylor III* (pp. 297–303). Cambridge Univ Press, Cambridge.
10. Kambouchev, N., Noels, L., & Radovitzky, R. (2007). Numerical simulation of the fluid-structure interaction between air blast waves and free-standing plates. *Computers and Structures, 8,* 923–931.
11. Sirivolu, D. (2016). Marine composite panels under blast loading. *Doctoral dissertation*. The University of Akron. https://etd.ohiolink.edu/pg_10?0::NO:10:P10_ACCESSION_NUM:akron1467993101.
12. Deshpande, V. S., & Fleck, N. A. (2001). Multi-axial yield behavior of polymer foams. *Acta Materialia, 49,* 185–186.
13. Gdoutos, E. E., Daniels, I. M., Wang, K. –A. (2002). Failure of cellular foams under multiaxial loading. *Composites Part A: Applied Science and Manufacturing*, *33*, 163–176.
14. Oller, S., Car, E., & Lubliner, J. (2003). Definition of a general implicit orthotropic yield criterion. *Computer Methods in Applied Mechanics and Engineering, 192,* 895–912.
15. Chen, L., & Hoo Fatt, M. S. (2013). Transversely isotropic mechanical properties of PVC foam under cyclic loading. *Journal of Materials Science, 48*(19), 6786–6796.

Nanowire Reinforcements for Improving the Interlaminar Properties of Textile Composites

Pavana Prabhakar

1 Introduction

Composite materials have become an attractive replacement of conventional materials such as steel or aluminum in order to improve the performance and reduce the weight of high-performance structures [1]. Their use has been successfully integrated into aerospace vehicles, wind energy turbine blades, rockets, marine structures and automobiles [2] due to their tailorable mechanical properties, high specific stiffness, strength-to-weight ratios, and corrosion and fatigue resistance [3, 4]. In particular, sandwich composites are used in ship hulls due to their high bending stiffness. Sandwich composites consist of two facesheets and core sandwiched between them. For improving the damage resistance and durability of sandwich composites, it is essential to improve the properties of facesheet and core. In the research presented in this chapter, the focus is on improving the interlaminar fracture toughness and impact response of carbon woven fiber reinforced facesheet composites.

Carbon fiber reinforced woven composites consist of layers of woven carbon fabric in polymer matrix. Although the in-plane mechanical properties of these composites are strong and stiff, the resin-rich region between the carbon fiber layers of the composite, which is known as interlaminar region, is susceptible to damage and can result in premature failure of the composite [5, 6]. The life of a composite structure depends on its response to different failure mechanisms, such as delamination or interlaminar fracture, matrix cracking, matrix–fiber debonding, fiber breaking fiber pullout, etc. [7, 8].

Delamination or interlaminar fracture is one of the most common failure mechanisms in composites [7]. Delamination can occur due to manufacturing defects such as bad layup, crack between layers, weaker matrix phase, etc. or in-service due to interlaminar stresses, impact, static overload, and fatigue [9–13]. This often results in a reduction of stiffness and strength of the composites leading to global failure of the composite structure. Low-velocity impacts can also occur during manufacturing, tool dropping during maintenance activities, accidental impacts in-service,

P. Prabhakar (✉)
University of Wisconsin-Madison, 1415 Engineering Drive, Madison, WI, USA
e-mail: pprabhakar4@wisc.edu

S. Gopalakrishnan and Y. Rajapakse (eds.), *Blast Mitigation Strategies in Marine Composite and Sandwich Structures*, Springer Transactions in Civil and Environmental Engineering, https://doi.org/10.1007/978-981-10-7170-6_15

hail strikes, etc. [14–17] Such events can cause significant damage in the interior of these composites, with barely visible damage (BVD) on the exterior. This is particularly dangerous as BVD has the potential to cause catastrophic failure without warning. Dynamic impact is generally divided into low-, intermediate-, or high-velocity impact. Typical low-velocity impact occurs at a velocity below 10 m/s. Common failure modes observed during low-velocity impact are fiber breakage, matrix cracking, and delamination [18–20]. Of these, delamination is one of the most common failure mechanisms [21] observed during low-velocity impact [22], which often results in the reduction of stiffness, strength, durability, and stability of the composite resulting in the global failure of the structure [23, 24].

In this chapter, interlaminar fracture toughness is investigated to establish the damage resistance and tolerance of a composite structure. Interlaminar fracture toughness is the amount of energy required to create fracture surfaces under three fracture modes: Mode-I (opening mode), Mode-II (sliding shear mode), and Mode-III (scissoring shear mode) [9, 25]. The focus is on enhancing the pure Mode-I and Mode-II interlaminar fracture of carbon fiber woven textile composites. Also, the influence of interlaminar reinforcements at selected regions on the impact response of these composites is explored here in terms of the impact force and energy absorbed.

Several through-thickness reinforcements have been investigated by earlier researchers for increasing the delamination resistance and extend the life of a composite structure. Sohn and Hu [24] explored chopped Kevlar fibers as reinforcements in unidirectional composites. A 100% increase in the interlaminar fracture toughness value was observed, while the compressive strength appeared to reduce up to 15%. The compressive strength reduced from 652.2 MPa without reinforcement to 559.5 MPa with reinforcement. Ren et al. [26] investigated flocked C-fibers to increase the fracture toughness, which showed an improvement of around 900%. Despite the advantages, flock fibers can be shaken loose during handling, it is a time-consuming process, and the quality of the reinforcement could be reduced as the fibers begin to lay flat on the surface of the fabric. Other methods such as z-pinning and stitching have shown to decrease the area of damage and increase the compression after impact (CAI) response. However, these methods appear to decrease the in-plane properties of the laminate due to undesired effects like fiber breakage and creation of large resin pockets around a z-pin or thread [27]. Another method is the use of nanofiber carbon nanotubes (CNTs) on the surface of the dry fabric by chemical vapor deposition. However, CNTs do not distribute uniformly and they tend to create bundles and branches [6, 28]. Further, the techniques that currently exist to disperse the CNTs tend to damage the carbon fiber [6, 29, 30]. Besides, several studies have reported a decrease in the tensile strength of the fibers after CNTs were grown on them [27]. Qian et al. [31] reported a decrease in the fiber tensile properties by nearly 55%. To prevent damage to the fiber due to high growth temperature and reduction of in-plane properties, a low-temperature solution-based fabrication of ZnO nanowires as interlaminar reinforcements is studied in the research reported here.

Previous researchers [28, 32] have verified that ZnO nanowires have a strong chemical bonding to carbon fibers. ZnO nanowires have very strong interaction with carbon fibers as previous studies have suggested [33]. Functional groups, like

hydroxyl, carbonyl, and carboxylic acid, have been found in carbon fibers that create a strong chemical bonding with ZnO [34–36]. Composites with ZnO nanowires have 23 times higher impact energy absorption compared to pristine composites [37]. Also, ZnO nanowires have piezoelectric and semiconducting properties, which make them suitable for solar cells [38], dynamic sensors [39], and energy-harvesting applications [40]. A recent study by Lin et al. [32] has shown that ZnO nanowires improve the interfacial shear strength of the individual carbon fibers by 113% and the lamina shear strength and modulus by 37.8% and 38.8%, respectively. In the current study, the influence of ZnO nanowire on the Mode-I and Mode-II interlaminar fracture toughness of carbon fiber woven composites is investigated (also reported in [41, 42]). This is the first time ZnO nanowires have been used as means to improve the interlaminar fracture toughness for woven composites.

Carbon fiber woven composites are studied here. ZnO nanowires are synthesized on dry fabric and the composites are manufactured using the vacuum-assisted resin transfer molding (VARTM) process. The interlaminar Mode-I and Mode-II fracture toughness with and without nanowires are compared using double cantilever beam (DCB) and end-notched flexure (ENF) tests, respectively. Significant improvement in Mode-I and Mode-II fracture toughness of the interfaces was observed due to ZnO nanowire reinforcement. Then, the impact response and degree of damage of the laminates with and without ZnO nanowires are compared to draw conclusions on the influence of interlaminar reinforcements on damage resistance. The chapter is organized in the following sections: Sect. 2.1 presents the description of the laminate manufacturing process and synthesis of ZnO nanowire on fabric. This is followed by Sects. 2.2 and 2.3 describe the test method for interlaminar fracture toughness measurements and impact response, respectively. This is followed by Sect. 3 on Results and Discussion, where detailed comparisons of responses between laminates with and without ZnO nanowire reinforcement are provided. The chapter will conclude with Sect. 4, which summarizes the key findings of the research.

2 Methods

2.1 Manufacturing

2.1.1 VARTM Process for Composite Manufacturing

VARTM process [43] was used to manufacture the woven composites with and without ZnO nanowires. Laminates were fabricated by placing layers of dry carbon fabric in a mold with flow media, like breather, nylon peel ply, etc. as shown in Fig. 1a. This was followed by enclosing the mold in a vacuum bag and drawing it into a vacuum in order to aid infiltration of the resin [43]. Laminates with 8 layers of dry fabric for Mode-I, 20 layers for Mode-II, and 16 layers for impact samples were manufactured. Dry fabrics of woven (plain weave) were used as reinforcement with

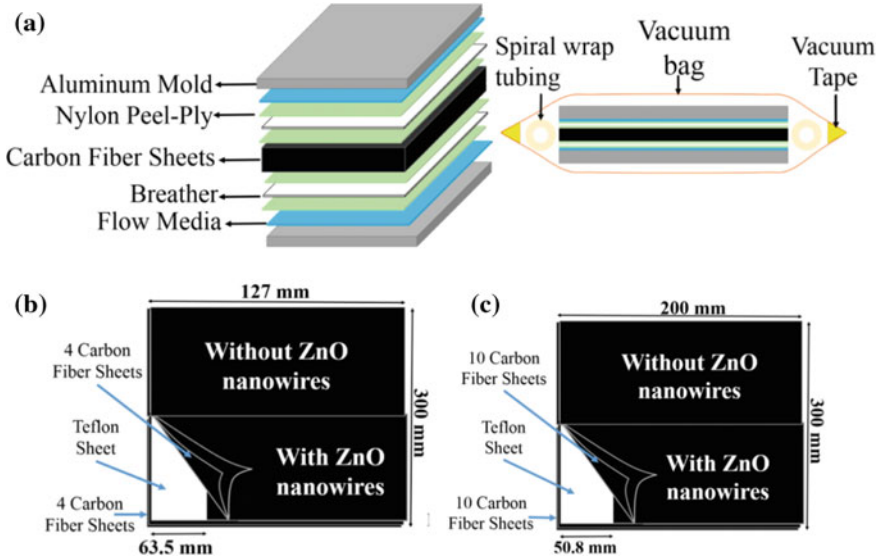

Fig. 1 **a** VARTM configuration for the 2D carbon woven composite; **b** Teflon sheet insert to simulate a crack for DCB sample; **c** Teflon sheet insert to simulate a crack for ENF sample

vinyl ester resin and methyl ethyl ketone peroxide (MEKP) hardener as matrix material. The resin was catalyzed with 1.25% MEKP (by weight) and mixed thoroughly for one minute as recommended by the manufacturer. All the specimens (with and without ZnO nanowires) for DCB and ENF tests were fabricated as one laminate as shown in Fig. 1b and c to ensure that the curing conditions were identical. Teflon sheet of 0.05 mm (0.002 in.) thickness was placed between the fourth and the fifth layers to create a pre-crack for the DCB samples (Fig. 1b), and between the tenth and eleventh layers for the ENF samples (Fig. 1c). Further, ZnO nanowires were synthesized on the surfaces of the fourth and the fifth layers for Mode-I and on the surfaces of the tenth and eleventh layers for Mode-II, thereby, reinforcing the fracturing interface of the DCB and ENF samples, respectively. In the case of impact samples, nanowire reinforcements were added at selected interlaminar regions that manifested high stresses in a computational simulation of the impact tests. Details of the simulation can be found in the article by Castellanos et al. [42]. Nanowire synthesis on dry fabric is described in the following section.

2.1.2 ZnO Nanowire Synthesis on Dry Fabric

ZnO nanowires have very strong interaction with carbon fibers as previous studies have suggested [33]. Functional groups, like hydroxyl, carbonyl, and carboxylic acid, have been found in carbon fibers that create a strong chemical bonding with ZnO [34–36]. ZnO nanowires added at the mid-plane of the laminate were synthesized

using a hydrothermal method, where ZnO nanoparticle seed layer was deposited on a woven carbon fiber surface by dip coating [44]. ZnO nanoparticles were formed by mixing together solutions of zinc acetate dihydrate and ethanol with sodium hydroxide and ethanol at a volume ratio of 18:7 at 55 °C [45]. Then, the carbon fibers were covered by ZnO nanoparticles by dip coating [32]. After that, nanowires were grown in a glass beaker on a hot plate, where the deposition on carbon fibers occurred in an aqueous solution of zinc nitrate hydrate and hexamethylenetetramine (HMTA). The temperature of the solution was maintained at 90 °C for 4 h. Finally, the carbon fiber layers were removed from the solution and were rinsed with 18.2 MΩ water and dried at 100 °C [32]. A low-molecular-weight polyethylenimine (PEI, Aldrich, M_w = 25,000) was added to aid uniform growth of nanowires [46]. The morphology (diameter, length, and orientation) and quality of ZnO nanowires synthesized on carbon fibers can be controlled through multiple parameters: temperature, solution concentration, ZnO nanoparticle size, and growth time. The approximate final geometry of the ZnO nanowires in the current study was 50 nm diameter and 500 nm length [32].

2.2 Interlaminar Fracture Toughness Tests

Mode-I fracture toughness tests were performed following the double cantilever beam (DCB) test method. Other possible tests are the wedge-insert-fracture (WIF) [8] and compression tension (CT) [7]. Mode-II fracture toughness tests were performed following the end-notched flexure (ENF) test method. According to Wang and Williams [47], the two common test geometries for Mode-II tests are the end-loaded-split (ELS) and the ENF specimens. 3-ENF was originally proposed for testing, which was later developed into the S-ENF, T-ENF, and 4-ENF methods [48]. However, according to Morais and Pereira [49], ENF test is the best method for Mode-II due to its simplicity, negligible friction effects, and low tendency for geometric nonlinearity [50].

2.2.1 Mode-I Fracture Toughness: Double Cantilever Beam (DCB)

Mode-I interlaminar fracture toughness, which is the critical strain energy release in J/m^2, was determined using DCB test. The DCB specimen typically consists of a rectangular uniform thickness laminated composite with a nonadhesive insert at the mid-plane that serves as a delamination initiator [51]. Opening forces are applied to the DCB specimen using hinges on the top and bottom surfaces at one end of the specimen by controlling the opening displacement, while the load and delamination length are recorded [51].

According to the ASTM Standard D5528-13 [51], the dimensions (Fig. 2) of each specimen were 127 mm (5.0 in.) long, 25.4 mm (1.0 in.) wide, and 2.54 mm (0.1 in.) thick. A Teflon sheet of 63.5 mm (2.5 in.) length × 25.4 mm (1.0 in.)

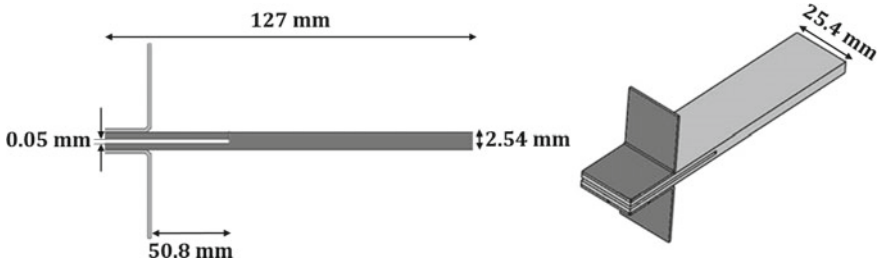

Fig. 2 Sample dimensions for DCB test

Fig. 3 DCB test in progress of a carbon fiber laminate with ZnO nanowires

width × 0.0508 mm (0.002 in.) thickness was inserted to simulate a pre-crack. A pre-crack (about 2 mm) was propagated by loading the hinges with the Instron machine. Eight specimens were tested in total (four specimens with ZnO nanowires and four without ZnO nanowires). The initial delamination length was measured from the point where the load was applied to the end of the pre-crack. Tests were performed on an Instron 8801 with a displacement control unit at a loading rate of 5 mm/min (recommended loading rate was 1–5 mm/min by ASTM D5528-13). A loading–unloading procedure was followed for crack propagation. That is, the applied displacement was stopped when a significant crack growth accompanied by an abrupt load drop was observed. The crack extension was recorded and the specimens were restored to their original position at an unloading rate of 25 mm/min. About 4–5 loading–unloading cycles were conducted for each DCB specimen.

Complex data reduction methods were used to calculate the critical strain energy release rate, G_{IC}, which is influenced by the accuracy of the measured load, displacement, crack length, and the change in compliance with crack length. Three data reduction methods were applied to the load–displacement data obtained from the tests: (1) modified beam theory (MBT), (2) compliance calibration (CC), and (3) modified compliance calibration method (MCC) as specified in ASTM D5528-13 [51]. Figure 3 shows the DCB test in progress for one of the specimens.

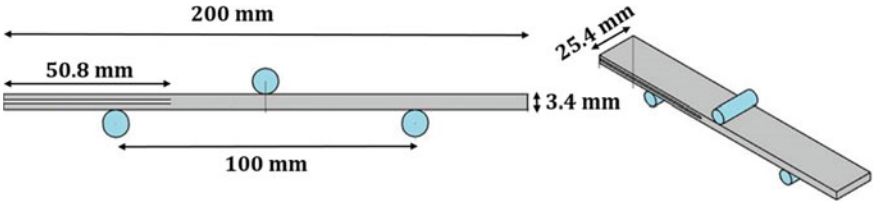

Fig. 4 Sample dimensions for ENF test

2.2.2 Mode-II Fracture Toughness: End-Notched Flexure (ENF)

Mode-II interlaminar fracture toughness, which is the critical strain energy release rate in J/m^2, was calculated using ENF test. The ENF specimen consists of a rectangular, uniform thickness laminated composite with a nonadhesive insert at the mid-plane that acts as a crack initiator [52]. The ENF specimen is loaded in a three-point bend fixture that consists of two support points at the bottom and one load point at the top of the specimen at the mid-span [53]. The load, center point displacement, and crack length are measured and recorded during displacement controlled tests.

According to the ASTM Standard D7905/D7905M-14 [52], the dimensions (Fig. 4) of each specimen were 200 mm (8.0 in.) long, 25.4 mm (1.0 in.) wide, and 3.4 mm (0.1 in.) thick. A Teflon sheet of 50.8 mm (2.5 in.) length × 25.4 mm (1.0 in.) width × 0.05 mm (0.002 in.) thickness was inserted to simulate a pre-crack. Tests were performed on an Instron 8801 at a loading rate of 0.5 mm/min. Eight specimens were tested in total (four specimens with ZnO nanowires and four without ZnO nanowires).

Compliance calibration (CC) method is provided in ASTM D7905 [52] to calculate the Mode-II interlaminar fracture toughness value. The specimen was positioned in a three-point bend fixture when the crack length was equal to 30 mm. The specimen was loaded until the crack propagates and an abrupt drop in force was observed. The unloading rate was 0.5 mm/min. The compliance (C) was determined by linear least squares regression analysis of slope of the load–displacement response. Then, the fracture toughness was calculated using the CC method as described in ASTM D7905. Figure 5 shows the ENF test in progress for one of the specimens.

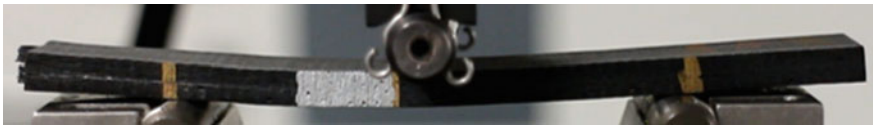

Fig. 5 ENF test in progress of a carbon fiber laminate with ZnO nanowires

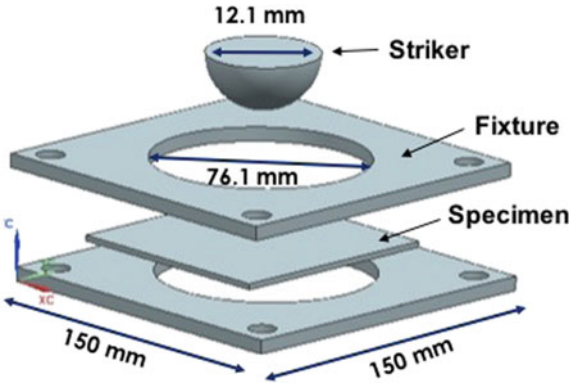

Fig. 6 Schematic of a dynamic impact text fixture

2.3 Dynamic Impact Tests

Drop-weight impact tests were performed using a CEAST 9340 Drop Tower Impact System on rectangular laminate specimens of 6.0 in. (150 mm) length × 4.0 in. (100 mm) width and thicknesses 4.49 ± 0.08 mm. Each specimen consisted of 16 layers of woven fabric. Regions for nanowire interlaminar reinforcements were computationally determined and synthesized at the selected interlaminar regions, which were the interlaminar region underneath the impacted layer and three interlaminar regions toward the back surface of the laminate. The laminates were clamped between two metal fixtures with a test area of 7.07 in^2 (45.6 cm^2).

The impact load using a hemispherical impactor (striker) with a mass of 3.01 kg and a diameter of 0.5 in. (12.7 mm) was concentrated at the center of the specimen in the out-of-plane direction [32] with kinetic energies of 2, 5, 10, 20, and 25 J for both types of samples (with and without ZnO nanowires). Kinetic energy is calculated based on the mass of the impactor and impact velocity. Here, the mass of the striker was fixed to 3.01 kg. For a particular impact energy, the impact velocity and the striker falling height were adjusted accordingly by the Instron machine CEAST 9340. A schematic of an impact test is shown in Fig. 6. Three samples were impacted for each impacted energy and sample type. Corresponding force–time, energy–time, and force–displacement plots were obtained from each test.

3 Discussion of Results

Interlaminar Fracture toughness values of composites with and without nanowires were compared to evaluate the influence of ZnO nanowire reinforcement.

3.1 Mode-I Fracture Toughness: Double Cantilever Beam (DCB)

Mode-I fracture toughness (G_{IC}) values of composites with and without nanowires were compared. Figure 7 shows the load–displacement response of one specimen without nanowires. As explained before, the specimen was loaded until an abrupt drop in load was observed. The extent of crack propagation was measured, and then the specimen was unloaded to restore to its original position. This process was repeated until the next load drop occurred and the load–displacement plot for four cycles for a specimen is shown in Fig. 7.

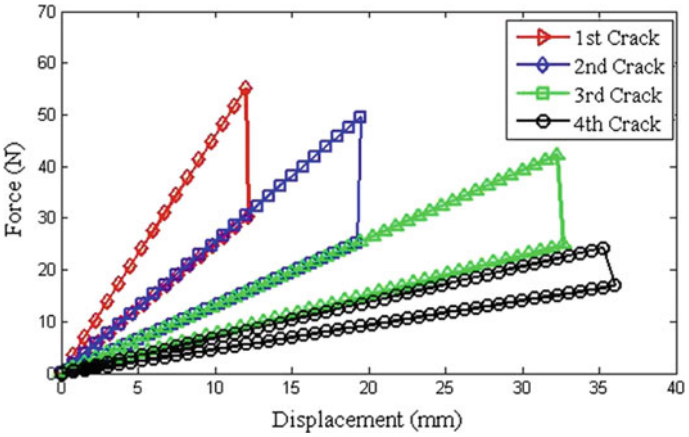

Fig. 7 Typical load–displacement response of a DCB test specimen without nanowires

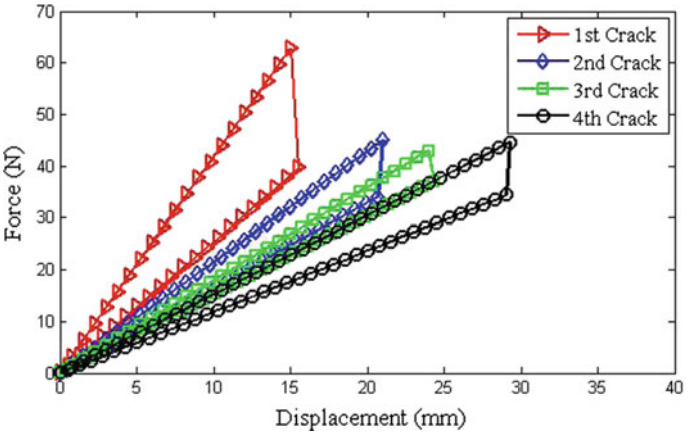

Fig. 8 Typical load–displacement response of a DCB test specimen with nanowires

Table 1 G_{IC} (kJ/m^2) without ZnO nanowires

Specimen	MBT	CC	MCC
1	0.442	0.414	0.465
2	0.424	0.427	0.477
3	0.424	0.376	0.418
4	0.454	0.505	0.434
Average	0.430 ± 0.001	0.431 ± 0.047	0.449 ± 0.023

Table 2 G_{IC} (kJ/m^2) with ZnO nanowires

Specimen	MBT	CC	MCC
1	0.747	0.772	0.726
2	0.683	0.777	0.734
3	0.718	0.726	0.809
4	0.760	0.914	0.832
Average	0.716 ± 0.026	0.797 ± 0.070	0.775 ± 0.056

Figure 8 shows the load–displacement response of one of the specimens with ZnO nanowires. The sample without ZnO nanowires (Fig. 7) showed larger drops in load corresponding to crack extension. On the other hand, the load did not drop as drastically in the specimen with ZnO nanowires (Fig. 8). As stated before, G_{IC} values were calculated with three reduction methods: MBT, CC, and MCC, and the values are shown in Tables 1 and 2 for specimens without and with ZnO nanowires, respectively. ZnO nanowire interlaminar reinforcement showed an increase of approximately 66.5% with MBT method, approximately 84.9% with CC method, and approximately 72.6% with MCC method. Therefore, ZnO nanowires appear to greatly improve the Mode-I interlaminar fracture toughness of carbon woven composites. This increase can be attributed to the bridging effect and cohesive matrix failure of the laminate. An analysis of the surface of single fiber showed a cohesive matrix failure, which supports the resistance of the nanowire toward the formation of new surfaces at the interlaminar regions [32].

3.2 Mode-II Fracture Toughness: End-Notched Flexure (ENF)

Figures 9 and 10 show the load–displacement response of specimens without and with ZnO nanowire reinforcement for ENF tests. The displacements are normalized by the displacement corresponding to the peak load to account for the slight increase in thickness due to nanowire reinforcement.

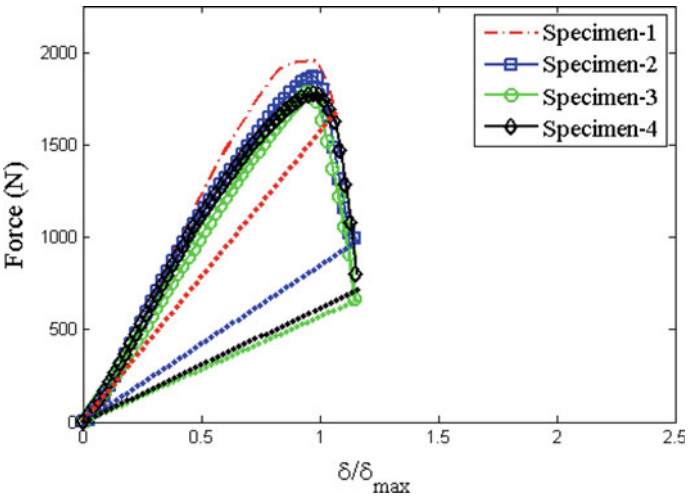

Fig. 9 Load–displacement response for specimens without nanowires for ENF

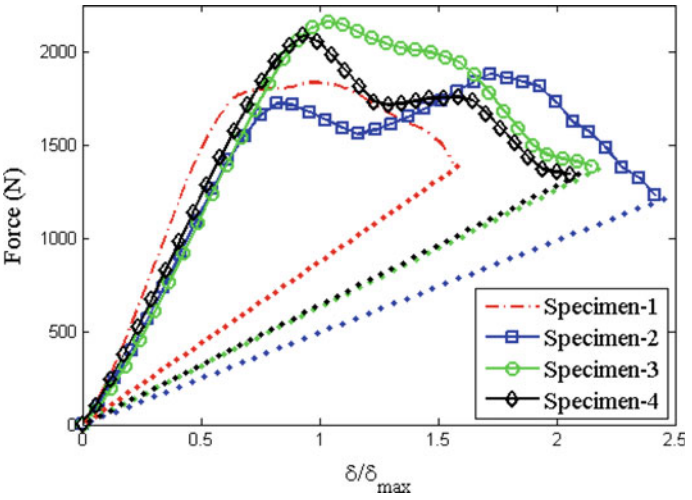

Fig. 10 Load–displacement response for specimens with nanowires

During the experiments, it was noticed that the crack progression in the sample without ZnO nanowires was more sudden as compared to the samples with ZnO nanowires. This is manifested by steeper drop in the post-peak response of the samples without ZnO nanowires (Fig. 9) as compared to the gradual drop in peak load for samples with ZnO nanowires (Fig. 10).

As stated before, G_{IIC} values were calculated using the CC reduction method. G_{IIC} values calculated for the specimens without and with ZnO nanowires are given in Table 3. ZnO nanowire reinforcement showed an average increase of

Table 3 G_{IIC} (kJ/m^2)

Specimen	Without ZnO	With ZnO
1	0.422	0.584
2	0.459	0.557
3	0.426	0.513
4	0.437	0.571
Average	0.436 ± 0.014	0.556 ± 0.027

approximately 28% with CC method. This increase is attributed to the shearing effect of ZnO nanowires at the laminate interfaces, thus reducing the ease of creating new smooth fracture surfaces. Therefore, ZnO nanowires appear to improve the Mode-II interlaminar fracture toughness of carbon woven composites.

3.3 Fractographic Analysis of Fractures Surfaces

The fractured surfaces were examined under a scanning electron microscope (SEM) in order to explore the interlaminar fracture mechanism of the specimens with and without ZnO nanowires. Fracture surfaces in both cases were restricted in the mid-plane interlaminar region of the composite. In samples without ZnO nanowires, the crack propagated predominantly through the resin as observed in Fig. 11b. That is, the interface is smooth with only a small amount of fiber separation at the interface, whereas, for samples with ZnO nanowires, a large amount of fiber separation at the interface was observed as shown in Fig. 11a, which is attributed to the ZnO nanowires at the interfaces. Based on the observations, it is hypothesized that the ZnO nanowires improve the bonding between the interfaces. Due to enhanced shear resistance imparted by the ZnO nanowires, the fracture surface progression is accompanied by fiber separation from the layers, which appears to improve the Mode-II interlaminar fracture toughness. That is, a higher resistance is present in the sample with ZnO nanowires, where the fracture surface not only propagates through the interlaminar region but also pulls the carbon fibers, as shown in Fig. 11c and d.

3.4 Dynamic Impact Response

The kinetic energies considered for the impact tests were 2, 5, 10, 20, and 25 J. 3 samples were impacted with the same energy for nanowire reinforced and unreinforced samples. The impact responses were evaluated in terms of visual damage of the impacted specimens and by calculating the degree of damage. The time, deformation, energy, force, velocity, and voltage were recorded by the data acquisition system

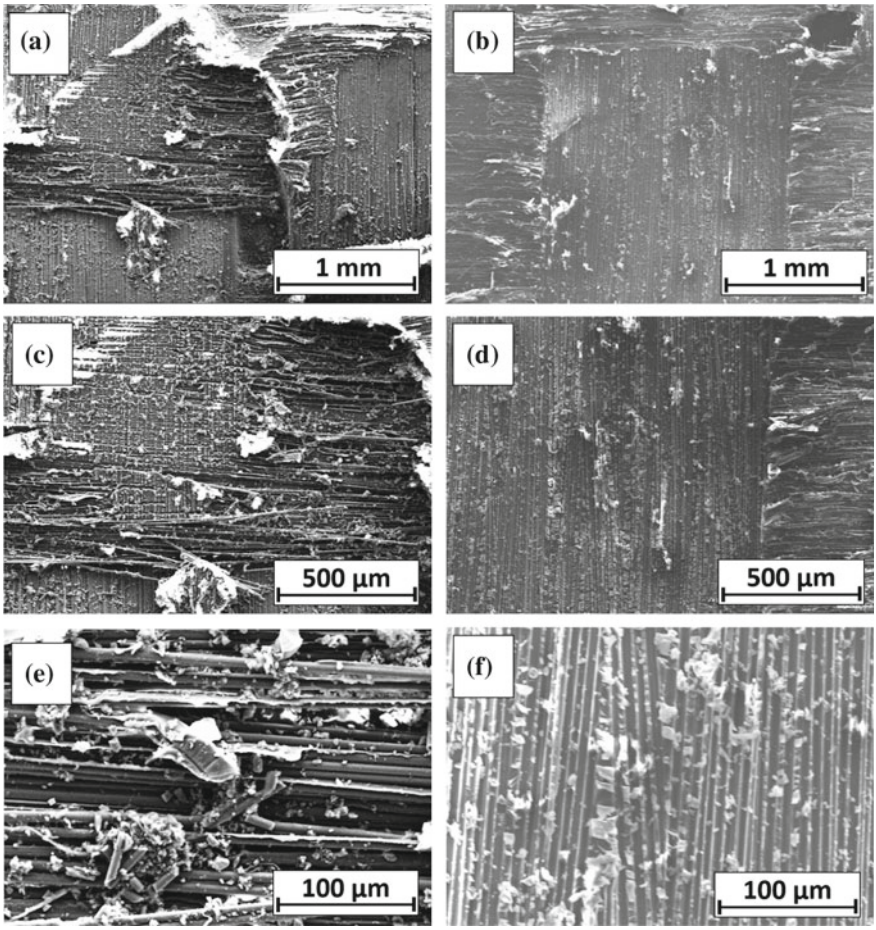

Fig. 11 **a** Fracture surface for a specimen with ZnO nanowires (Scale: 1 mm); **b** Fracture surface for a specimen without ZnO nanowires (Scale: 1 mm); **c** Fracture surface for a specimen with ZnO nanowires (Scale: 500 µm); **d** Fracture surface for a specimen without ZnO nanowires (Scale: 500 µm); **e** Fracture surface for a specimen with ZnO nanowires (Scale: 100 µm); **f** Fracture surface for a specimen with ZnO nanowires (Scale: 100 µm)

CEAST DAS 8000 Junior of the impact machine for each test conducted. Figure 12 shows the sample thickness normalized force–time responses from the impact tests of one set of samples with and without nanowire reinforcements impacted at different energies.

The force is generated by the contact of the striker with the impacted face of the sample, which is recorded with the data acquisition system of the impact machine. Table 4 summarizes the average peak force and average maximum deflection obtained for each impact energy. Predominantly, samples with ZnO nanowires displayed higher peak force and lower deflection than the samples without ZnO. This

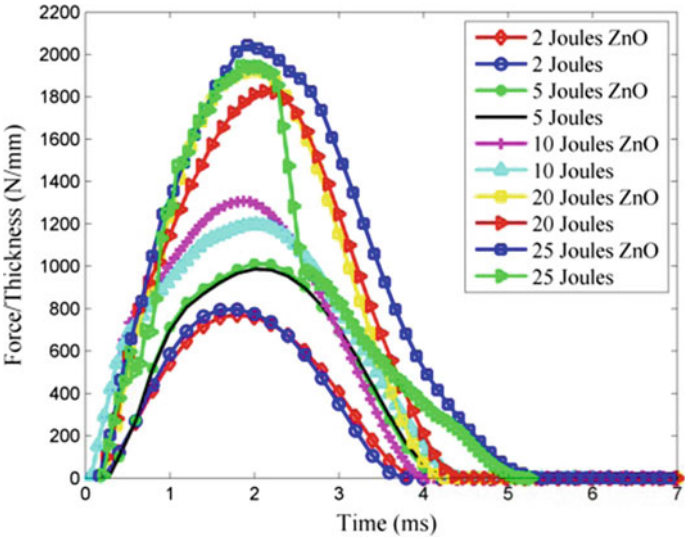

Fig. 12 Normalized force–time response for one set of samples impacted at 2, 5, 10, 20, and 25 J energies

Table 4 Normalized peak force (F) and maximum deflection (Def) for samples with and without ZnO nanowires

Energy (J)	F w/ ZnO (N/mm)	Def w/ ZnO (mm)	F w/o ZnO (N/mm)	Def w/o ZnO (mm)
2	641 ± 146	1.02 ± 0.04	629 ± 129	1.06 ± 0.04
5	813 ± 192	1.92 ± 0.33	812 ± 191	2.47 ± 0.67
10	1252 ± 51	3.06 ± 0.50	1122 ± 72	3.33 ± 0.40
20	1769 ± 141	4.17 ± 0.34	1684 ± 133	4.67 ± 0.54
25	1884 ± 241	4.73 ± 1.18	1844 ± 59	5.37 ± 1.23

implies that the load carrying capacity of the reinforced samples increased and the overall deformation of the laminate reduced as well.

Figure 13a shows representative energy–time responses of 10 specimens (five with and five without ZnO nanowire samples) that were impacted with five energies mentioned above. A schematic of a typical energy–time response is shown in Fig. 13b, where the peak value corresponds to the impact energy and the plateau region represents the absorbed energy.

In Fig. 13a, the difference between the absorbed energy (plateau region) and the impacted energy appears to increase with increasing impact energies. In addition, the samples without nanowires manifested higher absorbed energy for a particular impact energy as shown in Fig. 13a. For this reason, the specimens without nanowires experienced more damage. Further, to measure the damage experienced

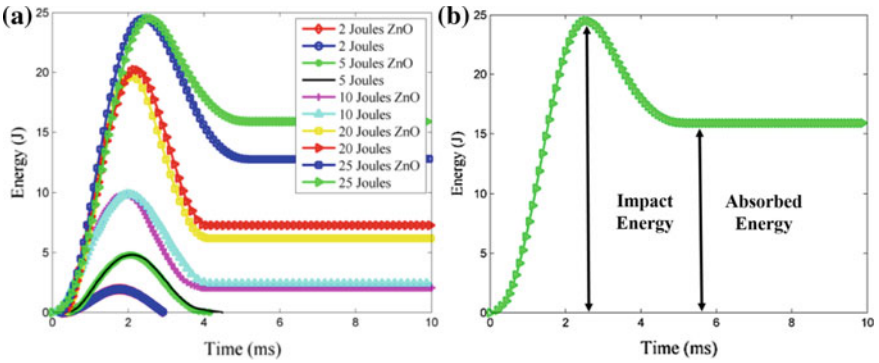

Fig. 13 **a** Energy–time responses of 10 specimens (five with and five without ZnO nanowire samples); **b** Schematic of degree of damage definition

Table 5 Percentage change in the degree of damage (D) values for samples with and without ZnO nanowires

Energy (J)	D w/ ZnO	D w/o ZnO	Percentage change
5	0.29 ± 0.03	0.21 ± 0.04	23% ± 0.02
10	0.44 ± 0.03	0.35 ± 0.02	22% ± 0.03
20	0.58 ± 0.01	0.44 ± 0.03	25% ± 0.02
25	0.71 ± 0.04	0.53 ± 0.06	24% ± 0.02

by the impacted specimens, the degree of damage [40] was calculated using the following equation:

$$D = \frac{Absorbed\ Energy}{Impact\ Energy} \tag{1}$$

Table 5 shows the average calculated degree of damage for each impact energy for samples with and without nanowire reinforcement. For impact energies 5, 10, 20, and 25 J, the samples with nanowires manifested lower values of D than the samples without ZnO nanowires, with up to 25% reduction. It should be noted that the degree of damage was zero for specimens impacted with 2 J energy, which indicates that no damage was imparted to those laminates and the striker rebounded from the impacted surface. Hence, ZnO nanowire reinforcement showed an improvement in damage resistance for low-velocity impact loading.

4 Conclusion

A novel fabrication technique for imparting ZnO nanowire interlaminar reinforcements in woven carbon fiber reinforced polymer composites was presented in this chapter. The objective was to improve the interlaminar fracture toughness and through-thickness impact response of the laminates without degrading the in-plane properties. Mode-I and Mode-II interlaminar fracture toughness values of carbon fiber woven composite facesheets with and without ZnO nanowire reinforcement at the interlaminar regions were compared. Double cantilever beam (DCB) tests were used to determine the Mode-I fracture toughness values with three data reduction methods: modified beam theory (MBT), compliance calibration (CC), and modified compliance calibration (MCC). End-notched flexure (ENF) tests were used to determine the Mode-II fracture toughness values by compliance calibration (CC) method. Eight specimens were tested for each mode, four with ZnO nanowires and four without. Next, low-velocity impact responses of these composites with and without ZnO nanowire interlaminar reinforcements were investigated and the degree of damage was experimentally determined.

Key findings of the research presented in this chapter are as follows:

1. Mode-I interlaminar fracture toughness increased significantly: approximately 66.5% from MBT, 84.9% from CC method, and 72.6% MCC method.
2. Mode-II interlaminar fracture toughness increased by approximately 28% in comparison to the samples without ZnO nanowires.
3. The impact tests revealed that the samples with ZnO nanowires experienced a lower degree of damage, up to a maximum of 25% for different impact energies, in comparison to the samples without ZnO nanowires for a range of impact energies between 5 and 25 J.
4. An increase in the impact peak load and reduction in maximum deflection was observed from the impact tests between samples with and without nanowire reinforcement.
5. A low absorption of energy by the samples with ZnO nanowires was observed, which can be attributed to the bridging and resistance of failure initiation caused by the ZnO nanowires at the interlaminar regions.

To summarize, this study revealed that ZnO nanowire interlaminar reinforcements improved the Mode-I and Mode-II fracture toughness values and impact resistance of woven carbon polymeric composites. Even though the improvement in the impact response is not drastic (approximately 25%), it can be improved further by exploring the wide range of nanowire synthesis parameters, like temperature, solution concentration, ZnO nanoparticle size, and growth time, as well as reinforcing all interlaminar regions. The current study serves as a preliminary work for further investigation into ZnO nanowires as potential interlaminar reinforcements for woven composites for improving their impact damage resistance. These nanowires have shown great potential for preventing or minimizing the degree of damage which would improve the overall damage tolerance of composite structures.

Acknowledgements The author would like to thank Ms. Alejandra Castellanos, doctoral student under the guidance of the author, for contributing key findings for this chapter. The author would also like to acknowledge the support of Mr. Emilio Tarango and Dr. Yirong Lin from the University of Texas at El Paso, TX for their support for initial synthesis of nanowires. Finally, the author would like to acknowledge the support through the DoD HBCU/MI Basic Research Grant (W911NF-15-1-0430) for conducting the research presented in this chapter.

References

1. Smiley, A. J., & Pipes, R. B. (1987). Rate effects on mode I interlaminar fracture toughness in composite materials. *Journal of Composite Materials*, *21*, 1–18.
2. Tenney, D., Davis, J., Byron, R., & Johnston, N. (2009). NASA composite materials development: Lessons learned and future challenges. *Conference Paper* (pp. 1–58), LF99-9370.
3. Bortz, D. R., Merino, C., & Martin-Gullon, I. (2011). Mechanical characterization of hierarchical carbon fiber/nanofiber composite laminates. *Composites Part A: Applied Science and Manufacturing*, *42*, 1584–1591.
4. Lars, B., Sumfleth, J., Hedemann, H., & Schulte, K. (2010). Improvement of fatigue life by incorporation of nanoparticles in glass fibre reinforced epoxy. *Composites Part A: Applied Science and Manufacturing*, *41*, 1419–1424.
5. Galan, U., Lin, Y., Ehlert, G. J., & Sodano, H. (2011). Effect of ZnO nanowire morphology on the interfacial strength of nanowire coated carbon fibers. *Composites Science and Technology*, *71*(7), 946–954.
6. Wicks, S., Wang, W., Williams, M. R., & Wardle, B. L. (2014). Multi-scale interlaminar fracture mechanisms in woven composite laminates reinforced with aligned carbon nanotubes. *Composites Science and Technology*, *100*, 128–135.
7. Szekrenyes, A. (2002). Overview on the experimental investigations of the fracture toughness in composite materials. *Hungarian Electronic Journal*, MET-020507-A, 1–19.
8. Czabaj, M., & Ratcliffe, J. (2012). Comparison of intralaminar and interlaminar mode-I fracture toughness of unidirectional IM7/8552 graphite/epoxy composite. In: *2012 American Society for Composites*, Arlington, TX, 1–3 Oct.
9. Arguelles, A., Vina, J., Canteli, A. F., Castrillo, M. A., & Bonhomme, J. (2008). Interlaminar crack initiation and growth rate in a carbon-fibre epoxy composite under mode I fatigue loading. *Composites Science and Technology, 68*, 2325–2331.
10. Khan, R., Rans, C. D., & Benedictus, R. (2009). Effect of stress ratio on delamination growth behavior in unidirectional carbon/epoxy under mode I fatigue loading. *ICCM-17 International Conferences on Composite Materials* (pp. 1–11). Scotland.
11. O'Brien, K. (1981). Characterization of delamination onset and growth in a composite laminate. *NASA Technical Memorandum*, 1–63.
12. Rikards, R., Buchholz, F. G., Bledzki, A. K., Wacker, G., & Korjakin, A. (1996). Mode I, mode II and mixed-mode I/II interlaminar fracture toughness of GFRP influenced by fiber surface treatment. *Mechanics of Composite Materials*, *32*(5), 1–24.
13. Dransfield, K. A., Jain, K. L., & Mai, Y. W. (1998). On the effects of stitching in CFRPs-I mode I delamination toughness. *Composite Science and Technology*, *58*, 815–827.
14. Kostopoulos, V., Baltopoulos, A., Karapappas, P., Vavouliotis, A., & Paipetis, A. (2010). Impact and after-impact properties of carbn fibre reinforced composites enhanced with multi-wall carbon nanotubes. *Composites Science and Technology*, *70*, 553–563.
15. Malhotra, A., & Guild, F. J. (2014). Impact damage to composite laminates: effect of impact location. *Applied Composite Materials*, *21*, 165–177.
16. Safri, S., Sultan, M., Yidris, N., & Mustapha, F. (2014). Low velocity and high velocity impact test on composite materials—a review. *International Journal of Engineering and Science*, *3*(9), 50–60.

17. Julias, A., & Murali, V. (2014). Effect of carbon fiber position on the impact behavior of glass/carbon fiber hybrid composite laminates. *International Journal of Applied Engineering Research*, *9*(26), 9103–9106.
18. Caprino, V., Lopresto, V., Scarponi, C., & Briotti, G. (1999). Effect of ZnO nanowire morphology on the interfacial strength of nanowire coated carbon fibers. *Composites Science and Technology*, *59*, 2279–2286.
19. Karakuzu, R., Erbil, E., & Mehmet, A. (2010). Impact characterization of glass/epoxy composite plates: An experimental and numerical study. *Composites: Part B*, *41*, 388–395.
20. Serenest, A. (2011). Overview on the experimental investigations of the fracture toughness in composite materials. *Journal of Engineering Materials and Technology*, *100*, 1–19.
21. Kim, J.-K., & Sham, M.-L. (2000). Impact and delamination failure of woven-fabric composites. *Composite Science Technology, 60*, 745–761.
22. Sheer, T. W., & Pan, Y. H. (2003). Impact resistance and damage characteristic of composite laminates. *Composite Structures*, *62*, 193–203.
23. Babe, S., & Shiva, H. K. (2014). Impact analysis of laminated composite on glass fiber and carbon fiber. *International Journal of Emerging Technology and Advanced Engineering*, *4*, 824–829.
24. Sohn, M. S., & Hu, X. Z. (1998). Processing of carbon-fibre/epoxy composites with cost-effective interlaminar reinforcement. *Composite Science and Technology*, *58*, 211–220.
25. Prasad, M. S., Venkatesha, C. S., & Jayaraju, T. (2011). Experimental methods of determining fracture toughness of fiber reinforced polymer composites under various loading conditions. *Journal of Minerals & Materials Characterization & Engineering*, *10*(13), 1263–1275.
26. Ren, J., Kim, Y. K., & Rice, J. (2011). Comparing the fracture toughness of 3-d braided preform composites with z-fiber reinforced laminar composites. *Textile Research Journal*, *81*, 335–343.
27. Sager, R. J., Klein, P. J., Davis, D. C., Lagoudas, D. C., Warren, G. L., & Sue, H. (2010). Interlaminar fracture toughness of woven fabric composite laminates with carbon nanotube/epoxy interleaf films. *Wiley Online Library*. https://doi.org/10.1002/app.33479:1-12.
28. Kong, K., Deka, B. K., Kim, M., Oh, A., Kim, H., Park, Y., et al. (2014). Interlaminar resistive heating behavior of woven carbon fiber composite laminates modified with ZnO nanorods. *Composites Science and Technology*, *100*, 83–91.
29. Fan, Z., Santare, M. H., & Advani, S. G. (2008). Interlaminar shear strength of glass fiber reinforced epoxy composites enhanced with multi-walled carbon nanotubes. *Composites Part A: Applied Science and Manufacturing*, *39*, 540–554.
30. Ashrafi, B., Guan, J., Mirjalili, V., Zhang, Y., Chun, L., Hubert, P., et al. (2011). Enhancement of mechanical performance of epoxy/carbon fiber laminate composites using single-walled carbon nanotubes. *Composites Science and Technology*, *71*, 1569–1578.
31. Qian, H., Bismarck, A., Greenhalgh, E. S., Kalinka, G., & Shaffer, M. S. P. (2008). Hierarchical composites reinforced with carbon nanotube grafted fibers: the potential assessed at the single fiber level. *Chemistry of Materials*, *20*(5), 1862–1869.
32. Lin, Y., Ehlert, G., & Sodano, H. (2009). Increased interface strength in carbon fiber composites through a ZnO nanowire interphase. *Advanced Functional Materials*, *19*, 2654–2660.
33. Crook, S., Dhariwal, H., & Thornton, G. (1997). HREELS study of the interaction of formic acid with ZnO(1010) and ZnO(0001)-O. *Surface Science*, *382*(1–3), 19–25.
34. Dilsiz, N., & Wightman, J. P. (1999). Surface analysis of unsized and sized carbon fibers. *Carbon*, *37*(7), 1105–1114.
35. Dilsiz, N., & Wightman, J. P. (2000). Effect of acid-base properties of unsized and sized carbon fibers on fiber/epoxy matrix adhesion. *Colloids and Surfaces A: Physicochemical and Engineering Aspects*, *164*, 325–336.
36. Turgeman, R., Gershevitz, O., Deutsch, M., Ocko, B. M., Gedanken, A., & Sukenik, C. N. (2005). Crystallization of highly oriented ZnO microrods on carboxylic acid-terminated SAMs. *Chemistry of Materials*, *17*, 5048–5056.
37. Hwang, H., Malakooti, M., Patterson, B., & Sodano, H. (2014). Increased interyarn friction through ZnO nanowire arrays grown on aramid fabric. *Composites Science and Technology*, *107*, 75–81.

38. Baxter, J. B., & Eray, S. A. (2005). Nanowire-based dye-sensitized solar cells. *Applied Physics Letters, 86*(5), 053114, 1–3.
39. Wang, X. D., Song, J. H., Liu, J., & Wang, Z. L. (2007). Direct-current nanogenerator driven by ultrasonic waves. *Science*, *316*, 102–105.
40. Wang, Z. L., & Song, J. (2006). Piezoelectric nanogenerators based on zinc oxide nanowire arrays. *Science*, *312*, 242–246.
41. Castellanos, A. G., Islam, M. S., Shuvo, M. A. I., Lin, Y., & Prabhakar, P. Nanowire reinforcement of woven composites for enhancing interlaminar fracture toughness. *Journal of Sandwich Structures and Materials*.
42. Castellanos, A. G., Islam, M. S., Tarango, E., Lin, Y., & Prabhakar, P. (2017). Interlaminar reinforcement for enhancing low-velocity impact response of woven composites. *Textile Research Journal*, (Accepted, in press).
43. Chittajallu, K. (2004). Computational modeling of the vacuum assisted resin transfer molding (VARTM) process (master's thesis). Clemson University.
44. Ehlert, G. J. (2009). Development of a zinc oxide nanowire interphase for enhanced structural composites. *Doctoral Dissertation. Retrieved from: US National Library of Medicine National Institutes of Health* (pp. 1–247).
45. Hu, Z., Oskam, G., & Searson, P. (2003). Influence of solvent on the growth of ZnO nanoarticles. *Journal of Colloid and Interface Science*, *263*(2), 454–460.
46. Law, M., Greene, L. E., Johnson, J. C., Saykally, R., & Yang, P. (2005). Nanowire dye-sensitized solar cells. *Nature Materials*, *4*, 455–459.
47. Wang, Y., & Williams, J. G. (1992). Corrections for mode-II fracture toughness specimens of composite materials. *Composites Science and Technology*, *43*, 251–256.
48. Yoshihara, H. (2005). Mode II initiation fracture toughness analysis for wood obtained. *Composites Science and Technology*, *65*, 2198–2207.
49. Pereira, A. B., De Morais, A. B., Marques, A. T., & Castro, P. T. (2004). Mode II interlaminar fracture of glass/epoxy multidirectional laminates. *Composites Part A: Applied Science and Manufacturing*, *35*(2), 265–272.
50. Reis, P. N. B., Ferreira, J. A. M., Costa, J. D. M., & Pereira, A. M. (2014). Interlaminar fracture in woven carbon/epoxy laminates. *Frattura ed Integrita Strutturale*, *30*, 431–437.
51. ASTM International. (2013). Standard test method for mode I interlaminar fracture toughness of unidirectional fiber-reinforced polymer matrix composites. D5528 (13 pages). ASTM International, West Conshohocken, PA. https://doi.org/10.1520/D5528, https://www.astm.org.
52. ASTM International. (2014). Standard test method for mode II interlaminar fracture toughness of unidirectional fiber-reinforced polymer matrix composites. *D7905/D7905M-14* (pp. 1–18).
53. Zhu, Y. (2009). Characterization of interlaminar fracture toughness of a carbon/epoxy composite material. *Master's thesis*. The Pennsylvania State University.

Shock Wave Mitigation Using Liquids

H. Jeon and V. Eliasson

1 Introduction

The understanding of shock wave propagation through various types of media is essential for the safety of humans and buildings because shock or blast waves can cause serious damage [1, 2]. With the advent of new technology, humans have learned to deposit high-density energy (up to megatons of TNT) by explosives, thereby generating shock waves with incredible strength. Explosives are often used for mining, excavation, and demolition. However, there are also negative effects of the development of technology. These include explosives as weapons that can potentially harm soldiers during a war or civilians during a terror attack. Further, explosions may occur unintentionally due to accidents that damage property and cost lives. With so much at stake, an understanding of how to reduce the energy contained in a blast wave is motivated by more than academic curiosity. Consequently, over the past few decades, many researchers have studied shock wave mitigation. There are various approaches to attenuate shock or blast waves using different materials and geometries [3]. Among the different approaches, environmentally friendly and readily available liquids such as water have been considered for cost-effective shock attenuation methods. The acoustic impedance of water is about 3500 times greater than that of air at atmospheric pressure. Therefore, only a small fraction of energy can be transmitted into the water. In addition, solid-like shock-absorbing properties can be achieved by adding dense particles into the water. Using experimental methods for more practical purposes, this chapter focuses on the use of liquids to dissipate and reflect incom-

H. Jeon
Department of Aerospace and Mechanical Engineering, University of Southern California, Los Angeles, CA 90089-1191, USA

V. Eliasson (✉)
Department of Structural Engineering, University of California, San Diego, La Jolla, CA 92093-0085, USA
e-mail: eliasson@ucsd.edu

S. Gopalakrishnan and Y. Rajapakse (eds.), *Blast Mitigation Strategies in Marine Composite and Sandwich Structures*, Springer Transactions in Civil and Environmental Engineering, https://doi.org/10.1007/978-981-10-7170-6_16

ing energy induced by shock waves. The chapter begins with a brief overview of the literature and experimental methods. Experimental results and analysis are then provided to demonstrate the potential possibilities of liquids to protect humans and building structures from shock waves.

1.1 Shock and Blast Waves

A shock wave is a very thin discontinuous region where a transient change in pressure, density, temperature, and velocity of the media in which the shock wave is propagating in takes place. Before introducing possible methods to study shock mitigation, the properties behind the actual shock front should be addressed. Typically, there are two scenarios that occur depending on the method used to generate the shocks: (1) a shock front followed by constant properties lasting for some time; and (2) a shock front followed by an exponential decay in properties (often referred to as a "blast wave"), as illustrated in Fig. 1. The first scenario is unrealistic unless the shock wave is confined to propagate in some direction with constant area cross section, the way most shock tubes are designed.

As shown in Fig. 1, the *overpressure* or *underpressure* can be defined by the relative pressure induced by shock or blast wave compared to the ambient pressure. A parameter often used to quantify the potential damage caused by a shock or blast wave is *impulse*, which is defined as the integral of the pressure over a certain time interval.

1.2 A Brief Overview of the Literature

The understanding of shock/blast mitigation requires knowledge of multidisciplinary research areas including the flow field behind the shock front and the dynamical re-

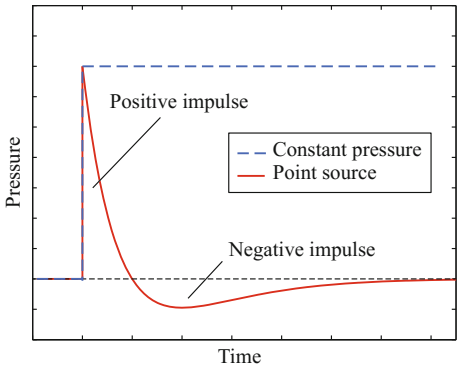

Fig. 1 Examples of pressure profiles behind shock waves. For constant area shock tubes, the pressure behind the shock remains constant for some time. For point source explosions, the pressure profile behind the shock front decays exponentially before returning to ambient conditions

sponse of materials and structures under extreme loading conditions. As discussed in [3] and previously presented in [4], the method of attenuating shock waves can be divided into several categories. **Path-changing methods** can be used to attenuate shock waves inside tunnels by using large-scale changes in geometry to force the shock wave to change direction thereby reducing the energy of the shock wave due to friction, heat transfer, diffraction, and multiple shock wave reflections. Igra et al. [5] performed experimental and numerical studies of shock wave propagation through double-bent ducts with smooth and rough walls. Results showed that a double-bent duct geometry with a rough wall was an effective method to attenuate the transmitted shock wave. The authors deduced that a certain aspect ratio of the width and height of the duct determined the peak pressure caused by the transmitted shock wave. **Obstacle methods** use complex large or small-scale geometries to attenuate shock waves by providing means to dissipate the energy of the shock wave by creating excessive vorticity (losses due to viscous fluid interaction), path changes of the shock, and multiple shock interactions. As an example, rigid obstacles with different barrier angles, shapes, and arrangements have been investigated using experimental different methods [6, 7]. Chaudhuri et al. [8] numerically studied shock wave attenuation effects using array-matrix obstacle arrangements in both non-staggered and staggered columns. Results showed that the strengths of the transmitted shock waves depended on different parameters such as the geometry of the obstacles, obstacle orientation in space, and the relaxation length. **Barrier methods** transfer kinetic energy of the shock wave to the potential energy of a solid or liquid barrier. Many experiments and simulations have been performed in this area using foam barriers [9–12], rigid porous media [13, 14], and solid barriers [15].

Liquid barriers can be used in different forms such as sprays, droplets, sheets, and bulk. Using liquids, the kinetic energy of the shock wave can be transferred to the liquid droplets. Water is a liquid with highly promising physical properties for use in shock mitigation techniques, and because it is both readily available and environmentally friendly makes it a candidate that can possibly be used in large-scale shock mitigation applications. The first attempts to mitigate shock waves using water invoked the process of water droplet atomization [16–18]. Water can be deformed and fragmented by aerodynamic forces and it is known as *secondary atomization* [19]. The main process of *secondary atomization* is divided into two stages: (1) Each droplet experiences deformation by the outside forces, called *deformation process*. Here, if the interfacial tension and viscous forces are smaller than the outside forces, the droplet enters the second stage. (2) Each droplet is broken into smaller ones, called *fragmentation process*. In this stage, aerodynamic forces generated by the shock wave can be used to increase the exchange surface of droplets and the heat energy also can be effectively exchanged between the surrounding air and water droplets at the same time. *The fragmentation process* is known as the main process that can decrease the pressure and gas velocity of shocked gas flow, mainly due to momentum exchange between the shocked air and the water [17].

Bulk water can be also used to mitigate the strength of shock waves. A large body of water can economically replace existing conventional concrete barriers or protective gear and armor. Blast mitigation using bulk water was conducted by many

international organizations and results showed that the shocked-gas pressure and impulse from explosions can be significantly reduced [16]. Meekunnasombat et al. [20] investigated shock wave accelerated liquid layers using a vertical shock tube to understand the impulsive load with applications related to inertial fusion energy reactors. Results showed that multiple water layers for a given volume of water can be used to decrease the end-wall loading of the shock tube. However, this study focused mainly on the impulsive load caused by the shock-accelerated liquid layer rather than the overall shock wave mitigation effects. Chen et al. [21] investigated shock wave mitigation using body armor containing water-filled plastic tubings. Results showed that the overpressure caused by the shock wave was reduced by as much as 97% using the water-filled body armor compared with cases without any protection. However, the results are not clear in terms of how much attenuation was achieved due to the water itself. Son et al. [22] studied blast mitigation using unconfined 3-mm-thick water sheets with an explosively driven shock tube. Results showed that different degrees of blast mitigation effects were observed in different locations and reductions up to 82% of the peak pressure and 75% of the impulse were achieved by using a water sheet. However, the drawback was that the results could not provide a detailed explanation for the pressure-time history results due to a limited visualization area of the shock tube setup.

The stiffness of a liquid can be increased by adding dense particles to achieve solid-like behavior such as shear thickening fluids. Shear thickening is a type of non-Newtonian fluids in which the liquid's viscosity increases with shear rate. One common and widely used shear thickening fluid is created by mixing cornstarch in water, known as a cornstarch suspension. A cornstarch suspension is a type of discontinuous shear-thickening fluids because its viscosity dramatically jumps with increasing shear rate [23]. Discontinuous shear-thickening fluids can be used in a variety of applications including shock absorptive gear, such as skis or tennis rackets [24], and flexible protective armor [25], which can dissipate vibrations without losing stiffness. There exist different theories to understand the physics of shear-thickening materials, but recently the concept of dynamics jamming has been accepted by many researchers [23]. Jiang et al. [26] studied the impact resistance and solid-like behavior of shear-thickening fluids at high-strain loading rates using Kolsky bar (split Hopkinson pressure bar) experiments. Results showed that the amplitude and width of the transmitted pulse were much weaker and longer, compared to cases using ethylene glycol. Petel et al. [27] investigated ballistic resistance in different particle-based shear-thickening fluids using gas gun experiments. Results showed that the loss of ballistic resistance was caused by the material strength of the particles in suspensions. Furthermore, Waitukaitis and Jaeger [28] conducted aluminum rod impact experiments to understand the energy absorption mechanism of a cornstarch suspension. Results showed that the growth of a dynamic jamming region generated by the impact is the main mechanism that absorbs the impact energy of the mechanical rod. Roché et al. [29] investigated dynamic fracture of a cornstarch suspension impacted by a cylindrical metal rod and showed detailed results of fluid-to-solid transition. The authors quantified the velocity of the crack tip and the number of cracks and then estimated the shear modulus of the fractured material. However, it is not clear

if conclusions drawn from the previous research can be extended to a non-physical impact caused by a shock wave.

This chapter focuses on investigating whether a transmitted shock wave through planar liquid sheets can be observed, and if so, then obtain detailed information on the pressure-time history during and after the shock wave impacts the liquid sheet. Finally, the shock wave mitigation effect is quantified for two different types and thicknesses of liquid sheets.

2 Experimental Setup

Experiments were conducted using a pressure-driven shock tube and a high-speed visualization method. This approach and setup have been described elsewhere [4] but will be repeated here for the convenience of the reader.

A shock tube is a fundamental instrument often used to investigate shock and blast wave mitigation because it provides a highly controlled environment in which pressure measurements and simultaneous optical visualizations can be performed. The experiments were conducted in a 3.8 -m-long shock tube with a circular cross section (96.8 mm inner diameter) of the driver section and square cross sections (63.5 mm internal sides) of both the driven section and the test section, as shown in Fig. 2. The length of the driven section was long enough to create a planar shock front once it arrives to the test section [30]. The driver section was filled with compressed air, while the rest of the shock tube remained at atmospheric pressure (101 kPa) and room temperature (297 K). Driver pressures were set to 310 and 586 kPa (45 and 85 psi) to create incident shock Mach numbers, $M_s = 1.34$ and 1.46, respectively. The driver pressure was measured with a digital pressure gauge (GE DPI 104, ±0.05%, full-scale accuracy).

The test section is made up of three separate parts: an upstream section, a square frame, and a downstream section. The test section has ports for four pressure sensors (S_1 and S_4: PCB 113B21, S_2 and S_3: PCB 113B31, flush mounted). Each sensor was mounted with a threaded Delrin adapter to minimize the influence of disturbances propagating in the shock tube walls. The pressure sensors, S_1 and S_2, are referred to as the upstream sensors, and S_3 and S_4 are referred to as the downstream sen-

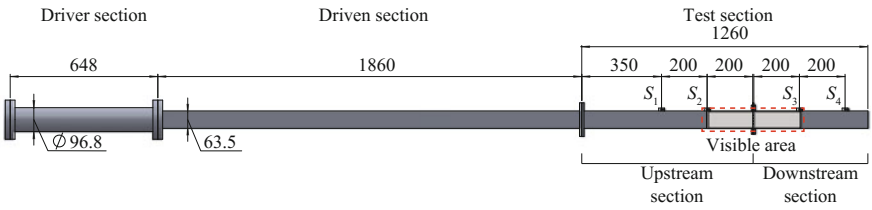

Fig. 2 Schematic side view drawing of the shock tube. Dimension is mm

sors. A signal conditioner (PCB 482C), a digital oscilloscope (LeCroy, Wave Surfer 24Xs-A), and a high-speed camera (Phantom V711) are used to record pressures and schlieren images during the experiment. The shock Mach numbers could be reproduced within ±0.75% with a measurement uncertainty less than ±0.82% in each experiment. The sides of the test section were made of transparent windows (impact-resistant polycarbonate, 12.7 mm thickness) to provide a long enough visualization area to study the breakup of the liquid sheets.

The square frame (similar to what was used in [20]) was designed to hold a 5- or 10-mm-thick liquid sheet in the test section with the desired planar shape by using two plastic sheets (12.5 μm, Saran wrap) and cotton wires (5 μm thickness, 12.7 mm distance), as shown in Fig. 3. The reason for using plastic sheets instead of an unconfined free-falling liquid sheets [22] was because of its reliability to provide shock–liquid interactions with liquid sheets of specific thicknesses repeatedly in all experiments. To prevent leakage between the square frame and the test sections, o-rings were used on both sides. Experiments were performed by the following procedure: (1) the plastic sheets and cotton wires were attached to the square frame; (2) the square frame was mounted into the test section using bolts; (3) water or a cornstarch suspension was filled through a top slit of the square frame; and (4) the top slit was covered by a cap to prevent leakage during the experiment. In the current study, 55 wt.% of cornstarch suspension (a concentration of 55 wt.% of cornstarch and 45 wt.% water) was used as previous studies [29, 31, 32]. More details are outlined in our previously published work [4].

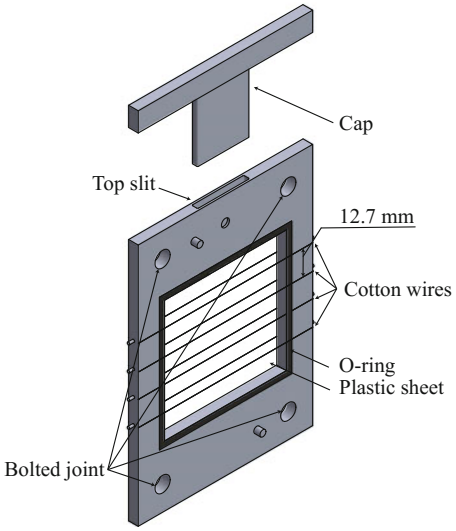

Fig. 3 Schematic drawing of the square frame. One layer of plastic sheet and four cotton wires are used on each side to maintain constant sheet thickness and to minimize bulge

2.1 Visualization Method

The schlieren visualization technique is based on the deflection of light caused by density and temperature changes in solids, liquids, and gases. For a detailed historical background on the schlieren visualization method, see [33]. Figure 4 shows a schematic representation of schlieren visualization techniques. In Fig. 4, the visualization system contains a z-folded schlieren setup, a light source, and a high-speed camera. Parallel light between the 254 mm flat mirrors, originating from the light source, is achieved using the 254 mm spherical mirror. A density change in the test section deflects the parallelized light and causes a phase difference. A knife edge is located in the focal point to cut off parts of the light. In the present study, the knife edge was placed vertically with a 50% cutoff to satisfy both resolution and sensitivity. The direct high-speed visualization method was achieved through the use of two light sources mounted alongside the high-speed camera pointed directly at the test section.

In the current study, a high-power light-emitting diode (Cree XLamp, XP-G2 LEDs, Cool white) was used as a light source for the schlieren system. The high-speed camera was equipped with a 50 mm focal length lens (Nikkor 50 mm $f/1.4$ lens). Two different visualization settings were used in this study, as summarized in Table 1.

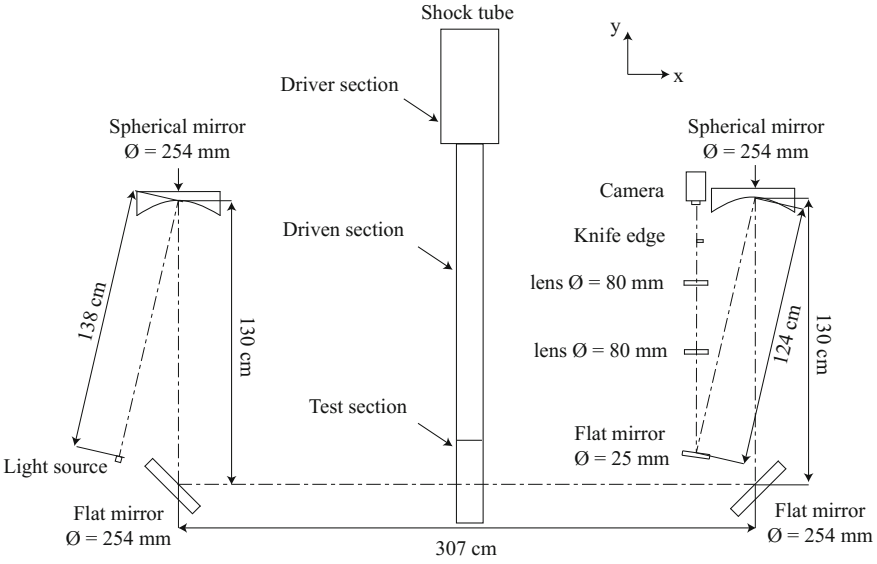

Fig. 4 An overview of the z-folded schlieren visualization setup. The dashed-dotted line represents the light path

Table 1 Summary of camera settings

Visualization	Resolution [pix]	Scale factor [mm/pix]	Exposure time [μs]	Frame rate [fps]	Inter-frame time [μs]
Schlieren	272 × 160	0.384	0.294	96,045	11.4
Direct	720 × 264	0.312	10	35,015	28.6

3 Experimental Results

First, experimental results [4] were obtained from an empty test section having only plastic sheets and cotton wires but no liquid inside. Quantitative and qualitative experimental results of shock wave attenuation by water or cornstarch suspension sheets are presented in the following section.

3.1 Shock Wave Interaction with Plastic Sheets and Cotton Wires

Figure 5 shows a sequence of high-speed schlieren photographs of shock wave interactions with the square frame containing only the plastic sheets and cotton wires but no liquid. Stress concentrations caused by the bolted joints were visible as dark regions between the square frame and windows. After the incident shock impacted the square frame, the transmitted and reflected shock waves were generated and these are clearly shown in Fig. 5c and d. The plastic sheets instantaneously broke upon contact with the shock wave and expanded toward downstream. In Fig. 5d, two reflected shock waves were generated by the upstream and downstream located plastic sheets. The second reflected shock wave caught up with the first and they coalesced into a single shock wave due to the different flow conditions behind the incident and reflected shock waves, as shown in Fig. 5d–f. Both the transmitted and reflected shock waves were slightly curved because of the slightly uneven surface and deformation of the plastic sheets.

An $x - t$ diagram for the flow in the shock tube is presented in Fig. 6 in which the paths of the incident waves, reflected waves, compression waves, and expansion waves are shown with plastic sheets and cotton wires inserted but without liquid between the plastic sheets. The incident shock wave interacts with the plastic sheets in the test section, resulting in the transmitted and reflected shock wave. A part of the transmitted wave through the upstream plastic sheet can be reflected by the downstream plastic sheet, resulting in repeated wave reflections within two sheets. The compression and expansion waves are generated when the plastic sheets expand toward the downstream section. The time, t_0, denotes the arrival time of the incident shock wave and t_1 represents the arrival of the expansion fan at S_1 and t_3 at S_3.

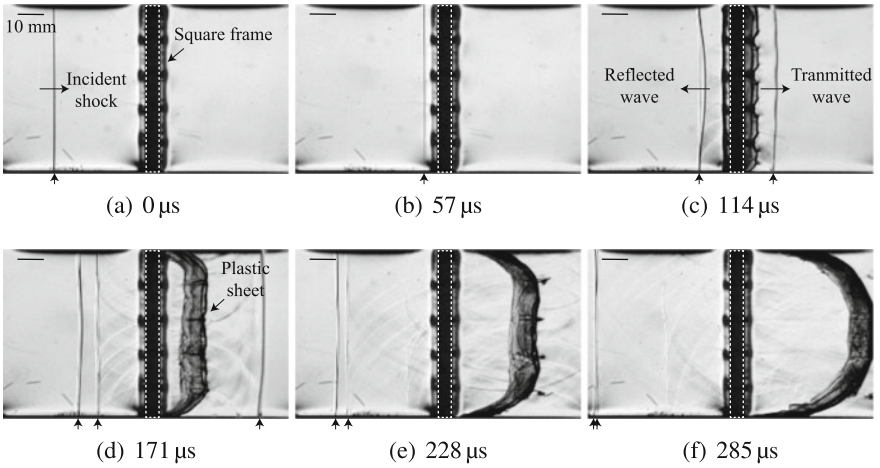

Fig. 5 A series of high-speed schlieren images of shock wave interaction with the plastic sheets and cotton wires but no liquid for an incident Mach number $M_s = 1.46$. The white-dashed lines denote the location of the square frame. This figure is reproduced from [4]

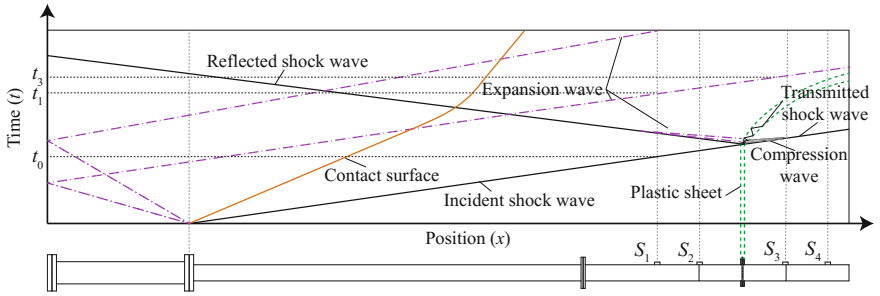

Fig. 6 An $x - t$ diagram depicting the shock wave interaction for a shock tube containing the two plastic sheets and cotton wires but without water in between the plastic sheets. This figure is reproduced from [4]

In Fig. 7, pressure and impulse histories measured from the sensors S_1 and S_3 are plotted to illustrate the effect of the plastic sheets and cotton wires at two incident shock Mach numbers, $M_s = 1.34$ and 1.46. The pressure signals were filtered out 20% of the natural frequency of the sensors (500 kHz for S_1 and S_4 and 400 kHz for S_2 and S_3) to avoid nonlinearity of the signals. Here, only averaged pressure impulses from at least three times of experiments under the same conditions are shown. The first step measured by the sensor S_1 and S_3 is caused by the incident shock wave and the transmitted shock wave, respectively. It can be seen that there is no significant difference between the two cases. Figure 7a and b shows sharp jumps occurring between time $t = 2$ and 3 ms, which were generated by the reflected shock wave. Figure 7c

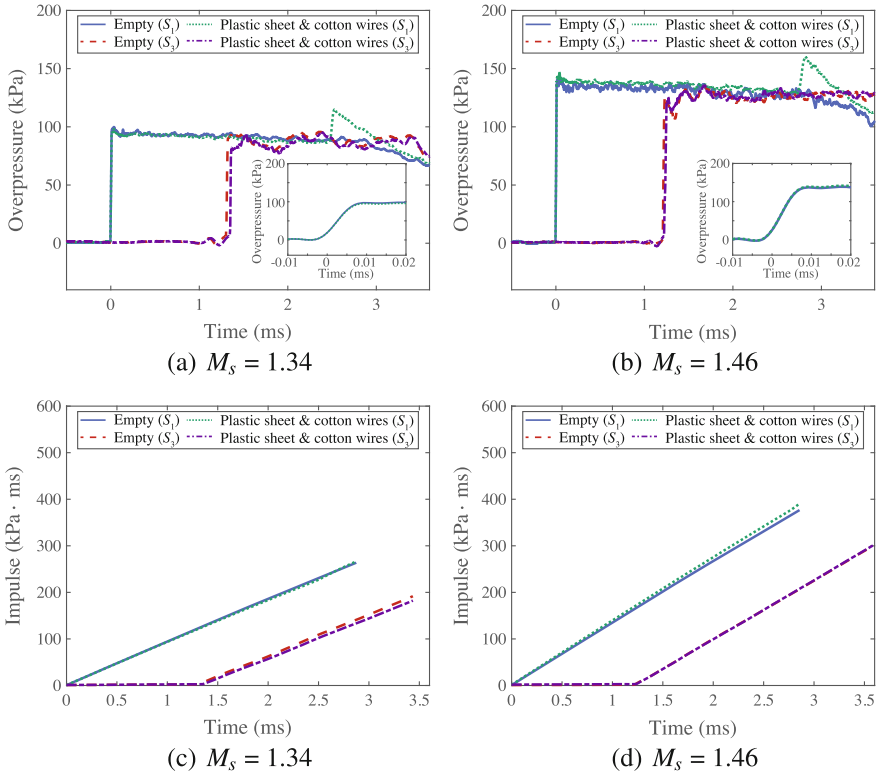

Fig. 7 Comparison of the overpressure and impulse histories recorded by the sensors S_1 and S_3 for two shock Mach numbers of $M_s = 1.34$ and 1.46 during experiments with an empty test section containing only the two plastic sheets and cotton wires: **a** and **b** overpressure versus time; **c** and **d** impulse versus time. The insets in **a** and **b** show overpressure versus time from −0.01 to 0.02 ms. This figure is reproduced from [4]

and d shows impulse histories as a function of time. Here, impulse, I, is calculated as

$$I = \int_{t_0}^{t_{1,3}} (p - p_0) dt, \tag{1}$$

where t is the time, p is the overpressure, and p_0 is the ambient atmospheric pressure. In Fig. 7c and d, the impulse shows a small deviation of less than 5% caused by the reflected wave from the plastic sheets and cotton wires. In addition, shock Mach numbers measured by the upstream and downstream sensors show a consistent wave speed with empty square frame and the plastic wrap and cotton wires. Therefore, shock wave attenuation by the plastic sheets and cotton wires is negligible (<5%), which agrees with previous results [20].

3.2 Shock Wave Interaction with Liquid Sheets

Both high-speed schlieren and direct photography are used to visualize the details of the interaction of the incident shock wave and the liquid sheets. Figure 8 shows a sequence of schlieren high-speed photographs for a 5-mm-thick water sheet impacted by $M_s = 1.46$. It can be seen that no transmitted wave is observed through the water sheet. The multiple circular arcs seen behind the reflected shock wave were generated by the cotton wires.

Figures 9 and 10 show direct high-speed photographs of the breakup processes of the liquid sheets when subjected to the incident shock Mach number $M_s = 1.46$. The time $t = 0$ ms corresponds to the time instant when the shock wave arrives at sensor S_1.

Figure 9 shows a sequence of high-speed photographs for the 10-mm-thick water sheet impacted by the incident shock Mach number $M_s = 1.46$. In Fig. 9b, the water sheet was deformed by the high pressure developed by the incident and reflected shock waves at the upstream section. The deformation generates the upstream-propagating expansion waves and the downstream-propagating compression waves. In Fig. 9c and d, the top and bottom parts of the sheet were broken first and the water was fragmented by the high pressure. The larger fragmented-water volume fraction indicates more energy dissipation of the shocked-gas flow. The fragmented water droplets arrived at sensor S_3 after approximately 3.3 ms.

Figure 10 shows the breakup of the 10-mm-thick cornstarch sheet impacted by the incident shock wave Mach number $M_s = 1.46$. In Fig. 10b, the evenly deformed surface, compared to the water as shown in Fig. 9b, was caused by shock-activated solidification of cornstarch suspensions. As discussed in [28], a rapidly growing jammed region was developed by the shock wave impact onto the surface of the cornstarch sheet, resulting in solidification of cornstarch suspensions. In Fig. 10c and d, the

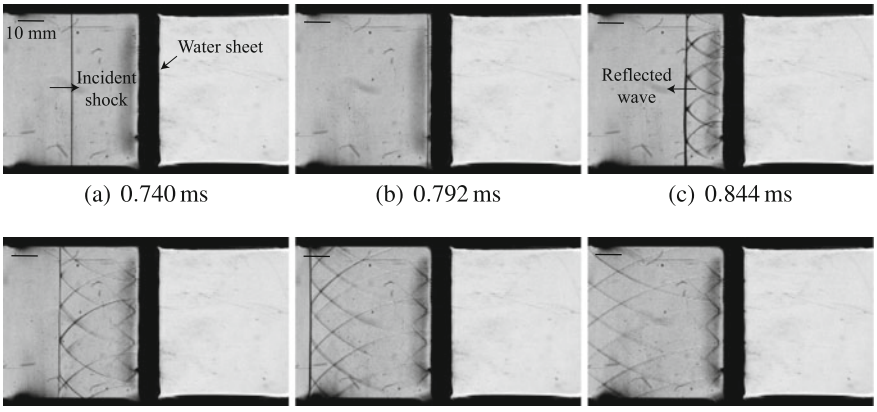

Fig. 8 A series of schlieren high-speed images for a 5-mm-thick sheet at $M_s = 1.46$

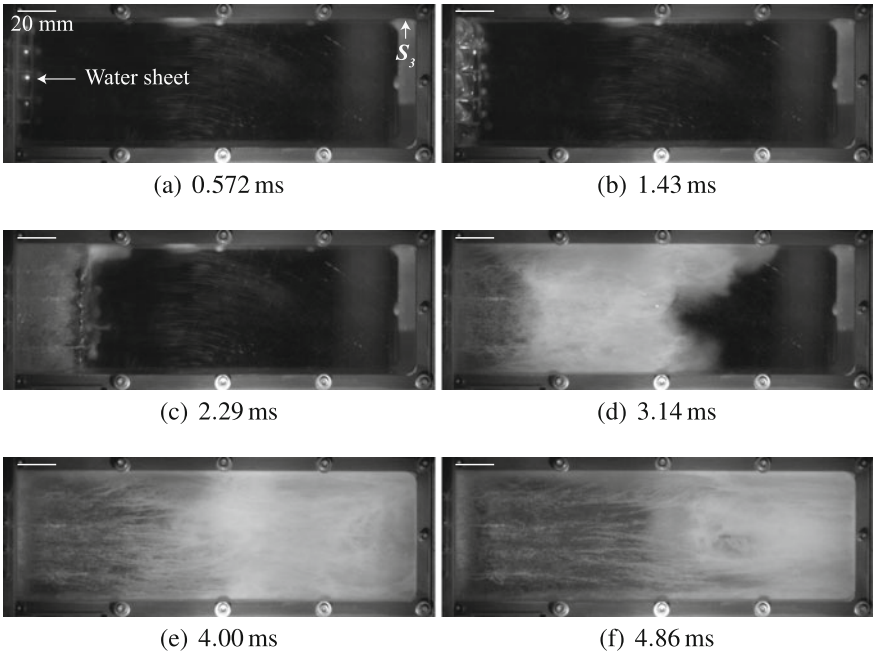

Fig. 9 A series of high-speed images for a 10-mm-thick water sheet at $M_s = 1.46$. S_3 is located in the top-right side of the test section. This figure is reproduced from [4]

cornstarch sheet shows piston-like motion or a solid-like behavior in contrast to the fragmented water as shown in Fig. 9c and d. In Fig. 10d, fragmented water droplets were squeezed out from the cornstarch suspension and this phenomenon can be explained by shear thickening in colloidal dispersions [34]. The shock wave impacted onto the cornstarch sheet caused the hydrodynamic pressure between the particles so multiple cornstarch particles approached each other, extracting water from the cornstarch suspension. The hydrodynamic pressure made the particle concentration became denser by water being extracted from the suspension. Therefore, the energy from the shock wave impact can be dissipated by a higher viscosity. In Fig. 10e and f, brittle fracture is observed on the surface of the cornstarch suspension to dissipate the impact energy but the size of fragmented cornstarch sheets is larger than those of the water droplets under the same experimental conditions.

A similar breakup behavior was observed for the 5-mm-thick cornstarch sheet impacted by an incident shock wave with Mach number $M_s = 1.46$, as shown in Fig. 11. The breakup time of the 5-mm-thick cornstarch sheet was reduced and the size of the fragmented particles was smaller than compared to the 10-mm-thick cornstarch sheet.

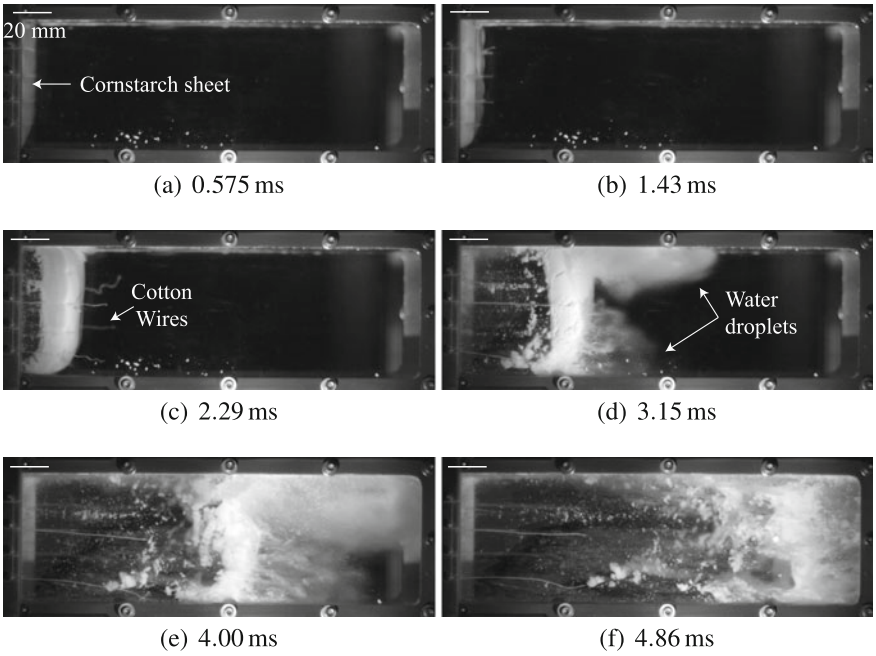

Fig. 10 A series of high-speed images for a 10-mm-thick cornstarch suspension sheet at $M_s = 1.46$

3.2.1 Pressure Profile

Figure 12 shows the pressure and impulse histories measured by S_1 and S_3 with shock Mach numbers, $M_s = 1.34$ and 1.46, during experiments with 5 and 10-mm-thick water and cornstarch sheets [4].

In Fig. 12a, the first pressure jump was created by the incident shock wave. Consistent amplitude and width of the first pressure jump confirm repeatable results of the experiments. After the incident shock impacted the liquid sheet, the reflected shock wave was generated and the strength of the reflected wave was considerably weaker than the reflection off a rigid-solid wall, which was calculated using the Rankine–Hugoniot shock relation. The stronger incident shock wave generated the stronger reflected shock wave. The overpressure caused by the reflected shock wave slowly decreases as a function of time, compared to the nearly constant overpressure caused by the incident shock wave, due to the liquid sheet deformation and breakup toward downstream. For an incident shock Mach number $M_s = 1.34$, the reflected shock wave was arrived at the sensor S_1 at $t = 2.10$ ms with the overpressure of 230 kPa. For an incident shock Mach number $M_s = 1.46$, the arrival time of the reflected shock wave was $t = 2.05$ ms and overpressure was 358 kPa (5 mm thick) and 378 kPa (10 mm thick) for both water and cornstarch sheets. The varia-

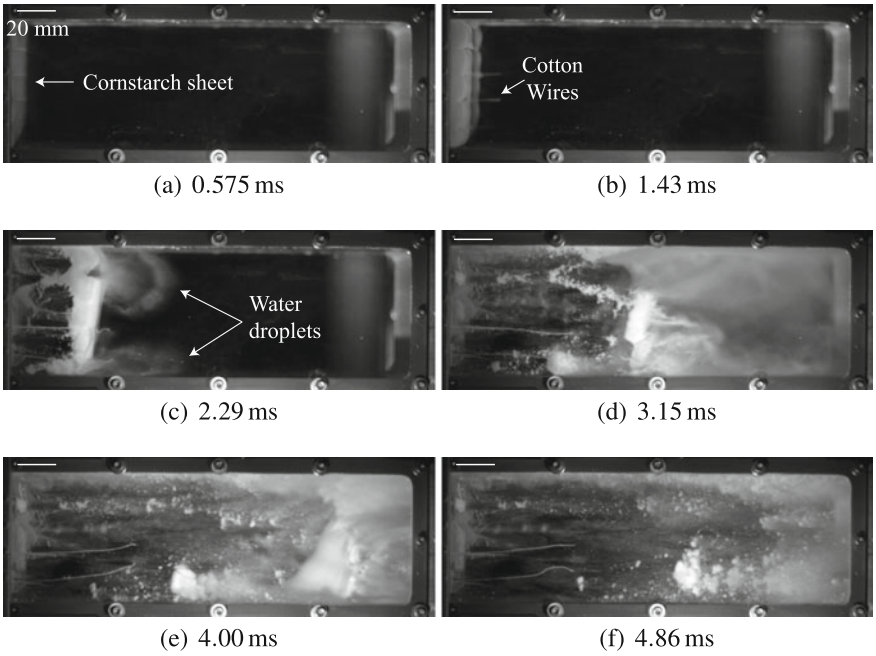

(a) 0.575 ms (b) 1.43 ms

(c) 2.29 ms (d) 3.15 ms

(e) 4.00 ms (f) 4.86 ms

Fig. 11 A series of high-speed images for a 5-mm-thick cornstarch suspension sheet at $M_s = 1.46$

tion in reflected overpressure of the 5 mm liquid sheets for both water and cornstarch suspensions was caused by an early breakup of liquid sheets.

In Fig. 12b, the peak overpressure measured at the sensor S_3 is much lower than that recorded at the upstream sensor S_1 since nearly all of the incident shock wave is reflected by the liquid sheets due to the impedance mismatch, in agreement with previous results [35, 36]. The acoustic impedance of air (414 kg/m^{2}s) based on 1.2 kg/m^3 density and 345 m/s speed of sound are several orders of magnitude less than that of both water (1.5×10^6 kg/m^{2}s) and cornstarch (2.3×10^6 kg/m^{2}s). Oscillatory traces of the pressure measurements are caused by vibrations of the side windows, which occur in every experiment no matter if the test section is empty or equipped with a liquid sheet. The highest peak overpressure was observed for the case of the 5-mm-thick water sheet with incident shock Mach number $M_s = 1.46$.

In Fig. 12b, two sharp jumps were generated by compression waves and liquid impacts. The high pressure generated by the incident and reflected shock waves deforms and breaks the liquid sheet toward downstream, resulting in compression waves. Further downstream, the compression waves coalesce into a shock wave that moves ahead of the shocked liquid layer, as shown in [20]. Later, the fragmented water droplets and cornstarch suspension particles arrive at the downstream sensor and generate the second pressure jump. However, those two jumps were not observed for the 10-mm-thick cornstarch sheet. A higher peak overpressure was measured by water sheets compared to the same thickness of cornstarch sheets.

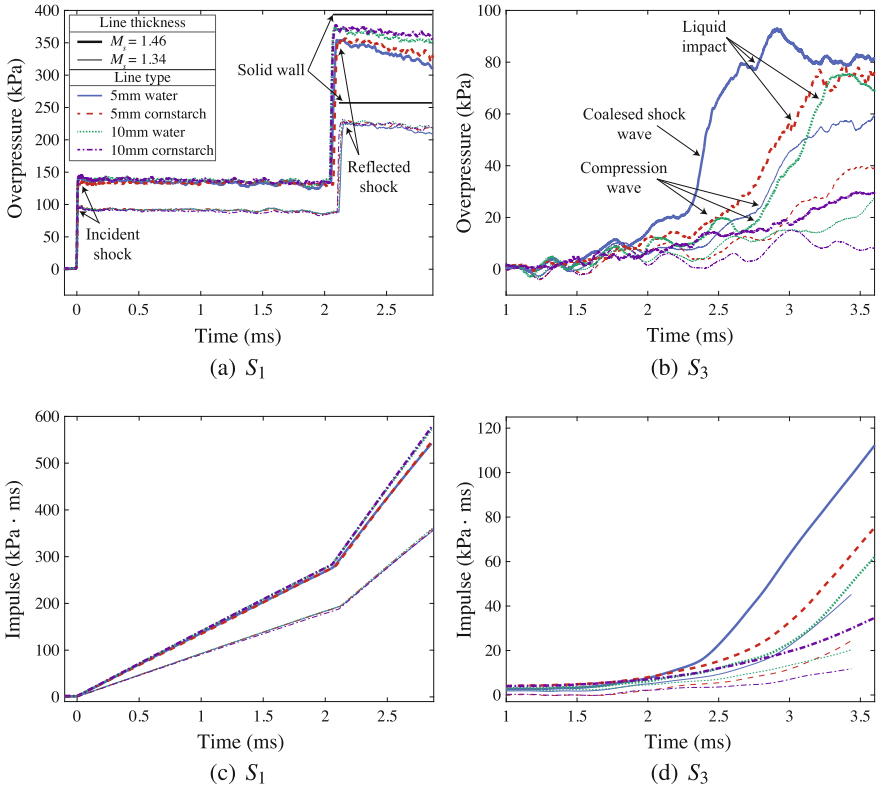

Fig. 12 Comparison of the overpressure and impulse histories measured at S_1 and S_3 during experiments with 5-mm- and 10-mm-thick water or cornstarch suspension sheets for incident Mach shock numbers of $M_s = 1.34$ and 1.46: **a** overpressure versus time at S_1; **b** overpressure versus time at S_3; **c** impulse versus time at S_1; **d** impulse versus time at S_3. Results for overpressure and impulse are averaged over three separate experiments. This figure is reproduced from [4]

In Fig. 12c, no discrepancy in the total impulse can be seen at $M_s = 1.34$ in upstream sensors, but a small discrepancy (6%) is shown at $M_s = 1.46$ after $t = 2$ ms, which is caused by the different amplitudes of the reflected shock waves. This is caused by the early breakup of 5-mm-thick water and cornstarch sheet. In Fig. 12d, the overall trend shows a similar result in the overpressure history.

On the basis of the pressure profile and high-speed photographs, an $x - t$ diagram for the case with a planar liquid sheet is presented in Fig. 13. As discussed in Fig. 6, repeated wave reflections within the liquid sheet are also shown in Fig. 13.

Table 2 shows reflected and coalesced shock Mach numbers, M_r and M_c, calculated by the upstream and downstream sensors using a speed of sound calculated based on the Rankine–Hugoniot relations. The reflected and coalesced shock Mach numbers increased with the higher incident shock Mach number. The reflected shock Mach number was not significantly affected by the types and thicknesses of the liquid

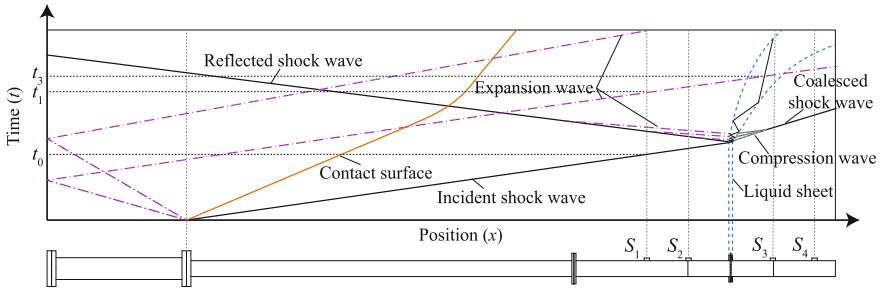

Fig. 13 A schematic $x - t$ diagram of the shock wave interaction with a liquid sheet. This figure is reproduced from [4]

Table 2 Reflected and coalesced Mach numbers (M_r and M_c) are calculated based on the time of arrival of the shock wave between sensors S_1 and S_2 and sensors S_3 and S_4, respectively

Type	$M_s = 1.34$		$M_s = 1.46$	
	M_r	M_c	M_r	M_c
5 mm water	1.26	1.03 ± 0.06	1.35	1.22 ± 0.02
5 mm cornstarch	1.27	0.844 ± 0.06	1.35	1.03
10 mm water	1.27	1.00 ± 0.02	1.35	1.00 ± 0.08
10 mm cornstarch	1.27	[N/A]	1.36	[N/A]

sheets but the coalesced shock Mach number decreased with the thicker liquid sheet. The measured coalesced Mach numbers were near or under sonic velocity, except for the 5 mm water sheet featuring $M_s = 1.46$. It is interesting that the coalesced shock Mach number generated by the cornstarch sheet was lower than that generated by the water sheet. The coalesced shock Mach number resulting from the experiment with the 10 mm cornstarch sheet was not available since the measured overpressure was significantly lower and cannot be distinguished from the noise level of the sensor.

Based on the pressure and impulse traces, several results can be concluded as follows: (a) transmitted shock wave through liquid sheets was not measured and visualized in the current study; instead, compression waves were generated by the shock-accelerated liquid sheet in downstream and compression waves later coalesce into a shock wave; (b) a thinner liquid sheet resulted in a higher peak overpressure (up to 200% higher) and impulse (up to 15% higher), and it caused a stronger coalesced shock wave, especially for a 5 mm water sheet at $M_s = 1.46$ in which $M_c = 1.22 \pm 0.02$; (c) a cornstarch sheet showed a lower peak overpressure (up to 35% lower) and impulse (up to 12% lower) when the same thickness of water and cornstarch suspension were compared, while the strength of coalesced wave resulted in a similar speed (near sonic velocity); and (d) a cornstarch sheet showed a delayed break-up time compared to water sheets.

Based on the impulse profile, a shock wave reflection factor, K_R, and a shock wave attenuation factor, K_A, were calculated for combinations of liquid sheets for

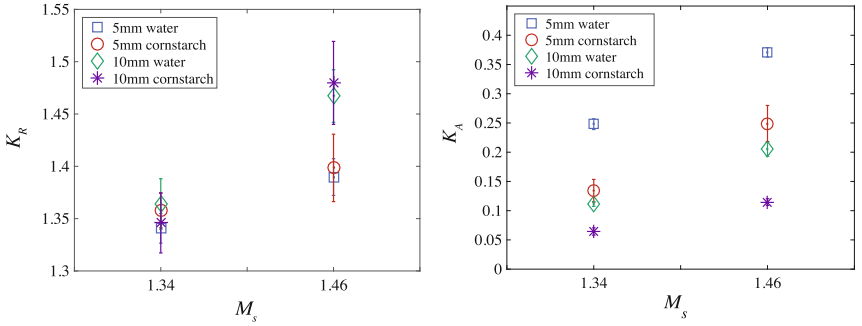

(a) Shock wave reflection factor (b) Shock wave attenuation factor, from [33]

Fig. 14 Shock wave reflection and attenuation factor, K_R and K_A, for 5-mm-thick- and 10-mm-thick-thick water and cornstarch sheets for incident shock Mach numbers $M_s = 1.34$ and 1.46. Error bars represent standard deviations

incident shock Mach numbers $M_s = 1.34$ and 1.46, as shown in Fig. 14. The shock wave reflection and attenuation factor, K_R and K_A, are defined as

$$K_R = \frac{I_1}{I_0}, \tag{2}$$

$$K_A = \frac{I_3}{I_0}, \tag{3}$$

where I_1 is the impulse recorded at sensor S_1 with a liquid sheet (water or cornstarch), I_3 is the impulse recorded at sensor S_3 with a liquid sheet, and I_0 is the impulse for a square frame without liquid between the plastic sheets. Therefore, the shock wave attenuation factor represents the value of the impulse with a liquid sheet normalized by the impulse without the liquid.

As shown in Fig. 14a, the shock wave reflection factors obtained for an incident shock Mach number of $M_s = 1.34$ are not statistically different from case to case. However, there is a difference in the results for the higher shock Mach number $M_s = 1.46$. This difference was mainly caused by a variation of breakup time instants of the liquid sheets. The shock wave attenuation factors for 10 mm water and 5 mm cornstarch sheets at $M_s = 1.34$ and 1.46 are not significantly different, as shown in Fig. 14b. However, the cornstarch sheet shows lower attenuation factor (higher attenuation effect) compared to the same thickness of the water sheet. The shock wave attenuation factor was mainly influenced by the compression waves (due to the shock-accelerated liquid layer) that later coalesced into a shock wave. One can note that the shock wave attenuation was mainly achieved by bulk viscosity of the cornstarch suspension caused by rapid compression regions [37].

4 Conclusions

This chapter discussed the shock wave mitigation with liquid sheets using experimental methods, including a high-speed visualization and a pressure-driven shock tube. Experimental investigation of shock wave mitigation is essential to understand fluid–structure interactions due to the difficulties of performing numerical simulations dealing with multiphase phenomena including viscosity and liquid surface tension. Here, shock wave mitigation using a 5-mm and a 10-mm-thick liquid sheet was investigated at two incident shock Mach numbers, $M_s = 1.34$ and 1.46. High-frequency pressure sensors were utilized to measure overpressure, impulse, and shock velocity. High-speed schlieren and direct photographs were used to understand the details of the pressure profiles. A test section and a square frame were designed to visualize the details of shock wave interactions with liquid sheets without gas leakage. The planar liquid sheet was generated by a square frame using plastic sheets and cotton wires to support and hold liquids inside. Results showed that a negligible amount of the shock wave was attenuated by the plastic sheets and cotton wires of the square frame. Based on the pressure profiles and the flow visualization, the results can be concluded as follows:

- Nearly, all of the incident shock wave was reflected by a liquid sheet of water or cornstarch suspensions and no transmitted shock wave was observed downstream of the liquid sheet.
- The waves detected in the downstream section behind the liquid sheet were compression waves that were generated by the liquid sheet breakup. Further downstream, these compression waves coalesced into a shock wave.
- A cornstarch sheet showed lower peak pressure and impulse compared to the same thickness of a water sheet in downstream. This was caused by the bulk viscosity and shock-driven solidification of the cornstarch sheet.

These results show promise that water or cornstarch suspensions may have a significant effect on attenuating the strength of shock waves and could possibly be incorporated into protective armor and barriers. However, the momentum of the shock-accelerated liquid layer can cause a high peak pressure and impulse although it results in no transmitted shock wave. To further understand the dynamic behavior of liquid sheets, the analysis of the breakup processes of water and cornstarch sheets must be performed including the details of the dispersal characteristics of liquid droplet clouds during and after interactions with shock waves. To achieve these goals, future experiments could consider using unconfined liquid sheets (without the plastic sheets and cotton wires because these can generate unnecessary and complex boundary conditions). Additionally, these results will be used as a baseline for future studies to compare with numerical studies for modeling shock-free surface interactions.

Acknowledgments We would like to thank the National Science Foundation sponsor award No. CBET-1437412. Special thanks to Mr. N. Amen, Ms. H. Geozalian, and Mr. H. Wei for their assistance in designing the test section of the shock tube and conducting the experiments. The authors also want to thank the USC Viterbi/Dornsife Machine Shop.

References

1. Mallonee, S., Shariat, S., Stennies, G., Waxweiler, R., Hogan, D., & Jordan, F. (1996). *JAMA*, *276*, 382.
2. National Research Council. (1995). *Protecting buildings from bomb damage*. Washington, D.C.: National Academy Press.
3. Igra, O., Falcovitz, J., Houas, L., & Jourdan, G. (2013). *Progress in Aerospace Sciences*, *58*, 1.
4. Jeon, H., & Eliasson, V. (2017). *Experiments in Fluids*, *58*(24)
5. Igra, O., Wu, X., Falcovitz, J., Meguro, T., Takayama, K., & Heilig, W. (2001). *Journal of Fluid Mechanics*, *437*, 255.
6. Berger, S., Sadot, O., & Ben-Dor, G. (2010). *Shock Waves*, *20*(1), 29.
7. Ohtomo, F., Ohtani, K., & Takayama, K. (2005). *Shock Waves*, *14*(5–6), 379.
8. Chaudhuri, A., Hadjadj, A., Sadot, O., & Ben-Dor, G. (2013). *Shock Waves*, *23*(1), 91.
9. Britan, A., Shapiro, H., Liverts, M., Ben-Dor, G., Chinnayya, A., & Hadjadj, A. (2013). *Shock Waves*, *23*(1), 5.
10. Britan, A., Shapiro, H., Liverts, M., & Ben-Dor, G. (2014). *Shock Waves*, *24*(3), 241.
11. Skews, B., Atkins, M., & Seitz, M. (1993). *Journal of Fluid Mechanics*, *253*, 245.
12. Kitagawa, K., Yasuhara, M., & Takayama, K. (2006). *Shock Waves*, *15*(6), 437.
13. Ram, O., & Sadot, O. (2013). *Journal of Fluid Mechanics*, *718*, 507.
14. Ram, O., & Sadot, O. (2015). *Journal of Fluid Mechanics*, *779*, 842.
15. Britan, A., Igra, O., Ben-Dor, G., & Shapiro, H. (2006). *Shock Waves*, *16*(1), 1.
16. Kailasanath, K., Tatem, P. A., & Mawhinney, J. (2002). Blast mitigation using water-a status report. Technical Report No. NRL/MR/6410-02-8606, Naval research lab, Washington, D.C.
17. Chauvin, A., Jourdan, G., Daniel, E., Houas, L., & Tosello, R. (2011). *Physics of Fluids*, *23*, 113301.
18. Jourdan, G., Biamino, L., Mariani, C., Blanchot, C., Daniel, E., Massoni, J., et al. (2010). *Shock Waves*, *20*, 285.
19. Guildenbecher, D. R., López-Rivera, C., & Sojka, P. E. (2009). *Experiments in Fluids*, *46*, 371.
20. Meekunnasombat, P., Oakley, J. G., Anderson, M. H., & Bonazza, R. (2006). *Shock Waves*, *15*, 383.
21. Chen, Y., Huang, W., & Constantini, S. (2012). *PLoS ONE*, *7*, e39353.
22. Son, S. F., Zakrajsek, A. J., Miklaszewski, E. J., Kittell, D. E., Wagner, J. L., & Guildenbecher, D. R. (2014). *Blast mitigation*. New York: Springer.
23. Brown, E., & Jaeger, H. M. (2014). *Reports on Progress in Physics*, *77*, 046602.
24. Fischer, C., Braun, S. A., Bourban, P. E., Michaud, V., Plummer, C. J. G., & Månson, J. A. E. (2006). *Smart Materials and Structures*, *15*, 1467.
25. Lee, Y. S., Wetzel, E. D., & Wagner, N. J. (2003). *Journal of Materials Science*, *38*, 2825.
26. Jiang, W., Gong, X., Xuan, S., Jiang, W., Ye, F., Li, X., et al. (2013). *Applied Physics Letters*, *102*, 101901.
27. Petel, O. E., Ouellet, S., Loiseau, J., Marr, B. J., Frost, D. L., & Higgins, A. J. (2013). *Applied Physics Letters*, *102*, 064103.
28. Waitukaitis, S. R., & Jaeger, H. M. (2014). *Nature*, *487*, 205.
29. Roché, M., Myftiu, E., Johnston, M. C., Kim, P., & Stone, H. A. (2013). *Physical Review Letters*, *110*, 148304.
30. Bleakney, W., Weimer, D. K., & Fletcher, C. H. (1949). *Review of Scientific Instruments*, *20*, 807.
31. Fall, A., Huang, N., Bertrand, F., Ovarlez, G., & Bonn, D. (2008). *Physical Review Letters*, *100*, 018301.
32. Bischoff White, E. E., Chellamuthu, M., & Rothstein, J. P. (2009). *Rheologica Acta*, *49*, 119.

33. Settles, G. S. (2012). *Schlieren and shadowgraph techniques: Visualizing phenomena in transparent media*. New York: Springer.
34. Wagner, N. J., & Brady, J. F. (2009). *Physics Today*, *62*, 27.
35. Henderson, L., Ma, J. H., Sakurai, A., & Takayama, K. (1990). *Fluid Dynamics Research*, *5*, 337.
36. Sakurai, A. (1974). *Journal of Applied Physics JAP*, *36*, 610.
37. Brady, J. F., Khair, A. S., & Swaroop, M. (2006). *Journal of Fluid Mechanics*, *554*, 109.

Coatings for Mitigating the Effects of Underwater Shock Waves on Structures

Serge Abrate

1 Introduction

The effects of underwater explosions on marine structures have been studied extensively for many years. Cole's book [1] summarizes the state of knowledge in 1948 and remains the reference on underwater explosions to this day. These explosions generate a shock wave and an oscillating bubble. The pressure generated by the shock wave at a point located at a distance R from the charge is given by

$$p(t) = p_o e^{-t/t_o} \tag{1}$$

The peak pressure p_o and the characteristic time t_o can be estimated given the mass of the explosive charge and the standoff distance R [1]. This pressure pulse can induce local damage to nearby structures but its duration is short so it does not transfer enough momentum to induce overall deformation of marine vessels. The interaction of these shock waves with submerged structures has been studied extensively. For example, see Kennard [2] for plates, Hansen [3–8] for interactions with cylindrical shells and, for interactions with cylindrical shells, Hansen [8–10] Iakovlev [11–23], and Abrate [24].

Explosion bubbles with diameters measured in meters oscillate at very low frequencies and migrate towards the free surface of the water. The oscillations of gas bubbles were first studied by Rayleigh [25] and Plesset [26]. If the bubble comes near a structure, it can generate some strong overall motion and excite some of the lowest vibrations modes. When the bubble comes near a structure, typically less than two to three times the maximum radius reached during the oscillations, it can become attracted towards the structure and collapse against it [27], [28].

S. Abrate (✉)
Mechanical Engineering and Energy Processes, Southern Illinois University, Carbondale, IL, USA
e-mail: abrate@engr.siu.edu; siu1521@siu.edu

S. Gopalakrishnan and Y. Rajapakse (eds.), *Blast Mitigation Strategies in Marine Composite and Sandwich Structures*, Springer Transactions in Civil and Environmental Engineering, https://doi.org/10.1007/978-981-10-7170-6_17

The collapse produces a high-speed jet of water that can perforate the hull of a ship. Some of the early investigators of the dynamic response of ships excited by explosion bubbles include Chertock [29], Keil [30], Hicks [31], [32], and Vernon [33].

This chapter discusses the use of coatings to reduce the pressures applied on marine structures subjected to underwater blasts. It describes the response of plates subjected to an exponentially decaying pulse and reviews the development of sandwich coatings, polymer coatings, and claddings.

2 Elastic Layer in Contact with Water

When a pressure pulse $p(t)$ traveling through the water reaches the interface with a solid we show that the pressure at the interface depends on the impedance of the water and the solid. When the impedance of the solid is much larger than that of the water, the pressure at the interface can be assumed to be $2p(t)$ after reflection. This is the case for steel but for the softer materials to be used here, the reflected pressure will be much lower.

This section will also show the response of freestanding air-backed plate to an underwater blast. The motion of the plate away from the incident pulse makes the pressure drop faster and reduces the impulse applied. The loading ends as cavitation occurs at the interface. The simple model presented here also shows that a free-standing water-backed plate is essentially transparent to the wave.

2.1 Half-Space in Contact with Water

When an elastic solid occupying the half-space x > 0 is in contact with water (x < 0), a pressure pulse p(t) traveling in the +x-direction reflects from the interface. After reflection, the pressure T_2 and particle velocity at the interface v_2 are

$$T_2 = 2\frac{z_s}{z_s + z_w}p(t) v_2 = 2p(t)/(z_s + z_w) \tag{2}$$

where z_s and z_w are the impedances of the solid and the water, respectively. When $z_s \to \infty$ the well-known result for a pulse reflecting from a rigid surface is recovered: the pressure is twice the incident pressure and the particle velocity is zero. With the properties listed in Table 1, the pressure at the interface is $1.93\,p(t)$ if the solid is steel and $0.182\,p(t)$ if it is the material used for coatings in Ref. [34]. Therefore, the deformation of the solid can have a significant effect on the pressure at the interface.

When a pulse given by Eq. 1 hits a stationary half-space at time t = 0, the impulse imparted to the plate is

Table 1 Impedance and wave velocity for water steel, and a typical coating [34]

Material	Impedance (kg/m^2/s)	Phase velocity (m/s)
Water	1.5×10^6	1500
Coating	0.15×10^6	500
Steel	40.472×10^6	5188

$$I_o = 2\frac{z_s}{z_s + z_w}\int_0^\infty p_o e^{-t/t_o} dt = 2\frac{z_s}{z_s + z_w} p_o t_o \tag{3}$$

If the half-space is stationary and rigid, the impulse applied to the plate is $I_o = 2p_o t_o$.

2.2 Air-Backed Plate

For a free-standing, air-backed, rigid plate the plate moves with a velocity v and the pressure at the interface is reduced by $z_w v$. The motion of the plate is governed by

$$\rho_s h\dot{v} + z_w v = 2p_o e^{-t/t_o} \tag{4}$$

where ρ_s is the density of the plate, h is its thickness. Solving this equation we find that the velocity of the plate and the pressure at the interface are given by

$$v = \frac{2p_o}{z_w\left(1 - \frac{t^*}{t_o}\right)}\left\{e^{-t/t_o} - e^{-t/t^*}\right\}, T = 2p_o e^{-t/t_o} - z_w v \tag{5}$$

where $t^* = \rho_s h/z_w$ is a constant that characterizes the response of the system while t_o characterizes the pressure pulse.

Consider the example of a steel plate with $\rho_s = 7850$ kg/m^3, h = 0.1 m, $\rho_w = 1000$ kg/m^3, $c_w = 1000$ m/s, $t_o = 0.1$ ms, and $p_o = 10$ MPa. The velocity and interface pressure predicted by Eq. 5 are plotted versus time in Fig. 1. The pressure drops to zero when t = 0.074 ms beyond that this model predicts negative pressures that cause cavitation. The model is not valid once cavitation occurs. The solution of this problem depends on $\psi = t_o/t^* = \rho_w c_w t_o/(\rho_s h)$, the ratio of the two-time constants. It has been shown [35] that cavitation occurs at time t_c and that I_t, the momentum per unit area transmitted to the plate is given by

$$t_c/t_o = (\psi - 1)^{-1}\ln\psi, I_t = \zeta I_o \tag{6}$$

where $\zeta = \psi^{\psi(1-\psi)}$. Figure 2 shows that when $\psi > 3$ the momentum transferred to the plate is essentially zero ($\zeta = 0$). In other words, when the mass of the plate per

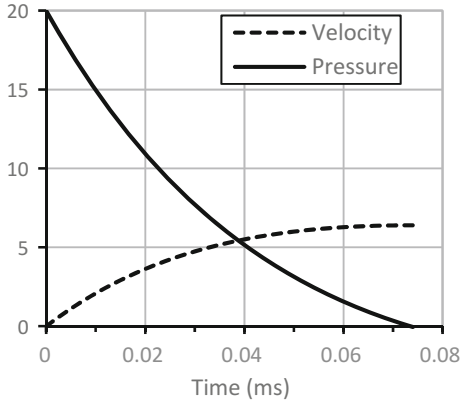

Fig. 1 Velocity (m/s) and interface pressure (MPa) for an air-backed, free-standing, steel plate subjected to a 10 MPa exponential pressure pulse

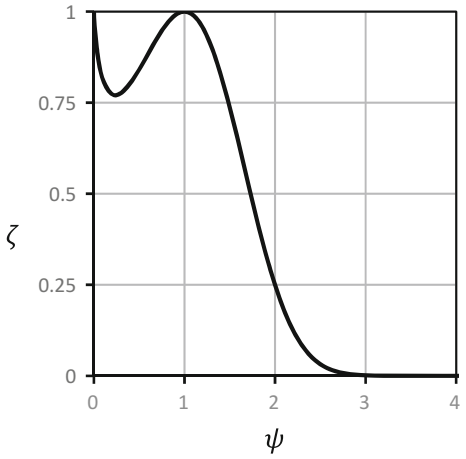

Fig. 2 Fraction of the momentum transmitted to the plate as a function of ψ

unit area is less than one-third of the mass of water swept during the time t_o, the plate is too thin to absorb any momentum.

2.3 Water-Backed Plate

If the plate is in contact with water on both sides, z_w is replaced by $2z_w$ in the equation of motion (Eq. 4). Using the same parameters as in the previous section, Fig. 3 compares the pressures on the right and left faces of the plate to the incident pulse (Eq. 1). It shows that shortly after the passage of the wavefront, the pressures are the same as if the incident wave had moved through unimpeded by the presence of the plate. It is said that the plate is transparent to the shock wave.

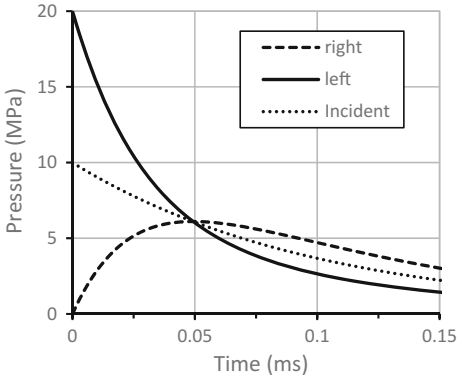

Fig. 3 Pressures on the right and left faces of a water-backed plate compared to the incident pulse

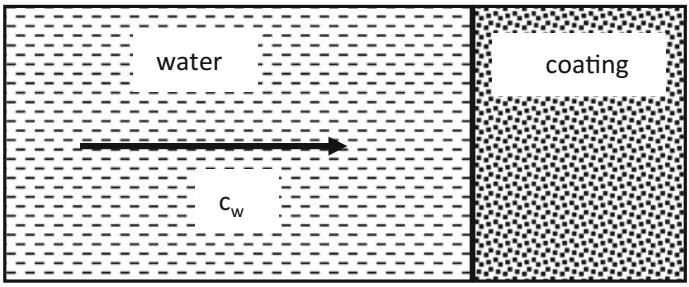

Fig. 4 Coating in contact with water on the left and fixed on the right

The mechanical impedance and the phase velocity of water, steel, and a typical coating are given in Table 1.

3 Elastic Layer Bonded to a Rigid Surface

In this section, we consider a single layer of a typical coating material in contact with water on the left and with fixed conditions on the right (Fig. 4). Properties of water and the coating are given in Table 1. The length of the coating is 50 mm unless indicated otherwise. Exact solutions obtained using the method of characteristics are presented for step pressure pulses and exponentially decaying pulses.

The step pressure example shows that the presence of the coating delays changes in pressure at the interfaces. It also shows a qualitative difference between coatings with impedances lower than water and those with impedances higher than water. Examples with exponentially decaying pulses show that the combination of the delaying effect of the coating and the decay of the pulse with time can significantly lower the peak pressure at the interface. This requires a significant thickness of the coating.

3.1 Step Pressure Pulse

A coating is bonded to a rigid surface on the right and is in contact with a semi-infinite expanse of water on the left (Fig. 4). A step pulse travels the through the water and reaches the interface with the coating at time t = 0. The Lagrange diagram (Fig. 5a) shows that the water is at rest before the arrival of the wave (region 0) and then is in a state defined by the compressive stress $T_1 = p_o$ and the particle velocity $v_1 = T_1/z_w$ in region I. After this incident wave reaches the interface, one part is reflected backwards in the water and one part is transmitted into the coating. In region II, the stress

$$T_2 = 2z_c T_1/(z_c + z_w) \tag{7}$$

and $v_2 = T_2/z_c$ where z_c is the impedance of the core. After reflection from the rigid surface, the stress doubles and the particle velocity is zero. The diagram (Fig. 5a) shows how the domain is divided by characteristic lines describing the wave transmission and reflection process.

The stress-particle velocity diagram or T-v diagram (Fig. 5b) shows a line connecting points representing the various regions in the Lagrange diagram. Starting with the point (v_2, T_2), vertices on the line with slope $-z_w$ passing through that point represent regions II, IV, … on the left side of the coating. Vertices on the axis v = 0 give the stress and particle velocity on the right side of the facing. The slope of the line connecting two consecutively numbered regions is $\pm z_c$. If the interface with the water was a rigid surface, the pressure would double and the particle velocity would be zero after reflection of the incident wave. Figure 5b shows that the solution converges to that point after many reflections. The pressure on the interface increases with time and reaches this limit asymptotically (Fig. 5c) and the particle velocity decreases exponentially (Fig. 5d).

Equation 7 indicates that $T_2 < T_1$ when $z_c < z_w$. In that case, the pressure on the water-coating interface is always less than $2p_o$. On the other hand, when $z_c > z_w$, the pressure exceeds $2p_o$. Figure 6 shows that when the coating is replaced by a steel plate of the same thickness, z_c being much larger than z_w, $T_2 > T_1$. Vertices on the line v = 0 indicate that stress on the right side of the plate far exceed $2p_o$. Coatings with higher impedances than water make the situation worse since the pressure applied on the fixed boundary is higher than it would be without the coating.

3.2 Exponentially Decaying Pulse

With the same geometry and material properties used above in this section, the response to an exponential pulse (Eq. 1) with $p_o = 10$ MPa and $t_o = 0.5$ ms is determined using the method of characteristics. The pressure at the interface with the water predicted with this approach (Fig. 7) is in excellent agreement with the

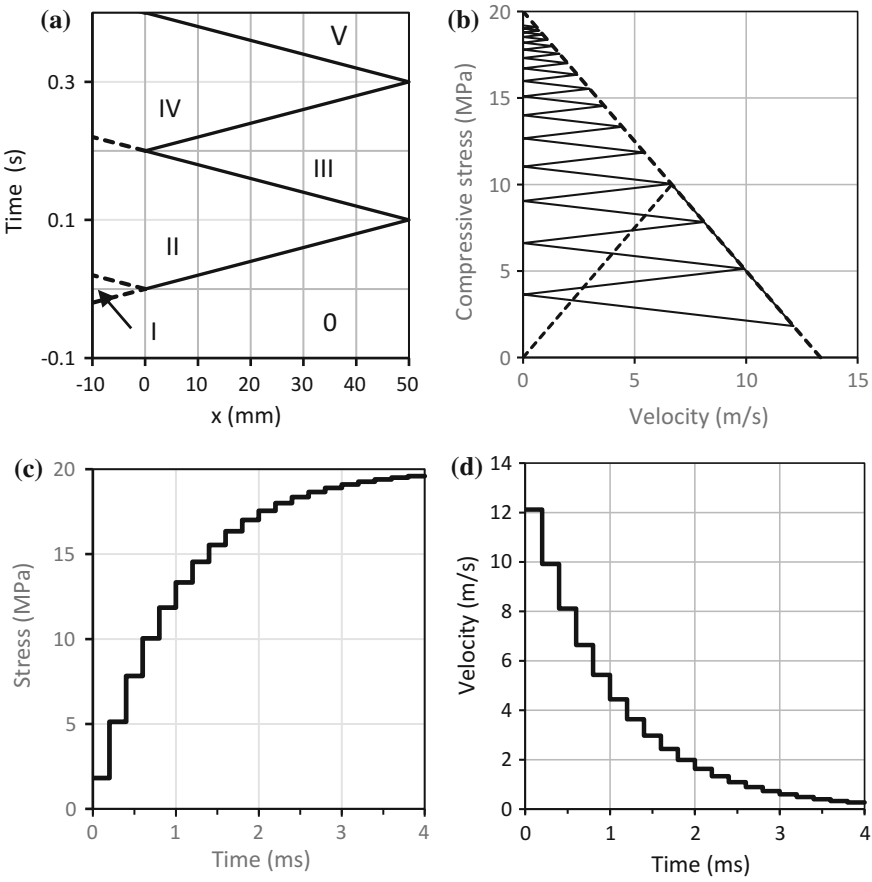

Fig. 5 Coating bonded to a rigid surface and subjected to an incident step pressure pulse **a** Lagrange diagram; **b** stress-velocity diagram

finite element results in [34]. The pressure decays between each successive reflection because the incident pulse decays with time. The pressure reaches a maximum of approximately 6 MPa with is less than the maximum of 10 MPa for the incident pulse and the 20 MPa that would be reached had the coating not been there.

The figure shows that the delay in the pressure build-up due to the travel of the waves through the thickness of the coating allows the amplitude to decay at every step. The time step in this process is twice the travel time through the thickness. This suggests that the response depends on that thickness. Order to see this effect, the thickness was reduced from 50 mm in Fig. 7 to 25 mm in Fig. 8 where the maximum pressure has increased from 6 MPa to 8 MPa and the total duration has decreased significantly.

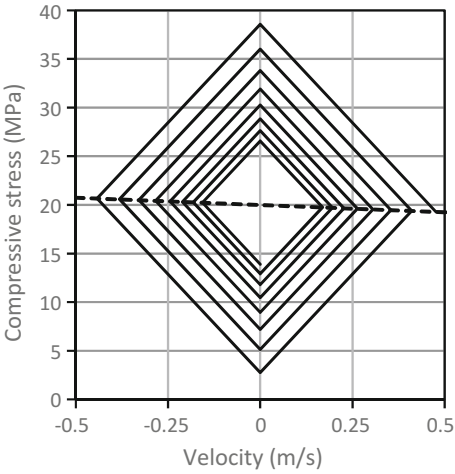

Fig. 6 Coating bonded to a rigid surface and subjected to an incident step pressure pulse

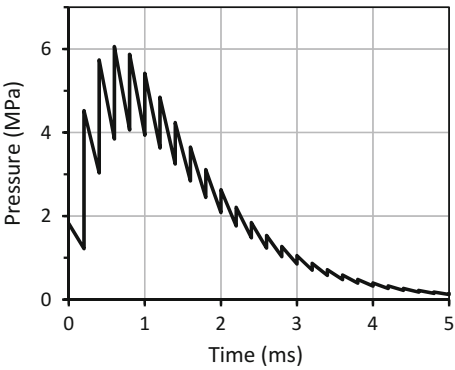

Fig. 7 Pressure on the wet face of a coating bonded to a rigid surface and subjected to an exponential pulse ($p_o = 10$ MPa, $t_o = 0.5$ ms, $h_c = 50$ mm)

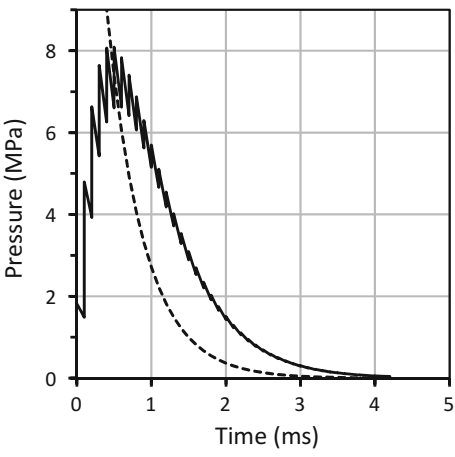

Fig. 8 Pressure on the wet face of a coating bonded to a rigid surface and subjected to an exponential pulse ($p_o = 10$ MPa, $t_o = 0.5$ ms, $h_c = 25$ mm)

4 Sandwich Coatings

Several studies examine the use of a coating to mitigate the effects of underwater explosions on marine structures. In Refs. [36], [37], the coating consists of a square honeycomb core with a face sheet of the top. This unit is made in one piece out of neoprene and the bottom of the honeycomb core is bonded directly to a steel structure. Experiments [37] show that the transmitted impulse at the initial FSI stage can be reduced by almost 50%.

The coating in Ref. [38], also made out of neoprene, has a quadrilateral honeycomb core, a top layer, and a bottom layer. The top facesheet is reinforced by a type of nylon cords used in tires. This type of coating was bonded to the hull of a boat that was subjected to underwater explosions. After firing three shots, the rubber sandwich coatings were removed and three more shots were fired so that the effectiveness of the coating can be evaluated.

Neoprene sandwich coatings with other types of honeycomb cores have also been tested: (a) chiral honeycomb cores [39]; (b) hexachiral honeycomb, reentrant honeycomb, and circular honeycomb [40], [41]; hexagonal honeycomb [42], [43].

5 Polymer Layers

A second approach is to apply a layer of polymer on one side of the structure to be protected. Kim and Shin [44] consider using a type of rubber material employed in tire construction and placing on the front face of the original plate. They also consider the use of a sandwich layer that consists of an upper skin and a honeycomb core both of which made of aluminum alloy 6061. The bottom of the core is bonded directly to the original plate.

Chen et al. applied a 20 mm thick neoprene coating with a density of 1060 kg/m^3 and acoustic wave speed of 212 m/s corresponding to an initial elastic modulus of 0.449 MPa [45], solid rubber [46], and both rubber and polyurethane foam layers in [47]. Such polymer layers can alter the pressure transmitted to the primary structure as discussed earlier. They also affect the subsequent response by changing the dynamics of the primary structure mainly because of the added mass. Both effects can be beneficial but the first one is negated when the coating enters the densification phase.

A particular type of coating material is polyurea, a polymer for which the material properties have been studied extensively [48, 49]. It has been used to retrofit masonry walls subjected to air blasts [50]. Polyurea is used in an attempt to mitigate the effect of underwater explosions on composite plates [51, 52] and steel plates [53–57]. These studies concluded that polyurea coatings are most effective when applied to the back side of the plate.

Underwater explosions can lead to the implosion of shells that will emit pressure pulses which in turn can cause the implosion of nearby structures and sometimes

cause a chain reaction. Polyurea applied to the inside surface of aluminum tubular structures was shown to reduce the amount of energy emitted during the implosion [58, 59].

6 Cladding

Another configuration used in several studies is to coat the structure to be protected with a layer of foam covered by a thin metal layer. The analysis of protective claddings (also called sacrificial claddings) to protect buildings from in-air explosions has received considerable attention. For example, Ma et al. [60, 61] studied single layer foam, Ye and Ma [62] use a layered foam, Li et al. [63] use gradient metallic foam. Reid and Peng [64] presented the first "shock wave" theory for a rigid-perfectly plastic- locking (RPPL) crushing material. This widely used model assumes that compaction of the cellular material is caused by a shock wave. With the RPPL idealization, the dynamic crushing stress σ_d is given by

$$\sigma_d = \sigma_o + \frac{\rho v^2}{\varepsilon_d} \tag{8}$$

in terms of the velocity of the front face v, the plateau stress σ_o, and the densification strain ε_d [65]. The condition for the occurrence of shock waves in such a material is that the velocity v should be larger than or equal to the critical velocity

$$v_{cr} = \sqrt{(\sigma_d - \sigma)\varepsilon_d / \rho} \tag{9}$$

Several references adopted different representations of the material behavior [66–68]. The analysis of the deformation of single layer cores [69], two-layer cores [69, 70], three-layer [71], and cellular materials with continuously varying density [72] revealed how complex the problem can be depending on the stress-strain behavior of the material and the initial velocity of the cover. Several studies concluded that a process of a full densification within the primary compaction wave would be a preferable scenario for blast attenuation which requires using foams with negligible strain hardening [73]. In the case of multilayer cores, higher density foam layer near to the loaded end while lower density foam layer is preferably near to the stationary end of the cladding [69, 71].

The use of sacrificial claddings for marine structures subjected to underwater blasts has been explored recently. Yin et al. [74] used a single layer cladding consisting of a 50 mm thick Rohacell foam to mitigate the effects of underwater blasts on a steel submersible hull. Chen et al. [75] used a single layer of soft polyurethane foam with a density of 1200 kg/m^3 and a 0.045 GPa elastic modulus. Sacrificial claddings with stepwise graded cellular cores are studied in Yin et al. [76], Chen et al. [77, 78].

7 Conclusion

This chapter presents an analysis of a linear elastic coating bonded to a rigid surface and subjected to a shock wave generated by an underwater explosion. This analysis brings insight into the response to a water-borne pulse and explains why a coating can reduce the pressure applied to the structure to be protected. Some limitations are brought out: (1) the coating could have negative effects when its impedance is larger than that of the water; (2) the length of the coating should be large enough to delay the pressure buildup at the interface and take advantage of the decay in the incident pressure pulse. An overview of the three practical implementations of the basic idea of using a coating to mitigate the effect of underwater shock waves is presented. In some of these designs, the main element displays a strong nonlinear material behavior. This complicating effect is currently handled numerically on a case by case basis. An in-depth study of the effect of nonlinearity on the response to a shock wave is left for future work. In conclusion, the concept of using coatings for blast mitigation could lead to more efficient designs of marine structures if proven effective.

References

1. Cole, R. H. (1948). *Underwater explosions*. New Jersey: Princeton University Press.
2. Kennard, E. H. (1944). The Effect of a Pressure Wave on a Plate or a Diaphragm, Taylor Model Basin, Washington, D.C., TMB 527.
3. Huang, H. (1969). Transient interaction of plane acoustic waves with a spherical elastic shell. *Journal of the Acoustic Society of America, 45*(3), 661–670.
4. Huang, H. (1979). Transient response of two fluid-coupled spherical elastic shells to an incident pressure pulse. *Journal of the Acoustic Society of America, 65*(4), 881–887.
5. Huang, H. (1975). Scattering of spherical pressure pulses by a hard cylinder. *Journal of the Acoustic Society of America, 58*(2), 310–317.
6. Huang, H., & Gaunaurd, G. C. (1995). Acoustic scattering of a plane wave by two spherical elastic shells. *Journal of the Acoustic Society of America, 98*(4), 2149–2156.
7. Huang, H., & Gaunaurd, G. C. (1998). Transient diffraction of a plane step pressure pulse by a hard sphere: Neoclassical solution. *Journal of the Acoustic Society of America, 104*(6), 3236–3244.
8. Huang, H., & Kiddy, K. C. (1995). Transient interaction of a spherical shell with an underwater explosion shock wave and subsequent pulsating bubble. *Shock and Vibration, 2*(6), 451–460.
9. Huang, H. (1970). An exact analysis of the transient interaction of acoustic plane waves with a cylindrical elastic shell. *ASME Journal of Applied Mechanics, 37*(4), 1091–1099.
10. Huang, H., & Wang, Y. F. (1970). Transient interactions of spherical acoustic waves and a cylindrical elastic shell. *Journal of the Acoustic Society of America, 48*(1B), 228–235.
11. Iakovlev, S. (2002). Interaction of a spherical shock wave and a submerged fluid-filled circular cylindrical shell. *Journal of Sound and Vibration, 255*(4), 615–633.
12. Iakovlev, S. (2004). Influence of a rigid coaxial core on the stress–strain state of a submerged fluid-filled circular cylindrical shell subjected to a shock wave. *Journal of Fluids and Structures, 19*(7), 957–984.

13. Iakovlev, S. (2006). External shock loading on a submerged fluid-filled cylindrical shell. *Journal of Fluids and Structures, 22*(8), 997–1028.
14. Iakovlev, S. (2007). Submerged fluid-filled cylindrical shell subjected to a shock wave: Fluid–structure interaction effects. *Journal of Fluids and Structures, 23*(1), 117–142.
15. Iakovlev, S. (2008). Interaction between a submerged evacuated cylindrical shell and a shock wave—Part I: Diffraction–radiation analysis. *Journal of Fluids and Structures, 24*(7), 1077–1097.
16. Iakovlev, S. (2008). Interaction between a submerged evacuated cylindrical shell and a shock wave—Part II: Numerical aspects of the solution. *Journal of Fluids and Structures, 24*(7), 1098–1119.
17. Iakovlev, S., Furey, C., Pyke, D., & Lefieux, A. (2015). Shock response of a system of two submerged co-axial cylindrical shells coupled by the inter-shell fluid. *Journal of Fluids and Structures, 55,* 1–24.
18. Iakovlev, S., Dooley, G., Williston, K., & Gaudet, J. (2011). Evolution of the reflection and focusing patterns and stress states in two-fluid cylindrical shell systems subjected to an external shock wave. *Journal of Sound and Vibration, 330*(25), 6254–6276.
19. Iakovlev, S., Gaudet, J., Dooley, G., & MacDonald, B. (2010). Hydrodynamic fields induced by the shock response of a fluid-filled submerged cylindrical shell containing a rigid co-axial core. *Journal of Sound and Vibration, 329*(16), 3359–3381.
20. Iakovlev, S., Mitchell, M., & Dooley, G. (2011). Modeling two-fluid response of thin elastic shells. *International Journa for Numerical Methods in Fluids, 65*(11–12), 1389–1406.
21. Iakovlev, S., Sigrist, J.-F., Leblond, C., Santos, H., Lefieux, A., & Williston, K. (2012). Mathematical modeling of the acoustic radiation by submerged elastic structures. In *Acoustics 2012*.
22. Iakovlev, S. (2014). On the possibility of shock-induced cavitation in submerged cylindrical shell systems. *Journal of Fluids and Structures, 50,* 437–460.
23. Iakovlev, S., Mitchell, M., Lefieux, A., & Murray, R. (2014). Shock response of a two-fluid cylindrical shell system containing a rigid core. *Computers and Fluids, 96,* 215–225.
24. Abrate, S. (2013). Interaction of underwater blasts and submerged structures. In *Dynamic failure of composite and sandwich structures* (pp. 93–150). Springer.
25. Rayleigh, L. (1917). VIII. On the pressure developed in a liquid during the collapse of a spherical cavity. *London*, *Edinburgh and Dublin Philosophical Magazine and Journal of Science, 34*(200), 94–98.
26. Plesset, M. S. (1949). The dynamics of cavitation bubbles. *Journal of Applied Mechanics, 16,* 277–282.
27. Blake, J. R., & Tong, R. P. (1995). Jet impact in collapsing bubbles. In *Proceedings of the 12th Australian Fluid Mechanics Conference, Sydney* (pp. 819–822).
28. Blake, J. R., Hooton, M. C., Robinson, P. B., & Tong, R. P. (1997). Collapsing cavities, toroidal bubbles and jet impact. *Philosophical Transactions of the Royal Society of London: Mathematical, Physical and Engineering Sciences, 355*(1724), 537–550.
29. Chertock, G. (1970). Transient flexural vibrations of ship-like structures exposed to underwater explosions. *Journal of the Acoustic Society of America, 48*(1B), 170–180.
30. Keil, A. H. (1961). The response of ships to underwater explosions, DTIC Document.
31. Hicks, A. N. (1970). A Method for Determining the Virtual Mass Distribution around a Vibrating Ship, DTIC Document.
32. Hicks, A. N. (1972). The theory of explosion induced ship whipping motions, DTIC Document.
33. Vernon, T. A. (1986). Whipping response of ship hulls from underwater explosion bubble loading, DTIC Document.
34. Jin, Z., Yin, C., Chen, Y., & Hua, H. (2015). One-dimensional analytical model for the response of elastic coatings to water blast. *Journal of Fluids and Structures, 59,* 37–56.
35. Fleck, N. A., & Deshpande, V. S. (2004). The resistance of clamped sandwich beams to shock loading. *Journal of Applied Mechanics, 71*(3), 386.

36. Chen, Y., Tong, Z. P., Hua, H. X., Wang, Y., & Gou, H. Y. (2009). Experimental investigation on the dynamic response of scaled ship model with rubber sandwich coatings subjected to underwater explosion. *International Journal of Impact Engineering, 36*(2), 318–328.
37. Chen, Y., Zhang, Z., Wang, Y., Hua, H., & Gou, H. (2009). Attenuating performance of a polymer layer coated onto floating structures subjected to water blasts. *European Journal of Mechanics—A/Solids, 28*(3), 591–598.
38. Du, Z. P., Wang, Y., Chen, Y., & Hua, H. X. (2009). A new type of rubber sandwich coated onto ship for the use of underwater explosion shock mitigating. *Advanced Materials Research, 79–82,* 291–294.
39. Xiao, F., Chen, Y., Wang, Y., Hua, H., & Zhu, D. (2014). Experimental research on the dynamic response of floating structures with coatings subjected to underwater explosion. *Shock and Vibration, 2014,* e705256.
40. Xiao, F., Chen, Y., Hua, H., & Zhu, D. (2015). Experimental and numerical investigation on the shock resistance of honeycomb rubber coatings subjected to underwater explosion. *Proceedings of the Institution of Mechanical Engineers, Part M*: *Journal of Engineering for the Maritime Environment, 229*(1), 77–94.
41. Xiao, F., Chen, Y., & Hua, H. (2014). Comparative study of the shock resistance of rubber protective coatings subjected to underwater explosion. *Journal of Offshore Mechanics and Arctic Engineering, 136*(2), 021402.
42. Zhang, Z.-H., Chen, Y., Hua, H.-X., & Wang, Y. (2015). Underwater explosion research on ship with polymer hull coating. *Proceedings of the Institution of Mechanical Engineers Part M: Journal of Engineering for the Maritime Environment, 229*(2), 147–56.
43. Zhang, Z.-H., Chen, Y., Huang, X.-C., & Hua, H.-X. (2016). Underwater explosion approximate method research on ship with polymer coating. *Proceedings of the Institution of Mechanical Engineers Part M: Journal of Engineering for the Maritime Environment,* 1–11.
44. Kim, C.-H., & Shin, Y. S. (2013). Numerical simulation of surface shield effects to waterblast wave. *Ocean Engineering, 60,* 99–114.
45. Chen, Y., Wang, Y., Zhang, Z., & Hua, H. (2013). Experimental research on the responses of neoprene coated cylinder subjected to underwater explosions. *Journal of Offshore Mechanics and Arctic Engineering*, *135*(1), 011102–011102-8.
46. Chen, Y., Chen, F., Du, Z. P., Zhang, W., & Hua, H. X. (2016). Influence of solid rubber coating on the response of floating structure to underwater shock wave. *Journal of Offshore Mechanics and Arctic Engineering, 138*(6), 061302.
47. Chen, Y., Chen, F., Du, Z. P., Wang, Y., Zhao, P. D., & Hua, H. X. (2015). Protective effect of polymer coating on the circular steel plate response to near-field underwater explosions. *Marine Structure, 40,* 247–266.
48. Amirkhizi, A. V., Isaacs, J., McGee, J., & Nemat-Nasser, S. (2006). An experimentally-based viscoelastic constitutive model for polyurea, including pressure and temperature effects. *Philosophy Magazine, 86*(36), 5847–5866.
49. Mohotti, D., Ali, M., Ngo, T., Lu, J., & Mendis, P. (2014). Strain rate dependent constitutive model for predicting the material behaviour of polyurea under high strain rate tensile loading. *Materials and Design, 53,* 830–837.
50. Davidson, J. S., Porter, J. R., Dinan, R. J., Hammons, M. I., & Connell, J. D. (2004). Explosive testing of polymer retrofit masonry walls. *Journal of Performance of Constructed Facilities, 18*(2), 100–106.
51. LeBlanc, J., & Shukla, A. (2015). Response of polyurea-coated flat composite plates to underwater explosive loading. *Journal of Composite Materials, 49*(8), 965–980.
52. LeBlanc, J., Shillings, C., Gauch, E., Livolsi, F., & Shukla, A. (2016). Near field underwater explosion response of polyurea coated composite plates. *Experimental Mechanics, 56*(4), 569–581.
53. Amini, M. R., Isaacs, J., & Nemat-Nasser, S. (2010). Investigation of effect of polyurea on response of steel plates to impulsive loads in direct pressure-pulse experiments. *Mechanics of Materials, 42*(6), 628–639.

54. Amini, M. R., Simon, J., & Nemat-Nasser, S. (2010). Numerical modeling of effect of polyurea on response of steel plates to impulsive loads in direct pressure-pulse experiments. *Mechanics of Materials, 42*(6), 615–627.
55. Amini, M. R., Amirkhizi, A. V., & Nemat-Nasser, S. (2010). Numerical modeling of response of monolithic and bilayer plates to impulsive loads. *International Journal of Impact Engineering, 37*(1), 90–102.
56. Amini, M. R., Isaacs, J. B., & Nemat-Nasser, S. (2010). Experimental investigation of response of monolithic and bilayer plates to impulsive loads. *International Journal of Impact Engineering, 37*(1), 82–89.
57. Ackland, K., Anderson, C., & Ngo, T. D. (2013). Deformation of polyurea-coated steel plates under localised blast loading. *International Journal of Impact Engineering, 51,* 13–22.
58. Matos, H., & Shukla, A. (2016). Mitigation of implosion energy from aluminum structures. *International Journal of Solids and Structures, 100–101,* 566–574.
59. Matos, H., Gupta, S., & Shukla, A. (2017). Structural instability and water hammer signatures from shock-initiated implosions in confining environments. *Mechanics of Materials*.
60. Ma, G. W., & Ye, Z. Q. (2007). Analysis of foam claddings for blast alleviation. *International Journal of Impact Engineering, 34*(1), 60–70.
61. Ma, G. W., & Ye, Z. Q. (2007). Energy absorption of double-layer foam cladding for blast alleviation. *International Journal of Impact Engineering, 34*(2), 329–347.
62. Ye, Z. Q., & Ma, G. W. (2007). Effects of foam claddings for structure protection against blast loads. *Journal of Engineering Mechanics, 133*(1), 41–47.
63. Li, J. D., Zhou, H. Y., & Ma, G. W. (2011). Numerical simulation of blast mitigation cladding with gradient metallic foam core. *Applied Mechanics and Materials, 82,* 461–466.
64. Reid, S. R., & Peng, C. (1997). Dynamic uniaxial crushing of wood. *International Journal of Impact Engineering, 19*(5–6), 531–570.
65. Liang, M., Li, Z., Lu, F., & Li, X. (2017). Theoretical and numerical investigation of blast responses of continuous-density graded cellular materials. *Composite Structures, 164,* 170–179.
66. Tan, P. J., Reid, S. R., Harrigan, J. J., Zou, Z., & Li, S. (2005). Dynamic compressive strength properties of aluminium foams. Part I—Experimental data and observations. *Journal of the Mechanics and Physics of Solids, 53*(10), 2174–2205.
67. Tan, P. J., Reid, S. R., Harrigan, J. J., Zou, Z., & Li, S. (2005). Dynamic compressive strength properties of aluminium foams. Part II—'Shock' theory and comparison with experimental data and numerical models. *Journal of the Mechanics and Physics of Solids, 53*(10), 2206–2230.
68. Harrigan, J. J., Reid, S. R., Tan, P. J., & Reddy, T. Y. (2005). High rate crushing of wood along the grain. *International Journal of Mechanical Sciences, 47*(4), 521–544.
69. Karagiozova, D. (2011). Velocity attenuation and force transfer by a single-and double-layer claddings made of foam materials. *International Journal of Protective Structures, 2*(4), 417–437.
70. Karagiozova, D., Langdon, G. S., & Nurick, G. N. (2013). Compaction of metal foam subjected to an impact by a low-density deformable projectile. *International Journal of Impact Engineering, 62,* 196–209.
71. Karagiozova, D., & Alves, M. (2015). Stress waves in layered cellular materials—dynamic compaction under axial impact. *International Journal of Mechanical Sciences, 101,* 196–213.
72. Karagiozova, D., & Alves, M. (2015). Propagation of compaction waves in cellular materials with continuously varying density. *International Journal of Solids and Structures, 71,* 323–337.
73. Langdon, G. S., Karagiozova, D., Theobald, M. D., Nurick, G. N., Lu, G., & Merrett, R. P. (2010). Fracture of aluminium foam core sacrificial cladding subjected to air-blast loading. *International Journal of Impact Engineering, 37*(6), 638–651.
74. Yin, C., Jin, Z., Chen, Y., & Hua, H. (2016). Shock mitigation effects of cellular cladding on submersible hull subjected to deep underwater explosion. *Ocean Engineering, 117,* 221–237.

75. Chen, Y., Wang, Y., & Hua, H. X. (2010). An analytic model for the water blast response of one-dimensional marine structure coated with elastic foam. *Archive of Applied Mechanics, 80* (11), 1243–1253.
76. Yin, C., Jin, Z., Chen, Y., & Hua, H. (2017). The underwater blast resistance of sacrificial claddings with stepwise graded cellular cores. *Journal of Offshore Mechanics and Arctic Engineering, 139*(2), 021602.
77. Chen, Y., Chen, F., Du, Z., Wang, Y., & Hua, H. (2015). Mitigating performance of elastic graded polymer foam coating subjected to underwater shock. *Composites Part B: Engineering, 69,* 484–495.
78. Chen, Y., Chen, F., Zhang, W., Du, Z. P., & Hua, H. X. (2016). Transient underwater shock response of sacrificed coating with continuous density graded foam core. *Composites Part B: Engineering, 98,* 297–307.

Shock Tubes: A Tool to Create Explosions Without Using Explosives

I. Obed Samuelraj and G. Jagadeesh

1 Introduction

With a view to design structures that are capable of resisting an impulsive load, experimental research has been carried out right from the advent of the space age. The focus on experimental research was primarily due to a poor understanding of material behavior at high strain rates and large loads that are inherent to an actual impact event. A general lack of material models at high strain rates and the absence of computation power as available today, precluded the use of numerical methods to understand this phenomenon.

1.1 Blast Wave Studies on Scaled Models

To design a spacecraft that may be subject to "high-intensity, asymmetric, short duration external pressures", Menkes and Opat [20] embarked on a basic study to understand the response of beams to impulse loading using sheet explosives. They identified three modes of failure, classified as *Mode I*—large inelastic deformation, *Mode II*—tensile failure at supports, and *Mode III*—shear failure at supports and cap (plug) formation. These failure modes were verified for metal plates by the works of Nurick et al. for circular plates [36]; and later on for square plates [23].

Apart from metals, woven composite plates have been a material of interest for blast wave studies [18]. The failure modes for such composite plates under high-velocity impact loading have also been identified by various researchers. A summary of these may be found in [3] and the failure modes may again be broadly classified into *matrix failure mode*, *fiber tow failure mode*, and *delamination failure mode*.

I. Obed Samuelraj · G. Jagadeesh (✉)
Department of Aerospace Engineering, Indian Institute of Science, Bangalore, India
e-mail: jaggie@aero.iisc.ernet.in

I. Obed Samuelraj
e-mail: obed.isaac@gmail.com

S. Gopalakrishnan and Y. Rajapakse (eds.), *Blast Mitigation Strategies in Marine Composite and Sandwich Structures*, Springer Transactions in Civil and Environmental Engineering, https://doi.org/10.1007/978-981-10-7170-6_18

While model studies such as these help in identifying and narrowing down the best possible material for a given type of impulsive loading, predicting the corresponding prototype structure's response requires a reliable scaling law. Such a law is also required to understand and develop blast mitigation strategies and other protective technologies as there is no scope of conducting reliable and repeatable outdoor experiments. All of these studies require a good understanding of similitude theory and its limitations with regard to these experiments.

1.2 Aspects of Scaling

From similitude theory, a recent review of which may be found in [7], it may be understood that scaling a test structure by β for an impulsive load having a very short rise time [34] would require the impulse also to be reduced by the same factor β. The pressure value, however, needs to remain unchanged for both model and the prototype. This means that if one were to simulate the effect of a 1 kg TNT explosion at a stand-off distance of 1 m on a 1 m $\times$ 1 m square plate, the scaled experiment ($\beta = 2$) would have to have a $1/2^3 = (0.125)$ kg TNT explosive at a stand-off distance of 0.5 m from a 0.5 m $\times$ 0.5 m square plate of the same material. The reflected pressures would then be 80 *bar* for both experiments and the impulses would be 884 *Pa-s* and 442 *Pa-s* for the prototype and the scaled experiments respectively. Similarly, the corresponding decay times (t_{blast}) would be 1.74 ms and 0.87 ms.

The underlying assumptions in such a simple geometric scaling law as this are that the structure's response is elastic, its material strain rate effects are negligible, and fracture, or even ductile–brittle transition is completely absent [13].

Elastic regime

Such a scaling law was experimentally validated for both complete and incomplete[1] the geometric scale model response of a cross-ply laminated E-glass/epoxy plate within the elastic regime [32]. For blast loading on metal plates, however, experimental data that validates scaling is scarcely available. Neuberger et al. [22] in their work on rolled homogeneous armor (RHA) steel plates with scaling factors of 2 and 4 show scaling to be valid when most of the dynamic loading is in the elastic regime.

Plastic regime and material strain rate effects

Although this law does not hold when the loading is inelastic and when strain effects are prominent—because the scaling law takes into account the (constant) static yield stress and not the (variable) dynamic one—researchers had carried out experiments to check the veracity of this claim and found mixed results.

Neuberger and Rittel report that the effect of strain rate was barely seen in their experiments [22]. Schleyer et al. [31] had low loading rates in his experimental facility, so he reports that the final deflections for mild steel loaded with a slow rising

[1] when all dimensions are not scaled down by a single scaling factor.

pulse (∼15 ms) at pressures of the order of 1 *bar* were scalable ($\beta = 0.5$) in the inelastic regime. While the dynamic deflections did not quite scale-up for the inelastic case, the error involved was not high (<10%) and he reports the effect of strain rate to be minimal. However, in the work of Snyman [33], where he reports blast loading on mild steel plates with scaling factors of 1.6 and 2, a discrepancy as high as 35% was noticed for the mid-point deflection when subjected to a blast pulse that would have been around 250 *bar* having a decay time of 70 μs. A general consensus for scaling in the inelastic regime is that using the dynamic yield stress in place of static yield stress would be better if the material can be modeled as a rigid perfectly plastic material. This is valid only when the impact energy is absorbed mostly by means of plastic bending and stretching throughout the volume of the material [14]. In other words, this holds only when almost all of the energy is absorbed in the plastic regime rather than the elastic regime.

In addition to this, it is known that the strain rate effects are amplified by β times that of the value in a prototype [13]. Since the dynamic yield strength usually increases with increasing strain rate, the scale model tests would under predict the prototype's response. Thus, the strain rate effects need to be taken into account to obtain some reliable data from model experiments. To this end, Oshiro and Alves [24] and then Kong et al. [17] propose an approach to account for the effect of strain rate. Oshiro and Alves [24] propose the use of a different basis set to implement the scaling—initial impact velocity-dynamic yield stress-impact mass as against the traditional mass-length-time. They show the validity of this approach for scaling factors all the way up to 1000. Kong et al. [17] had recently proposed a method for obtaining the corrected impulse (after accounting for scaling) to be imparted to the structure to factor in the strain rate effects using an appropriate version of the Johnson–Cook plasticity model. This data, which has been validated numerically, is very helpful to decide on the exact amount of impulse that is to be imparted to a model so as to achieve the correct response in a prototype.

Fracture scaling

The reasons for the non-scalability of fracture lie in the fact that the energy stored in the material is a volumetric one, whereas the energy release that occurs, via fracture, is area dependent [4], making it incongruent for scaling to be possible. Thus, the scaled-down models appear to fail at a higher fracture modulus, by a factor β, where $\beta > 1$. Anderson, on the other hand, suggests that it might be due to the limited time available for damage to accumulate in a scaled-down model [1], thus necessitating a higher stress in the model before a fracture occurs. However, if the proportion of energy absorbed by the failed area is very less compared to the elastic and plastic energy contained in the bulk of the material—which can happen in thin plates—the geometric laws have been shown to be valid within experimental error [15], based on some experiments using blunt impactors (traveling at speeds up to 119 m/s) on mild steel plates. Still, there remains further work to be done as the experimental data correlating fracture in a model and prototype is very scarce.

From the above discussion, the importance of considering all these factors while scaling-up the model response may be appreciated. The effects of strain rate partic-

ularly, help show the importance of impulse in any blast–structure interaction study and so this is one aspect which has to be carefully incorporated while carrying out scaled-down experiments in any lab-scale facility where the focus is in acquiring quantitative information.

1.3 Fluid–Structure Interaction (FSI) Effects

Within these broad contours given under scaling, since the scaling law does not take into account the interaction between the load and the structure, the proportion of impulse transferred, and the nature of the loading needs to be preserved. This implies that the ratio of blast pulse duration (t_{blast}) to the natural time period of the plate (T_n) in both model, and prototype has to be retained. Kambouchev et al. [16] had shown that the amount of impulse that is transmitted to the structure depends on the mass of the structure and the impedance of the loading medium. Along these lines, Xue and Hutchinson [38] had shown that all of the impulse in the air is imparted to the structure, whereas this is partial in the case of water. This implies that one cannot use a different loading medium, say water, to simulate an air blast.

In all of these situations, it is to be recollected that the case of a blast loading and not a gas explosion is being addressed. While blast loading involves extremely short rise times, in the latter case, a finite rise time of the order of a few milliseconds is implied. For this latter case, the ratio of both the rise time and the pulse duration with respect to the natural time period of the structure is to be considered, thus giving us the classic segregation into quasi-static, dynamic and impulse types of loading. For shock loading, however, since the rise time is of the order of microseconds [11], the pulse duration alone is to be considered in order to classify a given loading. While different authors cite different numbers for the limits of the time ratio ($\tau = t_{blast}/T_n$) to determine the type of loading, Li and Meng [19] had come up with some numbers based on the response of a single degree-of-freedom spring–mass model to a blast pulse. Since it is known that the shape of the blast pulse [9] has a serious impact (up to 40% [19]) on the final response, they carried out this analysis for three different types of pulses that have a zero rise time. Such ratios which determine the nature of the loading are provided in Table 1. Since a blast pulse may be considered to be a triangular pulse [2], a shock response spectrum analysis gives the degree to which a single degree-of-freedom system would respond to a given magnitude of load having different t_{blast} durations. Figure 1 plots the ratio of dynamic deflection to the static one versus the time ratio (τ). For the special case $\tau < 0.271$ (cf. Table 1) which constitutes an impulse load, irrespective of the nature of the pulse, as long as the impulse value is the same, the response should not differ. But Xue and Hutchinson had shown that the response to an ideal zero-pulse impulse is the maximum [37], suggesting that the pulse shape does play a role. This perhaps needs to be interpreted in terms of the differing peak pressures of each of those pulses since Jones [13] defines an impulse as a pulse having both a short duration, and a loading pressure that is much higher than its corresponding static collapse load (p_c). Thus, the response

Table 1 Defining [a]the three regimes based on τ $(= t_{blast}/T_n)$

Type of load	τ_{max} for impulsive regime	τ_{min} for quasi-static regime
Rectangular pulse	0.171	0.402
Triangular pulse	0.211	5.159
Exponential decay	0.275	19.029

[a]From Li and Meng [19], after incorporating the factor—2π

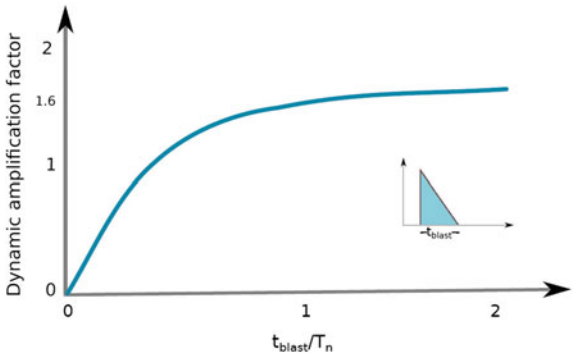

Fig. 1 A representative blast wave response curve for a triangular pulse

of a structure is sensitive to the ratio of the loading pressure to the static collapse pressure $(\eta = p/p_c)$ as well. This means that as long as the peak pressure is the same and the time duration is short enough to be in the impulsive regime, the responses will be identical. Thus, the magnitude of the pressure load is also important if a blast event is to be recreated.

1.4 Importance of Impulse and Pressure

From the discussion in Sects. 1.2 and 1.3, impulse and pressure, respectively, were shown to be very crucial for the recreation of a blast–structure interaction study. Thus, given a blast event to be recreated, the pressure and a scaled-down impulse value—that has been additionally corrected for (possible) strain rate effects—has to be reproduced. The loading medium also should, preferably, be unchanged.

While small-scale explosives can be used for these experiments, there remain several challenges in terms of getting repeatable results, aligning the charge and detonating it exactly with reference to the model (very crucial as the wavefront is not planar), the associated safety hazards, etc. In view of this, alternate techniques have been explored to carry out these scaled-down experiments. A shock tube being capable of generating a planar wave quite repeatadly—making it easier for numerical modeling—and also being capable of generating a controllable duration of the blast load, it has become a popular device of experimentation for studies on blast wave interaction with structures. While Celander [6] had proposed the use of shock tube

for blast studies on animals back in 1955, it was Stoffel (2001) who first proposed the use of shock tube for impact loading studies on plates. Since then, several researchers have been using the shock tube for blast mitigation and related studies [5, 18, 25, 35].

2 Shock Tubes

A shock tube is a simple device that uses the sudden release of a compressed gas to generate a shock wave. In this section, a description of how a shock tube works and how it may be tailored to generate a blast wave is provided.

2.1 Working of a Shock Tube

The shock tube consists of a high-pressure (driver) and a low-pressure (driven) chamber separated by a diaphragm (Fig. 2) and the shock loading occurs at the far end of the shock tube, where the test plate may be clamped. The rupture of the diaphragm, which for the time being may be assumed to be instantaneous, leads to the formation of a shock wave (an instantaneous pressure rise) that propagates into the low-pressure-driven region and an expansion wave (a pressure drop) that moves at a finite speed into the high-pressure driver side. This expansion fan reflects at the end and then starts propagating into the opposite side, which is now along the direction of propagation of the shock wave. In a typical shock tube experiment, the driver chamber is kept long enough so that this pressure drop (expansion fan) cannot catch up with the shock wave, thus giving rise to a flat-topped pressure pulse at the driven end of the shock tube as illustrated in Fig. 3a. Now, if the test plate were to fail catastrophically after absorbing some impulse from this curve, the pressure would drop rapidly

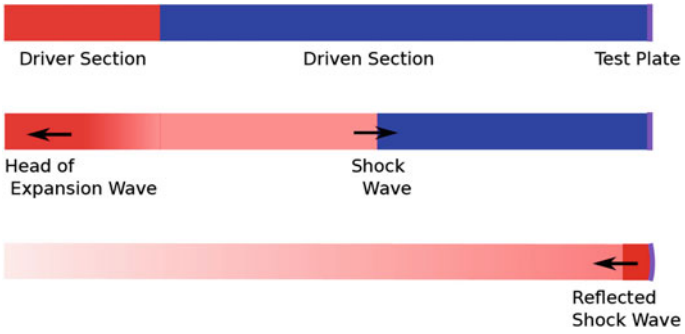

Fig. 2 A schematic drawing showing the working of a shock tube in blast tube mode

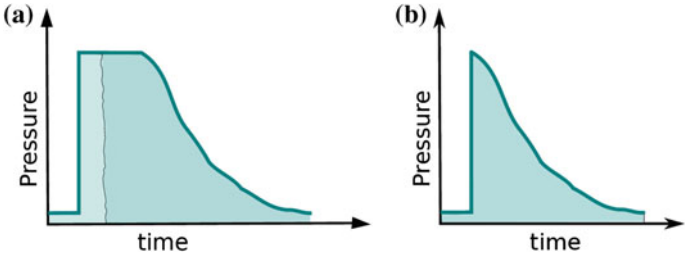

Fig. 3 A typical pressure trace for a shock wave (**a**) and a blast wave (**b**). While the pressure pulse in a typical shock tube is as in **a**, the lengths of the shock tube need to be tailored to obtain **b**. The first shaded area under the curve in **a** represents a portion of the impulse that may be absorbed by a structure that fails abruptly

after failure ensues and we would then obtain an extremely short duration pulse as depicted by the left half of the shaded area under the pressure–time curve. But since we are not primarily interested in fracture, we need a pulse with no flat-top region or no dwell time, as in Fig. 3b. To achieve this, we need to tailor the length of the driver side so that this expansion just catches up with the shock wave at the end of the driven chamber.

Using an x-t diagram, where the distance traveled by the wave is shown along the abscissa and the lapsed time is the ordinate, we can better understand the effect of the lengths of the driver and driven sections.

x-t diagram: Figure 4 shows a typical x-t diagram. The shock wave and the contact surface move down the driven section and the expansion wave travels toward the end of the driver section. Once the expansion wave reflects off the driver end wall, it then starts moving along the direction of the shock wave. When the expansion wave catches up with the shock wave after it reaches the end wall, we will have a dwell

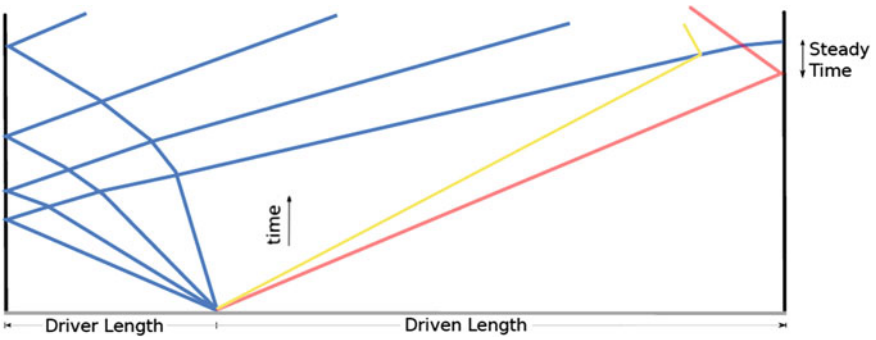

Fig. 4 An x-t diagram showing the shock wave (*red*), the contact surface (*yellow*), and the expansion wave (*blue*). The expansion wave has not caught up with the shock wave before the end wall. It catches up a little later, thus giving a small decay time as in Fig. 3a

time in the pressure trace recorded at the end wall before the decay begins (Fig. 3a). If instead, it catches up with the shock wave either before or just at the end wall, we will have a decaying pressure trace as represented in Fig. 3b. The optimal condition is achieved when it catches up just at the end wall, since an expansion wave catching up earlier would mean a continual reduction in peak pressure until the shock wave reaches the end wall. From the x-t diagram, it is quite clear that we can achieve such a condition, all other parameters remaining unchanged, by making the driven length slightly longer. Assuming that this is done, we next proceed to look at the decay time of the pulse—t_{blast} (cf. inset of Fig. 1). The expansion waves that keep reaching the end wall are the ones that are responsible for decay of the pressure. If we were to assume that three of these "rays" or "fans" are required to bring the pressure down to the ambient value, the longer the length of the driven tube, the longer would be the decay time as may be realized from Fig. 4. This is because these three waves "spread" over time as the tube gets longer, thus delaying the arrival of the final wave. So to have shorter decay times, the driven length needs to be kept short and the driver length would have to be commensurately reduced to obtain a blast profile at the end wall.

But then, a reduction in the driven length is limited by the shock formation distance, which is ultimately proportional to the opening time of the diaphragm, the shock speed, the inner diameter of the shock tube, and the speed of sound in the driven gas [10]. Accordingly, to obtain the shortest possible pulse, the driven length has to be the shock formation distance, and the driver length will then have to be optimized for this driven length.

Gas properties: From the discussion in Sect. 1.3, it is evident that the gas in the driven chamber cannot be different from that in an actual event, which thus has to be *air* for an air blast. On the other hand, the choice of the driver gas is based on gas dynamic considerations of how a shock wave reflects from a contact surface. A contact surface is an interface that separates the shocked gas and the non-shocked gas (*yellow*-colored line in Fig. 4). The reflected shock wave (Fig. 2) would have to cross this interface (which cannot be represented in Fig. 2 as it depicts pressures and not densities) as may be visualized in Fig. 4. If the impedance of the downstream gas is higher, we will have a shock reflection off this interface that would then travel toward the end wall, which is clearly not a desirable condition. So we need to choose a driver gas such that we have an expansion wave reflecting off the contact surface. For the driver pressures that are usually encountered, ~20–60 *bar*, the choice falls on helium, which incidentally also gives higher reflected shock pressures for a driver-driven gas pressure ratio.

Test sample: Another important aspect that has to be taken care of is with regard to the mounting of the specimen. Consider the progress of the shock wave once it exits the shock tube. Figure 5a shows a shadowgraph image, an image whose intensity is proportional to the second derivative of density, which can thus highlight a shock wave which is characterized by density jumps. As the image shows, expansion waves that emanate from the corner slowly catch up with the shock wave and progressively weaken the shock wave, thus making the shock nonplanar. Thus, it would be incorrect

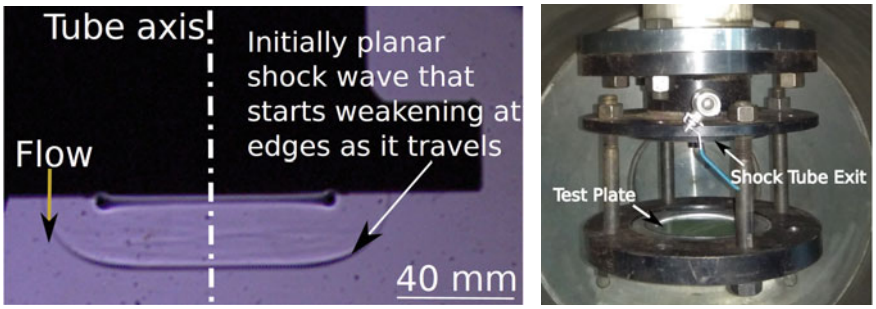

(a) Shadowgraph (b) Faulty placement of sample

Fig. 5 **a** Shadowgraph image of flow exiting a shock tube. **b** An illustrative photograph that shows the *wrong* positioning of a sample. The gap between the shock tube exit and the sample should ideally be zero

to position the sample at a distance from the exit of the shock tube as shown in Fig. 5b. Instead, the gap between the flange and the sample should ideally be zero so that a planar shock impingement is realized on the sample plate.

3 Shock Tubes at IISc

At the Laboratory for Hypersonic and Shock wave Research (LHSR) in Indian Institute of Science, we have shock tubes that are capable of simulating an air blast and an underwater blast event. The following subsections explain each of these facilities, and the work that is usually carried out in them.

3.1 Vertical Shock Tube

A shock tube that has a provision to vary the driver and driven lengths was designed based on the ideas presented in Sect. 2. This facility, a photograph of which is provided in Fig. 6a, has two shock tubes, each with an inner diameter of 136 mm and having a compartmentalized driver section (three tubes of 0.5 m each) and driven section (one tube of 1.5 m, three tubes of 0.6 m, one tube of 0.5 m, and one tube of 0.39 m), thus permitting a good number of combinations of driver and driven tube lengths. The shock tubes have been vertically positioned for ease of carrying out shock impingement studies on a liquid medium. These tubes open into a tank that was primarily intended for noise attenuation and safety purposes. It also has viewing windows to monitor the deformation of the test plate(s).

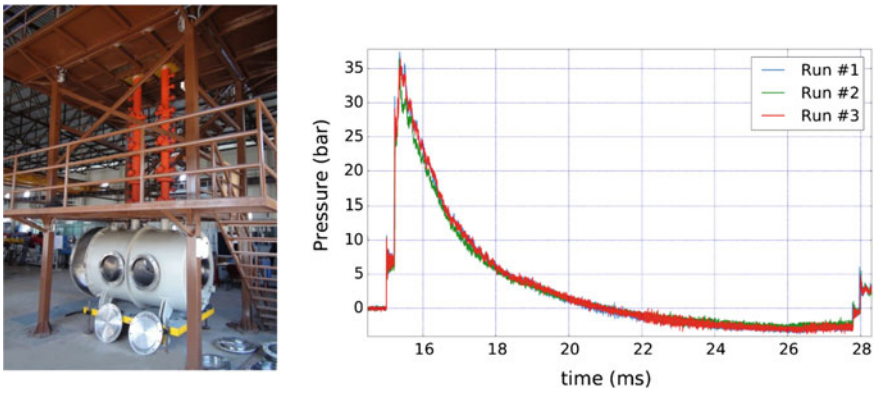

(a) Photograph of the facility (b) Side-on pressures

Fig. 6 **a** A photograph of the vertical shock tube showing the safety tank and the two variable length shock tubes that sit atop the tank. Three of the five viewing windows may also be seen in this photograph. **b** Side-on pressures measured closed to the exit of the shock tube

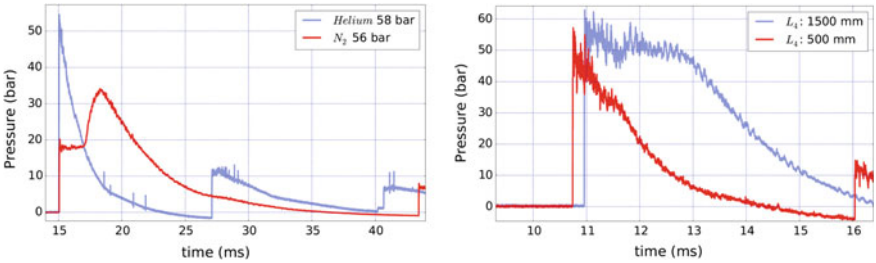

(a) Different driver gases (b) Effect of driver length

Fig. 7 The effect of driver gas and the length of the driver tube on the pulse formation

Figure 6b shows side-on pressures which were measured close to the exit of the shock tube (50 mm) upstream when a rigid concrete block was being loaded by a shock wave generated using 59.3 ± 2.8 *bar* of helium gas. The repeatability in peak pressure was found to be better than 3% and the repeatability in impulse was found to be 4.5%, the wide scatter largely due to the variability in the burst pressures of the metal diaphragm.

As mentioned in the previous section, helium is to be the preferred choice of driver gas. Figure 7a shows what would happen if nitrogen were to be used instead and a demonstrative experiment was carried out using nitrogen at 56 *bar*, and helium at 58 *bar*, as the driver gas. The shock tube had a 700 mm long driver and a 4500 mm long driven tube. For the case of nitrogen as the driver gas, we see the shock wave reflecting from off the contact surface as another shock wave, thus giving rise to the second peak, which is clearly to be avoided. The higher reflected pressures that are achieved using helium as the driver gas, for the same driver-driven gas pressure

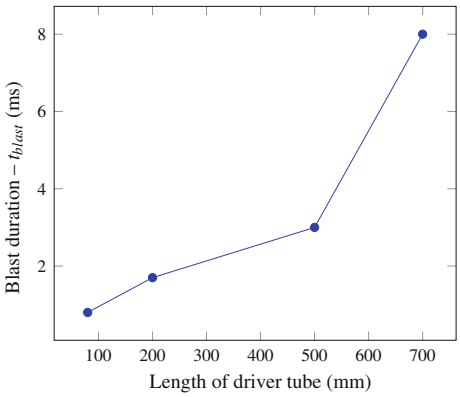

Fig. 8 An experimental plot showing the effect of driver length on the pulse duration of the blast wave

ratio is also worth being noted. To show the effect of the driver length, consider the plots shown in Fig. 7b. The driver gas used was helium and the burst pressures were 61 ± 1 *bar*, and the driven length was 2100 mm. It may be seen that by varying the driver length, with all the other parameters unchanged, we can get either a shock pulse or a blast pulse. Figure 8 further shows how a reduction, or increase in the driver length gave us different blast pulse durations.

For a blast loading test that we carried out on a fully clamped 2 mm-thick Aluminium 6061-T6 plate, a failure that is characteristic of an impulse load was recorded when the pressure loading conditions were similar to the helium signal shown in Fig. 7a. A photograph of the failed sample is given in Fig. 9a. Side-on pressure sensors on the shock tube were mounted at two locations, one each, before and after the plate. The signal is not clean perhaps due to noise in the cables, but it shows that the aluminum plate took about 700 μs to rupture. A correlation with a high-speed

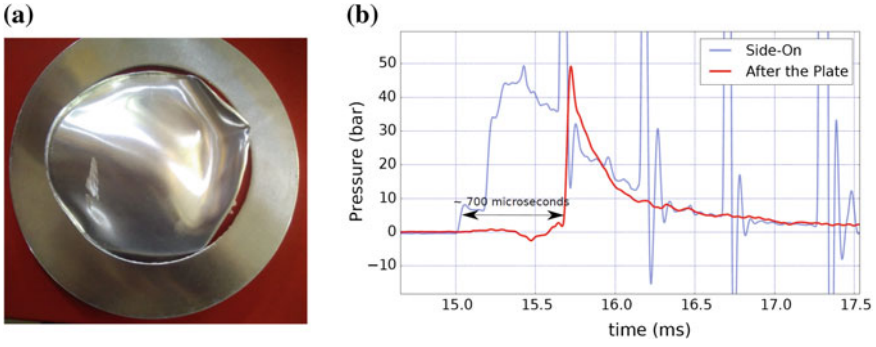

Fig. 9 **a** A photograph showing a 2 mm-thick Al 6061-T6 plate (Φ 136 mm exposed area) that showed an impulse failure and **b** A typical pressure signal showing the side-on pressure from sensors that were placed on the tube. The first signal was from a sensor that was 50 mm above the plate and the second one was at 40 mm after the plate

image recording will help us obtain an exact idea of how the failure had occurred. We had also carried out experiments on a 0.8 mm-thick copper plate and it also showed an impulse type of failure [29]. The experimentally measured impulse value matches well with the impulse value reported in existing literature for this type of failure mode. Since the data in the literature is from small-scale explosive-based experiments, it shows that a shock tube is certainly a capable device for recreating small-scale explosions.

3.2 Automated Shock Tube

For accurate control over experiment, the use of diaphragms is to be eliminated as their variable burst pressures are a major source of uncertainty in any meticulously executed experiment. The use of a diaphragmless system, wherein a fast acting valve performs the role of the diaphragm gives the desired control over such an experiment. Figure 10 shows such a facility at the lab, where the fast open valve is located at the left end and the test specimen may be clamped to the tube at the right end. Nagaraja and others [21] had used this facility to study shock wave-assisted metal forming of thin copper plates (0.15–0.5 mm). The reflected shock pressures were less than 5 *bar*, and a rectangular pulse was obtained at the end of the tube. For this pressure loading, they observed Mode II (impulse) failure for thin aluminum plates and copper plates. It is interesting to note that an impulsive failure was recorded although the pulse was of much longer duration than the natural time period of the plate. This may be attributed to the plate having failed after absorbing the corresponding damage impulse as mentioned in Sect. 2.1 and as illustrated by the shaded portion in Fig. 3a.

3.3 Free-Piston Shock Tube

From the discussion in Sect. 1.2, it is clear that failure cannot be scaled up. But since there is an absence of more experimental data on verifying scalability of fracture for thin plates, some high-pressure experiments were carried out on (composite) plates, with a view to not only understand the material response to shock loading, but also to obtain data for code validation. In this section and the subsequent one, we describe two facilities that are capable of generating high pressures—one for air blast and the other one for UNDEX.

Free-piston shock tube [27] uses the compressive action of a freely moving piston to heat up the driver gas (helium) adiabatically. This hot gas (up to ∼1600 K) which is also at high pressure (∼100 *bar*), bursts a diaphragm, giving rise to high reflected shock pressures. Tailoring the driver length is not an easy task in this device as the piston continues to move even after the rupture of the diaphragm. This facility, thus, generates a shock wave (like the automated shock tube) rather than a blast wave and it was used by Reddy and Madhu [26] as it is capable of generating high pressures.

For experiments on this tube, it was assumed that FSI effects are negligible and so argon, rather than air, was used as the driven gas to achieve higher reflected shock pressures.

FRP plates (courtesy of Defence Metallurgical Research Laboratory (DMRL), Hyderabad) that were 3 mm thick were tested by clamping them between two flanges and placing them at the end of the shock tube. Various patterns of failure were observed as we increased the loading pressure from 70 *bar* to 200 *bar* by increasing the initial pressure in the driven section (Fig. 11).

3.4 Liquid Blast Tube

To generate high pressures of the order of tens of *MPa*, a fast moving piston that hits a water surface may be used to generate a blast wave [8]. This may be used to simulate an UNDEX event.

As the piston hits the surface of the water, momentum is transferred to water, and so an elastic wave is generated in the water that travels at the speed of sound in water (∼1400 m/s). The initial velocity of the piston is thus imposed on the water at the boundary. Since water is nearly incompressible, it resists the motion of the piston, thereby decelerating it. Thus, the velocity of the piston, and that of the water interface keeps reducing. This leads to a drop in the pressure of the wave that propagates in the water, giving a decaying pressure profile, that is exponential in nature. The peak pressure (p_0) of this wave is related to the density of the liquid (ρ), the speed of sound in the liquid (a), and the velocity of the piston hitting the water interface (v_p) by the

Fig. 10 A photograph of the diaphragmless shock tube at IISc. The inset at the lower right shows failed aluminum and copper samples. The loading area was ϕ 50 mm

Eq. 1. Similarly, the time constant of decay for the blast wave (τ) is related to the mass of the piston (m_p), the cross-sectional area of the piston or the shock tube (A), and the acoustic impedance of the medium (ρa). The cross-sectional area was not explicitly included in [8]. The correct relation is Eq. 2.

$$p_0 = \rho a v_p \tag{1}$$

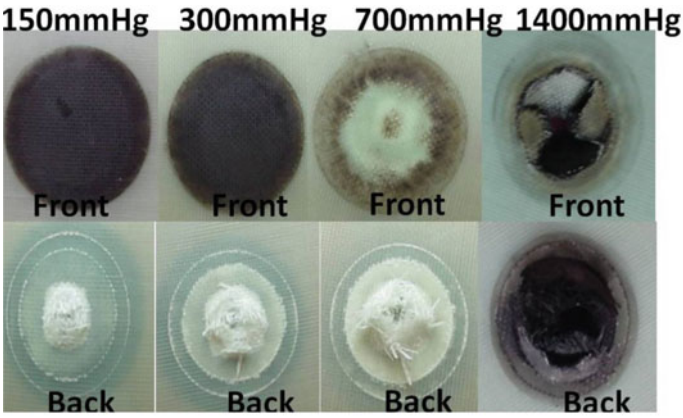

(a) Damaged composite plates

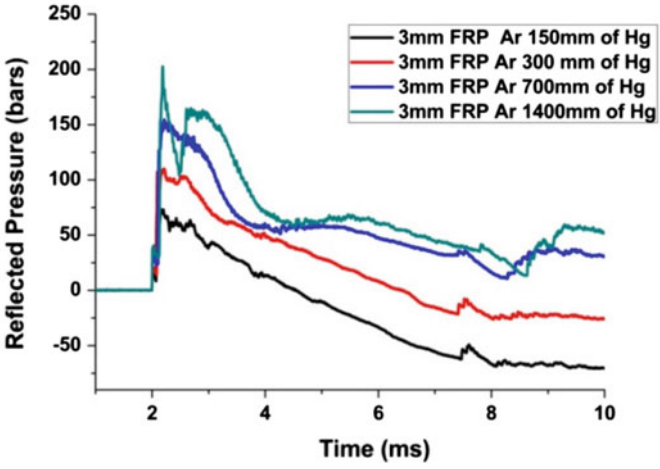

(b) Reflected shock pressures

Fig. 11 **a** Blast testing of 3 mm thick FRP plates showing different patterns of damage that were observed as we ramped up the loading pressure. The loading area is Φ 50 mm. The pressures mentioned above each sample refer to the initial pressure of the driven gas. **b** The reflected shock pressures were measured by a sensor that was flush mounted onto the side-wall of the shock tube near the end

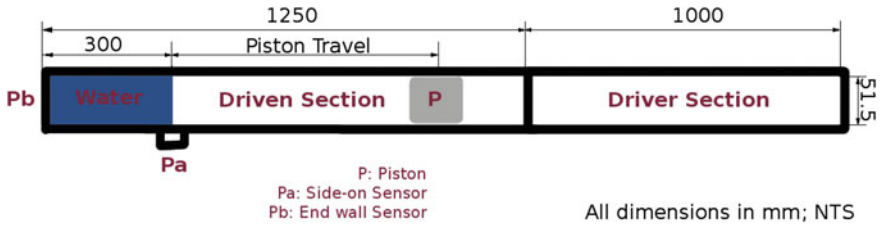

Fig. 12 A schematic diagram showing the major dimensions of the Φ 50 mm vertical shock tube that was used for this experiments. The illustration has been rotated clockwise by 90°

$$\tau = \frac{m_p}{\rho a A} \tag{2}$$

A schematic drawing of the facility has been provided in Fig. 12. A close-fitting piston, made of aluminum, and weighing 0.137 kg was used in these experiments, which was placed at a distance of 500 mm from the diaphragm station. The driver side of the shock tube was filled with water up to the pressure port (P_a), located at ∼900 mm from the diaphragm, thus giving an effective travel length of about 400 mm for the piston. For the experiments as blast tube, the side-on pressure port (P_a) was left open. This was done both to enable the air that is compressed by the piston to escape and to be used as an inlet to fill the tube with water. The initial pressure rise followed by the exponential decay and the subsequent peak due to the reflection from the end wall of the shock tube may be seen in the experimentally obtained pressure trace (Fig. 13a). Further, it may also be noticed that the rise time is quite significant. This may be attributed to the non-evacuation of the region between the piston and the air–water interface. The air that is being compressed in this intervening region due to the motion of the piston may have contributed to the pressure rise noticed before the peak pressure.

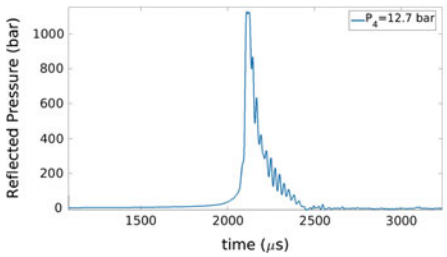

(a) Reflected pressure of the blast wave

(b) Damaged composite sample

Fig. 13 **a** A typical pressure signal at the end wall of the blast tube. The piston was fired using nitrogen gas at 12.4 *bar* **b** A photograph of the top and bottom side of the composite plate subjected to an underwater blast. The damaged area is a circle of Φ 50 mm

An E-glass/epoxy composite plate was clamped to the end of this shock tube and was exposed to the shock pressure, a typical signal of which is shown in Fig. 13a. The sample was damaged and exhibited fiber failure as shown in Fig. 13b. As reported elsewhere [28], a delamination type of failure was recorded when the specimen was subjected to a lower pressure.

3.5 Miniature Devices

To understand the microstructural response of a material being deformed by a blast wave, samples, whose microstructural and material parameters (stacking fault energy and grain size for a FCC material) have been carefully grown are required. However, samples of such controlled nanocrystalline material may be obtained in bulk only to a maximum size of Φ30−40 mm at a thickness of 1 mm, due to limitations in its manufacturing process (pulsed electrodeposition). To study the blast response of such small samples, the use of a miniaturized shock tube was proposed.

Nonel® tube: The Nonel® tube (M/s Orica Mining Services) is a small plastic tube (Φ3 mm and 300 mm long) that is coated on the inside with a layer of HMX explosive. On initiating a spark at one end, a detonation wave propagates down the tube, and a high-pressure pulse may be obtained at the other end. We can now clamp a small test specimen onto the other end of this tube using an appropriate fixture and subject it to blast loads that can be as high as 130 *bar* peak pressure. The pressures obtained from this tube were found to be highly repeatable [30], and it has been used for blast mitigation studies elsewhere [39]. But then, the exit pressure of this tube cannot be varied as the tube comes pre-coated with an explosive, which cannot be redone. This led us to develop a new hydrogen–oxygen-based detonation shock tube that was capable of generating repeatable and desired pressures.

Miniature detonation-driven shock tube: A photograph of this tabletop device is shown in Fig. 14a. The inner diameter of the tube is 6 mm, and the detonation length is 270 mm. A spark plug is located near the center of this tube, and the test plate is clamped to one end of this tube. The other end of this tube is closed. A mixture of hydrogen and oxygen from an in-situ hydrogen–oxygen generator that uses electrolysis of water is filled in the tube and then detonated using a spark plug [12]. A detonation wave is formed once the spark plug is initiated, and this travels down the tube and impinges on the test sample. A typical pressure signal that was obtained at the end wall is shown in Fig. 14b. Since the fill pressure of this shock tube controls the detonation pressure in this device, it is capable of generating repeatable variable shock pressures.

Nanocrystalline Nickel samples (Φ 12 mm) that were 120 and 200 μm thick were tested on these two devices—Nonel tube and the miniature detonation-driven shock tube.

Microstructure studies: Using Nonel tube, nanocrystalline nickel having (200) fiber was deformed and a significant weakening of bulk texture was observed. The forma-

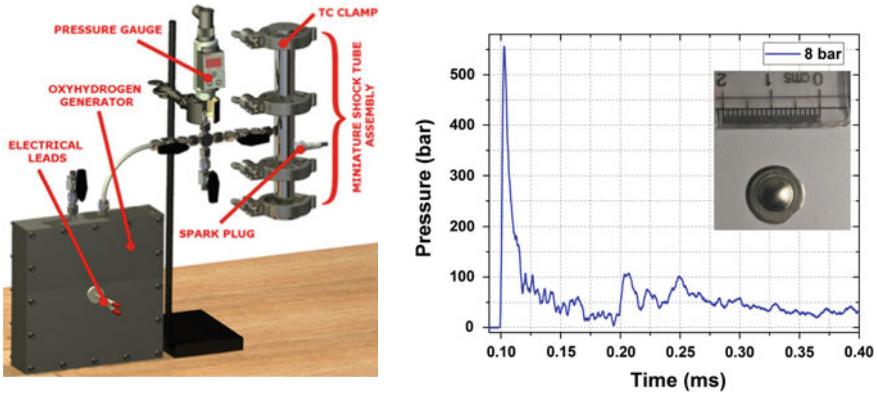

(a) The device (b) Typical pressure signal

Fig. 14 **a** A photograph of the miniature detonation-driven shock tube and **b** A typical pressure signal at the end of the shock tube. The inset shows a deformed nickel sample

tion of sub-grains was not observed but the grains were highly strained suggesting minimum recovery process which are generally formed in high stacking fault energy FCC metals. The grains were also found to be elongated and shear bands were observed parallel to grain elongation direction. These devices are, thus, being used to carry out basic studies with a view to understand how blast loading can change the microstructure of a material.

4 Summary and Conclusion

The guidelines under which scaled experiments may be carried out were outlined in this work. The importance of matching the pressures and obtaining a pulse duration that is consistent with the geometric scaling laws after incorporating corrections for the strain rate was highlighted in this work. Shock tubes being devices that are capable of generating pressures with extremely short rise times, and fairly repeatable planar waves, with the ability to vary the pulse duration were shown to be invaluable tools in recreating a scaled-blast event. Even if the scale-up of the experiment is not accurate, we may still use this data for validating numerical codes.

The repeatability of 4.5% (impulse) and 3% (pressure) achieved using the vertical shock tube needs to be contrasted against the difficulty in obtaining repeatable experiments using explosives [20], where the repeatability is rarely better than 10%. Based on the shortest duration of 0.8 ms that was achieved on the vertical shock tube, and knowing that a maximum pressure of 100 *bar* may be achieved on this tube, a 3*D* graph showing the range and masses of a scaled TNT explosion that can be recreated was plotted in Fig. 15. In this figure, the colored region represents the explosion parameters that may be simulated using this shock tube. While the lower

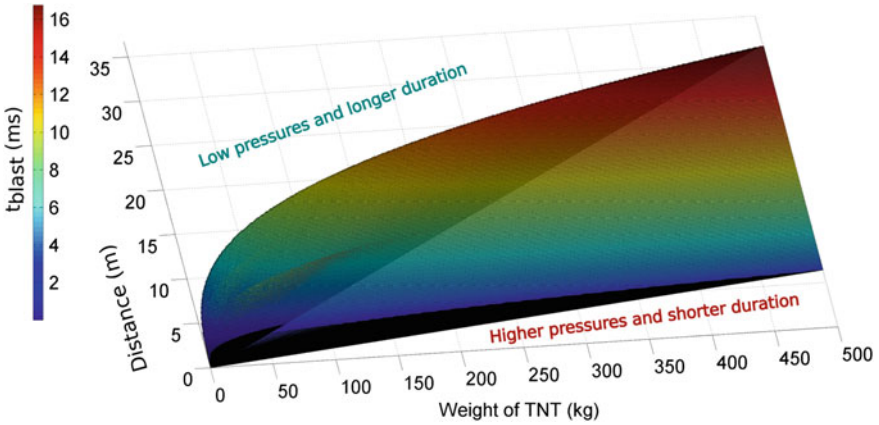

Fig. 15 A 3D plot showing the possible range of TNT weights and distances that may be simulated using the vertical shock tube. The lower and the upper parts including the (*dark*) regions are outside the simulation capability of the shock tube. This graph is for a scaled-down experiment and the corresponding full-scale values may be calculated using an appropriate scaling factor

half represents pressures and decay times that are outside the scope of a shock tube, the upper half corresponds to very low pressures (<2 *bar*) and longer time durations (>16 ms), which is not of interest for blast interaction with metal plates.

By tailoring the lengths of the vertical shock tube facility, blast wave formation was demonstrated and the diaphragmless shock tube facility may be used to generate repeatable rectangular pulses. These devices were shown to be capable of replicating an impulse failure that has been well documented for small-explosion-based experiments. The liquid blast tube may be used for underwater blast experiments. Finally, we described how a miniature version of a shock tube may be used for a careful study of the effect of shock loading on the grain size and other microstructural aspects of any material.

Acknowledgements We would like to thank the Defence Research and Development Organization (DRDO), New Delhi for funding the research reported in this work. The help received from the staff at the Laboratory for Hypersonic and Shock wave Research (LHSR), IISc is acknowledged with thanks. We also wish to thank Dr. Janardhanraj and Mr. Anuj Bisht of our laboratory, and Mr C J Reddy of DMRL, Hyderabad for sharing some of their data and figures for this article.

References

1. Anderson, C. E. (2003). From fire to ballistics: a historical retrospective. *International Journal of Impact Engineering*, *29*(1), 13–67.
2. Anderson, J. C., & Naeim, F. (2012). *Basic structural dynamics*. Hoboken, NJ: Wiley.
3. Ansar, M., Xinwei, W., & Chouwei, Z. (2011). Modeling strategies of 3D woven composites: a review. *Composite Structures*, *93*(8), 1947–1963.

4. Atkins, A. (1999). Scaling laws for elastoplastic fracture. *International Journal of Fracture*, *95*(1), 51.
5. Aune, V., Fagerholt, E., Langseth, M., & Borvik, T. (2016). A shock tube facility to generate blast loading on structures. *International Journal of Protective Structures*, *7*(3), 340–366.
6. Celander, H. (1955). The use of a compressed air operated shock tube for physiological blast research. *ACTA Physiologica Scandinavica*, *33*, 6–13.
7. Coutinho, C. P., Baptista, A. J., & Rodrigues, J. D. (2016). Reduced scale models based on similitude theory: a review up to 2015. *Engineering Structures*, *119*, 81–94.
8. Deshpande, V., Heaver, A., & Fleck, N. A. (2006). An underwater shock simulator. In: *Proceedings of the Royal Society of London. Series A, 462*, 1021–1041.
9. Fallah, A. S., Nwankwo, E., & Louca, L. A. (2013). Pressure-impulse diagrams for blast loaded continuous beams based on dimensional analysis. *Journal of Applied Mechanics*, *80*(5), 051011.
10. Ikui, T., & Matsuo, K. (1959). Investigations of the aerodynamic characteristics of shock tubes. *Bulletin of JSME*, *12*(52), 774–782.
11. Jahnke, D., Azadeh-Ranjbar, V., Yildiz, S., & Andreopoulos, Y. (2017). Energy exchange in coupled interactions between a shock wave and metallic plates. *International Journal of Impact Engineering*, *106*, 86–102.
12. Janardhanraj, S., & Jagadeesh, G. (2016). Development of a novel miniature detonation-driven shock tube assembly that uses in situ generated oxyhydrogen mixture. *Review of Scientific Instruments*, *87*(8):085114
13. Jones, N. (1989). *Structural impact*. New York: Cambridge University Press.
14. Jones, N. (2009). Hazard assessments for extreme dynamic loadings. *Latin American Journal of Solids and Structures*, *6*, 35–49.
15. Jones, N., & Kim, S. B. (1997). A study on the large ductile deformations and perforation of mild steel plates struck by a mass—Part II: Discussion. *Journal of Pressure Vessel Technology*, *119*(2), 185–191.
16. Kambouchev, N., Noels, L., & Radovitzky, R. (2006). Nonlinear compressibility effects in fluid-structure interaction and their implications on the air-blast loading of structures. *Journal of Applied Physics*, *100*(6), 063519.
17. Kong, X., Li, X., Zheng, C., Liu, F., & Guo Wu, W. (2017). Similarity considerations for scale-down model versus prototype on impact response of plates under blast loads. *International Journal of Impact Engineering*, *101*, 32–41.
18. LeBlanc, J., Shukla, A., Rousseau, C., & Bogdanovich, A. (2007). Shock loading of three-dimensional woven composite materials. *Composite Structures*, *79*(3), 344–355.
19. Li, Q. M., & Meng, H. (2002). Pressure-impulse diagram for blast loads based on dimensional analysis and single-degree-of-freedom model. *Journal of Engineering Mechanics*, *128*(1), 87.
20. Menkes, S. B., & Opat, H. J. (1973). Broken beams—tearing and shear failures in explosively loaded clamped beams. *Experimental Mechanics*, *13*(11), 480–486.
21. Nagaraja, S. R., Prasad, J. K., & Jagadeesh, G. (2012). Theoretical and experimental study of shock wave-assisted metal forming process using a diaphragmless shock tube. *Proceedings of the Institution of Mechanical Engineers, Part G: Journal of Aerospace Engineering*, *226*(12), 1534–1543.
22. Neuberger, A., Peles, S., & Rittel, D. (2007). Scaling the response of circular plates subjected to large and close-range spherical explosions. Part I: Air-blast loading. *International Journal of Impact Engineering*, *34*(5), 859–873.
23. Olson, M., Nurick, G., & Fagnan, J. (1993). Deformation and rupture of blast loaded square plates-predictions and experiments. *International Journal of Impact Engineering*, *13*(2), 279–291.
24. Oshiro, R., & Alves, M. (2009). Scaling of structures subject to impact loads when using a power law constitutive equation. *International Journal of Solids and Structures*, *46*(18–19), 3412–3421.
25. Pankow, M., Justusson, B., & Waas, A. M. (2010). Three-dimensional digital image correlation technique using single high-speed camera for measuring large out-of-plane displacements at high framing rates. *Applied Optics*, *49*(17), 3418–3427.

26. Reddy, C. J., & Madhu, V. (2017). Dynamic behaviour of foams and sandwich panels under shock wave loading. *Procedia Engineering*, *173*, 1627–1634.
27. Reddy, K. P. J. (2007). Hypersonic flight and ground testing activities in India. In: Peter Jacobs, Tim McIntyre, Matthew Cleary, David Buttsworth, David Mee, Rose Clements, Richard Morgan, Charles Lemckert (Ed.), *16th Australasian Fluid Mechanics Conference (AFMC), Gold Coast, Queensland, Australia*, pp. 32–37, 3–7 Dec.
28. Samuelraj, I. O., & Jagadeesh, G. (2015). *Development of a liquid blast tube facility for material testing*. In: R. Bonazza & D. Ranjan (Eds.) 29th International Symposium on Shock Waves 1. Springer, Cham.
29. Samuelraj, I. O., & Jagadeesh, G. (2017). Development of a vertical shock tube facility for blast testing applications. In: *30th International Symposium on Shock Waves* (to be published)
30. Samuelraj, I. O., Jagadeesh, G., & Kontis, K. (2013). Micro-blast waves using detonation transmission tubing. *Shock Waves*, *23*(4), 307–316.
31. Schleyer, G., Hsu, S., & White, M. (2004). Scaling of pulse loaded mild steel plates with different edge restraint. *International Journal of Mechanical Sciences*, *46*(9), 1267–1287.
32. Simitses, G. J., Starnes, J. H, Jr., & Rezaeepazhand, J. (2000). Structural similitude and scaling laws for plates and shells: a review. *41st AIAA/ASME/ASCE/AHS/ASC Structures, Structural Dynamics, and Materials Conference and Exhibit, AIAA Paper 2000–1383* (pp. A00–24525). GA: Atlanta.
33. Snyman, I. (2010). Impulsive loading events and similarity scaling. *Engineering Structures*, *32*(3), 886–896.
34. Sorrell, F. Y., & Smith, M. D. (1991). Dynamic structural loading using a light gas gun. *Experimental Mechanics*, *31*(2), 157–162.
35. Stoffel, M., Schmidt, R., & Weichert, D. (2001). Shock wave-loaded plates. *International Journal of Solids and Structures*, *38*, 7659–7680.
36. Teeling-Smith, R., & Nurick, G. (1991). The deformation and tearing of thin circular plates subjected to impulsive loads. *International Journal of Impact Engineering*, *11*(1), 77–91.
37. Xue, Z., & Hutchinson, J. W. (2003). Preliminary assessment of sandwich plates subject to blast loads. *International Journal of Mechanical Sciences*, *45*(4), 687–705.
38. Xue, Z., & Hutchinson, J. W. (2004). A comparative study of impulse resistant metal sandwich plates. *International Journal of Impact Engineering*, *30*(10), 1283–1305.
39. Zare-Behtash, H., Gongora-Orozco, N., Kontis, K., & Jagadeesh, G. (2014). Detonation-driven shock wave interactions with perforated plates. *Proceedings of the Institution of Mechanical Engineers, Part G: Journal of Aerospace Engineering*, *228*(5), 671–678.

Elastic Metamaterials for Blast Wave Impact Mitigation

H. Chen, M. V. Barnhart, Y. Y. Chen and G. L. Huang

1 Introduction

Unlike naturally occurring materials or traditional composites, metamaterials exhibit peculiar frequency dependent effective properties owing to their specifically designed microstructures. Although the field of metamaterials is relatively young, it has seen a significant increase in theoretical and experimental research efforts in the field of electromagnetics for applications including electromagnetic wave absorption, negative refractive index materials, electromagnetic cloaking and super resolution imaging [1–3]. Analogous to electromagnetic metamaterials, acoustic metamaterials have also been explored more recently for potential applications similar to their electromagnetic counterparts but for acoustic waves [4–9]. A fundamental microstructural design aspect of acoustic metamaterials is the utilization of locally resonant subwavelength structures, or, resonators. Because of the subwavelength design aspect, an effective continuum model can be used to represent acoustic metamaterials including their frequency dependent properties such as effective mass density or bulk moduli.

Similar to the types of metamaterials previously mentioned, the field of elastic metamaterials (EMMs) comprises a relatively young field of composites research with potential applications involving the control or manipulation of longitudinal and transverse waves. A locally resonant microstructure is also a key design feature of EMMs typically in the form of periodically arranged locally resonant inclusions (resonators) embedded within a rigid host medium. The first experimental demonstration of a locally resonant acoustic metamaterial was carried out by Liu et al. [10], in which locally resonant unit cells consisting of lead (Pb) spheres coated with a compliant silicone rubber were arranged periodically in an epoxy matrix. It

H. Chen · M. V. Barnhart · Y. Y. Chen · G. L. Huang (✉)
Department of Mechanical and Aerospace Engineering, University of Missouri, Columbia, MO 65211, USA
e-mail: huangg@missouri.edu

S. Gopalakrishnan and Y. Rajapakse (eds.), *Blast Mitigation Strategies in Marine Composite and Sandwich Structures*, Springer Transactions in Civil and Environmental Engineering, https://doi.org/10.1007/978-981-10-7170-6_19

was experimentally demonstrated that the effective medium produced strong sound attenuation regions restricting the transmission of incident waves referred to as "bandgaps". More recently, it has been demonstrated that if the mass-in-mass lattice model is used to represent a locally resonant metamaterial microstructure, the mass density will become effectively negative near the local resonance frequency of the internal resonators [11, 12]. However, an inherent drawback of traditional EMM microstructural designs is that the frequency region of the bandgap(s) are predetermined by the microstructural configuration and are therefore fixed. Because of this, practical engineering applications of EMMs are often limited as there is no way to tune or shift the bandgap frequency ranges without physical microstructural modifications which are unrealistic. Steps have been taken to address this weakness by incorporating microstructural designs utilizing arrays of multiple resonant masses embedded in a compliant rubber matrix [13]. It was found that the effective medium exhibited two negative dispersion bands in which one supported only compressional waves similar to a liquid while the other displayed super anisotropy where compression and shear waves could only propagate along different directions. This means that the effective medium could possess a simultaneously negative effective mass density and effective elastic modulus. More recently, chiral EMM designs were presented in which three- or single-phase microstructural designs exhibited both dipolar as well as rotational resonant modes [14, 15]. Inspired by the working mechanism of the EMMs, Chen and Sun [16] proposed a sandwich structure with the addition of mass-spring units into the core for blocking incident impact-induced elastic waves from entering the sandwich structure. A volume averaging approach was used to analyze the effect of the internal resonators where it was assumed the interior resonant masses were periodically arranged along the beam. The concept of including locally resonant structures to manipulate the dynamic response of sandwich beams was then demonstrated experimentally and provided validation to the previous theoretical modeling [17, 18]. Although previous work has been conducted to address the fundamental design challenge of achieving tunable or shifting the frequency locations of bandgaps in traditional passive EMM designs, it persists as a challenging engineering endeavor that needs to be addressed.

From previous metamaterial research, it has been clearly demonstrated that utilizing multiple resonant inclusions will result in additional bandgap frequency regions and thus increase the overall attenuation bandwidth. Huang and Sun [19] presented one such model in which two internal resonators were shown to exhibit multiple bandgaps in the theoretical analysis. The underlying mechanism responsible for the bandgap formation can be attributed to the reflection or temporary storage of incident wave energy by the internal resonators. Building on this work, a similar multi-resonator microstructural design was considered for the potential application of shielding structures from blast waves [20]. Chiral multi-resonator EMM microstructural designs have also been proposed to achieve broadband energy absorption both numerically and experimentally by exploiting individual local resonance bandgaps [21]. To produce more significant band gap characteristics compared to single-resonator designs, a sandwich beam with multiple

resonators embedded was presented which can lead to multiple resonant-type bandgaps with remarkable wave attenuation capabilities [22]. However, for the EMM designs previously mentioned, the energy attenuation mechanism is due to the reflection or temporary storage of energy while the dissipation of energy due to damping is neglected.

To this end, the significance of damping which is an intrinsic material property that describes a materials energy dissipation potential under dynamic loading can be examined for its potential application in EMM microstructural designs. However, in traditional non-dissipative EMM designs damping is often avoided as it inhibits the resonant motions of the EMM microstructure, and thus, reduces the overall attenuation of propagating elastic waves. This presents an interesting conundrum that will be analyzed further in later sections of this chapter where the two critical design features of locally resonant motions and the effects of damping will be explored in-depth. Early work by Hussein and Frazier [23] and Manimala and Sun [24] on the effects of damping in a single-resonator mass-in-mass lattice found that the proposed "metadamping" concept could increase the attenuation width and increase the range of attenuated frequencies. More recently, Pai et al. applied a similar approach by incorporating damping elements to a multi-resonator metamaterial beam which resulted in the two bandgap frequency regions effectively merging to form a single broadband energy absorption region [25]. Furthermore, it was discovered that damping applied to one or both of the two resonant masses significantly impacted the numerically calculated energy absorption performance. The fundamental EMM design challenge to achieve broadband energy absorption is to first create a locally resonant microstructure where the two resulting bandgaps are close in proximity (close resonant frequencies). The second challenge is to properly utilize the damping properties between each of the resonant masses such that the out-of-phase motions are not totally suppressed.

To address these challenges, two different multi-resonator EMM designs that incorporate dissipative (damping) properties will be comprehensively analyzed. To quantify their potential application for broadband blast or shock wave mitigation, analytical and numerical modeling will be used where dynamic loading in the form of longitudinal and flexural waves is considered. The first microstructural design consists of a dissipative three degree-of-freedom (3-DOF) lattice system where attention is paid to effects of damping applied to the two interior resonant masses. After obtaining results from analytical modeling, a two-dimensional (2D) numerical model is formulated to calculate the dispersion bands for an effective medium comprised of more realistic continuum media. Furthermore, transient analysis is carried out to demonstrate the proposed EMMs broadband energy absorption capabilities under simulated blast wave loading using a typical blast wave loading profile. Finally, the second microstructural design which consists of a multi-resonator EMM sandwich beam design in considered with similar analyses conducted. The two proposed EMM designs will hopefully provide new outlooks for the development of novel multifunctional composites capable of effectively mitigating blast or shock waves which are broadband by nature.

2 Discrete Mass-Spring-Damper Model of Dissipative Elastic Metamaterials

2.1 Transient Analysis Under Blast Loadings

Building on the non-dissipative multi-resonator EMM design [19] and incorporating damping elements in the microstructure [24], a dissipative multi-resonator mass-in-mass lattice system is considered as shown in Fig. 1. In the figure, damping elements connect the outermost mass, m_1, and the two internal resonant mass m_2 and m_3 in the one-dimensional (1D) lattice. The damping element c_1 denotes the damping coefficient of the background medium while c_2 and c_3 respectively denote the damping coefficients of the middle and innermost resonator masses. Each unit cell in the lattice is connected to its neighboring cells by a linear spring with stiffness k_1 while the middle and innermost masses in each unit cell by springs with stiffness's denoted by k_2 and k_3, respectively.

To begin the analysis of the dissipative EMM microstructure the innermost damping coefficient is examined to quantify its impact on the overall attenuation performance of an incident blast wave signal. For the two internal resonators, m_2 and m_3, a significantly larger mass for the innermost resonator is chosen such that the mass ratio, m_3/m_2, will be reasonably large. A layout of the system is illustrated in Fig. 2 where the 1D lattice structure consists of 15 dissipative EMM unit cells situated between the sufficiently long incident and transmission sections. For the incident section of the lattice, 400 monatomic unit cells consisting of only the mass m_1 and spring k_1 are assumed. The same is true for the transmission section of the lattice with the only difference being that it is only 385 unit cells in length. To simulate a typical blast wave in the time domain, a force is applied to the left-most cell of the lattice with the force function written as

$$F = F_{\max} e^{-\frac{t-t_0}{t_d}}. \tag{1}$$

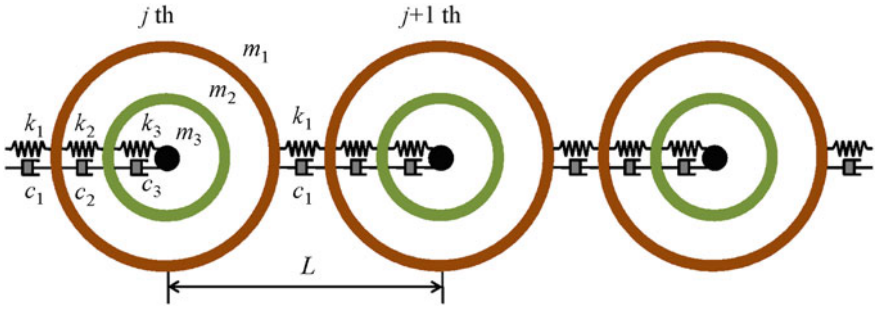

Fig. 1 One-dimensional mass-in-mass lattice with damping elements included

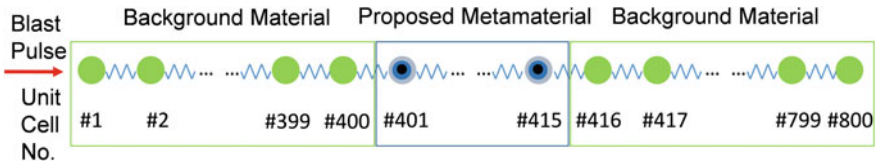

Fig. 2 1D dissipative EMM lattice analyzed under simulated blast wave loading

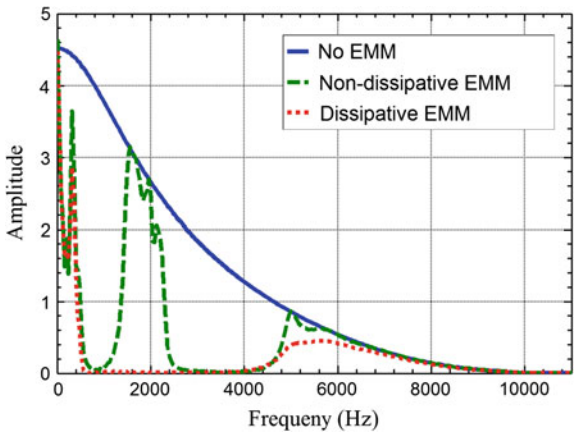

Fig. 3 Incident and transmission signals obtained from the Fast Fourier Transform

In Eq. (1), the maximum force amplitude, F_{max}, is defined as 1000 N while the parameters t_0 and t_d are defined as 0.5 and 0.1 ms, respectively, and simulate a typical air blast profile [20].

To quantify the frequency domain amplitudes of the incident and transmitted the Fast Fourier Transform (FFT) is applied to the time domain signals as shown in Fig. 3. As previously mentioned and clearly illustrated from the incident signal (solid-blue line) in Fig. 3, the incident blast wave signal is broadband in nature with a large low-frequency amplitude that decays exponentially for higher frequencies. The mass, stiffness and damping coefficients using in the lattice are listed in Table 1.

The frequency domain amplitudes of the transmitted signals for a non-dissipative and lattice with damping included are also obtained using the FFT and are plotted alongside the incident blast signal in Fig. 3. For the non-dissipative lattice (dotted-green curve), two transmission dips can be seen at 0.6–1.2 kHz and 2.4–4.6 kHz. The two bandgap regions are separated by a passing band present from

Table 1 Mass, stiffness and damping coefficients used in transient blast wave simulation

Mass (kg)			Stiffness (N/m)			Damping (Ns/m)		
m_1	m_2	m_3	k_1	k_2	k_3	c_1	c_2	c_3
0.002	0.01	0.04	7.90E6	1.58E6	0.79E6	1.26	1.26	125.66

1.7–2.2 kHz in which waves with frequency components in this range can freely propagate through the 15 multi-resonator portion of the lattice system. However, when damping is applied to the multi-resonator section of the lattice (red-dotted curve) this passing band is effectively suppressed leaving a single broadband energy absorption region of 0.6–4.6 kHz. Based on these results, it is apparent that the utilization of damping components in a traditional multi-resonator EMM design has very good potential for applications involving the mitigation of blast waves.

3 Design of Spherical Dissipative EMM Microstructure

As blast-induced shockwaves have become an increasing threat in both civilian and military conditions, interest has grown on developing efficient systems to mitigate against their damaging effects. Some traditional protective systems consist of structures that are engineered to undergo large plastic deformations as an energy absorption mechanism [26], or, energy redirection mechanisms that redirect incident blast pulses away from the shielded object [27–29]. While these systems have shown the ability to provide significant energy absorption and protection, they are usually only able to undergo a single blast event before needing to be replaced. The complexity, size, and weight of these systems also limit their practical application in most realistic circumstances.

To address this, a multi-resonator EMM design is proposed using realistic constituent materials as shown in Fig. 4. The continuum model shown in the figure is analogous to the mass-spring-damper system previously analyzed where compliant materials 2 and 4 represent the middle and innermost spring-damper components, respectively. The background material denoted by material 1 in Fig. 4 can be seen as representing both the outermost spring k_1, as well as mass m_1 from the previous 1D microstructural model. Finally, the middle and innermost resonant masses are then denoted by materials 3 and 5, respectively.

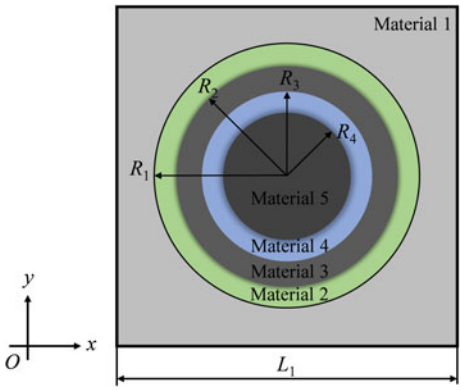

Fig. 4 Multi-resonator microstructural design using continuum media

3.1 Two-Dimensional Dispersion Bands Using the Finite Element Method

To numerically obtain the 2D dispersion bands a using the finite element method (FEM), a $\omega(k)$ approach is typically used in which the wavenumber k is swept over the first irreducible Brillouin zone and the eigenfrequencies obtained. With the application of material damping, however, these frequencies will be complex and therefore have no clear meaning. Therefore, a $k(\omega)$ numerical approach must be adopted to obtain the complex dispersion bands of the dissipative EMM microstructure. Using this approach with periodic Bloch boundary condition, the complex wavenumber can be obtained as a function of the frequency where the real and imaginary components of the wavenumber represent the propagation and attenuation coefficients, respectively.

To obtain the complex wavenumber of the dissipative EMM microstructure with plane-strain assumption and periodic boundary conditions, the commercial FEM software COMSOL Multiphysics is employed. For the incident longitudinal wave, an angle of incidence of 0° is used and each of the constituent materials used are defined with the properties listed in Table 2. Using the previously observed correlation between the innermost damping coefficient and broadband attenuation performance, Rayleigh damping is applied to only the innermost compliant layer (material 4) with a coefficient denoted by β_d.

The complex wavenumber components are obtained as shown in Fig. 5 for increasing values of damping applied to material 4. As previously mentioned, the real and imaginary parts of the complex wavenumber represent the propagation and attenuation coefficients of the dissipative EMM microstructure. For the real portion of the wavenumber shown in Fig. 5a it is apparent that as the inner damping is increased, the two pure bandgaps present in the zero-damping case will no longer be zero ($\mathrm{Re}\{kL\} \neq 0$) within the bandgap frequency ranges. However, the propagation amplitude will be reduced for all frequency components outside of the bandgap regions. This is due to the suppression of the locally resonant motions of the resonant masses as larger damping is applied to the system. For the imaginary

Table 2 Multi-resonator EMM microstructural geometry and constituent material properties

Material properties					
	Material 1	Material 2	Material 3	Material 4	Material 5
Lamé's first constant (Pa)	2.0×10^9	5.0×10^5	2.0×10^{12}	2.0×10^5	2.0×10^{12}
Lamé's second constant (Pa)	1.0×10^9	2.5×10^5	1.0×10^{12}	1.0×10^5	1.0×10^{12}
Density (kg/m^3)	1000.0	1000.0	20000.0	1000.0	20000.0
Geometrical parameters					
L_1 (mm)		R_1 (mm)	R_2 (mm)	R_3 (mm)	R_4 (mm)
20.0		9.0	8.5	8.0	7.5

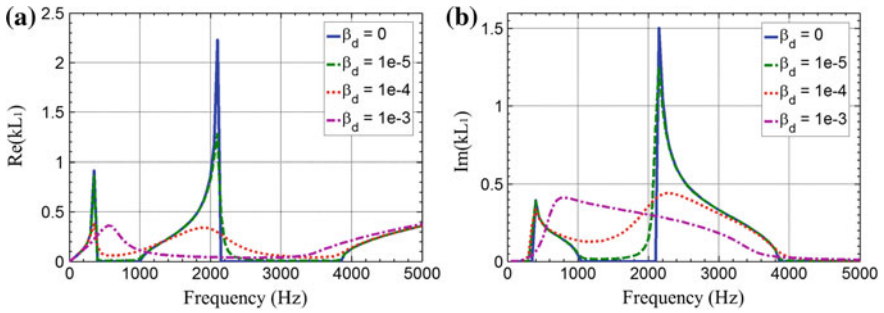

Fig. 5 Numerically obtained complex dispersion bands of dissipative EMM: **a** Re{kL}; **b** Im{kL}

component of the wavenumber shown in Fig. 5b, it is obvious that with increased damping applied to material 4 the two strong attenuation regions can be effectively merged resulting in a single broadband attenuation region for the β_d = 1e-3 case.

3.2 *Numerical Modeling of Blast Wave Transmission in a Dissipative EMM*

In this section, a finite 2D lattice of the dissipative EMM microstructure previously discussed is now analyzed for its energy absorption performance of simulated blast wave excitation. The 2D numerical model is similar to the 1D analytical lattice previously considered with sufficiently long (8 m) incident and transmission domains and five unit cells (N = 5) situated between them as shown in Fig. 6. Also similar to the previous analytical model, the incident and transmission beams in the numerical model are also defined as the background medium (material 1) and all of the constituent materials properties are left unchanged from those in Table 2. An input force is applied to the left-most boundary of the incident beam to simulate a realistic air blast is defined as $F = F_0 \exp[-(t-t_0)/t_d]$, where F_0 = 100 N/m, t_0 = 0.5 ms and t_d = 0.2 ms. To measure the incident and transmitted signals for the dissipative multi-resonator EMM lattice, two-point probes are used to measure the particle velocity amplitudes located 0.2 m before and after the lattice section. It should be noted that the relatively long length of the incident and transmission beam sections is to avoid secondary reflections from the left- and right-most

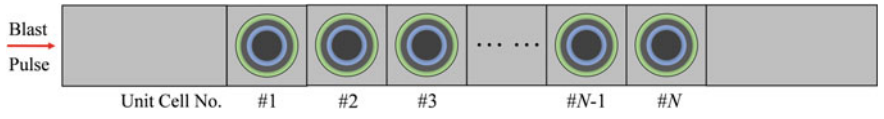

Fig. 6 Numerical model of finite dissipative EMM lattice used for transient blast wave excitation analysis

boundaries which would create unwanted 'noise' in the frequency domain amplitudes.

Similar to the numerical frequency domain analysis previously presented, damping is only considered for the innermost elastic layer (material 4). In Fig. 7a the time domain signals for the incident blast pulse and three cases of increasing Rayleigh damping coefficients are shown. In the top portion of Fig. 7a, the initial blast wave signal and the subsequent reflected signal from the EMM lattice is clearly visible. In the bottom three portions of the figure, it is apparent that as the damping amplitude is increased the amplitude of the transmission signal through the lattice will decrease and reach a steady-state in a much shorter time. To obtain the frequency domain amplitudes of the signal, the FFT is once again applied to the time domain signals to obtain the incident and transmitted frequency domain amplitudes shown in Fig. 7b. Just like the previously discussed 1D analytical model, as the inner Rayleigh damping coefficient is increased the broadband absorption performance of the dissipative EMM also increases. In Fig. 7b, it is clear that for the zero-damping case there are two separate bandgap regions divided by a narrow passing band at ~2 kHz. As the Rayleigh damping coefficient of material 4 in the EMM microstructure is increased to 1e-3 however, the passing band is effectively suppressed and the two bandgap regions are combined to form a single broadband energy absorption region.

For the final analysis of this dissipative EMM microstructural design, the effects of increasing the number of unit cells in the lattice are studied. Figure 8a shows the incident and transmitted time domain signals for a lattice consisting of $N = 15$ dissipative EMM unit cells. Comparing the time domain amplitudes in Fig. 8a with those in Fig. 7a it is hard to interpret any significant difference. However, for the frequency domain signals in Figs. 7b and 8b it is clear that increasing the number of unit cells significantly impacts the low-frequency attenuation performance for each case that damping is considered.

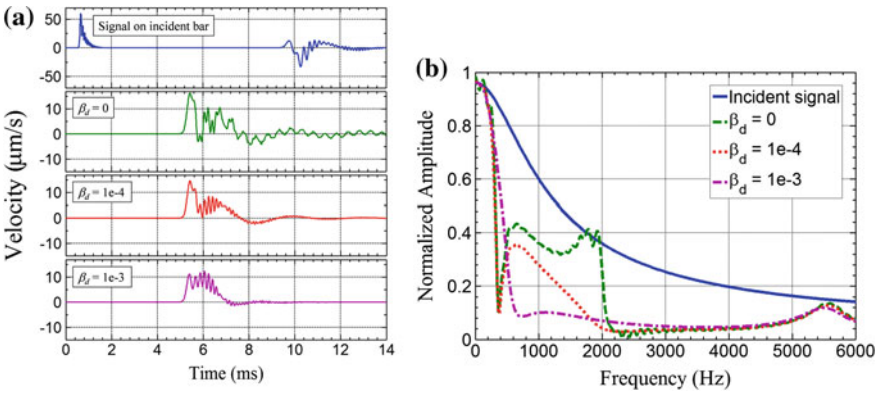

Fig. 7 Incident and transmitted signals under blast wave excitation for a five unit cell dissipative EMM lattice in **a** time and **b** frequency domains

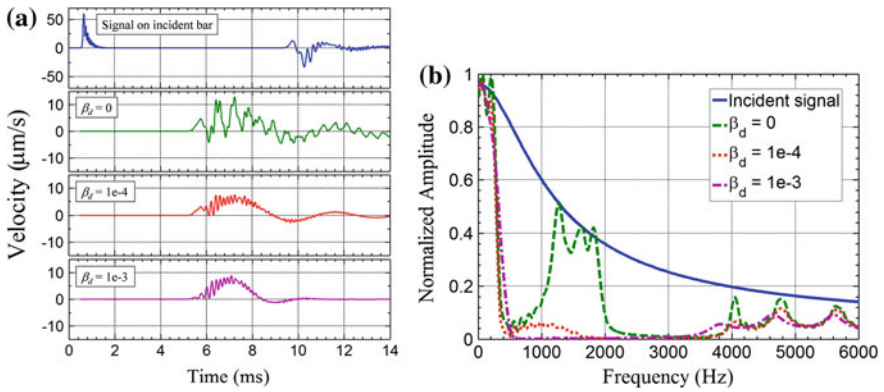

Fig. 8 Incident and transmitted signals under blast wave excitation for a 15 unit cell dissipative EMM lattice in **a** time and **b** frequency domains

4 Design of Sandwich Beams Containing Interior Dissipative Multi-resonators for Broadband Absorption and Mitigation

4.1 Modeling of an Infinite Sandwich Beam with Multiple Dissipative Resonators

A sandwich beam with multiple dissipative resonators embedded in the core is considered as shown in Fig. 9a. The dissipative resonators are represented by mass-spring-dashpot systems which are uniformly distributed over the entire length of the core. Generally, when the internal resonators are embedded into the sandwich core, some portion of the sandwich core materials will be drilled out. Thus, the bending stiffness or the strength of the sandwich host medium would be reduced slightly, and the total weight will be increased. However, through the design of special frames fitted into the voided areas, the strength of the sandwich host beam can be ensured as the original one.

The transfer matrix method is adopted for the derivation of the dispersion relations of this sandwich beam [30]. In the design for low-frequency wave attenuation, the lattice constant of the inner dissipative resonator is usually much larger than the dimension of the voided area in the sandwich core, which is used for inserting dissipative multi-resonators. For simplicity, we assume that the mechanical degradation (stiffness reduction) of the original sandwich material can be ignored because the void volume is much smaller than the overall volume of the sandwich core. Therefore, this composite structure is modeled as an equivalent sandwich beam periodically attached by two dissipative resonators on its face sheet, as shown in Fig. 9b. In the figure, the lattice constant of the beam is denoted as a. Also illustrated in the figure, the two resonant masses m_1 (inner mass), and m_2

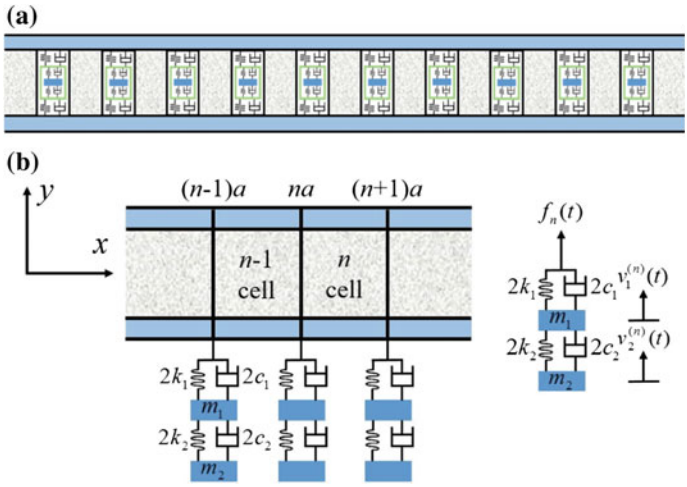

Fig. 9 **a** Schematic of a sandwich beam with embedded dissipative multi-resonators in the core. **b** An equivalent beam model of the sandwich structure

(outer mass) are connected by two linear springs and two dashpots in parallel and attached to the host sandwich beam. The linear spring constants and damping coefficients are represented by k_1, k_2, c_1, and c_2, respectively. In the model, the x-axis is defined on the neutral plane of the sandwich beam.

The sandwich beam is analytically modeled based on Timoshenko beam assumptions

$$GA\left[\frac{\partial\varphi(x,t)}{\partial x}-\frac{\partial^2 v(x,t)}{\partial x^2}\right]+\rho A\frac{\partial^2 v(x,t)}{\partial t^2}=0, \tag{6a}$$

$$EI\frac{\partial^2\varphi(x,t)}{\partial x^2}+GA\left[\frac{\partial v(x,t)}{\partial x}-\varphi(x,t)\right]-\rho I\frac{\partial^2 v(x,t)}{\partial t^2}=0, \tag{6b}$$

where EI is the bending rigidity, GA is the shear rigidity, ρA is the mass of the sandwich beam per unit length, and ρI is the rotatory inertia. v and φ denote the transverse displacement and the angle of rotation of the cross section of the sandwich beam around the z-axis, respectively.

The interactions between the host beam and dissipative resonators are represented by periodically distributed out of plane point forces. By considering the Bloch theorem and the continuity of the displacement, slope, bending moment and shear force at the interfaces between two adjacent unit cells, the wave dispersion relations can be calculated, from which the complex wavenumber is determined as a function of frequency [31].

4.2 Wave Transmission and Absorption in a Finite Sandwich Beam

When a flexural wave travels through a sandwich beam containing dissipative resonators, the wave would experience reflection, transmission, and absorption. Now we consider a unit section of the sandwich beam to investigate the wave power flow along a finite number of unit cells. For harmonic incidents, the input power flow can be written as [32]

$$P_{\text{in}} = \frac{1}{2}\text{Re}[-\text{i}\omega F_0 V^*(0)], \tag{7}$$

where the superscript, *, denotes the complex conjugate, F_0 and $V(0)$ are the amplitudes of the excited force and displacement at $x=0$. The wave energy absorption power by the dissipative resonators is given by

$$\begin{aligned} P_{\text{ab}} = \frac{1}{2}\text{Re}\{&2c_1\omega^2[V_1(l)-V(l)][V_1(l)-V(l)]^* \\ &+2c_2\omega^2[V_1(l)-V_2(l)][V_1(l)-V_2(l)]^*\}, \end{aligned} \tag{8}$$

where $V_1(l)$ and $V_2(l)$ are the displacements of masses m_1 and m_2 at $x=l$. $V(l)$ is the displacement of the sandwich beam at $x=l$. The wave absorption coefficients can be defined as $P_{\text{ab}}/P_{\text{in}}$.

To obtain the wave transmission and absorption coefficients of a sandwich beam with a finite number of unit cells, the transfer matrix method is applied. The flexural wave transmittance is defined as

$$T_N = \log\left|\frac{V_R^N}{V_L^1}\right|, \tag{9}$$

where V_L^1 is the transverse displacement at the left edge of the first unit cell and V_R^N is the transverse displacement at its right edge with N unit cells, respectively.

To quantitatively characterize wave attenuation in the sandwich beam, the flexural wave transmission properties of a finite sandwich beam containing 50 unit cells are performed and illustrated in Fig. 10. In the simulation, the sandwich beam is excited by transverse harmonic loads with different frequencies at the left side of the first unit cell. The dimensions and material constants of face sheets and foam core used in the calculation are summarized in Table 3, where the face sheets are laminated AS4/3501-6 $[0_2/90_2/0_2]$, and the core is Rohacell IG-51 foam [16]. The effective bending rigidity, shear rigidity, mass per unit length, and rotatory inertia of the sandwich beam are listed in Table 4. In the tables, h_f and h_c are the thickness of face sheets and foam core, respectively. b is the width of the beam. ρ_f and ρ_c are the density of face sheets and foam core, respectively. Because we are interested in demonstrating the optimal wave absorption properties in the low-frequency region,

Table 3 Dimensions and material constants of face sheets and foam core

h_f(m)	h_c(m)	a(m)	b(m)	ρ_f(kg/m^3)	ρ_c(kg/m^3)
7.62×10^{-4}	3.02×10^{-2}	0.048	0.019	1550	52.1

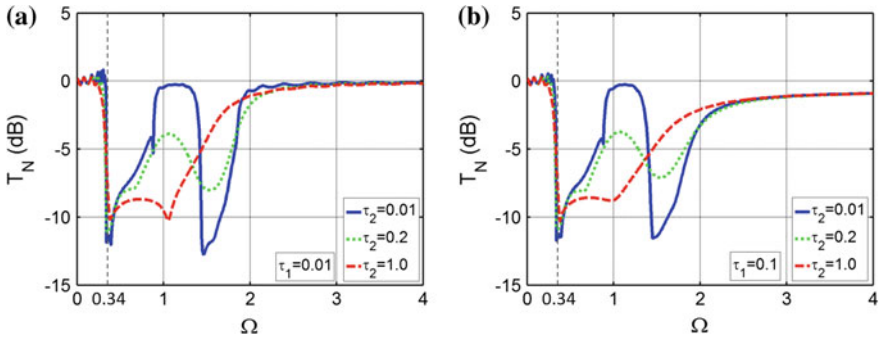

Fig. 10 Wave transmittance of a sandwich beam containing 50 unit cells with different damping coefficients: **a** $\tau_1 = 0.01$; **b** $\tau_1 = 0.1$

the inner damping coefficient is fixed as $\tau_1 = 0.01$ in the following simulation. As shown in Fig. 10a, strong wave attenuation in the two bandgap frequency regions is observed when the outermost damping coefficient is sufficiently small ($\tau_2 = 0.01$). However, when τ_2 is increased to 0.2 (dotted curve), the wave attenuation reduction around the second bandgap frequency range is 38%, and the bandwidth increment is 59%. A broad wave attenuation frequency range can still be observed when τ_2 is increased further to 1.0 (dashed curve). Therefore, with the increase of the outermost damping coefficient, the wave attenuation ability will be reduced although the wave attenuation frequency region will increase. Therefore, there is a trade-off between the wave attenuation amplitude and frequency range by selecting different damping coefficients τ_2. Similar wave transmission properties can also be observed with the increase of the damping coefficient τ_1, as shown in Fig. 10b. At lower frequencies, the transmission curves in Fig. 11 is almost the same for $\tau_1 = 0.01$ and $\tau_1 = 0.1$. Specifically, as illustrated in Fig. 7, the attenuation constants for the $\tau_2 = 0.01$ cases are almost unchanged in the region with the normalized frequency $\Omega < 1.3$, when τ_1 is increased from 0.01 to 0.1. Therefore, the transmission curves are shown in Fig. 10 are almost the same at the normalized frequency $\Omega < 1.3$ for the two cases. However, the second attenuation peak ($\Omega = 1.4$) is decreased when τ_1 is increased from 0.01 to 0.1, and thus produces an increased wave transmission amplitude in Fig. 10b. By increasing τ_1 from 0.01 to 0.1, the attenuation constant is increased at higher frequencies ($\Omega > 1.9$), and therefore, the wave transmission is reduced when $\Omega > 1.9$. Thus, it can be concluded that the damping effects could increase or decrease wave attenuation abilities of the metamaterial-based sandwich beams in which the wave attenuation ability is mainly caused by the local resonant motion when the input frequency approaches the local resonance.

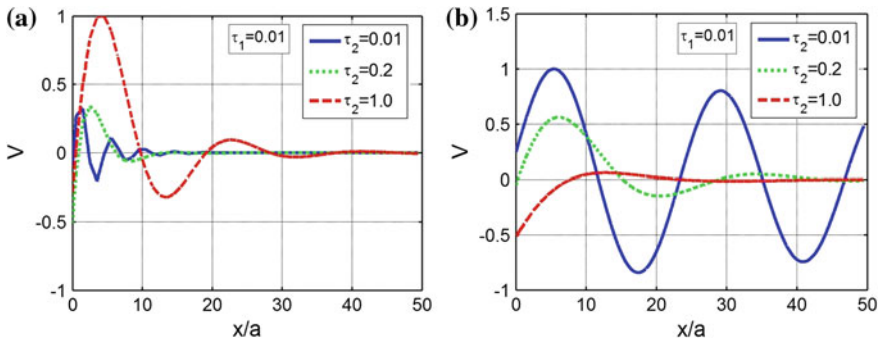

Fig. 11 **a** Wave profiles of the sandwich beam at the first resonant frequency ($\Omega = 0.34$) and $\tau_1 = 0.01$ when $\tau_2 = 0.01$, 0.2, and 1.0, respectively. **b** Wave profiles of the sandwich beam at $\Omega = 1.0$ and $\tau_1 = 0.01$ when $\tau_2 = 0.01$, 0.2, and 1.0, respectively

Table 4 Dimensions and material constants of face sheets and foam core

$EI(\text{Pa} \cdot \text{m}^4)$	$GA(\text{Pa} \cdot \text{m}^2)$	$\rho A(\text{kg/m})$	$\rho I(\text{kg} \cdot \text{m})$
677	1.15×10^4	0.075	1.31×10^{-5}

The global wave profiles of the sandwich beam with different damping coefficients, τ_2, are calculated in Fig. 11a, b for the normalized frequencies $\Omega = 0.34$ and $\Omega = 1.0$, respectively. In the simulation, the frequency $\Omega = 0.34$ is close to the first local resonant frequency of the multi-resonators. As illustrated in Fig. 11a, a significant spatial attenuation amplitude of the metamaterial-based sandwich beam is observed for the small damping constant $\tau_2 = 0.01$, and most of the incident wave energy is absorbed within ten unit cells. This is expected because most of the wave energy is transferred and absorbed by the large out-of-phase motions of the resonators instead of propagating through the system and therefore the out-of-phase mechanical motions (inertia forces) coupled with the damping eventually absorb the incoming wave. This holds true even if the damping coefficient is small, which is the so-called "metadamping" behavior. However, when the outermost damping coefficient τ_2 is increased to 1.0, which means a very large damping coefficient between the two local resonators, the connection between these two masses will become more rigid. Therefore, it can be observed from Fig. 11a that the attenuation constant is smallest at this frequency when τ_2 is increased to 1.0 and the flexural wave can travel a long distance and be attenuated mainly by the metadamping effect. On the other hand, as shown in Fig. 11b, when the input frequency is $\Omega = 1.0$ which is away from the local resonance, the wave attenuation ability of the metamaterial-based sandwich beam increases with the increase of the outermost damping coefficient τ_2. This is because the conventional damping plays a more important role in wave attenuation or absorption than the anti-resonant motions of the multi-resonators at this frequency. However, the conventional damping is not very efficient for wave absorption, especially for low-frequency cases.

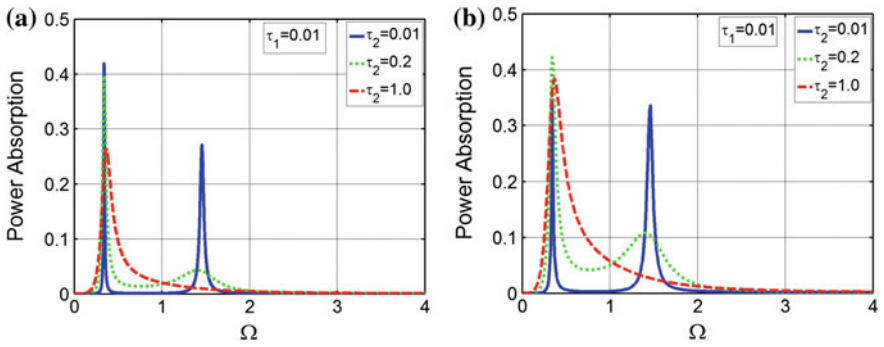

Fig. 12 **a** Power absorption efficiencies of the sandwich beam within one unit cell at $\tau_1 = 0.01$ when $\tau_2 = 0.01$, 0.2, and 1.0, respectively. **b** Power absorption efficiencies of the sandwich beam within two unit cells at $\tau_1 = 0.01$ when $\tau_2 = 0.01$, 0.2, and 1.0, respectively

Compared with the wave attenuation and reflection by conventional metamaterials, the wave absorption in the dissipative metamaterial has not been quantitatively investigated yet. By considering the effects of dissipative resonators on the power flow in the sandwich beam, the power absorption efficiencies (P_{ab}/P_{in}) of the sandwich beam within one unit cell are calculated based on Eqs. (7) and (8), respectively, and illustrated in Fig. 12a. In the simulation, the properties of the sandwich beam are the same as those in Fig. 11. The harmonic point force is applied at $x = 0$ and the magnitude of the force is assumed to be 1.0. As shown in Fig. 12a, the metadamping behavior can be further observed at the two resonant frequencies especially for the low damping coefficient $\tau_2 = 0.01$, and the power absorption is as high as 42% at the first resonant frequency. With the increase of the damping coefficient τ_2, the frequency absorption region becomes broader and the wave absorption efficiencies become lower especially for higher frequency cases. Therefore, to demonstrate the high wave absorption in a broadband frequency region, the number of the unit cell of dissipative metamaterials should be increased. Figure 12b shows the power absorption efficiencies (P_{ab}/P_{in}) of the sandwich beam within two unit cells. The material properties in the simulation are the same as those in Fig. 12a. It is interesting to note that the wave absorption efficiency will not increase at the first resonant frequency but will increase significantly at the second resonant frequency for a low damping coefficient $\tau_2 = 0.01$ with an increased number of unit cells. This means that the metadamping at the second resonant frequency could be enhanced by increasing the number of unit cells in the metamaterial beam. It should also be mentioned that the wave absorption efficiency could be enhanced in a very broad frequency region for the damping coefficient $\tau_2 = 0.2$. This result is very encouraging for developing a metamaterial-based sandwich beam for broadband wave absorption.

4.3 Transient Analysis of Blast-Induced Elastic Wave Mitigation

To validate the proposed design and demonstrate practical applications, we conduct a transient analysis of a sandwich beam with 20 unit cells of the proposed dissipative resonators to examine blast-induced elastic wave mitigations, as shown in Fig. 13. In the analysis, the linear wave response is considered for the sandwich structure, which should be very useful and adequate to capture the basic broadband wave attenuation and propagation mechanisms under the blast-induced elastic wave. The time domain finite element analysis is performed based on plane stress assumptions by using a commercial software, Abaqus/Explicit. The length of the host sandwich beam is carefully selected to suppress the wave reflected from the beam boundaries in simulations [16, 17]. The first group of dissipative resonators is located at $x = 0$ m and equally spaced with intervals being 0.01 m. Two probes are inserted into the left-hand side (5 m away from the first dissipative resonators) and right-hand side (2.2 m away from the 20th dissipative resonators) regions of the metamaterial section to measure the incident and transmitted signals. In simulations, the material and geometric parameters are the same as those used in Fig. 12. A transverse pulse is excited 10 m away from the metamaterial with the incident wave profile calculated as $F = F_0 \exp[-(t - t_0)/t_d]$, is applied to the left edge of the incident bar to generate a blast wave profile, where $F_0 = 1000$ N, $t_0 = 0.5$ ms and $t_d = 0.1$ ms.

Figure 14a shows time domain blast-induced elastic wave signals measured on the incident and transmission beams from the wave transmission simulations of the proposed sandwich beam. The signal presented in the upper window of Fig. 14a illustrates the applied force on the incident beam. The other two windows in the figure show transmitted signals without and with the proposed dissipative resonators, respectively. It can be seen from the figure that the peak amplitude of the transmitted signal will be decreased and the blast-induced elastic wave can be effectively attenuated in the proposed sandwich beam. Figure 14b shows the incident and transmitted blast-induced elastic wave signals in the frequency domain

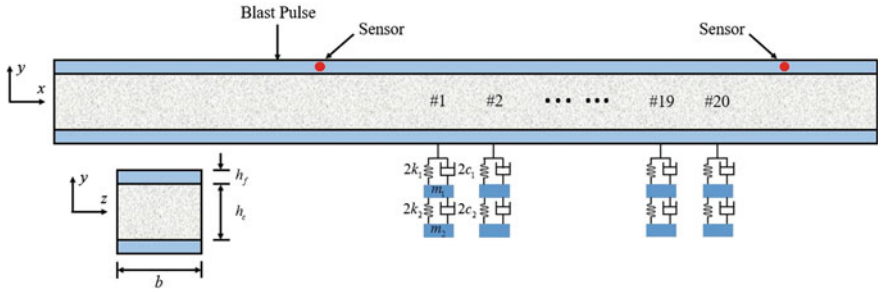

Fig. 13 Schematic design of transient analysis of a sandwich beam containing 20 unit cells under a blast-induced elastic pulse

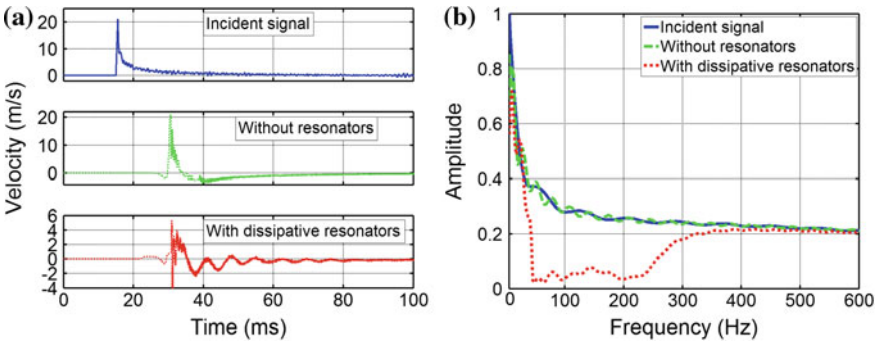

Fig. 14 Blast-induced elastic wave signals on the incident and transmitted beams of the sandwich beam containing 20 unit cells in the **a** time and **b** frequency domain

acquired from the sandwich beam with dissipative resonators. The frequency domain signals are calculated from the corresponding time domain signals through the Fast Fourier Transform (FFT). In the figure, a broadband wave transmission dip from approximately 40–350 Hz is observed, which agrees very well with that from analytical predictions (49–371 Hz). At those frequencies, the blast-induced elastic wave energy is significantly reflected and/or absorbed, compared with the incident blast-induced elastic wave. Thus, the metadamping behavior has been clearly illustrated through the time domain analysis. Since some low-frequency wave components are leaked from the dissipative metamaterials, geometric optimizations of the design will still be needed in future applications.

5 Conclusions

Concluding on the analysis presented in this chapter, two dissipative elastic metamaterial microstructural designs were evaluated for broadband energy absorption performance for the application of mitigating blast waves. Analytical and numerical models were used to obtain time and frequency domain transmission amplitudes to quantify the attenuation performance of the dissipative elastic metamaterial designs considered. It was found that specific damping components within the microstructural design have a significant impact on the final attenuation performance under incident blast wave signals. In each stage of the previous analysis, it was clearly demonstrated that by carefully selecting the constituent microstructural elements to maintain the locally resonant motions of the resonant masses, appropriate damping resulted in a significant increase in attenuation performance. The information presented in this chapter hopes to serve as a motivation for the development of multifunctional composite materials that can be used to effectively mitigate incident blast and/or shockwaves.

Acknowledgements This work was supported by the Air Force Office of Scientific Research under No. AF 9550-15-1-0061 with Program Manager Dr. Byung-Lip (Les) Lee.

References

1. Pendry, J. B. (2000). Negative refraction makes a perfect lens. *Physical Review Letters, 85,* 3966–3969.
2. Tanaka, T., Ishikawa, A., & Kawata, S. (2006). Unattenuated light transmission through the interface between two materials with different indices of refraction using magnetic metamaterials. *Physical Review B, 73,* 125423.
3. Cai, W., & Shalaev, V. (2010). *Optical metamaterials: fundamentals and applications*. New York: Springer.
4. Li, J., & Chan, C. T. (2004). Double-negative acoustic metamaterial. *Physical Review E, 70,* 055602(R).
5. Fang, N., Lee, H., Sun, C., et al. (2005). Sub-diffraction-limited optical imaging with a silver superlens. *Science, 308,* 534–537.
6. Yang, Z., Mei, J., Yang, M., et al. (2008). Membrane-type acoustic metamaterial with negative dynamic mass. *Physical Review Letters, 101,* 204301.
7. Mei, J., Ma, G. C., Yang, M., et al. (2012). Dark acoustic metamaterials as super absorbers for low-frequency sound. *Nature Communication, 3,* 756.
8. Chen, Y. Y., Huang, G. L., Zhou, X. M., et al. (2014). Analytical coupled vibroacoustic modeling of membrane-type acoustic metamaterials: Membrane model. *Journal of the Acoustic Society of America, 136,* 969–979.
9. Chen, Y. Y., Huang, G. L., Zhou, X. M., et al. (2014). Analytical coupled vibroacoustic modeling of membrane-type acoustic metamaterials: Plate model. *Journal of the Acoustic Society of America, 136,* 2926–2934.
10. Liu, Z., Zhang, X., Mao, Y., et al. (2000). Locally resonant sonic materials. *Science, 289,* 1734–1736.
11. Yao, S. S., Zhou, X. M., & Hu, G. K. (2008). Experimental study on negative effective mass in a 1D mass-spring system. *New Journal of Physics, 10,* 043020.
12. Huang, H. H., Sun, C. T., & Huang, G. L. (2009). On the negative mass density in acoustic metamaterials. *International Journal of Engineering Science, 47,* 610–617.
13. Lai, Y., Wu, Y., Sheng, P., et al. (2011). Hybrid elastic solids. *Nature Materials, 10,* 620–624.
14. Liu, X. N., Hu, G. K., Huang, G. L., et al. (2011). An elastic metamaterial with simultaneously negative mass density and bulk modulus. *Applied Physics Letters, 98,* 251907.
15. Zhu, R., Liu, X. N., Hu, G. K., et al. (2014). Negative refraction of elastic waves at the deep subwavelength scale in a single-phase metamaterial. *Nature Communication, 5,* 5510.
16. Chen, J. S., & Sun, C. T. (2011). Dynamic behavior of a sandwich beam with internal resonators. *Journal of Sandwich Structures & Materials, 13,* 391–408.
17. Chen, J. S., Sharma, B., & Sun, C. T. (2011). Dynamic behaviour of sandwich structure containing spring-mass resonators. *Composite Structures, 93,* 2120–2125.
18. Sharma, B., & Sun, C. T. (2016). Impact load mitigation in sandwich beams using local resonators. *Journal of Sandwich Structures & Materials, 18,* 50–64.
19. Huang, G. L., & Sun, C. T. (2010). Band gaps in a multiresonator acoustic metamaterial. *Journal of Vibration and Acoustics, 132,* 031003.
20. Tan, K. T., Huang, H. H., & Sun, C. T. (2014). Blast-wave impact mitigation using negative effective mass density concept of elastic metamaterials. *International Journal of Impact Engineering, 64,* 20–29.
21. Zhu, R., Liu, X. N., Hu, G. K., et al. (2014). A chiral elastic metamaterial beam for broadband vibration suppression. *Journal of Sound and Vibration, 333,* 2759–2773.

22. Chen, J. S., & Huang, Y. J. (2016). Wave propagation in sandwich structures with multiresonators. *Journal of Vibration and Acoustics, 138,* 041009.
23. Hussein, M. I., & Frazier, M. J. (2013). Metadamping: An emergent phenomenon in dissipative metamaterials. *Journal of Sound and Vibration, 332,* 4767–4774.
24. Manimala, J. M., & Sun, C. T. (2014). Microstructural design studies for locally dissipative acoustic metamaterials. *Journal of Applied Physics, 135,* 023518.
25. Pai, P. F., Peng, H., & Jiang, S. (2014). Acoustic metamaterial beams based on multi-frequency vibration absorbers. *International Journal of Mechanical Sciences, 79,* 195–205.
26. Del Prete, E., Chinnayya, A., Domergue, L., et al. (2013). Blast wave mitigation by dry aqueous foams. *Shock Waves, 23,* 39–53.
27. Su, Z., Peng, W., Zhang, Z., et al. (2007). Numerical simulation of a novel blast wave mitigation device. *International Journal of Impact Engineering, 35,* 336–346.
28. Su, Z., Peng, W., Zhang, Z., et al. (2009). Experimental investigation of a novel blast wave mitigation device. *Shock and Vibration, 16,* 543–553.
29. Chen, Y., Huang, W., & Constantini, S. (2012). Blast shock wave mitigation using the hydraulic energy redirection and release technology. *PLoS ONE, 7,* e39353.
30. Liu, L., & Hussein, M. I. (2012). Wave motion in periodic flexural beams and characterization of the transition between Bragg scattering and local resonance. *Journal of Applied Mechanics, 79,* 011003.
31. Collet, M., Ouisse, M., Ruzzene, M., et al. (2011). Floquet-Bloch decomposition for the computation of dispersion of two-dimensional periodic, damped mechanical systems. *International Journal of Solids and Structures, 48,* 2837–2848.
32. Pinnington, R. J., & White, R. G. (1981). Power flow through machine isolators to resonant and non-resonant beams. *Journal of Sound and Vibration, 75,* 179–197.

Blast Mitigation Through the Operation of Steering the Incoming Wave by the Use of Active Metamaterial Structure

Sathya Hanagud and Pavitra Manghaiapathy

1 Introduction

The currently used procedures for blast mitigation are as follows. The first option is to design and fabricate the structure to withstand the expected blast wave. A second option is to design, fabricate a protective shield, and place the shield between the structures to be protected and the blast wave. It is expected that the shield absorbs the energy of the incoming blast wave and attenuates the stresses to a level that the protected structure can withstand the stresses safely (Fig. 1).

The goals of this paper are to propose a new option that has the potential to steer the incoming blast wave away from the structure, to be protected (Fig. 2).

The steering of the wave is planned by the use of tunable or active metamaterial structural (AMMS) system. In the following sections, different steps of the foundations, the design, and implementation of the AMMS system are explained.

S. Hanagud (✉) · P. Manghaiapathy
School of Aerospace Engineering, Georgia Institute of Technology,
Atlanta, GA 30332-0150, USA
e-mail: hanagud@ae.gatech.edu

S. Gopalakrishnan and Y. Rajapakse (eds.), *Blast Mitigation Strategies in Marine Composite and Sandwich Structures*, Springer Transactions in Civil and Environmental Engineering, https://doi.org/10.1007/978-981-10-7170-6_20

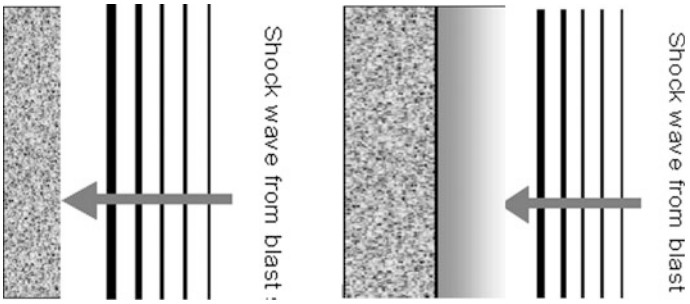

Fig. 1 Current blast wave mitigation options

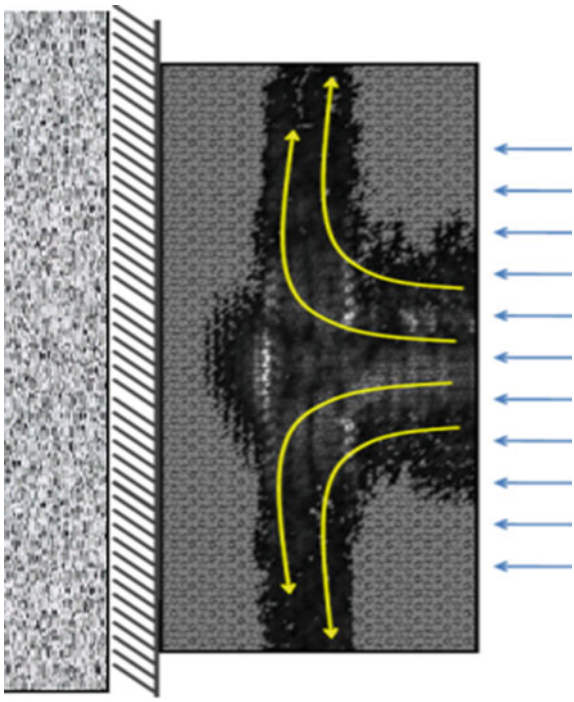

Fig. 2 Blast mitigation through steering the incoming wave

2 Background 1: Veselago and the Negative Refractive Index

The basic foundations are from the 1968 paper of Veselago [1] and his work on the concept of negative refraction in optical or electromagnetic waves.

$$\nabla \cdot \mathbf{E} = 0 \quad \nabla \times \mathbf{E} = -\frac{\partial \mathbf{B}}{\partial t},$$
$$\nabla \cdot \mathbf{B} = 0 \quad \nabla \times \mathbf{B} = \frac{1}{c^2}\frac{\partial \mathbf{E}}{\partial t}.$$

$$c = \frac{1}{\sqrt{\mu_0 \varepsilon_0}} = 2.99792458 \times 10^8 \,\mathrm{m\,s^{-1}} \tag{1}$$

$$\mathbf{B} = \mu \mathrm{H}$$
$$\mathbf{D} = \varepsilon \mathbf{E}.$$

In this equation, E is the electric field, B is the magnetic field, c is wave velocity in a vacuum, ε is the electrical permeability, μ is the magnetic permittivity, D is electrical displacement, and H is the magnetizing field. Veselago clearly shows that negative refraction is the result when at the same frequency ω,

$$\varepsilon(\omega) < 0 \text{ and } \mu(\omega) < 0, \tag{2}$$

the resulting refractive index n is negative.

$$\mathrm{n} = -\sqrt{\varepsilon \mu} \tag{3}$$

Optical rays through a material, with positive refractive index, bend as shown in the Fig. 3a. However, an optical ray through a material, with a negative refractive index, bend in the opposite direction as shown in the Fig. 3b.

If such a negative refractive index material is available one can think of several options. A first option is the optical cloaking. Because the wave propagation characteristics are similar, a second option is acoustic cloaking. Another option is cloaking in elastodynamic solids and efforts to steer blast waves away from the protected structure. However, at the time of Veselago's paper, no natural negative

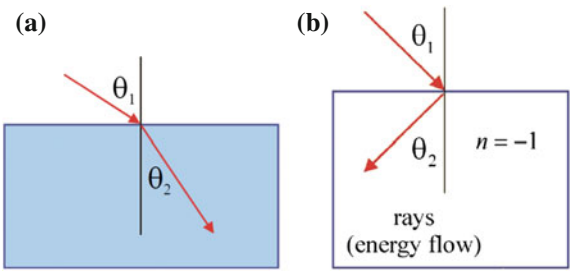

Fig. 3 **a** A ray through a positive refractive index material. **b** A ray through a negative refractive index material

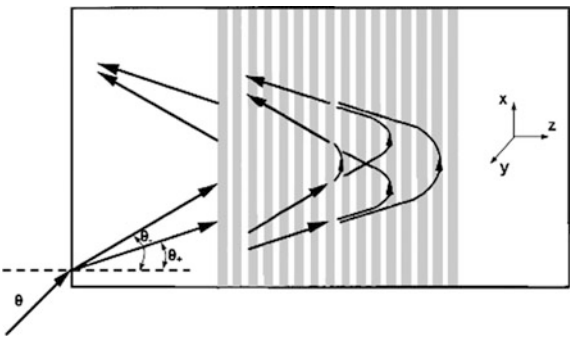

Fig. 4 A cartoon of expectation

index material existed. Thus, one could only think of a cartoon of possibilities, as shown in the following figure (Fig. 4).

3 Background 2: Option of Metamaterials

Approximately, 30 years, following the paper by Veselago, scientists started thinking of the concept metamaterials or materials with embedded structures. Pendry and others [2–4] explored the techniques to design and build metamaterials that had the negative refractive index. The results of the research indicated the possibility to design such a needed metamaterial. However, from the point of view of optical applications, it was observed that the internal structure that was to be embedded inside the host of the metamaterial had to be smaller than the optical wavelengths. Optical wavelengths are very small. Thus, Cummer et al. [5–10] initiated research to explore acoustic cloaking concepts where the wavelengths are larger than the optical wavelengths. They had a notable success.

In 2006, Pendry et al. [10–12] reported a new powerful technique to control the electromagnetic field. This technique was to design the needed subwavelength structure by using by coordinate transformation technique. The goal of the technique was to hide an arbitrary object. For illustration, they selected a sphere of radius R_1. In order to cloak this sphere, they applied the coordinate transformation, from the coordinates $\mathrm{r}, \vartheta, \varphi$ to $\mathrm{r}', \vartheta', \varphi'$ in the region $R_1 < r < R_2$. The transformation is achieved by taking all the fields in the region $\mathrm{r} < R_2$ and compressing them into the region $R_1 < r < R_2$, with the following transformation

$$\begin{aligned} \mathrm{r}' &= R_1 + \mathrm{r}(R_2 - R_1)/R_2 \\ \vartheta' &= \vartheta \\ \varphi' &= \varphi \end{aligned} \tag{4}$$

Then, as described by the authors the transformation and Maxwell's equations yield a spatial distribution of permeability and permittivity to realize the cloaking of the region $r < R_1$.

In the region $R_1 < r < R_2$,

$$\begin{aligned} \varepsilon_{r'}' &= \mu_{r'}' = [R_2/(R_2 - R_1)]\left[(r' - R_1)^2/r'\right] \\ \varepsilon_{\vartheta'}' &= \mu_{\vartheta'}' = [R_2/(R_2 - R_1)] \\ \varepsilon_{\phi'}' &= \mu_{\phi'}' = [R_2/(R_2 - R_1)]. \end{aligned} \tag{5}$$

Thus, the permeability and permittivity varied depending on the spatial location. Thus, it became necessary to fabricate a metamaterial with spatially varying permeability and permittivity. Again, because of very small wavelengths in optical systems methods were not available to fabricate such metamaterials.

However, Cummer and Schurig [7] thought that it is possible to achieve acoustic cloaking because of larger acoustic wavelengths and analogy between acoustic equations and Maxwell's equations, where the equation structure did not change with the transformation of coordinates. Unlike the anisotropic distribution of electric permeability and magnetic permittivity in optical cloaking, the acoustic cloaking required metamaterials with anisotropic mass density distribution in the metamaterial. The work was on cylindrical symmetric cloaking. Later Chen and Chan [6] extended the work to spherical symmetrical cloaking, with anisotropic density distribution. There are also some reported literature on acoustic carpet cloaking, with experiments, to hide selected objects. Other acoustic cloaking works include sound cancellation and directional cloaking. These works are reviewed by Noriss [8].

4 Background 3: Cloaking of Elastodynamic Systems

Cloaking in fields other than the electromagnetic field and acoustic field, by using transformational techniques pose problems. The inherent two waves in elastic structures pose a challenge to cloaking. Yet there are some interesting papers by Brun et al. [13].

Because Maxwell's equations retain their form, with coordinate transformations, authors such as Pendry et al., were able to bend electromagnetic waves around selected objects of varying sizes and shapes, to produce invisibility cloaking. However, the coordinate transformation, resulted in heterogeneous and anisotropic permeability and permittivity. Yet, elastodynamic waves and shock waves in solids have not received the same level of attention as electromagnetic waves or acoustic waves. Even the simpler case of Navier's equations that govern elastodynamics do not always retain their form under a coordinate transformation.

In 2009, Brun et al. [13–17] showed that it is possible to design elastic-cylindrical cloaking for in-plane coupled pressure and shear waves. However with transformed coordinates, they had to allow the elasticity tensor in transformed coordinates to become asymmetric, in addition to the spatial variation of the density. They also used finite element calculations to validate their results through numerical simulation. In 2014, Diatta and Guenneau [18] showed that it also is possible design cloaking with spherical elastic waves

5 Contributions of This Paper

By using the concept of transformation of coordinates, Pendry obtained spatial distributions of electrical permeability and magnetic permittivity that can successfully conceal or cloak a sphere from incoming radiation. Similarly, Brun, Norris, Guenneau, Diatta, and others have discussed cloaking for elastic waves by using the concept of transformation of coordinates. The requirements for cloaking resulted in a spatial distribution of density and asymmetric elastic constants. The derived elastic cloaking has also been validated by finite element calculations.

However, in the case of cloaking with electromagnetic waves or cloaking or with elastic waves, techniques do not extend to the level of practically producing natural materials or metamaterials that have these properties that can cloak a selected object. For example, we do not have materials or metamaterials that have such distributions of permeability and permittivity for cloaking with electromagnetic waves. Similarly, we do not have natural materials or metamaterials, with desired density distributions or elastic modulus distributions for controlling elastic waves. Thus, the objective of this paper is to develop and demonstrate AMMS that can provide the needed density or elastic modulus through selected actuators that can function on the basis of active control laws. This new concept of AMMS is based on the previous demonstration of active damping AAMS that was developed and practically demonstrated by one of the authors [19, 20] of this paper. A brief description of the active damping AAMS is as follows.

Many high-performance aircraft are designed to operate at high angles of attack. For example, F-15 aircraft can fly at 23° of the angle of attach and FA/18 up to 35°. These high-performance aircraft also have twin vertical tails. When operating at high angles of attack vortices form at the intersection of the fuselage and the wing. As they flow down the aircraft vortices break-up due to instability and impact the vertical tails, with a broad band of frequencies and induce what is known as “buffet-induced vibrations.” Buffet or buffeting is a nonlinear aeroelastic phenomena. The effect of such buffet-induced vibrations results in fatigue damage and cannot be eliminated by passive structural design changes. It is necessary to design (Fig. 5) and Implement active controllers to alleviate these buffet-induced vibrations. Hanagud and his colleagues have designed and shown via tests that such controllers need AMMS.

Fig. 5 High-performance aircraft with buffet

For purposes of illustration, we assume that the structural system of the vertical tail, with its attachment to the fuselage can be represented approximately by one degree of system. The equation is as below:

$$\xi + 2\zeta_s \omega_s \xi + \omega_s^2 \xi = (\mathrm{f(t)/m}) \tag{6}$$

In this equation, ξ is the deflection of the vertical tail, ω_s is the natural frequency, and ζ_s = (c/2 m ω_s) is known as the damping ratio that governs the rate of alleviation of vibration amplitudes. Usually in most structural systems and in our case $\zeta_s = 0.02$. To alleviate buffet-induced vibrations, we need values of ζ_s upto 0.2. Currently, there are no such aircraft structural materials, with such a damping ratio.

Thus, our option was to develop a AMMS to provide the high damping ratio. This development was in two steps. In the first step, we developed a compensator that was used to achieve the needed damping ratio, up to 0.2. The compensator resides in a computer that received an input from the measurements on the vertical tail. Then, the combined equations for the vertical tail and the compensator took the following form.

$$\xi + 2\zeta_s \omega_s \xi + \omega_s^2 \xi = (\mathrm{f(t)/m}) + \mathrm{g}\omega_c^2 \eta \tag{7}$$

$$\ddot{\eta} + 2\zeta_c \omega_c \dot{\eta} + \omega_c^2 \eta = \omega_s^2 \xi \tag{8}$$

Then, the parameters ω_c, ζ_c and the gain g were designed by Hanagud and his colleagues to achieve the closed-loop damping ratio of 0.2. This completed the first step. In the second step, we had developed a metamaterial structure to implement the control force or control effort (g ω_c^2 η), in Eq. (7), on the structure. Unlike the compensator that resides in a computer, it was necessary to develop technique to

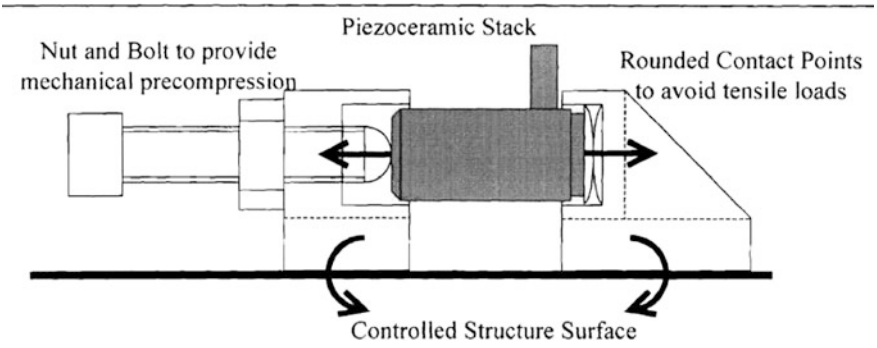

Fig. 6 Offset piezoceramic stack AMMS assembly

implement on the structure of the vertical tail and was known as efforts to achieve the control authority. This was achieved by designing, fabricating and attaching an "offset piezoceramic stack assembly" that was as shown in the following figure (Fig. 6).

The metamaterial structural assembly consists of a piezoceramic stack that had the capability of providing very high actual forces (with an appropriate electric field) that are converted into large bending moments through a carefully designed assembly.

The metamaterial structural assembly was tested in wind tunnel tests, with a one-sixteenth aeroelastic scale model of F-15 and a full scale F-15 vertical tail. The effectiveness of the AMMS in alleviating the buffet-induced vibration was evident in the following figure (Fig. 7).

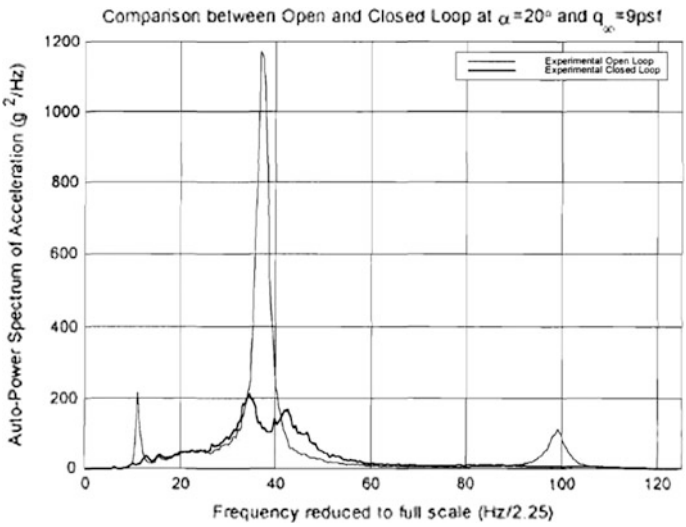

Fig. 7 Effect of active MMS for large damping

The previous few paragraphs explain the feasibility of AMMS for damping applications. Now, the application to elastic cloaking application is explored.

6 Active MMS for Cloaking in Elastodynamic Systems

The concept of AMMS concept has been discussed with reference to acoustic cloaking. They use piezoelectric materials to change the dynamic density or to control the directional propagation of the acoustic energy. With reference to elastic cloaking, periodically placed piezoelectric sensor and actuator pairs and proportional feedback control are used to actively change the stiffness of linear elastic beAAMS. However, as described later, the elastic cloaking concepts require changing specified elastic constants, specified densities, or a combination of specified elastic constants and densities in the form of wave velocities.

Specifically, let us consider, the work of Brun et al., in achieving cylindrical cloaking for in-plane shear and pressure waves. They start with Navier's equations for elastodynamics and use a transformation of coordinates, similar to the transformation by Pendry and others for electromagnetic systems. The objective of the transformation is to cloak a cylindrical region r_0 to r_1, by transforming the coordinates from (r, ϑ) to (r′, ϑ′).

$$\mathrm{r}' = r_0 + \mathrm{r}(r_1 - r_0)/r_1; \vartheta' = \vartheta \quad \mathrm{r} < r_1 \tag{9}$$

$$\mathrm{r}' = \mathrm{r}; \vartheta' = \vartheta \quad \mathrm{r} > r_1 \tag{10}$$

Following the transformation the form of the Navier's equation changes. The density

$$\mathrm{P} = \rho\{(\mathrm{r} - r_0)/\mathrm{r}\}\{r_1(r_1 - r_0)\}^2 \tag{11}$$

The elastic constants λ and μ change to

$$C_{ijkl} = \mathrm{F}(\lambda, \mu, \mathrm{r}, r_0) \tag{12}$$

Thus, we need metamaterials with density and elastic constants and their changes as functions of r. If we consider segments of width Δr, we can approximate each segment to have new constant density and new elastic constants. The next questions are as follows. How to we design such a material and produce those densities and elastic constants, in practice. In the next paragraphs, a two step procedure is described to design such an AMMS and produce the material using the concept.

To explain and demonstrate the two step procedure, we consider, the case of longitudinal vibrations. As a first case, we consider a uniform linearly elastic rod of length L, modulus of elasticity E, and density ρ. The wave velocity is c. The rod

extends from x, ξ = 0 to ξ = L. The boundary x • ξ = L is a fixed end and a time-dependent displacement u = A sin Ωt is applied at x, ξ = 0. The differential equation for the problem is as follows.

$$c^2 \frac{\partial^2 u}{\partial x^2} = \frac{\partial^2 u}{\partial t^2} \tag{13}$$

To accommodate the inhomogeneous boundary condition at x,ξ = 0, we introduce a function g

$$u(x,t) = u_1(x,t) + g(x)(A \sin \Omega t) \tag{14}$$

By solving the resulting homogeneous equation and the resulting forced vibration problem; retaining only the first mode equation as an approximate representation of the forced vibration problem; and adding a modal damping term, we obtain the following equation.

$$\ddot{\xi} + 2\zeta_s \omega_s \dot{\xi} + \omega_s^2 \xi = Q_1(\mathrm{t}) \tag{15}$$

In this equation, ω_s is the first natural frequency and equal to (πc/L) = (π/L) $\left(\sqrt{(E)}/\rho\right)$. The quantity ζ_s is the damping ratio and is usually 0.02 for many structural materials.

In elastic cloaking, by the use of transformation of coordinates, the new MMS contains changed elastic constants and changed density ρ in each strip of width Δr. Also, the elastic constant and density distribution can change spatially. First, we describe how the elastic constants and density can be changed from E to a different value E_1 and ρ to a different value ρ_1. Then, we address the issue of changing the spatial distributions of elastic constants and densities.

In the Eq. (15), E and ρ are combined in the form of ω_s.

$$\omega_s = (\pi \mathrm{c}/\mathrm{L}) = (\pi/\mathrm{L})(\sqrt{(E/\rho)}). \tag{16}$$

Thus, the first objective is to change ω_s to $\omega_f = A\omega_s$, where A can have different values specified values such as 1.1, 0.9, 1.2, 1.5, 2.0. 6.0. This process is in two steps. In the first step, we introduce a compensator which receives an input from the elastodynamic system represented by the Eq. (15). The compensator resides in a computer and feeds back the results of the computations to the elastodynamic system to achieve the following result.

$$\omega_s \rightarrow \omega_f = A\omega_s \tag{17}$$

The combined elastodynamic equation, the compensator, including feedback are as follows (Fig. 8).

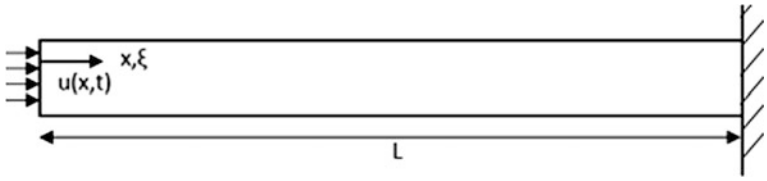

Fig. 8 Elastodynamic system for longitudinal vibrations

$$\begin{aligned} \ddot{\xi} + 2\zeta_s\omega_s\dot{\xi} + \omega_s^2\xi &= Q_1 + g\omega_c^2\eta \\ \ddot{\eta} + 2\zeta_c\omega_c\dot{\eta} + \omega_c^2\eta &= \omega_s^2\xi \end{aligned} \tag{18}$$

In these equations, the compensator receives the input in the form of the position ξ of the elastodynamic system. The quantity Q_1 represents the external input at the boundary of the elastodynamic system. 'g $\omega_c^2\eta$' is the feedback to the elastodynamic system from the compensator. In practice, this needs an actuator assembly or AMMS assembly, similar to the one described for buffet-induced damping alleviation.

To change ω_s to $\omega_f = A\omega_s$, we first obtain the following transfer function.

$$\frac{\xi(s)}{Q_1(s)} = \frac{\left[s^2 + 2\zeta_c\omega_c s + \omega_c^2\right]}{\left[s^2 + 2\zeta_s\omega_s s + \omega_s^2\right]\left[s^2 + 2\zeta_c\omega_c s + \omega_c^2\right] - g\omega_s^2\omega_c^2} \tag{19}$$

To realize desired frequency ω_f, we equate the denominator of the transfer function to the expected square of the desired denominator of the transfer function. The operation of squaring is to obtain only one desired frequency in the closed-loop system.

$$\left[s^2 + 2\zeta_s\omega_s s + \omega_s^2\right]\left[s^2 + 2\zeta_c\omega_c s + \omega_c^2\right] + abg\omega_c^2 s^2 = \left(s^2 + 2\zeta_f\omega_f s + \omega_f^2\right)^2 \tag{20}$$

The quantity $\omega_f = A\omega_s$ = A(π/L) $\left(\sqrt{(E)}/\rho\right)$ is specified, for each given value of A. Then, the objectives of the design are to determine ζ_c, ω_c, g and ζ_f, from Eq. (20). This requires equating the coefficients of different powers of the s. Thus, we obtain four equations for four unknowns.

$$\begin{aligned} &\mathbf{S^3}: \mathbf{2}(\boldsymbol{\zeta_c\omega_c} + \boldsymbol{\zeta_s\omega_s}) = \mathbf{4}\boldsymbol{\zeta_f\omega_f} \\ &\mathbf{S^3}: \boldsymbol{\omega_c^2} + \mathbf{4}\boldsymbol{\zeta_c\zeta_s\omega_c\omega_s} + \boldsymbol{\omega_s^2} = \mathbf{2}\boldsymbol{\omega_f^2} + \mathbf{4}\boldsymbol{\zeta_f^2\omega_f^2} \\ &\mathbf{S^1}: \mathbf{2}\boldsymbol{\omega_c\omega_s}(\boldsymbol{\zeta_s\omega_c} + \boldsymbol{\zeta_c\omega_s}) = \mathbf{4}\boldsymbol{\zeta_f\omega_f^3} \\ &\mathbf{S^0}: -(\mathbf{-1} + g)\boldsymbol{\omega_c^2\omega_s^2} = \boldsymbol{\omega_f^4} \end{aligned} \tag{21}$$

The following table shows the possible solution sets since the value of A = 1.1 and 2.0 gives two possible solutions:

	Sol 1: $A = 1.1$	Sol 2: $A = 1.1$	Sol 1: $A = 2.0$	Sol 2: A = 2.0
ζ_f	0.0272727	3.20909	0.015	25.015
$\frac{\omega_c}{\omega_s}$	1.19164	7.1007	2.64575	100.035
ζ_c	0.0251754	0.990043	0.0113389	0.99995
g	−0.0310563	0.970962	−1.28571	0.998401

These values of parameters are checked for stability by using Routh–Hurvitz criteria; and examined for practical implementation. For practical implementation, it is important that the controller parameters are close to the structural parameters. Thus, solution 1 is selected.

6.1 Acceleration Feedback

Instead of an input of deflected position ξ to the compensator, we input the acceleration to the compensator.

$$\begin{aligned} &\ddot{\xi} + 2\zeta_s\omega_s\dot{\xi} + \omega_s^2\xi = Q_1 - ag\omega_c^2\eta \\ &\ddot{\eta} + 2\zeta_c\omega_c\dot{\eta} + \omega_c^2\eta = b\ddot{\xi} \end{aligned} \tag{23}$$

The constants a and b result from the measurement system that converts the acceleration to electrical signals. As in the case of the position feedback the next step is to obtain the needed transfer function.

$$\frac{\xi(s)}{Q_1(s)} = \frac{\left[s^2 + 2\zeta_c\omega_c s + \omega_c^2\right]}{\left[s^2 + 2\zeta_s\omega_s s + \omega_s^2\right]\left[s^2 + 2\zeta_c\omega_c s + \omega_c^2\right] + abg\omega_c^2 s^2} \tag{24}$$

Then, equate the denominator of the transfer function to the denominator of the desired transfer function in terms of ω_f and has coincident natural frequency because we need only one ω_f.

$$\left[s^2 + 2\zeta_s\omega_s s + \omega_s^2\right]\left[s^2 + 2\zeta_c\omega_c s + \omega_c^2\right] + abg\omega_c^2 s^2 = \left(s^2 + 2\zeta_f\omega_f s + \omega_f^2\right)^2 \tag{25}$$

To determine compensator parameters and, we equate the coefficients of the powers of s.

$$\begin{aligned} &\mathbf{S^3}: \mathbf{2}(\boldsymbol{\zeta_c\omega_c + \zeta_s\omega_s}) = \mathbf{4}\boldsymbol{\zeta_f\omega_f} \\ &\mathbf{S^2}: (\mathbf{1} + \boldsymbol{abg})\boldsymbol{\omega_c^2} + \mathbf{4}\boldsymbol{\zeta_c\zeta_s\omega_c\omega_s} + \boldsymbol{\omega_s^2} = \mathbf{2}\boldsymbol{\omega_f^2} + \mathbf{4}\boldsymbol{\zeta_f^2\omega_f^2} \\ &\mathbf{S^1}: \mathbf{2}\boldsymbol{\omega_c\omega_s}(\boldsymbol{\zeta_s\omega_c + \zeta_c\omega_s}) = \mathbf{4}\boldsymbol{\zeta_f\omega_f^3} \\ &\mathbf{S^0}: \boldsymbol{\omega_c^2\omega_s^2} = \boldsymbol{\omega_f^4} \end{aligned} \tag{26}$$

To solve this system of equations, $\zeta_s = 0.03$, consider $\omega_f = A\omega_s$ and $\omega_c = B\omega_s$ and solve for the ration B and the values of ζ_c, ζ_f and gain constant g.

	$A = 1.1$	$A = 1.2$	$A = 0.9$	A = 2.0	$A = 0.5$
ζ_f	0.0301364	0.0305	0.0301667	0.0375	0.0375
$\frac{\omega_c}{\omega_s}$	1.21	1.44	0.81	4	0.25
ζ_c	0.03	0.03	0.03	0.03	0.03
g	$\frac{-0.0300938}{ab}$	$\frac{-0.0932802}{ab}$	$\frac{-0.0549726}{ab}$	$\frac{-0.561994}{ab}$	$\frac{-8.9919}{ab}$

7 Active MMS Where Elastic Constants' Density and ω_f Vary as Functions of Space

As Brun et al., indicate the transformation of coordinates for cloaking the elasto-dynamic system result in a spatial distribution of elastic constants and densities. By considering strips of segments of radius Δr, the elastic constants and densities are constant in each segment. Again, the example of longitudinal vibration of a linear elastic rod is used illustrate how the concept of the two-step AMMS design can be used accomplish the design. The following figure illustrates the original beam, with one elastic constant E and one density ρ throughout the beam, before implementing the coordinate transformation (Fig. 9).

Following the coordinate transformation, for cloaking, a simple configuration has E_1 and ρ_1, for $0 < x_1 < \mathrm{L}$; and E_2 & ρ_2, for $0 < x_2 < \mathrm{l}$ (Fig. 10).

The objective is to design procedures to change E, ρ, c to E_1, ρ_1, c_1 for $0 \le x_1 \le \mathrm{L}$; and E_2, ρ_2, c_2 for $0 \le x_2 \le \mathrm{L}$. The procedure is as follows.

First consider the uniform beam, with same elastic constants and density on both sides, the equations are as follows.

$$\begin{aligned} &\text{For } 0 \le x_1 \le L \quad c^2 \frac{\partial^2 u_1}{\partial x^2} = \frac{\partial^2 u_1}{\partial t^2} \\ &\text{For } 0 \le x_2 \le L \quad c^2 \frac{\partial^2 u_2}{\partial x^2} = \frac{\partial^2 u_2}{\partial t^2} \end{aligned} \tag{27}$$

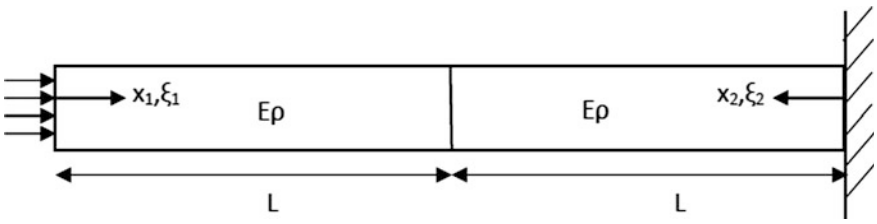

Fig. 9 Longitudinal vibrations with same E and ρ in both section

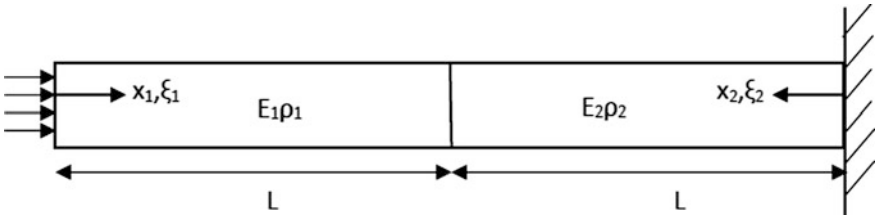

Fig. 10 Longitudinal vibrations with spatial distribution of E and ρ

To include homogeneous boundary conditions, consider

$$\begin{aligned} u_1 &= \overline{u_1}(x_1, t) + g_1(x_1)u_o(t) \\ u_2 &= \overline{u_2}(x_2, t) + g_2(x_2)u_o(t) \end{aligned} \tag{28}$$

We obtain functions g_1 and g_2 to make the boundary conditions homogeneous and simplify the resulting transformed differential equations by setting

$$\frac{d^2 g_1}{dx_1^2} = 0 \text{ and } \frac{d^2 g_1}{dx_1^2} = 0, \tag{29}$$

Then,

$$\begin{aligned} g_1 &= -\frac{1}{2L}x_1 + 1 \\ g_2 &= -\frac{1}{2L}x_2 \end{aligned} \tag{30}$$

We find natural frequencies, modes, and solve the resulting inhomogeneous differential equations.

$$\begin{aligned} c_1^2 \frac{\partial^2 \overline{u}}{\partial x_1^2} &= \frac{\partial^2 \overline{u}}{\partial t^2} + g_1(x)\ddot{u}_0 \quad \text{for} \quad 0 \le x_1 \le L \\ c_2^2 \frac{\partial^2 \overline{u}}{\partial x_2^2} &= \frac{\partial^2 \overline{u}}{\partial t^2} + g_2(x)\ddot{u}_0 \quad \text{for} \quad 0 \le x_2 \le L \end{aligned} \tag{31}$$

From solution to these equations, we identify a single degree of freedom approximation.

$$\ddot{\xi} + 2\zeta_s \omega_s \dot{\xi} + \omega_s^2 \xi = Q_1 \tag{32}$$

$$\omega_s = \frac{\pi c}{2L}, \text{with } \zeta_s = 0.01 \tag{33}$$

The next step is to follow a similar procedure and solve the differential equations for the regions with E_1, ρ_1, c_1 for $0 \leq x_1 \leq$ L; and E_2, ρ_2, c_2 for $0 \leq x_2 \leq$ L, to obtain new needed natural frequencies.

$$\phi + \frac{\omega L}{c_1} = n\pi n = 1, 2, \ldots \tan\phi = \frac{E_1 c_2}{E_2 c_1} \quad \tan\frac{\omega L}{c_1} \tag{34}$$

Then, the design of the 2D of AMMS is to design two compensators. One to change from ω_s to ω_{f1} and a second one to change from ω_s to ω_{f2}. The procedure for the design is as follows. For the first compensator, equations are as follows.

$$\xi + 2\zeta_s\omega_s\xi + \omega_s^2\xi = Q_1 - ag\omega_c^2\eta \tag{35}$$

$$\ddot{\eta} + 2\zeta_c\omega_c\dot{\eta} + \omega_c^2\eta = b\xi \tag{36}$$

Control 1

Using two coincident frequencies for the closed-loop system gives:

$$\left[s^2 + 2\zeta_s\omega_s s + \omega_s^2\right]\left[s^2 + 2\zeta_c\omega_c s + \omega_c^2\right] + abg\omega_c^2 s^2 = \left(s^2 + 2\zeta_{f1}\omega_{f1}s + \omega_{f1}^2\right)^2$$

With the Routh–Hurwitz stability criteria, the condition for stability for the fourth-order denominator of the transfer function are $a_1a_2 - a_0a_3 > 0$ and $a_1a_2a_3 - a_0a_3^2 - a_1^2a_4 > 0$ which calls for

$$g > \frac{-2\left(\zeta_s\omega_s^3 + \zeta_c\omega_c^3\right) - 8\zeta_c\omega_c\zeta_s\omega_s(\zeta_c\omega_c + \zeta_s\omega_s)}{2ab\left(\zeta_s\omega_c^2\omega_s + \zeta_c\omega_c^3\right)}$$

and

$$g > \frac{1 + 4\omega_c^2\omega_s^2(\zeta_s\omega_s + \zeta_c\omega_c)^2 - 4\omega_s\omega_c\left(\omega_c^2 + 4\zeta_s\zeta_c\omega_s\omega_c + \omega_s^2\right)(\zeta_s\omega_c + \zeta_c\omega_s)(\zeta_s\omega_s + \zeta_c\omega_c)}{4ab\omega_s\omega_c\left(\omega_c^2 + 4\zeta_s\zeta_c\omega_s\omega_c + \omega_s^2\right)(\zeta_s\omega_c + \zeta_c\omega_s)(\zeta_s\omega_s + \zeta_c\omega_c)}$$

Using two coincident frequencies for the closed-loop system and comparing the coefficients for the different powers of s gives rise to the following equalities:

$$\begin{aligned}
&\mathbf{S^3 = a_1}: \mathbf{2}(\boldsymbol{\zeta_c\omega_c + \zeta_s\omega_s}) = \mathbf{4}\boldsymbol{\zeta_{f1}\omega_{f1}} \\
&\mathbf{S^2 = a_2}: (\mathbf{1} + \boldsymbol{abg})\boldsymbol{\omega_c^2} + \mathbf{4}\boldsymbol{\zeta_c\zeta_s\omega_c\omega_s} + \boldsymbol{\omega_s^2} = \mathbf{2}\boldsymbol{\omega_{f1}^2} + \mathbf{4}\boldsymbol{\zeta_{f1}^2\omega_{f1}^2} \\
&\mathbf{S^1 = a_3}: \mathbf{2}\boldsymbol{\omega_c\omega_s}(\boldsymbol{\zeta_s\omega_s + \zeta_c\omega_s}) = \mathbf{4}\boldsymbol{\zeta_{f1}\omega_{f1}^3} \\
&\mathbf{S^0 = a_4}: \boldsymbol{\omega_c^2\omega_s^2} = \boldsymbol{\omega_{f1}^4}
\end{aligned} \tag{37}$$

For this control problem, we want to solve for ωf_1, therefore taking $\frac{\omega f_1}{\omega_s} = A = 1$.

	Solution 1	Solution 2
ζ_{f1}	0.6091	9.554
$\frac{\omega c_1}{\omega s_1}$	1.19164	21.038
ζ_{c1}	0.60839	0.9989
g_1	0.0311	0.9967
$a_1\ a_2 - a_0\ a_3$	0.0484	1.862E04
$a_1\ a_2\ a_3$ $-a_0\ a_3^2$ $-a_1^2\ a_4$	7.761E-07	9.448E08

Control 2

Using two coincident frequencies for the closed-loop system gives:

$$\left[s^2 + 2\zeta_s\omega_s s + \omega_s^2\right]\left[s^2 + 2\zeta_c\omega_c s + \omega_c^2\right] + abg\omega_c^2 s^2 = \left(s^2 + 2\zeta_{f2}\omega_{f2} s + \omega_{f2}^2\right)^2$$

Using two coincident frequencies for the closed-loop system and comparing the coefficients for the different powers of s gives rise to the following equalities:

$$\begin{aligned}
&\mathbf{S^3 = a_1}: \mathbf{2}(\boldsymbol{\zeta}_c\boldsymbol{\omega}_c + \boldsymbol{\zeta}_s\boldsymbol{\omega}_s) = \mathbf{4}\boldsymbol{\zeta}_{f\mathbf{2}}\boldsymbol{\omega}_{f\mathbf{2}}\\
&\mathbf{S^2 = a_2}: (\mathbf{1} + \boldsymbol{abg})\boldsymbol{\omega}_c^2 + \mathbf{4}\boldsymbol{\zeta}_c\boldsymbol{\zeta}_s\boldsymbol{\omega}_c\boldsymbol{\omega}_s + \boldsymbol{\omega}_s^2 = \mathbf{2}\boldsymbol{\omega}_{f\mathbf{2}}^2 + \mathbf{4}\boldsymbol{\zeta}_{f\mathbf{2}}^2\boldsymbol{\omega}_{f\mathbf{2}}^2\\
&\mathbf{S^1 = a_3}: \mathbf{2}\boldsymbol{\omega}_c\boldsymbol{\omega}_s(\boldsymbol{\zeta}_s\boldsymbol{\omega}_s + \boldsymbol{\zeta}_c\boldsymbol{\omega}_s) = \mathbf{4}\boldsymbol{\zeta}_{f\mathbf{2}}\boldsymbol{\omega}_{f\mathbf{2}}^3\\
&\mathbf{S^0 = a_4}: \boldsymbol{\omega}_c^2\boldsymbol{\omega}_s^2 = \boldsymbol{\omega}_{f\mathbf{2}}^4
\end{aligned} \tag{38}$$

The resulting parameters and g are as follows:

For this control problem, we want to solve for $\boldsymbol{\omega}_{f\mathbf{2}}$. Therefore with $\zeta_s = 0.03$, and taking $\frac{\omega f_2}{\omega_s} = 2.2$.

	Solution 1	Solution 2
ζ_{f2}	0.00454	87.27
$\frac{\omega_{c2}}{\omega_{s2}}$	2.94	384
ζ_{c2}	0.003394	0.99997
g_2	-	0.9984
$a_1\ a_2 - a_0\ a_3$	-1-699	1.13E08
$a_1\ a_2\ a_3$ $-a_0\ a_3^2$ $-a_1^2\ a_4$	3.043E-06	4.21E11

7.1 Practical Implementation of Active MMS

In the past several paragraphs, we have described the two-step procedure to design AMMS. First, techniques were described to change the elastic constant, density, and wave velocity from the original or host material to new specified values of the new elastic constant, new density and new wave velocity. Next, we extended the technique to change E, ρ, and the wave velocity c to E_1, ρ_1, c_1 for $0 \leq x_1 \leq \mathrm{L}$; and E_2, ρ_2, c_2 for $0 \leq x_2 \leq \mathrm{L}$. This showed that, we were able to accommodate spatial variations of elastic constants, densities, and wave velocities that were needed in elastodynamic cloaking.

Then, it is necessary to practically implement the AMMS on the given elastodynamic system. This means that force terms such as "ag ω_c^2 η_c" on the elastodynamic system. This can be done actuator assembly that was described, for implementing large damping ratio on the vertical tail of the high-performance aircraft. Both controls can be implemented with one actuator.

8 Case of Blast Waves with Finite Deformations

Until now, the discussions, in the paper, are for, electromagnetic waves, acoustic waves, and waves in elastodynamic systems. The main interest is in blast mitigation. This involves shock waves in solids, with finite deformations. The transformation of coordinates to realize cloaking started with electromagnetic systems and associated waves. Because the wavelengths are very small, scientists initiated studies in acoustic cloaking, where wavelengths are large and the transformation of coordinates preserved the acoustic equations, in a way similar to the electromagnetic equations of Maxwell. Then the design of metamaterials for acoustic cloaking, including active metamaterials are being explored.

In elastodynamic solids, the transformation of coordinates does not preserve the governing equations. Many scientists and engineers are exploring cylindrical and spherical cloaks in elastodynamic solids. They have explored coordinate transformation to design metamaterials for cloaking, by using the transformation similar to those used and discussed by Pendry, Schurig and Smith [2–4]. The result shows a need for metamaterials with the spatial distribution of unsymmetrical elastic constants and spatial distribution of densities. No such materials exist. To accommodate such spatial distribution of elastic constants and densities, we have presented the concept of AMMS in this paper. The paper also includes methods of designing the AMMS and implementing by the use of piezoelectric stack assemblies.

The next step is to explore the application of the concepts of the transformation of coordinates to design metamaterials for blast waves, with finite deformations.

This is to be followed by a two-step design of AMMS to realize the designed metamaterials and develop procedures for practical implementation.

The governing equations are as follows;

Conservation of mass:

$$\frac{\partial^s \rho}{\partial t} + \frac{\partial}{\partial x_i}\left({}^s\rho^s v_i\right) = {}^s\zeta^s \mathrm{M}\theta \tag{39}$$

Conservation of momentum:

$${}^s\rho \frac{D^s v_i}{Dt} = \frac{\partial^s \sigma_{ji}}{\partial x_j} \tag{40}$$

Conservation of Energy:

$${}^s\rho \frac{D^s e}{Dt} = \frac{\partial^s q_i}{\partial x_i} + {}^s\sigma_{ji}\frac{\partial^s \nu_i}{\partial x_j} \tag{41}$$

Constitutive equations;

$$\sigma_{ij} = -\mathrm{p}\delta_{ij} + \sigma'_{ij} \tag{42}$$

$$\mathrm{p} = \mathrm{p}(\rho, \mathrm{e}) \tag{43}$$

$\sigma'_{ij'}$ is elastic-plastic. However, to keep the coordinate transformation results simple, we assume rigid-plastic behavior and p = p (ρ).

Next, we use the conservation equations in cylindrical coordinates to cloak a cylindrical geometry. Following this cloaking, we consider coordinate transformation to steer the blast wave away from the cylinder. In order to cloak the cylinder, we use the following transformation.

$$\begin{aligned} r' &= r_0 + \frac{r_1 - r_0}{r_1} r, \quad \theta' = \theta \quad \text{for} \quad r \le r1, \\ r' &= r, \quad \theta' = \theta \quad \text{for} \quad r > r1, \end{aligned} \tag{44}$$

The result of the coordinate transformation, following the guidelines of Pendry, Schurig, and Smith, yields spatial distribution of the pressure–density relationship and spatial distribution of the density distribution. However, the application of the two-step procedure is to design the AMMS, the basic equations are nonlinear and require nonlinear control concepts. Also, the numerical methods to validate the results of the two-step procedure, requires significant modification because of the spatial distribution of the constitutive equations and density. The complete description the cylindrical cloaking and the transformation of the coordinates to achieve steering the incoming blast wave will be discussed in a separate paper.

9 Conclusions

The publication of Veselago' paper on the negative refractive index, in1968, created a significant of interest in developing materials that provided negative refractive index and in cloaking selected objects. A next significant progress was by Pendry, Schurig, and Smith who introduced coordinate transformation techniques to design metamaterials to reach the goal of cloaking. Because the optical wavelengths are very small Cummer. Bogdan and Popa resorted to acoustical cloaking where wavelengths are large. Later, Brun and others showed that it is possible to cloak objects in elastodynamic systems, where the basic differential equations changed resulting the asymmetric elastic constants, as well as the density, that were spatially distributed. Even though they made some suggestions to develop materials, with such properties there were no materials for practical use. The contributions, in this paper, are to formulate a two-step procedure to design and implement an AMMS technique to design elastodynamic cloaking that can achieve elastodynamic cloaking. Practical feasibility was based on the application of such a technique to create large damping in a structure when no such damping material excited in nature. Next steps to steer a blast wave, with finite deformations are briefly described.

References

1. Veselago, V. G. (1968). The electrodynamics of substances with simultaneously negative values of permeability and permittivity. *Soviet Physics Uspekhi*, *10*(4), 509.
2. Pendry, J. B., et al. (1996). *Physical Review Letters,* 76, 4773.
3. Pendry, J. B., et al. (1999). *IEEE Transactions on Microwave Theory and Techniques*, *47*, 2075.
4. Smith, D. R., et al. (2000). *Physical Review Letters, 84*, 4184.
5. Cummer, S., & Schurig, D. (2007). One path to acoustic cloaking. *New Journal of Physics, 9,* 45.
6. Chen, H., & Chan, C. T. (2000). Acoustic cloaking in three dimensions using acoustic metamaterials. *Applied Physics Letters*, *91*, 183518.
7. Zhang, S., Xia, C., & Fang, N. (2011). Broadband acoustic cloak for acoustic waves. *Physical Review Letters, 106,* 024301.
8. Norris, A. N. (2015). Acoustic cloaking. *Acoustics Today*, *11*, 1.
9. Cummer, S., Rahm, A., & Schurig, D. (2008). Material parameters and vector scaling in transformation acoustics. *New Journal of Physics, 10,* 115025.
10. Zigoneanu, L., Popa, B., & Cummer, S. (2014, April) Three dimensional broadband omnidirectional acoustic ground cloak. *Nature Materials*, *13*.
11. Pendry, J., Schurig, D., & Smith, D. (2006). Controlling electromagnetic fields. *Science, 312,* 1780–1782.
12. Schurig, D., Pendry, J., & Smith, D. (2007, October 29). Transformation-designed optical element. *Optics Express*, *15*(22), 14772,
13. Brun, M., Gunneau, S., & Movchan, A. B. (2006). Achieving control in plane elastic waves. *Applied Physics Letters, 94,* 061903.

14. Milton, G. W., Briane, M., & Willis, J. R. (2006). On cloaking for elasticity and physical equations with a transformation invariant form. *New Journal of Physics, 8*.
15. Norris, A. N., & Shuvalov, A. N. (2011). Elastic cloaking theory. *Wave Motion, 49,* 525.
16. Parnell, W. J., & Shearer, T. (2013, November). Antiplane elastic wave cloaking using metamaterials, homogenization and hyperelasticity. *Wave Motion*.
17. Brun, M., Colquitt, D. J., Jones, I. S., Movchan, A. B., & Movchan, N. V. (2014). Transformation cloaking and radial approximations for flexural waves in elastic plates. *New Journal of Physics, 16,* 093020.
18. Diatta, A., & Gunneau, S. (2014). Controlling solid elastic waves with spherical cloaks. *Applied Physical Letters*, *105*, 021901.
19. Hanagud, S., Bayon de Noyer, M., Luo, H., Henderson, D., & Nagaraja, K. S. (2002). Tail buffet alleviation in high performance twin-tailed aircraft using piezostack actuators. *AIAA Journal, 40,* 4.
20. Bayon de Noyer, M., & Hanagud, S. (1997). Single actuator and multi-mode acceleration feedback control. In *Adaptive Structures and Materials Systems* (Vol. 54, pp. 227–235). Aerospace Division, ASME.

Bioinspired Layered Composite Principles of Biomineralized Fish Scale

M. D. Nelms, W. D. Hodo and A. M. Rajendran

1 Introduction

Over the last two decades, both design engineers and researchers have turned to nature with the hopes of understanding how biological materials are efficiently created to have superior properties such as high strength, high toughness, while being lightweight [1]. Researchers have learned nature does not design structures rather it designs for functionality using whatever materials are indigenous to the geographical location. Functionality is what dictates the formation of the structure [2, 143]. From an evolutionary standpoint, the biological materials adapted to their environment by enhancing their functionality in response to external stimuli.

Nature has evolved specific groups of ancient fish that possess an outer exoskeleton layer, known as biomineralized fish scales to cover its body [3]. The boney scales that cover various fish species can be grouped as follows: (a) elasmoids, (b) placoids, and (c) ganoids [4] as well as dermal armors in other marine species [5]. The collection of fish scale is thought to be used as a protective layer for the fish from predatory events. Meaning the scales have shown to successfully mitigate penetration damage and tend to exhibit energy absorptive/dissipative characteristics under dynamic, high-strain loading conditions. The exoskeletal scales are considered to be a biocomposite that exhibits the mutually exclusive engineering attributes of high strength, lightweight, and toughness sought after for protection from extreme loading conditions, i.e., blast and impact. In contrast, man-made engineered composites can also have superior engineering properties

M. D. Nelms (✉) · A. M. Rajendran
University of Mississippi, Oxford, MS, USA
e-mail: mnelms@go.olemiss.edu

W. D. Hodo
US Army ERDC-GSL, Vicksburg, MS, USA

S. Gopalakrishnan and Y. Rajapakse (eds.), *Blast Mitigation Strategies in Marine Composite and Sandwich Structures*, Springer Transactions in Civil and Environmental Engineering, https://doi.org/10.1007/978-981-10-7170-6_21

(high strength, high fracture toughness, and lightweight). However, man-made composites are prone to delamination at the bonded interface when impacted or penetrated [6, 7].

Recently, engineers and scientists have become interested in understanding both the materials and mechanical mechanisms that may contribute to the fish scale's resilient performance. The fish scale uses limited constituents that are individually weak, but when combined they are very strong. Nature has synthesized the multilayered composite uniquely by embedding hard materials into soft material phases. Additionally, the material phases have been optimally arranged and assembled uniquely at each length scale (nano-to-millimeter). Furthermore, the hydration state, volume fraction, orientation and mechanical interaction for the bio-apatite (hard) minerals and (soft) protein-based collagen fiber bundles are believed to control the preferential response of the biocomposite (Fig. 1).

Fish scales and related biomineralized structures have been of recent interest for their penetration resistance [8–12], flaw tolerant behavior [13–15], damage mitigation [16, 17], crack arresting, and lightweight biologically inspired composite (biocomposite) design [5, 18]. Ganoid fish scales, such as the alligator gar (*Atractosteus spatula*) [8, 17, 19, 20] and gray bichir (*Polypetreus senegalus*) [16], teleost fish scales from striped bass (*Marone saxitilis*) [11, 12] as well as generalized structures based elasmoid fish [18], have been researched due to their articulating armor characteristics and complex multiscale biocomposite structure. Penetration experiments on striped bass fish have shown a significant increase in penetration resistance due to the presence of fish scale covering, Fig. 2 [12]. The multilayer structure was shown to have length scale dependent geometrical features and material components with potential applications to advanced composite and 3-D printed materials. Recently, the biomineralized fish scale has emerged as a lightweight bioinspired design architecture that has been used to develop articulating armor for use in solider protection applications [5, 10].

Protective biomaterials have had a marked increase in interest due to unique characteristics and properties that are typically sought in engineered material systems [21, 22]. The biomineralized composites are a distinct subclass that can provide inspiration when designing composites that have the attributes of high strength, tough, and energy dissipation [23, 24]. Within the subclass of biomineralized composites fish scale, bone, nacre, antlers, and teeth have shown to possess the advantageous characteristics described above [97]. Researchers have summarized the fish scale as a hierarchical biocomposite structure, having the resilient characteristics of thin, lightweight, crack resistant, and durable [11, 12, 17, 25, 26].

In general, biomineralized materials have both short and long range ordering of materials that define the gradation of engineering properties and behavior from nano-to-macro scale [16, 27]. When the relatively weak individual constituents of hard minerals and soft collagen fibers of the fish scales are combined, they form a bilayered material system. The protective nature of fish scales tends to exhibit the

attributes of exceptional fracture toughness and stiffness that are greater than or equal to most of the currently available man-made engineering composites, see Fig. 1 [25]. The unique combination of engineering properties, often found in fish exoskeleton, has eluded composite material scientist and engineers. As a result, the exoskeleton's robust engineering attributes have led to recent interest into mechanical aspects of biological material characterization and the correlation to bioinspired design of novel protection systems [5, 9, 16, 18, 28, 29]. The goal of this chapter is to provide a prospectus into the current state of fish scale experimentation and modeling as it pertains to bioinspired protective material design as well discussion on the correlation between fish scale and bone/bone-like materials.

Fish scales serve a unique dual purpose, such that they provide insight into a multiscale hierarchy of structural–material interactions that improve highly sought after, and often disparate, characteristics of engineering composites. Additionally, they are an exciting platform for the basic science of bone and related hard tissues. The fundamental mechanisms are still being discovered within the complexity that defines their advantageous characteristics. Researchers would like to understand the intrinsic features at play between the hard–soft material interactions, both chemically and mechanically, as well as the layering and gradation of mechanical properties [16].

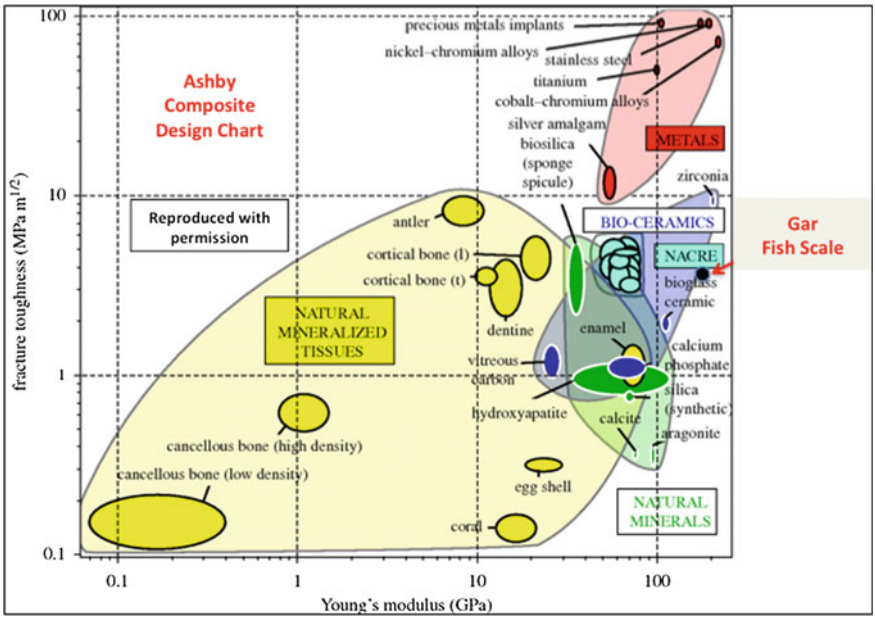

Fig. 1 Ashby design chart of mechanical properties for biological materials [25, 146] (Reprinted with permission from [25] Copyright (2015))

2 General Background

The motivation for this review is to gain: (a) sufficient knowledge on how to best understand the protective nature through a combination of materials science and numerical modeling and (b) provide the reader with a road map that discusses the current state of knowledge for fish scale research from the perspective of both experimental and computational characterization. Additionally, the review describes the multiscale (macro, micro, and nano) structural and mechanical features that are thought to contribute to fish scale's exceptional performance. The complexity and specific performance of fish scale start with the biological classifications at the macroscale.

2.1 Fish Scale Classifications: The Macroscale

Fish scales can be categorized based on general characteristics into placoid, ganoid, elasmoid, which are then subdivided into ctenoid and cycloid, and cosmoid classifications [4] as well as dermal armor [5]. The primary distinction between classifications is the volume fraction of the protein and mineral phases, as well as variations in structural and material arrangement. As an example, shown in Fig. 2 is a visual illustration of Alligator fish scales structural layered arrangement that consists of a bone-like inner layer, covered by a ganoine layer, followed by epidermis covering [3].

Placoid scales are most commonly found in sharks and ray-finned fish; primarily consisting of bone and dentin with an enameloid covered spine that protrudes through the skin or epidermis. Research has been primarily focused on the hydrodynamic properties and abrasion resistance, but tend to offer limited predator protection [21]. Given their minimal strength and puncture resistance, they will not be reviewed in detail. Within the other fish classifications, particularly from the ganoid class, the

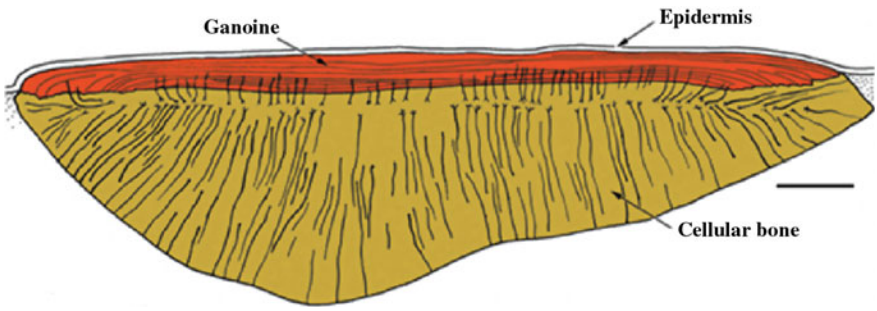

Fig. 2 Lepisosteoid-type ganoid scale structural arrangement found in alligator gar. Scale bar: 250 μm [3] (Reprinted/adapted with permission from [3] Copyright (2009) Wiley Online Library)

multiscale variations are thought to have a pronounced effect on the mechanical properties [25]. The mineral component, bio-substitutable apatite (B/Ap), the organic component, collagen fibers, and porosity are consistent features. Current research has been focused on elasmoid and ganoid scales with interest into the dermal armor of the three-spine stickleback for potential insights into penetration resistance [4, 5, 11, 16, 17, 30, 38, 56, 145]. Cosmoid fish scales are only found on extinct species but are similar in structure to ganoid scales. The external layer is the enamel-like material vitrodentine (similar to ganoine), followed by cosmine (a dentine-like material), then two basal layers, one of spongy bone and the inner most layer being isopedine. Cosmoid scales are known from fossil records to be highly protective, so the correlation to ganoid scales can allow for understanding into the more protective, but untestable, ancient version.

2.2 *Biomineralized Fish Scales: A Multilayer Composite Material*

The elasmoid scales are characteristic of most "modern" fish species, teleost fish. The scale is bilayer bio-composite comprised of an external bone layer and woven "thread like" collagen fibers in its internal layer [135]. The infraclass of teleost comprises 96% of all modern fish. Specifically, scales from the striped bass (*Marone saxatilis*) [11, 12] and Arapaima (*Arapaima gigas*) [32–34] have been researched for their bite or puncture resistance. Zhu et al. [11] showed a 400% increase in penetration load resistance when including elasmoid fish scale shown in Fig. 3.

Teleost scales contain the least mineralized external layer of the fish scales reviewed [18]. They can be divided into cycloid and ctenoid subtypes based on collagen fibular orientation, with cycloid being circumferential, and ctenoid being radially dominated. The bone is composed of a hard B/Ap mineral and randomly oriented soft collagen fibers. The mineral has a ceramic-like response while strong in compression and weak in tension. The collagen has hyperelastic, entropic elastic

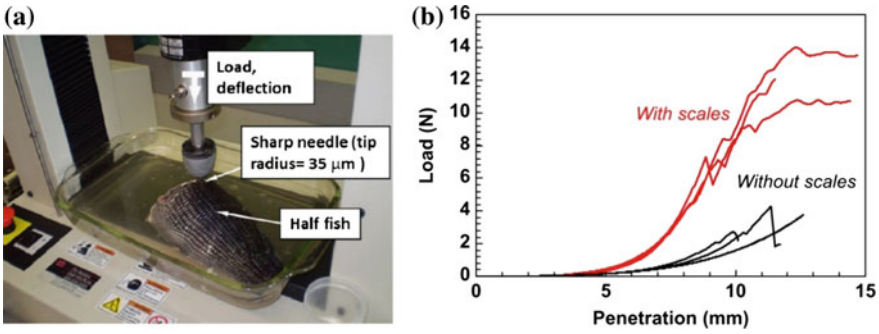

Fig. 3 Stripped bass (*Marone saxitilis*) penetration testing [12]

responses similar to engineering polymers. While the scales do contain a mineralized layer, the elasmoid scales are significantly less resistant to penetration than other classifications but have provided insight into the effects of the scale layup and embedment into an elastic protein matrix on both external and internal surfaces [18], see Fig. 2.

Ganoid fish scales are ancient and have adapted to its environmental surroundings but experienced very little evolution in its structural makeup since its inception during the "Cretaceous" time period, occurring 66–144 million years ago [35, 36] and are typically rhombic in shape. The exoskeleton scales are biomineralized and have a multilayered structure [4, 5, 20, 145]. The ganoid structure can be as complex as the quad-layered biocomposite of gray bichir. The lamellar structure is as follows from external to internal, or lateral to medial, respectively: highly mineralized external layer of ganoine, then the random, less mineralized structure of dentine, a lamellar bone structure of isopedine and a highly collagenous osseous inner layer [16]. The alligator gar is a bilayer composite having a ganoine outer layer covering up to 70% most of the bone inner layer, see Fig. 4 (left) [17]. The ganoid scales for the alligator garfish have varying volume ratios of minerals-to-fibers within the individual layers and at the interfacial transition zones between layers where the composition has a sudden drastic change [17, 25]. In bone-like materials, nanoindentation has been used to determine each layer's gradation of modulus and hardness, which typically decrease from the external (radial) surface toward the internal (medial) layers [16, 17, 25, 37]. As previously stated, ganoid scales are considered to be a more primitive variation of fish scale and seem to provide improved penetration resistance; thus, there is greater interest in understanding the structure–mechanical property relationships. The current research in ganoid fish scales has primarily focused on gray [16] and alligator gar due to the armor-like characteristics of the "ancient" scale [4, 16, 17, 25].

Like the ganoid, cosmoid scales have a layered structure with a functionally graded composition. Lastly, there are fish groups that exhibit what is designated as flexible dermal armor, which seems to provide protection against predators. Due to

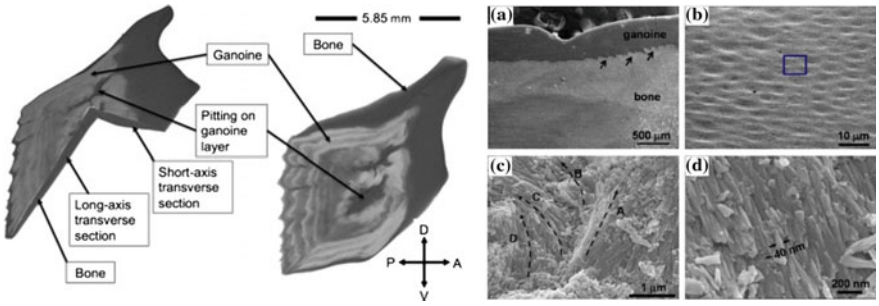

Fig. 4 Alligator gar fish scale and (right) [3] (Reprinted with permission from [3] Copyright (2013) Elsevier) and SEM images for the alligator gar micro and nanostructure [20] (Adapted with permission from [20] Copyright (2013) Elsevier)

the exoskeletal plates thought to be dermal armor: the three-spine stickleback (*Gasteroseus aculeatus)* has been researched for bioinspired design Song et al. [145]. The armor plates consist of primarily (58–68%) of a biologically produced version of mineral apatite, B/Ap, the ceramic-like component, and porosity (20–35%). Song et al. [145], [5] used the additive manufacturing technique to 3-D print scaled up models of the stickleback to better understand the mechanics and articulating structure of the dermal armor. The layering of fish scales, in general, is typically a thin, highly mineralized external layer with decreasing mineralization and increasing collagen content progressing inward with sharp decrease in degree of mineralization at layer interfaces [25]. The alligator gar scaled has the characteristic "*sawtooth*" interlocking, see Fig. 5a, pattern between layers, functionally graded interface, and a tough-soft bone inner layer [4, 17, 25]. In this case, highly mineralized means greater than 95% inorganic material, with the other 5% being pores and interstitial proteinaceous (i.e., consisting of proteins) inclusions. The mechanical behavior of ganoine, obtained from microindentation experimentation, has shown to be brittle in nature due to the cone cracking under the indenter tip [17]. Porosity has been observed from the micro-to-nanolength scales in both the ganoine and bone layers. The pore geometry and volume fraction are layer specific. In the dense ganoine layer, the pore volume fraction and the pore geometry are small. However, in the less dense bone layer, the pore volume fraction and the pore geometry increase through the layer's thickness. The ganoine's hardness and strength characteristics have been attributed to the B/Ap phase. Mechanically, ganoine is similar to dental enamel in behavior having high modulus, hardness, and brittle failure characteristics analogous to engineering ceramics. In ganoid scales, ganoine is the thinnest layer with the alligator gar having a thickness of ~45 μm when compared to the total thickness of 750 μm, Fig. 5 [19].

Comparatively, in the gray bichir, measured thickness was ~10 μm when compared to the total thickness of 400 μm, but both exhibit similar results during indentation testing. Using nanoindentation experimentation, the elastic modulus ranged from 55 to 80 + GPa [8, 17, 19, 25, 38]. The material properties for the various constituents present in typical ganoid scales are listed in Table 1.

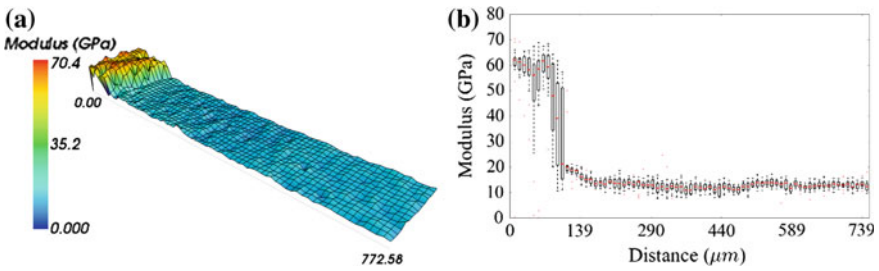

Fig. 5 Elastic modulus present in the alligator gar determined through **a** dynamic nanoindentation mapping and **b** the Tukey's boxplot data reduction [19] (Reprinted with permission from [19]. Copyright (2017) Elsevier)

Table 1 Summary of fish scale constituents and mechanical properties

Biocomposite microconstituents	Composition	Structure, geometry, dimensions	Material properties
Ganoine layer	Primarily calcium deficient hydroxyapatite[f] (<5% organic)	Rod-like with an average orientation 45 off the surface normal axis.	E = 55 GPa[a] E = 69 GPa[b] H = 3.3 GPa[b] E = 70.8 ± 4.5 GPa[c] H = 3.6 ± 4.5 GPa[c]
Dentine layer	Collagen and hydroxyapatite	Unknown	E = 20 GPa[a]
Bone	Significantly less mineralized than ganoine and is characterized by tubules and collagen fibers	Corn flake like platelets[j] embedded in collagen matrix[k]	E = 13.5 GPa[a] E = 14.5 GPa[b] H = 0.5 GPa[b] E = 20.5 ± 2.4 GPa[c] H = 0.7 ± 0.1 GPa[c]
Collagen fibers	Alligator gar: collagen fibrils bundles to make fibers	Molecular: rod-like[h] Molecular collagen: length = 290 nm[h] Diameter = 1.5 nm[h] Alligator gar : fibers ~100 nm	Nanofiber: 2.82 GPa rupture stress = 25 MPa @ 2% strain Max strain: 33%[d] E = 1 GPa[e] σ_y = 200 MPa
Bio-substitutable[i] Apatite	$Ca_{(10-x)} \cdot []_x[(PO_4)_{(6-x)}(CO_3)_x] \cdot (OH)_{(2-x)} \cdot []_x$	Alligator gar: columnar crystals—length ~220 nm; diameter ~40 nm[f]	E = 150.38 GPa[g] H = 7.06 GPa[g] E = 143.56 GPa[g] Hardness = 6.41 GPa[g]

[a]Song et al. [38], [b]Allison et al. [17], [c]Chen et al. [8], [d]Carlisle et al. [142], [e]Zhu et al. [12], [f]Yang et al. [4], [g]Saber-Samandari and Gross [143], [h]Gautieri et al. [79], [i]Tonsuaadu et al. [98] [j]Hodo [25], [k]Ikoma et al. [30]

Progressing internally, the gray bichir next has a dentine layer. The dentine layer has a reduced B/Ap mineral content (~50%), increased organic content (~30%) with the organic phase being primarily mineralized collagen, and the rest being interstitial fluids or proteins [16]. The layer thickness was measured by Bruet et al. [16] to be 50 μm. Next is the isopedine layer for the bichir, which is described having a uniquely layered structure similar to lamellar bone and the interior most layer being comprised of porous bone. Ganoid scales exhibit a geometrically interlocked interface between the ganoine and the bone layers. For the gar fish, the interface has a periodic sawtooth structure intruding into the interfacial region of the fish scale [25].

The gray bichir has a less distinct more randomly varying interface interlocking between layers. Hodo [25] showed, using transmission electron microscopy (TEM), that the B/Ap are thin mineralized platelets with "corn flake like" geometric structure. The inner bone layer is a combination of B/Ap platelets and collagen fiber bundles producing viscoelastic material behavior [25, 39]. The local material and geometric property variations are thought to be responsible for the observed gradation of properties within a scale. The material properties show a distinct piecewise gradation as shown in Fig. 5. Bruet et al. [16] have found graded properties that include elastic modulus, yield, strength, and density. Provided in Table 1 is a summary of the common constituents found in fish scales as well as their experimentally determined material composition, unique features, and mechanical properties. The inter- and intra-layer features, listed in Table 1, provide a basis for three-dimensional design of materials that take advantage of rapidly advancing additive manufacturing. In biomaterials, the complexity goes well beyond the structural features; the mechanical response is hydration state dependent.

Hydration state appears to have two effects [40]: (a) facilitates the kinetic reactions used for development and assemblage of the discrete units used in forming the overall fish structure and (b) contributes to mechanical strengthening.

(a) When biomineralized (mineral matrix + soft reinforcement) composite materials are hydrated, the osmotic fluids can be used to facilitate the kinetic reactions that drive the transportation and deposition of minerals and nutrients used for the growth and development of intra- and extracellular materials [41–43].
(b) In the mechanical sense, hydration state aides in maintaining the integrity of highly organic collagen fiber reinforcement phases and tends to aid the toughening mechanisms used to bind the biomineralized hydroxyapatite mineral matrix phases [43–49]. For natural materials, full saturation produces swelling pressures that help create residual compressive loads, thus reducing crack-inducing tensile stresses [40]. Likewise, when the fish scale saturation level drops, non-load related volume shrinkage and tensile cracks can possibly appear at the boundaries of the discrete materials and in the layers at the system level; especially in the more porous collagen-rich bone layers [44, 45, 50–55].

Tensile and notched beam experiments of dog bone shaped specimens cut from garfish scales highlighted the effects of water inclusion. When dehydrated, fish scales exhibited linear elastic response with brittle failure as compared to the nonlinear, large ductility of rehydrated specimens before failure. When dry, the scales were determined to have a maximum strain of 0.03–0.06 whereas the maximum strain for the wet samples was up to 0.12. Material nonlinearity was observable only for the wet samples and was induced at strains of 0.03 [56]. Researchers have postulated bone-like materials exhibit varied stress transfer with the biomineral phase resisting the majority of the applied loading and the protein phase transfers shear at multiple length scales, see Fig. 6 [57] often termed shear lag by the engineering community.

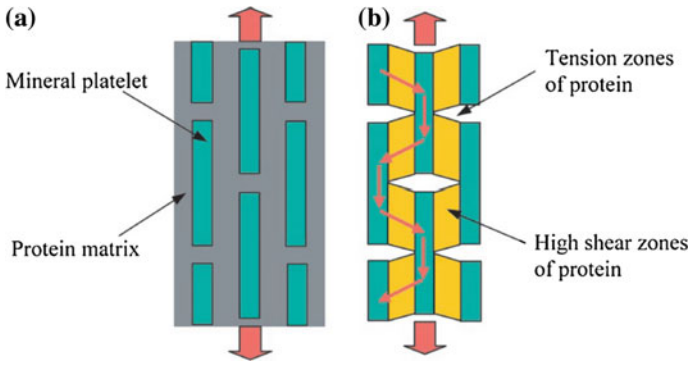

Fig. 6 Jaeger–Fratzel model for shear transfer via protein phase in bone-like materials [61] (Reprinted with permission from [61]. Copyright (2012) Springer Publishing Company)

3 Existing Micromechanical and Computational Models for B/Ap-Based Materials and Structures

Although B/Ap based materials have discrete nano constituents that are uniquely arranged/assembled from the nano-to-macro level, it is the characteristic length scale that determines what is physically measurable as well define the structures behavior [58, 144]. For example, research conducted by Nelms [19], Hodo [25], Nelms [59], Chandler [29], Allison [17], Wang [60], and Bruet [16] further show there is a relationship between the materials microlevel morphology (volume fractions, spatial proximity, and directional placement) and macrolevel mechanical response observed in B/Ap-based fish scale. Yet, the exact nature of relationship between structure and mechanical properties is not well understood. However, several models have been developed for investigating B/Ap-based materials and structures, such as bone, teeth, fish, etc.

When dealing with the multiple material phase and combined structural interactions occurring, at several spatial and temporal scales, in biomaterials robust modeling methods are often used to assist with decomposing the contributing effects the interactions may have on the engineering response. The models provide a means to investigate and discern the mechanisms that lead to elastic, creep, damage, and failure in the complex hierarchical structure. Micromechanical approximations for the B/Ap material response are often determined using a variety of modeling methodologies. In addition, material model development is continually ongoing as new experimental evidence sheds light on the never seen before underlying geometries and mechanisms at each length scale. Our goal is not to summarize all models in existence, but highlight the progression and provide detail for those that are thought to appropriately describe the microstructural and material property relationships.

3.1 Micromechanical Models for Biomineralized Composites

The previous efforts in bone research provide a starting point for the following discussion of candidate modeling approaches for biomineralized tissues. At the continuum level, strength models have been used to approximate the material response to external loading for mineralized collagen fibers. The geometry for the individual B/Ap mineral (hard) and collagen fiber (soft) phases has been incorporated into composite material models by Hill, Walpole, Hirsh, Cox, Currey (bone specific), Padawer-Beecher [66], Halpin-Tsai and Katz (bone specific) [61]. In the following constitutive relationships, the elastic modulus and relative volume fractions are represented for the collagen phase by E_c and ν_c, respectively, and for apatite mineral phase by E_{HA} and ν_{HA}. Hirsh proposed combining aspects from the Voigt and Reuss models so that the geometric effects can be captured through a strengthening parameter. The strengthening parameter describes the material orientation with the relative volume fractions of material that coincide with Voigt and Reuss descriptions, respectively.

Recently, experimental research efforts by Zimmerman et al. [62] have shown that the complex load transfer mechanisms, occurring at the nanoscale, may be a key aspect in the mechanical response of collagen + B/Ap biomaterials. However, both still provide more accurate representations of bone-like microstructure than the classical Voigt and Ruess bounds approximations for elastic moduli, which is defined each constituents' volume fractions (ϕ), and respective, moduli. The interactions have been extended to the individual constituents bulk (K) and shear (G) moduli and Poisson's ratio (ν) as well as different geometric descriptions for the particulate hydroxyapatite phase. The properties for each phase is designated by a HA or C subscripts for hydroxyapatite and collagen, respectively. The formulation provides upper and lower bounds of bulk and shear moduli as well as the elastic modulus for an isotropic material. When considering the platelet or flake-like geometry of the B/Ap, the Halpin-Tsai is the most widely used semiempirical composite model. The Halpin-Tsai model [63] has been modified for use in studying platelet reinforcement by including a strengthening parameter for hexagonal platelet reinforced composite materials. [136] generalized the Halpin–Tsai equations for particulate composites, Eq. 1, which have been implemented on bone specific models that include Poisson's ratio and fiber misorientation within a single bone lamella through the β parameter defined in Eq. 2; misorientation being defined as the angle between fiber direction and loading axis, θ_i and their relative volume fractions, f_i.

Katz		Geometric parameters
Longitudinal	(1) $E_l = \frac{\phi_C E_C (1 - \nu_C \nu_{HA})}{1 - \nu_C^2} + \beta$	(2) $\sum \phi_{HA} E_{HA} f_i \left(\cos^4 \theta_i - \nu_m \cos^2 \theta_i \sin^2 \theta_i\right)$

Currey [64] proposed a mesoscale bone specific extension to the Cox model to capture the geometry of hexagonal platelet geometry of B/Ap. Padawer and Beecher [65] described the interaction between flake reinforcements using geometrically defined strengthening parameters as an extension of the Voigt model Eqs. 3–8. The Padawer–Beecher model was extended to include fiber-to-fiber interactions by Lusis et al. [66], Eqs. 9 and 10. Both have been applied by Weiner and Wagner [67] for Collagen + B/Ap-based biocomposites.

Padawer-Beecher		Geometric parameters
Longitudinal	(3) $E_l = \phi_C E_C + \eta_1 \phi_{HA} E_{HA}$	(4) $\eta_1 = 1 - \frac{\tanh(u_1)}{u_1}$ (5) $u_1 = \alpha_1 \sqrt{\frac{G_C v_{HA}}{E_{HA} v_C}}$ $\alpha_1 = \frac{w}{t}$
Transverse	(6) $E_t = \phi_C E_C + \eta_2 \phi_{HA} E_{HA}$	(7) $\eta_2 = 1 - \frac{\tanh(u_2)}{u_2}$ (8) $u_2 = \alpha_2 \sqrt{\frac{G_c v_{HA}}{E_{HA} v_c}}$ $\alpha_2 = \frac{w}{t}$;
Extension by Lusis et al. [67]		Geometric parameters (9) $\boldsymbol{\eta_1} = 1 - \frac{\mathbf{tanh}(u_1 + 1)}{u_1}$ (10) $\boldsymbol{\eta_2} = 1 - \frac{\mathbf{tanh}(u_2)}{u_2}$

Jaeger and Fratzel [68] proposed a shear-lag model that includes the thin hexagonal platelet shape and overlap to better captures the geometry effects of orientation and mineralization present in a given RVE, Fig. 6. This model assumes that the mineralized protein transfers the load from platelet to platelet via shear. This model has been the predominantly model used in bone finite element modeling [61].

In a shear-lag model, the assumption is the collagen fibers transfer stress via simple shear and the B/Ap platelet effectively support the majority of the applied load. Figure 6 from [61] illustrates the hierarchal load transfer between the mineral and protein phases from the fiber to TC-mineral particle level. The degree of mineralization is captured through ϕ_m.

Jaeger - Fratzel		Geometric parameters
Longitudinal	(11) $\frac{1}{E_l} = \frac{4(1-\phi_m)}{G_C \phi_m^2 \rho^2} + \frac{1}{\phi_m E_m}$	

Given the significant hydration and entropic effects exhibited of collagen, models will need to be adapted for the hierarchal load transfer that includes intrafiber penetration of the mineral phase. Future constitutive material model enhancements will then be able to extend beyond simple shear transfer so that the dominant deformation mechanisms at play can be better captured during complex loading applications. Also needed is an approach that can include the effects of repeating structuring which is typical of all biomaterials [69]. Provided in Table 2 is a brief summary of commonly used continuum material models that have been used

Table 2 Summary of continuum bone models

Systems modeled	Author/Reference	Model description
Bone & Bone-like hierarchical materials	Pistoia et al. [99]	Strain energy density
	Schileo et al. [100]	Comparative study: von Mises and maximum principal strain criterion
	Carnelli et al. [101]	Extended Drucker–Prager
	Shuchan and Yuenuang [102]	1) Shear Lag 2) Tension shear
General bone tissue	Chevalier et al. [71] Charlebois et al. [103]	Damage couple with anisotropic elastoplasticity using density and fabric tensor
Cortical Bone	Mercer et al. [104]	Bilinear (elastic, Drucker–Prager yield surface)
	Natali et al. [105]	Phenomenological viscoelastic-plastic
	Cezayirlioglu et al. [106]	Asymmetric plastic tangent modulus and Hill's yield criterion
	Johnson et al. [107]	Low and high strain rate viscoelastic-viscoplastic
Intervertebral disc	Ehlers et al. [108]	Theory of Porous Media
Low-density trabecular bone	Bayraktar et al. [109] Stölken et al. [110]	Cast-iron Axisymmetric with von Mises yield criterion
Mineralized collagen fiber	Barkaoui and Hambli [111] Hambli and Barkaoui [112]	Isotropic elasticity Quasi-brittle
Parallel-fibered lamaller bone	Akiva et al. [113]	Micromechanical
Trabecular bone	Carretta et al. [70]	Bilinear Isotropic/maximum strain yield criterion
	Verhulp et al. [114]	Isotropic hardening (Hill's yield function)
	Yeh and Keaveny [115]	3-D lattice model Microfracture using strain-based criterion
	Keaveny et al. [116]	Tsai-Wu yield criterion
	Zysset and Rincon [117]	Explicit damage mechanics
	Moore and Gibson [118]	Compressive damage
	Kosmopoulos and Keller [119]	Elastic damage
	Komospoulos et al. [120]	Fatigue damage
	Kosmopoulos and Keller [121]	Nonlinear damage
	Garcia et al. [122]	Elastic-plastic damage
	Stölken et al. [110]	Smear crack

to numerically investigate bone behavior [70]. Also included in Table 2 are references for porous, damage, and plasticity-based constitutive relations that are thought to be consistent with the composite structure of bone. Most recently, the shear-lag model has been implemented by Gao [13] for FEM modeling and fracture analysis of bone-like materials. The collagen fibers provide large plasticity zone and crack branching which aides in arresting crack propagation through the brittle B/Ap bio-ceramic. Plasticity zones also provide energy dissipation through the large-strain capacity collagen fibers and inter-platelet motion (i.e., plasticity) [26]. Furthermore, the plasticity zones allow increased load carrying capacity of the bulk material. A promising approach that can be useful in capturing the nature of the repeating structure is fractals. Fractals have previously been used to capture the three-dimensional micro-texture of bone and to model the hierarchical architecture in biomaterials [71–73]. Giving potential to better represent the physical biomaterials structure but will also lead to a more efficient models. Improved models can led to more accurately predicting/capturing the phenomenological mechanisms that may be contributing to deformation which will allow engineers to discern which effects are pertinent to include in bioinspired composites.

Collagen fibers have been shown to aid in principal loading response and current efforts neglect the complex nanoscale 3-D geometric interactions of both collagen and B/Ap phases as well as hydration state effects on nonlinear response. The Gao and Buehler research groups, using a linear elastic fracture mechanics approach, proposed that the protein phase allows for larger flaw tolerance approaching the nanoscale compared to the atomic level flaw tolerance of carbon nanotube based composites [130, 13, 74, 75]. Thus far, the unique mechanisms at play have been difficult to determine experimentally and direct observation has yet to be performed. The understanding of 3-D structures has been captured using 3-D micro-computed tomography for various human bone structures [76]. On the other hand, a well-posed micromechanical modeling approach that considers the lower length scale features could provide the necessary information for understanding the characteristic deformation and its propagation through lengths scales. As stated earlier, the exoskeleton fish scale has the B/Ap biomineral platelets and fibrous protein collagen fibers which are the two predominate submicroscale material phases. Each has a distinct mechanical behavior and deformation mechanism, and when coupled in bone-like materials, it has been shown to play a significant role in defining the continuum level behavior [77, 126]. The B/Ap platelets are assumed to provide the significant strength characteristics while the collagen is believed to improve toughness and fracture resistance [125, 129, 133, 134, 137, 140, 141]. Generally, collagen fibers are organic proteins that have long chain molecule containing various amino acid residues that define the protein conformation (3-D shape), solvency, chemical, thermal, structural, and mechanical behavior through various molecular interactions. Hydrogen bonds are largely responsible for the unique collagen triple helix and chain-to-chain interaction of collagen fibers [79, 89]. The polymeric-like behavior of collagen's fibrous helical structure and its unfolding ability are believed to be key components for the existing crack mitigation properties [13].

The behavior of the collagen unfolding (and conversely conformation) is protein specific. Proteins exhibit a ratcheting behavior for the stress–strain rate dependent

response when modeled using steered MD simulations [80–82, 141]. The ratcheting behavior has been attributed to the entropic elasticity of the side-chain bonds breaking and rupture occurring when the protein has been fully unfolded [83–85]. This has been attributed to molecular chain extension with a following "decrease in configurational entropy" [86]. Currently, the experimental techniques used for understanding the micromechanical strength of proteins (Atomic Force Microscopy and optical tweezers) are unable to accurately describe the protein-unfolding path [87]. The current assumption about the deformation occurring due to protein unfolding is a result of the rotation about the C_α atoms with negligible extension between neighboring C_α atoms. Collagenous materials when hydrated exhibit strong viscous effects that are attributed to chain-to-chain slip and reduced intramolecular interactions [88, 89]. The proteins can aid in energy dissipation and eliminate stress concentration near crack-like flaws by introducing a large plasticity zone at the crack tip. In addition, weak sacrificial molecular bonding at the biomineral–protein interface dissipates energy as well increase crack path length [13, 15, 74, 90]. Sacrificial sulfur bonds can be broken and reformed as the protein extends thereby increasing the energy to unfold the protein and ultimately the proteins mechanical failure [85, 91, 132].

In general, the true effect of protein unfolding has yet to be included in micromechanical formulations. Nevertheless, there are two candidate continuum models that have been previously used to describe polymer deformation. The worm-like chain polymer models are capable of predicting the characteristic ratcheting pattern of protein extension. Proteins have been modeled as either freely jointed chain (FJC) or worm-like chain (WLC) using solutions to the Kratky–Porod model for polymeric chains [92] and adapted for FEM by Qi et al. [86]. The continuum Kratky–Porod model describes the change in the Hamiltonian entropy dissipation due to protein extension. It assumes that the bond energy is proportional to the distance between bonds, but not on the bond plane. Given proteins are chain-like molecules, their Kuhn length, l, and the number on Kuhn segments, N. Proteins are categorized as self-avoiding since two segments of the protein cannot occupy the same space define their structure for mechanical modeling. The FJC is a statistical approach used to model unfolding assuming a 3-D random walk of protein segments. Basically, it treats the proteins as collection of stiff segments that are freely jointed and randomly oriented. The FJC model is applied to polymers that have an end to length that is significantly longer than the number of Kuhn segments times the square of the Kuhn length, $\langle R^2 \rangle \geq Nl^2$. For shorter, semiflexible biopolymers, the WLC is a statistical mechanics based model that treats the protein as a continuous, inextensible and isotropic rod being extended by a force [92]. Semiflexible biopolymers are defined as $\langle R^2 \rangle \geq 2l$.

The WLC was originally developed to describe the extension of the polymers that exhibit a self-avoiding walk (protein unfolding path for the individual links in the polymer chain) [93]. The WLC was then adopted to model the fibrous proteins, specifically the DNA double helix [92]. Later, [86] developed 2-D (4-chain) and 3-D (8-chain) continuum level models for both the FJC and WLC to predict the

unfolding of proteinaceous material using a modified version of the Arruda–Boyce model [94] developed for hyperelastic rubbers. Both the FJC and WLC models disregard the protein's main chain extension and torsional potential for specific bond rotations under mechanical loading and attribute the entropic elasticity to the change in conformation. Given the extension is predominately due to the protein unfolding; the backbone extension is considered negligible to the description of the overall deformation. Given the FLC and WLC use a Hamiltonian potential that captures the entropic nature of the deformation, it would be possible to account the effects of torsion bond rotation or hydration states [95]. The H-bonds define the bound water molecules for protein structure and interactions within biomaterials and therefore key to understanding the mechanical behavior of fibular biopolymers. The water molecules contribute to the toughening mechanisms that are often observed in biological structures [96]. Additionally, by adapting the current constitutive and micromechanical formulations, a variety of loading conditions and specific unfolding path (e.g., rotational for collagen or hydration state effects on the hydrogen bonding) can be investigated to determine their effects on the collagen proteins mechanical response.

3.2 Finite Element Modeling of Fish Scale Structures

Recently, researchers have used finite element analysis (FEA) to aide in the interpretation of the layering effect on the engineering properties for the Alligator gar and Gray bichir fish scales. Bruet et al. [16] and Han et al. [28] on the gray bichir as well as Chandler et al. [29] on alligator gar have used two-dimensional (2-D) axis-symmetric approach. Bruet et al. [16] focused on the difference between discrete and linear graded material properties. Han et al. [28] investigated the effects of B/Ap crystal orientation on the mechanical properties as well the effects of variable geometry within ganoine layer. Chandler et al. [29] employed a cohesive zone model to analyze potential delamination at the ganoine–bone interface. The FE modeling effort showed that the microindentation could lead to interface delamination between the ganoine and bone layer, but did not consider the interface geometry. The model does not account for the brittle damage characteristics by assuming perfectly plastic behavior. To determine such phenomena, collagen fibers have been shown to aid in principal loading response and current efforts neglect the complex nanoscale multidimensional geometric interactions of both collagen and B/Ap phases as well as hydration state effects on nonlinear response.

The 2-D axis-symmetric modeling has shown that the heterogeneous material variations aid in elastic energy dissipation [97]. Furthermore, the interface and internal geometric complexity has been computationally investigated to show stress redistribution [8, 11, 59]. Nelms has shown in his research using a 3-D Representative Volume Element (RVE) modeling approach that material variation induces transversely isotropic effective elastic response in fish scale [19]. Vernerey and Barthelet [9] and Vernerey et al. [10] investigated the fish scale overlap

(imbrication) and showed the scale layup can increase the penetration load resistance up to 40% when overlapping a single scale and 700% when overlapping the skin, or epidermis, itself. In addition, experimentation on bone and fish scale has shown that the structural response is a function of the variation of material properties with respect to spatial proximity and volume fractions. In other words, nature uses the material's anisotropy as one of its favorable attributes that contributes to the composite structures enhancement in strength and toughness [26]. Still needed is a model that can better describe the anisotropic response from the composite biomaterials mineral, B/Ap, and fibrous collagen phases. The current material models and FEM for fish scale have employed traditional linear elastic and bilinear material descriptions. While the bilinear material description provides necessary insights into nanoscale material behavior, it does not adequately capture the energy dissipative nature, provided by viscoelastic fiber material response, observed during experimentation.

4 Summary

This chapter provided the reader with a road map that describes the current state of knowledge for biomineralized fish scales research. Discussed were the material components and how they are thought to be assembled across the multiple length scales. The bilayered structure was shown to have length scale dependent geometrical features and material components. The structure has been optimized by nature and has shown to possess the attributes of high strength and high toughness, while being lightweight. The hydration state, mixture proportioning, and orientation for the hydroxyapatite (hard) minerals and (soft) protein-based collagen bundles are believed to control the mechanical response of the biocomposite. However, the experiments alone could not identify how nature may have optimized the geometry and materials components for biocomposite's superior mechanical attributes of energy dissipation. Additionally, an overview was provided from a mechanics perspective of what techniques have been previously applied when using modeling to identify the structure–property relationships for the exoskeleton fish scale structure and similar structural components found in other related biological systems. Still needed is the technological development of laboratory equipment, refinement of experimental protocols, and enhancements of phenomenological models so that can be better capture the viscous and rate dependent nature of the energy absorptive/dissipative mechanisms.

Acknowledgements The authors from the University of Mississippi, Oxford and US. Army ERDC, Vicksburg, MS acknowledge the support by the US. Army Research Office under a cooperative agreement award contract No. W911NF-11-2-0043 (Program Manager: Dr. Joseph Myers) and US. Army Research Office under a cooperative agreement award contracts No. W911NF-11-2-0043 (Program Manager: Dr. Joseph Myers), No. W911NF-14-2-0119 (Program Manager: David Grove) and the US. Army ERDC Military Engineering 6.1-ILIR Basic Research Project on "Investigation of Delamination Resistant Bio-Laminates". Permission granted

to publish by the ARO and US Army ERDC-GSL. Additionally, discussions with several researchers at Engineering Research and Development Center, Vicksburg, MS, and US. Army Research Laboratory are gratefully acknowledged.

References

1. Wegst, U. G. K., & Ashby, M. F. (2004). The mechanical efficiency of natural materials. *Philosophical Magazine, 84*(21), 2167–2186.
2. Weiner, S., Addadi, L., & Wagner, H. D. (2000). Materials design in biology. *Materials Science and Engineering C, 11*(1), 1–8.
3. Sire, J. Y., Donoghue, P. C., & Vickaryous, M. K. (2009). Origin and evolution of the integumentary skeleton in non-tetrapod vertebrates. *Journal of Anatomy, 214*(4), 409–440.
4. Yang, W., Chen, I. H., Mckittrick, J., & Meyers, M. A. (2012). Flexible dermal armor in nature. *JOM Journal of the Minerals Metals and Materials Society, 64*(4), 475–485.
5. Song, J. (2011). Multiscale materials design of natural exoskeletons: fish armor (Doctoral dissertation, Massachusetts Institute of Technology).
6. Cantwell, W. J., & Morton, J. (1991). The impact resistance of composite materials—a review. *composites*, 22(5), 347–362.
7. Sela, N., & Ishai, O. (1989). Interlaminar fracture toughness and toughening of laminated composite materials: a review. *Composites, 20*(5), 423–435.
8. Chen, P. Y., Schirer, J., Simpson, A., Nay, R., Lin, Y. S., Yang, W., et al. (2012). Predation versus protection: fish teeth and scales evaluated by nanoindentation. *Journal of Materials Research, 27*(1), 100.
9. Vernerey, F., & Barthelat, F. (2010). On the mechanics of fishscale structures. *International Journal of Solids and Structures, 47*(17), 2268–2275.
10. Vernerey, F. J., Musiket, K., & Barthelat, F. (2014). Mechanics of fish skin: A computational approach for bio-inspired flexible composites. *International Journal of Solids and Structures, 51*(1), 274–283.
11. Zhu, D., Ortega, C. F., Motamedi, R., Szewciw, L., Vernerey, F., & Barthelat, F. (2012). Structure and mechanical performance of a modern fish scale. *Advanced Engineering Materials, 14*(4), B185–B194.
12. Zhu, D., Szewciw, L., Vernerey, F., & Barthelat, F. (2013). Puncture resistance of the scaled skin from striped bass: collective mechanisms and inspiration for new flexible armor designs. *Journal of the Mechanical Behavior of Biomedical Materials, 24,* 30–40.
13. Gao, H. (2006). Application of fracture mechanics concepts to hierarchical biomechanics of bone and bone-like materials. *International Journal of Fracture, 138*(1–4), 101–137.
14. Gao, H., & Ji, B. (2004). Modeling fracture in nano materials. In *IUTAM Symposium on Asymptotics, Singularities and Homogenisation in Problems of Mechanics* (pp. 307–316). Netherlands: Springer.
15. Gao, H., Ji, B., Buehler, M. J., & Yao, H. (2004). Flaw tolerant bulk and surface nanostructures of biological systems. *Mech. Chem. Biosyst, 1*(1), 37–52.
16. Bruet, B. J., Song, J., Boyce, M. C., & Ortiz, C. (2008). Materials design principles of ancient fish armour. *Nature Materials, 7*(9), 748–756.
17. Allison, P. G., Chandler, M. Q., Rodriguez, R. I., Williams, B. A., Moser, R. D., Weiss, C. A., et al. (2013). Mechanical properties and structure of the biological multilayered material system. *Atractosteus spatula scales. Acta Biomaterialia, 9*(2), 5289–5296.
18. Browning, A., Ortiz, C., & Boyce, M. C. (2012). Mechanics of composite elasmoid fish scale assemblies and their bioinspired analogues. *Journal of the Mechanical Behavior of Biomedical Materials, 19,* 75–86.

19. Nelms, M., Hodo, W., & Rajendran, A. M. (2017). A representative volume element based micromechanical analysis of a Bi-layered Ganoid Fish scale. *Journal of the Mechanical Behavior of Biomedical Materials, 69,* 395–403.
20. Yang, W., Gludovatz, B., Zimmermann, E. A., Bale, H. A., Ritchie, R. O., & Meyers, M. A. (2013). Structure and fracture resistance of alligator gar (*Atractosteus spatula*) armored fish scales. *Acta Biomaterialia, 9*(4), 5876–5889.
21. Meyers, M. A., Lin, A. Y., Seki, Y., Chen, P. Y., Kad, B. K., & Bodde, S. (2006). Structural biological composites: an overview. *Journal of Materials, 58*(7), 35–41.
22. Sanderson, K. (2015). Structure: Artificial armour. *Nature, 519*(7544), S14–S15.
23. Hollister, S. J., & Kikuchi, N. (1994). Homogenization theory and digital imaging: a basis for studying the mechanics and design principles of bone tissue. *Biotechnology and Bioengineering, 43*(7), 586–596.
24. Jeronimidis, G., & Atkins, A. G. (1995). Mechanics of biological materials and structures: Nature's lessons for the engineer. *Proceedings of the Institution of Mechanical Engineers, Part C: Journal of Mechanical Engineering Science, 209*(4), 221–235.
25. Hodo, W. (2015) *Investigation of the inherent chemical, structural, and mechanical attributes of bio-engineered composites found in nature: Alligator gar's exoskeleton fish scales*. Ph.D. Dissertation, University of Arkansas, Fayetteville, Arkansas, USA.
26. Ritchie, R. O., Buehler, M. J., & Hansma, P. (2009). Plasticity and toughness in bone. *Physics Today, 62*(6), 41–47.
27. Buehler, M. J. (2010). Multiscale mechanics of biological and biologically inspired materials and structures. *Acta Mechanica Solida Sinica, 23*(6), 471–483.
28. Han, L., Wang, L., Song, J., Boyce, M. C., & Ortiz, C. (2011). Direct quantification of the mechanical anisotropy and fracture of an individual exoskeleton layer via uniaxial compression of micropillars. *Nano Letters, 11*(9), 3868–3874.
29. Chandler, M. Q., Allison, P. G., Rodriguez, R. I., Moser, R. D., & Kennedy, A. J. (2014). Finite element modeling of multilayered structures of fish scales. *Journal of the Mechanical Behavior of Biomedical Materials, 40,* 375–389.
30. Ikoma, T., Kobayashi, H., Tanaka, J., Walsh, D., & Mann, S. (2003). Microstructure, mechanical, and biomimetic properties of fish scales from Pagrus major. *Journal of Structural Biology, 142*(3), 327–333.
31. Youn, H. S., & Shin, T. J. (2009). Supramolecular assembly of collagen fibrils into collagen fiber in fish scales of red seabream, Pagrus major. *Journal of Structural Biology, 168*(2), 332–336.
32. Torres, F. G., Troncoso, O. P., Nakamatsu, J., Grande, C. J., & Gomez, C. M. (2008). Characterization of the nanocomposite laminate structure occurring in fish scales from Arapaima gigas. *Materials Science and Engineering C, 28*(8), 1276–1283.
33. Lin, Y. S., Wei, C. T., Olevsky, E. A., & Meyers, M. A. (2011). Mechanical properties and the laminate structure of Arapaima gigas scales. *Journal of the Mechanical Behavior of Biomedical Materials, 4*(7), 1145–1156.
34. Yang, W., Sherman, V. R., Gludovatz, B., Mackey, M., Zimmermann, E. A., Chang, E. H., et al. (2014). Protective role of Arapaima gigas fish scales: structure and mechanical behavior. *Acta Biomaterialia, 10*(8), 3599–3614.
35. Daget, J., Gayet, M., Meunier, F. J., & Sire, J.-Y. (2001). Major discoveries on the dermal skeleton of fossil and recent polypteriforms: a review. *Fish and Fisheries, 2,* 113–124.
36. Gottfried, M. D., & Krause, D. W. (1998). First record of gars Lepissteidae Actionoterygii on Madagascar Late Cretaceous remains from the Mahajanga Basin. *Journal of Vertebrate Paleontology, 18*(2), 275–279.
37. Oyen, M. L. (2011). *Handbook of nanoindentation with biological applications*. Singapore, China: Stanford Publishing.
38. Song, J., Ortiz, C., & Boyce, M. C. (2011). Threat-protection mechanics of an armored fish. *Journal of the Mechanical Behavior of Biomedical Materials, 4*(5), 699–712.
39. Tennyson, R. C., Ewert, R., & Niranjan, V. (1972). Dynamic viscoelastic response of bone. *Experimental Mechanics, 12*(11), 502–507.

40. National Research Council Commission on Engineering and Technical Systems National Materials Advisory Board. (1994). Hierarchical Structures in Biology as a Guide for New Materials Technology. NMAB-64, National Academy Press, Washington, D.C.
41. Boskey, A. L. (2007). Mineralization of bones and teeth. *Elements, 3*(6), 385–391.
42. Mann, S. (2001). *Biomineralization principles and concepts in bioinorganic materials chemistry*. New York: Oxford University Press.
43. Rai, R. K., & Sinha, N. (2011). Dehydration-induced structural changes in the Collagen-Hydroxyapatite interface in bone by high-resolution solid-state NMR spectroscopy. *The Journal of Physical Chemistry C, 115,* 14219–14227.
44. Bembey, A. K., Bushby, A. J., Boyde, A., Ferguson, V. L., & Oyen, M. L. (2006). Hydration effects on the micro-mechanical properties of bone. *Journal of Materials Research, 21*(08), 1962–1968.
45. Bembey, A. K., Oyen, M. L., Bushby, A. J., & Boyde, A. (2006). Viscoelastic properties of bone as a function of hydration state determined by nanoindentation. *Philosophical Magazine, 86*(33–35), 5691–5703.
46. Bertassoni, L. E., & Swain, M. V. (2012). Influence of hydration on nanoindentation induced energy expenditure of dentin. *Journal of Biomechanics, 45*(9), 1679–1683.
47. Garrano, A. M. C., La Rosa, G., Zhang, D., Niu, L. N., Tay, F. R., Majd, H., et al. (2012). On the mechanical behavior of scales from Cyprinus carpio. *Journal of the Mechanical Behavior of Biomedical Materials, 7,* 17–29.
48. Rho, J. Y., & Pharr, G. M. (1999). Effects of drying on the mechanical properties of bovine femur measured by nanoindentation. *Journal of Materials Science Materials in Medicine, 10* (8), 485–488.
49. Rodriguez-Florez, N., Oyen, M. L., & Shefelbine, S. J. (2013). Insight into differences in nanoindentation properties of bone. *Journal of the Mechanical Behavior of Biomedical Materials, 18,* 90–99.
50. Hughes, C. E., & White, C. A. (2009). Crack propagation in teeth: A comparison of perimortem and postmortem behavior of dental materials and cracks. *Journal of Forensic Sciences*, *54*(2), 263–266.
51. Kishen, A., & Asundi, A. (2005). Experimental investigation on the role of water in the mechanical behavior of structural dentine. *Journal of Biomedical Materials Research, Part A, 73*(2), 192–200.
52. Lievers, W. B., Lee, V., Arsenault, S. M., Waldman, S. D., & Pilkey, A. K. (2007). Specimen size effect in the volumetric shrinkage of cancellous bone measured at two levels of dehydration. *Journal of Biomechanics, 40*(9), 1903–1909.
53. Lievers, W. B., Poljsak, A. S., Waldman, S. D., & Pilkey, A. K. (2010). Effects of dehydration-induced structural and material changes on the apparent modulus of cancellous bone. *Medical Engineering & Physics, 32*(8), 921–925.
54. Panighi, M., & G'Sell, C. (1993). Effect of the tooth microstructure on the shear bond strength of a dental composite. *Journal of Biomedical Materials Research, Part A, 27*(8), 975–981.
55. Wood, J. D., Wang, R., Weiner, S., & Pashley, D. H. (2003). Mapping of tooth deformation caused by moisture change using moiré interferometry. *Dental Materials, 19*(3), 159–166.
56. Yang, W., Chen, I. H., Gludovatz, B., Zimmermann, E. A., Ritchie, R. O., & Meyers, M. A. (2013). Natural flexible dermal armor. *Advanced Materials, 25*(1), 31–48.
57. Gupta, H. S., Seto, J., Wagermaier, W., Zaslansky, P., Boesecke, P., & Fratzl, P. (2006). Cooperative deformation of mineral and collagen in bone at the nanoscale. *Proceedings of the National Academy of Sciences, 103*(47), 17741–17746.
58. Öchsner, A., & Ahmed, W. (Eds.). (2011). *Biomechanics of Hard Tissues*. Wiley.
59. Nelms, M. (2014) *Finite element analysis of shear resistant mechanisms for biolaminate interfaces*. Masters Thesis, University of Mississippi, Oxford, Mississippi, USA.
60. Wang, L., Song, J., Ortiz, C., & Boyce, M. C. (2009). Anisotropic design of a multilayered biological exoskeleton. *Journal of Materials Research, 24*(12), 3477–3494.

61. Hamed, E., & Jasiuk, I. (2012). Elastic modeling of bone at nanostructural level. *Materials Science and Engineering: R: Reports, 73*(3), 27–49.
62. Zimmermann, E. A., Gludovatz, B., Schaible, E., Dave, N. K., Yang, W., Meyers, M. A., & Ritchie, R. O. (2013). Mechanical adaptability of the Bouligand-type structure in natural dermal armour. *Nature communications*, 4.
63. Halpin, J. C., & Tsai, S. W. (1967). Environmental factors estimation in composite materials design. *AFML Trans*, 67–423.
64. Currey, J. D. (1969). The relationship between the stiffness and the mineral content of bone. *Journal of Biomechanics, 2*(4), 477–480.
65. Padawer, G. E., & Beecher, N. (1970). On the strength and stiffness of planar reinforced plastic resins. *Polymer Engineering & Science, 10*(3), 185–192.
66. Lusis, J., Woodhams, R. T., & Xanthos, M. (1973). The effect of flake aspect ratio on the flexural properties of mica reinforced plastics. *Polymer Engineering & Science, 13*(2), 139–145.
67. Weiner, S., & Wagner, H. D. (1998). The material bone: structure-mechanical function relations. *Annual Review of Materials Science, 28*(1), 271–298.
68. Jäger, I., & Fratzl, P. (2000). Mineralized collagen fibrils: a mechanical model with a staggered arrangement of mineral particles. *Biophysical Journal, 79*(4), 1737–1746.
69. Goodsell, D. S. (2004). *Bionanotechnology: lessons from nature*. Wiley.
70. Carretta, R., Lorenzetti, S., & Müller, R. (2012). Towards patient-specific material modeling of trabecular bone post-yield behavior. *International journal for numerical methods in biomedical engineering*.
71. Carpinteri, A., Cornetti, P., Pugno, N. M., & Sapora, A. (2008). Fractals to model hierarchical biomaterials. In *Advances in Science and Technology* (Vol. 58, pp. 54–59). Trans Tech Publications.
72. Cho, Y., Shin, J. H., Costa, A., Kim, T. A., Kunin, V., Li, J., et al. (2014). Engineering the shape and structure of materials by fractal cut. *Proceedings of the National Academy of Sciences, 111*(49), 17390–17395.
73. Pothuaud, L., Benhamou, C. L., Porion, P., Lespessailles, E., Harba, R., & Levitz, P. (2000). Fractal dimension of trabecular bone projection texture is related to three-dimensional microarchitecture. *Journal of Bone and Mineral Research, 15*(4), 691–699.
74. Ji, B., & Gao, H. (2010). Mechanical principles of biological nanocomposites. *Annual Review of Materials Research, 40,* 77–100.
75. Launey, M. E., Buehler, M. J., & Ritchie, R. O. (2010). On the mechanistic origins of toughness in bone. *Annual Review of Materials Research, 40,* 25–53.
76. Alexander, T., Antonis, L., Savvas, S., & Nikolaos, M. (2012). Nonintrusive 3D reconstruction of human bone models to simulate their bio-mechanical response. *3D. Research, 3*(2), 1–10.
77. Katz, J. L., Misra, A., Spencer, P., Wang, Y., Bumrerraj, S., Nomura, T., et al. (2007). Multiscale mechanics of hierarchical structure/property relationships in calcified tissues and tissue/material interfaces. *Materials Science and Engineering C, 27*(3), 450–468.
78. Fritsch, A., Hellmich, C.,& Young, P. (2011) Porosity-dependent elasticity and strength of ceramic bone biomaterials: Micromechanics-based assessment of power functions. Baumgartner, C. Biomedical Engineering. (2011). *Paper presented at IASTED International Conference: Bimedical Engineering, Innsbruck*. Austria. Online: Actapress.
79. Gautieri, A., Pate, M. I., Vesentini, S., Redaelli, A., & Buehler, M. J. (2012). Hydration and distance dependence of intermolecular shearing between collagen molecules in a model microfibril. *Journal of biomechanics, 45*(12), 2079–2083.
80. Buehler, M. J., & Wong, S. Y. (2007). Entropic elasticity controls nanomechanics of single tropocollagen molecules. *Biophysical Journal, 93*(1), 37–43.
81. Gautieri, A., Buehler, M. J., & Redaelli, A. (2009). Deformation rate controls elasticity and unfolding pathway of single tropocollagen molecules. *Journal of the Mechanical Behavior of Biomedical Materials, 2*(2), 130–137.

82. Gautieri, A., Vesentini, S., Montevecchi, F. M., & Redaelli, A. (2008). Mechanical properties of physiological and pathological models of collagen peptides investigated via steered molecular dynamics simulations. *Journal of Biomechanics, 41*(14), 3073–3077.
83. Buehler, M. J. (2006). Nature designs tough collagen: Explaining the nanostructure of collagen fibrils. *Proceedings of the National Academy of Sciences, 103*(33), 12285–12290.
84. Buehler, M. J. (2007). Hierarchical chemo-nanomechanics of proteins: Entropic elasticity, protein unfolding and molecular fracture. *Journal of Mechanics of Materials and Structures, 2*(6), 1019–1057.
85. Buehler, M. J., & Ackbarow, T. (2007). Fracture mechanics of protein materials. *Materials Today, 10*(9), 46–58.
86. Qi, H. J., Ortiz, C., & Boyce, M. C. (2006). Mechanics of biomacromolecular networks containing folded domains. *Transactions-American Society of Mechanical Engineers Journal of Engineering Materials And Technology, 128*(4), 509.
87. Eom, K., Yoon, G., Kim, J. I., & Na, S. (2010). Coarse-grained elastic models of protein structures for understanding their mechanics and dynamics. *Journal of Computational and Theoretical Nanoscience, 7*(7), 1210–1226.
88. Gautieri, A., Vesentini, S., Redaelli, A., & Buehler, M. J. (2011). Hierarchical structure and nanomechanics of collagen microfibrils from the atomistic scale up. *Nano Letters, 11*(2), 757–766.
89. Gautieri, A., Vesentini, S., Redaelli, A., & Buehler, M. J. (2012). Viscoelastic properties of model segments of collagen molecules. *Matrix Biology, 31*(2), 141–149.
90. Qin, Z., Gautieri, A., Nair, A. K., Inbar, H., & Buehler, M. J. (2012). Thickness of Hydroxyapatite nanocrystal controls mechanical properties of the collagen–Hydroxyapatite interface. *Langmuir*, *28*(4), 1982–1992. Raton, FL: Taylor and Francis.
91. Fantner, G. E., Hassenkam, T., Kindt, J. H., Weaver, J. C., Birkedal, H., Pechenik, L., et al. (2005). Sacrificial bonds and hidden length dissipate energy as mineralized fibrils separate during bone fracture. *Nature Materials, 4*(8), 612–616.
92. Marko, J. F., & Siggia, E. D. (1995). Stretching DNA. *Macromolecules, 28*(26), 8759–8770.
93. Jernigan, R. L., & Flory, P. J. (1969). Moments of chain vectors for models of polymer chains. *The Journal of Chemical Physics, 50*(10), 4178–4185.
94. Boyce, M. C., & Arruda, E. M. (2000). Constitutive models of rubber elasticity: a review. *Rubber Chemistry and Technology, 73*(3), 504–523.
95. Marko, J. F. (1997). *Stretching must twist DNA. EPL (Europhysics Letters), 38*(3), 183.
96. Keten, S., & Buehler, M. J. (2008). Geometric confinement governs the rupture strength of H-bond assemblies at a critical length scale. *Nano Letters, 8*(2), 743–748.
97. Tai, K., Dao, M., Suresh, S., Palazoglu, A., & Ortiz, C. (2007). Nanoscale heterogeneity promotes energy dissipation in bone. *Nature materials, 6*(6), 454–462.
98. Tõnsuaadu, K., Gross, K. A., Plūduma, L., & Veiderma, M. (2012). A review on the thermal stability of calcium apatites. *Journal of Thermal Analysis and Calorimetry, 110*(2), 647–659.
99. Pistoia, W., Van Rietbergen, B., Lochmüller, E. M., Lill, C. A., Eckstein, F., & Rüegsegger, P. (2002). Estimation of distal radius failure load with micro-finite element analysis models based on three-dimensional peripheral quantitative computed tomography images. *Bone, 30* (6), 842–848.
100. Schileo, E., Taddei, F., Cristofolini, L., & Viceconti, M. (2008). Subject-specific finite element models implementing a maximum principal strain criterion are able to estimate failure risk and fracture location on human femurs tested in vitro. *Journal of Biomechanics, 41*(2), 356–367.
101. Carnelli, D., Gastaldi, D., Sassi, V., Contro, R., Ortiz, C., & Vena, P. (2010). A finite element model for direction-dependent mechanical response to nanoindentation of cortical bone allowing for anisotropic post-yield behavior of the tissue. *Journal of Biomechanical Engineering, 132*(8), 081008.
102. Shuchun, Z., & Yueguang, W. (2007). Effective elastic modulus of bone-like hierarchical materials. *Acta Mechanica Solida Sinica, 20*(3), 198–205.

103. Charlebois, M., Jirásek, M., & Zysset, P. K. (2010). A nonlocal constitutive model for trabecular bone softening in compression. *Biomechanics and Modeling in Mechanobiology, 9*(5), 597–611.
104. Mercer, C., He, M. Y., Wang, R., & Evans, A. G. (2006). Mechanisms governing the inelastic deformation of cortical bone and application to trabecular bone. *Acta Biomaterialia, 2*(1), 59–68.
105. Natali, A. N., Carniel, E. L., & Pavan, P. G. (2008). Constitutive modelling of inelastic behaviour of cortical bone. *Medical Engineering & Physics, 30*(7), 905–912.
106. Cezayirlioglu, H., Bahniuk, E., Davy, D. T., & Heiple, K. G. (1985). Anisotropic yield behavior of bone under combined axial force and torque. *Journal of Biomechanics, 18*(1), 61–69.
107. Johnson, T. P. M., Socrate, S., & Boyce, M. C. (2010). A viscoelastic, viscoplastic model of cortical bone valid at low and high strain rates. *Acta Biomaterialia, 6*(10), 4073–4080.
108. Ehlers, W., Karajan, N., & Markert, B. (2006). A porous media model describing the inhomogeneous behaviour of the human intervertebral disc. *Materialwissenschaft und Werkstofftechnik, 37*(6), 546–551.
109. Bayraktar, H. H., Morgan, E. F., Niebur, G. L., Morris, G. E., Wong, E. K., & Keaveny, T. M. (2004). Comparison of the elastic and yield properties of human femoral trabecular and cortical bone tissue. *Journal of Biomechanics, 37*(1), 27–35.
110. Stölken, J. S., & Kinney, J. H. (2003). On the importance of geometric nonlinearity in finite-element simulations of trabecular bone failure. *Bone, 33*(4), 494–504.
111. Barkaoui, A., & Hambli, R. (2014). Nanomechanical properties of mineralised collagen microfibrils based on finite elements method: biomechanical role of cross-links. *Computer Methods in Biomechanics and Biomedical Engineering, 17*(14), 1590–1601.
112. Hambli, R., & Barkaoui, A. (2012). Physically based 3D finite element model of a single mineralized collagen microfibril. *Journal of Theoretical Biology, 301,* 28–41.
113. Akiva, U., Wagner, H. D., & Weiner, S. (1998). Modelling the three-dimensional elastic constants of parallel-fibred and lamellar bone. *Journal of Materials Science, 33*(6), 1497–1509.
114. Verhulp, E., van Rietbergen, B., Müller, R., & Huiskes, R. (2008). Indirect determination of trabecular bone effective tissue failure properties using micro-finite element simulations. *Journal of Biomechanics, 41*(7), 1479–1485.
115. Yeh, O. C., & Keaveny, T. M. (2001). Relative roles of microdamage and microfracture in the mechanical behavior of trabecular bone. *Journal of Orthopaedic Research, 19*(6), 1001–1007.
116. Keaveny, T. M., Wachtel, E. F., Zadesky, S. P., & Arramon, Y. P. (1999). Application of the Tsai–Wu quadratic multiaxial failure criterion to bovine trabecular bone. *Journal of Biomechanical Engineering, 121*(1), 99–107.
117. Zysset, P., & Rincón, L. (2006). An alternative fabric-based yield and failure criterion for trabecular bone. In *Mechanics of Biological Tissue* (pp. 457–470). Berlin Heidelberg: Springer.
118. Moore, T. A., & Gibson, L. J. (2002). Microdamage accumulation in bovine trabecular bone in uniaxial compression. *Journal of Biomechanical Engineering, 124*(1), 63–71.
119. Kosmopoulos, V., & Keller, T. S. (2003). Finite element modeling of trabecular bone damage. *Computer Methods in Biomechanics and Biomedical Engineering, 6*(3), 209–216.
120. Kosmopoulos, V., Schizas, C., & Keller, T. S. (2008). Modeling the onset and propagation of trabecular bone microdamage during low-cycle fatigue. *Journal of Biomechanics, 41*(3), 515–522.
121. Kosmopoulos, V., & Keller, T. S. (2008). Predicting trabecular bone microdamage initiation and accumulation using a non-linear perfect damage model. *Medical Engineering & Physics, 30*(6), 725–732.
122. Garcia, D., Zysset, P. K., Charlebois, M., & Curnier, A. (2009). A three-dimensional elastic plastic damage constitutive law for bone tissue. *Biomechanics and Modeling in Mechanobiology, 8*(2), 149–165.

123. Buehler, M. J. (2006). Atomistic and continuum modeling of mechanical properties of collagen: elasticity, fracture, and self-assembly. *Journal of Materials Research, 21*(08), 1947–1961.
124. Buehler, M. J. (2006). Mechanics of protein crystals: Atomistic modeling of elasticity and fracture. *Journal of Computational and Theoretical Nanoscience, 3*(5), 670–683.
125. Buehler, M. J. (2007). Molecular nanomechanics of nascent bone: fibrillar toughening by mineralization. *Nanotechnology, 18*(29), 295102.
126. Buehler, M. J. (2007). Nano-and micromechanical properties of hierarchical biological materials and tissues. *Journal of Materials Science, 42*(21), 8765–8770.
127. Buehler, M. J. (2008). Molecular architecture of collagen fibrils: a critical length scale for tough fibrils. *Current Applied Physics, 8*(3), 440–442.
128. Buehler, M. J. (2008). Nanomechanics of collagen fibrils under varying cross-link densities: atomistic and continuum studies. *Journal of the Mechanical Behavior of Biomedical Materials, 1*(1), 59–67.
129. Buehler, M. J. (2009, January). Defining nascent bone by the molecular nanomechanics of mineralized collagen fibrils. In *ASME 2009 International Mechanical Engineering Congress and Exposition* (pp. 795–798). American Society of Mechanical Engineers.
130. Buehler, M. J., Yao, H., Ji, B., & Gao, H. (2005). Atomistic and continuum studies of flaw tolerant nanostructures in biological systems. In *Materials Research Society Symposium Proceedings* (Vol. 844, p. 207). Warrendale, Pa.; *Materials Research Society*; 1999.
131. Chevalier, Y., Charlebois, M., Pahr, D., Varga, P., Heini, P., Schneider, E., et al. (2008). A patient-specific finite element methodology to predict damage accumulation in vertebral bodies under axial compression, sagittal flexion and combined loads. *Computer methods in biomechanics and biomedical engineering, 11*(5), 477–487.
132. Gupta, H. S., Wagermaier, W., Zickler, G. A., Hartmann, J., Funari, S. S., Roschger, P., et al. (2006). Fibrillar level fracture in bone beyond the yield point. *International Journal of Fracture, 139*(3–4), 425–436.
133. Gupta, H. S., Wagermaier, W., Zickler, G. A., Raz-Ben Aroush, D., Funari, S. S., Roschger, P., et al. (2005). Nanoscale deformation mechanisms in bone. *Nano Letters, 5*(10), 2108–2111.
134. Gupta, H. S., & Zioupos, P. (2008). Fracture of bone tissue: The hows and the whys. *Medical Engineering & Physics, 30*(10), 1209–1226.
135. Ikoma, T., Kobayashi, H., Tanaka, J., Walsh, D., & Mann, S. (2003b). Physical properties of type I collagen extracted from fish scales of Pagrus major and Oreochromis niloticas. *International Journal of Biological Macromolecules*, 32(3), 199-204. *International, 48,* 407–413.
136. Katz, J. L. (1971). Hard tissue as a composite material—I. Bounds on the elastic behavior. *Journal of Biomechanics, 4*(5), 455–473.
137. Libonati, F., Nair, A. K., Vergani, L., & Buehler, M. J. (2013). Fracture mechanics of hydroxyapatite single crystals under geometric confinement. *Journal of the Mechanical Behavior of Biomedical Materials, 20,* 184–191.
138. Peterlik, H., Roschger, P., Klaushofer, K., & Fratzl, P. (2005). From brittle to ductile fracture of bone. *Nature Materials, 5*(1), 52–55.
139. Ritchie, R. O., Kinney, J. H., Kruzic, J. J., & Nalla, R. K. (2005). A fracture mechanics and mechanistic approach to the failure of cortical bone. *Fatigue and Fracture of Engineering Materials and Structures, 28*(4), 345–371.
140. Srinivasan, A. V., Haritos, G. K., Healberg, H. L., & Jones, W. F. (1996). Biomimetics: Advancing man-made materials through guidance from nature-Update. *Applied Mechanics Reviews, 49,* S194–S200.
141. Tang, Y., Ballarini, R., Buehler, M. J., & Eppell, S. J. (2010). Deformation micromechanisms of collagen fibrils under uniaxial tension. *Journal of the Royal Society, Interface, 7* (46), 839–850.
142. Carlisle, C. R., Coulais, C., & Guthold, M. (2010). The mechanical stress–strain properties of single electrospun collagen type I nanofibers. *Acta biomaterialia, 6*(8), 2997–3003.

143. Saber-Samandari, S., & Gross, K. A. (2010). The use of thermal printing to control the properties of calcium phosphate deposits. *Biomaterials, 31*(25), 6386–6393.
144. Nudelman, F., Pieterse, K., George, A., Bomans, P. H., Friedrich, H., Brylka, L. J., ... & Sommerdijk, N. A. (2010). The role of collagen in bone apatite formation in the presence of hydroxyapatite nucleation inhibitors. *Nature materials, 9*(12), 1004–1009.
145. Song, J., Reichert, S., Kallai, I., Gazit, D., Wund, M., Boyce, M. C., & Ortiz, C. (2010). Quantitative microstructural studies of the armor of the marine threespine stickleback (Gasterosteus aculeatus). *Journal of structural biology, 171*(3), 318–331.
146. Wegst, U., Schecter, M., Donius, A., and Hunger, P. (2010). "Biomaterials by Freeze Casting." *Philosophical Transactions of The Royal Society: A* 368: 2099–2121.

Constitutive Material Models for High Strain Rate Behavior of Cementitious Materials from Material Chemistry—Molecular Dynamics Modeling Methodology with Illustrative Application to Hydrated Calcium Silicate Hydrate Jennite

J. Rivas Murillo, R. Mohan and A. Mohamed

1 Introduction

Studies of high strain rate (HSR) behavior of cementitious materials and cement-based structures are important to predict their performance when shock waves are expected to propagate, for instance, when cement-based structures are subjected to blast loads or ballistic impacts [10, 39, 40]. Design and understanding of cement-based structures capable of withstanding HSR deformation depend on proper characterization of the cementitious materials under HSR loading conditions and development of accurate material models. However, this is a very contentious area due to wide variability of the reported experimental data [4, 10]. A comprehensive review of experimental work that had been performed to characterize the rate-dependent behavior of cementitious materials up to the 1980s was provided by Bischoff et al. [4] and summarized in a series of graphs shown in Figs. 1, 2, and 3.

The wide variability of experimental data is due to complex nature of the cementitious materials. Not only are the nano- and microstructural properties of cementitious materials highly sensitive to cement clinker composition, hydration process, and curing conditions during their formation, but also their mechanical response is affected by specimen storage and test conditions [10, 16, 31, 38–41]. Additionally, most commonly used method to measure and probe HSR behavior in materials, the split Hopkinson pressure bar test, has a very important intrinsic difficulty, which requires a constant or nearly constant strain rate to be maintained

J. Rivas Murillo · R. Mohan (✉) · A. Mohamed
Department of Nanoengineering, Joint School of Nanoscience and Nanoengineering, North Carolina A&T State University, Greensboro, NC, USA
e-mail: rvmohan@ncat.edu

S. Gopalakrishnan and Y. Rajapakse (eds.), *Blast Mitigation Strategies in Marine Composite and Sandwich Structures*, Springer Transactions in Civil and Environmental Engineering, https://doi.org/10.1007/978-981-10-7170-6_22

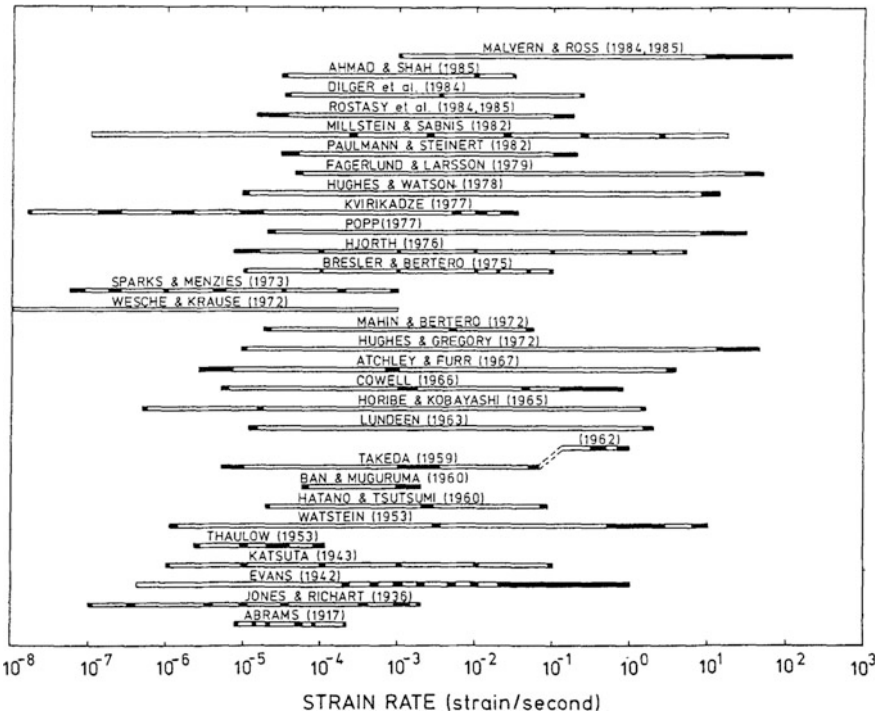

Fig. 1 Range of strain rates used in experimental characterization of the strain rate-dependent properties of cementitious materials before 1990 [27] (Reproduced with Permission)

during test [10], that contributes to the great dispersion of experimental data reported.

Some of the most recent studies highlight variety of experimental conditions employed in cementitious materials following split Hopkinson pressure bar testing. Chen et al. [10] reported experimental characterization of cement paste, mortar, and concrete samples (ASTM type I cement with 0.45 water/cement ratio, strain rates from ~25 to ~150 s^{-1}) using a pulse-shape split Hopkinson pressure bar that led to the development of empirical relations for the dynamic increase factor, the ratio between dynamic and static strength of material, and a constitutive model for cement paste, mortar, and concrete accounting for strain rate. Wang et al. [39, 40] reported results from plain and fiber-reinforced (straight steel fibers, polyethylene fibers, and a combination of the two) high-strength concrete (ASTM type I cement with 0.36 water/cement ratio) with strain rates ranging from 40 to 300 s^{-1} [40] and from 10^{-4} to 300 s^{-1} [39]. Rong et al. [31] studied ultra-high performance cement-based composites (Portland cement with silica fume, fly ash, and slag), with applicability of Johnson–Holmquist concrete material model shown using finite element (FE) modeling. Wu et al. [41] focused on the effect of strain rate on the dynamic tensile strength of concrete and the spalling phenomenon and compared

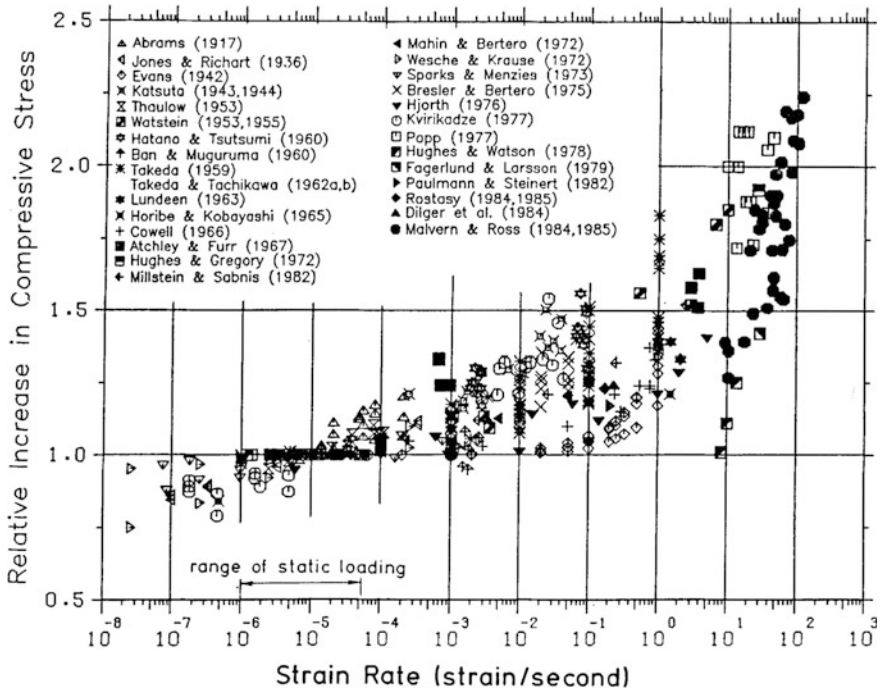

Fig. 2 Relative change in compressive strength due to changes in strain rate for cementitious materials. Results reported before 1990 [27] (Reproduced with Permission)

experimental results to an FE model defined by a continuous damage accumulation model. Wang et al. [38] reported an experimental study of HSR response of mortar under one-dimensional stress, one-dimensional strain at high pressure using a gas gun, and quasi-one-dimensional strain using a passive confining technique in a split Hopkinson pressure bar. Strain rate dependency of mechanical properties was found not to be linear with the damage evolution, and results support use of a damage-modified nonlinear viscoelastic constitutive relation for mortar. Grote et al. [16] investigated mortar (with fly ash) and concrete (42% aggregate in volume) specimens at strain rates between 250 and 1700 s^{-1}, bar and plate impact machine (strain rate of 10^4 s^{-1} with pressures between 1 and 1.5 GPa) to formulate a constitutive model for concrete and mortar at strain rates between 10^{-3} and 10^4 s^{-1} [16].

In all cases, experimental data is typically used to create material constitutive models or identified parameters for equations aimed at explaining the mechanisms responsible for changes in the mechanical behavior of cementitious materials under HSR conditions [10, 39, 40]. Experimental information for such models, however, always comes from a very narrow sampling of the spectrum of cementitious materials, and each experimental study observes the behavior of specimens that are intrinsically different.

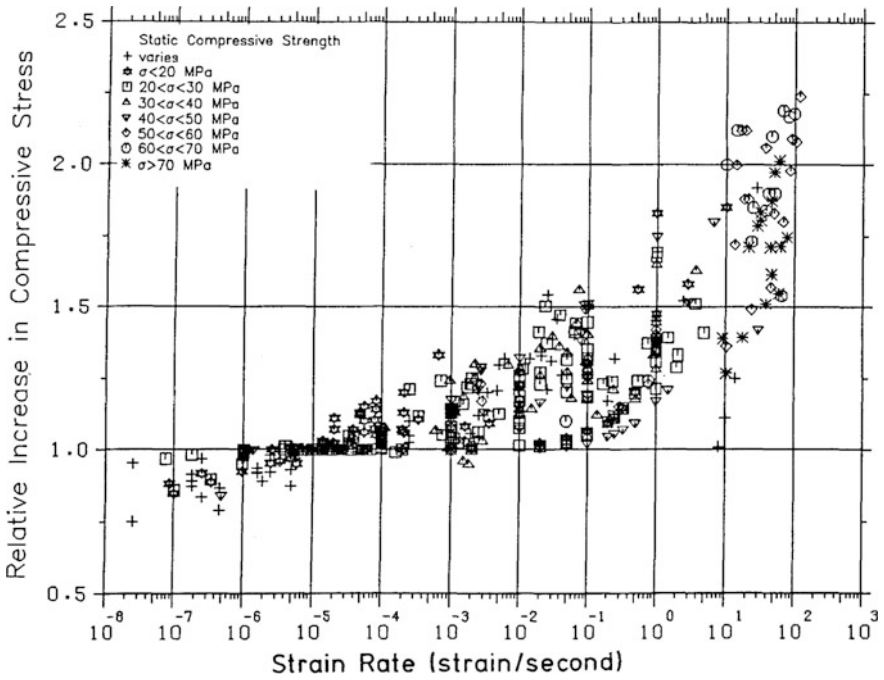

Fig. 3 Relative change in compressive strength due to changes in strain rate for cementitious materials based on the quasi-static compressive strength of the specimens. Results reported before 1990 [27] (Reproduced with Permission)

Chen et al. [10] estimated parameters for a constitutive model of the form

$$\sigma = \left(1 - \left(D_1 + D_0 * \left(\dot{\varepsilon}_{dyn}\right)^{\zeta}\right) * \varepsilon\right) * \left(A_0 + A_1 * \left(\dot{\varepsilon}_{dyn}/\dot{\varepsilon}_{sta}\right)^{B}\right) * \varepsilon, \tag{1}$$

where σ represents the stress in the specimen, ε is the strain, $\dot{\varepsilon}_{sta}$ is the quasi-static strain rate, and $\dot{\varepsilon}_{dyn}$ represents the dynamic strain rate. Zhou et al. [44] used numerical models to investigate the effect of confinement of specimens in experimental setup used in typical HSR experiments of cementitious materials on the observed dynamic increase factor. This study indicated that dynamic increase factor observed in physical experiments has a component due to material response under high strain rate conditions and another due to confinement of specimens. A 2D axisymmetric finite element model with circular inclusion to represent large sand aggregate in mortar, plus a thin interfacial transition zone, was used to explain the phenomena affecting perceived dynamic increase factor of cementitious materials using a basic constitutive theoretical model recommended by the Comite Euro-International du Beton [11]. Lu et al. [20] proposed a constitutive model for cementitious materials based on continuum fracture theory of microcrack nucleation. Predicted properties based on the application of this model compare well with

experimental results; however, they do not offer any insights into the phenomena governing the response of cementitious materials under high strain rate loading. Hentz et al. [17] used a 3D discrete element model to investigate response of cementitious materials under dynamic loading with the model calibrated to reproduce experimentally observed behavior in macroscopic specimens of concrete under quasi-static testing conditions creating a quasi-empirical model that was a good predictor of macroscopic behavior of concrete. It, however, does not provide insights into the mechanisms in the behavior of cement under HSR conditions, with response of strain rate dependence of cement modeled using a simple theoretical approach [20]. Park et al. [27] developed a finite element model built on experimental results [38] using a two-phase microstructure model of concrete. Drucker–Prager constitutive material model was calibrated with parameters determined from experimental data [38]. Majority of deformation is found to be in mortar phase, which controls HSR behavior, but do not provide insights into the factors that dominate HSR response.

Unlike with other material systems, power of computational modeling at nano- and microscale has not been fully applied toward understanding mechanisms driving behavior of cementitious materials under HSR conditions. HSR behavior of nanoscale metallic systems is commonly investigated by directly simulating deformation of material under HSR loading and using different structural measurements to estimate effects of change in strain rate. These studies for metallic systems under HSR include shock-induced breaking of single crystals and nanowires [18, 19, 36, 37], plastic deformation [29, 32], void nucleation and collapse [13, 33], ablation and spallation in single crystals [43], hydrostatic and shock-induced melting [2], and changes in material properties induced by shock [7]. The study of the HSR behavior of nanoscale metallic systems by direct simulation of HSR loading is aided by well-established quantitative measures of structural changes in crystalline materials. In metallic systems, quantification of coordination numbers and centro-symmetry parameters lead to the identification of dislocations, twinning regions, and grain boundaries in polycrystalline metals, which allows a clear observation of the changes induced by the HSR loading. Although quantities such as the centro-symmetry parameter have not yet been established for complex nanoscale structures of cement paste, direct simulation of deformation of this material system under HSR would enable observation of important damage-related phenomena like void formation and collapse, crack initiation and propagation, and ablation and spallation.

Computational modeling can also be used to estimate and predict constitutive material models from nanoscale material chemistry structures of cement-based materials. Such an approach would allow overcoming the need for purely phenomenological constitutive models. A modeling method based on material chemistry for relevant constitutive material models for behavior under HSR loading with an illustrative application to hydrated cement paste constituent calcium silicate hydrate (CSH), with a molecular structure represented by Jennite [26], is presented in this chapter. Thermodynamic state of a material involving longitudinal plane

shock waves can be represented in the form of a relation between the axial stress, or pressure, in the material and the specific volume as discussed next.

2 Hugoniot Curves

Longitudinal plane shock wave propagation through a solid leads it to develop a uniaxial strain state. The description of effects of shock on thermodynamic properties of a material can be obtained from the solution of system of equations given by the formulation of conservation of mass, linear momentum, and energy across the shock wave front. The set of equations typically known as jump equations [3, 12] is given by

$$\begin{aligned} [[\rho]][u_s] - [[\rho\dot{x}]] &= 0 \\ [[\rho\dot{x}]]u_s - \left[\left[\rho\dot{x}^2 - \sigma_{11}\right]\right] &= 0 \\ \left[\left[\rho\left(\left[\varepsilon + \frac{1}{2}\dot{x}^2\right]\right)\right]\right]u_s - \left[\left[\left(\left(\varepsilon + \frac{1}{2}\dot{x}^2\right) - \sigma_{11}\right)\dot{x}\right]\right] &= 0, \end{aligned} \tag{2}$$

where ρ is the density of material, u_s is the speed of propagating shockwave, $\dot{x}$ is the velocity of particles of material, σ_{11} is the axial stress in the material, and ε is the specific internal energy of the material. Notation $[.15em[\xi].15em]$ indicates the jump of a quantity ξ across the wavefront, i.e., the difference between its value after and before the passing of the shockwave front, $[.15em[\xi].15em] = [\xi^+] - \xi^-$. The passing of a shockwave effectively creates two domains in the material, namely, un-shocked or reference state, characterized by ξ^- properties, and shocked state, characterized by properties ξ^+. From Eq. (2), it can be seen that nine quantities define the state of material affected by passing of a shockwave, namely four un-shocked quantities $\left([\rho^-], \dot{x}^-, \sigma_{11}^-, [\varepsilon^-]\right)$ typically known, four shocked quantities $\left([\rho^+], \dot{x}^+, \sigma_{11}^+, \varepsilon^+\right)$ typically unknown, and shockwave speed [12]. If the shockwave speed or any of the shocked properties is known, jump equations along with a material equation of state (EOS) can be used to fully describe effects of passing of a shockwave.

Estimating and obtaining the EOS for materials is a fundamental part of modeling shocks physics, as without appropriate material models, predictions about material behavior under HSR loading conditions cannot be made. Although not a full EOS, a Hugoniot curve provides a relation between pairs of thermodynamic properties of a material undergoing effects of a passing shock wave. In essence, it represents thermodynamic state changes that a material experiences due to effect of a shockwave. Such relationship can be used to characterize a material model and complements jump equations in the study of shockwave propagation [12].

A Hugoniot curve can be obtained from physical experimentation [6, 15], or using theoretical and numerical models. Among numerical approaches [8, 9, 14, 21, 30], it is common to use computational models based on molecular dynamics

(MD) or Monte Carlo simulations (MC) to estimate points on the surface of a function defined as

$$h(T,v) = \varepsilon(T,v) - \varepsilon_R(T_R, v_R) - \frac{1}{2}(p(T,v) + p_R(T_R, v_R))^*(v_R - v), \tag{3}$$

where T, v, ε, *and* p represent the temperature, specific volume, internal specific energy, and the pressure in the material, respectively. The subscript R indicates that the properties are measured at certain reference state, typically the un-shocked state. Equation (3) is defined as Rankine–Hugoniot equation. Computational modeling analysis can be used to obtain points on the surface $h(T,v)$ and interpolation techniques applied to find properties corresponding to $h(T,v) = 0$, corresponding to Hugoniot state of the material. This might require a large amount of computational simulations in order to obtain enough points on $h(T,v)$ surface for interpolation and extrapolation purposes. The technique developed by Maillet et al. [21] does not map points on $h(T,v)$ for later interpolation and extrapolation of the quantities leading to $h(T,v) = 0$ but rather uses MD with a set of variations to dynamic equations in order to satisfy the condition $h(T,v) = 0$ directly. This approach seems more suited for in-house MD implementations where researchers can modify the equations and analysis code describing evolution of the system. A more suitable technique is, however, required employing available MD analysis codes and modeling capabilities directly.

The modeling approach described in this chapter uses Mie–Grüneisen EOS [15] and Rankine–Hugoniot equation to formulate a methodology to obtain axial stress/pressure versus specific volume Hugoniot curves using MD modeling, without a need for mapping points on the surface described in Eq. (3). Theoretical background followed by our MD modeling methodology and demonstrative application to calcium silicate hydrate (CSH) Jennite representation of hydrated cement past is presented. Our MD material modeling methodology is, however, applicable to any solid-state material system based on its molecular configuration and provides an effective material modeling methodology to understand the effect of material chemistry level variations, and materials by design tailoring of associated material chemistry.

3 Axial Stress/Pressure Versus Specific Volume Hugoniot

For an isotropic material under uniaxial strain, axial stress is given by Eq. (4):

$$\sigma_{11} = -p - \frac{4}{3}\tau_{max}, \tag{4}$$

where p and τ_{max} represent the hydrostatic pressure and maximum shear stress. Stress state developed in a material under shock would involve shear stresses that are higher than shear strength of the material. This is particularly true for components of cement paste that are brittle in nature. However, since the material is confined, failure due to shear stress will not occur; instead, the maximum shear stress developed would be equal to or exceed the shear strength of the material. In the development of modeling approach presented in this chapter, τ_{max} is thus replaced by shear strength of the material, τ_s.

$$\sigma_{11} = -p - \frac{4}{3}\tau_s \tag{5}$$

Thermodynamic processes occurring during propagation of a shock wave are adiabatic, and Hugoniot curves represent the behavior of material under adiabatic conditions, though their effects can be estimated based on a study of isothermal processes [12, 15]. According to Mie–Grüneisen EOS [15]

$$p(v) = p^{(H)}(v) + \frac{\gamma(v)}{v}\left(\varepsilon(v) - \varepsilon^{(H)}(v)\right) \tag{6}$$

where the super-index (H) indicates a property that is measured along the Hugoniot. v and ε represent the specific volume and the specific internal energy of the material, respectively. γ is a material property known as Grüneisen parameter, given by Eq. (7)

$$\gamma = v\left.\frac{\partial p}{\partial \varepsilon}\right|_v \tag{7}$$

If isothermal pressure and isothermal specific internal energy versus specific volume relationships for a material are known, indicated with superscript (θ) in Eq. (8), Hugoniot pressure versus specific volume can be obtained from Eq. (6) as

$$p^{(H)}(v) = \frac{p^{(\theta)}(v) + \frac{\gamma(v)}{v}\left(\varepsilon_R - \varepsilon^{(\theta)}(v)\right)}{1 - \frac{\gamma(v)}{2v}(v_R - v)} \tag{8}$$

In Eq. (8), specific internal energy along the Hugoniot, $\varepsilon^{(H)}$, was replaced using its relation with Hugoniot pressure presented in Eq. (9), which is known as Rankine–Hugoniot equation [12, 15]

$$\varepsilon^{(H)} = \varepsilon_R + \frac{1}{2}(p(v) - p_R)(v_R - v) \tag{9}$$

In Eqs. (8) and (9), subscript R indicates that properties are measured at a certain reference state, typically un-shocked state of the material. Following these discussions, for a full description and material modeling of axial stress versus specific volume Hugoniot, knowledge of four quantities are required: (i) isothermal pressure, and (ii) isothermal specific internal energy versus specific volume variation, (iii) Grüneisen parameter, and (iv) shear strength as a function of the specific volume of the material. All these quantities can be obtained from MD modeling analysis employing material molecular configurations as discussed next.

4 Molecular Dynamics Methodology

This section describes MD methodologies to estimate axial stress versus specific volume Hugoniot for a material system based on material chemistry molecular structure.

4.1 Grüneisen Parameter Modeling

For a system with a constant specific volume v, solution of Eq. (7) can be written as

$$\Delta p = \left(\frac{\gamma}{v}\right)\Delta\varepsilon \tag{10}$$

A change in specific internal energy and pressure is produced by a change in any thermodynamic property other than specific volume. Based on Eq. (10), a series of MD modeling analysis is set up using a Canonical ensemble to estimate the Grüneisen parameter for any given specific volume. An MD canonical ensemble (*NVT* ensemble) is one where a number of particles in system (N), volume (V), and temperature (T) are kept constant [1], and ensuring that specific volume remains constant. If the system is equilibrated at different temperatures, data for pressure and specific internal energy at different constant temperatures can be obtained. Following Eq. (10), relation between change in pressure and change in specific internal energy is given by a linear function, slope of which gives Grüneisen parameter for a given specific volume.

4.2 Isothermal Compression Model

An isothermal compression model is setup using a series of isothermal–isobaric MD ensembles (*NPT* ensemble), where a number of particles (*N*), temperature (*T*), and pressure (*P*) remain constant [1]. Isothermal compression model is set up by gradually increasing the pressure on a molecular system. Specific internal energy and specific volume are obtained as time averages after equilibration at each pressure increment. Results of this MD model are two sets of data for isothermal pressure and specific internal energy variation with specific volume. Following Eq. (8) these two sets of data, along with Grüneisen parameter function, lead to constitutive material modeling of pressure versus specific volume Hugoniot curve. This, along with shear strength versus specific volume of material, allows calculating axial stress versus specific volume Hugoniot curve (Eq. 6).

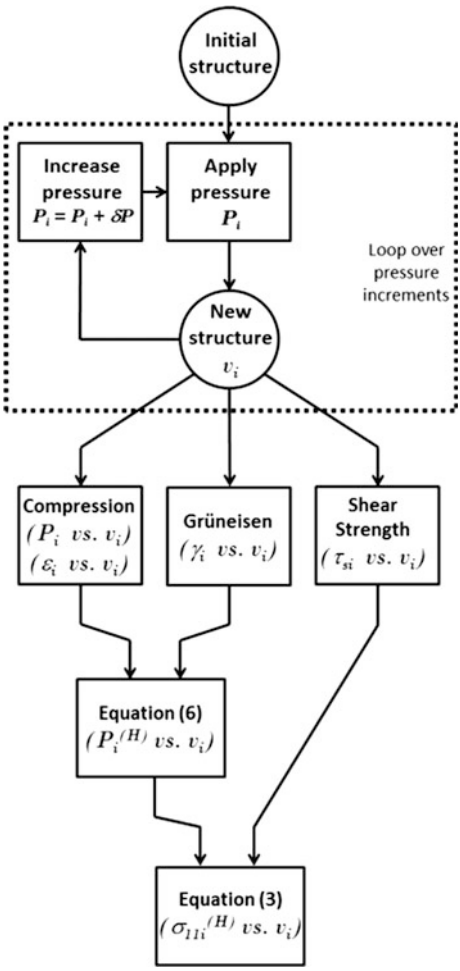

Fig. 4 Flow diagram of MD modeling methodology

4.3 Shear Strength Model

MD modeling analysis is set up by using a series of Canonical (NVT) ensembles. In order to simulate effect of shear deformation on the material, a series of deformations are applied to the molecular system according to a procedure described in Pellenq et al. [28]. The molecular system is deformed, as it would deform by a shear force, and it is subsequently equilibrated. The shear stress is obtained as a time average after the equilibration. Applying shear deformation in small increments provides a shear stress versus shear strain at a given specific volume, and predictive shear strength. This leads to characterizing shear strength versus specific volume data needed to produce the axial stress versus specific volume Hugoniot curve. Complete MD modeling methodology with all sub-models is illustrated in Fig. 4.

5 Demonstrative and Illustrative Application to CSH Jennite

Cement paste, consisting of hydrated and unhydrated cement material constituents, is formed during hydration when the dry cement clinkers are mixed with water. Complex microstructures and associated hydrated material chemistry are of significant interest. Nanoscale models built from molecular material configurations coupled with MD modeling (Sect. 4) provide an effective means to understand material chemistry effects on property changes, and associated material constitutive models employed at engineering scale. The methodology described in Sect. 4 is applied and demonstrated to obtain axial stress–specific volume behavior of nanoscale calcium silicate hydrate (CSH) Jennite (CSH Jennite), which is a mineral structure commonly used to represent the hydrated binder material [5, 34]. MD modeling analyses were implemented using Discover module of Accelrys Material Studio®, with complete details of MD implementation presented in Mohamed [24]. Molecular structure of CSH Jennite used for this study was published by Bonaccorsi et al. [5]. In this illustrative application, material chemistry molecular model consisted of a single unit cell structure of CSH Jennite (68 atoms) that was modeled using periodic boundary conditions in all directions. Results based on MD analysis from the demonstrative application are illustrated. MD modeling analysis is thus effective to estimate high strain rate behavior of cement-based materials and associated constitutive material models, which are essential to understand shock and blast loading conditions and their mitigation in defense applications.

High strain properties of cement-based materials are generally studied using experimental setups to obtain their EOS or their Hugoniot curves [23, 35]. Number of costly experiments required can be reduced through effective implementation of computational material modeling techniques, such as the one introduced and presented in this chapter.

5.1 Ghrüneisen Parameter Model

Although the Grüneisen parameter is a function of the specific volume of the material, the quantity $\left[\left(\frac{\gamma}{v}\right)\right]$ can be assumed to be constant [15]. Therefore, if $\left[\left(\frac{\gamma}{v}\right)\right]$ is estimated for certain reference state, defined by a specific volume, v_R, the quantity $\left(\frac{\gamma_R}{v_R}\right)$ can be used instead of $\left(\frac{\gamma}{v}\right)$ in Eq. (8); γ_R represents the Grüneisen parameter at the chosen reference state. For the hydrated CSH Jennite molecular structure illustrated in this chapter, reference state chosen corresponds to a specific volume of 0.424 cm^3/g (single unit cell of CSH Jennite molecular structure with a volume of 759.5 $Å^3$). Six canonical ensembles were set up at temperatures of 200, 300, 400, 500, 600, and 700 K. Equilibrium specific internal energy and pressure of each of these models were used to obtain the Grüneisen parameter, γ_R, for chosen reference specific volume according to Eq. (10). Pressure versus specific internal energy from this series of MD modeling analysis for CSH Jennite molecular chemistry structure is shown in Fig. 5. The slope of the fitting line in Fig. 5 corresponds to the quantity $\left(\frac{\gamma}{v}\right)$, and is computed to be 1342 ± 444 kg/m^3, with the Grüneisen parameter of 0.57 ± 0.188.

5.2 Isothermal Compression Model

Using a single unit cell molecular structure of CSH Jennite, pressure in the system was gradually increased from 0.0001 GPa (atmospheric pressure) to 5 GPa in increments of 0.1 GPa. Specific volume and specific internal energy were obtained using time averages after the system has reached equilibrium. More details of MD implementation can be found in Mohamed [24] and Rivas Murillo et al. [26]. The isothermal pressure versus specific volume and specific internal energy versus

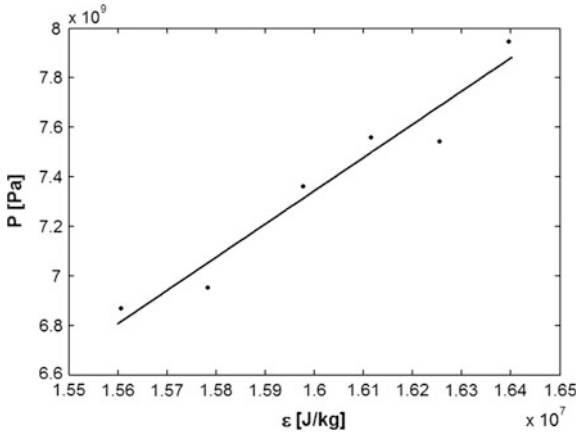

Fig. 5 Pressure versus specific internal energy for CSH Jennite modeled using canonical ensembles at different temperatures

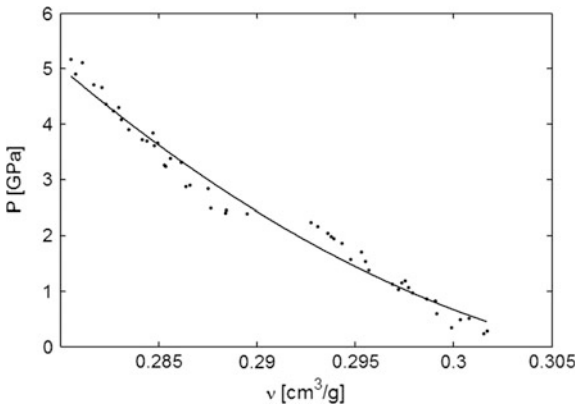

Fig. 6 Isothermal pressure versus specific volume for CSH Jennite molecular structure

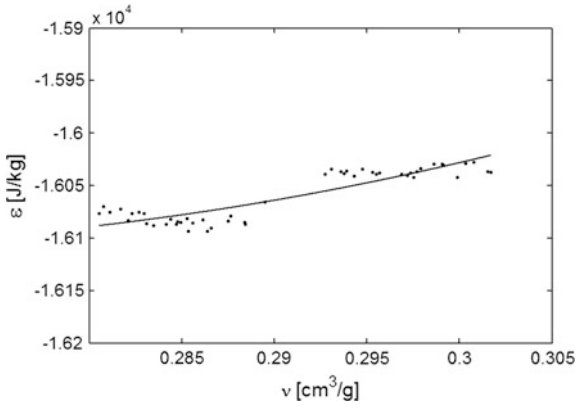

Fig. 7 Specific internal energy versus specific volume for CSH Jennite molecular structure

specific volume that are obtained for illustrative CSH Jennite configuration are presented in Figs. 6 and 7.

These along with Grüneisen parameter in Eq. (8) is used to obtain the pressure versus specific volume along the Hugoniot path shown in Fig. 8.

5.3 Shear Strength Model

Shear strength of the material was assumed not to vary with the volume of the material for this illustrative demonstration of MD modeling methodology. This assumption does not hinder potential applicability of MD modeling methodology for equation of state material modeling of CSH Jennite. The shear strength was obtained by applying the procedure outlined in Sect. 4.3 to six molecular systems made of a single unit cell of CSH Jennite, with specific volumes of 0.302, 0.300, 0.290, 0.288, 0.281, and 0.280 cm^3/g at a temperature of 300 K. The average of

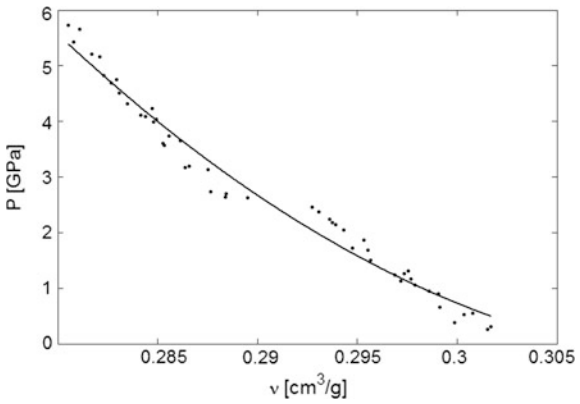

Fig. 8 Pressure versus specific volume Hugoniot for CSH Jennite molecular structure

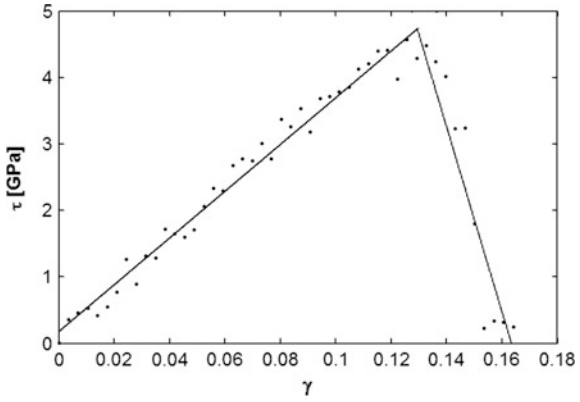

Fig. 9 Shear stress versus shear strain for sample of CSH Jennite molecular structure with a specific volume of 0.288 cm^3/g

maximum stress from each molecular system was taken as shear strength of the material. In Fig. 9, shear stress versus shear strain curves for a representative sample of CSH Jennite is shown. The average value of shear strength from MD modeling analyses involving a single unit cell CSH Jennite molecular structure was 3.75 ± 0.95 GPa, which is comparable to the value reported for CSH gel structure [5]. Additionally, average shear modulus obtained from shear stress–strain material deformation modeling was 29.6 ± 5.3 GPa, which is also in good agreement with values obtained using other MD modeling approaches [22, 23, 42]. This average strength value obtained can now be used in Eq. (5) to estimate and obtain the predictive axial stress versus specific volume Hugoniot curve.

5.4 Axial Stress Versus Specific Volume Hugoniot

The axial stress–specific volume Hugoniot obtained using Eq. (5) for demonstrative application to CSH Jennite based on molecular modeling is illustrated in Fig. 10.

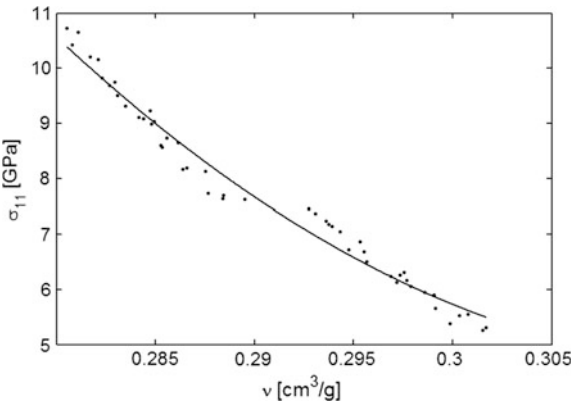

Fig. 10 Axial stress versus specific volume Hugoniot for CSH Jennite molecular structure

For this, it has been assumed that shear strength for the molecular and nanoscale CSH Jennite does not change significantly with compression. The emphasis of the current chapter is primarily on the development of MD modeling methodology. In a more detailed study, shear strength should be calculated for larger molecular material chemistry configurations at different compression levels. Additionally, it is assumed that the shear strength under adiabatic and isothermal conditions does not change significantly; hence, the isothermal value obtained as explained in Sect. 4.3 has been used.

6 Pressure–Specific Volume Relationship for Nanoscale CSH Jennite

MD modeling methodology discussed in Sects. 4.2 and 5.2 was applied to model pressure versus specific volume relationship for CSH Jennite [26]. Model configuration consisted of multiple unit cells of CSH Jennite (23324 atoms), arranged as a triclinic single crystal structure of dimensions $a = 7.4$ nm, b = 5.1 nm, and c = 7.7 nm, and angles $\alpha = 101.3°, \beta = 97.0°$, *and* $\gamma = 109.7°$. Complete details are discussed in Murillo et al. [26]. MD modeling results indicate that pressure–specific volume and the specific energy–specific volume can be described by a linear and a quadratic function, respectively, as presented in Figs. 11 and 12. The constitutive material models are thus given by

$$P(v) = (-270 \pm 8)v + (81 \pm 2) \tag{11}$$

$$\varepsilon(v) = (4864 \pm 559)v^2 - (2827 \pm 326)v - (144 \pm 48) \tag{12}$$

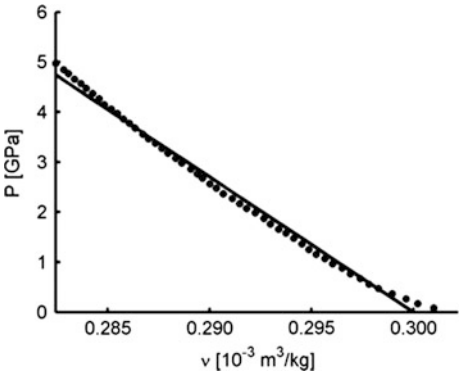

Fig. 11 Pressure versus specific volume for nanoscale mineral Jennite under isothermal conditions at 298 K. Constitutive model obtained by linear fitting of modeling data: $P(v) = (-270 \pm 8)v + (81 \pm 2)$. P in [GPa] and v in $[10^{-3}\mathrm{m}^3\mathrm{kg}^{-1}]$ (Reproduced with Permission)

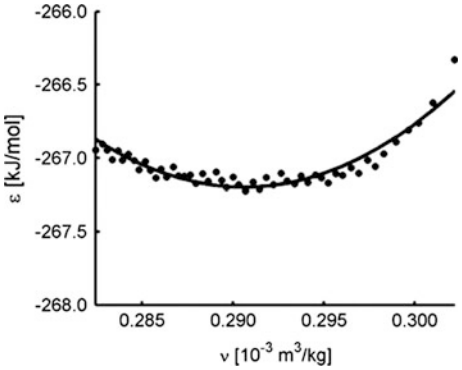

Fig. 12 Specific internal energy versus specific volume for nanoscale mineral Jennite under isothermal conditions at 298 K. Modeling data fitted to quadratic function. $\varepsilon(v) = (4864 \pm 559)v^2 - (2827 \pm 326)v - (144 \pm 48)$. ε in $[\mathrm{kJ*mol}^{-1}]$ and v in $[10^{-3}\mathrm{m}^3\mathrm{kg}^{-1}]$ (Reproduced with Permission)

where $P, v,$ *and* ε represent pressure, specific volume, and specific internal energy, respectively. The quantities are given in [GPa], $[10^{-3}\mathrm{m}^3\mathrm{kg}^{-1}]$, and $[\mathrm{kJ*mol}^{-1}]$, respectively.

The data presented in Rivas Murillo et al. [26] fits well the constitutive model described by the Birch–Murnaghan equation of state [25], as shown in Fig. 13. Additionally, modeling results compare exceptionally well to theoretical data, obtained from first principle calculations, and experimental data [25], as shown in Fig. 14.

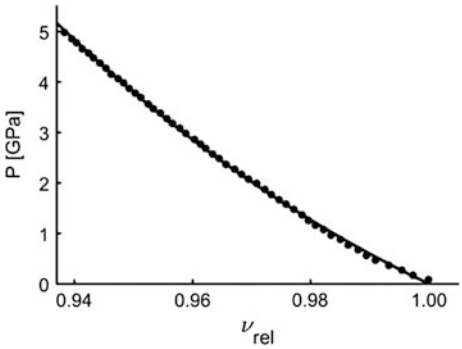

Fig. 13 Pressure versus specific volume for nanoscale mineral Jennite under isothermal conditions at 298 K. Modeling data fitted to Birch–Murnaghan equation of state [25] (Reproduced with Permission)

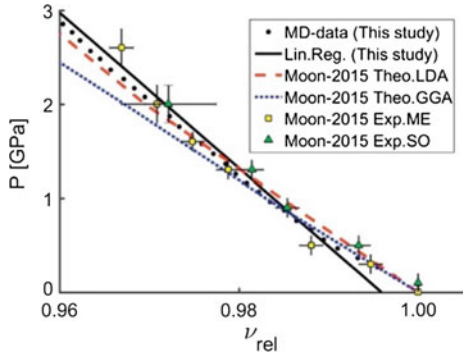

Fig. 14 Pressure versus relative volume for nanoscale mineral Jennite under isothermal conditions at 298 K. Comparison to modeling and experimental data from Moon *et al.* [25]. Theo.LDA: Theoretical estimation by Local Density Approximation; Theo.GGA: Theoretical estimation by Generalized Gradient Approximation; Exp.ME: Experimental measurements by isometric compression in methanol–ethanol mixture; Exp.SO: Experimental measurements by isometric compression in silicone oil mixture (Reproduced with Permission)

7 Concluding Remarks

Significant interest currently exists in the materials and mechanics research community in predictive constitutive material models, understanding material behavior and characteristics starting from material chemistry molecular representations following MD modeling methodologies. The MD-based material modeling methodology presented in this chapter allows obtaining necessary quantities to investigate the behavior of materials subjected to uniaxial strain from the propagation of a longitudinal plane shock wave, and material models for high strain rate behavior. Ideally, application of this methodology, using material chemistry models for

developing associated constitutive material models, would allow reducing amount and cost of physical experimentation. For illustrative purposes, results of the application of this material chemistry and molecular modeling methodology using molecular structure of hydrated cement past constituent CSH Jennite have been shown and demonstrated. Larger material chemistry molecular structures and a convergence of the material model equation parameters are required to be established following the presented methodology [26].

Acknowledgements The authors acknowledge the support by the U.S. Army Research Office under a cooperative agreement award contract No. W911NF-11-2-0043 (Program Manager: Dr. Joseph Myers).

References

1. Allen, M. P., & Tildesley, D. J. (1989). *Computer simulation of liquids.* Oxford University Press.
2. An, Q., Luo, S. -N., Han, L. -B., Zheng, L., & Tschauner, O. (2008). Melting of Cu under hydrostatic and shock wave loading to high pressures. *Journal of Physics: Condensed Matter, 20,* 095220.
3. Asay, J. R., & Chhabildas, L. C. (2003). High-pressure shock compression of solids VI. In: Y. Horie, L. Davison, & N. N. Thadhani (Eds.), *Old paradigms and new challe*nges. New York: Springer.
4. Bischoff, P. H., & Perry, S. H. (1991). Compressive behaviour of concrete at high strain rates. *Materials and Structures, 24,* 425–450.
5. Bonaccorsi, E., Merlino, S., & Taylor, H. F. W. (2004). The crystal structure of Jennite, $Ca_9Si_6O_{18}(Oh)_6 \cdot 8h_2O$. *Cement and Concrete Research, 34,* 1481–1488.
6. Bourne, N., Millett, J., Rosenberg, Z., & Murray, N. (1998). On the shock induced failure of brittle solids. *Journal of the Mechanics and Physics of Solids, 46,* 1887–1908.
7. Bringa, E. M., Caro, A., Wang, Y., Victoria, M., McNaney, J. M., Remington, B. A., et al. (2005). Ultrahigh strength in nanocrystalline materials under shock loading. *Science, 309,* 1838–1841.
8. Chantawansri, T. L., Byrd, E. F., Rice, B. M., & Andzelm, J. W. (2011). Molecular Dynamics Simulations of Hugoniot Relations for Poly [Methyl Methacrylate], DTIC Document.
9. Chantawansri, T. L., Sirk, T. W., Byrd, E. F. C., Andzelm, J. W., & Rice, B. M. (2012). Shock Hugoniot calculations of polymers using quantum mechanics and molecular dynamics. *The Journal of chemical physics, 137,* 204901.
10. Chen, X., Wu, S., & Zhou, J. (2013). Experimental and modeling study of dynamic mechanical properties of cement paste, mortar and concrete. *Construction and Building Materials, 47,* 419–430.
11. CEB-FIP Model Code. (1993). Comite Euro-International Du Beton. *Bulletin d'information, 213,* 214.
12. Davison, L. (2008). *Fundamentals of shock wave propagation in solids.* Springer Science & Business Media.
13. Erhart, P., Bringa, E. M., Kumar, M., & Albe, K. (2005). Atomistic mechanism of shock-induced void collapse in nanoporous metals. *Physical Review B, 72,* 052104.
14. Erpenbeck, J. J. (1992). Molecular dynamics of detonation. I. Equation of state and Hugoniot curve for a simple reactive fluid. *Physical Review A, 46*, 6406.
15. Grady, D. E. (1998). Shock-wave compression of brittle solids. *Mechanics of Materials, 29,* 181–203.

16. Grote, D. L., Park, S. W., & Zhou, M. (2001). Dynamic behavior of concrete at high strain rates and pressures: I. Experimental characterization. *International Journal of Impact Engineering, 25,* 869–886.
17. Hentz, S., Donzé, F. V, & Daudeville, L. (2004). Discrete element modelling of concrete submitted to dynamic loading at high strain rates. *Computers & Structures, 82*, 2509–2524.
18. Koh, S. J. A., & Lee, H. P. (2006). Molecular dynamics simulation of size and strain rate dependent mechanical response of Fcc metallic nanowires. *Nanotechnology, 17,* 3451.
19. Liu, Y., Zhao, J., & Wang, F. (2009). Influence of length on shock-induced breaking behavior of copper nanowires. *Physical Review B, 80,* 115417.
20. Lu, Y., & Xu, K. (2004). Modelling of dynamic behaviour of concrete materials under blast loading. *International Journal of Solids and Structures, 41,* 131–143.
21. Maillet, J. -B., Mareschal, M., Soulard, L., Ravelo, R., Lomdahl, P. S., Germann, T. C., et al. (2000). Uniaxial Hugoniostat: A method for atomistic simulations of shocked materials. *Physical Review E, 63,* 016121.
22. Manzano, H., Dolado, J. S., & Ayuela, A. (2009). Elastic properties of the main species present in Portland cement pastes. *Acta Materialia, 57,* 1666–1674.
23. Mazzatesta, A. D., Rosen, M., Sidhu, H., & Lindgren, E. A. (1998). Equation of state of cementitious materials by ultrasonic methodology. *Materials Science and Engineering A, 251,* 121–128.
24. Mohamed, A. (2013). *Computational material modeling for mechanical properties prediction and a methodology for Mie Gruneisen equation of state characterization via molecular/nano scale cementitious material constituents*. North Carolina Agricultural And Technical State University.
25. Moon, J., Yoon, S., & Monteiro, P. J. M. (2015). Mechanical properties of Jennite: A theoretical and experimental study. *Cement and Concrete Research*, *71*, 106–114.
26. Murillo, J. S. R., Hodo, W., Mohamed, A., Mohan, R. V., Rajendran, A., & Valisetty, R. (2017). A molecular dynamics investigation of hydrostatic compression characteristics of mineral Jennite. *Cement and Concrete Research, 99,* 62–69.
27. Park, S. W., Xia, Q., & Zhou, M. (2001). Dynamic behavior of concrete at high strain rates and pressures: Ii. Numerical simulation. *International Journal of Impact Engineering, 25,* 887–910.
28. Pellenq, R. J. -M., Kushima, A., Shahsavari, R., Van Vliet, K. J., Buehler, M. J., Yip, S., et al. (2009). A realistic molecular model of cement hydrates. *Proceedings of the National Academy of Sciences, 106,* 16102–16107.
29. Ravelo, R., Germann, T. C., Guerrero, O., An, Q., & Holian, B. L. (2013). Shock-induced plasticity in tantalum single crystals: Interatomic potentials and large-scale molecular-dynamics simulations. *Physical Review B, 88,* 134101.
30. Rice, B. M., Mattson, W., Grosh, J., & Trevino, S. F. (1996). Molecular-dynamics study of detonation. I. A comparison with hydrodynamic predictions. *Physical Review E, 53*, 611.
31. Rong, Z., Sun, W., & Zhang, Y. (2010). Dynamic compression behavior of ultra-high performance cement based composites. *International Journal of Impact Engineering, 37,* 515–520.
32. Rudd, R. E. (2010). High-rate plastic deformation of nanocrystalline tantalum to large strains: Molecular dynamics simulation. *Materials Science Forum* Trans Tech Publ (pp. 3–19).
33. Shao, S., Zbib, H. M., Mastorakos, I. N., & Bahr, D. F. (2014). The void nucleation strengths of the Cu–Ni–Nb-based nanoscale metallic multilayers under high strain rate tensile loadings. *Computational Materials Science, 82,* 435–441.
34. Thomas, J. J., Jennings, H. M., & Allen, A. J. (2010). Relationships between composition and density of tobermorite, Jennite, and nanoscale $Cao-Sio_2-H_2o$. *The Journal of Physical Chemistry C, 114*, 7594–7601.
35. Tsembelis, K., Proud, W. G., Field, J. E., Furnish, M. D., Thadhani, N. N., & Horie, Y. (2002). The dynamic strength of cement paste under shock compression. In: *AIP Conference Proceedings* AIP (pp. 1414–1418).

36. Wang, F., Gao, Y., Zhu, T., & Zhao, J. (2011). Shock-induced breaking in the gold nanowire with the influence of defects and strain rates. *Nanoscale, 3,* 1624–1631.
37. Wang, F., Gao, Y., Zhu, T., & Zhao, J. (2011). Shock-induced breaking of the nanowire with the dependence of crystallographic orientation and strain rate. *Nanoscale Research Letters, 6,* 291.
38. Wang, L. -L., Shi, S. -Q., Chen, J. -Y., Huang, D. -J., & Shen, L. -J. (2003). Influences of strain-rate and stress-state on dynamic response of cement mortar. *International Journal of Structural Stability and Dynamics, 3,* 419–433.
39. Wang, S., Zhang, M. -H., & Quek, S. T. (2011). Effect of high strain rate loading on compressive behaviour of fibre-reinforced high-strength concrete. *Magazine of Concrete Research, 63*, 813–827.
40. Wang, S., Zhang, M. -H., & Quek, S. T. (2012). Mechanical behavior of fiber-reinforced high-strength concrete subjected to high strain-rate compressive loading. *Construction and Building Materials, 31,* 1–11.
41. Wu, H., Zhang, Q., Huang, F., & Jin, Q. (2005). Experimental and numerical investigation on the dynamic tensile strength of concrete. *International Journal of Impact Engineering, 32,* 605–617.
42. Wu, W., Al-Ostaz, A., Cheng, A. H. -D., & Song, C. R. (2011). Computation of elastic properties of Portland cement using molecular dynamics. *Journal of Nanomechanics and Micromechanics, 1*, 84–90.
43. Zhakhovskii, V. V., Inogamov, N. A., Petrov, Y. V., Ashitkov, S. I., & Nishihara, K. (2009). Molecular dynamics simulation of femtosecond ablation and spallation with different interatomic potentials. *Applied Surface Science, 255,* 9592–9596.
44. Zhou, X. Q., & Hao, H. (2008). Modelling of compressive behaviour of concrete-like materials at high strain rate. *International Journal of Solids and Structures, 45*, 4648–4661.

Geometry and Size Effects in Response of Composite Structures Subjected to Water-Based Impulsive Loading

Siddharth Avachat, Tao Qu and Min Zhou

1 Introduction

The response of composite structures to both contact-induced dynamic and water-based impulsive loads is of great importance in the design of failure-resistant marine structures for naval and offshore industry applications in which composite materials have been increasingly employed. As a consequence, there is an increasing need to understand and quantify the response of composite structures to such intense dynamic loads. Minnaar and Zhou [1] showed that interlaminar crack speeds are significantly higher when subjected to shear loads, and mode II loading rate determines crack speeds. The matrix material, composite layup, and geometric aspects such as size, thickness, and loading area all have a significant influence on the deformation and damage response of composite laminates [2–4]. Chang and coworkers [5–7] carried our low-velocity impact testing of composite laminates and concluded that in-ply matrix cracking preceded delamination nucleation, which was followed by shear and bending crack initiation.

A high-speed servo-hydraulic testing system was developed by Battley and coworkers [8, 9] to evaluate slamming impact on deformable sandwich panels, which showed markedly different peak and residual pressures from those for a rigid panels. Espinosa and coworkers [10–12] carried out experiments and computation focusing on a range of designs to identify morphologies that offer the highest blast mitigation capabilities. A combined experimental and computational analysis of deformation in composite structures subjected to underwater blasts carried out [13]

S. Avachat · T. Qu · M. Zhou (✉)
The George W. Woodruff School of Mechanical Engineering,
Atlanta, USA
e-mail: min.zhou@gatech.edu

S. Avachat · T. Qu · M. Zhou
School of Materials Science and Engineering, Georgia Institute of Technology,
Atlanta, GA 30332-0405, USA

S. Gopalakrishnan and Y. Rajapakse (eds.), *Blast Mitigation Strategies in Marine Composite and Sandwich Structures*, Springer Transactions in Civil and Environmental Engineering, https://doi.org/10.1007/978-981-10-7170-6_23

shows that sandwich structures significantly outperform monolithic structures. Shukla and coworkers [14–18] found similar trends in planar and curved structures.

Comparative analyses of the blast resistance and dynamic performance of different reinforcements (glass-fiber, carbon-fiber), varying anisotropy, different matrix materials (epoxy, polyester, etc.), and varying loading conditions (planar, oblique, cylindrical) are lacking. The damage response of composite laminates with different reinforcements and structural geometries subjected to underwater explosions. The focus is on understanding the deformation and failure mechanisms and quantifying damage as a function of structural attributes, material properties, loading conditions, and loading rates. We have developed a novel experimental setup called the Underwater Shock Loading Simulator (USLS) to generate planar impulses resembling those resulting from underwater explosions. The USLS consists of a projectile-impact-based impulsive loading system, a fluid chamber, a target support, and a transparent polycarbonate fitted enclosure for safety.

Coupled Eulerian–Lagrangian simulations are carried out to account for the fluid–structure interaction (FSI) effect at the water–composite interface, blast intensity, material properties, and interfacial effects. The simulations focus on shear cracking and fragmentation, tensile cracking, compressive kinking, and interfacial debonding in the early stage of deformation (~1500 μs) since the load-carrying capacity is most critically reflected then. This combined approach allows us to identify factors that play important roles in determining the dynamic response of the materials.

2 Technical Approach

2.1 Composites Manufacturing

Fiber matrix composites are composed of two distinct phases: (1) reinforcements like glass-fibers or carbon-fibers and (2) matrix materials like epoxy, polyester, etc. The strength and stiffness of the finished composite is determined by the volume fraction and directionality of fibers with respect to external loads. Two types of composite materials are used in this analysis: glass-fiber reinforced epoxy and carbon-fiber reinforced epoxy. The glass-fiber reinforced prepregs are 24 in. wide *XF0920/346-AA-675 E-Glass 300 GSM 36% RW*. *XF0920* is the resin designation, *346-AA-675* is the identification number of Owens Corning 346 Type 30 roving, *300 GSM* denotes the 300 g/m^2 areal mass of the aforementioned glass-fiber, *675* denotes the length of the roving in yards per pound, and *36% RW* denotes resin weight in each lamina. The carbon-fiber reinforced prepregs are 24 in. wide *VTM 264/792/HTR40-300gsm 36% RW*. *VTM 264* is a variable temperature, vacuum processable epoxy resin developed by Cytec, *HTR40* is the identification number of Toho Tenax continuous fiber reinforcement, *300 GSM* denotes 300 g/m^2 areal mass of the aforementioned fiber reinforcement, and *36% RW* denotes resin weight in each lamina. The composite laminates are manufactured by curing the prepregs under pressure in a high temperature oven at 100 °C. The thickness of each cured lamina is calculated using

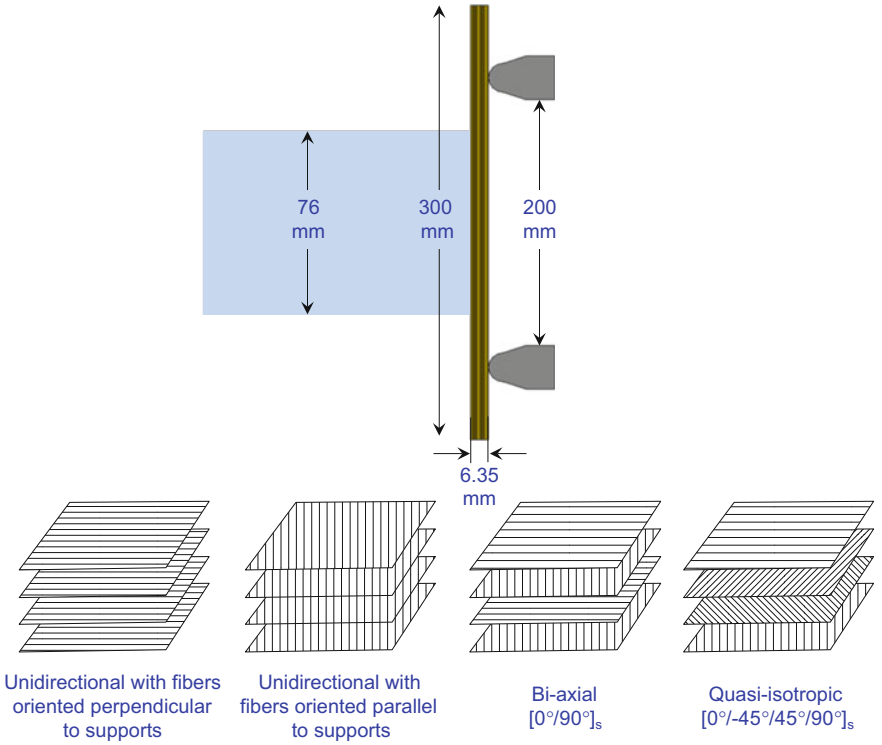

Fig. 1 Schematic illustration showing the simply supported loading configuration with planar incident impulsive load and different composite layups of the test specimens

$$\text{Cured Ply Thickness} = \frac{\text{Fiber Areal Weight}\,(\text{g}\cdot\text{m}^{-2})}{\text{Fiber density}\,(\text{g}\cdot\text{m}^{-3}) \times \text{Fiber Volume}\,(\%) \times 10}, \qquad (1)$$

giving a cured ply thickness of approximately 0.23 mm per layer or lamina. Each composite laminate is constructed by stacking unidirectional prepregs in the required orientations to create a dense, thick laminate with a total thickness of 6.5 mm. The layups studied in this analysis are biaxial (0/90), quasi-isotropic (0/−45/45/90), unidirectional with fibers perpendicular to supports (90) and unidirectional with fibers parallel to supports (0). Figure 1 shows the simply supported planar impulsive loading configuration and the different layups used in laminate construction.

Marine vessels consist of geometrical nonlinearities like inclined and curved surfaces. Such sections interact with high-intensity impulsive loads rather differently from the way planar sections do under normal load incidence. The deformation and damage due to such geometric factors need to be considered for effective structure design.

2.2 Water-Based Impulsive Loading Experiments

Gas gun impact has been successfully used to generate impulsive loading through water [11, 19–22]. It has been shown that this FSI effect can be exploited to improve the blast mitigation capability of structures subjected to transient loads [23, 24]. The facility shown in Fig. 2 is designed to obtain controlled loading and simulate different water–structure contact conditions and allow concurrent real-time quantification [19–21]. USLS can generate water-based loads with a range of intensities to impulsively load composite structures [25]. The impulsive load induces deformation at strain rates up to 10^4 s^{-1}. We have also integrated high-speed photographic and laser interferometric diagnostics with the USLS. The USLS is capable of creating underwater impulses with pressures exceeding 200 MPa similar to underwater explosions [26–29].

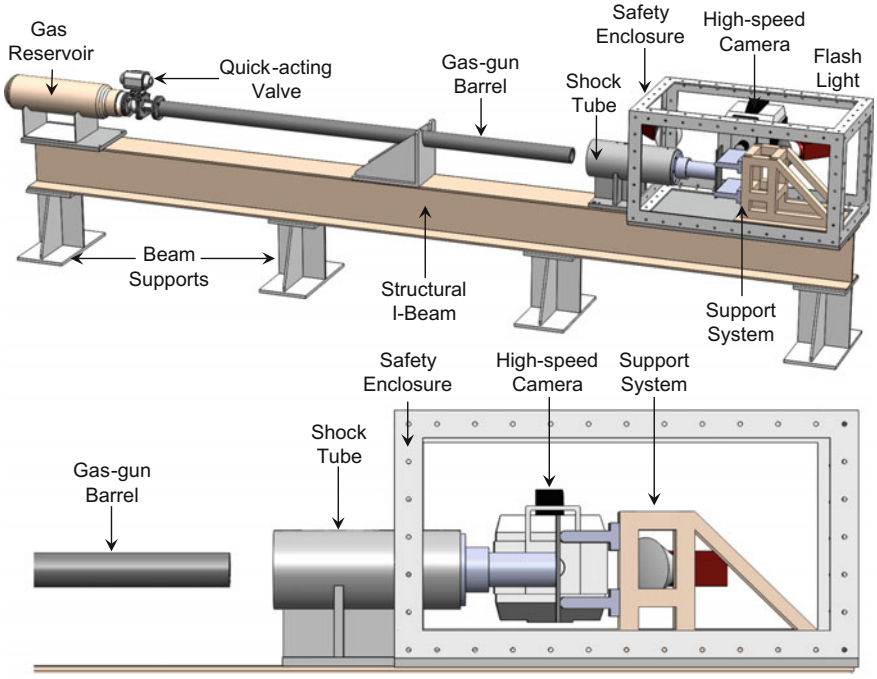

Fig. 2 An illustration of the underwater shock loading simulator (USLS) for testing simply supported thick laminates. Components shown include gas reservoir, gun barrel, water chamber, support system, specimen, and high-speed camera

2.3 Modeling of In-ply Cracking and Failure

Based on the energy required for initiation, matrix damage through cracking occurs first, followed by combined fiber matrix debonding or "fiber-pullout" and finally fiber fracture. Damage occurring in the facesheets is accounted for using an energy-based damage evolution law [30, 31]. The models assume a transversely isotropic solid which is perfectly elastic until the onset of damage. After damage initiation, following damage modes are accounted for through the simulations: (1) matrix tension; (2) matrix compression; (3) fiber tension; and (4) fiber compression. The parameters used in these calculations can be found in [32, 33]. The material properties of glass-fiber reinforced epoxy and carbon-fiber reinforced epoxy are provided below [34, 35] (Tables 1, 2 and 3).

Table 1 Material properties for unidirectional glass-fiber/epoxy laminates in [32]

Parameter	Symbol	Unit	Value
Density	ρ	kg · m^{-3}	1850
Tensile modulus	E_{11}	MPa	39000
Transverse modulus	E_{22}	MPa	9000
Shear modulus	G_{12}, G_{13}	MPa	3500
Longitudinal tensile strength	T_{11}	MPa	1200
Longitudinal compressive strength	C_{11}	MPa	900
Transverse tensile strength	T_{22}	MPa	45
Transverse compressive strength	C_{22}	MPa	128
Longitudinal shear strength	S_{12}, S_{21}	MPa	51
Transverse shear strength	S_{23}	MPa	51

Table 2 Material properties for unidirectional carbon-fiber/epoxy laminates [33]

Parameter	Symbol	Unit	Value
Density	ρ	kg · m^{-3}	1580
Longitudinal tensile modulus	E_{11}	MPa	138000
Transverse tensile modulus	E_{22}	MPa	10000
Shear modulus	G_{12}, G_{13}	MPa	5240
Longitudinal tensile strength	T_{11}	MPa	2280
Longitudinal compressive strength	C_{11}	MPa	1440
Transverse tensile strength	T_{22}	MPa	57
Transverse compressive strength	C_{22}	MPa	228
Longitudinal shear strength	S_{12}, S_{21}	MPa	71
Transverse Shear strength	S_{23}	MPa	71

Table 3 Material properties for epoxy [36]

Parameter	Symbol	Unit	Value
Normal stiffness	K_n	MPa	2000
Shear stiffness	K_s, K_t	MPa	2000
Critical normal traction	t_{n}^0	MPa	50
Critical shear traction	t_{s}^0, t_{t}^0	MPa	50
Critical normal fracture energy	G_n^C	N/mm	4.0
Critical shear fracture energy	G_s^C, G_t^C	N/mm	4.0

The characteristic length, L_C, is based on the element geometry and formulation: it is a typical length of a line across an element for a first-order element. The damage variable will evolve such that the stress–displacement behaves as shown in each of the four failure modes. The positive slope of the stress–displacement curve prior to damage initiation corresponds to linear elastic material behavior; the negative slope after damage initiation is achieved by evolution of the respective damage variables according to the equations shown below. For each failure mode, the energy dissipated due to failure, which corresponds to the area of the triangle OAC, must be specified.

2.4 *Modeling of Interfacial Effects Using Cohesive Elements*

The cohesive finite element method (CFEM) model explicitly represents the laminar nature of the structure of the entire carbon-fiber/epoxy laminate and capture damage and deformation. The epoxy layers between two laminas are modeled using cohesive elements to capture interfacial fracture and delamination. Interfacial separation of directionally stacked layers in the composite is called delamination. Delamination requires very little energy and is the dominant damage mode in composite materials subjected to impact or impulsive loads. Core-facesheet separation is an important damage mode that occurs due to interfacial separation and fracture. If the bond between facesheet and core is weak, interfacial separation occurs. If the bond between the facesheet and the core is strong, tensile fracture in the foam leads to separation. Some commonly used metrics to evaluate the damage resistance of composites to impact loads are impact energy, displacement, delamination area, and extent of rupture.

The CFEM has been extensively used to study fracture and surface creation in a range of deformation modes [37], quasi-static crack growth [38], ductile fracture [39, 40], dynamic fracture [41], dynamic fragmentation [42, 43], delamination in composites [44, 45], and microstructural fracture [46]. In this set of simulations, cohesive elements are present at the interfaces between individual layers as well as

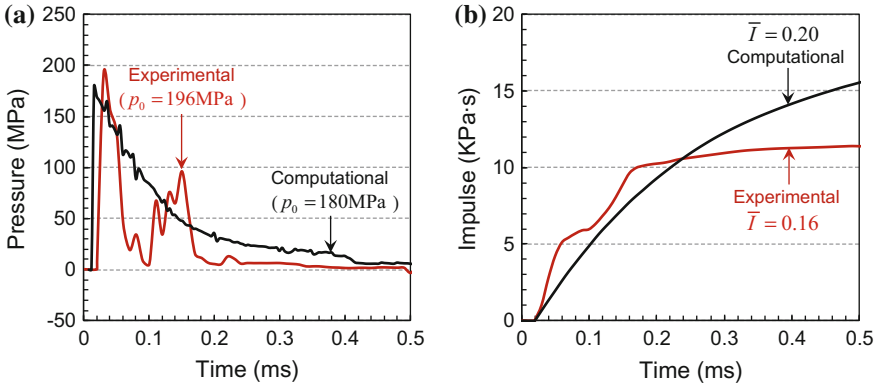

Fig. 3 Experimentally measured and numerically calculated pressure and impulse histories in the water chamber for a gas reservoir base pressure of 350 psi and a projectile velocity of ~110 ms^{-1}

the interfaces between the aluminum and composite sections in the hybrid plates. The cohesive elements allow damage initiation and development in the interlaminar regions to be captured. A bilinear traction-separation law is adopted to describe the behavior of the cohesive elements [44]. The parameters for all cohesive relations used are obtained from the work performed by Lapczyk and Hurtado [36].

The measured and calculated peak pressures and decay times are consistent, as shown in Fig. 3. The calculations capture most of the essential features of the loading in the experiments [25]. Although the peak pressures are similar for experiments and simulations, the decay times are slightly different. The normalized impulse magnitude is $\bar{I} = 0.20$ for experiments and $\bar{I} = 0.16$ for simulations.

3 Results and Discussion

3.1 Experiments and Validation of Model

The deformation in a dynamically loaded composite laminate can be divided into two regimes: (1) flexural wave propagation toward the supports and (2) structural deflection. The flexural wave travels toward the supports in a very short time (~50 μs). Although the resolution of the camera is sufficient to capture this phenomenon, we are more interested in structural response in the form of damage and out-of-plane deflection, which take place over a longer time span. Consequently, the temporal resolution of the camera is selected to capture the behavior over a duration of 2 ms. The experiments and simulations are considered together in order to develop a detailed analysis and intimate understanding of structural failure in blast-loaded monolithic composite plates. Both quantitative and qualitative approaches are used to evaluate blast response.

In order to accurately compare the performance of composite structures under blast loading, we need to consider laminates of equal areal mass subjected to similar incident impulses. Since quasi-isotropic laminates are most widely used in commercial applications, we identified the incident failure impulse for a 6.35 mm thick quasi-isotropic laminate. A number of experiments were carried out to determine that the quasi-isotropic laminate fails under an impulsive load with a peak pressure of ~196 MPa. It was found that a gas reservoir base pressure of 350 psi generated an underwater pressure wave with a peak pressure of ~196 MPa with a variation of up to 20 MPa. Although the peak pressures are similar for experiments and simulations, the decay times are slightly different. The normalized impulse magnitude is $\bar{I} = 0.20$ for experiments and $\bar{I} = 0.16$ for simulations.

As discussed previously, the loading configuration consists of a simply supported composite beam which undergoes bending deformation. The magnitude and rate of bending is determined by the incident impulse. Figure 4 shows a sequence of high-speed photographs showing the deformation in a monolithic carbon-fiber/epoxy composite laminate with a quasi-isotropic layup subjected to $\bar{I} = 0.08$. In this case, the composite laminate undergoes bending deformation, but the impulsive load is insufficient to cause failure. Since there is no failure, the water in the shock tube does not breach the laminate and instead, escapes the chamber by flowing sideways with respect to the composite, in the direction of high-speed camera. Note the lack of any water in the space directly behind the composite as shown at

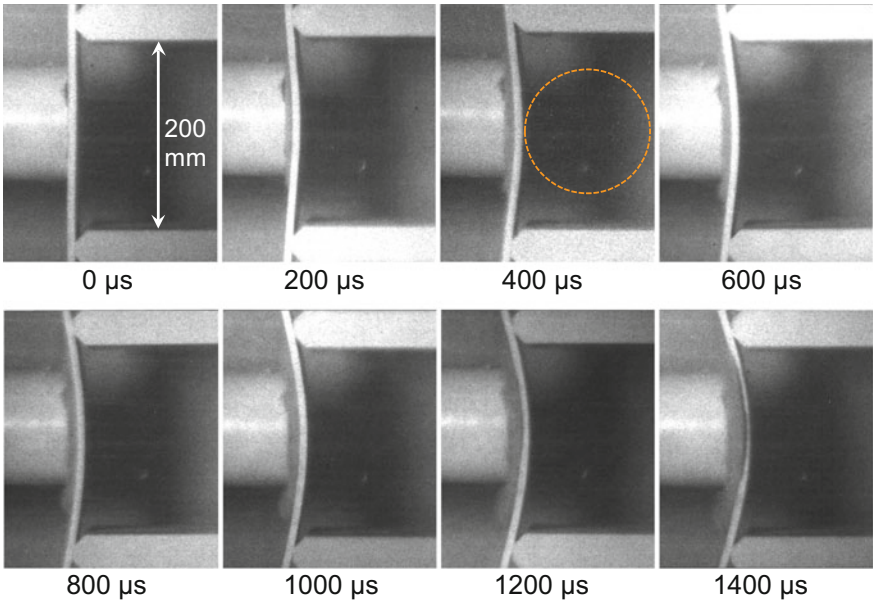

Fig. 4 Sequence of high-speed photographs showing the deformation in a monolithic carbon-fiber/epoxy composite plate with a quasi-isotropic layup subjected to $\bar{I} = 0.08$

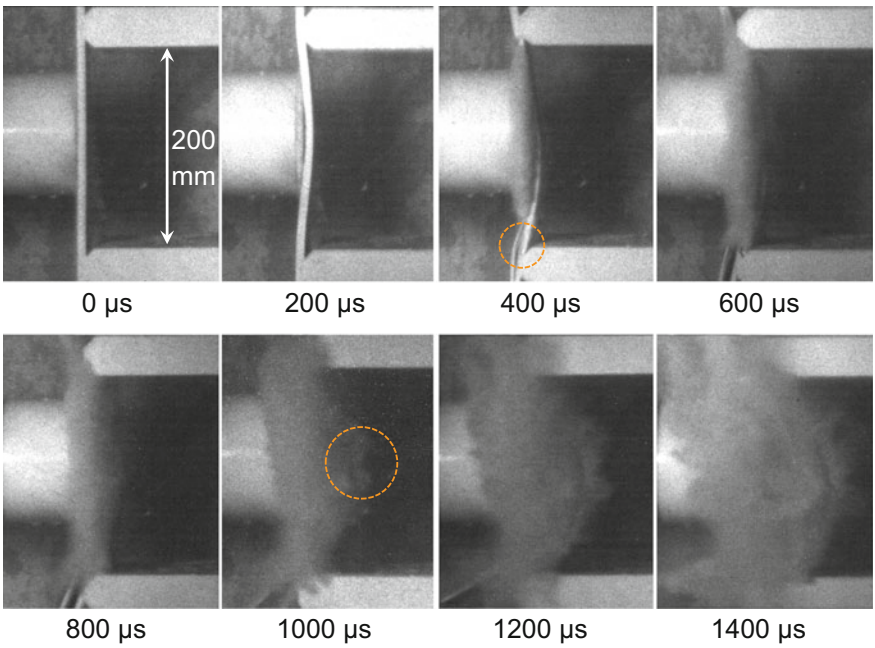

Fig. 5 Sequence of high-speed photographs showing the deformation in a monolithic carbon-fiber/epoxy composite laminate with a biaxial layup subjected to $\bar{I} = 0.16$

$t = 400$ μs. Figure 5 shows the sequence of high-speed photographs of deformation in a monolithic carbon-fiber/epoxy composite laminate with a biaxial layup subjected to $\bar{I} = 0.16$. A comparison of deformation at two different impulse magnitudes shows that at $\bar{I} = 0.16$, the pressurized water breaches the composite laminate and flows through the back side of the bending plate, clearly signifying rupture and catastrophic failure. In summary, tracking the behavior of the water column in touch with the specimen using high-speed digital imaging can provide an insight into the structural response, failure modes, and collapse of each composite laminate.

Figure 6 shows a sequence of high-speed photographs of a quasi-isotropic carbon-fiber/epoxy laminate subjected to $\bar{I} = 0.16$. Figure 7 shows the in-ply damage contours for a quasi-isotropic carbon-fiber/epoxy laminate subjected to $\bar{I} = 0.20$. After the onset of bending deformation at $t = 200$ μs, the quasi-isotropic plate undergoes delamination near the midplane at $t = 400$ μs.

The interlaminar cracks propagate toward the supports and cause further delamination near the edge at $t = 600$ μs. Since a simply supported loading configuration causes maximum stresses near the midplane, a "hinge" or localized deformation develops in the laminate due to a combination of compressive and tensile stresses through the thickness. This observation is supported by the computational results shown in Fig. 7. It should be noted that although there is widespread delamination and in-ply damage, water flowing out of the shock tube does

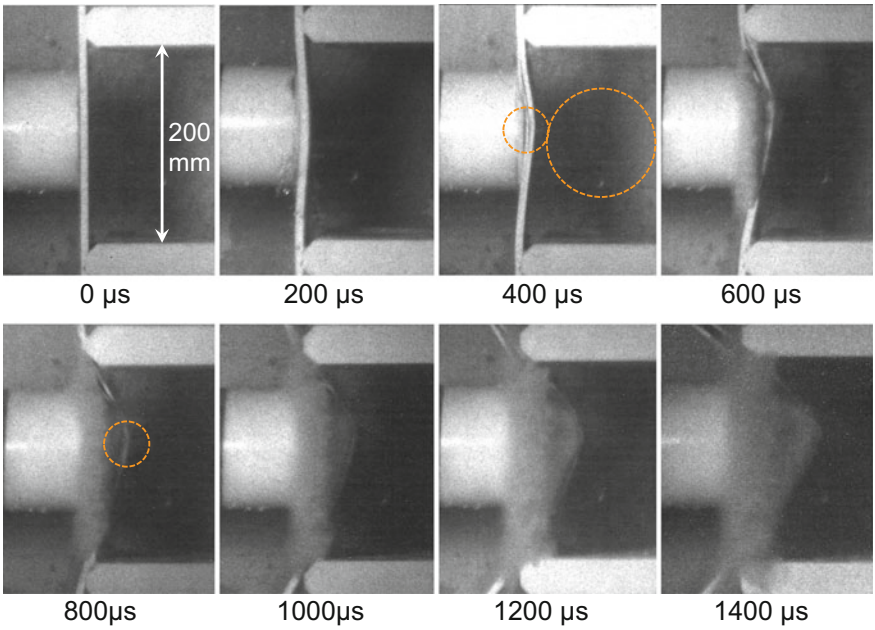

Fig. 6 Sequence of high-speed photographs showing the deformation in a monolithic carbon-fiber/epoxy composite plate with a quasi-isotropic layup at $\bar{I} = 0.16$

not breach the plate, instead flowing out of the sides as observed in Fig. 4. Results indicate that the computational model accurately captures the deformation observed in experiments. As discussed previously, the quasi-isotropic layup exhibits large-scale delamination but does not experience failure. In order to determine whether delamination can be localized to smaller region by modifying the laminate layup, laminates are constructed such that all laminas have fibers oriented parallel to the supports. Figure 8 shows a sequence of high-speed photographs of a carbon-fiber/epoxy laminate with fibers oriented in a direction parallel to the supports subjected to underwater impulsive loads of similar magnitudes.

After the onset of bending delamination at $t = 200$ μs, the plate experiences delamination at $t = 400$ μs. After delamination initiation, the delaminated sections of the laminate experience severe bending stresses leading to in-ply rupture at $t = 1000$ μs, followed by perforation of the plate near the midplane and catastrophic failure at $t = 1200$ μs. The computational framework accounts for the effects of fiber orientation and captures the flow of water through the structure post-failure. Since the fibers are oriented parallel to the supports, a relatively smaller fraction of the incident impulse is transmitted to the supports leading significantly higher deflection and localized in-ply damage and fracture in close proximity to the impulsive wave loading area. Delamination is observed over a smaller area than the quasi-isotropic laminate, primarily near the loading region.

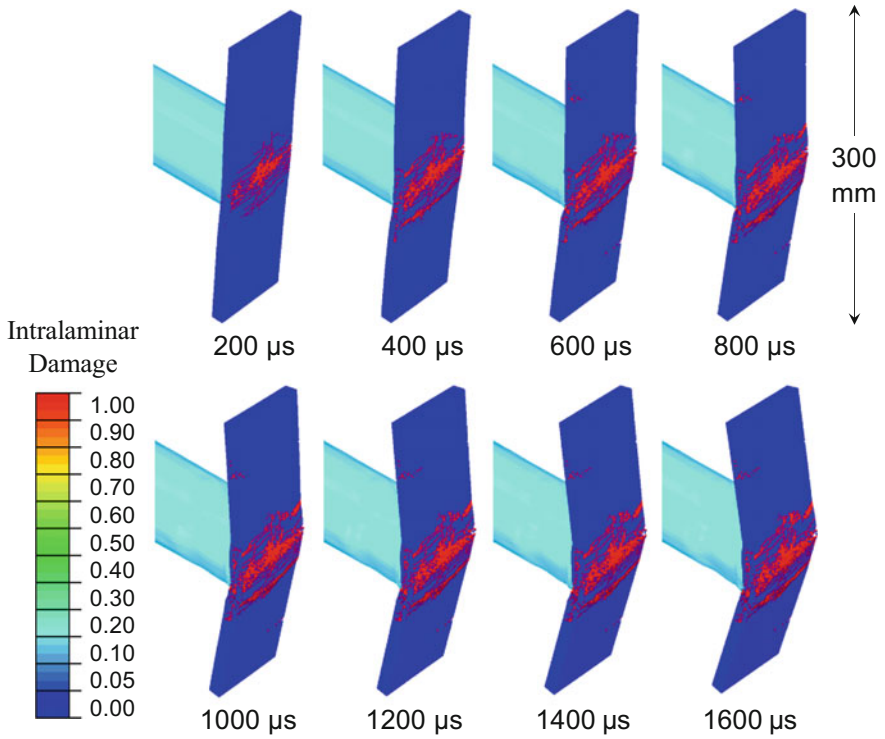

Fig. 7 Distributions of in-ply damage in quasi-isotropic carbon-fiber/epoxy composite laminate at $\bar{I} = 0.20$

Figure 9 shows a sequence of high-speed photographs of a carbon-fiber/epoxy laminate with fibers oriented in a direction perpendicular to the supports subjected to underwater impulsive loads of similar magnitudes. In this case, the plate is extremely stiff in the vertical direction and resists bending much more than the other layups. However, the lack of bending causes high shear stresses in the laminate. Since the laminate lacks stability in the horizontal direction, the high transverse shear stresses cause "splitting" in the composite structure leading to failure at $t = 400$ μs. A comparison of the finite element simulations of the quasi-isotropic laminate with respect to the uniaxially oriented laminates reveals that the quasi-isotropic layup provides superior blat resistance by minimizing shear stresses in any particular region and distributing the incident impulsive load in a uniformly to avoid localized rupture.

Carbon-fiber/epoxy laminates exhibit exceptionally high stiffness and bending resistance due to the high elastic modulus of carbon-fibers. Investigation of the underwater blast resistance of such laminates indicates that the composite plates are quite stable and blast resistant prior to damage initiation. However, after damage initiates, the laminates experience a dramatic loss in stiffness and undergo

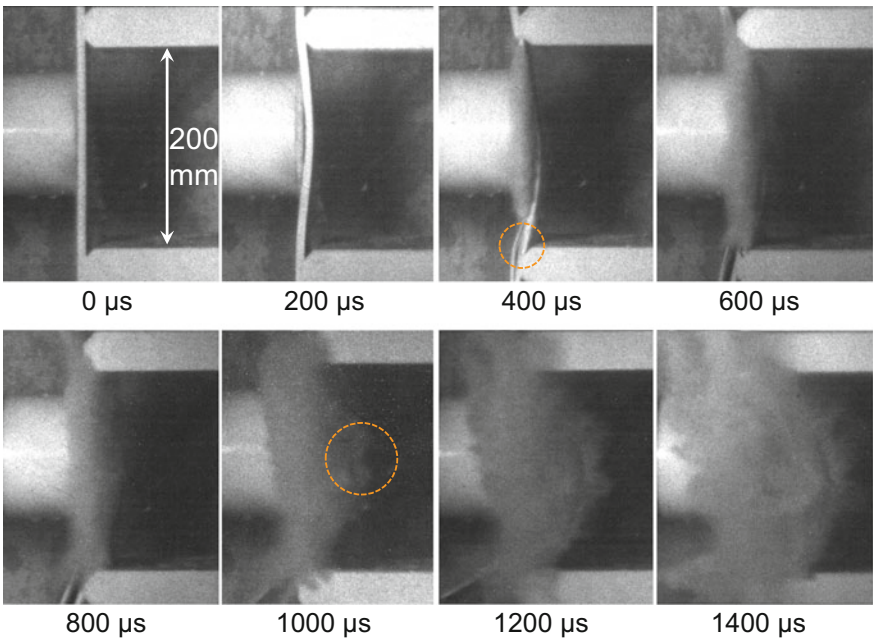

Fig. 8 Sequence of high-speed photographs showing the deformation in a monolithic carbon-fiber/epoxy composite laminate with fibers oriented parallel to the supports subjected to $\bar{I} = 0.16$

catastrophic failure and collapse. Additionally, carbon-fiber/epoxy laminates significantly more expensive in comparison to glass-fiber/epoxy laminates. With respect to the materials studied here and reported in this analysis, the carbon-fiber/epoxy laminates have a unit cost that is more than twice as much as that of glass-fiber/epoxy laminates. Since marine structures often require large quantities of composite materials, cost considerations can play a major role in materials selection. To evaluate the differences in structural response of carbon-fiber and glass-fiber/epoxy laminates, a set of experiments and simulations is carried consisting of glass-fiber/epoxy laminates with different fiber layups subjected to incident impulses similar to those for the carbon-fiber/epoxy laminates. For brevity, high-speed photographs of all layups and computational results for only the quasi-isotropic layup are reported. The high-speed photographs are followed by a quantitative analysis of the blast response of both carbon-fiber and glass-fiber/epoxy laminates.

Figure 10 shows a sequence of high-speed photographs of a biaxially oriented glass-fiber/epoxy laminate subjected to $\bar{I} = 0.16$. After the onset of bending at $t = 200$ μs, an in-ply crack initiates at the backface and propagates toward the frontface at $t = 600$ μs. This propagating crack deflects into two interlaminar cracks at $t = 800$ μs. The composite laminate loses stiffness and undergoes catastrophic failure at $t = 1200$ μs. Figure 11 shows a sequence of high-speed photographs of a

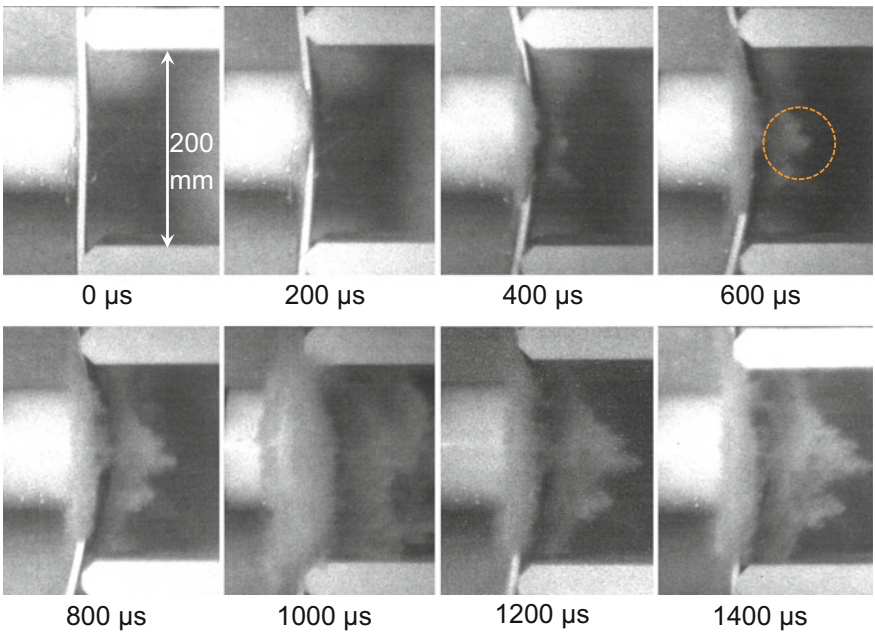

Fig. 9 Sequence of high-speed photographs showing the deformation in a monolithic carbon-fiber/epoxy composite laminate with fibers oriented perpendicular to the supports subjected to $\bar{I} = 0.16$

quasi-isotropic glass-fiber/epoxy laminate at $\bar{I} = 0.16$. Figure 12 shows the in-ply damage contours for a quasi-isotropic glass-fiber/epoxy laminate at $\bar{I} = 0.20$. The deformation in the composite plate is initially arrested as indicated by the smaller jump in displacement between $t = 400$ μs and $t = 600$ μs in comparison to the change in displacement between $t = 200$ μs and $t = 400$ μs. However, at $t = 800$ μs, the deforming laminate experiences cracking at the backface and a 45° crack travels from the backface to the frontface.

Comparing the computational results for the carbon-fiber laminate and glass-fiber laminate shows that the glass-fiber composite plate experiences significantly greater out-of-plane deflection for similar applied impulse. Since the tensile stresses created in a bending plate are strongly dependent on out-of-plane deflection, the glass-fiber laminate primarily undergoes damage and cracking at the midsection. Additionally, interlaminar damage, fracture, and separation are restricted to the region close to the center of the plate. Figure 13 shows the experimental and computational out-of-plane deflection histories for carbon-fiber/epoxy laminates with different layups. The quasi-isotropic laminate experiences the least deflection, followed by the biaxial laminate, laminate with fibers oriented perpendicular to supports, and parallel to supports, in that order. Initially, the rate of deformation for all plates is similar but as the deformation progresses. As

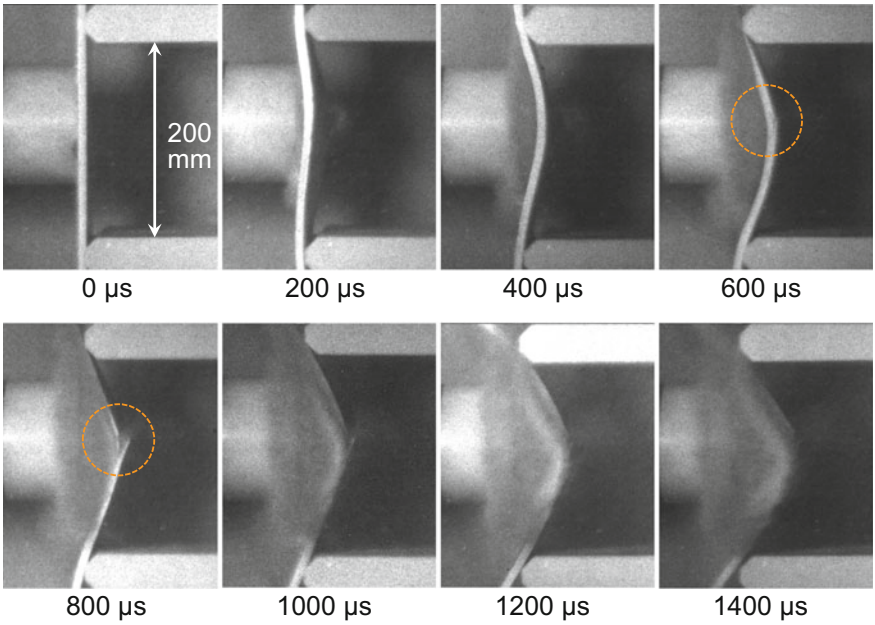

Fig. 10 Sequence of high-speed photographs showing the deformation in a monolithic glass-fiber/epoxy composite laminate with a biaxial layup subjected to $\bar{I} = 0.16$

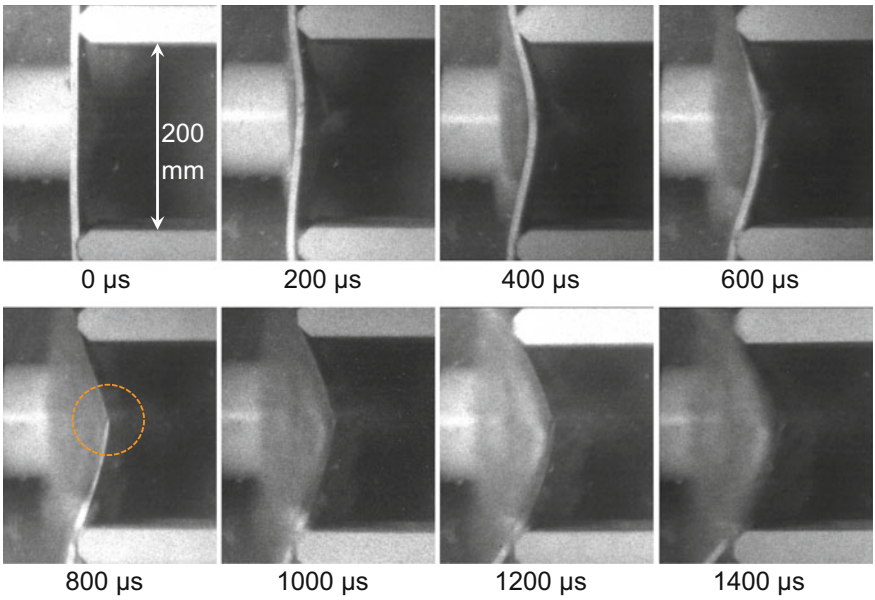

Fig. 11 Sequence of high-speed photographs showing the deformation in a monolithic glass-fiber/epoxy composite laminate with a quasi-isotropic layup subjected to $\bar{I} = 0.16$

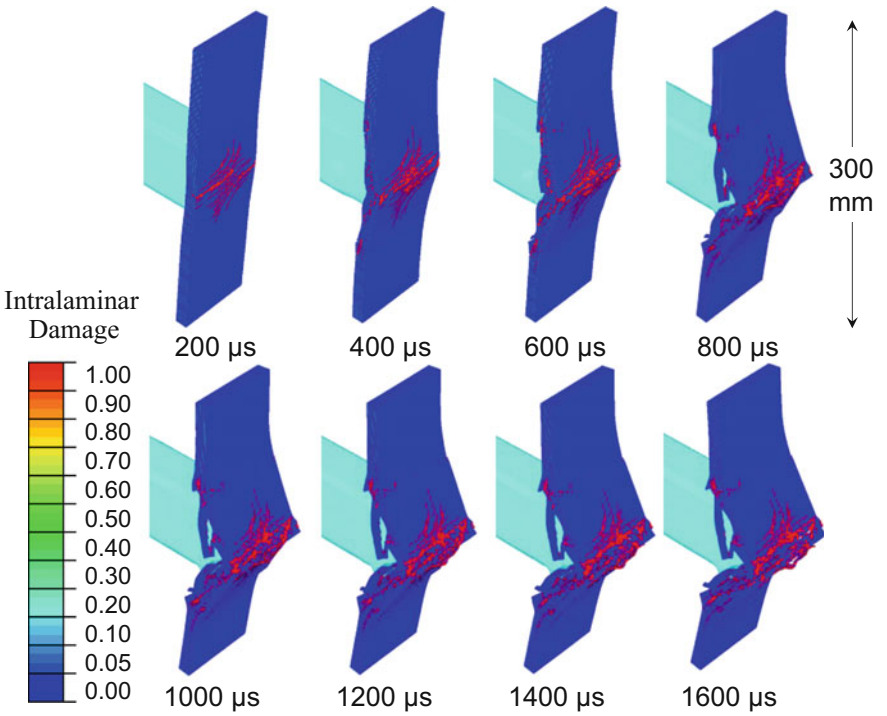

Fig. 12 Distributions of in-ply damage in a quasi-isotropic glass-fiber/epoxy composite laminate subjected to $\bar{I} = 0.20$

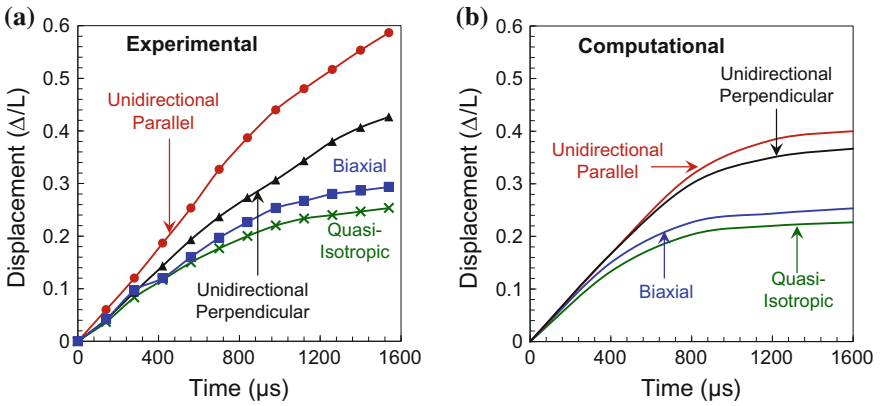

Fig. 13 Experimentally measured and numerically calculated midpoint displacements as functions of time for carbon-fiber/epoxy laminates to similar incident impulsive loads

deformation progresses, the quasi-isotropic and biaxial laminates experience a reduction in the rate of bending at $t = 800$ μs.

Laminates with fibers oriented parallel to the supports exhibit the least blast resistance, due to their inability to transmit the incident impulse to the supports and mitigate the effects of incident impulsive loads. The laminate with fibers oriented parallel to the supports undergoes the greatest deflection, with a normalized deflection ($\Delta/\Delta L$) of 0.6. The laminate with fibers oriented perpendicular to supports undergoes 60%, the biaxial plate undergoes 50%, and the quasi-isotropic plate experiences 40% of the deflection experienced by the laminate with fibers oriented parallel to the supports. The computational model accounts for the essential aspects of deformation but the continuum damage framework underestimates the stiffness of the plate resulting in artificial softening which leads to a lower rate of deformation post-failure in comparison to the experiments. However, the model accurately captures the relative blast resistance of each composite laminate.

3.2 *Out-of-Plane Deflection*

The out-of-plane deflection histories of glass-fiber/epoxy laminates with different fiber layups are shown in Fig. 14. Glass-fibers are inherently more compliant, possessing approximately 30% of the stiffness and strength of carbon-fibers despite being 20% heavier by weight. This is reflected in the deflection of the glass-fiber/epoxy plates which show a clear softening behavior under water-based impulsive loading. The quasi-isotropic laminate experiences the least deflection, with a normalized deflection ($\Delta/\Delta L$) of 0.35 with the biaxial plate experiencing 10% more deflection, the plate with fibers oriented parallel to supports experiencing 20% more deflection, and fiber oriented perpendicular to supports experiencing 40%

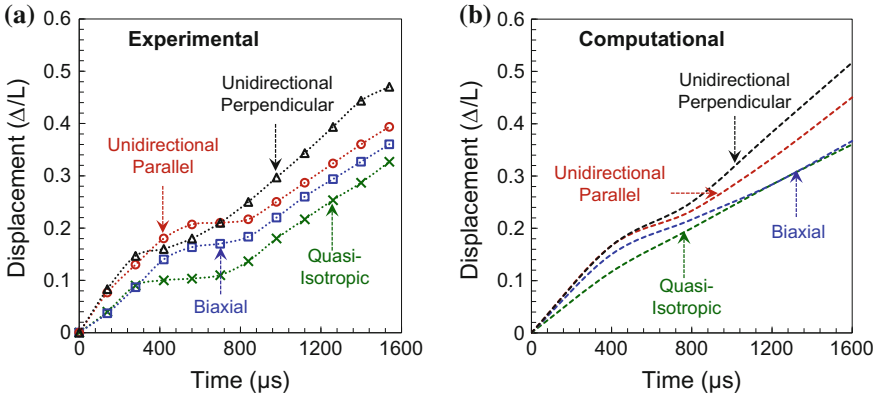

Fig. 14 Experimentally measured and numerically calculated midpoint displacements as functions of time for glass-fiber/epoxy laminates to similar incident impulsive loads

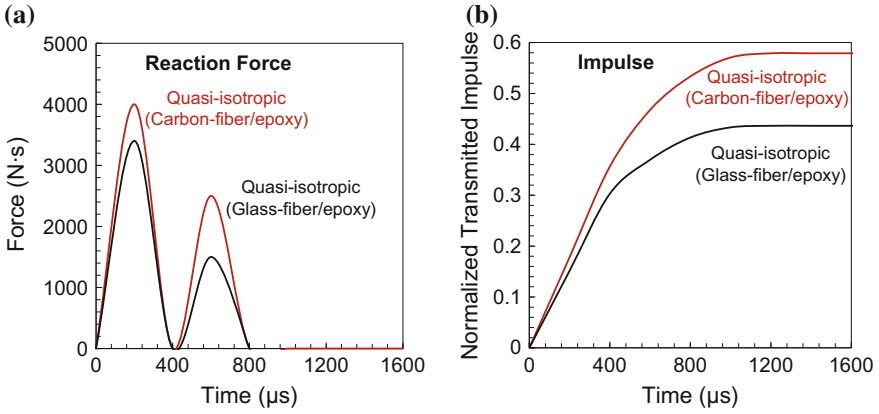

Fig. 15 Calculated reaction forces and transmitted impulses as functions of time for carbon-fiber/epoxy and glass-fiber/epoxy laminates subjected to similar incident impulsive loads

more deflection. The rate of impulse transmission and the magnitude of the transmitted impulse can provide valuable insight into the blast resistance and performance of composite structures. Figure 15a shows the reaction forces measured at the supports in finite element simulations while Fig. 15b shows the corresponding impulses calculated using $I = \int F \cdot dt$.

The Hashin damage model used in this computational approach consists of damage modes that encompass tensile matrix cracking, compressive matrix cracking, tensile fiber cracking, and compressive matrix cracking. Since cracking initiates due to high tensile stresses caused by bending, the intralaminar damage considered for the purposes of damage quantification is the tensile damage occurring in the matrix and fibers. A cohesive zone model is used to evaluate interlaminar cracking. Evaluating the rate and extent of damage can provide a deeper insight into the performance of each composite plate. In order to evaluate the total damage in impulsively loaded composite structures, we use a cumulative damage term called "accumulated damage" defined by $\bar{N}$ = Number of Failed Elements/Total Number of Elements.

Figure 16a shows the ratio of the number of elements undergoing intralaminar damage and the total number of elements described by the Hashin damage model as a function of time for quasi-isotropic carbon-fiber/epoxy and glass-fiber/epoxy laminates subjected to $\bar{I} = 0.20$. The glass-fiber/epoxy specimen experiences damage in ~40% of the laminate while the carbon-fiber/epoxy specimen experiences damage in ~10% of the laminate. Figure 16b shows the ratio of the number of elements undergoing interlaminar damage and the total number of cohesive elements as a function of time for quasi-isotropic carbon-fiber/epoxy and glass-fiber/epoxy laminates subjected to $\bar{I} = 0.20$. The glass-fiber/epoxy specimen experiences damage in ~60% of the interlaminar "resin-rich" regions while the carbon-fiber/epoxy specimen experiences damage in ~10% of the interlaminar regions.

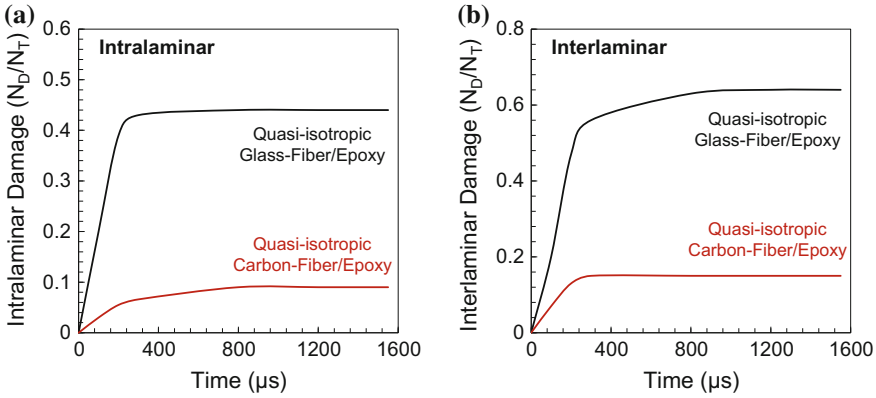

Fig. 16 Calculated reaction forces and transmitted impulses as functions of time for carbon-fiber/epoxy and glass-fiber/epoxy laminates subjected to similar incident impulsive loads

3.3 Implosion of Cylindrical Structures

The implosion of composite cylindrical shells in underwater blasts is a process in which a structure collapses inward onto itself and releases energy via outwardly radiating pressure pulses.

Experimentally, the USLS is used to characterize the dynamic deformations and damage response of composite tubes as a function of different core densities subjected to high-intensity underwater impulsive loads [47–49]. Figure 17 shows high-speed photographs of a monolithic composite cylinder subjected to an underwater impulsive load corresponding to a projectile velocity of 50 m/s. The high-speed photographs capture the deformation and warping in the composite cylinder. Visual inspection of posttest specimens reveals that four types of damage modes are observed in both monolithic and sandwich structures: (1) delamination, (2) matrix cracking and fiber rupture, (3) structural warping, and (4) core compression and partial recovery. Results showed that the transmitted impulse and overall damage increase as the core density increases. The fiber orientation of face sheets and the size of the cylinder affect the deflection and warping in the region subjected to impulsive loading. Overall, the monolithic structure showed more severe internal damage and warping comparing to the filament wound structure, and the sandwich structure has superior resistance to damage compared with the monolithic composite structure.

Numerically, the CEL framework is employed to finite element models to characterize the dynamic deformation and damage response of structures subjected to combined loads of hydrostatic pressure and high-intensity explosive loading. The primary driving force for implosion is the difference between higher external water pressure and lower internal air pressure.

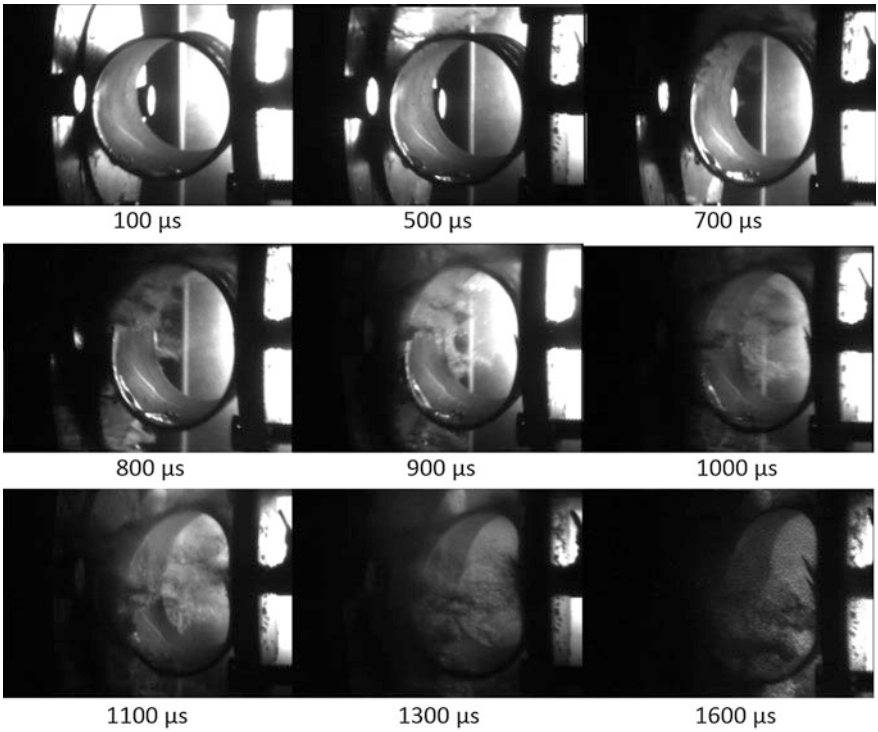

Fig. 17 High-speed photographs of a monolithic composite structure subjected to an impulsive load generated by a projectile velocity of $V_0 = 50$ m/s

Hydrostatically induced implosion is caused by quasi-static pressurization to the critical buckling pressure of a structure. Under purely hydrostatic loading, the composite cylindrical structure tends to buckle and implode in a symmetric fashion into one of several possible mode shapes, as shown in Fig. 18a. The mode shapes are determined through a linear buckling analysis conducted on carbon/epoxy composite tubes subjected to a uniform external pressure [50]. The buckling mode and the critical collapse pressure are affected by the length, diameter, and shell thickness of the cylinder, as well as material properties. Typically, cylinders with large length-to-diameter ratios (L/D) collapse in mode 2, while those with lower L/D ratios collapse in mode 3 or 4, as shown in Fig. 18b. However, it was observed in experiments that deformation of a composite cylinder with large L/D ratios initiates in a higher order shape early in an implosion event [51].

When hydrostatic loading is combined with UNDEX, the implosion process becomes more complex. Impulses with short pulse durations or low peak pressures not capable of causing collapse can excite vibrations and lead to local imperfections in the structure. Implosion can be triggered by subsequent bubble pulses or via further exposure to subcritical loading due to damage or resonance. Structures experiencing explosive-induced implosion tend to exhibit asymmetric collapse

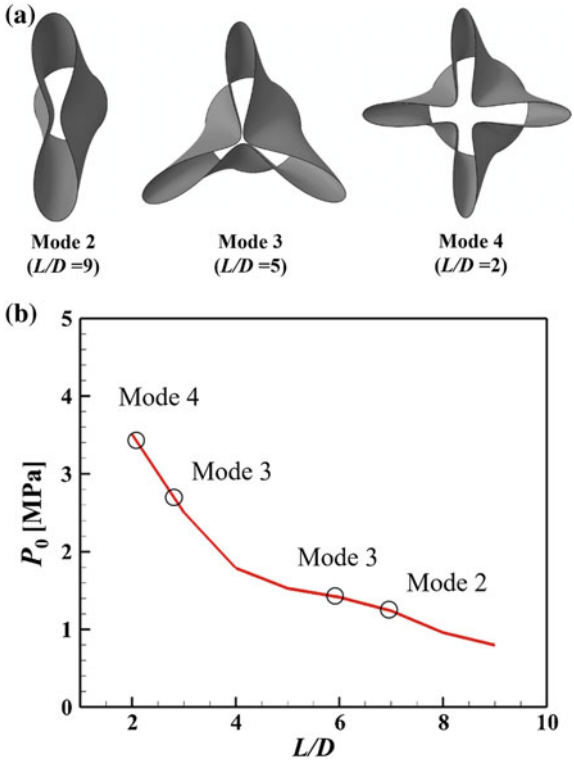

Fig. 18 **a** High-speed photographs of a monolithic composite structure subjected to an impulsive load generated by a projectile velocity of $V_0 = 50$ m/s, **b** the plot of the critical collapse pressure as a function of L/D ratios of cylindrical structures

modes. The dynamic deformation and damage response depend on many factors, including initial shock, hydrostatic pressure, orientation of the structure relative to the explosive source, loading time (damage accumulation), as well as factors such as the constitutive behavior of materials. In the CEL framework, the cylinder is located within an Eulerian domain where a blast wave is generated as shown in Fig. 19a. In relation to the latest experimental work on explosive-induced implosion of composite tubes [52], the composite specimen has a [±15°/0°/±45°/±15°] layup with a 380 mm length, 60 mm inner diameter and 1.5 mm wall thickness. The specimen is sealed with two aluminum end caps. Boundary conditions are applied at one of the end caps to prevent translation in all directions and rotations around all three axes. Translation in the axial direction is allowed at the other end. To study the effects of initial hydrostatic pressure, the initial stress state of the structure is first established in a static analysis. Then the static state is imported as the initial condition into the dynamic analysis [50–53], where FSI are modeled though general Eulerian–Lagrangian contact to allow the Eulerian domain (water) interacting with the Lagrangian domain (cylindrical structure). Simulations are carried out with various combinations of hydrostatic and explosive loading.

In the CEL framework, a high-pressure, exponentially decaying impulse is generated by a specified exponentially decaying v(t), defined in Eq. (10.7), at the

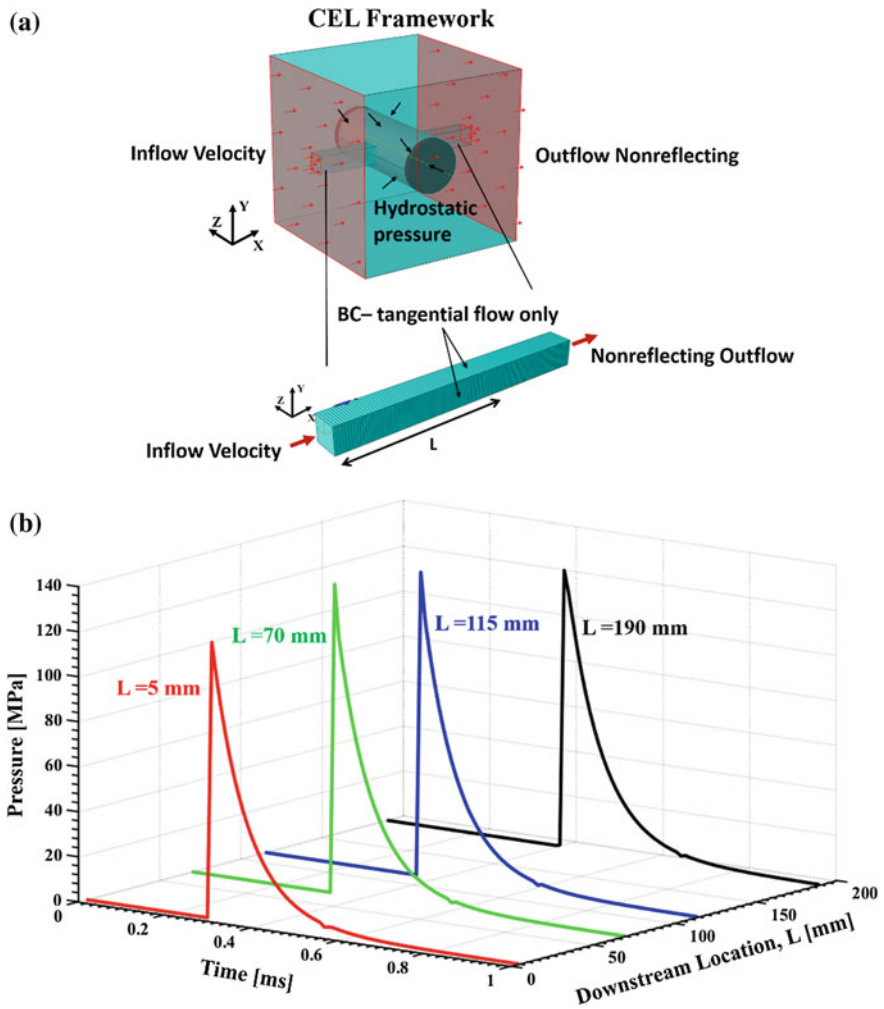

Fig. 19 **a** Schematic illustration showing the CEL framework for studying the explosive-induced implosion event, **b** output pressure histories at different downstream locations within the Eulerian domain

Eulerian inflow boundary and the pressure profile p(t) is measured at some distance L downstream [54, 55],

$$v(t) = v_0 + v_p \exp[-(t - t_0)/t_d]. \tag{4}$$

Here, v_0 is the initial particle velocity, v_p is the peak particle velocity, t_0 defines the start time, and t_d defines the duration of the exponentially decaying in the velocity profile. A one-dimensional Eulerian model is used to quantify blast waves

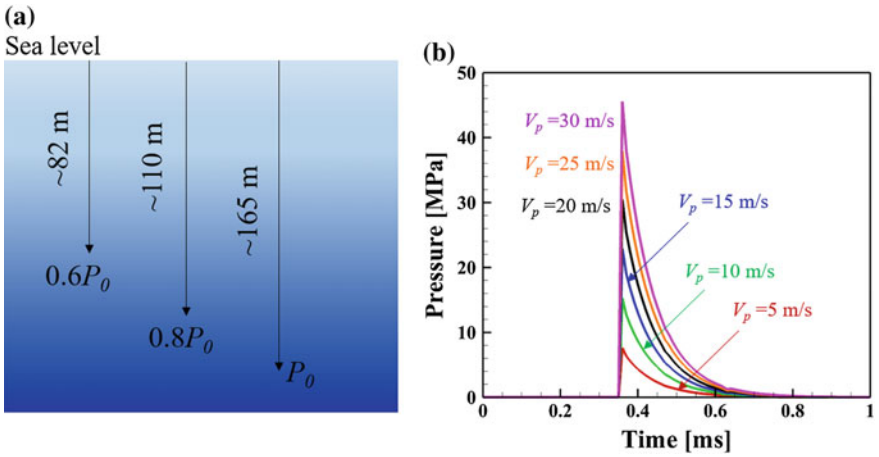

Fig. 20 **a** Schematic illustration showing the different hydrostatic pressure applied to the structure corresponding to different depths under sea level with $P_0 = 1.39$ MPa, **b** different impulsive loads, $\bar{I} = 0.0016, 0.0032, 0.0048, 0.0064, 0.0080, 0.0096$, applied to the structure corresponding to different input velocities

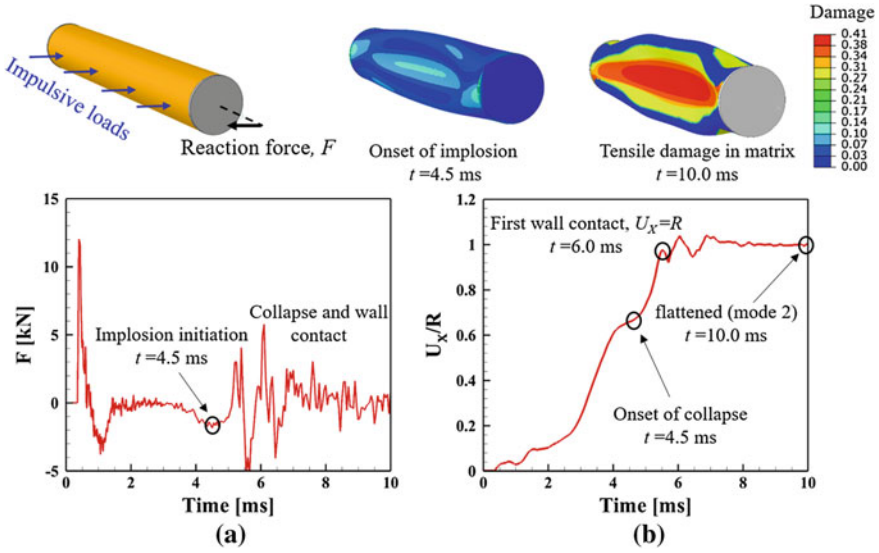

Fig. 21 **a** Reaction force and **b** deflection of the structure when loaded with $P = P_0, \bar{I} = 0.0016$

as shown in Fig. 19a. The front face of the model (inflow face) is prescribed a chosen particle velocity *v(t)*. This flow field simulates the effects of the incident blast wave on the specimen, as shown in Fig. 19b. Zero displacement boundary conditions are applied on the sides of the model to restrict flow normal to the walls

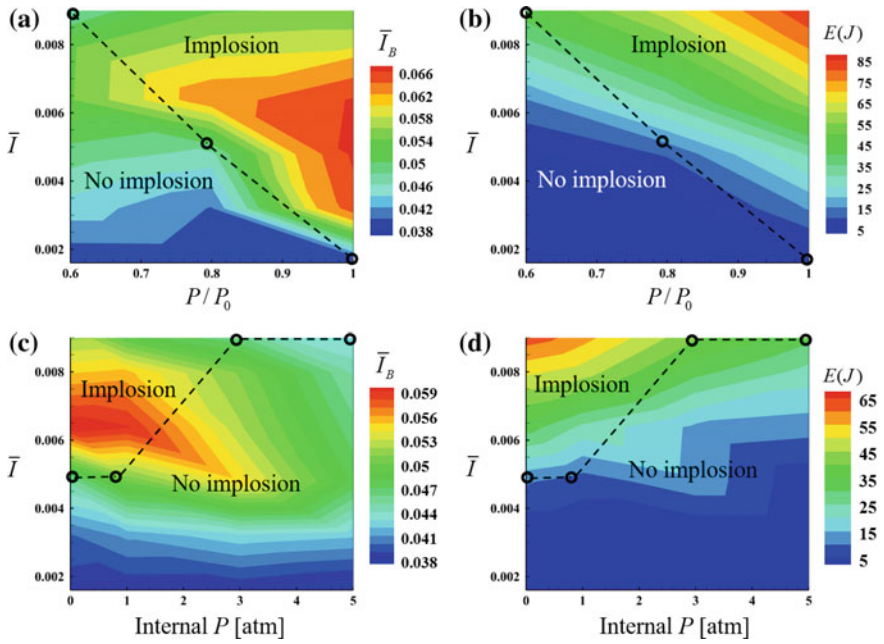

Fig. 22 **a** Transmitted impulse and **b** energy dissipation due to damage of the structure when loaded with different combinations of impulsive load intensity $\bar{I}$, initial hydrostatic pressure P ($0.6P_0$, $0.8P_0$, P_0), and internal $P_i = 0$. **c** Transmitted impulse and **d** energy dissipation due to damage of the structure when loaded with different combinations of impulsive load intensity $\bar{I}$, initial hydrostatic pressure $P = 0.8P_0$ and internal P_i(0, 1, 3, 5) atm

but allow tangential flow. Nonreflecting flow is defined at the Eulerian outflow boundary of the model.

Explosive-induced implosion is affected by factors such as initial shock, hydrostatic pressure, bubble pulse, and material properties [50–52, 56]. To mimic the effects of different stand-off distances of the explosives at sources, impulsive loading of different intensities is applied to the structure, as shown in Fig. 20. To mimic the effects of different depths where the structure is working under the sea level, uniform pressure of different magnitudes based on the critical collapse pressure (P_0) of the structure is applied to the cylinder surface, as shown in Fig. 20. Cylindrical structures with different levels of internal pressure (P_i), i.e., 0, 1, 3, and 5 atm, are imported to dynamic simulations to investigate the effect of initial internal pressurization on the structural performance.

Numerically measured reaction force combined with the deflection of the structure as a function of time is used to locate the onset of the implosion event. The negative force represents a change in load bearing capacity of the structure which corresponds to the initiation of implosion. The subsequent variations in the reaction force correspond to the deceleration of water when the deflection of the structure reaches the maximum, as shown in Fig. 21. Structures undergo asymmetric collapse

with higher mode numbers initiated by the impulsive loading and tend to settle to a mode 2 shape in all cases. The severe tensile matrix failure is the main damage mechanism, as shown in Fig. 21.

The performance of structures when loaded with different combinations of impulsive load intensity $\bar{I}$, initial hydrostatic pressure P, and internal P_i is measured as the transmitted impulse $\bar{I}_B = 0.0016 = \frac{I_B}{I_0} = \frac{\int \frac{F}{A} \cdot dt}{I_0}$ and the energy dissipated due to damage. Results of are summarized in Fig. 22. The loading threshold where the implosion event initiated is determined from the numerical results. The impulsive loading dominates the structural performance. Higher impulsive load intensity leads to larger transmitted impulse and higher damage dissipation energy. Initial internal pressurization of the structure significantly enhances the damage resistance of structures. However, the enhancement diminishes as the internal pressure further increases.

4 Concluding Remarks

Marine structures must balance stiffness and load-carrying capacity with the ability to minimize impulse transmission for high blast and impact resistance. Composite structures have higher stiffness and strength-to-weight ratios compared to metallic structures. Additionally, thick composite laminates provide very high bending and shear resistances with relatively small increases in total mass. However, due to the novelty and wide range of structural combinations, the relationships between structural responses and material heterogeneity in composite structures are not well quantified. In particular, the behavior of composite structures under extreme impulsive loading generated by underwater explosions needs to be systematically analyzed. This research has been carried out to address this need.

The composite structures consist of both carbon-fiber and glass-fiber reinforced epoxy resin, and are manufactured by curing commercially available prepregs. The composites consist of 34% epoxy by weight, with the rest containing fibers. Four different composite layups are analyzed: (1) biaxial; (2) quasi-isotropic; (3) unidirectional with fibers oriented parallel to supports; and (4) unidirectional with fibers oriented perpendicular to supports. It should be emphasized that the composite panels studied have quite similar in overall mass and thickness to enable comparison of performance. The combined experimental and computational research reported here focuses on the quantification of the water blast response of fiber-reinforced epoxy laminates with different material properties and layups. It is found that $\bar{I} = 0.16$ (peak pressure 196 MPa), causes failure of all structures analyzed. A three-dimensional computational framework which employs a Coupled Eulerian–Lagrangian (CEL) approach is used in conjunction with the experiments to capture the effects of underwater blasts and fluid–structure interactions (FSI). The calculations offer details of the deformation event and damage mechanisms not obtainable through experiments at this time.

Comparison of experiments and simulations shows that numerical calculations provide a reasonable representation of damage and dissipation mechanisms in the composite laminates. The finite element model captures the essential deformation mechanisms observed in both carbon-fiber and glass-fiber/epoxy laminates. Specifically, the following are replicated with reasonable accuracy: fluid−structure interaction effects at the water–structure interface, effects of fiber orientation, in-ply matrix and fiber cracking and rupture, and inter-ply delamination initiation and evolution. The Hashin damage model overestimates the softening effect resulting from cracking and fracture leading to a slight underestimation of backface deflection.

The unidirectional layups experience splitting due to a lack of stability in the transverse direction, while the bi-axial layups undergo failure near the loading circumference in close proximity to the impulsively loaded region. Quasi-isotropic layups provide the highest blast resistance for both the carbon-fiber and glass-fiber epoxy laminates. Additionally, the quasi-isotropic carbon-fiber/epoxy laminates experience 70% of the deflection experienced by glass-fiber/epoxy laminates. Since carbon-fiber laminates are nearly four times stiffer than glass-fiber laminates, it is expected that these laminates will transfer higher impulses due to more efficient load spreading. The impulse transmitted by the carbon-fiber laminates is ∼130% of that transmitted by glass-fiber laminates, which is relatively modest increase in comparison to superior deflection resistance and reduced in-ply as well as inter-ply damage. In terms of accumulated damage, the carbon-fiber laminates experience 25% of the damage experienced by glass-fiber laminates.

The dynamic deformation and damage response of composite cylinders during an explosive-induced implosion event is affected by many factors, such as initial shock, hydrostatic pressure, damage accumulation as well as material properties. Numerical approaches such as CEL-based finite element models are designed to allow exploration of design scenarios involving simultaneously varying loading, material, geometric, and size variables. The results obtained so far provide design recommendations for reducing the severity of implosion. Measures include internal pressurization and tailoring of fiber orientation of facesheets. For similar total mass, sandwich composites with rate-dependent cores as the energy absorbing material are shown to provide superior blast mitigation as compared with monolithic composite structures. Loading–structure–performance maps are developed, accounting for different combinations of impulsive load intensity, initial hydrostatic pressure, and internal pressure.

Acknowledgements The authors gratefully acknowledge support by the Office of Naval Research through grant numbers N00014-09-1-0808 and N00014-09-1-0618 (program manager: Dr. Yapa D. S. Rajapakse). Calculations were carried out on computers in the DOD High Performance Computing Modernization Program (HPCMP) and on the Athena HPC cluster in the Dynamic Properties Research Laboratory (DPRL) at Georgia Tech. MZ also acknowledges beneficial interactions through the CAS/SAFEA International Partnership Program for Creative Research Teams.

References

1. Minnaar, K., & Zhou, M. (2004). A novel technique for time-resolved detection and tracking of interfacial and matrix fracture in layered materials. *Journal of the Mechanics and Physics of Solids, 52*(12), 2771–2799.
2. Cantwell, W. J., & Morton, J. (1991). The impact resistance of composite-materials—a review. *Composites, 22*(5), 347–362.
3. Hashin, Z. (1986). Analysis of stiffness reduction of cracked cross-ply laminates. *Engineering Fracture Mechanics, 25*(5–6), 771–778.
4. Hashin, Z. (1987). Analysis of orthogonally cracked laminates under tension. *Journal of Applied Mechanics-Transactions of the Asme, 54*(4), 872–879.
5. Chang, F. K., Choi, H. Y., & Jeng, S. T. (1990). Study on impact damage in laminated composites. *Mechanics of Materials, 10*(1–2), 83–95.
6. Chang, F. K., Choi, H. Y., & Jeng, S. T. (1990). Characterization of impact damage in laminated composites. *Sampe Journal, 26*(1), 18–25.
7. Lessard, L. B., & Chang, F. K. (1991). Damage Tolerance of laminated composites containing an open hole and subjected to compressive loadings: Part 2—experiment. *Journal of Composite Materials, 25*(1), 44–64.
8. Battley, M., & Allen, T. (2012). Servo-hydraulic system for controlled velocity water impact of marine sandwich panels. *Experimental Mechanics, 52*(1), 95–106.
9. Battley, M., et al. (2005). Dynamic characterisation of marine sandwich structures. *Sandwich structures 7: Advancing with sandwich structures and materials* (pp. 537–546).
10. Espinosa, H. D., Lee, S., & Moldovan, N. (2006). A novel fluid structure interaction experiment to investigate deformation of structural elements subjected to impulsive loading. *Experimental Mechanics, 46*(6), 805–824.
11. Latourte, F., et al. (2011). Failure mechanisms in composite panels subjected to underwater impulsive loads. *Journal of the Mechanics and Physics of Solids, 59*(8), 1623–1646.
12. Wei, X. D., et al. (2013). A new rate-dependent unidirectional composite model—Application to panels subjected to underwater blast. *Journal of the Mechanics and Physics of Solids, 61*(6), 1305–1318.
13. Avachat, S., & Zhou, M. (2015). High-speed digital imaging and computational modeling of dynamic failure in composite structures subjected to underwater impulsive loads. *International Journal of Impact Engineering, 77,* 147–165.
14. Tekalur, S. A., Bogdanovich, A. E., & Shukla, A. (2009). Shock loading response of sandwich panels with 3-D woven E-glass composite skins and stitched foam core. *Composites Science and Technology, 69*(6), 736–753.
15. Tekalur, S. A., Shukla, A., & Shivakumar, K. (2008). Blast resistance of polyurea based layered composite materials. *Composite Structures, 84*(3), 271–281.
16. LeBlanc, J., et al. (2007). Shock loading of three-dimensional woven composite materials. *Composite Structures, 79*(3), 344–355.
17. Grogan, J., et al. (2007). Ballistic resistance of 2D and 3D woven sandwich composites. *Journal of Sandwich Structures and Materials, 9*(3), 283–302.
18. Wang, E. H., Gardner, N., & Shukla, A. (2009). The blast resistance of sandwich composites with stepwise graded cores. *International Journal of Solids and Structures, 46*(18–19), 3492–3502.
19. Avachat, S., & Zhou, M. (2011). Effect of facesheet thickness on dynamic response of composite sandwich plates to underwater impulsive loading. *Experimental Mechanics, 52*(1), 83–93.
20. Avachat, S., & Zhou, M. (2011). Dynamic response of composite sandwich structures subjected to underwater impulsive loads: Experiments and simulations. In Ferreira, A. J. M., (Ed.), *Conference Proceedings of the 16th International Conference on Composite Structures, ICCS-16.* FEUP, Porto.

21. Avachat, S., & Zhou, M. (2010). Dynamic response of submerged composite sandwich structures to blast loading. In Shukla, A. (Ed.), *Proceedings of the IMPLAST 2010—SEM Fall Conference*, October 12–14 2010 Providence. Rhode Island, USA.
22. Wei, X. D., et al. (2013). Three-dimensional numerical modeling of composite panels subjected to underwater blast. *Journal of the Mechanics and Physics of Solids, 61*(6), 1319–1336.
23. Kambouchev, N., Radovitzky, R., & Noels, L. (2007). Fluid-structure interaction effects in the dynamic response of free-standing plates to uniform shock loading. *Journal of Applied Mechanics-Transactions of the Asme, 74*(5), 1042–1045.
24. Hutchinson, J. W. (2009). Energy and momentum transfer in air shocks. *Journal of Applied Mechanics-Transactions of the Asme, 76*(5).
25. Avachat, S., & Zhou, M. (2016). High-speed digital imaging and computational modeling of hybrid metal-composite plates subjected to water-based impulsive loading. *Experimental Mechanics, 56*(4), 545–567.
26. Swisdak, M. M. (1978). Explosion effects and properties: Part II—explosion effects in water. *Technical Report.* Dahlgren, Virginia, USA: Naval Surface Weapons Center.
27. Taylor, G. I. (1941). The pressure and impulse of submarine explosion waves on plates. *The scientific papers of G I Taylor* (Vol. III, pp. 287–303). Cambridge: Cambridge University Press.
28. Arora, H., et al. (2014). Compressive strength after blast of sandwich composite materials. *Philosophical Transactions of the Royal Society a-Mathematical Physical and Engineering Sciences, 372*(2015).
29. Arora, H., Hooper, P. A., & Dear, J. P. (2012). The effects of air and underwater blast on composite sandwich panels and tubular laminate structures. *Experimental Mechanics, 52*(1), 59–81.
30. Hashin, Z. (1980). Failure criteria for unidirectional fiber composites. *Journal of Applied Mechanics-Transactions of the Asme, 47*(2), 329–334.
31. Puck, A., & Schürmann, H. (1999). Failure analysis of FRP laminates by means of physically based phenomenological models. *Composites Science and Technology, 62*(12–13), September–October, 2002, 1633–1662.
32. Schubel, P. M., Luo, J. J., & Daniel, I. M. (2005). Low velocity impact behavior of composite sandwich panels. *Composites Part A—Applied Science and Manufacturing, 36*(10), 1389–1396.
33. Kiel, A. H. (1961). *The response of ships to underwater explosions.* Department of the Navy.
34. Chan, S., et al. (2007). Ballistic limit prediction using a numerical model with progressive damage capability. *Composite Structures, 77*(4), 466–474.
35. Pinho, S. T., Robinson, P., & Iannucci, L. (2006). Fracture toughness of the tensile and compressive fibre failure modes in laminated composites. *Composites Science and Technology, 66*(13), 2069–2079.
36. Lapczyk, I., & Hurtado, J. A. (2007). Progressive damage modeling in fiber-reinforced materials. *Composites Part A—Applied Science and Manufacturing, 38*(11), 2333–2341.
37. Needleman, A. (1990). An analysis of tensile decohesion along an interface. *Journal of the Mechanics and Physics of Solids, 38*(3), 289–324.
38. Tvergaard, V., & Hutchinson, J. W. (1992). The relation between crack-growth resistance and fracture process parameters in elastic plastic solids. *Journal of the Mechanics and Physics of Solids, 40*(6), 1377–1397.
39. Tvergaard, V., & Needleman, A. (1992). Effect of crack meandering on dynamic, ductile fracture. *Journal of the Mechanics and Physics of Solids, 40*(2), 447–471.
40. Needleman, A., & Tvergaard, V. (1994). Mesh effects in the analysis of dynamic ductile crack-growth. *Engineering Fracture Mechanics, 47*(1), 75–91.
41. Xu, X. P., & Needleman, A. (1994). Numerical simulations of fast crack-growth in brittle solids. *Journal of the Mechanics and Physics of Solids, 42*(9), 1397.
42. Camacho, G. T., & Ortiz, M. (1996). Computational modelling of impact damage in brittle materials. *International Journal of Solids and Structures, 33*(20–22), 2899–2938.

43. Espinosa, H. D., Zavattieri, P. D., & Dwivedi, S. K. (1998). *A finite deformation continuum discrete model for the description of fragmentation and damage in brittle materials*. Pergamon-Elsevier Science Ltd.
44. Camanho, P. P., Davila, C. G., & de Moura, M. F. (2003). Numerical simulation of mixed-mode progressive delamination in composite materials. *Journal of Composite Materials, 37*(16), 1415–1438.
45. Minnaar, K., & Zhou, M. (2002). Characterization of impact in composite laminates. *AIP Conference Proceedings, 620*(1), 1208.
46. Zhai, J., & Zhou, M. (2000). Finite element analysis of micromechanical failure modes in a heterogeneous ceramic material system. *International Journal of Fracture, 101*(1–2), 161–180.
47. Qu, T., Avachat, S., & Zhou, M. (2017). Response of cylindrical composite structures subjected to underwater impulsive loading: Experimentations and computations. *Journal of Engineering Materials and Technology, 139*(2), 021020.
48. Avachat, S., & Zhou, M. (2013). *Response of Cylindrical Composite Structures to Underwater Impulsive Loading*.
49. Qu, T., & Zhou, M. (2017). Implosion of composite cylinders due to underwater impulsive loads. In Lopresto, V., Antonio, L., Serge, A. (Ed.) *Dynamic response and failure of composite materials and structures.* Woodhead Publishing.
50. Pinto, M., Gupta, S., & Shukla, A. (2015). Study of implosion of carbon/epoxy composite hollow cylinders using 3-D digital image correlation. *Composite Structures, 119,* 272–286.
51. Pinto, M., & Shukla, A. (2015). Dynamic collapse mode evolution in carbon composite tubes. *Extreme Mechanics Letters, 3,* 55–58.
52. Pinto, M., & Shukla, A. (2016). Shock-initiated buckling of carbon/epoxy composite tubes at sub-critical pressures. *Experimental Mechanics, 56*(4), 583–594.
53. Yin, C., et al. (2016). Shock mitigation effects of cellular cladding on submersible hull subjected to deep underwater explosion. *Ocean Engineering, 117,* 221–237.
54. Chen, A., Louca, L. A., & Elghazouli, A. Y. (2015). Blast assessment of steel switch boxes under detonation loading scenarios. *International Journal of Impact Engineering, 78,* 51–63.
55. Chen, A., Louca, L. A., & Elghazouli, A. Y. (2016). Behaviour of cylindrical steel drums under blast loading conditions. *International Journal of Impact Engineering, 88,* 39–53.
56. Gish, L. (2015). Designing implodable underwater systems to minimize implosion pulse severity. In *OCEANS'15 MTS/IEEE.* Washington: IEEE.